Characterisation of very thin epitaxial layers by high resolution x-ray diffraction

Miles, Simon Jonathon

Characterisation of Very Thin Epitaxial Layers by High Resolution X-ray Diffraction

by

Simon Jonathon Miles
B.Sc. (Dunelm)

Being a thesis submitted for the degree of
Doctor of Philosophy
of
The University of Durham
September 1989

Abstract

X-rays can be used as a sensitive, non-destructive probe for the characterisation of semiconductors. The energy and wavelength of X-rays is such that structural information down to the Ångstrom level can be yielded with a depth penetration of several microns. As a result X-rays are ideally suited to the study of thin layer semiconductors. Double crystal diffractometry in particular is widely used throughout industry for the characterisation of heteroepitaxial layers. As epitaxial growth techniques become more sophisticated the demand for more detailed structural information becomes even greater. In particular, the trend towards thinner and thinner layers in optoelectronic devices means that conventional characterisation methods are often lacking in sensitivity. This thesis concentrates on the development of new techniques used in the study of ultra thin epitaxial layers.

Skew beam paths have been utilised to provide enhanced sensitivity to thin surface layers. By choosing a suitable asymmetric reflection and rotating the sample through the reflection plane normal it is possible to tune the angle of incidence to that required. Experiments performed on a single epilayer yielded a fourfold increase in intensity of the layer diffraction effects compared to a conventional grazing incidence asymmetric reflection.

Two layer structures have been characterised using Pendellösung fringes. Although a conventional technique it has only recently been realised that errors may result in layer thickness determination due to direct measurement of fringe spacing from the rocking curve. Fourier Analysis has been used to accurately determine layer thickness and the conditions necessary for its use have been fully

investigated. By evaluating layer thickness in this fashion the process of matching theoretical rocking curves with those produced in experiment becomes more straightforward and close fits have been achieved.

X-ray reflectivity is a well established method sensitive to electron density change, although as yet it has had little application in the study of epitaxial layers. Angular reflectivity using both double and triple crystal diffractometers has been used to characterise thin epilayers, and the relative merits of each are discussed. A technique known as energy dispersive reflectivity has also been investigated and found to be an extremely rapid method of determining layer thickness. Theory describing X-ray reflectivity is discussed and a computer program has been written to model the experimental results.

Acknowledgements

Financial support from the Science and Engineering Research Council and British Telecommunications p.l.c through a CASE award is gratefully acknowledged.

I would like to acknowledge the help and assistance from the following people during the course of this work.

Firstly, I would like to thank Professor A. W. Wolfendale for making available the facilities of the Department of Physics at the University of Durham.

I am very grateful to Dr. B. K. Tanner for his supervision of this project and to Mrs. M. A. G. Halliwell and Dr. M. H. Lyons of British Telecom Research Laboratories for many useful discussions. I am also grateful to Mr. S. Cockerton for his help in designing and building the X-ray Laboratory, and to Dr. G. S. Green for his help with the simulation programs.

I would also like to thank Professor R. A. Cowley for his permission to use the triple crystal diffractometer at Edinburgh University and Dr. T. W. Ryan, Dr. P. D. Hatton and Dr. S. Bates for their collaboration. I am grateful to Professor M. Hart of Manchester University for use of diffraction equipment and to Dr. S. Cummings, Dr. D. K. Bowen and Miss L. Hart for assistance in the energy dispersive reflectivity experiments.

Thanks to Dr. E. G. Scott and Dr. P. C. Spurdens of British Telecom for the MBE and MOCVD samples provided and also to Dr. M. C. Petty of Durham University, Dr. C. Stanley of Glasgow University and Dr. T. Krier for allowing me to present results on their samples.

I would also like to thank the technical staff of the Department of Physics, especially Mr. P. Foley, Mr. D. Josling, Mr. T. Jackson, Mr. G. Teasdale, Mr. P. Armstrong and Mrs. P. Russell for their help and advice.

Finally, I would like to thank my parents and Kate for their encouragement and support.

List of Publications

Lucas, C. A., Hatton, P. D., Bates, S., Ryan, T. W., Miles, S. J. and Tanner, B. K. (1988) J. Appl. Phys. **63** 1936.

Bates, S., Hatton, P. D., Lucas, C. A., Ryan, T. W., Miles, S. J. and Tanner, B. K. (1988) Adv. X-ray Anal. **31** 155.

Tanner, B. K., Miles, S. J., Peterson, G. G. and Sacks, R. N. (1988) Mater. Lett. **7**(5) 239.

Miles, S. J., Green, G. S., Tanner, B. K., Halliwell, M. A. G. and Lyons, M. H. (1989) Mat. Res. Soc. Symp. Proc. **138** 539.

Cockerton, S., Miles, S. J., Green, G. S. and Tanner, B. K. (1989) J. Cryst. Growth (in press).

Abbreviations

DCD	Double Crystal Diffractometer/Diffraction
DCR	Double Crystal Reflectivity
FT	Fourier Transform
FWHM	Full Width at Half Maximum
GIABS	Glancing Incidence Asymmetric Bragg Scattering
GIXS	Glancing Incidence X-ray Scattering
LBF	Langmuir-Blodgett Film
LED	Light Emitting Diode
LHS	Left Hand Side
LPE	Liquid Phase Epitaxy
MBE	Molecular Beam Epitaxy
MCA	Multi-Channel Analyser
MOCVD	Metal-Organic Chemical Vapour Deposition
MOVPE	Metal-Organic Vapour Phase Epitaxy
MQW	Multi-Quantum-Well
PL	Photoluminescence
RHS	Right Hand Side
RMS	Root Mean Square
SIMS	Secondary Ion Mass Spectroscopy
SLS	Strained Layer Superlattice
S/N	Signal to Noise

TCD	Triple Crystal Diffractometer/Diffraction
TCR	Triple Crystal Reflectivity
TEM	Transmission Electron Microscopy
VPE	Vapour Phase Epitaxy
SARCA	Skew Asymmetrical Rocking Curve Analysis

Contents

Declaration

I declare that this thesis is original. No part of it has been submitted previously for a degree at any other university. All work shown is my own unless stated otherwise. Work done in collaboration with the Edinburgh, Manchester and Warwick groups is duely acknowledged.

Chapter I

Introduction

1.1 Optical Communications

It was in the 1960's when Kao and Hockham (1961) first proposed the use of optical fibres for communication purposes. Since that time the rapidity with which optical fibre communication systems have been transformed from a novel idea into the present day commercial exploitation on a vast scale, has been primarily due to the great advances made in reducing optical losses in silica fibres, coupled with the rapid development of reliable, long wavelength (1.3-1.6μm) transmitters and detectors. Semiconductor lasers operating at these wavelengths are now integral components of many new optical fibre communication systems. Higher optical power output and superior dynamic response, where very large light intensity changes can be achieved by a relatively small change of current through the device, has resulted in lasers almost completely replacing LED's for some applications. An excellent account of long-wavelength semiconductor lasers including their operation, growth and applications has been given by Agrawal and Dutta (1986) while $GaAs$ technology has been reviewed by Mellor (1987).

Figure 1.1 shows the range of emission wavelengths for various semiconductor lasers. Taken together, these materials cover the optical spectrum from near ultraviolet to far infrared (Bachman and Goslowsky, 1987). The most important criterion in selecting the semiconductor material for a specific heterostructure laser is related to the quality of the heterojunction interface between the two semiconductors of different band gaps. To reduce the formation of lattice defects, the lattice constants of the two materials should match to closer than 0.1%.

Figure 1.2 shows the interrelationship between the band gap E_g, and the lattice constant a, for several ternary and quarternary compounds (Glisson et al., 1978). $In_{1-x}Ga_xAs_yP_{1-y}$ lasers, for example, can cover a wavelength range of 1.1-1.65μm by choosing x and y such that the active layer is lattice-matched

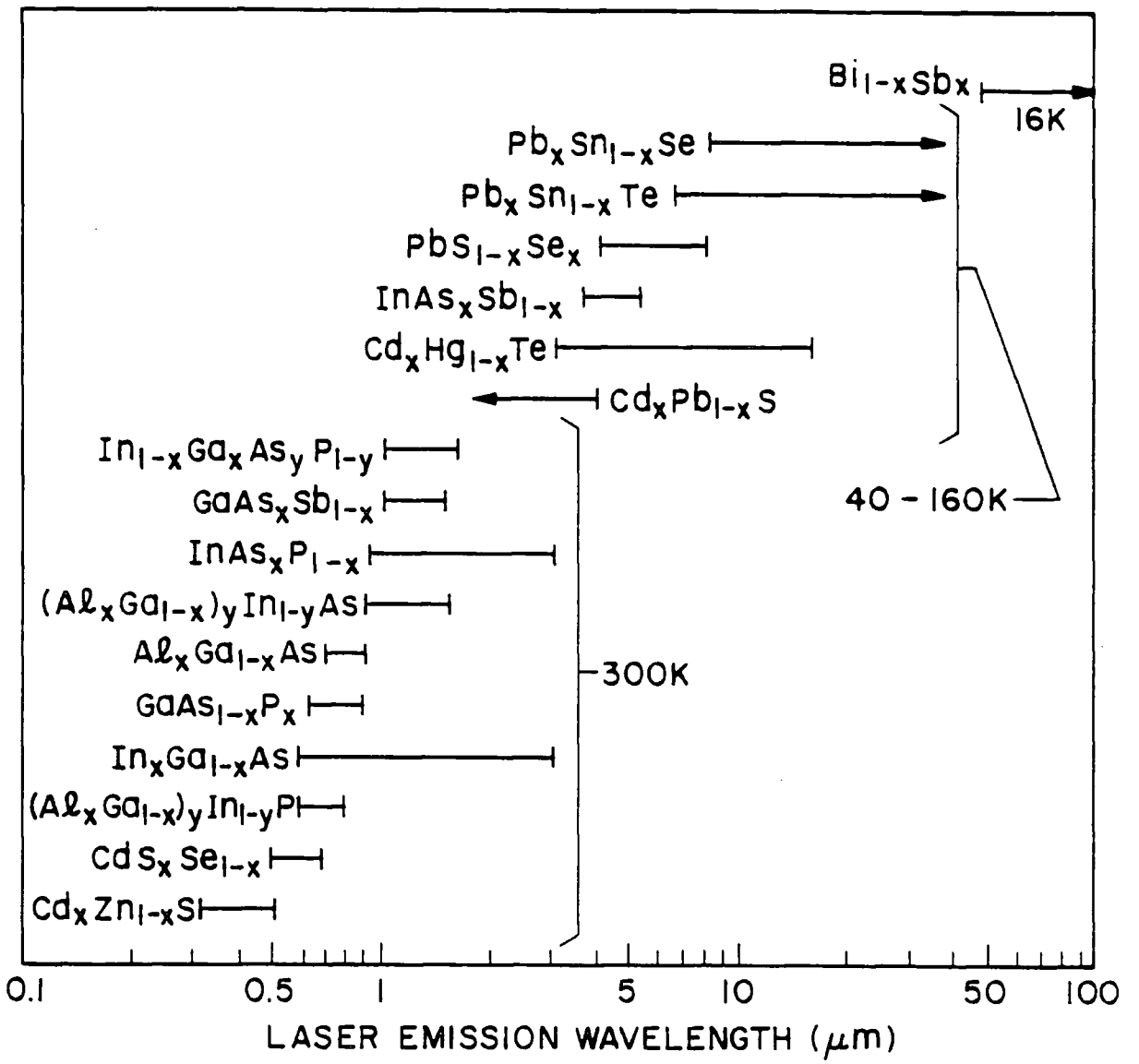

Figure 1.1: Wavelength range of semiconductor lasers covered by different material systems. After Agrawal and Dutta (1986).

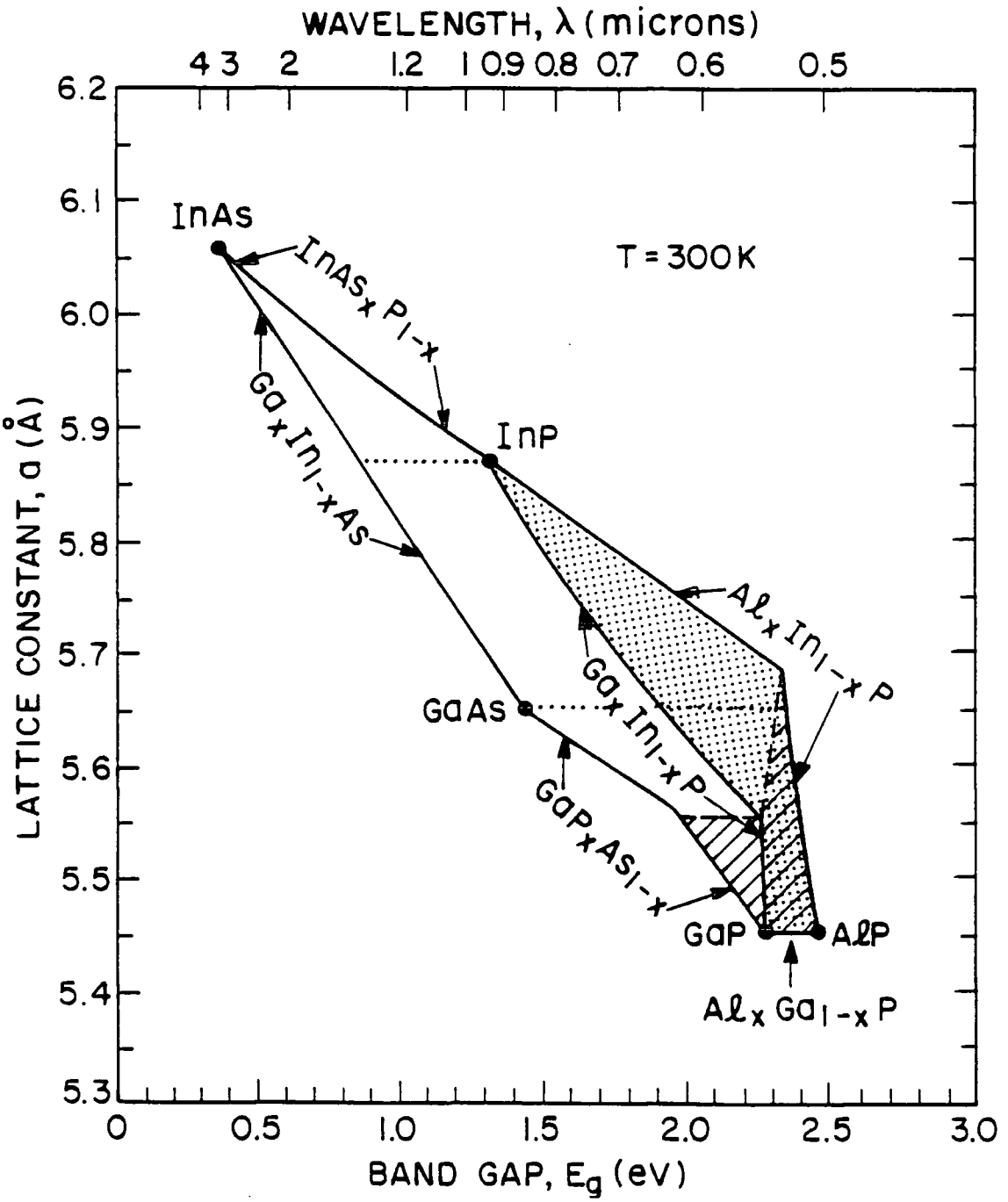

Figure 1.2: Band gap and lattice constant for $In_{1-x}Ga_xAs_{1-y}P_y$ (clear region) and $(Al_xGa_{1-x})_yIn_{1-y}P$ (shaded regions) obtained by varying compositions x and y. Dashed lines separate indirect- band-gap regions (shown hatched). Dotted lines show the wavelength range (top scale) for a semiconductor laser whose quaternary active layer is lattice-matched to the binary compound. After Agrawal and Dutta (1986).

to InP. Semiconductor lasers emitting at $1.3\mu m$ and $1.55\mu m$ wavelengths are of particular interest because of their application in optical fibre communications (Panish, 1987).

In an optical fibre communication system, information is transmitted by light propagation within an optical fibre as a coded sequence of light pulses. The signal weakens during propagation because of fibre loss and so it becomes necessary to regenerate the signal, after some distance, through the use of a repeater (essentially a detector-amplifier-transmitter combination). It is therefore necessary to maximise what is known as the bit rate-distance product, BL. The bit rate is limited inherently by chromatic dispersion in the fibre, which is responsible for the broadening of optical pulses during their propagation inside a fibre. The choice of the operating wavelength is therefore related to the loss and dispersion characteristics of the fibre. Figures 1.3 and 1.4 show the variation of the optical loss [in dB/km] and the dispersion coefficient [in $ps/(km.nm)$] as functions of the wavelength for typical single-mode fibres (Miya et al., 1979; Sugimura et al., 1980).

The first generation of optical transmission systems utilised $GaAs$ lasers operating at a wavelength of about $0.85\mu m$. Relatively high values of the loss and dispersion coefficients restricted the repeater spacing to $\sim 10km$ and the bit rate to $\sim 100Mb/s$. The second generation of systems made use of the wavelength region around $1.3\mu m$, where fibre dispersion is negligible. The use of $InGaAsP$ lasers coupled with the relatively low fibre loss allowed a repeater spacing of about $20km$. However, the bit rate had to be below $\sim 100Mb/s$ because of modal dispersion in multimode fibres. This problem was overcome in the third generation of lightwave transmission systems with the use of single-mode fibres, and the absence of chromatic dispersion near $1.3\mu m$ then allowed much higher bit rates ($B \leq 1Gb/s$). However, the repeater spacing ($\sim 50km$) was limited by the fibre loss at this wavelength. The fourth generation of optical communication systems is based on $1.55\mu m$ $InGaAsP$ lasers where the fibre loss is a minimum. At this wavelength the repeater spacing can easily exceed $100km$ for moderate bit rates. At high bit rates ($B \geq 1Gb/s$) the repeater station is not limited by fibre loss but by the extent of fibre dispersion. Two possible approaches have been followed to overcome this problem. In one the zero dispersion wavelength,

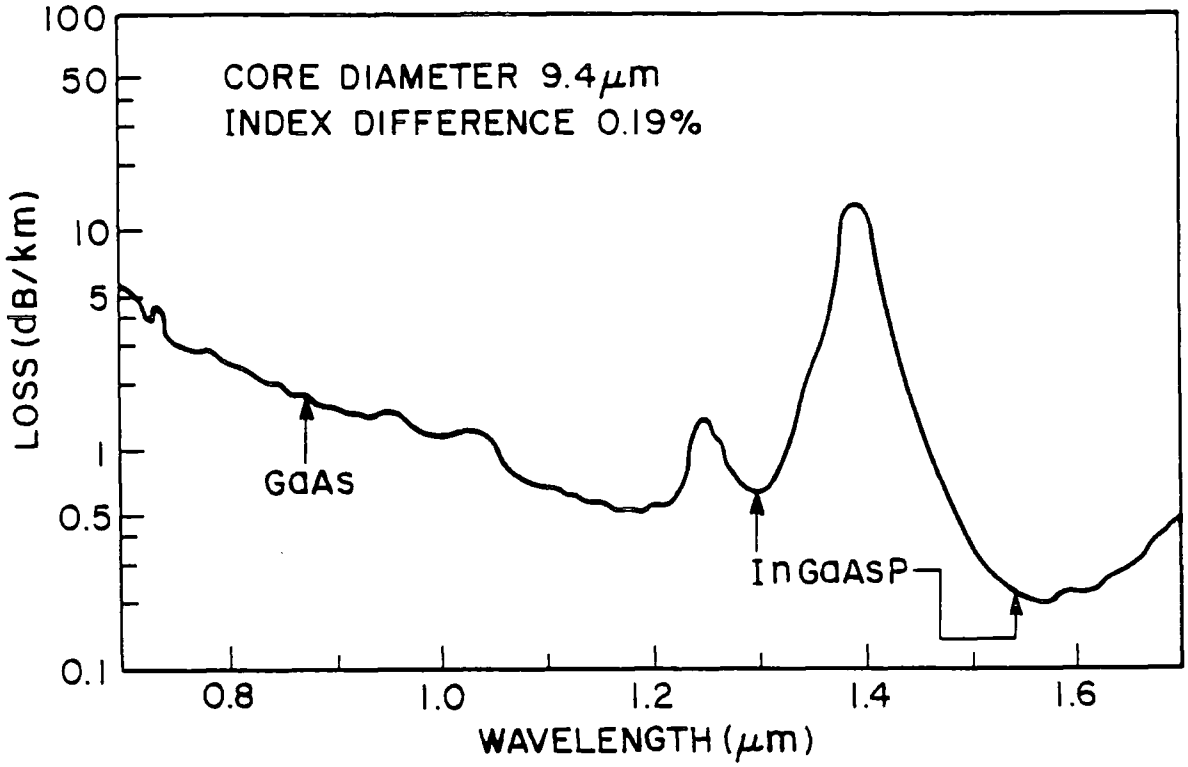

Figure 1.3: Measured loss in a single-mode silica fibre as a function of wavelength. Arrows indicate wavelength regions used for optical fibre communications. Minimum loss occurs around the $1.55\mu m$ wavelength. After Miya et al (1979).

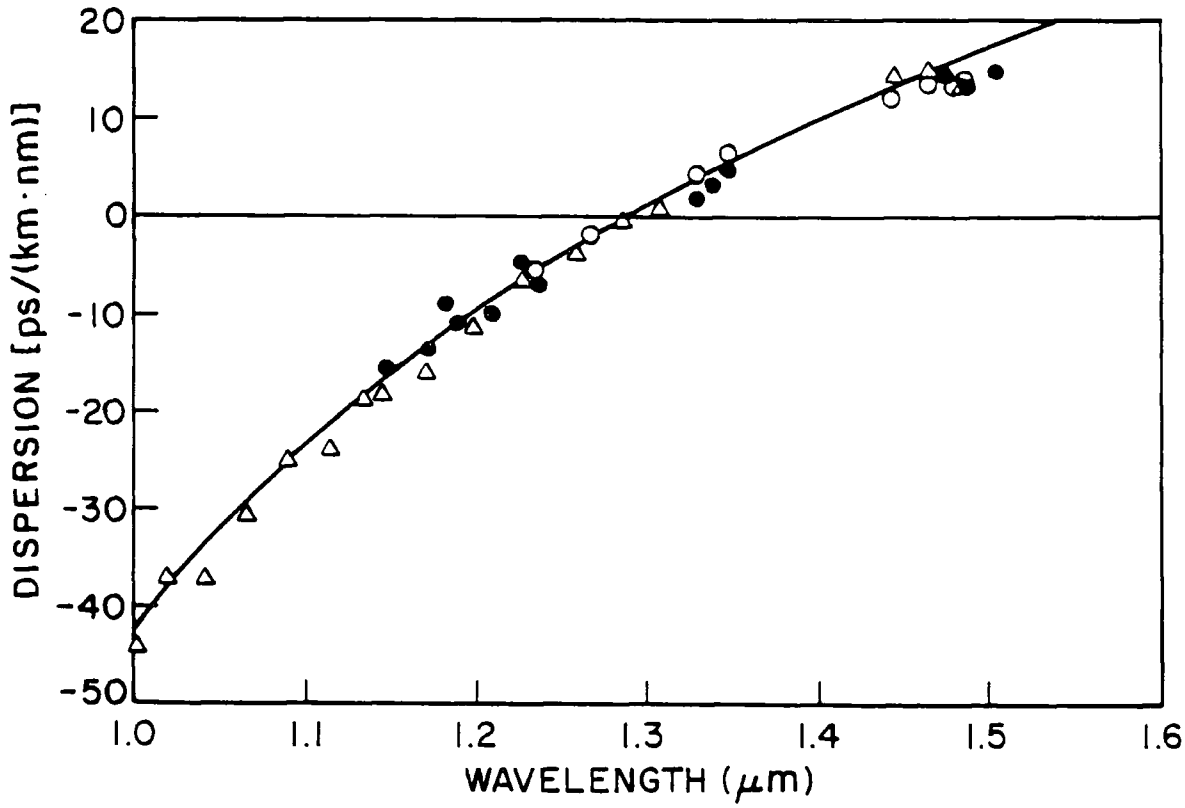

Figure 1.4: Measured material dispersion for typical single-mode silica fibres. Data points for three fibres are shown. After Sugimura et al (1980).

which is about $1.3\mu m$ for conventional silica fibres is shifted towards the desirable $1.55\mu m$ region by modifying the fibre characteristics (Okamoto, et al., 1979). In the other the effect of fibre dispersion is minimised by reducing the spectral width of the $1.55\mu m$ $InGaAsP$ laser source (Bell, 1983).

In general terms, a laser is an externally pumped self-sustained oscillator and consists of a gain medium that is placed inside an optical cavity to provide the necessary feedback. In semiconductor lasers a forward biased p-n diode structure electrically pumps a semiconductor material, and charge carriers injected into a thin active layer provide the gain. No external cavity is required since cleaved facets of the semiconductor gain medium itself can provide sufficient optical feedback. The strength of the external pumping is governed by the injected current density, J. The laser threshold is reached when J reaches a critical value J_{th} at which the gain is sufficient to overcome the cavity losses. Any further increase in J leads to light emission by stimulated emission. Figure 1.5 shows a schematic illustration of a laser.

Long wavelength photodetectors also form a vital part of any optical fibre communication system. The simplest practical detector is the unity gain PIN photodiode, as shown schematically in figure 1.6, which can be illuminated either through the substrate or by direct top illumination (Nelson et al., 1986). Radiation is absorbed in the $GaInAs$ region and the photogenerated carriers are separated by the electric field to produce a photocurrent in the external circuits. Another essential component for both integrated optics and coherent communication purposes is the guided wave device, which is necessary for the manipulation of optical signals. A cross sectional view through a ridge waveguide phase modulator is shown in figure 1.7. Essential requirements of this structure are firstly a low doped $GaInAsP$ guide layer to reduce optical transmission loss, and secondly a high quality p-n junction close to the guide layer which is used to deplete $GaInAsP$ layer of mobile carriers and thereby change the optical properties via the electro-optic effect.

Low dimensional structures are a powerful new class of semiconductor heterostructures in which periodic changes in the heterojunction band structures are engineered to occur over small dimensions (Chang, 1983, 1986). Confinement of

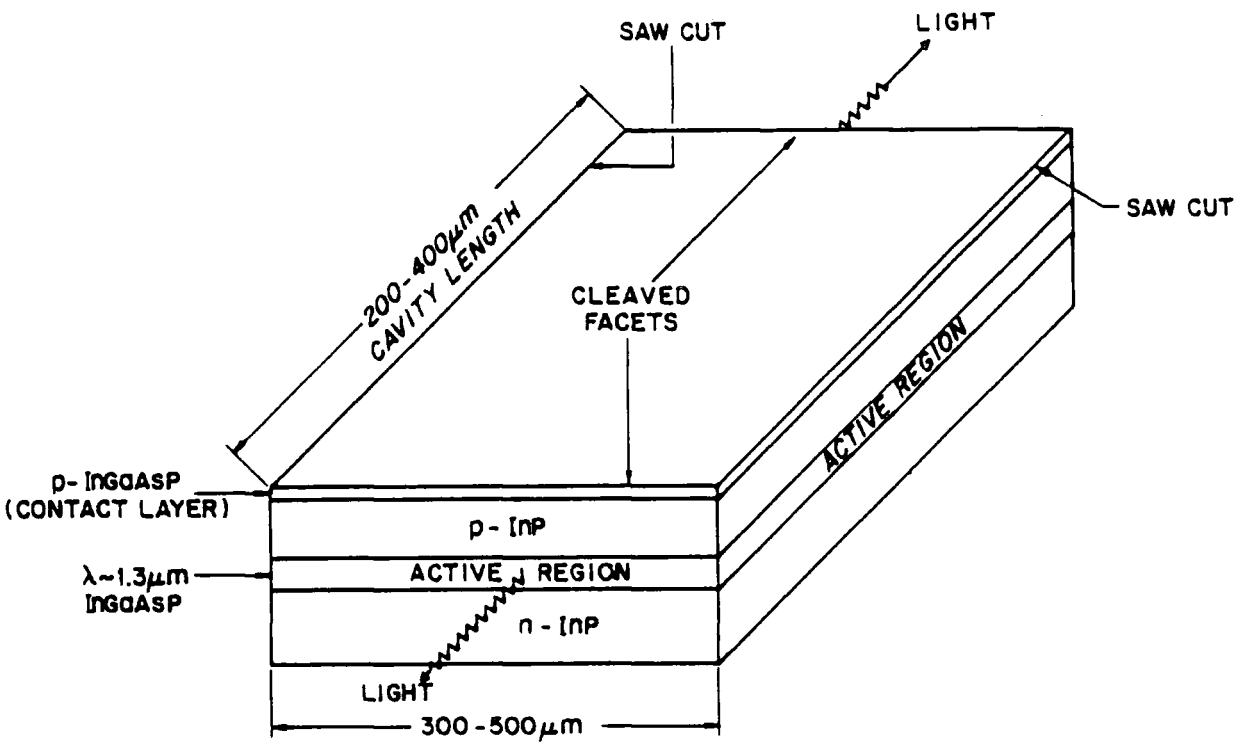

Figure 1.5: Schematic illustration of a broad- area laser chip for a $1.3\mu m$ $InGaAsP$ double- heterostructure laser. After Agrawal and Dutta (1986).

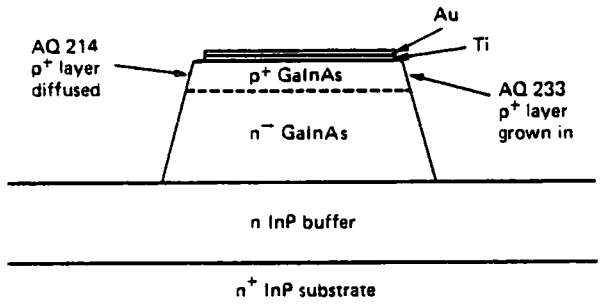

Figure 1.6: Schematic cross section of a PIN detector. After Nelson et al (1986).

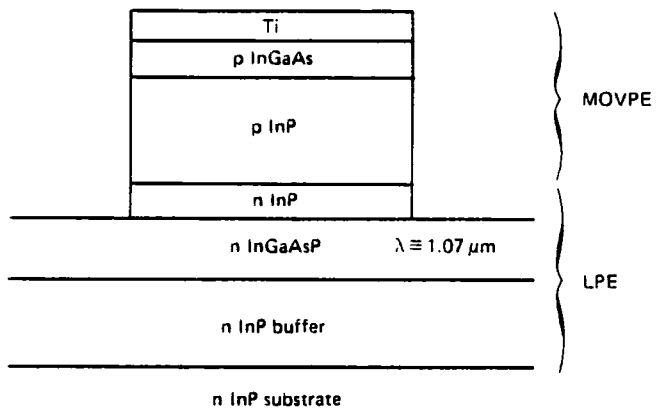

Figure 1.7: Schematic cross section of a ridge waveguide phase modulator. After Nelson et al (1986).

carriers within the band structure potential wells thus formed, results in the formation of quantised energy levels via the quantum size effect, thereby producing a range of new optical and electronic properties completely uncharacteristic of the original bulk semiconductors. Multi-quantum well (MQW) and superlattice structures, as they are know, therefore open up a completely new field of device physics (Orton, 1989).

1.2 Epitaxial Growth

The development of sophisticated epitaxial techniques has been of major significance in the development of high-quality, reliable devices. The commonly used techniques are liquid-phase epitaxy (LPE), vapour-phase epitaxy (VPE), and molecular-beam epitaxy (MBE). The VPE technique has also been called chemical vapour deposition (CVD) depending on the constituent of the reactants. A variant of the same technique is metal-organic chemical vapour deposition (MOCVD) also known as MOVPE, in which metal alkyls are used as the compound source.

1.2.1 Liquid-Phase Epitaxy

LPE is particularly suited to growing relatively thick layers (2-10μm) of high crystalline quality (Nakajima et al., 1980). In LPE a supersaturated solution of the material to be grown is brought in contact with the substrate for a desired period of time. Three basic types of growth apparatus have been used for LPE, illustrated in figure 1.8. They are (a) the tipping furnace, in which the substrate is brought in contact with the solution by tilting the furnace (b) the vertical furnace, in which the substrate is dipped into the solution and (c) the multibin furnace, in which the substrate can be brought in contact with different solutions kept in successive bins. The multibin furnace method is extensively used for the fabrication of laser structures that require successive growth of several epitaxial layers. LPE has been used in the growth of high purity InP and $InGaAsP$ (Cook et al., 1982) and in the fabrication of $InP/InGaAsP$ superlattices (Chang, 1983), although presently it is used mainly for the fabrication of LED's.

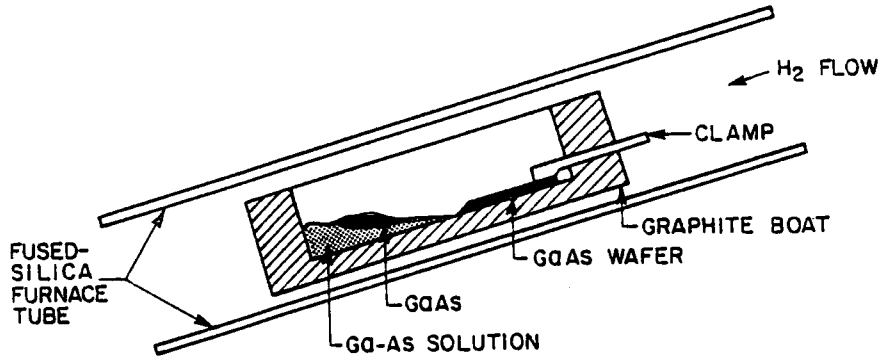

Figure 1.8(a): Schematic illustration of the tipping furnace used for liquid-phase epitaxy (LPE). After Agrawal and Dutta (1986).

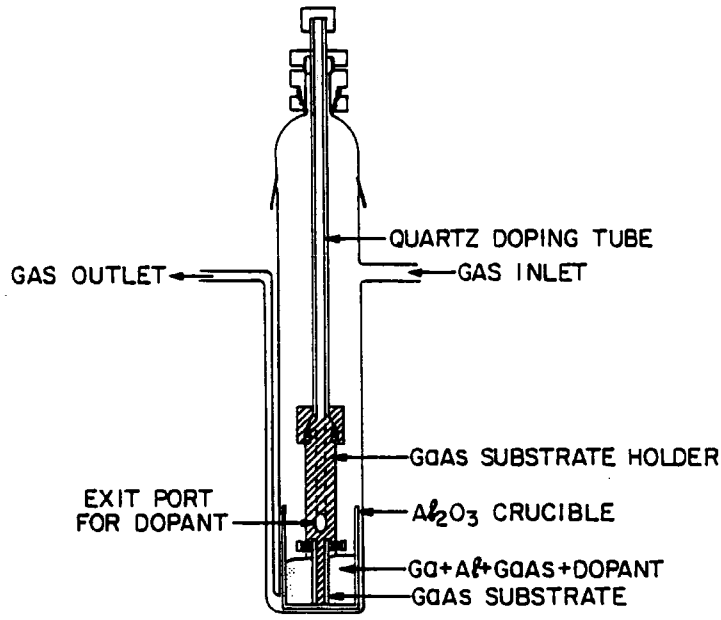

Figure 1.8(b): Schematic illustration of a vertical LPE apparatus. After Agrawal and Dutta (1986).

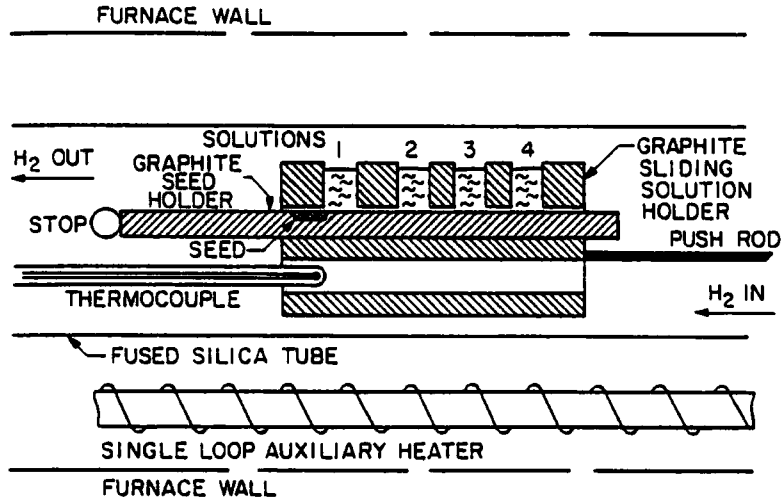

Figure 1.8(c): Schematic illustration of a multibin-boat LPE apparatus used for growing several epitaxial layers. After Agrawal and Dutta (1986).

1.2.2 Vapour Phase Epitaxy

In VPE the source chemicals from which the epitaxial layers are grown are gaseous (Chatterjee et al., 1982). VPE is often classified as one of two different methods; the chloride and the hydride techniques. In the chloride method, $AsCl_3$ or PCl_3 is passed over elemental Ga or In to form metal chlorides. These then react with AsH_3 or PH_3 near the InP substrate to form epitaxial layers of $InGaAsP$ on InP. The metal chlorides can also be formed by using source pieces of $GaAs$ or InP instead of elemental Ga or In. In the hydride method, metal chlorides are formed by passing HCl gas over hot In or Ga metal. Figure 1.9 shows a schematic diagram of the growth reactor for the growth of $InGaAsP$.

1.2.3 Metal-Organic Vapour-Phase Epitaxy

MOVPE (or MOCVD) is a variant of the VPE technique that uses metal alkyls as sources from which the epitaxial layers form (Stringfellow, 1985). Figure 1.10 shows a schematic illustration of the MOVPE growth process (Nelson et al., 1986). Group III alkyls [$Ga(C_2H_5)_3$ and $In(C_2H_5)_3$] and group V hydrides [AsH_3 and PH_3] are introduced into a quartz reaction chamber that contains a substrate placed on a radio-frequency heated ($\sim 500^{\circ}C$) carbon susceptor. The gas flow near the substrate is lam- inar, with velocities in the range of 1 to $15cms^{-1}$ for a working pressure between 0.1 and $0.5atm$. A stagnant boundary layer is formed near the hot susceptor and gas molecules diffuse to the hot surface of the substrate. At the hot surface the metal alkyls and the hydrides decompose, producing elemental In, Ga, P and As. The elemental species deposit on the substrate, forming an epitaxial layer. The gas-flow rates are determined by mass-flow controllers. $Zn(C_2H_5)_3$ and H_2S are used as sources for p-type and n-type doping respectively.

MOVPE has been used for the growth of high quality single thick layers and MQW's of $GaInAs$ and InP (Moss and Spurdens, 1984) as well as II-VI layers and superlattices (Bhat et al., 1987; Ahlgren et al., 1987). MOVPE has the ability to produce a wide variety of structures, as well as being capable of depositing metals and dielectric materials. Large area uniformity and precise thickness and composition control makes MOVPE an ideal technique for production (Nelson et al., 1986).

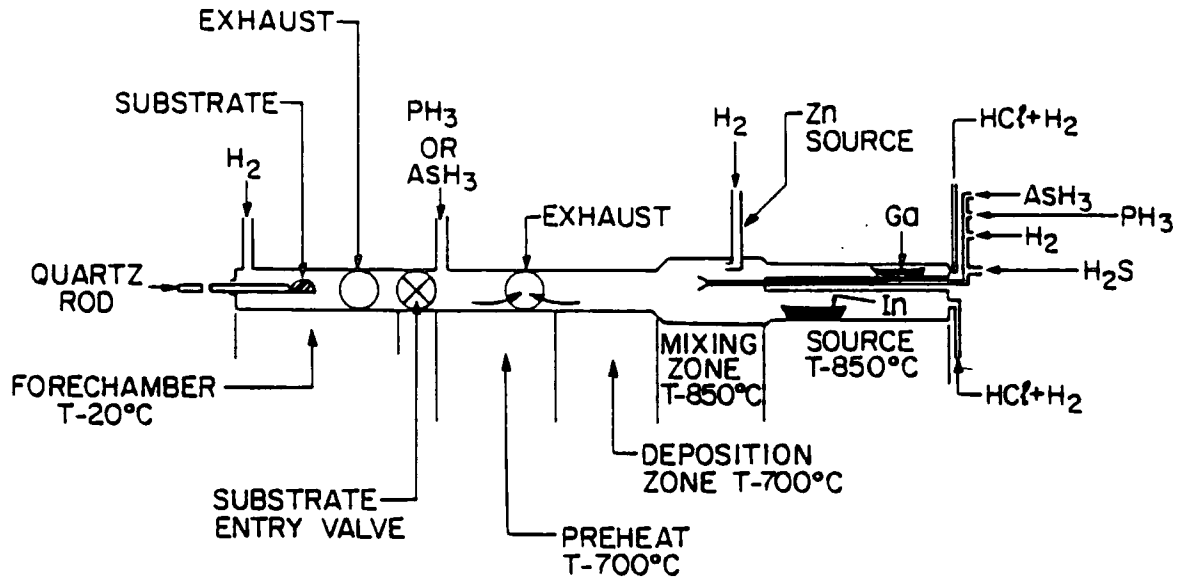

Figure 1.9: Schematic illustration of a vapour-phase epitaxy (VPE) reactor. After Agrawal and Dutta (1986).

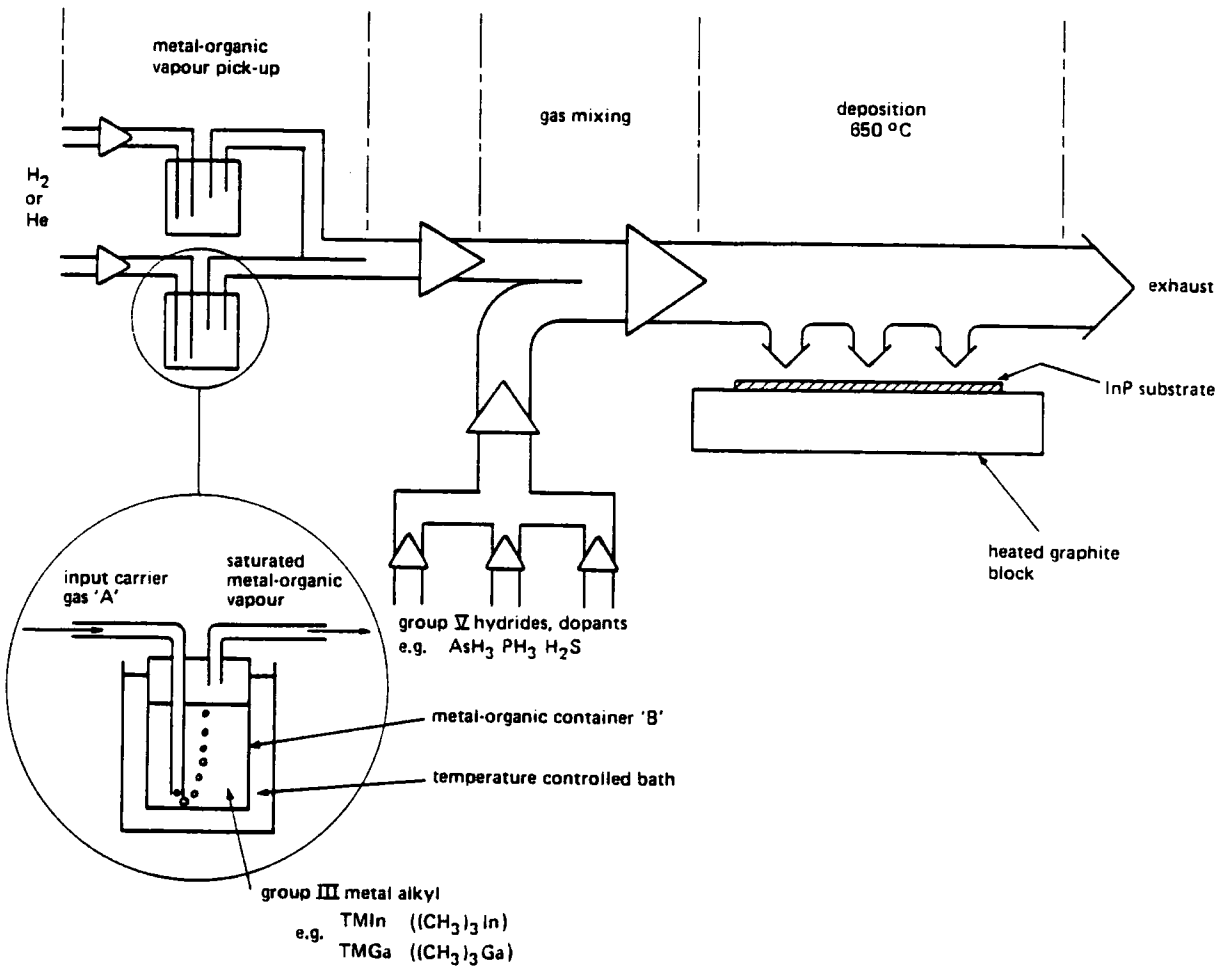

Figure 1.10: Schematic illustration of the MOVPE growth process. After Nelson et al (1986).

1.2.4 Molecular Beam Epitaxy

In MBE, epitaxial layers are grown by impinging atomic or molecular beams on a heated substrate in an ultrahigh vacuum. The constituents of the beam react with the substrate, resulting in a lattice-matched layer. The beam intensities can be separately controlled to take into consideration the difference between sticking coefficients of the various constituents of the epitaxial layers. Figure 1.11 shows a cross-sectional view of an MBE system illustrating the configuration of the major components (Davies and Andrews, 1985). The widespread use of MBE for the growth of different III-V semiconductors resulted from the original work of Cho and Arthur (1975). Since then, extensive work on heterostructure lasers, microwave devices, quantum-well lasers, and superlattice structures has been reported using $AlGaAs$ and other materials prepared by MBE (Chang, 1983; Holah, Meeks and Eisele, 1983; Davies and Andrews, 1985).

1.3 Lattice Mismatch and Végard's Law

Since ternary alloys of III-V elements are only lattice matched to binary III-V substrates at one composition, any deviation from this matched value will lead to misfit stress occurring during growth (Griesche et al., 1988). If the mismatch is relatively small the strain will be entirely taken up by tetragonal distortion of the layer (Olsen and Smith, 1975), whereby the lattice spacing in the substrate plane becomes equal to that of the substrate and the spacing perpendicular to the plane changes from its relaxed value. Clearly, any lattice parameter measurements performed will be of this final structure and it is therefore important to be able to relate these values to the initial compositions. Hill (1985) has given an account of tetragonal distortion and misfit stress in epilayers for growth on (001) substrates, while growth on other planes has been dealt with by Hornstra and Bartels (1978).

The relaxed lattice constant can be directly related to the composition for ternary alloys, using Végard's law, which states that the lattice parameter is a linear function of the composition (Mikkelsen and Boyce, 1982; Fukui, 1984). For example, for $Ga_xIn_{1-x}As$ as we have

$$a_{Ga_xIn_{1-x}As} = (1-x)a_{InAs} + xa_{GaAs} \ . \qquad 1.1$$

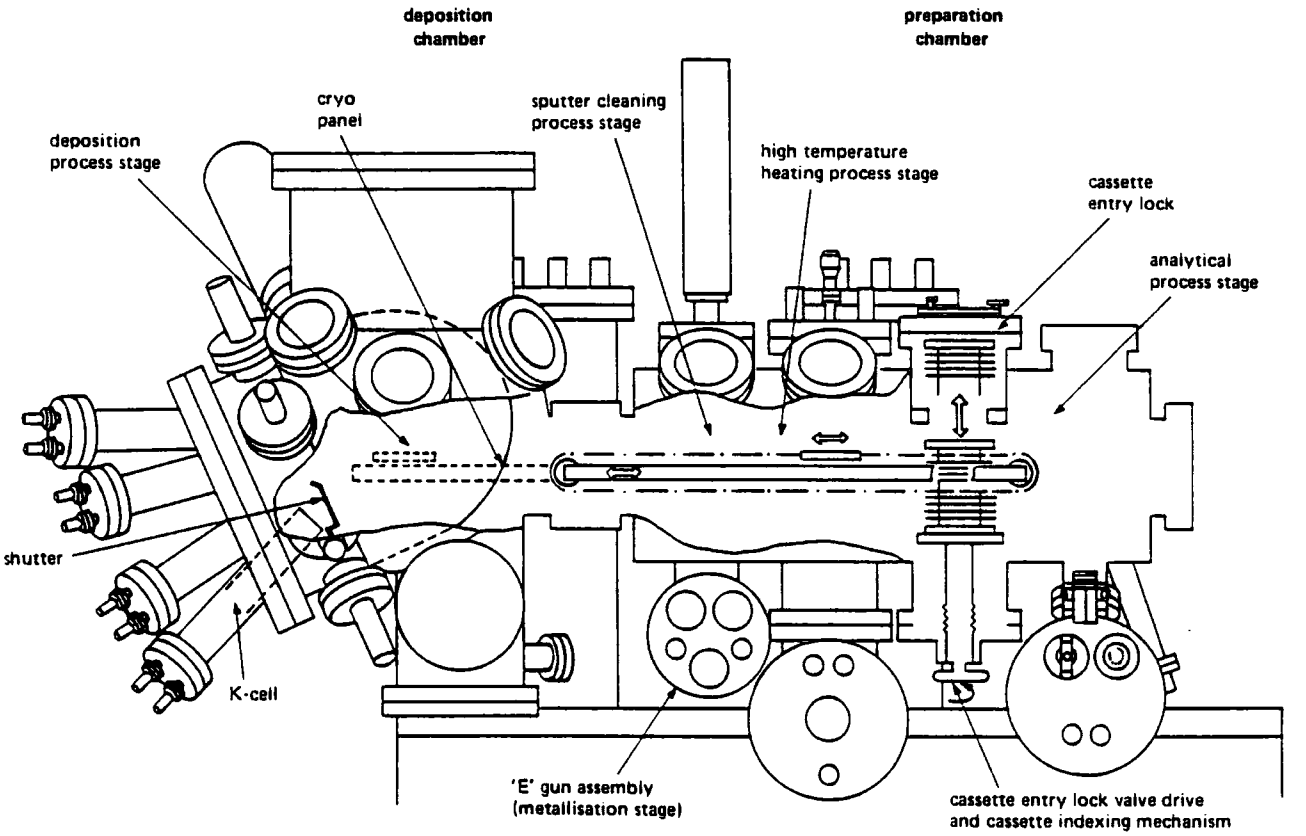

Figure 1.11: Cross-sectional view of an MBE system illustrating the configuration of the major components. After Davies and Andrews (1985).

where a is the relaxed lattice parameter. Similar equations exist for other ternaries, thus x can be easily determined.

For quaternaries the variation in lattice parameter is more complicated. Taking $Ga_xIn_{1-x}As_yP_{1-y}$ as an example, the lattice parameter is given by the surface shown in figure 1.12 (Hill, 1985). Considering the change in lattice parameter parallel to the x and y axes we obtain

$$\frac{\partial a}{\partial x} = ya_{GaAs} + (1-y)a_{GaP} - ya_{InAs} - (1-y)a_{InP} \ , \qquad 1.2$$

and

$$\frac{\partial a}{\partial y} = xa_{GaAs} + (1-x)a_{InAs} - xa_{GaP} - (1-x)a_{InP} \ . \qquad 1.3$$

Now at $x = 0$ and $y = 0$, $a = a_{InP}$, therefore

$$a_{Ga_xIn_{1-x}As_yP_{1-y}} = xya_{GaAs} + x(1-y)a_{GaP} + (1-x)ya_{InAs} + (1-x)(1-y)a_{InP}. \qquad 1.4$$

The lattice matched composition occurs when $a(x,y) = a_{InP}$, so that

$$x = \frac{0.4526y}{1 - 0.031y} \ . \qquad 1.5$$

As it is not possible to determine x and y individually from equation (1.4), it is necessary to use the empirical relationship between composition and band gap (Nahory, 1978). The best fits to the experimental data is shown in Table 1.1 and the values of the lattice parameters for some of the common III-V binary alloys are shown in Table 1.2.

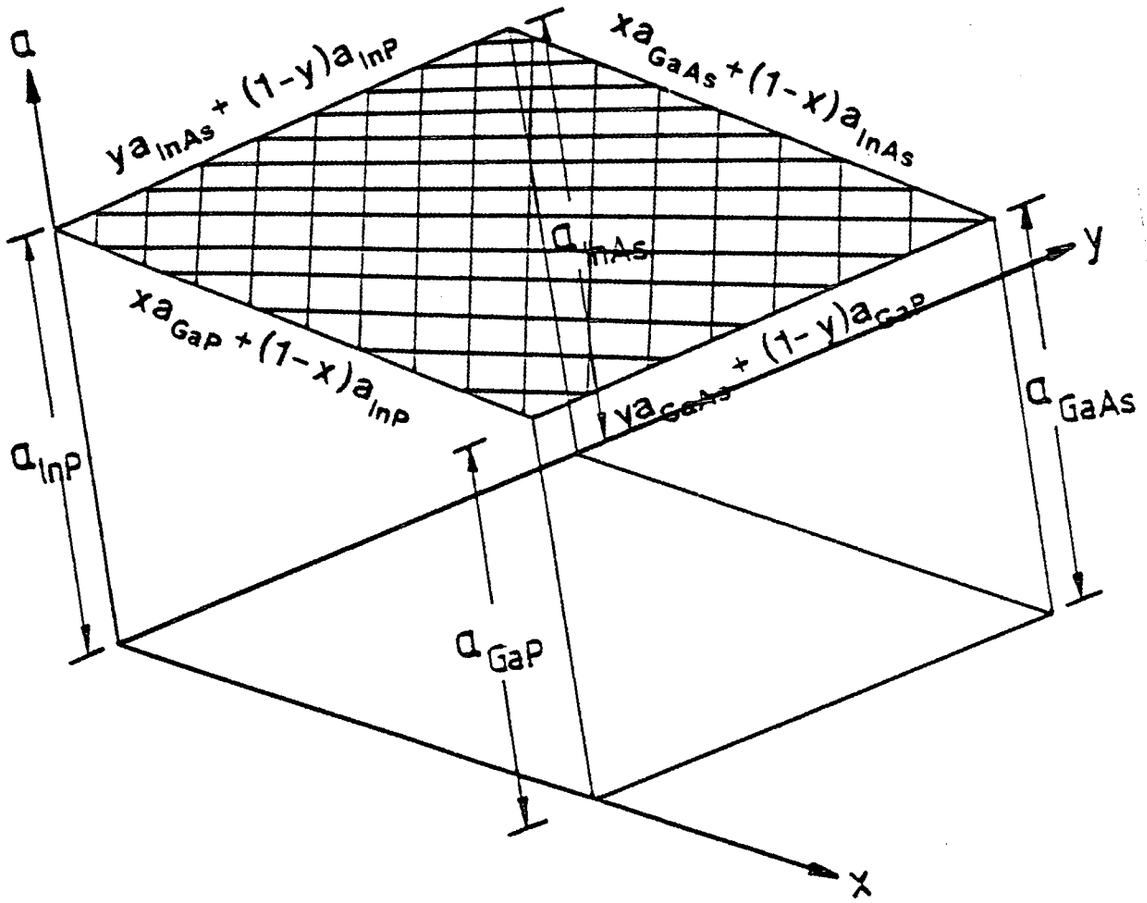

Figure 1.12: Surface representing the lattice parameter of $Ga_xIn_{1-x}As_yP_{1-y}$ as a function of x and y. After Hill (1985).

Ternary	Band gap (eV)
$In_{1-x}Ga_xAs$	$E_g(x) = 0.36 + 0.629 + 0.436x^2$
$InAs_yP_{1-y}$	$E_g(y) = 1.35 - 1.77y + 0.18y^2$
$In_{1-x}Ga_xP$	$E_g(x) = 1.35 + 0.668x + 0.758x^2$
$GaAs_{1-y}P_y$	$E_g(y) = 2.77 - 1.56y + 0.21y^2$
$In_{1-x}Ga_xAs_yP_{1-y}$	$E_g(x,y) = 1.35 - 0.72y + 0.12y^2$

Table 1.1: Band gaps of some common Ternary and Quaternary alloys

Binary	Lattice Parameter (Å)
$GaAs$	5.65325
InP	5.86875
$InAs$	6.0584
GaP	5.45117

Table 1.2: Lattice Parameters of III-V Binaries

1.4 Characterisation Methods for Semiconductor Materials

The precision and quality required of semiconductor materials for use in microelectronic and optoelectronic devices requires increasingly precise control of growth conditions. As future material and device requirements become increasingly sophisticated, so analysis techniques must develop to match them (Ambridge and Wakefield, 1985). Other than electrical assessment (Wood and Ambridge, 1986), characterisation methods for semiconductor materials can be divided into four main groups; optical probes, electron beams, X-ray probes and particle beams. Table 1.3 outlines some capabilities of common characterisation techniques used in the semiconductor industry today (Shaffner, 1986). Complementary types of information are provided by each of the groups and it is usually necessary to use several techniques in order to fully characterise a sample. For instance, particle techniques which are sensitive to trace impurities and dopants clearly complement those methods employing beams of electrons for defect and

Table 1.3: Capabilities of some commonly used techniques for semiconductor characterisation are compared relative to the type of probing radiation. After Shaffner (1986).

	Optical Micro-scopy	Fourier Transform Infrared (FTIR)	Photo Lumines-cence (PL)	Infrared and Ultra-Violet (IR & UV)	Raman Micro-Probe	Photo-Neutron Activation
Depth Analyzed	> 1-3 μm	1-10 mm	1-3 μm	1 mm IR 1 μm UV	1 μm	0.5 cm
Diameter of Analysis Region	~ 1 cm	2 mm	> 5 μm	1 mm	2 μm	0.5 cm
Detection Limit (atoms/cm^3)	visual inspect	$1x10^{11}$	$1x10^{11}$	$5x10^{18}$	$5x10^{19}$	$5x10^{15}$
Detection Limit (ppm)	visual inspect	$2x10^{-6}$	$2x10^{-6}$	100	1000	0.1
In-depth profiling resolution	none	none	none	none	none	none
Time for Analysis	< 1 hour	2 hours	2 hours	< 1 hour	< 1 hour	2 hours
Comments	In-depth profiling achieved by angle-lap cross section	Performed at 10-15°K tempera-tures	Performed at 4°K tempera-tures	Performed at room tempera-ture		Bulk measure-ment only

(a): Optical probes

	Scanning Electron Microscopy (SEM)	Auger Electron Spectroscopy (AES)	Scanning Auger Microprobe (SAM)	Electron Microprobe (EMP)	Analytical Electron Microscopy (AEM)	High Voltage TEM (HVTEM)
Depth Analyzed	~ 1000 Å	20 Å	20 Å	1 μm	< 1000 Å	< 1000 Å
Diameter of Analysis Region	50 Å - 5 mm	100 μm	1000 Å	1 μm	10 μm	10 μm
Detection Limit (atoms/cm^3)	surface image	$5x10^{19}$	$1x10^{21}$	$5x10^{19}$	defect imaging	lattice imaging
Detection Limit (ppm)	surface image	1,000	20,000	1000	defect imaging	lattice imaging
In-Depth Profiling Resolution	stereo microscopy	20 Å	20 Å	none	stereo microscopy	none
Time for Analysis	< 1 hour	< 1 hour	< 1 hour	< 1 hour	1-3 days	1-3 days
Comments	In-depth profiling achieved by angle-lap cross section	Profiling achieved by argon sputtering	Profiling achieved by argon sputtering	Wave-length & energy dispersive analysis	sample preparation requires specialized techniques and is time consuming	

(b): Electron beams

	Powder X-ray Diffraction (XRD)	Thin Film Analysis (Seeman-Bohlin)	Lang X-ray Topography (Lang)	Double Crystal Topography (DCT)	X-ray Fluorescence (XRF)	X-ray Photo-electron Spectro-scopy (XPS,ESCA)
Depth Analyzed	10-50 μm	100 Å - 1 μm	500 μm	5-100 μm	1-3 μm	20 Å
Diameter of Analysis Region	> 1 mm	1x5 mm	> 1 cm	> 1 cm	> 5 mm	5 mm
Detection Limit (atoms/cm^3)	$5x10^{19}$	$5x10^{19}$	$1x10^{-3}$ in $\Delta d/d$	$1x10^{-7}$ in $\Delta d/d$	$1x10^{19}$	$5x10^{19}$
Detection Limit (ppm)	1000	1000	—	—	200	1000
In-depth Profiling Resolution	none	none	stereo topography	none	none	20 Å
Time for Analysis	< 1 hour	2 hours	1 hour	4 hours	10 min	< 1 hour
Comments	sample cannot be amorphous	grazing incidence beam used	whole slice survey	whole slice survey	rapid & quanti-tative	In-depth profiling by argon sputtering

(c): X-ray probes

	Rutherford Backscattering Spectroscopy (RBS)	Neutron Activation Analysis (NAA)	Ion Microscope (IMS,SIMS)	High Energy Ion Channeling	Charged Particle Activation Analysis (CPA)
Depth Analyzed	200 Å - 1 μm	1 μm	50 Å	100 Å	300 μm
Diameter of Analysis Region	2 mm	> 1 cm	> 5 mm	1 mm	5 mm
Detection Limit (atoms/cm^3)	$5x10^{19}$	$5x10^{11}$ - $5x10^{18}$	$5x10^{15}$ - $5x10^{18}$	$5x10^{16}$	$5x10^{13}$
Detection Limit (ppm)	1000	0.00001 - 100	0.1 - 100	1.0	0.001
In-depth Profiling Resolution	200 Å	1 μm	50 Å	surface technique	25 μm
Time for Analysis	1 hour	2-5 days	1 hour	2 hours	2 hours
Comments	No standards needed	In-depth profiling by chemical etching	Spatial Resolution near 1 μm	crystal-line substrate required	In-depth profiling by chemical etching

(d): Particle beams

surface definition, while X-ray techniques specialise in crystalline imperfections and determination of composition.

In the growth of bulk crystals, characterisation methods are concerned with the identification of bulk impurities, dopants, defects and crystal damage (Dyer, 1983). *GaAs* stoichiometry, for instance, has been studied using composition sensitive X-ray methods (Cockerton, Green and Tanner, 1989), and infrared spectroscopy has been used for the characterisation of dopant species, determining the presence of carbon and oxygen in silicon (Stalhofer and Huber, 1983). X-ray topography (Halliwell, Childs and O'Hara, 1972; Hart, 1975; Tanner, 1976; Bhat, 1985) is a powerful technique which can be used not only to study macroscopic features such as flake chips, surface fractures, scratches, edge cracks and wafer warpage, but also microscopic defects including stacking faults, dislocation loops and slip. Double crystal topography, in particular, is highly sensitive to lattice strains and effects (Bonse and Kappler, 1958) and is ideally suited for study of epitaxial films (Riglet et al., 1980; Eaglesham et al., 1988).

Optical assessment techniques, including Raman spectroscopy and Photoluminescence spectroscopy are particularly valuable in the characterisation of quantum well and superlattice structures, as well as single epitaxial semiconductor layers (Davey, Wakefield and Ambridge, 1987). Raman spectroscopy is a technique based on focussing light from a laser into a micron sized spot on the specimen and collecting the light in a spectrometer for analysis. The Raman vibrational modes excited by the light can be used as a fingerprint to identify composition. Raman spectroscopy has been used to determine composition in *GaInAs/AlInAs* MQW structures (Davey, Scott, Wakefield and Davies, 1987; Scott, Davey, Halliwell and Davies, 1988; Davey et al., 1989) and in *InAs/GaAs* heterostructures (Diebold, Steinhauser and Mariella, 1989). In photoluminescence spectorscopy (PL), a population inversion of electronic excited states is created by visible laser light stimulation, and emissions resulting from relaxation to the ground state are analysed. Smith (1981) has given a review of the method and examples of its use have been in the study of impurity incorporation of *InGaAs* on *InP* (Goetz et al., 1983), optical properties of *InGaAs* (Skolnick et al., 1986) and determination of energy gaps in *AlGaAs* (Lambert et al., 1987).

For the characterisation of diffusions and implants one of the most useful tools is secondary ion mass spectroscopy (SIMS), (Asher, 1988). The technique involves bombarding a sample with a primary beam resulting in a gross disturbance of the near surface region. Sample atoms recoil from the surface, a small fraction of which will be ionised. These secondary ions are then focused into a mass analyser and the proportion of different element types in the surface can be determined. This destructive technique has been used, for example, by Macrander and Swaminathan (1987), to study $InGaAs$ on InP.

Diffraction based characterisation techniques are becoming increasingly important in the development of device technology (Halliwell, Taylor and Ambridge, 1985). A major difference in the experimental conditions used in X-ray and electron diffraction techniques arises because of the much stronger interaction between electrons and atoms than between X-rays and atoms. Electrons are rapidly scattered and absorbed on entering a sample and so only very thin layers (up to $1\mu m$) of a sample may be examined, whereas X-rays can penetrate through samples up to the thickness of a typical wafer. Electrons can be readily focused using electromagnetic lenses unlike X-rays, and so the spatial resolution is very high. X-rays can be used to assess large samples such as complete wafers, up to several inches in diameter. The major advantage of X-rays is that they are non-destructive. In electron diffraction techniques this is not the case, as the sample generally has to be thinned, however, because the magnification available is around four orders of magnitude greater than for the X-ray case, a much more detailed study of the defects can be made.

The Transmission Electron Microscope (TEM) consists of an electron source, two condenser lenses to focus the electrons on the specimen, an objective lens to form the image and diffraction pattern, and three post specimen lenses to magnify the image or diffraction pattern (Grundy and Jones, 1976). By the preparation of cross sections it is possible to obtain images of, for example, compositional change through a superlattice and misfit dislocations at strained layer interfaces (Chang, Bhattacharya and Gibala, 1989). TEM has been used for the observation of small periodic compositional variations in $GaInAs$ and $AlInAs$ layers grown by MBE (Alavi et al., 1983) as well as to identify defects in MOVPE grown $GaInAs$ (Carey, 1985). Schaus et al., (1986) have investigated the properties

of *GaAs/AlGaAs* quantum well heterostructures, using TEM together with PL, in order to optimise growth conditions. Dupuis et al. (1987) have observed dislocations in MOVPE *Ge* layers on *Si* using TEM before and after annealing, and together with double crystal diffraction an assessment of layer quality was made. Complementary information from X-ray diffraction, PL and TEM has been used to fully characterise MQW structures (Orton et al., 1987).

1.5 Introduction to X-ray Diffraction

This thesis concentrates on the use of X-ray diffraction methods in the characterisation of epitaxial layers. X-ray diffraction is now widely used in industry both as a routine assessment technique to aid crystal growth, and as a highly sensitive tool for detailed structural studies. It is especially useful for the characterisation of epitaxial layers, where the layer quality is high, and differences in lattice parameter between substrate and layer are at the parts per million (*ppm*) level.

Epitaxial layers are single crystals with the same orientation as the substrate. In a single crystal the atoms are arranged in a regular three dimensional array, known as the crystal lattice. The atoms within a lattice can be considered as lying on a series of equally spaced planes which diffract X-rays. The conditions under which an X-ray or electron beam is diffracted are given by Bragg's Law,

$$n\lambda = 2d_{hkl}\sin\theta \ . \qquad 1.6$$

This is illustrated in figure 1.13 where θ is known as the Bragg angle, for which constructive interference occurs between rays diffracted from adjacent atomic planes. d_{hkl} is the interplanar spacing and the diffracted radiation is said to have undergone on '*hkl* reflection' if the planes are separated by a/h, b/k and c/l respectively in the three axial directions, where h, k and l are integers. The interplanar spacing for an *hkl* reflection is then given by

$$d_{hkl} = \frac{1}{\sqrt{h^2/a^2 + k^2/b^2 + l^2/c^2}} \ . \qquad 1.7$$

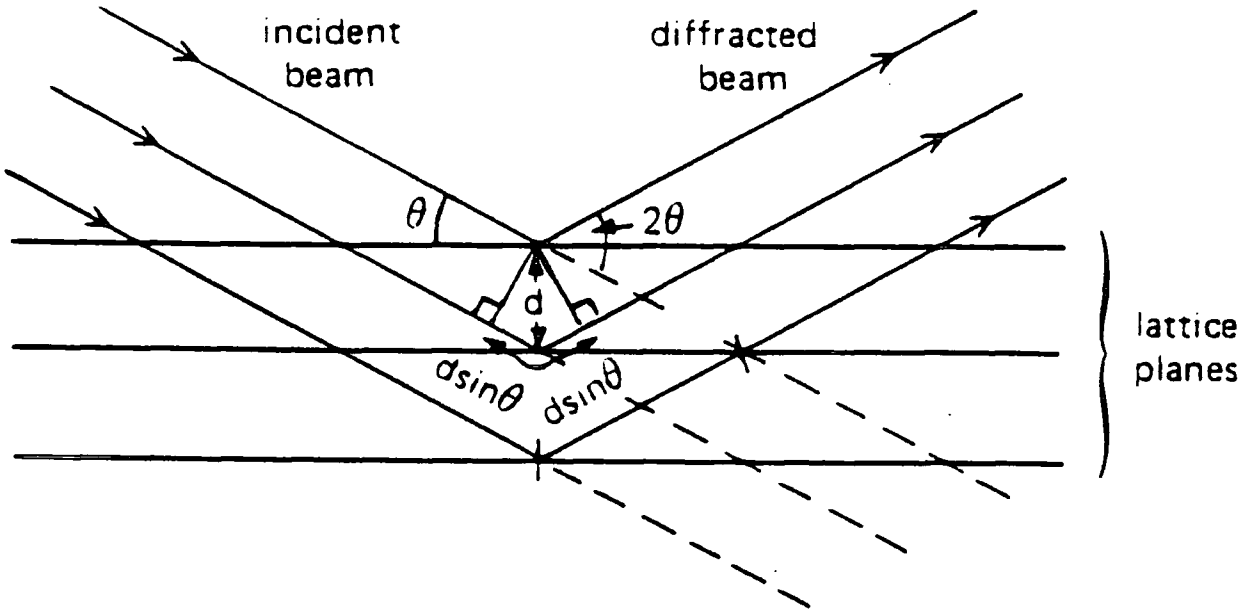

Figure 1.13: Diagram showing that the path difference for beams diffracted by planes d apart is $2d\sin\theta$. The Bragg condition for constructive interference is $\lambda = 2d\sin\theta$. After Halliwell et al (1985).

As a result, for a fixed wavelength λ, and interplanar spacing d, a strong diffracted beam only occurs at one fixed angle, which is the basis of X-ray diffraction.

If a sample consists of a mismatched epitaxial layer on a substrate then the layer and substrate will fulfil the Bragg condition at different angles. Hence by rocking the sample with respect to the X-ray beam over a range of angles and measuring the two Bragg angles corresponding to diffraction maxima, the layer interplanar spacing and therefore composition may be determined. This plot of diffracted intensity versus angle is known as a rocking curve. The simplest method of X-ray diffraction is the single crystal technique (Hart, 1981). For layers with lattice mismatch ($\Delta d/d$) of greater than 10^{-4}, single crystal methods can be used to give a rapid indication of layer composition. However, the technique is severely limited by beam divergence and wavelength dispersion, and for high resolution studies it is necessary to use double crystal diffraction.

Chapter II

Multiple Crystal Diffraction

2.1 Introduction

The previous chapter has described the various methods available for the characterisation of semiconductors. This chapter deals with multiple crystal X-ray diffraction techniques, where multiple implies more than one reflection. Single crystal diffraction has many limitations because the rocking curve is dominated by broadening due to beam divergence, source size and wavelength dispersion. The double crystal diffractometer (DCD) removes many of these limitations. Its theory has been known since the 1920's, and the reader is referred to the papers of Schwarzschild (1928); Allison and Williams (1930); Allison (1932); Compton and Allison (1936) and DuMond (1937). Double crystal diffractometers have been in existence since the early 1930's (Compton, 1931; DuMond and Marlow, 1937), although it is only with the recent development of highly perfect semiconductor crystals that their use has become more widespread. This chapter describes the theory of the double crystal diffractometer following the work of Compton and Allison; DuMond; and Pinsker (1978).

The triple crystal diffractometer (TCD) first proposed by Renninger (1955) is able to scan reciprocal space and so allows the study of diffuse scattering around the Bragg peaks yielding important information on the topography of the crystal surface. Examples of its use have been in the study of surface perfection of thin surface layers (Afanas'ev, Aleksandrov, Imamov, Lomov and Zavyalov, 1984) as well as multilayers and superlattices (Hornstrup, Christensen and Schnopper 1986; Christensen, Hornstrup and Schnopper, 1988). Cowley and Ryan (1987) have used the instrument to study thin surface layers and the theory presented in this chapter follows the work of Ryan (1986).

The use of four crystal monochromators to improve spectral resolution as well as angular resolution was first studied by Beaumont and Hart (1974). Since then

the monochromator has been used in high resolution five crystal diffractometers to study thin layers (Bartels, 1983), the resolution function of which has been described by Slusky and Macrander (1987). Fewster (1989) has recently combined the qualities of a four crystal monochromator with an analyser crystal in a six crystal diffractometer. The theory and relative merits of the various instruments are dealt with in this chapter.

2.2 Theory of the Double Crystal Diffractometer

Figure 2.1 shows the two possible settings of the DCD, with the second crystal either parallel or antiparallel to the first. The X-ray beam is collimated with two slits before being incident on the first crystal and it is this which defines the angular divergence of the beam. The divergence is made up of two components; the horizontal divergence of a ray, α, is defined as the angle made with its projection on a vertical plane and the vertical divergence of a ray, ψ, is the angle made with its projection on a plane perpendicular to the axes of the instrument (a horizontal plane). If the two slits are rectangular apertures, of equal width W and height H, separated by the distance L, then the maximum values of divergence are given by

$$\alpha_m = \frac{W}{L}, \qquad \psi_m = \frac{H}{L}. \tag{2.1}$$

Following Compton and Allison (1936), the first crystal is aligned such that a central ray in the incident beam makes an angle

$$\theta = \theta_0 + \Delta \tag{2.2}$$

with the reflecting planes, corresponding to the centre of the reflecting range. Δ is dependent on the refractive index of the crystal and its value is given in the next chapter. Consequently, the maximum of the reflecting profile does not correspond exactly with the kinematic Bragg angle, θ_0, given by

$$\sin\theta_0 = \frac{n\lambda}{2d}. \tag{2.3}$$

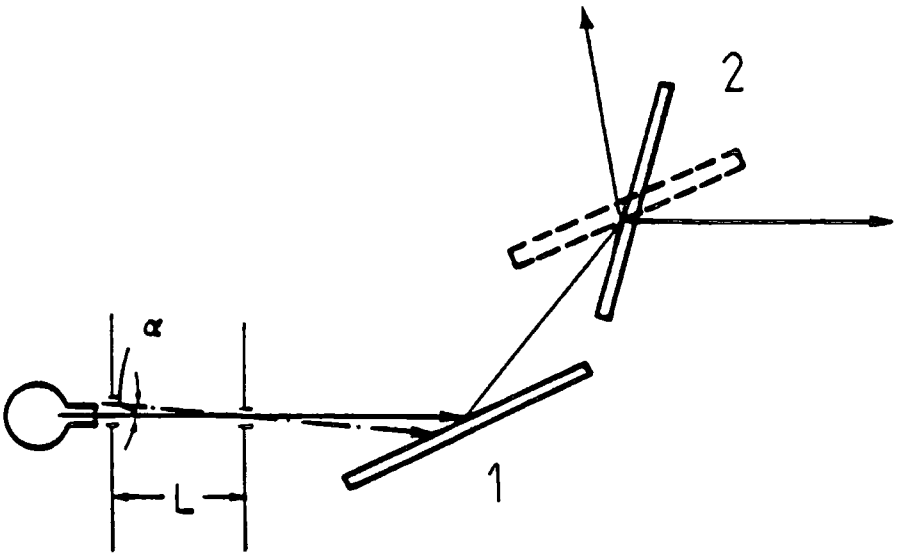

Figure 2.1: Illustration of the two settings of the double crystal diffractometer.

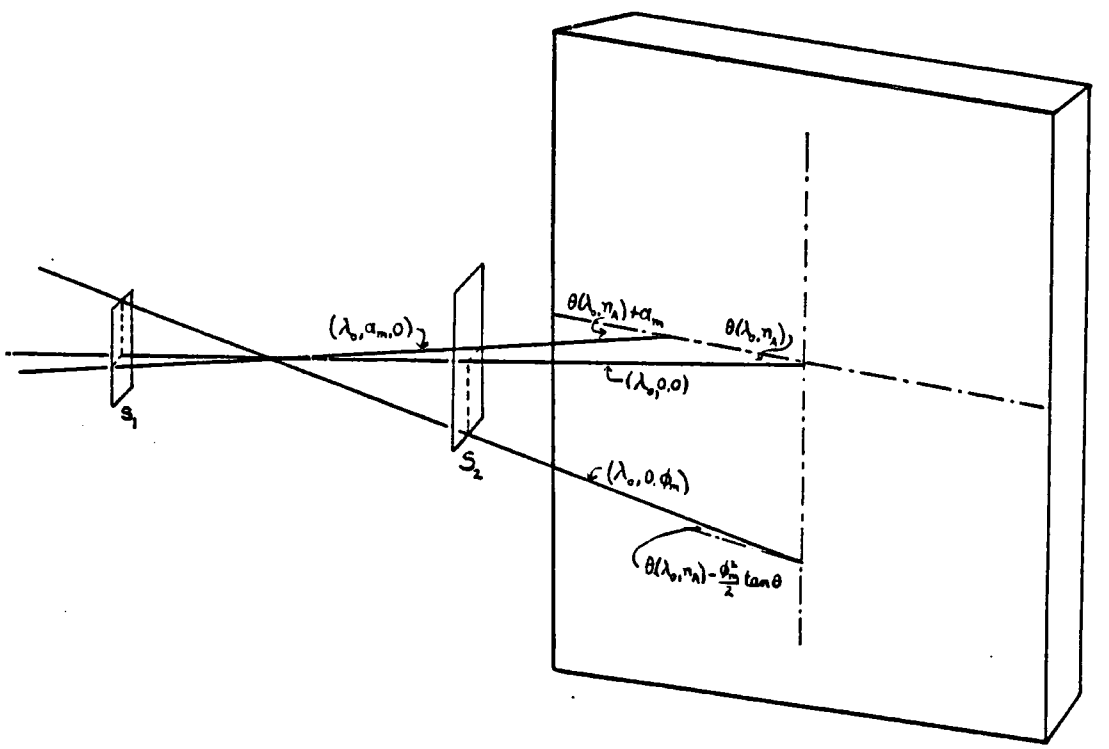

Figure 2.2: Deviation of an arbitrary ray from the central ray due to horizontal and vertical divergence. After Compton and Allison (1935).

The central ray, passing through the geometrical centre of the slit apertures, with $\alpha = \psi = 0$, makes a glancing angle of $\theta(\lambda_0, n_1)$ with the first crystal, where n_1 is the order of reflection. λ_0 may be thought of as some characteristic wavelength in the incident radiation, corresponding to the centre of a spectral line. In general, a ray incident on the first crystal may be characterised by three quantities (λ, α, ψ), giving its wavelength, and horizontal and vertical divergence respectively. It may be shown using figure 2.2 that the deviation of an arbitrary ray from the central ray is

$$\alpha - \frac{1}{2}\psi^2 \tan\theta(\lambda_0, n_1) - (\lambda - \lambda_0)\frac{\partial\theta}{\partial\lambda_0}(\lambda_0, n_1). \qquad 2.4$$

The second term corresponds to the deviation due to vertical divergence and the third due to monochromaticity, which takes this form after assuming that within the spectral width of the incident beam the reflection angles change only slightly.

Figure 2.3 shows the X-ray paths and angles for the two possible settings of the DCD. β is the angular deviation from a position in which the glancing angle of the central ray on the second crystal is $\theta(\lambda_0, n_2)$. The deviation of an arbitrary ray (λ, α, ψ) from the central ray is given by

$$\pm\beta \mp \alpha - \frac{1}{2}\psi^2 \tan\theta(\lambda_0, n_2) - (\lambda - \lambda_0)\frac{\partial\theta}{\partial\lambda_0}(\lambda_0, n_2), \qquad 2.5$$

where the upper signs correspond to type I and the lower to type II.

To determine the intensity reflected from the second crystal, for all angles of incident rays, the power in an element of the beam is considered. This element consists of radiation having wavelengths between λ and $\lambda + d\lambda$, and has the horizontal and vertical divergences $d\alpha$ and $d\psi$. The power in such an elementary beam may be written

$$G(\alpha, \psi)J(\lambda - \lambda_0)d\alpha d\lambda d\psi. \qquad 2.6$$

The function G arises from geometrical considerations of the instrument and J gives the distribution of energy in the incident spectrum.

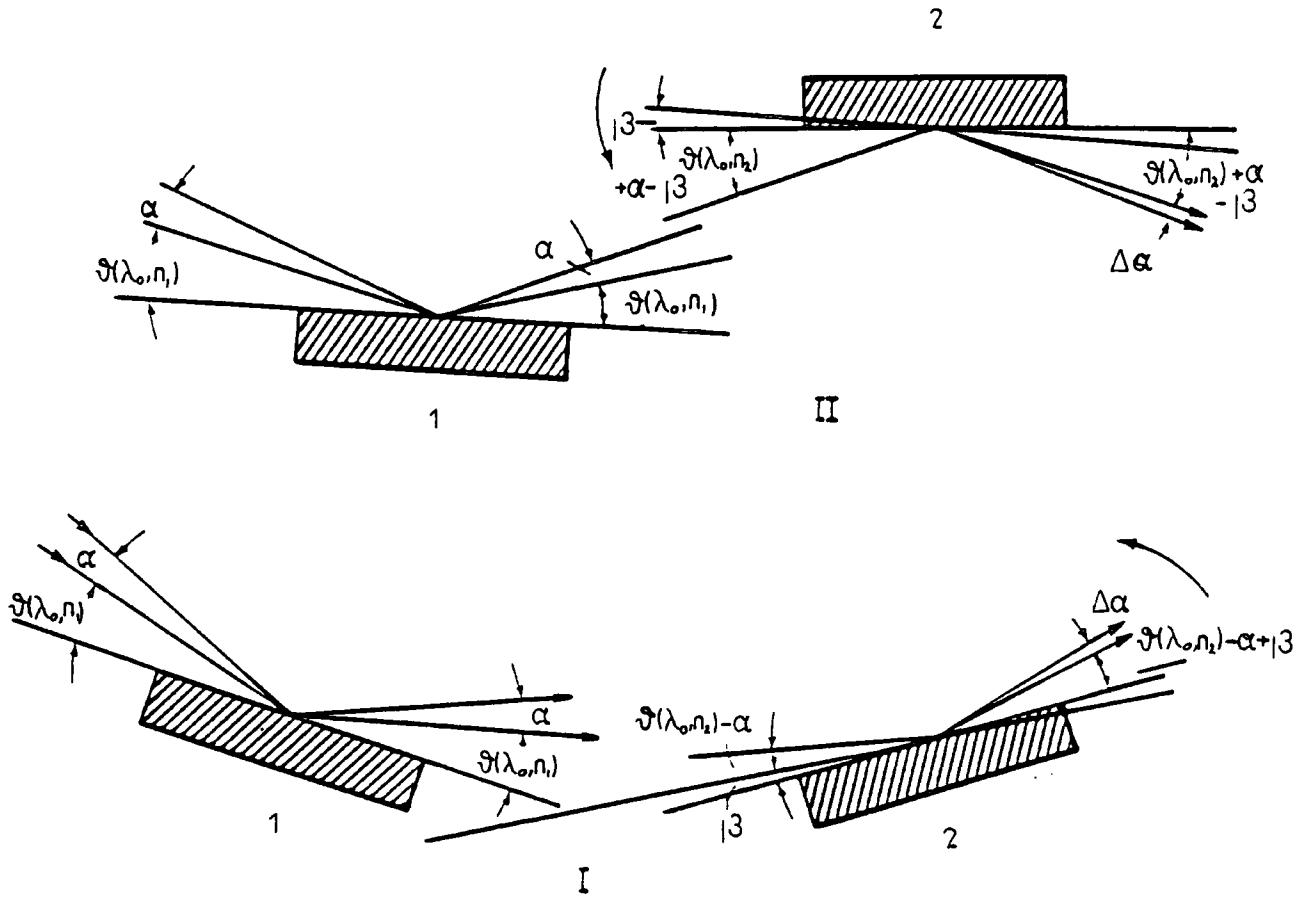

Figure 2.3: X-ray beam paths and angles of the two double crystal diffractometer settings. After Pinsker (1978).

The total integrated intensity reflected from the second crystal is then

$$P(\beta) = \int_{-\psi_m}^{\psi_m} \int_{\lambda_{min}}^{\lambda_{max}} \int_{-\alpha_m}^{\alpha_m} C_1\Big[\alpha - \frac{1}{2}\psi^2 \tan\theta(\lambda_0, n_1) - (\lambda - \lambda_0)\frac{\partial\theta}{\partial\lambda_0}(\lambda_0, n_1)\Big]$$

$$\times C_2\Big[\pm\beta \mp \alpha - \frac{1}{2}\psi^2 \tan\theta(\lambda_0, n_2) - (\lambda - \lambda_0)\frac{\partial\theta}{\partial\lambda_0}(\lambda_0, n_2)\Big] G(\alpha, \psi) J(\lambda - \lambda_0) d\alpha d\lambda d\psi, \tag{2.7}$$

where C_1 and C_2 are expressions corresponding to the reflection curves of the first and second crystals. The rocking curve is then given by $P(\beta)$ over the range of angles required.

The general properties of this equation can be studied by considering the limiting case in which the diffraction patterns of the two crystals are so narrow that the power is only non-zero when the arguments of both C functions are zero. Although this is non-physical it may be used to determine the dispersion of the instrument. Hence

$$\alpha - \frac{1}{2}\psi^2 \tan\theta(\lambda_0, n_1) - (\lambda - \lambda_0)\frac{\partial\theta}{\partial\lambda_0}(\lambda_0, n_1) = 0$$

$$\pm\beta \mp \alpha - \frac{1}{2}\psi^2 \tan\theta(\lambda_0, n_2) - (\lambda - \lambda_0)\frac{\partial\theta}{\partial\lambda_0}(\lambda_0, n_2) = 0$$

Eliminating α gives

$$\beta - \frac{\psi^2}{2}\Big\{\tan\theta(\lambda_0, n_1) \pm \tan\theta(\lambda_0, n_2)\Big\} - (\lambda - \lambda_0)\Big\{\frac{\partial\theta}{\partial\lambda_0}(\lambda_0, n_1) \pm \frac{\partial\theta}{\partial\lambda_0}(\lambda_0, n_2)\Big\} = 0. \tag{2.8}$$

Now define D to be

$$D = \frac{\partial\theta}{\partial\lambda_0}(\lambda_0, n_1) \pm \frac{\partial\theta}{\partial\lambda_0}(\lambda_0, n_2). \tag{2.9}$$

Differentiation of Bragg's law gives

$$D = \frac{n_1}{2d\cos\theta(\lambda_0, n_1)} \pm \frac{n_2}{2d\cos\theta(\lambda_0, n_2)} \tag{2.10}$$

or

$$D = \frac{1}{\lambda_0}\Big\{\tan\theta(\lambda_0, n_1) \pm \tan\theta(\lambda_0, n_2)\Big\}. \qquad 2.11$$

Substitution of equations (2.10) and (2.11) into (2.8) gives

$$\beta = \frac{1}{2}D\lambda_0\psi^2 + D(\lambda - \lambda_0). \qquad 2.12$$

The dispersion of the DCD is defined as $d\beta/d\lambda$, and so, from equation (2.12)

$$Dispersion = \frac{d\beta}{d\lambda} = D.$$

Hence, the dispersion in the parallel arrangement is zero when two identical reflections are used.

We will now consider the parallel (Type II) arrangement, denoted by $(n, -n)$. If both crystal reflections are of first order then the notation becomes $(1, -1)$. For two identical crystals we have $C_1 = C_2 = C$ and $\theta(\lambda_0, n_1) = \theta(\lambda_0, n_2) = \theta$, so that equation (2.7) simplifies to

$$P(\beta) = \int_{-\psi_m}^{\psi_m}\int_{\lambda_{min}}^{\lambda_{max}}\int_{-\alpha_m}^{\alpha_m} G(\alpha,\psi)J(\lambda-\lambda_0)C\Big[\alpha - \frac{1}{2}\psi^2\tan\theta - (\lambda-\lambda_0)\frac{\partial\theta}{\partial\lambda_0}\Big]$$

$$\times C\Big[\alpha - \beta - \frac{1}{2}\psi^2\tan\theta - (\lambda-\lambda_0)\frac{\partial\theta}{\partial\lambda_0}\Big]d\alpha d\lambda d\psi. \qquad 2.13$$

For nearly perfect crystals C is only non-zero over a range of a few seconds of arc. The function $G(\alpha, \psi)$ can be written as

$$G(\alpha,\psi) = G_1(\alpha)G_2(\psi). \qquad 2.14$$

The functions G_1 and G_2 are finite over the range of a few minutes of arc, but since the term $\frac{1}{2}\psi^2\tan\theta$ is very small, the effective region of variation of G_2 is about the same as function C. It can be shown, however, that the shape of the resultant

reflection curve is independent of the vertical divergence of the beam incident on the first crystal in the parallel arrangement (see section 2.4). The effective values of α for any monochromatic component of the beam of wavelength lie very close to the value $(\partial\theta/\partial\lambda_0)(\lambda - \lambda_0)$. The function $P(\beta)$ is only appreciably different from zero over a very narrow range of β. Thus the parallel position rocking curves have widths comparable to those of the diffraction pattern of a single crystal. The effective wavelength range reflected by the second crystal is estimated at

$$\lambda = \lambda_0 \pm \frac{\partial\lambda}{\partial\theta}\alpha_m \ . \qquad 2.15$$

In the parallel position, therefore, the beam entering the detector from the second crystal at any position on the rocking curve contains effective contributions from every wavelength reflected by the first crystal.

Considering the narrow range of the C functions, and the relatively wide ranges of the arguments ψ, α and λ, (the functions G_1, G_2 and J change gradually within seconds of arc), the reflection curve expression can be simplified to

$$P(\beta) = K \int_{-\infty}^{+\infty} C(\alpha)C(\alpha - \beta)d\alpha, \qquad 2.16$$

where K represents the functions G_1, G_2 and J. From inspection of this equation, it should be noted that the reflection curve is symmetrical about $\beta = 0$, even if the curves C are not symmetrical.

For unpolarised radiation, as produced in the characteristic lines of conventional X-ray sources, it is necessary to consider the contribution from both π and σ polarisations. The rocking curve for unpolarised radiation is therefore

$$P(\beta) = K \int_{-\infty}^{+\infty} [C_\sigma(\alpha)C_\sigma(\alpha - \beta) + C_\pi(\alpha)C_\pi(\alpha - \beta)]d\alpha. \qquad 2.17$$

The reflecting power, for this case, is given by

$$R(\beta) = \frac{\int_{-\infty}^{+\infty} [C_\sigma(\alpha)C_\sigma(\alpha-\beta) + C_\pi(\alpha)C_\pi(\alpha-\beta)]d\alpha}{\int_{-\infty}^{+\infty} [C_\sigma(\alpha) + C_\pi(\alpha)]d\alpha} \quad . \qquad 2.18$$

2.3 DuMond Diagrams

The theoretical discussion presented in the previous section, although necessary to the understanding of the double crystal diffractometer, is mathematically complicated and difficult to visualise. It was for this reason that a graphical representation was proposed by DuMond in 1937, which is especially useful if more than two reflections are considered. Figure 2.4 represents a plot of the Bragg equation known as the DuMond diagram. The individual curves correspond to the different orders n of reflection. Since the reflection occurs over a range of angles, a cross section along a line of constant wavelength yields the single crystal reflection curve.

The DuMond diagram may be extended to illustrate any number of crystal reflections. If the case of two identical symmetric crystals is first considered, figure 2.5(a), then it can be seen that an increase in angle of the first crystal corresponds to an equivalent increase in angle of the second. Figure 2.6(a) illustrates the DuMond diagram for this case, with an expanded reflection range. The traces are displaced slightly, corresponding to a small rotation of the second crystal relative to the first. The diffracted intensity corresponds to the area in the overlap of the two perfect crystal DuMond diagrams. Mathematically this is just the convolution of the two perfect crystal reflecting curves calculated from dynamical theory. Since the crystals are parallel, all wavelengths reflected by the first crystal are reflected by the second crystal at the same angle and hence the arrangement is non-dispersive in wavelength. Only a very small angular displacement leads to no wavelengths being doubly diffracted, (figure 2.6(b)), so it is possible to obtain rocking curve widths comparable to the intrinsic single crystal width with this configuration.

The case shown in figure 2.5(b) where the Bragg angles are not equal is illustrated by the DuMond diagram of figure 2.7(a). As the second crystal is rotated

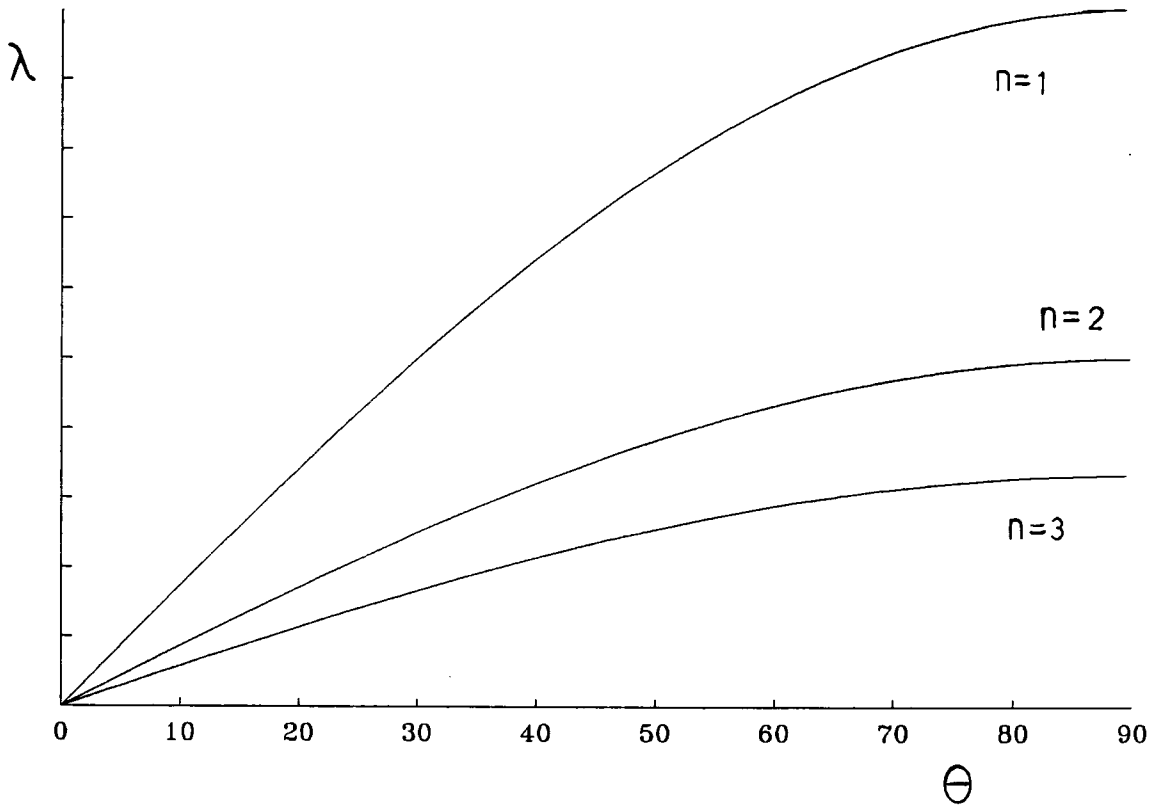

Figure 2.4: The DuMond diagram.

Figure 2.5: Double crystal arrangements.

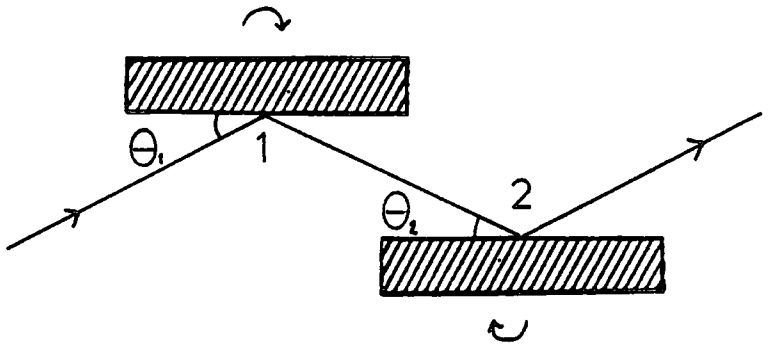

(a) $(n, -n)$ $\theta_1 = \theta_2$, non-dispersive

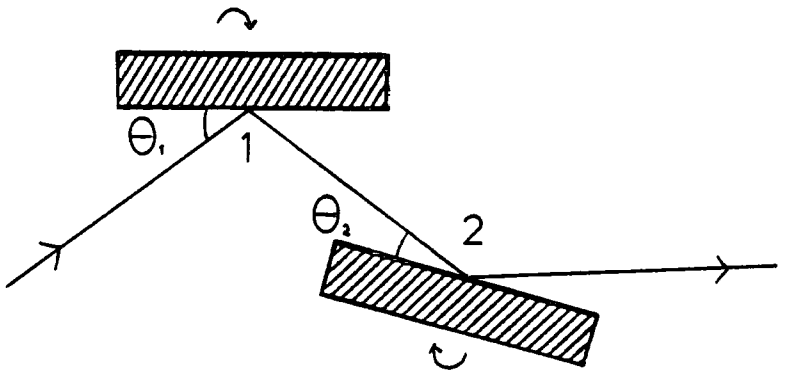

(b) $(n, -n)$ $\theta_1 \neq \theta_2$, dispersive

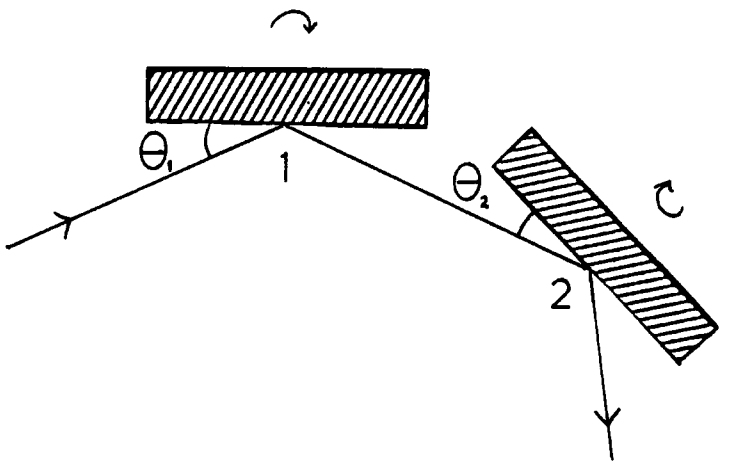

(c) $(n, +n)$ antiparallel, dispersive

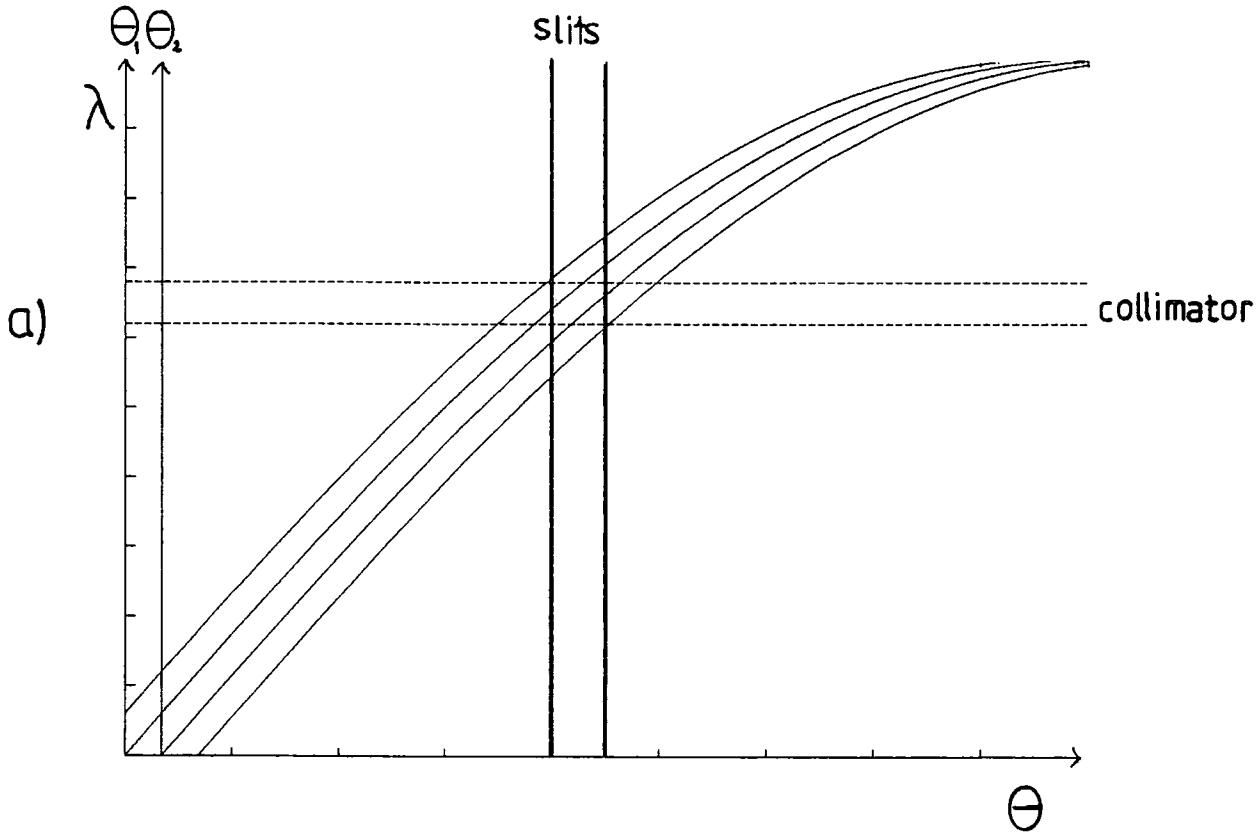

Figure 2.6: DuMond diagram for parallel $\theta_1 = \theta_2$ double crystal arrangement.

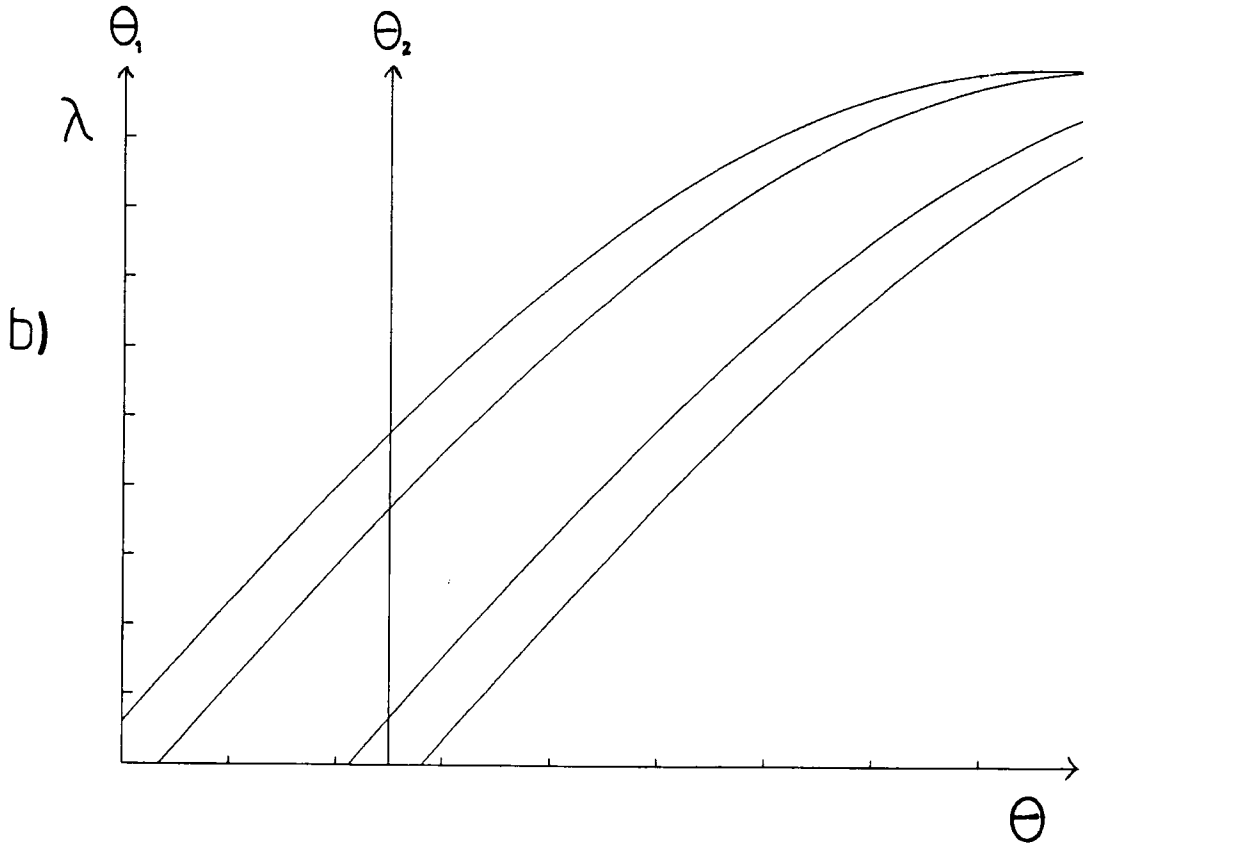

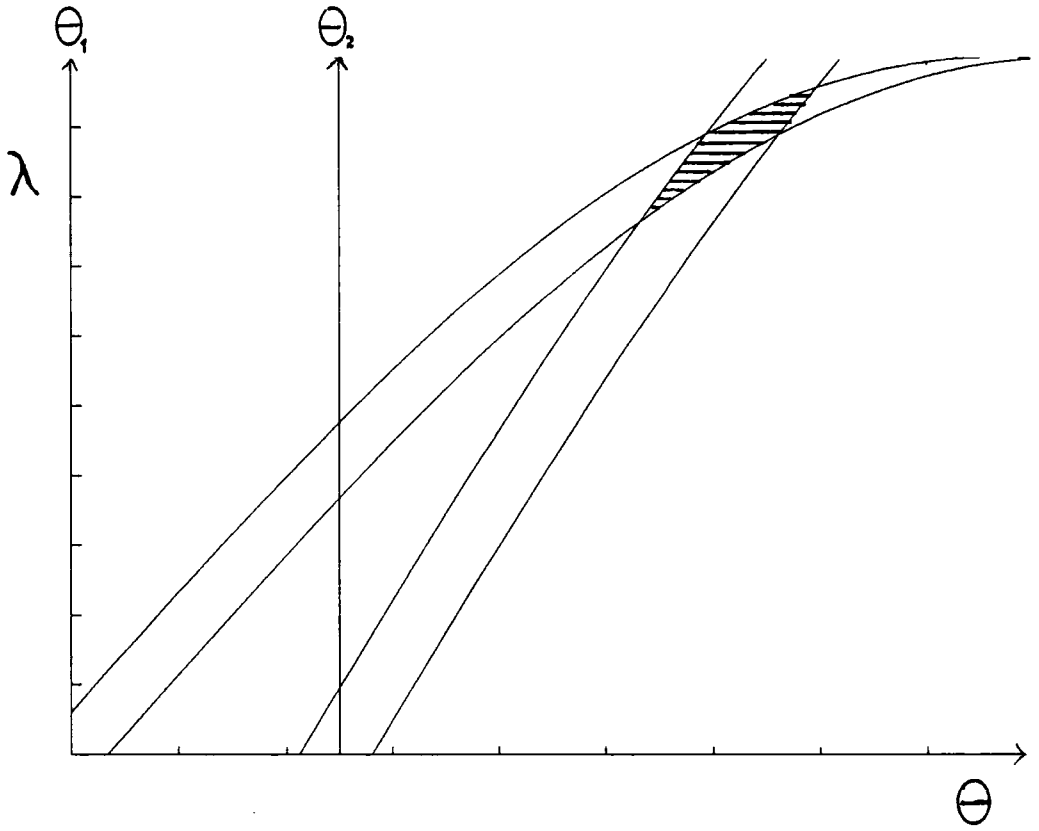

Figure 2.7(a): DuMond diagram for parallel $\theta_1 \neq \theta_2$ arrangement.

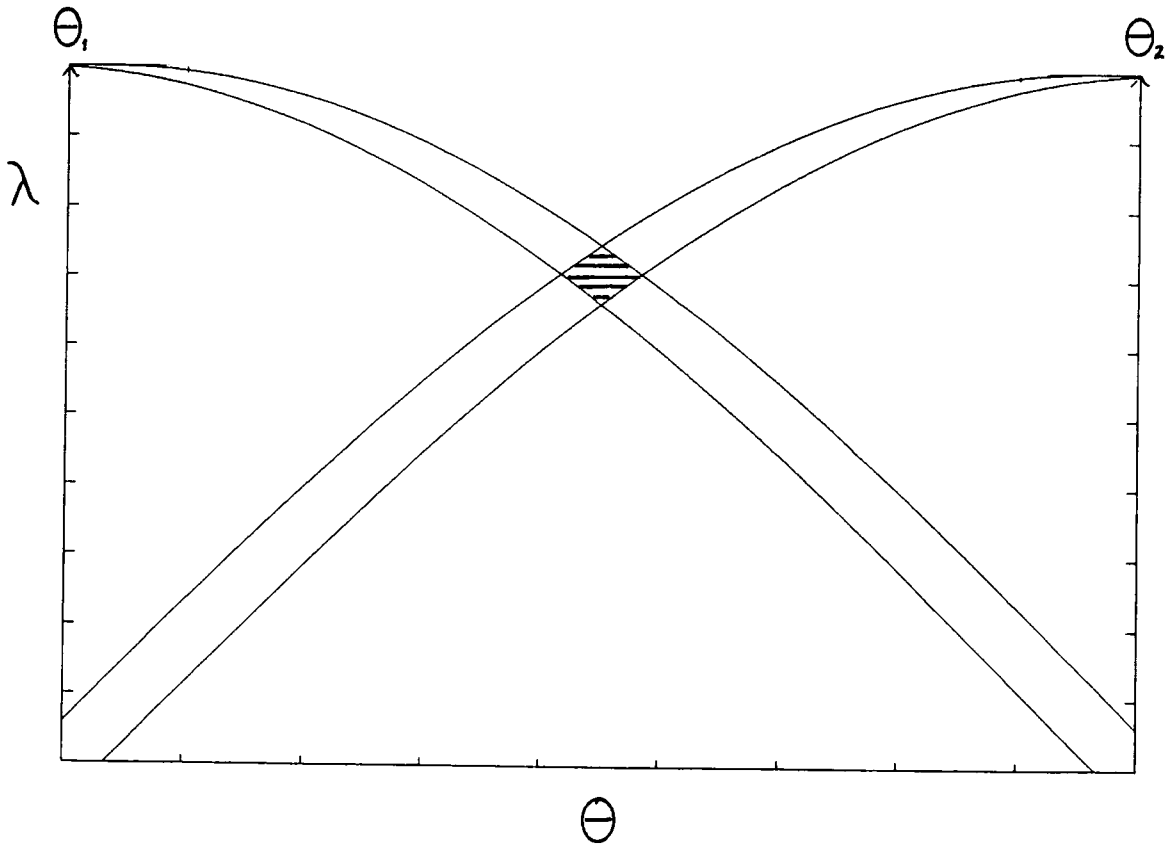

Figure 2.7(b): DuMond diagram for anti-parallel arrangement.

relative to the first, the area of intersection corresponding to diffracted intensity changes in wavelength. Hence this arrangement is dispersive in wavelength.

Figure 2.5(c) illustrates the antiparallel arrangement $(n, +n)$, where an increase in the angle of incidence on the first crystal corresponds to a decrease in the angle of the second for a Bragg reflection. Again, using the DuMond diagram shown in figure 2.7(b) a rotation of the second crystal results in a change of wavelength diffracted. This arrangement is also dispersive in wavelength and the magnitude of this dispersion is given in equation (2.11). Depending on the degree of dispersion in the arrangement, individual wavelengths may be resolved such as the $K\alpha_1$ and $K\alpha_2$ doublet on the rocking curve (Schnopper, 1965; Schumacher, 1987; Li and Xu, 1988).

2.4 The Effect of Vertical Divergence on the Rocking Curve

The DuMond diagrams presented so far have not included the effects of vertical divergence of X-ray beams. Even though DuMond considered total reflection due to dynamical scattering in the formation of a rocking curve, he did not put it into his λ-θ diagram, so the details of a rocking curve cannot be fully explained by a two dimensional λ-θ DuMond diagram.

Recently, the range of total reflection has been added to a DuMond diagram for a certain wavelength, and Yoshimura (1984) has discussed mathematically the influence of vertical divergence in DCD's. In order to include this, a three dimensional (3D) DuMond diagram can be constructed with three coordinate axes representing vertical divergence, horizontal divergence and X-ray wavelength. Xu and Li (1988) have used 3D DuMond diagrams to analyse successive diffraction of multiple crystals. The extent of the 3D DuMond diagram along the ψ, θ and λ axes represents the vertical and horizontal divergences, and wavelength dispersion respectively of X-rays emitted from the source, passing through a slit, and accepted or reflected by a crystal. DuMond diagrams of an X-ray source and slit are shown in figures 2.8(a) and (b), and a single crystal with the range of reflection exaggerated is shown in figure 2.8(c). Xu and Li have used these diagrams to graphically determine the effect of vertical divergence on double crystal diffractometers and have derived an expression for the resolution of a DCD.

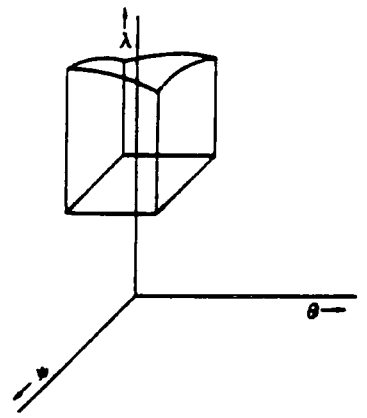

Figure 2.8(a): Three-dimensional DuMond diagram of an X- ray source.

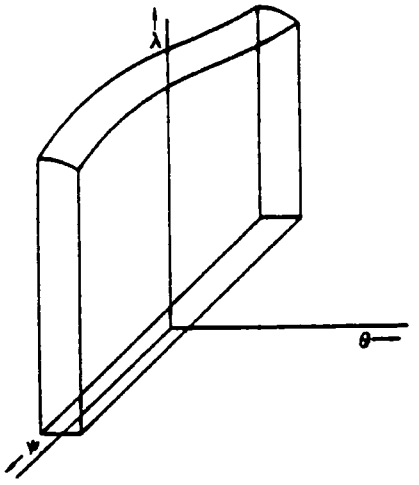

Figure 2.8(b): Three-dimensional DuMond diagram of a vertical slit.

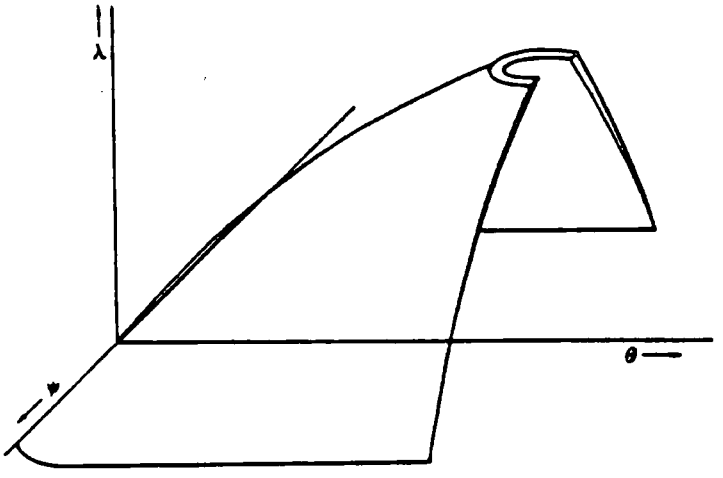

Figure 2.8(c): Three-dimensional dynamic DuMond diagram, where $\chi = 0$. After Xu and Li (1988).

Yoshimura (1984) has considered the effect of vertical divergence mathematically and for a full description the reader is referred to his paper. Hill (1985) also presents a summary of his work. A graph of vertical divergence, ψ, against the change in crystal angle, θ, required to diffract a beam with value W is shown in figure 2.9 for two silicon (333) reflections in the parallel setting $(+,-)$ for $CuK\alpha_1$, with varying values of the tilt angle, χ. The vertical divergence, ψ, is defined to be the vertical coordinate of the incidence beam on the first crystal divided by the distance to the X-ray source (for small angles) i.e. half of the full beam divergence. W represents the deviation from the exact Bragg angle, i.e. $-1 < W < 1$ corresponds to the total reflection range. The rocking curve for a particular divergence is given by traversing the curve along a line $y = \psi$ parallel to the θ axis. If there is no tilt, $\chi = 0$, the vertically divergent beam can be diffracted over its entire length with the same intensity. The curve for a non-parallel $(+,+)$ arrangement, with $Si(111)$ and $Si(220)$ reflections, is shown in figure 2.10. As can be seen the wavelength and parameter W vary rapidly with ψ along the line $\theta = 0$, and the distribution of high diffraction intensity is limited to a narrow vertical range. For a beam with a zero vertical coordinate on the first crystal the value of divergence is $\psi = 0$. The relationship between the tilt of the second crystal relative to the first, χ, and the value of θ for a beam with a zero vertical coordinate is shown in figure 2.11. This curve has been used to aid the rapid alignment of the double crystal arrangement to zero tilt (Fewster, 1985). The value of θ increases with either positive or negative tilt, and the curve becomes broader. In order to minimise the rocking curve width θ should be adjusted to a minimum. Yoshimura (1985) has shown that the half width of the rocking curve is related to the half width at zero divergence by

$$\omega = \frac{\omega(\psi = 0)}{[1 - \psi^2/\cos^2\theta_B]^{\frac{1}{2}}} \qquad 2.19$$

if the two reflection curves are assumed to be Gaussian and $\psi \ll 1$.

Wavelength dispersion is very small when both crystals are aligned in the parallel $(n,-n)$ configuration and the dominant broadening mechanism arises from tilt misalignment. Ignoring refraction and dynamical effects Schwarzschild

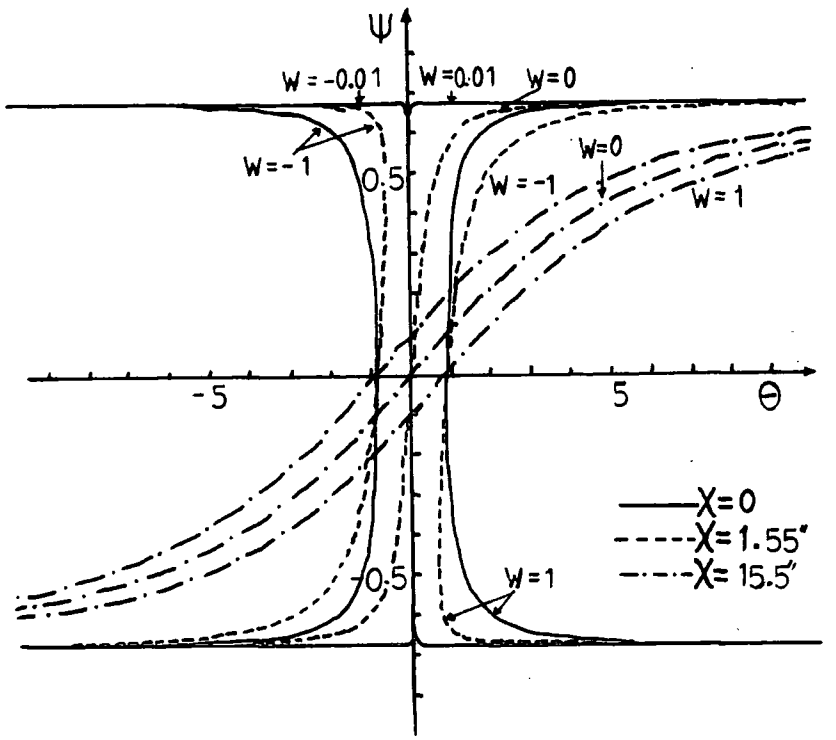

Figure 2.9: The change in crystal angle (θ) required to diffract a beam with value W as a function of ψ, the position of the incident beam on the first crystal, for a parallel $(+,-)$ setting with two silicon (333) reflections and CuK_{α_1} radiation, for varying values of χ the tilt angle. After Yoshimura (1984).

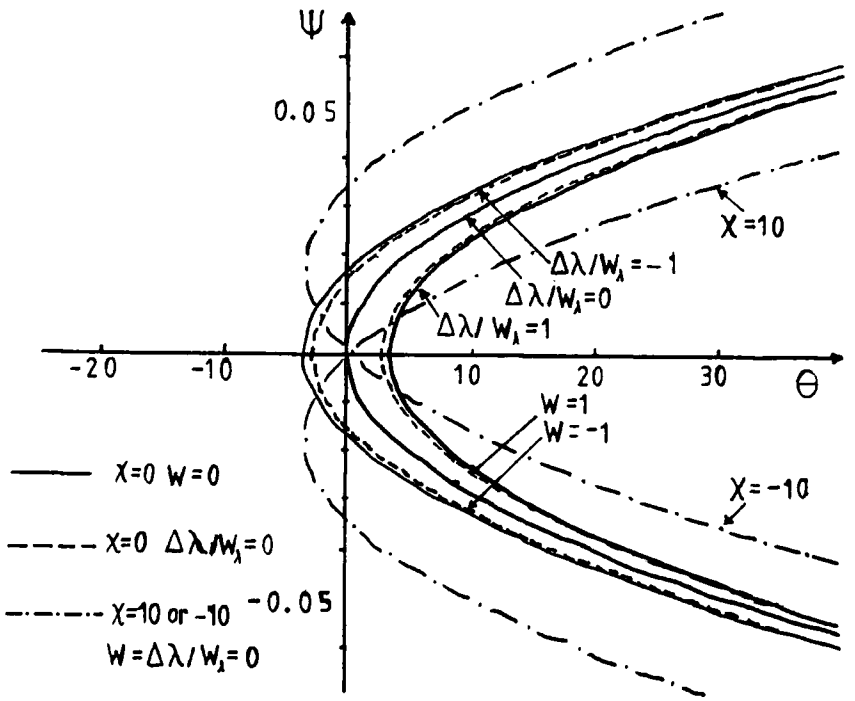

Figure 2.10: Curve of ψ vs (θ) for a non- parallel $(+,-)$ setting with $Si(111)$ and $Si(220)$ reflections. CuK_{α_1} radiation with the abscissa scaled in units of 1.55 arc seconds. After Yoshimura (1984).

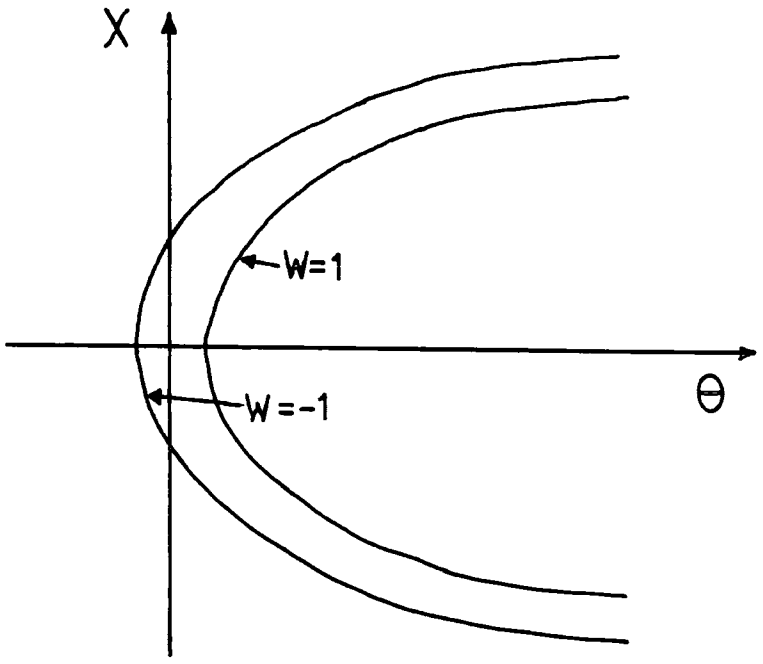

Figure 2.11: Change in angle θ required to give the centre of Bragg reflection with tilt angle χ. After Fewster (1985).

(1928) showed that the half width due to purely geometrical effects could be related to the tilt angle, χ, by

$$\omega_{\frac{1}{2}} = 2\chi\psi \qquad for \quad \chi > \psi(\tan\theta_1 \pm \tan\theta_2)$$

$$\omega_{\frac{1}{2}} = M\psi^2 + \chi\psi + \frac{\chi^2}{4M} \qquad for \quad \chi < 2M\psi, \tag{2.20}$$

where $M = \frac{1}{2}(\tan\theta_1 \pm \tan\theta_2)$ with the upper sign for the $(+,+)$ setting and the lower for the $(+,-)$ setting. For the parallel setting $M = 0$, so the geometrical half width varies linearly with tilt angle. For the dispersive setting the tilt broadening is usually small compared to dispersion broadening.

2.5 The Triple Crystal Diffractometer

The double crystal diffractometer offers a substantial improvement over a single crystal diffractometer essentially because of greater resolution. If a parallel arrangement is chosen wavelength dispersion disappears and rocking curves of width comparable to the perfect single crystal can be obtained. However, there is one essential limitation, sample curvature. Most epitaxial structures accommodate the lattice mismatch of the layer by tetragonal distortion, and as a result mismatched samples are curved. Effectively therefore, the sample crystal will satisfy the Bragg condition over a larger range of angles for a finite X-ray spot size. This has the effect of broadening the rocking curves and obscuring any interesting fine structure. One way of overcoming this problem is a fine slit over the detector which selects only those rays diffracted at the correct angle, and scanning the second crystal and detector in a θ-2θ scan. Unfortunately, this significantly reduces the recorded intensity. The solution is the triple crystal diffractometer first proposed by Renninger in 1955. The third crystal, known as the analyser, causes many of the resolution degrading effects of the DCD to simply disappear.

A major problem of the DCD is the collection of diffusely scattered radiation in addition to the Bragg diffracted intensity. TCD removes this problem and so gives rocking curves of higher sensitivity. The wide detector angle of the

DCD geometry integrates the thermal diffusely scattered intensities in a correspondingly wide angular range. TCD registers only the intensity in the angular interval of the width of the analyser reflection curve. The use of a perfect analyser crystal therefore allows the investigation of the angular distribution of the radiation dynamically diffracted by the sample and the angular separation of dynamical and diffuse intensities. Figure 2.12 shows a comparison of DCD and TCD curves taken from a sample of ion implanted silicon by Zaumseil, Winter, Cembali, Servidor and Sourek (1987). The fine structure oscillations are not visible with the DCD because of the higher diffuse background and the effects of curvature.

Figure 2.13 shows the crystal arrangement of the TCD in the $(n, -n, n)$ configuration with the Bragg angles for the monochromator, sample and analyser being θ_m, θ_s and θ_a respectively. Using the notation of Ryan (1986), the two instrument variables are Ψ, the sample crystal rocking angle, and Φ, the analyser detector angle. θ_m and θ_a remain fixed throughout a measurement.

The essential feature of the TCD is that it is sensitive only to the angle and wavelength of the scattered X-ray beam. In other words the instrument probes reciprocal space. The double crystal instrument, however, is also sensitive to the position of the scattered beam so that the resolution of the instrument depends on many geometrical factors such as source size and intensity distribution, slits and sample curvature. These effects simply vanish with the adoption of an analyser crystal.

The main resolution degrading effects of a TCD are the horizontal divergence and wavelength spread of the incident beam, α and $\Delta\lambda$ respectively; the angular range through which the sample and analyser crystals satisfy the Bragg condition $\Delta\theta_s$ and $\Delta\theta_a$ respectively, and the vertical divergence ψ. Following the same approach as section 2.2 the wavelength dispersion of the TCD is given by

$$\frac{d\Phi}{d\lambda} = \frac{1}{\lambda}[\tan\theta_1 - 2\tan\theta_2 + \tan\theta_3] \ . \qquad 2.21$$

The most common configuration used is the $(+1, -n, +1)$, with $\theta_m = \theta_a$. Hence,

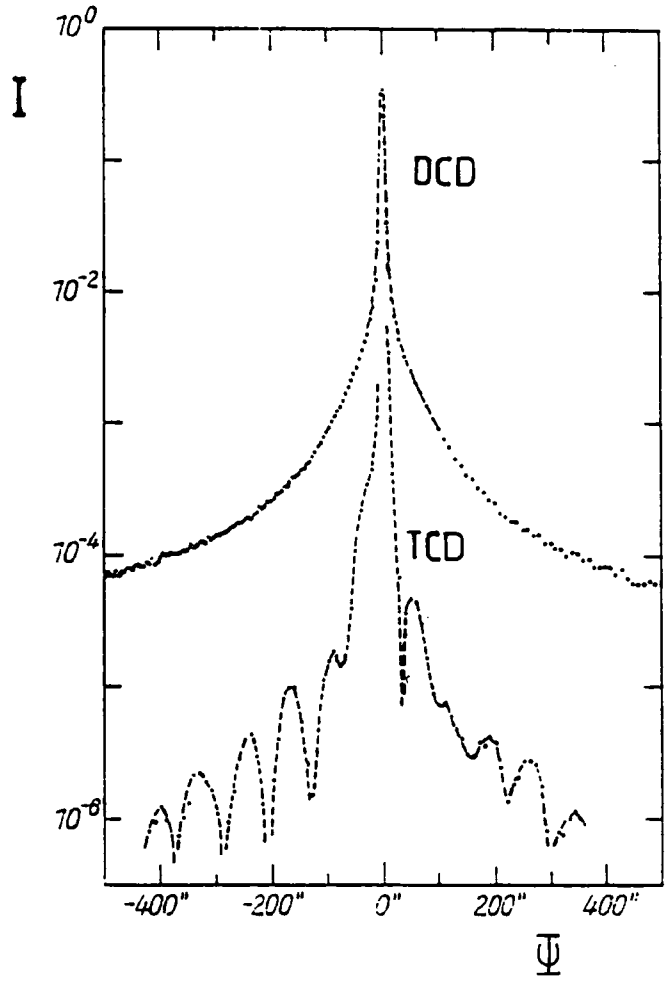

Figure 2.12: Comparison of DCD and TCD curves taken from a sample of ion implanted silicon. After Zaumseil et al (1987).

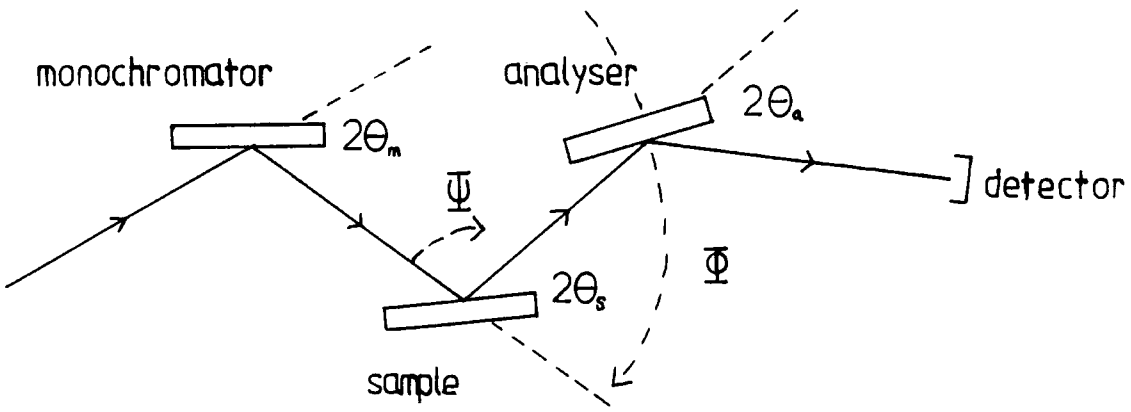

Figure 2.13: Arrangement of the triple crystal diffractometer.

the dispersion relationship simplifies to

$$\frac{d\Phi}{d\lambda} = \frac{2}{\lambda}[\tan\theta_1 - \tan\theta_2] \; . \qquad 2.22$$

When $\theta_m = \theta_s = \theta_a$, $\tan\theta_1 = \tan\theta_2$ and the dispersion becomes zero. This is known as the focusing, or $(+1,-1,+1)$ configuration, which totally eliminates wavelength dispersion.

The main resolution degrading effects may be transformed from real to reciprocal space in which they are more easily defined. Scattering in reciprocal space is extended in the direction normal to the surface, and as discussed by Andrews and Cowley (1985), this so called "surface streak" or "crystal truncation rod" contains important information on the topography of the crystal surface. The locus of the surface streak is well defined in reciprocal space but less well defined in Ψ/Φ space, depending as it does on the geometrical relationship between the scattering vector and the crystal surface.

Figure 2.14 shows a contour map in reciprocal space of a TCD focusing $(+1,-1,+1)$ configuration using $Si(111)$ monochromator, sample and analyser crystals (Ryan, 1986). The star shape is characteristic of TCD patterns with a conventional generator and single reflection beam conditioner and analyser crystals (Lucas, Garstein and Cowley, 1989).

2.6 Four Crystal Monochromators and N-Crystal Diffraction

The use of N-reflection monochromators was first proposed by DuMond (1937), although it was not until 1974 when Beaumont and Hart (1974) first studied multiple reflection monochromators experimentally using synchrotron radiation. Four reflection monochromators in particular, have since been used by Bartels (1983); Vandenberg, Hamm, Panish and Temkin (1987); Slusky and Macrander (1987); Fewster (1989); and Lyons, Scott and Halliwell (1989).

The TCD has been shown to give an improvement over the DCD in angular resolving power but no great improvement in spectral resolving power. If the instruments use two different crystals or reflections for instance, even in the $(n,-n)$ and $(n,-n,n)$ arrangements, significant peak broadening can occur from

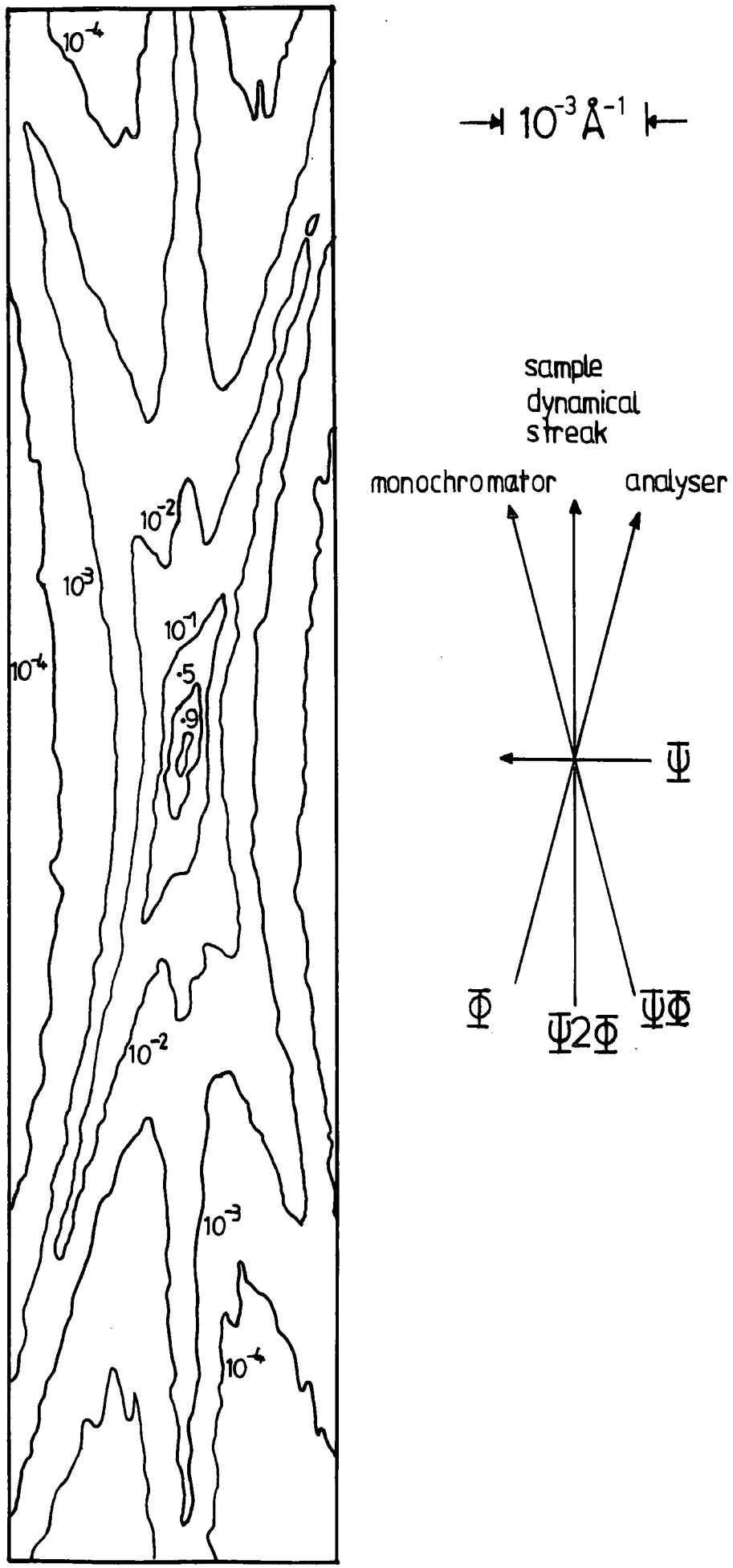

Figure 2.14: Triple crystal diffractometer contour map in reciprocal space with $Si(111)$ monochromator, sample and analyser crystals and a focussing $(+1,-1,+1)$ configuration. $CuK\alpha_1$, $\theta_m = \theta_s = \theta_a = 14.22°$. After Ryan (1986).

spectral dispersion (Nakayama et al., 1972). They therefore have the serious limitation that only one particular Bragg reflection from one particular sample material may be studied, without significantly changing arrangements, with high resolution. This lack of versatility may be overcome with a four crystal monochromator.

Figure 2.15 shows the arrangement of a four crystal monochromator in the $(+1,-1,-1,+1)$ geometry generally used. The first pair of crystals act as a DCD, allowing the whole spectral distribution to pass. The third crystal, however, is set in a non-parallel way, and only a small range of wavelengths can satisfy the Bragg condition for any fixed angle. The fourth crystal reflects the monochromatic beam back into its original direction. A DuMond diagram illustrating this is shown in figure 2.16(a), with the region of intersection expanded in 2.16(b). The reduction in size of the diamond shaped window at the fourfold intersection on the DuMond diagram means a serious reduction in available X-ray intensity. However, due to the decrease in the intensity of the tails of the rocking curve and reduction in the instrument background, the signal to noise ratio is effectively enhanced to allow sensitive study of weak scattering effects. Also, the shape of the rocking curve of a specimen can be shown to be independent of the vertical divergence (Bubáková, Drahokoupil and Fingerland, 1961), and so the full height of the beam may be used.

Slusky and Macrander (1987) have derived an expression for the reflecting power of the five crystal diffractometer for each of the configurations shown in figure 2.17. This expression is necessary for the simulation of five crystal rocking curves. Figure 2.18 shows the expanded DuMond diagrams from the two settings. The diamond shaped intersection of the four crystal curves illustrates the high spectral and angular resolution of the instrument. The extra band of intersection arises from the sample crystal.

The four crystal monochromator, therefore, solves the problems associated with angular and spectral dispersion, and there are no restrictions on studying any reflections, but it still does not overcome the problems associated with a curved sample. If a crystal is bent, then it will diffract over an angle given by that expected convoluted with a shape function. The shape function is given by

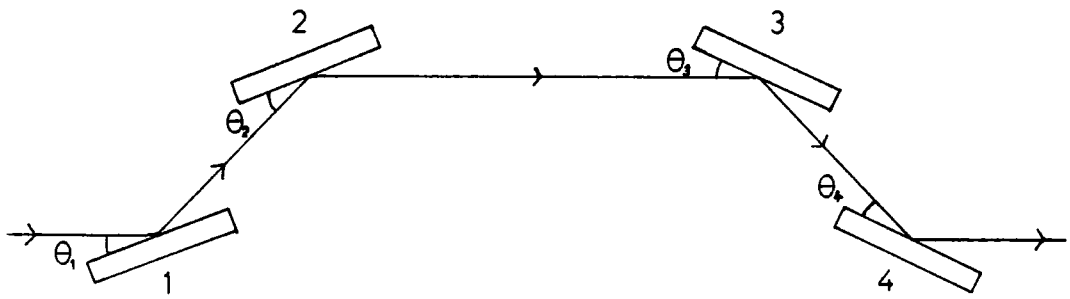

Figure 2.15: The four crystal monochromator in the $(+1, -1, -1, +1)$ configuration.

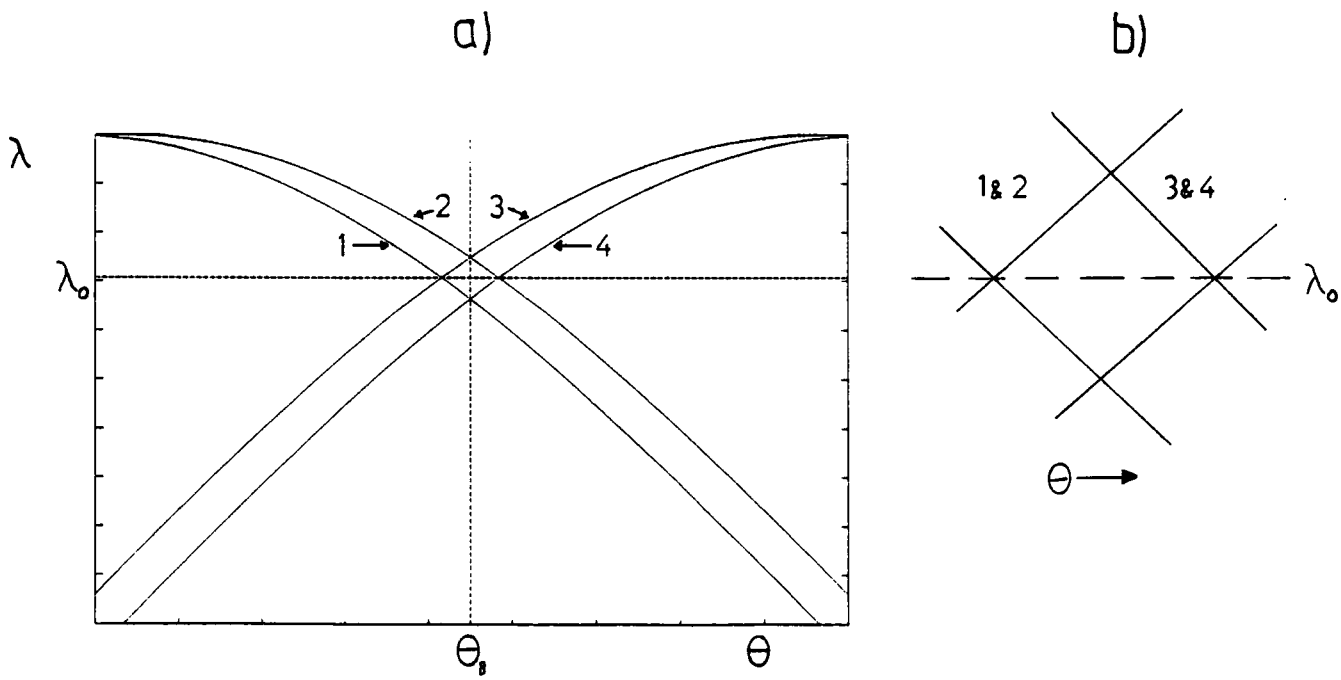

Figure 2.16: DuMond diagram of a four crystal monochromator.

(a) $(+,-,-,+,-)$ (b) $(+,-,-,+,+)$

Figure 2.17: Five crystal diffractometer arrangements

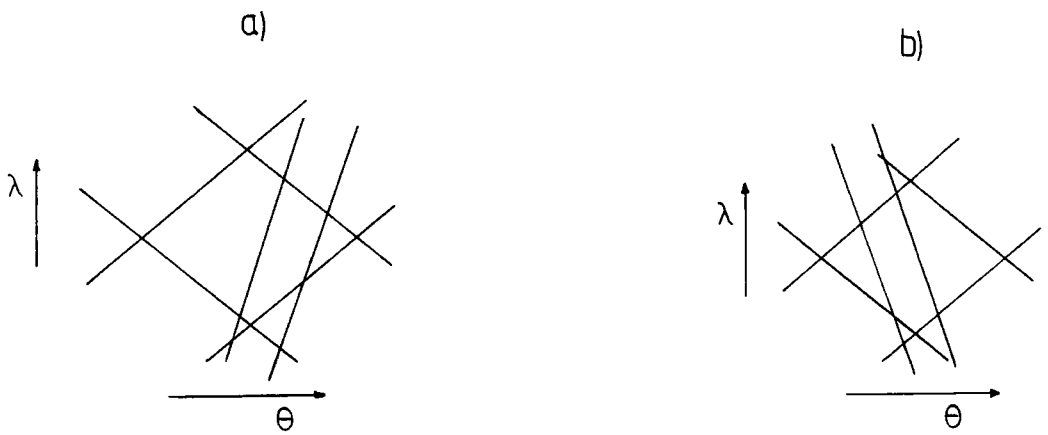

Figure 2.18: Expanded DuMond diagrams of the five crystal diffractometer arrangements shown in figure 2.17.

the intensity over the wavelength distribution $\Delta\lambda$, (Fewster, 1989),

$$\Delta\lambda = \lambda(\cot\theta)\xi \ , \qquad 2.23$$

where ξ = (length sampled in the diffraction plane)/(radius of curvature), neglecting vertical divergence effects. The problem is solved by combining the qualities of the TCD with a four crystal monochromator, to produce a six crystal diffractometer (Fewster, 1989). There are two possible modes of operation. In the first, the sample and analyser rotations are coupled to obtain near perfect rocking curves from distorted crystals, and in the second mode the two axes are decoupled to obtain a map of reciprocal space to study diffuse scattering. The result is a very high resolution instrument, with the ability to use any sample type or reflection without fear of dispersion broadening, and which enables the study of curved specimens.

Chapter III

X-Ray Scattering Theory

3.1 Dynamical Theory

An elementary treatment of X-ray scattering, known as kinematical theory, has been dealt with by many authors (James, 1948; Warren, 1969). It assumes that the amplitudes of the scattered waves are small compared with the incident wave amplitude. When crystals are small and for heavily deformed crystals having a mosaic structure, kinematical theory describes the scattering satisfactoraly. However, for large perfect single crystals the amplitude of the diffracted wave becomes comparable with that of the incident beam. In this situation, interchange of energy occurs between the beams as they pass through the crystal and kinematical theory cannot be applied. The occurrence of multiple scattering and absorption can be explained using Dynamical theory.

The first dynamical theory of X-ray diffraction was given by Darwin (1914), while a different treatment was presented independently by Ewald (1916,1917). Von Laue (1952) reformulated the Ewald treatment as a problem involving the solution of Maxwell's equations for a medium with a periodic complex dielectric constant. General introductions to the different forms of dynamical theory can be found in books by James (1948); Zachariasen (1945) and Pinsker (1978), and reviews have been given by Batterman and Cole (1964); Authier (1970) and Hart (1971,1980). The reader is referred to these works for a full description of dynamical theory.

For a Bragg reflection to occur, there will exist two waves inside the crystal whose difference in wave-vector is exactly equal to the reciprocal lattice vector corresponding to the Bragg reflecting planes. Therefore, inside the crystal a standing wavefield is set up whose spacing and orientation are exactly those of the diffracting planes. These are known as Bloch waves which form coherent solutions to Maxwell's equations. For a two beam approximation, where it is

assumed that only one Bragg reflection is excited for a given wavelength and angle, the dispersion surface linking the incident and scattered wave-vectors may be derived. Each point on the dispersion surface determines the allowed wave-vectors in the crystal and the amplitude ratio of the component plane wave in the Bloch wave.

In order to determine what is occurring outside the crystal when the crystal is excited by a plane wave, it is necessary to match wave-vector and wave amplitude at the surface. The boundary conditions for field vectors are that the tangential components of both $\underline{E}$ and $\underline{H}$ are continuous across the surface. Since the refractive index for X-rays is close to unity, the reflection amplitude at the crystal surface is negligible provided that the glancing angle is not comparable with the critical angle of total external reflection. This means that, to a very good approximation, all of the field vectors are continuous across the crystal surface. As well as amplitude matching, the components of the wave-vectors inside and outside the crystal must be the same. The dispersion surface is very useful in viewing these conditions geometrically.

Several important results arise from the dynamical theory treatment. The full width at half maximum of the Bragg reflection peak, for instance, is given by

$$\Delta\theta_{\frac{1}{2}} = \frac{2C(\chi_h\chi_{\bar{h}})^{\frac{1}{2}}}{\sin 2\theta_B}\sqrt{\frac{|\gamma_h|}{\gamma_0}} \ , \qquad 3.1$$

where C is the polarisation factor (1 for σ and $\cos 2\theta_B$ for π polarisations) and θ_B is the Bragg angle. γ_0 and γ_h are the direction cosines of the incident and diffracted beams respectively, while χ_h and $\chi_{\bar{h}}$ are the complex susceptibilities given by

$$\chi_h = \frac{-e^2\lambda^2}{\pi mc^2 V}F_h \ . \qquad 3.2$$

F_h is known as the structure factor which is a number dependent on the arrangement of atoms in a unit cell, essentially the scattering power of a material, and is given by

$$F_{hkl} = \sum_n f_n e^{2\pi i(hx_n+ky_n+lz_n)} \ . \qquad 3.3$$

The summation is over the n atoms within a unit cell where x_n, y_n and z_n are the fractional coordinates of individual atoms and f_n is the atomic scattering factor. For example, for InP which has a zinc-blende type crystal structure, the structure factor for an hkl reflection is given by

$$F_{hkl}^2 = 16(f_{In} + f_P)^2 \qquad hkl \quad even \qquad h+k+l = 4n$$

$$F_{hkl}^2 = 16(f_{In} - f_P)^2 \qquad hkl \quad even \qquad h+k+l = 4n+2$$

$$F_{hkl}^2 = 16(f_{In}^2 + f_P^2) \qquad hkl \quad odd$$

$$F_{hkl}^2 = 0 \qquad hkl \quad mixed.$$

For instance, the 004 is an allowed reflection, while the 002 is quasi-forbidden and the 112 is totally forbidden.

The integrated intensity, when absorption is neglected, of a single crystal rocking curve is given by

$$I = \frac{8}{3}|C|\frac{\chi_h}{\sin 2\theta}\sqrt{\frac{|\gamma_h|}{\gamma_0}}\,. \tag{3.4}$$

The intensity is therefore proportional to the structure factor for dynamical diffraction, compared to the square of the structure factor in kinematical diffraction. The refractive index of the crystal causes a shift in the position of the Bragg peak compared to the position expected from Bragg's law. This shift is given by

$$\Delta\theta = \frac{|\chi_0|}{2\sin 2\theta}\left(1 + \frac{|\gamma_h|}{\gamma_0}\right). \tag{3.5}$$

As a result of interference between the two wave-fields propagating within the crystal, oscillations known as Pendellösung fringes occur on the rocking curve, which were first observed by Batterman and Hilderbrandt (1968). The angular spacing of the Laue case Pendellösung fringes is given by

$$\delta\theta = \frac{\lambda(\gamma_0|\gamma_h|)^{\frac{1}{2}}}{Ct(\chi_h\chi_{\bar{h}})^{\frac{1}{2}}}\,, \tag{3.6}$$

where t is the thickness. The length $\lambda(\gamma_0|\gamma_h|)^{\frac{1}{2}}/C(\chi_h\chi_{\bar{h}})^{\frac{1}{2}}$ is known as the extinction distance, and corresponds to the separation of the maxima of the wavefield excited within the crystal due to the interference of the two Bloch waves propagating in the crystal. If absorption is included, the Bragg case Pendellösung oscillations become rapidly damped as the thickness of the crystal is increased; hence these fringes are only seen in thin crystals.

Clearly, the approach of dynamical theory could be used to calculate the rocking curve from a layered sample by matching the wave-vectors at each interface. However, this approach would be extremely laborious, especially for multi-layered or graded samples. A much simpler approach, which is well suited to computation, is to use the differential equations of Takagi (1962,1969) and Taupin (1964). Unfortunately, since only incident and diffracted wave amplitudes are retained at each interface, it is not possible to visualise physically what is occurring within the crystal.

3.2 The Takagi - Taupin Equations

For a full description of the derivation of Taupin (1964) the reader is referred to Pinsker (1978). A summary of the physics involved is given here.

We assume that the electric displacement vector in a vacuum, given by

$$\underline{D} = \underline{D}_0(\underline{r})exp\Big\{i[\omega_0 t - 2\pi\Phi_0(\underline{r})]\Big\} \qquad 3.7$$

is a plane wave, so that

$$\Phi_0(r) = \underline{k}_0.\underline{r}\ , \qquad |\underline{k}_0| = \frac{1}{\lambda}\ . \qquad 3.8$$

In the general case $\underline{D}$ satisfies the wave equation in a vacuum

$$\nabla^2\underline{D} + \frac{\omega_0^2}{c^2}\underline{D} = 0\ . \qquad 3.9$$

Considering spherical waves for which the radii of curvature are much larger than the wavelength λ, we have

$$|grad\Phi_0| \simeq \frac{1}{\lambda}\Big[1 + 0(\frac{\lambda^2}{R^2})\Big] \qquad 3.10$$

where $0(\lambda^2/R^2)$ represents small terms of higher orders of λ/R. For a nearly plane incident wave we have

$$grad\Phi_0 = \underline{k}_0 + \Delta\underline{k}_0 \qquad 3.11$$

and $\underline{k}_0.\Delta\underline{k}_0 = 0$, $|\Delta\underline{k}_0| \ll |\underline{k}_0|$, so that from (3.10) we have

$$|\underline{k}_0| = \lambda^{-1} , \qquad |\Delta\underline{k}_0| = R^{-1} , \qquad 3.12$$

corresponding to an incident wave packet with an angular width of the order of $1/R$.

The function $\underline{D}_0$ is retained for the phase when describing the wave inside the crystal. The amplitude $\underline{D}_0$ becomes a complex function of the coordinates, which is dependent on the differences in the paths of propagation in the crystal and the vacuum. The wavefield in the crystal can be described through the use of a variable amplitude Bloch function,

$$\underline{D} = \sum_m \underline{D}_m exp\Big\{ i[\omega_0 t - 2\pi(\underline{k}_m.\underline{r})] \Big\} . \qquad 3.13$$

For a perfect crystal and plane waves the following values remain constant

$$\underline{k}_m = \underline{k}_0 + \underline{h}_m , \qquad \underline{k}_0 = grad\Phi_0 . \qquad 3.14$$

However, generally $\underline{k}_0$ and $\underline{h}_m$ are functions of the coordinates. For each point in the crystal the vector $\underline{h}_m$ can be determined.

If the planes in a crystal, denoted by n_m, are regarded as a continuous function of the coordinates which takes integral values on each plane m, we find

$$\underline{h}_m = grad\ n_m \qquad 3.15$$

$$\underline{D} = \sum_m \underline{D}_m exp[i(\omega_0 t - 2\pi\Phi_m)] \qquad 3.16$$

where

$$\Phi_m(\underline{r}) = \Phi_0(\underline{r}) + n_m(\underline{r}) \ . \qquad 3.17$$

The dielectric constant remains a periodic function of the coordinates, but $\epsilon(\underline{r})$ can be approximately assumed to be an exponential function of n_m in each system of reflecting planes. The susceptibilities can therefore be written

$$\chi(\underline{r}) = \sum_m \chi_m exp[-2\pi i n_m(\underline{r})] \qquad 3.18$$

$$\chi_m \equiv \chi_{h_m} = -\frac{e^2}{mc^2}\frac{\lambda^2}{\pi V}F_{h_m} \ , \qquad 3.19$$

and for the general case of an absorbing crystal

$$\chi_0 = \chi_{0_r} + i\chi_{0_i} \ , \qquad \chi_h = \chi_{h_r} + i\chi_{h_i} \ . \qquad 3.20$$

The variable representing the angular departure from the Bragg condition is taken as

$$\alpha_m = 2\Delta\theta_m \sin 2\theta_m \ , \qquad 3.21$$

which is derived from the approximate values of the expressions

$$\alpha_m = k_0^{-2}[h_m^2 + 2(\underline{k}_0.\underline{h}_m)] = \lambda^2\left(\frac{1}{d_m^2} - \frac{2\sin\theta_m}{\lambda d_m}\right), \qquad 3.22$$

where both d_m and $\sin\theta_m$ are coordinate dependent.

The wave equation inside the crystal is derived from Maxwell's equations, which are

$$curl\ \underline{E} = -\frac{1}{c}\frac{\partial \underline{H}}{\partial t} \ , \qquad curl\ \underline{H} = \frac{1}{c}\left(\frac{\partial \underline{E}}{\partial t} + 4\pi \underline{J}\right) .$$

$$div\ \underline{E} = 4\pi\rho \ , \qquad div\ \underline{H} = 0 \ . \qquad 3.23$$

Taking the curl of both sides we obtain

$$curl\ curl\ \underline{E} = -\frac{1}{c} curl\ \frac{\partial \underline{H}}{\partial t} = -\frac{1}{c}\frac{\partial}{\partial t} curl\ \underline{H}\ , \qquad 3.24$$

$$curl\ \underline{H} = \frac{1}{c}\frac{\partial \underline{D}}{\partial t}\ , \qquad 3.25$$

and from $\underline{D} = \epsilon \underline{E} = (1+\chi)\underline{E}$, $\underline{E} \simeq (1-\chi)\underline{D}$ we obtain

$$curl\ curl\ (1-\chi)\underline{D} = \frac{4\pi^2}{\lambda^2}\underline{D}\ . \qquad 3.26$$

Evaluating the left hand side of equation (3.26) involves rewriting the value of $(1-\chi)\underline{D}$ using the solution of the wave equation and Fourier expansion of the polarisability. Given that

$$\underline{k}_0 = grad\ \Phi_0\ , \qquad \underline{h}_m = grad\ n_m\ , \qquad \underline{k}_m = grad\ \Phi_m\ , \qquad 3.27$$

and using the Bloch solution we get

$$\frac{4\pi^2}{\lambda^2}\sum_m \underline{D}_m \exp(-2i\pi\Phi_m) = \underline{A}\ , \qquad 3.28$$

where $\underline{A}$ is a function with terms of varying magnitude. Neglecting small terms (see Pinsker, 1978) we obtain

$$\alpha_m \underline{D}_m - \sum_h \chi_{m-h}\underline{D}_h \cos X_{mh} + \frac{i\lambda^2}{\pi}(\underline{k}_m grad)\underline{D}_m = 0\ , \qquad 3.29$$

where $\cos X_{mh}$ is the polarisation factor. The calculation of the solution for X-ray propagation in the perfect crystal is then the solution of this system in first order partial derivatives. The variable α_m is calculated to allow for local deformations at any point in the crystal.

For the two beam case we need only consider $m = 0$ and $m = h$. If $\underline{s}_0$ and $\underline{s}_h$ are unit vectors in the direction of the incident and diffracted beams respectively, then

$$\underline{s}_0 = \lambda \underline{k}_0 \ , \qquad \underline{s}_h = \lambda \underline{k}_h \ , \tag{3.30}$$

and for any point on the reflection plane

$$\underline{r} = s_0 \underline{s}_0 + s_h \underline{s}_h \ , \tag{3.31}$$

and the system (3.29) reduces to

$$\begin{aligned} \frac{i\lambda}{\pi} \frac{\partial D_0}{\partial s_0} &= \chi_0 D_0 + C\chi_{\bar{h}} D_h \\ \frac{i\lambda}{\pi} \frac{\partial D_h}{\partial s_h} &= (\chi_0 - \alpha_h) D_h + C\chi_h D_0 \ , \end{aligned} \tag{3.32}$$

where

$$C = \cos X_{0h} \ .$$

We can include the polarisation factor C in the values χ_h and $\chi_{\bar{h}}$ by adding the symbols σ and π, so that

$$\chi_h^\sigma = \chi_h^\pi (|\cos 2\theta|)^{-1} \ , \qquad \chi_{\bar{h}}^\sigma = \chi_{\bar{h}}^\pi (|\cos 2\theta|)^{-1} \ . \tag{3.33}$$

3.3 Solution of the Takagi - Taupin Equations

The Takagi-Taupin equations (3.32) can now be used to calculate the reflectively of a given crystal in the Bragg case. The amplitude ratio of the incident and diffracted beams is required. We will assume an incident plane wave, and that variations in diffracted intensity will be a function of depth only.

For asymmetric reflections γ_0 and γ_h, the direction cosines of the incident and diffracted beams with respect to the surface, are not equal. The depth below the surface z, is then given by

$$z = s_0 \gamma_0 + s_h \gamma_h \tag{3.34}$$

then (3.32) becomes

$$\frac{i\lambda}{\pi}\ \gamma_0\frac{\partial D_0}{\partial z} = \chi_0 D_0 + C\chi_{\bar{h}} D_h$$

$$\frac{i\lambda}{\pi}\ \gamma_h\frac{\partial D_h}{\partial z} = (\chi_0 - \alpha_h)D_h + C\chi_h D_0\ . \qquad 3.35$$

Note that in general, χ_h and $\chi_{\bar{h}}$ are not equal in a non-centrosymmetric crystal such as the zinc-blende structure except in special cases (such as the $00l$ reflection).

The complex reflection coefficient, X, is defined as

$$X = \frac{D_h}{D_0}\ . \qquad 3.36$$

Differentiating (3.36) we obtain

$$\frac{dX}{dz} = \frac{1}{D_0}\frac{\partial D_h}{\partial z} - \frac{D_h}{D_0^2}\frac{\partial D_0}{\partial z}\ , \qquad 3.37$$

and substituting into (3.35) we arrive at

$$\frac{dX}{dz} = \frac{i\pi}{\lambda\gamma_0}\left\{C\chi_{\bar{h}}X^2 + (\chi_0 - \frac{\gamma_0}{\gamma_h}\chi_0 + \frac{\gamma_0}{\gamma_h}\alpha_h)X - C\frac{\gamma_0}{\gamma_h}\chi_h\right\}\ . \qquad 3.38$$

For a crystal/layer structure containing compositional variations, α_h will be a function of the depth z, below the surface. Solution of (3.38) would then need to be performed numerically. However, if the crystal is divided into a number of laminae of constant composition, equation (3.38) can be solved analytically for each lamina. The complex amplitude ratios are then matched at each boundary in order to obtain the reflectivity at the surface.

Equation (3.38) can be written as

$$\frac{dX}{dz} = iD[AX^2 + 2BX + E]\ , \qquad 3.39$$

where

$$A = C\chi_{\bar{h}} \quad , \qquad B = (1-b)\frac{\chi_0}{2} + \alpha_h \frac{b}{2} \quad , \qquad D = \frac{\pi}{\lambda\gamma_0} \quad , \qquad E = -Cb\chi_h$$

and where $b = \gamma_0/\gamma_h$ is the ratio of the direction cosines of the incident and reflected beams relative to the surface normal. Note that if the angles of incidence and reflection with respect to the surface are i and e respectively, then

$$\gamma_0 = \sin i \ , \qquad \gamma_h = -\sin e \ , \tag{3.40}$$

and so for a symmetric Bragg case reflection $b = -1$.

Equation (3.39) can be written as

$$\frac{dX}{dz} = iDA\left[\left(X + \frac{B}{A}\right)^2 - \frac{B^2}{A^2} + \frac{E}{A}\right]. \tag{3.41}$$

With the substitution

$$X = -\frac{B}{A} + \frac{\sqrt{EA - B^2}}{A}\tan Y \ , \tag{3.42}$$

the RHS of (3.41) becomes

$$iDA\frac{(EA - B^2)}{A^2}(1 + \tan^2 Y),$$

and the LHS becomes

$$\frac{\sqrt{EA - B^2}}{A}(1 + \tan^2 Y)\frac{dY}{dz} \ ,$$

and so

$$\frac{dY}{dz} = iD\sqrt{EA - B^2} \ . \tag{3.43}$$

Assuming that the reflectively is known at a depth W, i.e. $X(W) = k$, we obtain

$$\int_{Y(W)}^{Y(z)} dY = \int_{W}^{z} iD\sqrt{EA - B^2}\, dz \ ,$$

so

$$Y(z) = iD\sqrt{EA - B^2}(z - W) + \tan^{-1}\Big(\frac{Ak + B}{\sqrt{EA - B^2}}\Big).$$

Therefore, from (3.42)

$$X = \frac{1}{A}\Big[-B\sqrt{EA - B^2} + B(Ak + B)\tan(iD\sqrt{EA - B^2}(z - W))$$

$$+(EA - B^2)\tan(iD\sqrt{EA - B^2}(z - W)) + (Ak + B)\sqrt{EA - B^2}\Big]$$

$$\times\Big[\sqrt{EA - B^2} - (Ak + B)\tan(iD\sqrt{EA - B^2}(z - W))\Big]^{-1}.$$

And so

$$X = \frac{k\sqrt{EA - B^2} + (E + Bk)\tan(iD\sqrt{EA - B^2}(z - W))}{\sqrt{EA - B^2} - (Ak + B)\tan(iD\sqrt{EA - B^2}(z - W))} \ . \qquad 3.44$$

Now

$$\tan[iD\sqrt{EA - B^2}(z - W)] = -\tan[D\sqrt{B^2 - EA}(z - W)],$$

so that (3.44) can be written as

$$X = \frac{k\sqrt{B^2 - EA} + i(Bk + E)\tan(D\sqrt{B^2 - EA}(z - W))}{\sqrt{B^2 - EA} - i(Ak + B)\tan(D\sqrt{B^2 - EA}(z - W))} \ . \qquad 3.45$$

The boundary condition is that $k = 0$ at a point deep within the substrate. Then equation (3.45) becomes

$$X = \frac{iE\tan(D\sqrt{B^2 - EA}(z - W))}{\sqrt{B^2 - EA} - iB\tan(D\sqrt{B^2 - EA}(z - W))} \ . \qquad 3.46$$

As

$$(z-W)\rightarrow-\infty \quad Im\left[D\sqrt{B^2-EA}(z-W)\right]\rightarrow+\infty \quad if \quad Im(\sqrt{B^2-EA})<0$$

$$Im\left[D\sqrt{B^2-EA}(z-W)\right]\rightarrow-\infty \quad if \quad Im(\sqrt{B^2-EA})>0$$

Therefore

$$\tan\left[D\sqrt{B^2-EA}(z-W)\right]\rightarrow -i \quad Sign\left[Im(\sqrt{B^2-EA})\right].$$

Hence (3.46) can be written as

$$X=-\left\{\frac{B+\sqrt{B^2-EA} \quad Sign\left[Im(\sqrt{B^2-EA})\right]}{A}\right\}. \qquad 3.47$$

The reflectively at the surface of the substrate is calculated using equation (3.47). This value serves as a boundary condition for the first epitaxial layer. The reflectively at the surface of the layer is then calculated from equation (3.45) and the process repeated for all the layers in the structure. The intensity ratio R, is then calculated from

$$R=\frac{|X|^2}{|b|}, \qquad 3.48$$

where the ratio of the direction cosines takes into account any beam expansion or compression.

Once the reflectively is obtained the rocking curve can be calculated using the convolution equation (2.17), which gives the total power reflected by the second crystal at an angle β. The rocking curve is calculated by performing this integration for the range of angles β, required. $C_{A,B}$ are the single crystal reflectivities for the first and second crystals respectively. For the first crystal the reflectively for an infinite crystal is used.

The rocking curve simulation program written by Hill (1985) contained several errors which, although irrelevant in the symmetric geometry, emerged when

using asymmetric geometries. For this reason the computational section of the program (CRUNCH) was rewritten, and the version based on the equations derived in this chapter is included in Appendix A. In addition, the input section of the program was extended to include a number of II-VI compounds. For a full description of the suite of programs, together with an account of the effects of sample curvature on the rocking curve, the reader is referred to Hill's thesis (1985). Examples of the use of simulation programs based on the Takagi-Taupin equations can be found in the work of Halliwell, Lyons and Hill (1984); Hill, Tanner, Halliwell and Lyons (1985); Fewster and Curling (1987); Bensoussan et al. (1987); Miltat (1987,1988); Barnett et al. (1988) and Fewster (1989).

Chapter IV

Experimental Techniques of Double Crystal Diffraction

4.1 Introduction

Although Double Crystal Diffractometers were first used in the 1920's it is only recently with the advancement in growth of high quality epitaxial layers that they have come into their own as highly sensitive instruments for determining growth structure. A great deal of information is contained in a rocking curve (Segmüller, 1986) concerning the quality of the layers and substrate, composition and thickness of layers and sample curvature. The use of a simulation program, which was introduced in the last chapter is essential, enabling much of the information to be recovered from the diffraction profile.

The primary function of the DCD is the determination of layer composition. The difference in lattice parameter of the layer compared to the substrate, known as the mismatch, may be measured from the separation of the Bragg peaks (Estrop, Izrael and Sauvage, 1976), and since the substrate parameter is known the layer composition may be determined. Halliwell (1981) showed that measurement of mismatch using a DCD was more precise than with other techniques and showed that it was accurate to within $20ppm$ with 004 and 115 reflections from $InGaAs$ and $InGaAsP$ grown on InP. However, when layers become thin peaks may become shifted from the position dictated by their composition and measurement of mismatch from peak separation is no longer accurate (Fewster and Curling, 1987) and it is then necessary to match experimental curves with simulation (Fewster, 1989). If layers are highly mismatched they may become partially or completely relaxed by the introduction of misfit dislocations at the growth interface. Asymmetric reflections with both high and low angle beam paths are utilised to determine lattice parameters of incoherent layers (Bartels and Nijman, 1978; Wang et al., 1988). Misfit dislocations can be imaged with X-ray topography (Oe et al., 1978), which can be used in combination with DCD to study strained layers (Chu, Wie, Kim and Lau, 1988). Chang, Bhattacharya

and Gibala (1989) have also used TEM to study misfit dislocations in strained $InGaAs/GaAs$ MQW's.

Layer thickness is indirectly obtained from the rocking curve by simulating experimental peak profiles (Hill, Tanner, Halliwell and Lyons, 1985; Chu and Tanner, 1986, 1987). A more accurate method of determining layer thickness is to measure Pendellösung fringe spacing which arises from interference in thin layers and whose period is directly related to layer thickness (Bartels and Nijman, 1978). This method has been used for VPE grown $InGaAs$ on InP (Macrander and Strege, 1986) and for MBE grown $InGaAs$ and $InGaAlAs$ on InP (Ferrari, Franzosi, Gastaldi and Taiariol, 1988) with a symmetric 004 reflection. In combination with simulation, Pendellösung fringe measurement has been used to characterise both composition and thickness in $AlGaAs$ on $GaAs$ (Bensoussan, Malgrange and Sauvage-Simkin, 1987; Bassignana, Springthorpe and Tan, 1987, 1989) and in $InGaAs$ on $GaAs$ (Jeong, Schilesinger and Milnes, 1988; Ferrari and Franzosi, 1989). Tanner and Halliwell (1988) have noted that direct measurement of fringe spacing in two layer structures can lead to deviations from the true Pendellösung frequencies and this is discussed in more detail in Chapter 6.

When characterising epilayers it is important to be aware of tilts of both substrate and layers away from the growth plane. Substrate misorientation generally leads to epilayer tilt (Nagai, 1974; Kleiman, Park and Mar, 1988) which will produce errors in mismatch measurement if neglected (Tanner, Miles, Peterson and Sacks, 1988). Both substrate and layer tilt can be evaluated straightforwardly by measuring peak separations from several sample orientations (Hattanda and Takeda, 1973) and there is no need to revert to measurement of rocking curve width at low incidence angles, as described by Slusky and Macrander (1988), which is difficult and too dependent on instrumental factors. An indication of sample quality can also be obtained from rocking curve widths, and compositional grading can be modelled using simulations (Halliwell, Juler and Norman, 1983; Bowen, Hill and Tanner, 1987).

There is presently much interest in the growth of II-VI semiconductors as well as III-V's. Qadri et al. (1988) used DCD and topography to study $ZnSe$ on $GaAs$ to give an indication of crystalline quality. Okamoto et al. (1988)

used the symmetric 004 reflection to measure alloy composition in ZnS_xSe_{1-x} on $GaAs$, and Bhat et al. (1987, 1988) considered the effect of substrate tilt on 004 and 115 rocking curves of $CdTe$ on $InSb$. Ion implanted layers are also important in the function of optoelectronic devices and DCD is a valuable tool in their characterisation. DCD has been used to study strain and damage in ion implanted garnet films (Speriosu, 1981; Speriosu and Wilts, 1983) with the aid of a kinematic model of X-ray diffraction. The introduction of strain in $GaAs$ by low dose ion implantation has been investigated with symmetric 004 reflections and the strain depth profile has been modelled kinematically (Paine, Hurvitz and Speriosu, 1987). Studies of strain in $GaAs$ by DCD after high doses of radiation have found that the strain saturates to a certain level resulting in uniform lattice spacing larger than the initial spacing of the lattice (Wie, Vreeland and Tombrello, 1985). Models based on dynamical X-ray diffraction theory have been used by Larson and Barhorst (1980) to study rocking curves of boron implanted laser annealed silicon, and by Capano et al. (1988) to investigate gallium implanted silicon.

Multi-quantum well and superlattice structures are now used in a variety of device structures including lasers, photodiodes and optical modulators. The first semiconductor superlattices were grown in the early 1970's (Esaki and Tsu, 1970) and since then their properties have been much investigated (Chang, 1983). Segmüller and Blakeslee (1973) used two different approaches to extract structural information from rocking curves showing superlattice reflections or so called satellites of the substrate Bragg reflection. The first one approximated the compositional and lattice distortion as a Fourier series. However, because the well-barrier composition profile is nearly rectangular it is not described well by a Fourier series with only a few harmonics. The second approach used a step function to describe the compositional profile (Segmüller, Krishna and Esaki, 1977). Fleming et al. (1980) considered the effect of interdiffusion in $AlAs/GaAs$ multilayers with a Fourier approach. Methods other than X-ray have been used to study superlattices, however X-ray diffraction data contains all the information needed to determine the structural parameters since diffraction angles are a function of lattice period and diffracted intensities depend on the nature and position of the atoms in the unit cell (Kervarec et al., 1984). Fewster (1986, 1987) presents a systematic approach to the analysis of multiple quantum well

structures using DCD and powder diffraction. Information may be obtained on the compositions and thicknesses of the individual wells and barriers as well as the average composition and period, and an indication of period fluctuations and interfacial quality. Recently models of interfacial roughness and period variations have been proposed (Fewster, 1988) and a new approach to modelling of interfacial grading has been developed (Lyons, 1989; Lyons, Scott and Halliwell, 1989). X-ray diffraction analysis has been performed on $AlGaAs/GaAs$ and $AlSb/GaSb$ superlattices (Paine, 1986), and $HgTe/CdTe$ superlattices (Paine, Vreeland and Cheung, 1986) with the aid of a kinematical model (Speriosu and Vreeland, 1984). The Takagi-Taupin equations have also been used for superlattice simulation in the symmetric (Halliwell, Lyons and Hill, 1984; Hill, Tanner, Halliwell and Lyons, 1985) and asymmetric cases (Bartels, Hornstra and Lobeek, 1986). Intentionally disordered $GaAlAs/GaAs$ superlattices have been studied by Auvray, Baudet and Regreny (1987) and a model has been developed which can be extended to account for interface roughness and period fluctuation.

MQW's are examples of band gap engineering whereby band gaps can be tailored to that desired using different combinations of thin layers of alternating composition. Strained layer heteroepitaxy gives a further degree of freedom allowing layer growth even if the lattice parameter is not exactly matched with the substrate. The strain in turn modifies the band gap and hence the electrical and optical properties of the materials in a manner which can be of benefit to device performance. However, layers will only be coherent if thin, and beyond a certain critical thickness (Van der Merwe and Jesser, 1989) strain will be released through the formation of misfit dislocations which have a detrimental effect on the electrical behaviour of the material. Fiory et al. (1984) and Aydinli et al. (1987) have measured critical thickness in Ge_xSi_{1-x} on Si and $InGaAs$ on $GaAs$ respectively with Rutherford Back Scattering while Orders and Usher (1987) have used DCD to measure it in $InGaAs/GaAs$ single heterostructures. It is important that critical thickness is known so that devices may be grown without relaxation occurring. Baribeau, Houghton and Kechang (1989) studied relaxation in Si/Ge_xSi_{1-x} heterostructures and found that previously coherently strained layers with good crystallanity become progressively relaxed upon annealing. The effect of layer strains in $InAlAs/GaAs$ strained

layer superlattices (SLS's) has been studied by Kato et al. (1986) and a shrinkage in the fundamental band gap for $GaAs$ wells has been observed. Relaxation also has the effect of broadening rocking curves (Wie, 1989). Characterisation of $Si_{1-x}Ge_x/Si$ SLS's using X-ray diffraction has been described by Lyons et al. (1987) and Baribeau (1988), where the superlattice period and average composition was determined by the symmetric 004 reflection. In order to determine the in-plane lattice parameter of the superlattice asymmetric reflections are required with which it is possible to determine the extent of relaxation (Halliwell et al., 1989). Barnett, Brown, Houghton and Baribeau (1989) have shown double-crystal X-ray diffraction to have the ability to distinguish between and quantify different types of non-uniformities in $Si_{1-x}Ge_x/Si$ superlattices. The effect of thick buffer layers of $InAlAs$ in $InAlAs/GaAs$ superlattices has been investigated by Kamigaki et al. (1987) who found that for buffer layer thicknesses of greater than $0.5\mu m$ the $InAlAs$ layers of both buffer layers and superlattices were in a strain free state, while the superlattice $GaAs$ layers showed large tetragonal distortions. The buffer was effectively acting as a substrate. II-VI semiconductor superlattices are also becoming increasingly important with improving crystal quality (Tanaka et al., 1987). Fantner (1987) has used X-ray diffraction to study $PbTe/Pb_{1-x}Sn_xTe$ SLS's while Villaflor et al. (1988) used the 004 reflection to study $GaAs/AlSb$ SLS's. $HgTe/CdTe$ superlattices grown for the first time with photo assisted MOCVD by Ahlgren et al. (1987) were found to be very high quality with satellite peaks up to third order shown by X-ray diffraction.

DCD's are used extensively in the analysis of single and multiple epitaxial layers as well as complex multi-quantum well structures. As a non-destructive relatively inexpensive method of characterisation, double crystal diffraction is now used routinely by crystal growers for optimisation of growth conditions and in detailed studies of device-quality samples.

4.2 Instrumentation and Experimental Alignment

The experiments in Durham were performed on a prototype Bede model 150 diffractometer, based on the design of Hart (1980). An Amstrad PC 1512 DD controlled the diffractometer via a Bede Minicam interface using Bede software.

The detectors used were a Nuclear Enterprises $DM1$-1 Sodium Iodide Scintillation counter and a Centronic $PX\ 28R/Xe$ proportional counter. Copper $K\alpha$ radiation from an AEG X-ray tube was used throughout, powered by a Hilton-brooks model $DG2$ X-ray generator. All experiments were run in a safely interlocked X-ray enclosure to avoid radiation hazards.

The Bede double crystal diffractometer is shown in figure 4.1. The first crystal axis is coaxial with the main diffractometer axis and the second crystal is positioned at an angle of twice the first crystal Bragg angle, with the detector mounted on an arm coaxial with the second axis. The first crystal must be aligned such that the reflected X-ray beam passes through the centre of the second crystal rotation axis and parallel to the plane of the diffractometer. The second crystal alignment may then be carried out.

Fewster's paper on DCD alignment (1985) suggests alignment methods for both crystals. The tilt of the first crystal which gives an X-ray beam parallel to the diffractometer plane is determined by recording the diffracted intensity as a function of tilt. The correct tilt occurs at the peak position in the tilt angle profile for crystal rotation angles below the Bragg angle, or the mid-point between the peaks in the high angle case. If the vertical divergence is too large for the tilt arm angle range then an alignment tool with a horizontal slit can be inserted on the second axis, at the correct height. The tilt arm is then rocked for maximum intensity.

For the reflected beam to pass through the centre of the second axis an alignment tool with a vertical slit is inserted and the whole diffractometer is rotated until the X-ray intensity is a maximum. The first crystal is then scanned in angle and accurately set on the peak of the intensity profile. When a small source spot size is used the $K\alpha_1$ $K\alpha_2$ doublet will be resolved and if required the $K\alpha_2$ peak may be removed using a slit in between the two crystals.

The second crystal is then mounted accurately over the centre of the axis and scanned to find the Bragg reflection. For the parallel $(n, -n)$ arrangement wavelength dispersion is small and most peak broadening arises from tilt misalignment. Fewster's method of tilt optimisation, mentioned in Chapter 2, searches for the minimum angle of the Bragg peak for a range of tilt values. The tilt angle

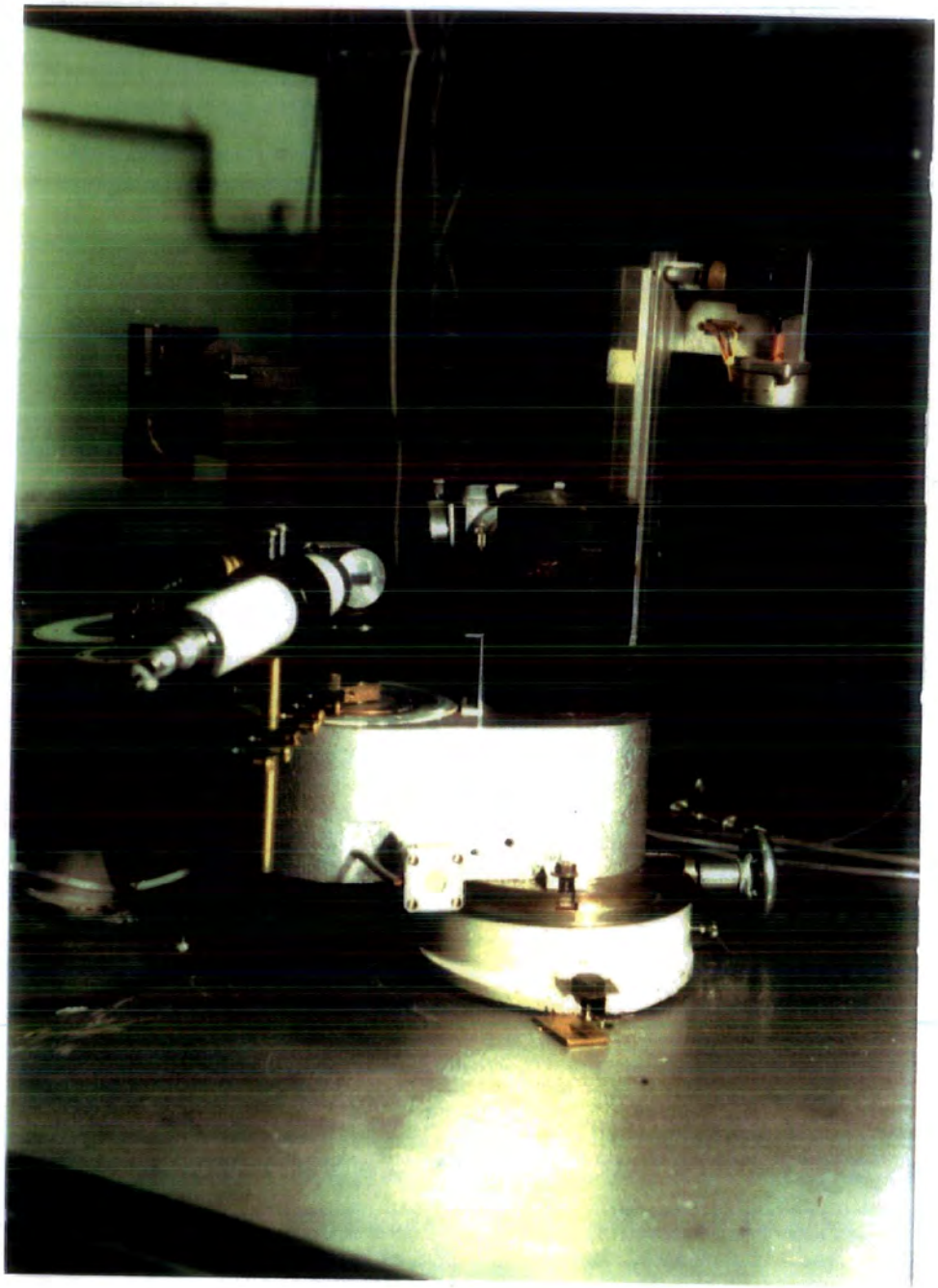

Figure 4.1: The prototype Bede model 150 diffractometer at Durham University.

giving the minimum peak angle brings the reflecting plane normal parallel to the incident beam. Alternatively, because the integrated intensity remains the same for any value of tilt, a maximum in peak intensity corresponds to a minimum in peak width. So an iterative process of maximising the peak intensity by tilting and rotating the second crystal will result in optimisation. Tanner, Chu and Bowen (1986) also suggested a method of tilt optimisation, by rotation about an axis almost normal to the Bragg planes, which is quick and accurate.

A rocking curve may now be taken, which is a plot of intensity against crystal rotation through the Bragg reflection. An important consideration for good rocking curves is the reduction of background noise. At no time should the detector see any part of the X-ray source or first crystal diffracted beam. This is ensured by surrounding the first crystal with a scatter shield with openings only at the correct angles, and by inserting a slit between the first and second axes. Additional scattered background is also reduced with a shield over the detector. Unless care is taken important information may be lost in background noise.

4.3 Composition and Thickness of Heteroepitaxial Layers

4.3.1 Mismatch

Consider the case of a single mismatched layer grown epitaxially onto a substrate. The rocking curve will generally exhibit two peaks corresponding to the Bragg angles of the layer and substrate. The separation of these peaks is directly related to the difference in lattice parameter, or mismatch, of the layer. The mismatch, m, is defined as

$$m = \frac{a_r - a_0}{a_0} , \qquad 4.1$$

where a_0 and a_r are the lattice parameters of the substrate and layer, respectively, in bulk form. When tetragonal distortion is present, the unit cell of the layer adopts the dimensions $a_0 \times a_0 \times c$, where c is the dimension perpendicular to the interface. The apparent mismatch, m^*, is then given by

$$m^* = \frac{c - a_0}{a_0} . \qquad 4.2$$

m^* and m are related from elastic theory (Hornstra and Bartels, 1978) by

$$m^* = m\frac{(1+\nu)}{(1-\nu)}\ , \qquad 4.3$$

where ν = Poisson's ratio (Halliwell, 1981). Values of ν for some common semiconductors are shown in Table 4.1 (Brantley, 1973). Published values are not available for ternary and quaternary compounds but they can be derived by extrapolating the binary values. Once m is found the composition of ternaries can be calculated using Végard's law. For quaternaries it is slightly more complicated and equation (1.4) should be used.

Semiconductor	ν
Si	0.278
Ge	0.273
$GaAs$	0.311
InP	0.360
GaP	0.271
$InAs$	0.353

Table 4.1: Poisson's Ratio

For substrates grown off axis the layer distortion will not be truly tetragonal and the layer becomes tilted relative to the substrate. If the stresses in the layer build up sufficiently for plastic distortion to occur the layer unit cell dimensions will become $a_1 \times a_1 \times c$. This plastic distortion takes the form of a network of misfit dislocations located close to and parallel with the interface. In the case of m^* positive a_1 will be greater than a_0, while c will be less than it would have been without plastic deformation. If m^* is negative a_1 will be less than a_0 and c will be greater than it would have been without plastic deformation. In both cases the layer lattice will begin to relax back towards cubic symmetry. Layers with $a_1 = a_0$ are said to be coherent while layers with misfit dislocations are said to be incoherent.

For symmetric reflections a relationship between peak splitting and mismatch is found from differentiating Bragg's law:

$$m^* = \frac{\Delta d}{d} = -\cot\theta\Delta\theta \ , \qquad 4.4$$

where $\Delta\theta = \theta_S - \theta_L$. m may now be calculated from equation (4.3).

For asymmetric reflections the reflecting planes are not parallel to the sample surface and the X-ray beam is either incident at an angle of $(\theta + \phi)$ or $(\theta - \phi)$ to the sample surface, for non-skew geometry. The peak separation is then $(d\theta - d\phi)$ for the high angle of incidence and $(d\theta + d\phi)$ for the low angle of incidence, with $d\phi = \phi_L - \phi_S$. If rocking curves are recorded using both beam paths $d\theta$ and $d\phi$ can be found independently, since $d\theta$ is half the sum of the two measured separations while $d\phi$ is half the difference. The diffracted radiation is said to have undergone an 'hkl reflection' if the planes are separated by a/h, a/k and c/l in the three axial directions respectively, where h, k and l are integers. The interplanar spacing for an hkl reflection is given by

$$d_{hkl} = \frac{1}{\sqrt{\frac{h^2+k^2}{a^2} + \frac{l^2}{c^2}}} \ , \qquad 4.5$$

where a and c are the parameters of the tetragonal unit cell which can then be calculated form the following equations.

$$\cos\phi_L = \cos(\phi_S + d\phi) = \left\{\frac{c^2(h^2+k^2)}{a^2l^2} + 1\right\}^{-\frac{1}{2}}$$

$$\sin\theta_L = \sin(\theta_S - d\theta) = \lambda\frac{\{h^2 + k^2 + a^2l^2/c^2\}^{\frac{1}{2}}}{2a} \ , \qquad 4.6$$

where the subscripts L and S refer to the layer and substrate respectively. a_r is then given by

$$a_r = a + (c - a)\frac{(1-\nu)}{(1+\nu)} \ , \qquad 4.7$$

and m can then be calculated using equation (4.1). If only one rocking curve is recorded in order to calculate m^* the interface is assumed to be coherent. Therefore

$$d\phi = \frac{m^* l (h^2 + k^2)^{\frac{1}{2}}}{(h^2 + k^2 + l^2)} ,$$

$$d\theta = \frac{m^* l \tan\theta}{(h^2 + k^2 + l^2)} , \qquad 4.8$$

and equation (4.3) is used to obtain m.

4.3.2 Thickness

Layer thickness determination is not quite as straightforward as the measurement of lattice mismatch. It is necessary to compare the experimental rocking curve with simulated curves until a close fit is obtained (Halliwell et al., 1984; Hill et al., 1985). However this method is also sensitive to many variables which are difficult to quantify such as crystalline quality, interfacial grading and sample curvature, and the fitting procedure can become tedious. A more sensitive method of determining layer thickness, for relatively thin layers, is the measurement of the Pendellösung fringe period discussed in Chapter 3. The fringe spacing, $\delta\theta$, is related to the layer thickness, t_L, by the following expression (Bartels and Nijman, 1978),

$$\delta\theta = \frac{\lambda \sin(\theta + \phi)}{t_L \sin 2\theta} . \qquad 4.9$$

The fringe spacing is independent of composition, layer quality and sample curvature, although the fringe amplitude is not. These effects are discussed further in Chapter 6. It is important to note, however, that Pendellösung fringes are only found on rocking curves of thin layers, and so the only way of determining layer thickness in thick layers is by matching experimental and theoretical curves.

4.4 Experimental Determination of Thickness and Mismatch

Four samples of single epitaxial layers of $AlGaAs$ grown by MBE at Glasgow University by C. Stanley were characterised. The substrates were $GaAs$, (001) oriented, and so to avoid dispersion effects a first crystal of $GaAs$ was used, with the surface symmetric 004 reflection for both crystals. The layers were nominally

$2\mu m$ in thickness and had expected Aluminium concentrations of 20%, 40%, 60% and 80%, corresponding to sample identification codes GAS1, GAS2, GAS3 and GAS4 respectively. Rocking curves were taken over on $800''$ range using a $4''$ step size with 5 seconds counting time a point.

Figure 4.2 shows the experimental and simulated rocking curves from the four samples. The mismatch used in the simulation was determined directly from the experimental peak separation and the thickness varied until a close match was attained. It was necessary to include curvature in the simulations to fit the peak widths, with more curvature required for the higher mismatched layers. The only sample not closely fitted using a single layer was GAS3. It is likely, in this case, that compositional grading exists at the interface, or possibly an actual interfacial layer, which causes the asymmetry of the substrate peak.

Table 4.2 shows the values of mismatch, Aluminium concentration, thickness and curvature of the samples determined from the simulations. The curvature is expressed in an angular deviation of the sample across the incident beam. The mismatches shown are accurate to within $\pm 20ppm$, or $\pm 1\%$ Aluminium. The error in the thickness determination is about $\pm 0.05\mu m$ ($\pm 500\AA$), but this is on the assumption that only one layer exists, as well as no compositional grading or layer imperfections.

Sample	Mismatch (ppm)	Al (%)	Thickness (μm)	Curvature ($''$)
GAS1	220	17.3	2.37	6
GAS2	490	38.5	2.33	8
GAS3	680	53.4	2.29	10
GAS4	920	72.3	2.25	12

Table 4.2

These layers were too thick to observe Pendellösung fringes and so the only method of layer thickness determination available is by matching experimental

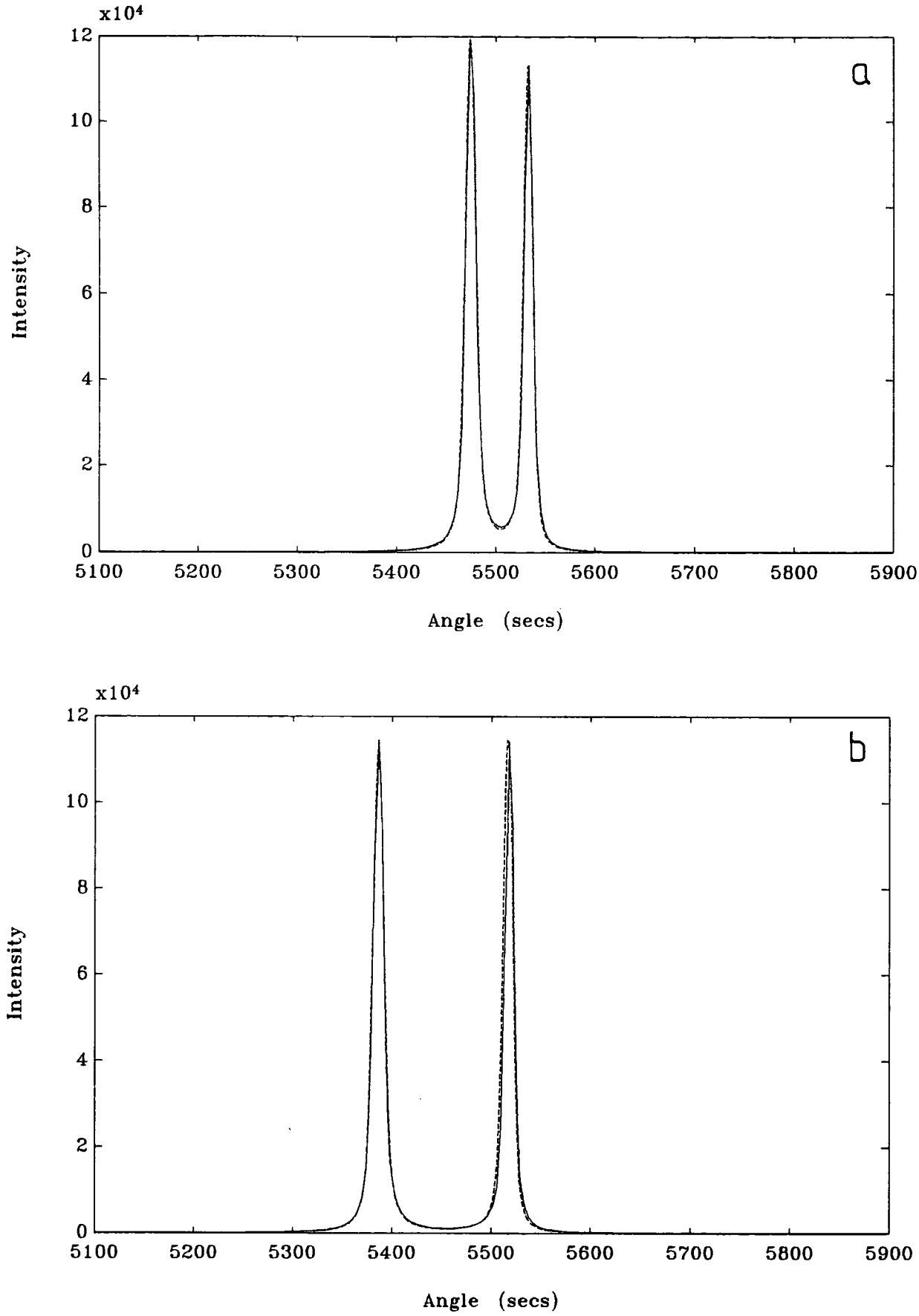

Figure 4.2: 004 experimental (solid) and theoretical (dashed) rocking curves; (a) GAS1, (b) GAS2, (c) GAS3, (d) GAS4.

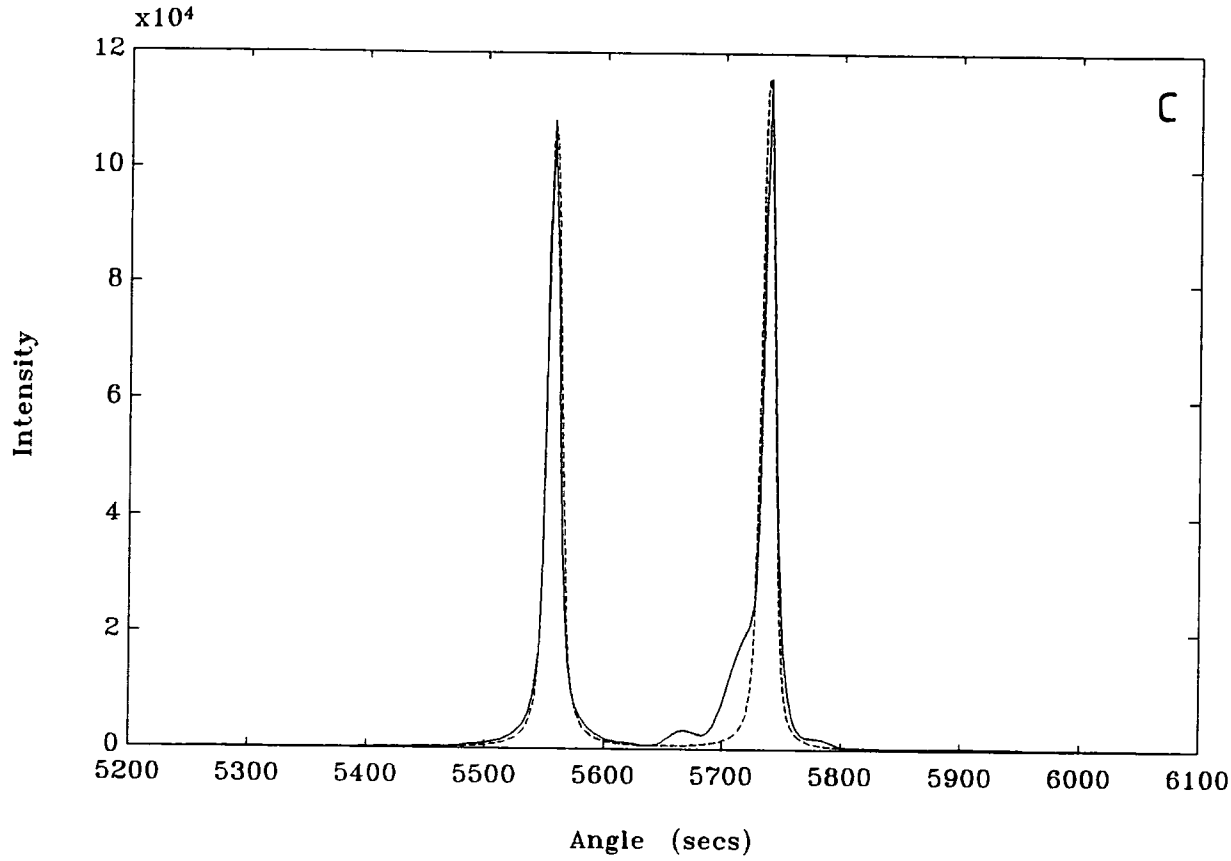
x10⁴
12
10
8
6
4
2
0
Intensity
c
5200
5300
5400
5500
5600
5700
5800
5900
6000
6100
Angle (secs)

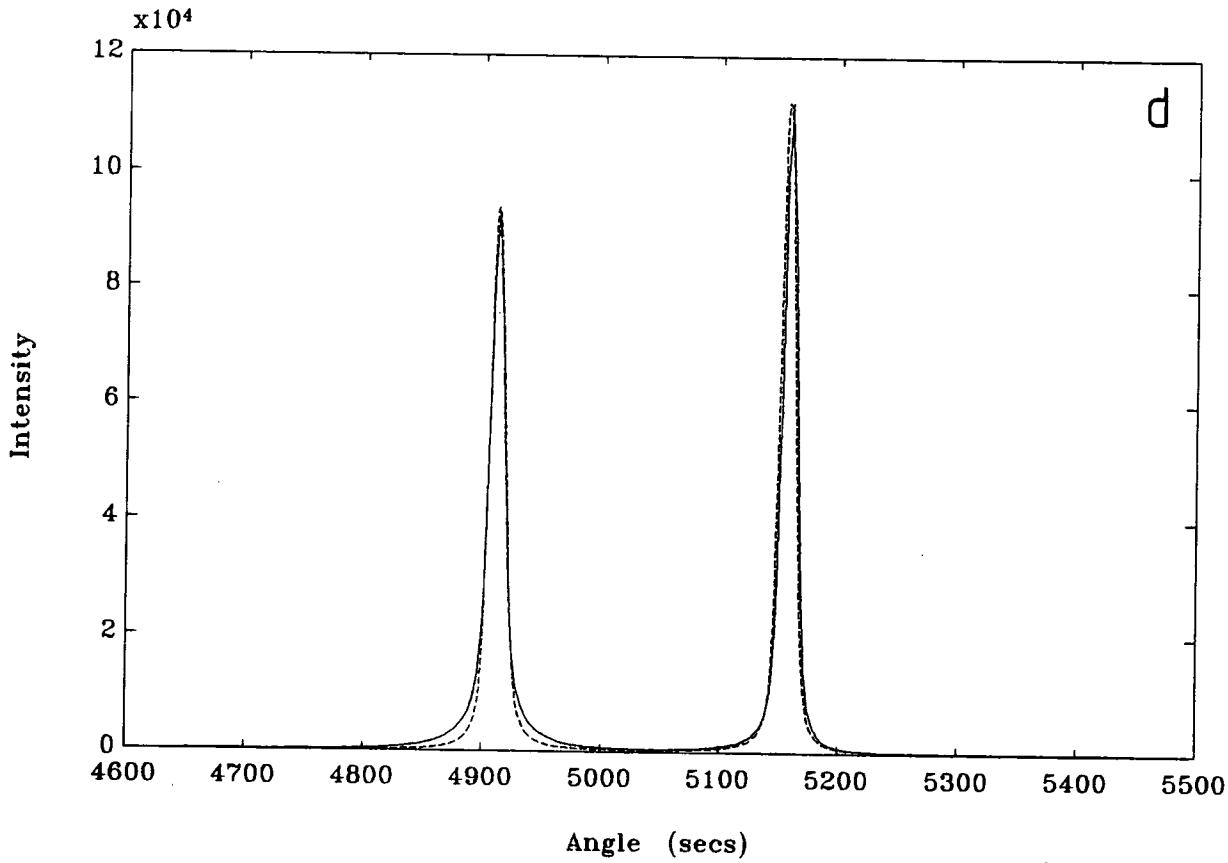
x10⁴
12
10
8
6
4
2
0
Intensity
d
4600
4700
4800
4900
5000
5100
5200
5300
5400
5500
Angle (secs)

and theoretical rocking curves. However, two further samples of $AlGaAs$ on $GaAs$, grown by C. Stanley, were characterised with nominal thicknesses of $1.2\mu m$ and 35% Aluminium; identification codes GAS5 and GAS6. This thickness of layer would be expected to show fringes.

The experimental conditions were the same as before but this time the layer thicknesses were characterised both by simulation and by measuring Pendellösung fringe spacing. The samples were long strips taken from a 2 inch wafer and information on uniformity of growth was required. The samples were mounted on a Bede X-Y Translation stage to allow a line scan across the sample without remounting the sample at each point. Five rocking curves were taken from each sample at points $4mm$ apart, going from the centre of the wafer to the edge. Each rocking curve had a range of $400''$, a step size of $2''$ and a counting time of 72 seconds for each step.

Figures 4.3 and 4.4 show the experimental and simulated rocking curves of GAS5 and GAS6. The fits were obtained by matching the peak separations, relative peak heights and widths only. Again curvature was required for a close match. Figures 4.5 and 4.6 show the corresponding experimental rocking curves with the intensity plotted on a logarithmic scale. The fringes are clearly visible on this type of graph, and the average fringe spacing may be measured. Using equation (4.9) the thickness can then be calculated. Table 4.3 illustrates the data yielded from both methods of characterisation.

Several points are evident from the data. Firstly, the layer thickness predicted from the simulation method is consistently smaller than from the Pendellösung technique. This can be explained because the simulation assumes a perfect layer with no compositional grading. This is unlikely in practice (Lyons, 1989) and so the thickness difference between the two methods gives an indication of the degree of grading and of layer quality, since Pendellösung fringe spacing is independent of composition. Therefore, it would appear that GAS6 is of better quality than GAS5 because the layer thickness difference between the two methods is only of the order of 5% compared to 10% for GAS5. This was corroborated by the crystal growers who in fact found considerable compositional grading in GAS5 using TEM. This grading was periodic and section 4.6.2 deals with its characterisation.

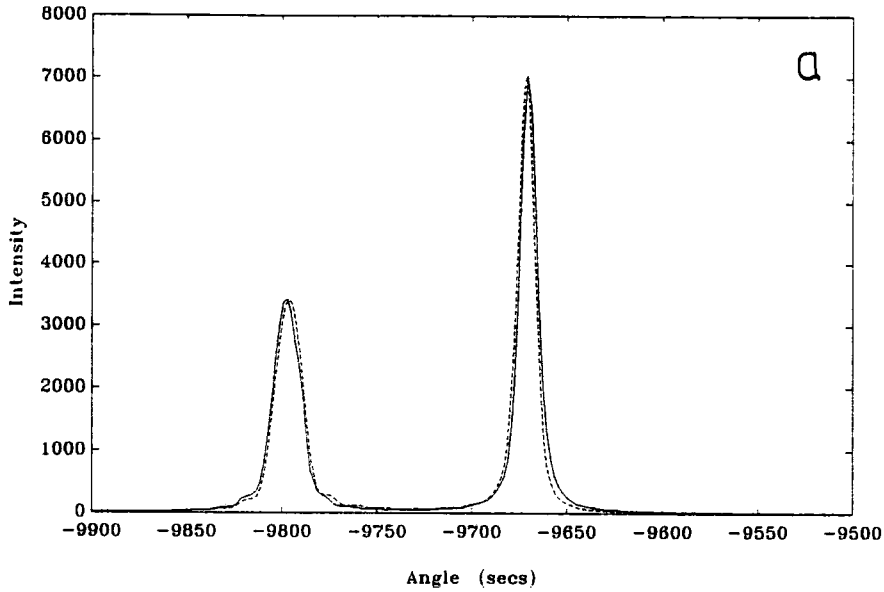

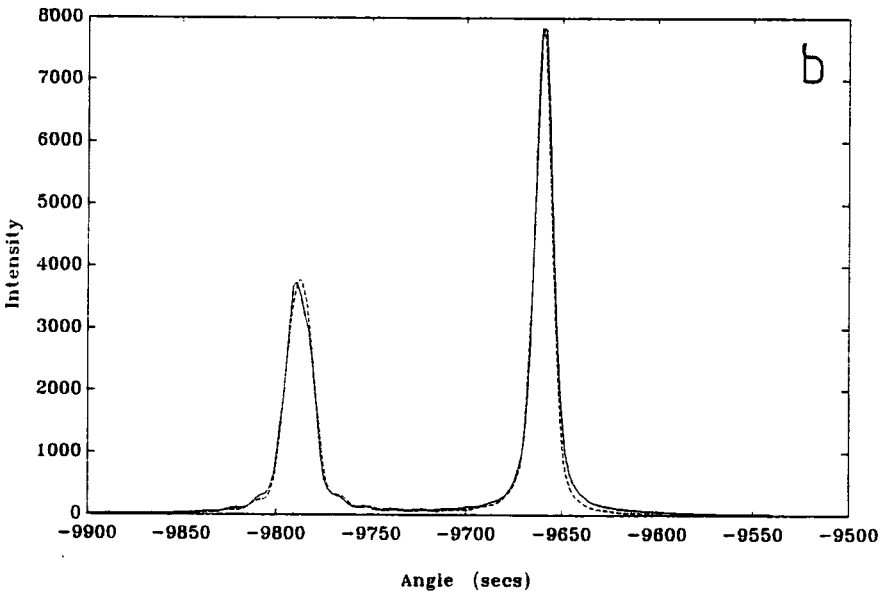

Figure 4.3: 004 experimental (solid) and theoretical (dashed) rocking curves of GAS5; (a) $2mm$, (b) $6mm$, (c) $10mm$, (d) $14mm$, (e) $18mm$ from wafer centre.

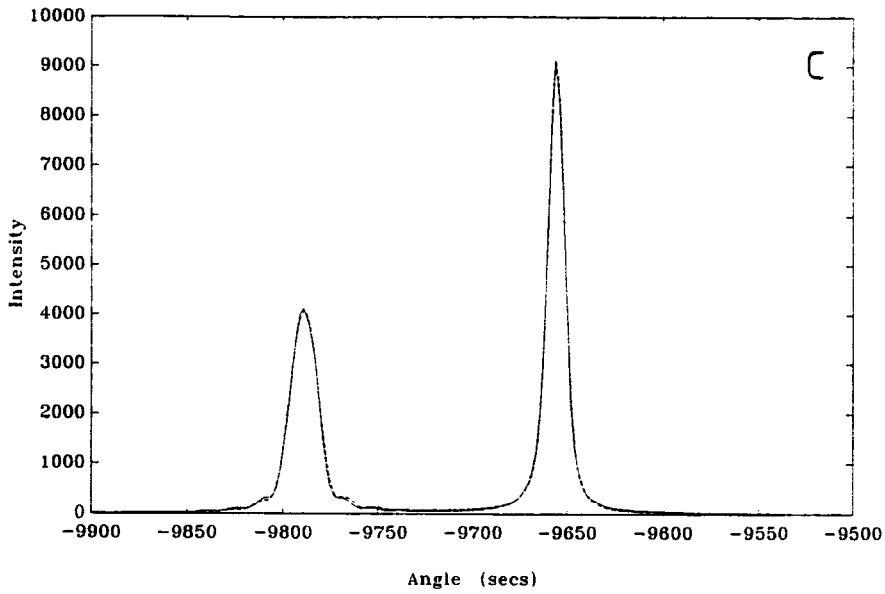
c
Intensity
10000
9000
8000
7000
6000
5000
4000
3000
2000
1000
0
-9900
-9850
-9800
-9750
-9700
-9650
-9600
-9550
-9500
Angle (secs)

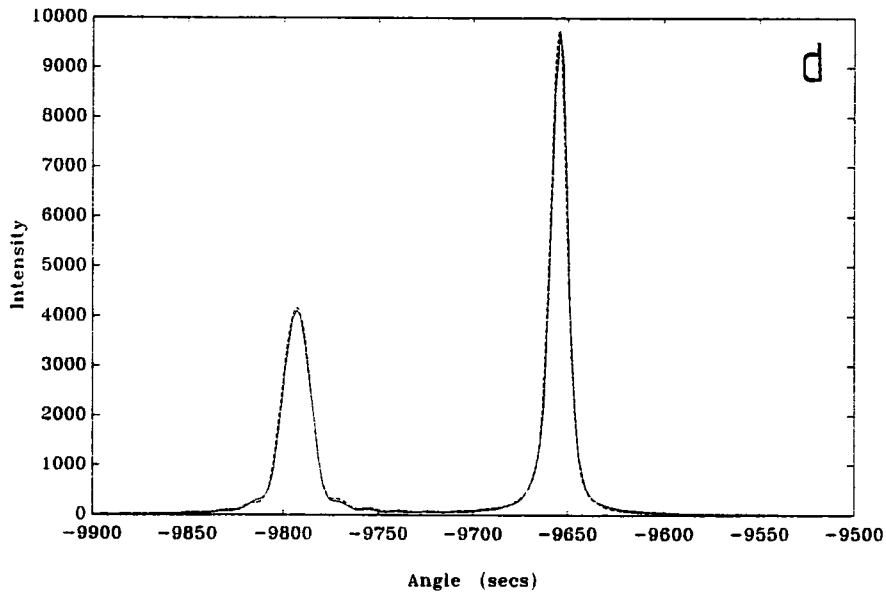
d
Intensity
10000
9000
8000
7000
6000
5000
4000
3000
2000
1000
0
-9900
-9850
-9800
-9750
-9700
-9650
-9600
-9550
-9500
Angle (secs)

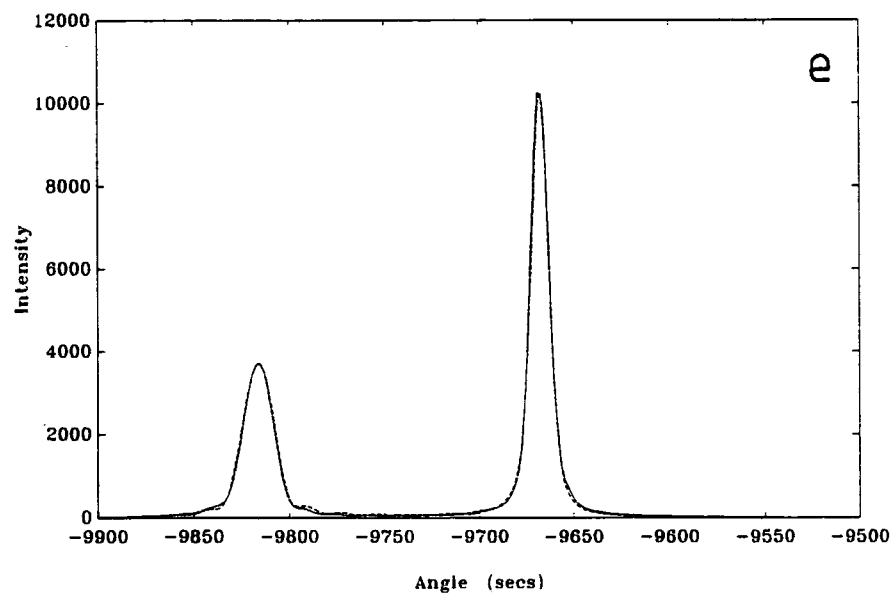
e
Intensity
12000
10000
8000
6000
4000
2000
0
-9900
-9850
-9800
-9750
-9700
-9650
-9600
-9550
-9500
Angle (secs)

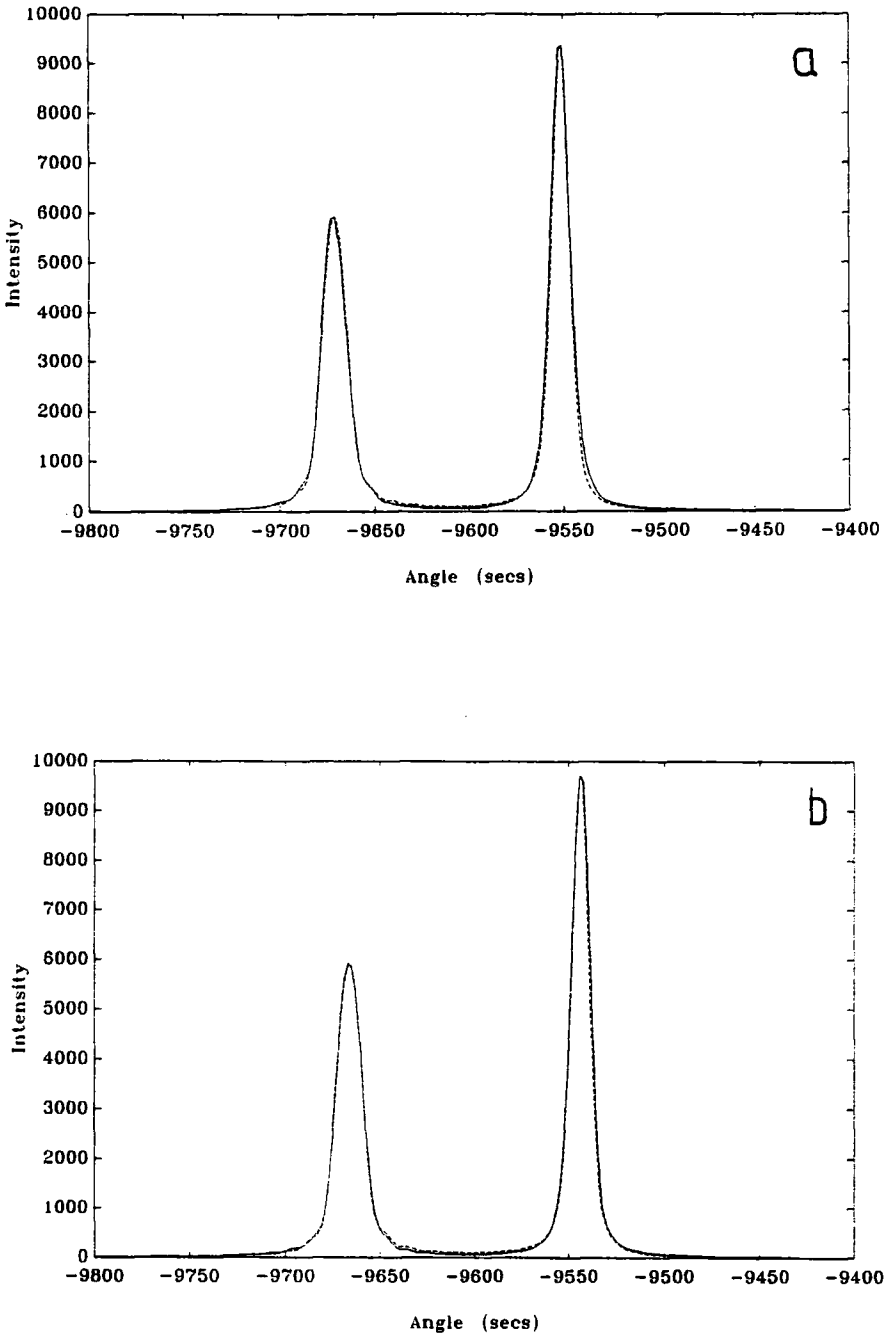

Figure 4.4: 004 experimental (solid) and theoretical (dashed) rocking curves of GAS6; (a) $2mm$, (b) $6mm$, (c) $10mm$, (d) $14mm$, (e) $18mm$ from wafer centre.

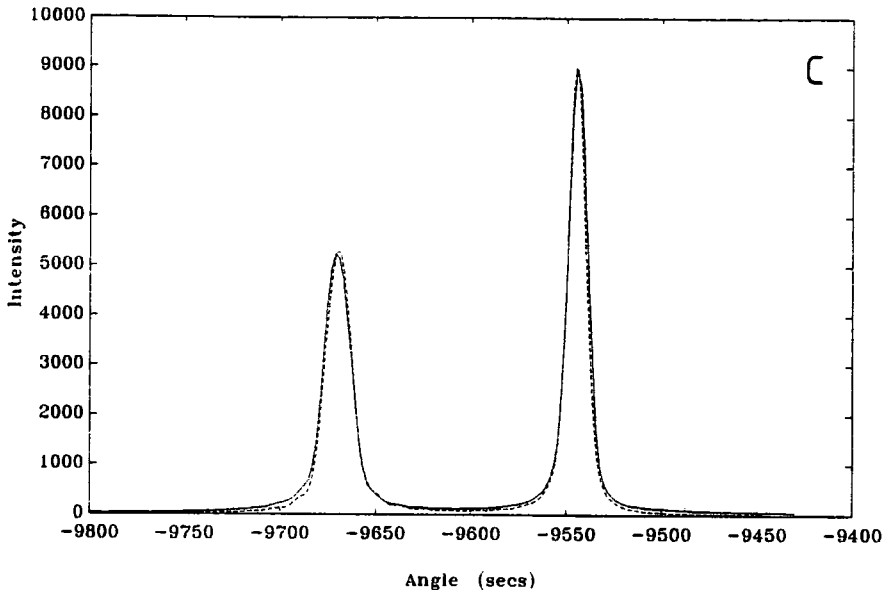
c
Intensity
10000
9000
8000
7000
6000
5000
4000
3000
2000
1000
0
-9800
-9750
-9700
-9650
-9600
-9550
-9500
-9450
-9400
Angle (secs)

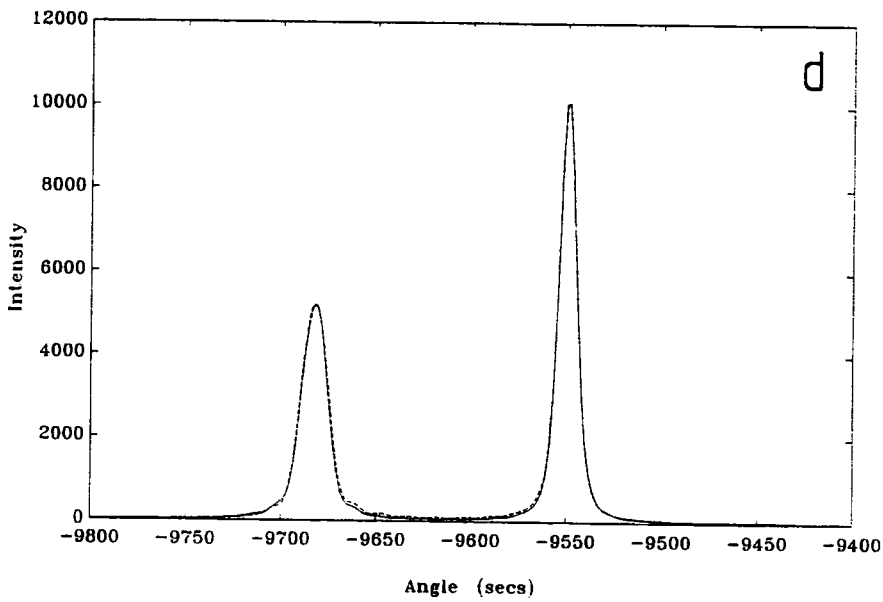
d
Intensity
12000
10000
8000
6000
4000
2000
0
-9800
-9750
-9700
-9650
-9600
-9550
-9500
-9450
-9400
Angle (secs)

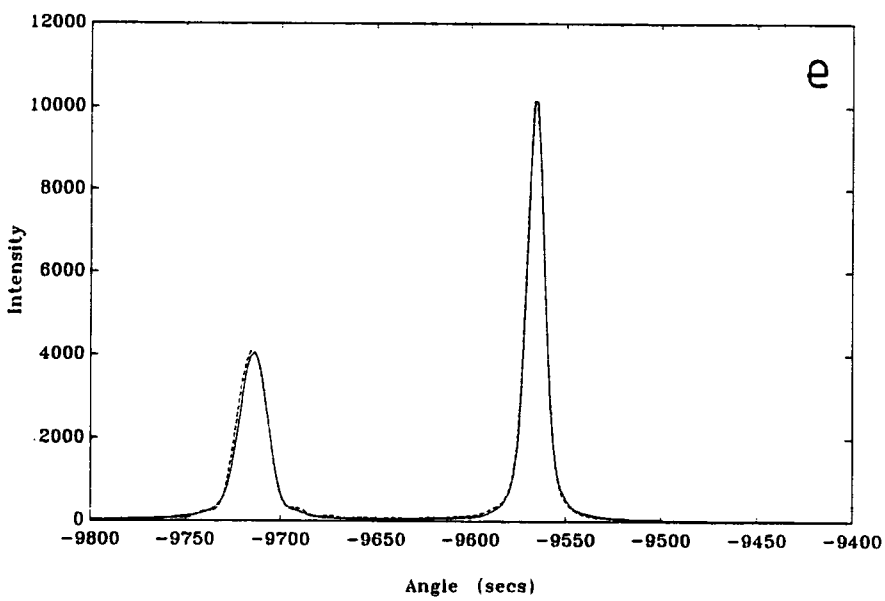
e
Intensity
12000
10000
8000
6000
4000
2000
0
-9800
-9750
-9700
-9650
-9600
-9550
-9500
-9450
-9400
Angle (secs)

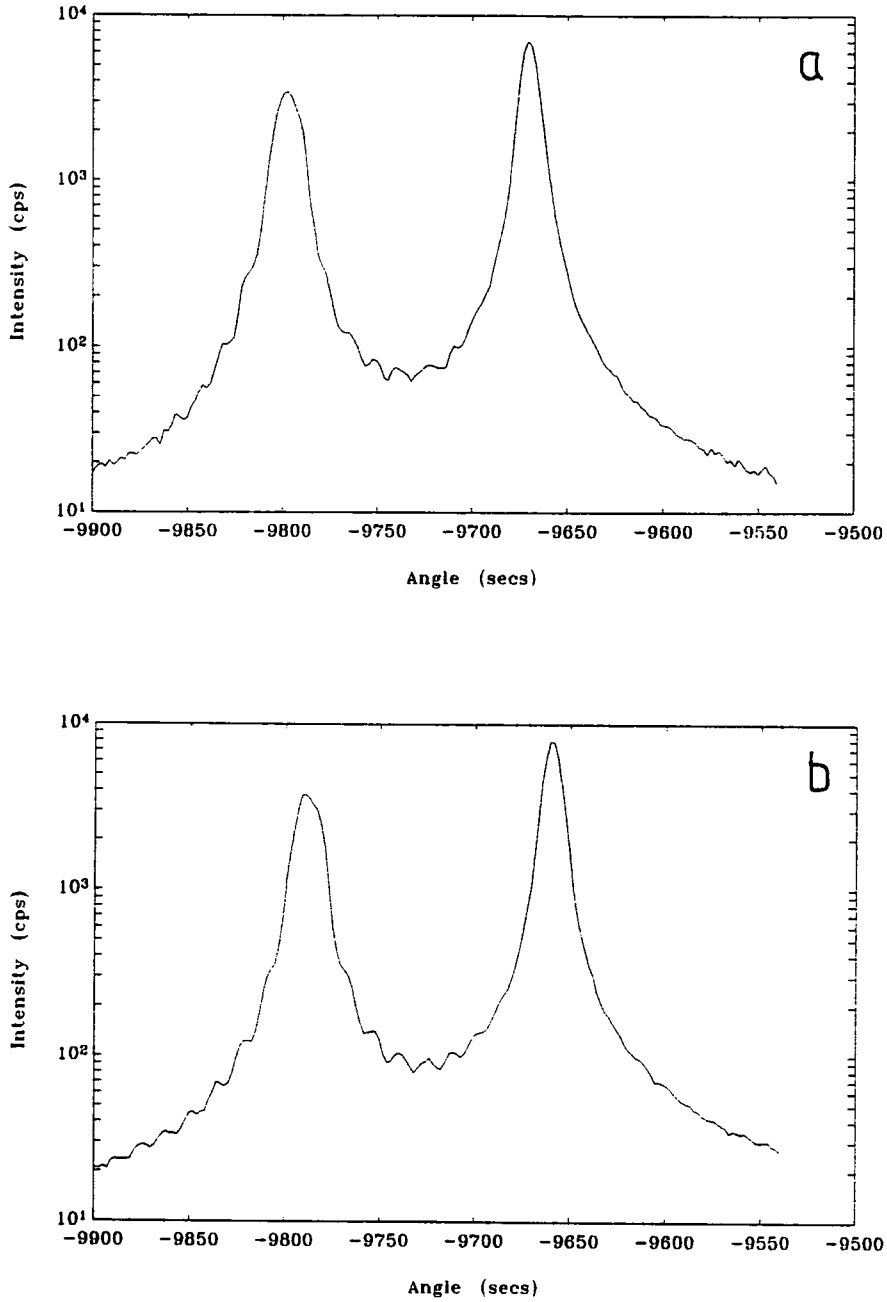

Figure 4.5: 004 experimental rocking curves of GAS5 on a logarithmic scale; (a) $2mm$, (b) $6mm$, (c) $10mm$, (d) $14mm$, (e) $18mm$ from wafer centre.

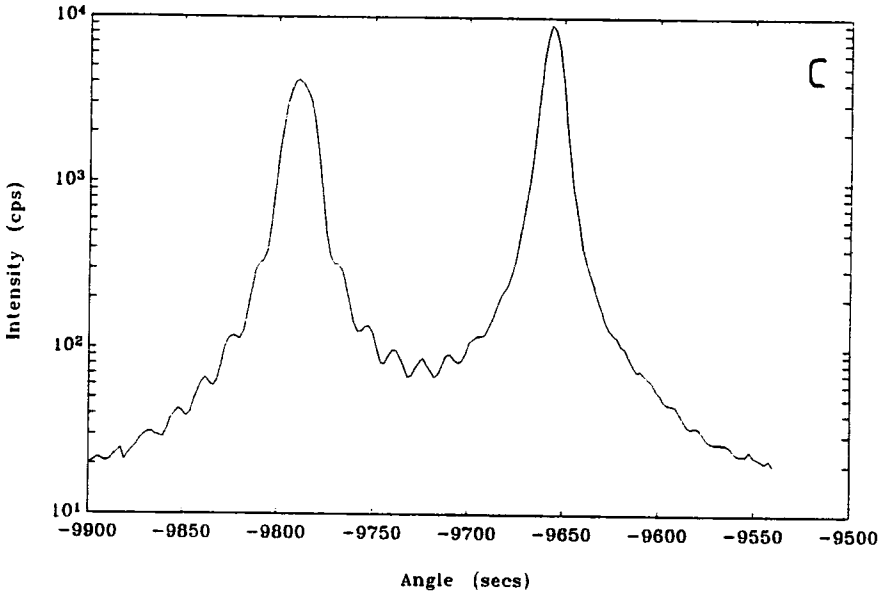
c
Intensity (cps)
10^4
10^3
10^2
10^1
-9900 -9850 -9800 -9750 -9700 -9650 -9600 -9550 -9500
Angle (secs)

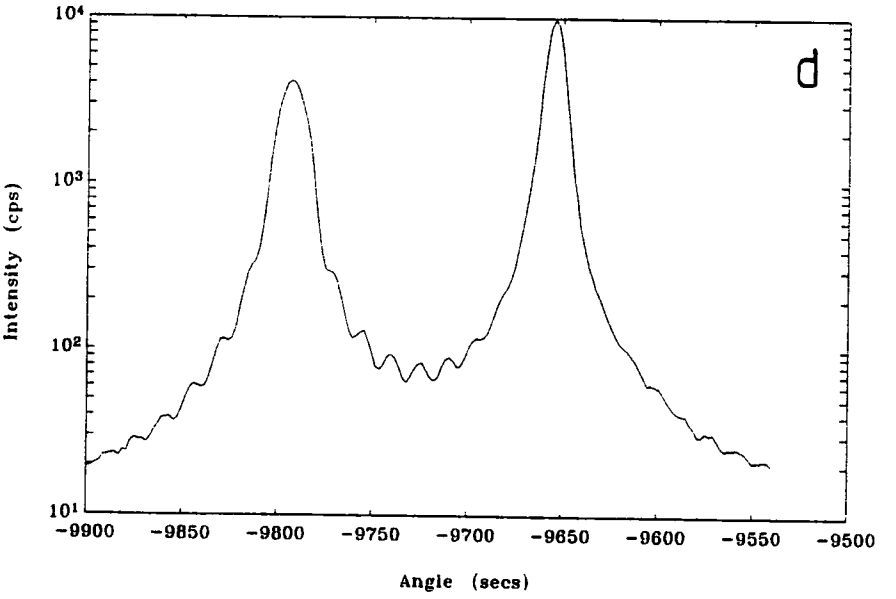
d
Intensity (cps)
10^4
10^3
10^2
10^1
-9900 -9850 -9800 -9750 -9700 -9650 -9600 -9550 -9500
Angle (secs)

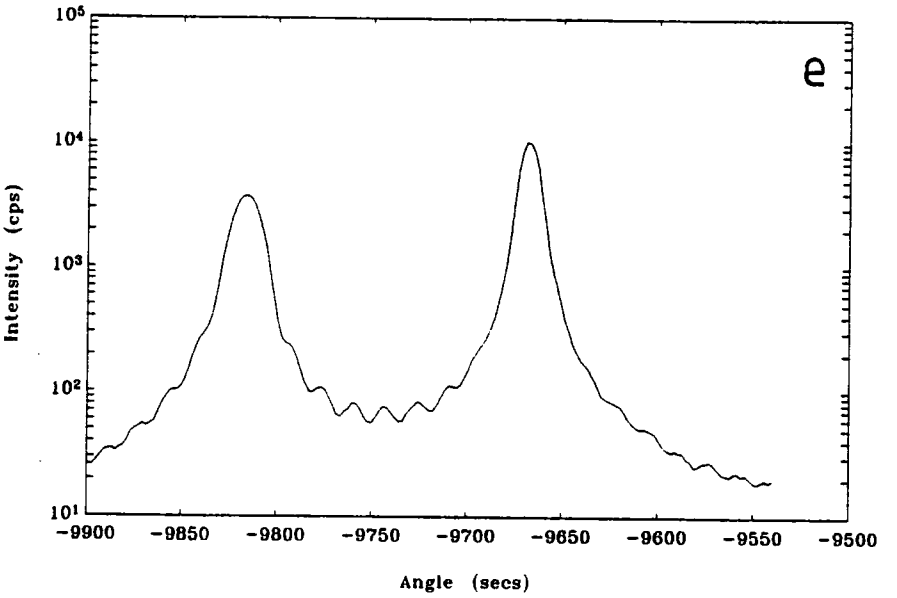
e
Intensity (cps)
10^5
10^4
10^3
10^2
10^1
-9900 -9850 -9800 -9750 -9700 -9650 -9600 -9550 -9500
Angle (secs)

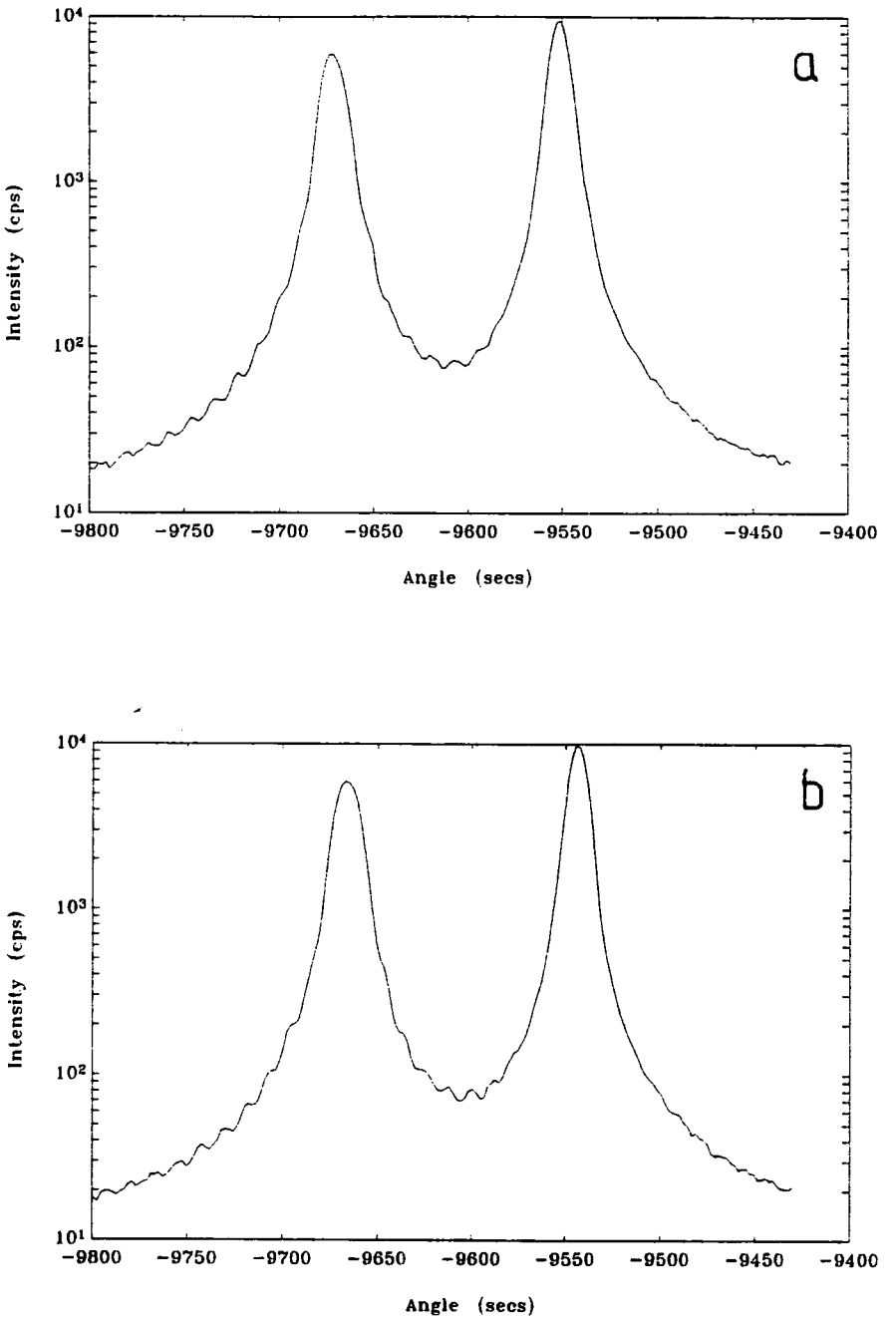

Figure 4.6: 004 experimental rocking curves of GAS6 on a logarithmic scale; (a) $2mm$, (b) $6mm$, (c) $10mm$, (d) $14mm$, (e) $18mm$ from wafer centre.

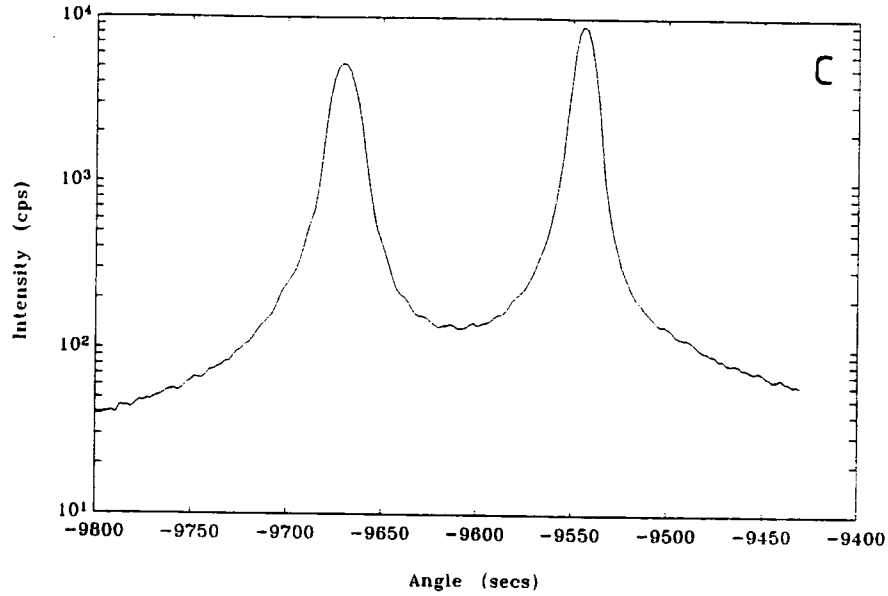
c
Intensity (cps)
10^4
10^3
10^2
10^1
-9800 -9750 -9700 -9650 -9600 -9550 -9500 -9450 -9400
Angle (secs)

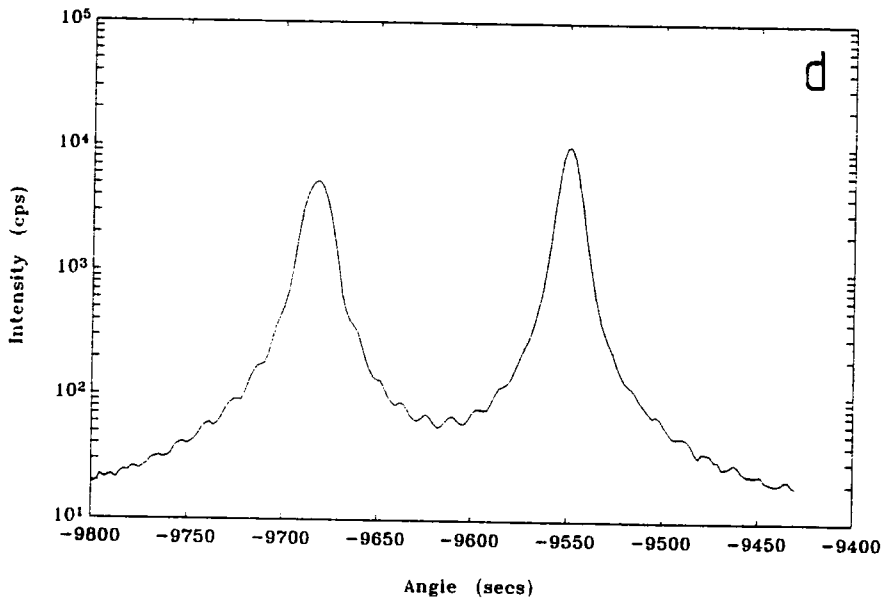
d
Intensity (cps)
10^5
10^4
10^3
10^2
10^1
-9800 -9750 -9700 -9650 -9600 -9550 -9500 -9450 -9400
Angle (secs)

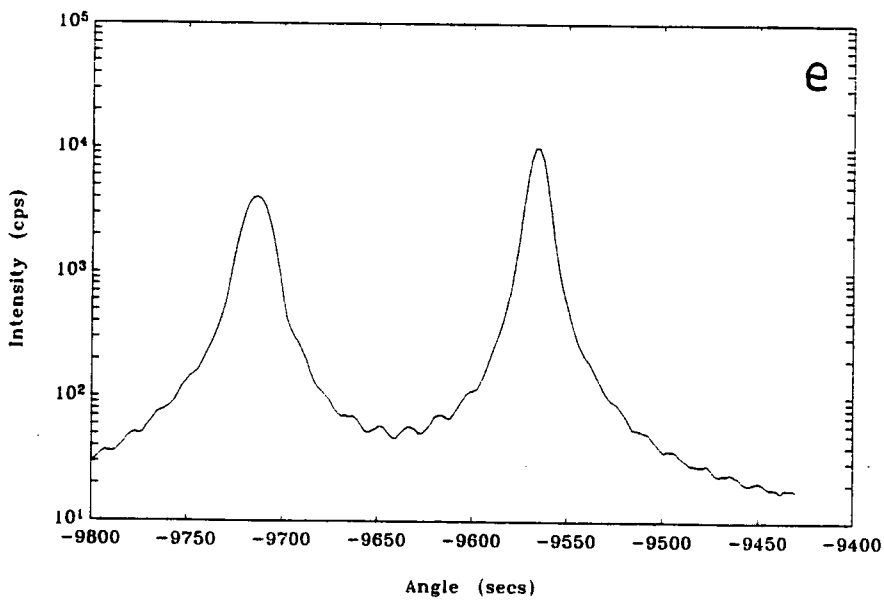
e
Intensity (cps)
10^5
10^4
10^3
10^2
10^1
-9800 -9750 -9700 -9650 -9600 -9550 -9500 -9450 -9400
Angle (secs)

In addition, the mismatch increases going from the centre to the edge of the wafer, while the thickness decreased, for both samples. The wafers were therefore not particularly uniform.

These results illustrate that is not enough to simply fit relative peak heights and widths to determine layer thickness accurately. It is evident that excellent matches can be obtained even when the layer thickness used is in fact incorrect, and compositional grading may be hidden if it is not significant.

Sample	Distance from wafer centre (mm)	Mismatch (ppm)	Composition $\%Al$	Curvature (")	Thickness (μm)	
					Simulation	Pendellösung
GAS5	2	470	35.9	5	1.28	1.47
	6	480	36.7	5	1.28	1.39
	10	500	38.2	5	1.22	1.30
	14	520	39.8	5	1.19	1.30
	18	560	42.8	6	1.05	1.13
GAS6	2	450	34.4	6	1.53	1.60
	6	460	35.2	6	1.49	1.56
	10	470	35.9	6	1.45	1.53
	14	500	38.2	6	1.32	1.43
	18	560	42.8	6	1.13	1.21

Table 4.3

4.5 Problems Associated with the Characterisation of Epilayers

4.5.1 The Effect of Epilayer Tilt on Mismatch Measurement

When substrates are misoriented with respect to the plane of growth, epitaxial layers tend to grow at an angle to the substrate (Nagai, 1974; Olsen and Smith, 1975). This epilayer tilt has been observed in $InGaAs$ layers grown by VPE on 3° misoriented InP substrates (Macrander and Strege, 1986), in $CdTe$

layers grown by MOVPE on 2° misoriented $InSb$ substrates (Bhat et al., 1988), and also in $GaAlAs$ grown on 2° misoriented $GaAs$ substrates (Tanner, Miles, Peterson and Sacks, 1988). Kleiman, Park and Mar (1988) have shown that the value of tilt between the layer and substrate planes depends on both the epilayer thickness and the orientation of the substrate plane. They proposed a simple model based on a stepped substrate surface responsible for a redistribution of the bond lengths between the atoms of the substrate and the epilayer in the interface region leading to the formation of tilt between the planes in the epilayer and the substrate.

In order to determine the composition of the layer it is not enough to use only one rocking curve measure of peak separation. Two rocking curves must be taken from the sample separated by 180° rotation about the surface normal (Hattanda and Takeda, 1973; Kawamura and Okamato, 1979). For symmetric reflections the peak separations, $\Delta\theta$, corresponding to the two cases are

$$\Delta\theta_a = m^* \tan\theta - \delta\phi \ , \qquad \Delta\theta_b = m^* \tan\theta + \delta\phi \ , \tag{4.10}$$

where $\delta\phi$ is the component of tilt between the layer and substrate in the incident plane. The mismatch is therefore determined from the average peak separation,

$$m^* = \frac{1}{2}(\Delta\theta_a + \Delta\theta_b)\cot\theta \ . \tag{4.11}$$

In order to measure the absolute tilt, rather than tilt component, it is necessary to record four rocking curves rotated 90° with respect to one another for convenience (Tanner, Miles, Peterson and Sacks, 1988) although only three are actually needed. If $\delta\phi_1$ is the tilt determined from the difference between the 0° and 180° positions and $\delta\phi_2$ is that determined from the difference between the 90° and 270° positions, then the maximum tilt $\delta\phi_0$ is given by

$$\tan^2\delta\phi_0 = \tan^2\delta\phi_1 + \tan^2\delta\phi_2 \ . \tag{4.12}$$

The direction of tilt is at an angle α away from the first measurement setting, given by

$$\tan\alpha = \frac{\tan\delta\phi_2}{\tan\delta\phi_1} \ . \tag{4.13}$$

Tanner et al. (1988) recorded a difference of 18″ between measurements of peak splitting taken from rocking curves 180° apart. If only one rocking curve had been taken the calculated aluminium concentration would have been inaccurate by 2%. Auvray, Baudet and Regreny (1989) have also reported similar possible errors from $AlAs$ epitaxial layers and $AlAs/GaAs$ superlattices MBE grown on misoriented (001) $GaAs$ substrates and for substrate misorientation above 0.5° the tilt is proportional to the miscut angle (Isherwood, Brown and Halliwell, 1981).

Figures 4.7(a) and (b) show two 004 rocking curves 180° apart, using a first crystal 004 reflection from a strained layer superlattice structure, sample identification Code SLS1, grown with MBE by C. Stanley, the structure of which is given in figure 4.8. The $1\mu m$ superlattice is surrounded by two $3\mu m$ cladding layers of $GaAs$, grown on a misoriented $GaAs$ substrate. The substrate tilt was determined to be 1.4° by taking four rocking curves 90° apart and using a modified form of equation (4.12)

$$\tan^2 \phi_0 = \tan^2 \phi_1 + \tan^2 \phi_2 \ , \qquad 4.14$$

where ϕ now represents the tilt of the substrate with respect to the (001) plane. The asymmetry seen does not in fact arise from the superlattice itself, as its mismatch is large and the angular range shown is small, but from the cladding. The asymmetry is probably due to the smaller unresolved substrate peak combining with the stronger cladding layer peak. Its movement with respect to the layer peak indicates a tilt between the substrate and superlattice stack. The average mismatch of the cladding, using equation (4.11), is zero, but the tilt causing the cladding to appear mismatched is $100 \pm 10''$.

Figure 4.9 shows two 004 rocking curves taken 180° apart along the direction of maximum substrate tilt from another strained layer superlattice, code SLS2. In this case the first crystal reflection was an 044 from an 011 surface, and so the arrangement was dispersive. The rocking curves had a step size of 4″ and 40 seconds counting time per step. The sample structure was nominally the same as SLS1 but the top cladding layer had not been deposited and the number of superlattice periods was reduced. Using the same method as before

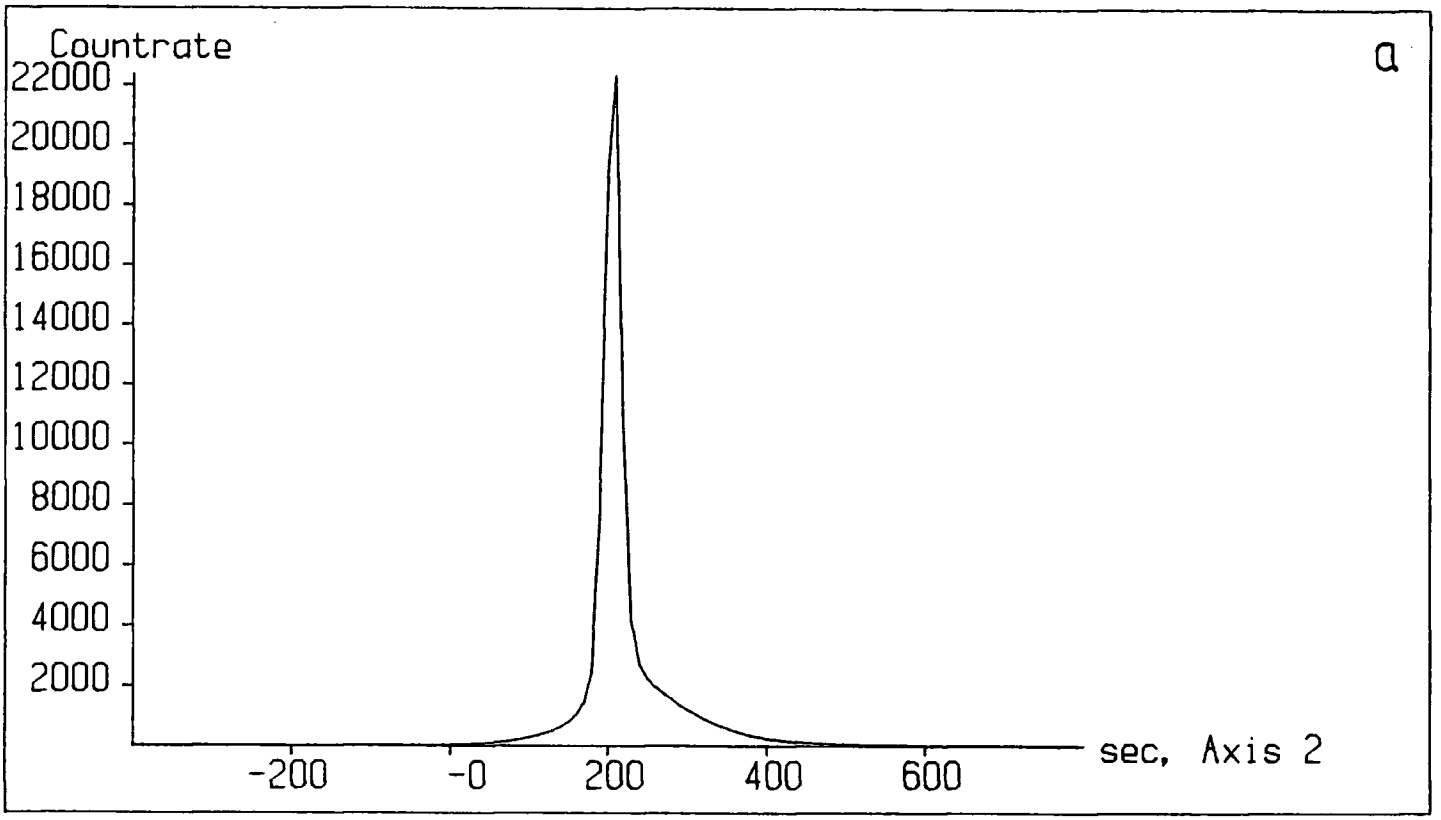

Figure 4.7: 004 rocking curves of SLS1 with (a) 0° and (b) 180° rotation about the surface normal.

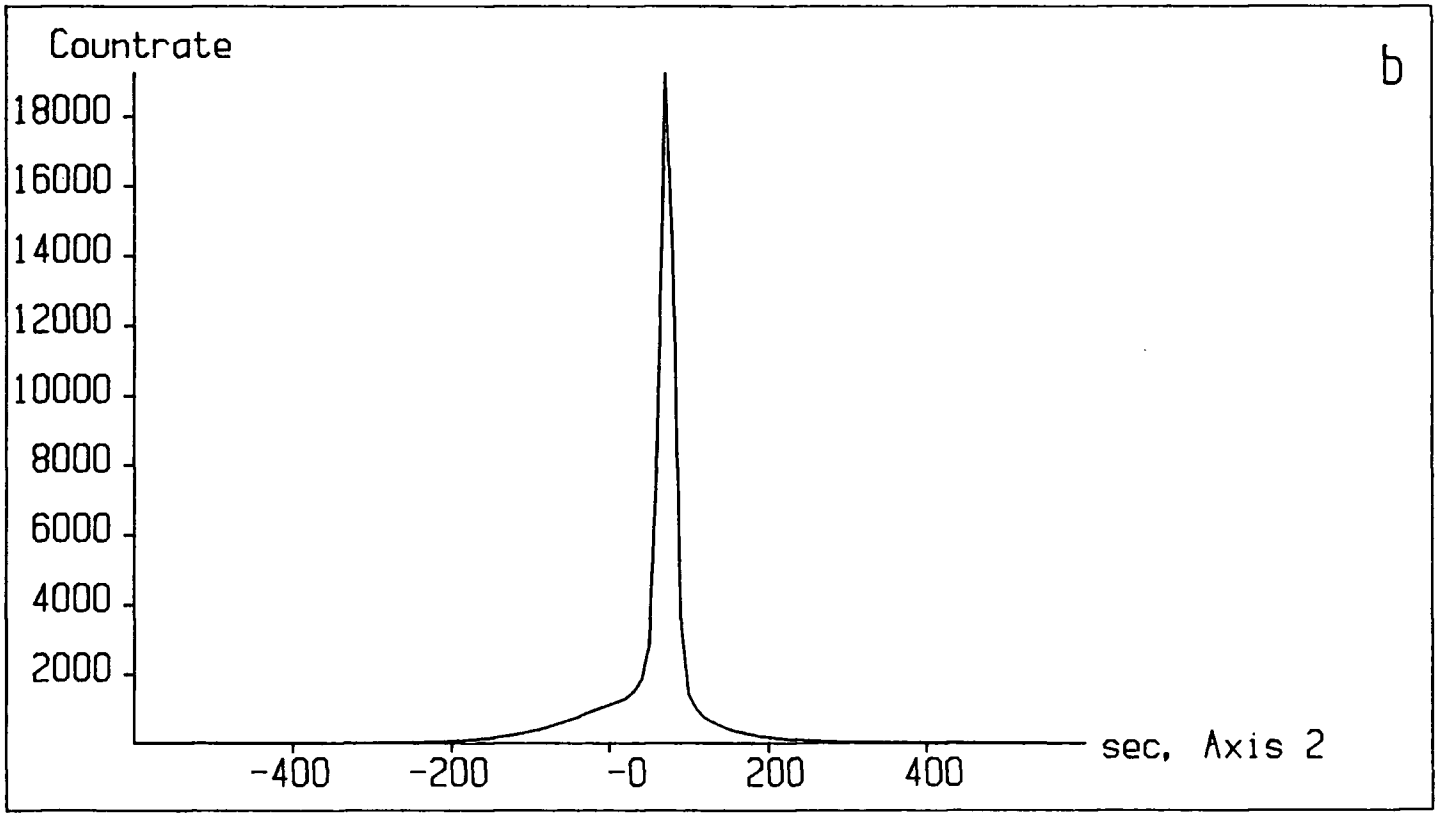

30% Indium well/GaAs barrier
grown on GaAs substrate

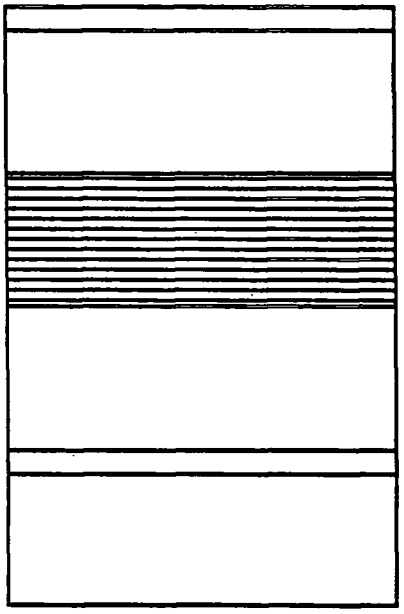

	Dimension	Doping (cm^{-3})
p+ GaAs Cap	100Å	$5x10^{18}$
p GaAs Cladding	3μm	$5x10^{16}$
i InGaAs/GaAs SLS	1μm	intrinsic
n GaAs Cladding	3μm	$5x10^{16}$
n+ GaAs	100Å	$5x10^{18}$
n+ GaAs Substrate	≈0.6mm	n+

Room Temperature
Band-edge of SLS

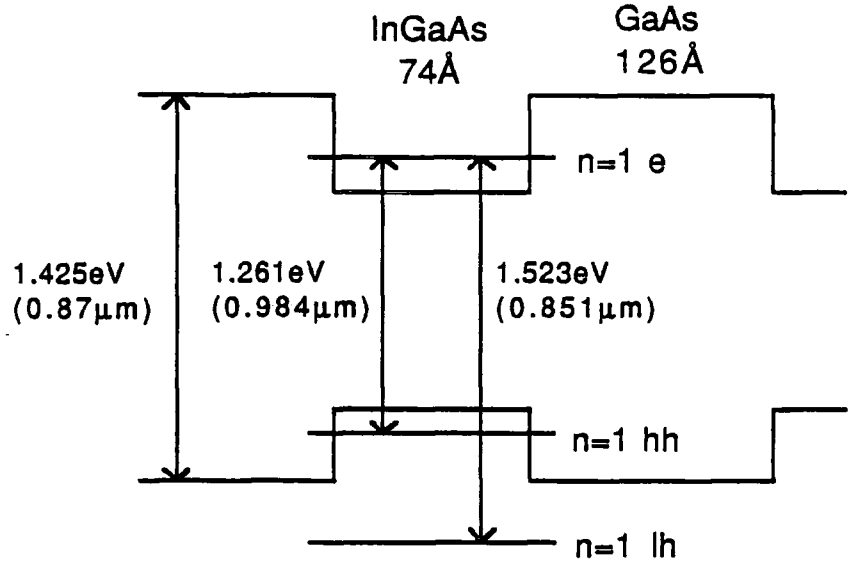

Figure 4.8: Structure of SLS1, *InGaAs/GaAs* strained- layer superlattice.

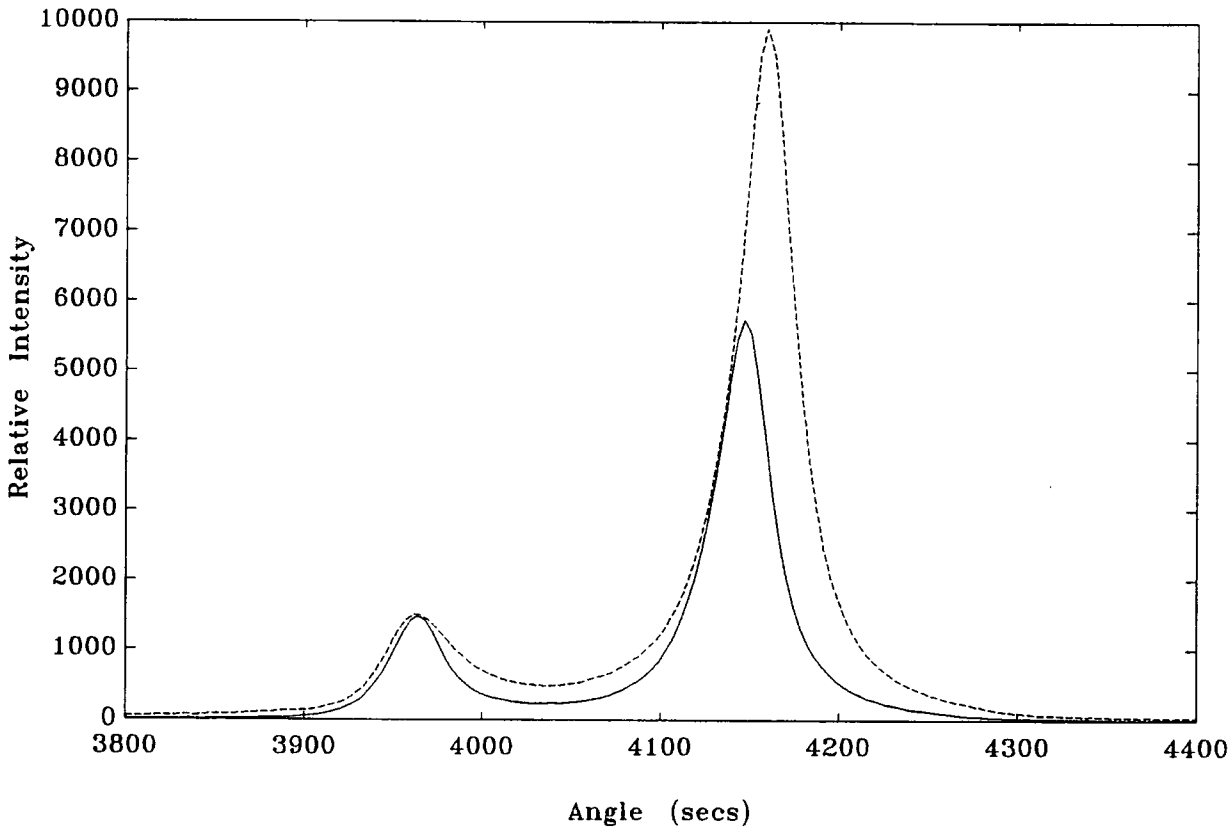

Figure 4.9: 004 rocking curves of SLS2 with 0° (solid) and 180° (dashed) rotation about the surface normal.

the maximum substrate tilt was found to be 1.6° with the 001 surface. The low intensity peaks on the rocking curves correspond to the substrate. The layer-substrate separation between the two rocking curves was 12″ corresponding to an epilayer tilt of 6″. In this sample the cladding layer was mismatched from the substrate by $+699ppm$ probably arising from the doping process. The substrate tilt of 1.6° also affects the relative peak heights and the difference between the layer peak in the high and low incidence cases is significant. It is vital, therefore, in order to measure mismatch and determine layer thicknesses from simulation, to record two rocking curves rotated by 180° about the surface normal. The characterisation of superlattices is dealt with in detail in section 4.6.

4.5.2 The Effect of Wavelength Dispersion in the Parallel Setting

Significant peak broadening can occur if the Bragg angles of the first and second crystals are different, even in the parallel setting. When both the $K\alpha_1$ and $K\alpha_2$ components are present in the incident beam they will be resolved on the rocking curve if the dispersion is large enough, which complicates its interpretation. This is illustrated in the following example.

A two layer structure grown by T. Krier was characterised using a Bede Scientific Instruments $QC1$ desk top diffractometer (Bede Scientific Instruments, 1987). This instrument had a fixed first crystal of $GaAs$ with both $CuK\alpha_1$ and $K\alpha_2$ components contained in the incident beam. The sample was grown on an $InAs$ substrate by LPE and consisted of two layers of nominal composition $InAs_{0.86}Sb_{0.06}P_{0.08}$, the first n-doped and the second p-doped. The sample was stepped across its surface to expose the first layer and substrate. Three rocking curves were taken over 1000″ ranges with 4″ step size and 2 second counting time a step. Since the Bragg angle of InAs is 30.6° compared to 33° for $GaAs$ the $K\alpha_1$ $K\alpha_2$ peak separation is calculated using equation (2.10) to be 30″. The rocking curves are shown in figures 4.10(a), (b) and (c), corresponding to two layers, one layer and the substrate respectively. The rocking curve in figure 4.10(a) is complicated and it is not immediately obvious that it arises from only two layers. However, the subsidiary maximum on the substrate peak at roughly half the peak intensity is present on the rocking curve from the part of the sample without growth, figure 4.10(c), and is simply the $K\alpha_2$ peak. The mismatch may

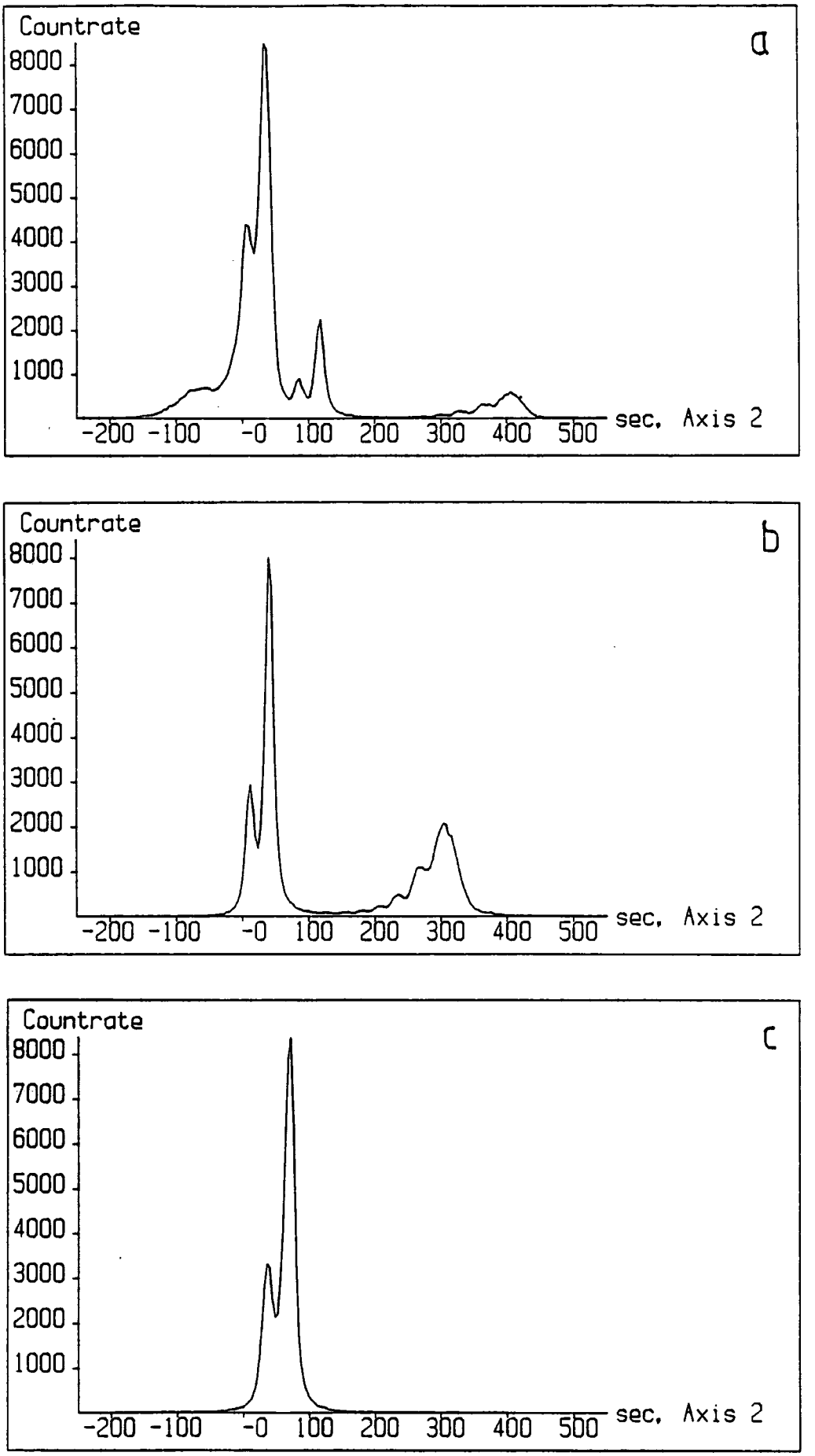

Figure 4.10: 004 rocking curves of a two layer structure of $InAsSbP$ on $InAs$ illustrating wavelength dispersion; (a) 2 layers, (b) 1 layer, (c) substrate only.

then be determined for each layer using only the separations between the $K\alpha_1$ peaks. The first layer (n-type), is of poor quality and graded in composition. Its rocking curve peak is very broad and the $K\alpha_2$ peak is not individually resolved as a result. The peak shape is characteristic of graded layers (Halliwell, Juler and Norman, 1983; Bowen, Hill and Tanner, 1987). In addition, the position of the peak changes for different points on the sample which means that the average layer composition changes significantly across the surface, from $-1400ppm$ to $-990ppm$ in $10mm$. The second layer, (p-type), is of better quality and has a mismatch of $-310ppm$.

It was not possible to simulate the structure to determine layer thickness because of the $K\alpha_2$ contamination. For the cases where a dispersive geometry cannot be avoided it is good practice to remove the $K\alpha_2$ peak with a slit between the two axes. The rocking curve peaks will then only be broadened by the linewidth of the $K\alpha_1$ peak.

4.5.3 The Interpretation of Complicated Rocking Curves

Figure 4.11 shows an 004 rocking curve of a multilayer structure grown at British Telecom by G. Scott using MBE, code INP1. The rocking curve was taken on a $QC1$ diffractometer having an InP first crystal with a step size of $4''$ and a counting time of 120 seconds per step. The sample structure consists of 15 layers and is shown in figure 4.12. The layer thicknesses have been measured by TEM but the mismatches are unknown. The rocking curve is highly complex and it is evident that there are just too many varying quantities for an interpretation to be achieved unless a great deal of time is spent simulating it. Although this is an extreme case it illustrates the need for cross referencing with other characterisation techniques or other reflections in order to reduce the number of unknowns, and hence allow complete characterisation.

4.6 Characterisation of Superlattices

4.6.1 Modelling Techniques

Superlattices and Multi-Quantum Well (MQW) structures generally consist of alternating layers of two semiconductors which are sufficiently thin to exploit

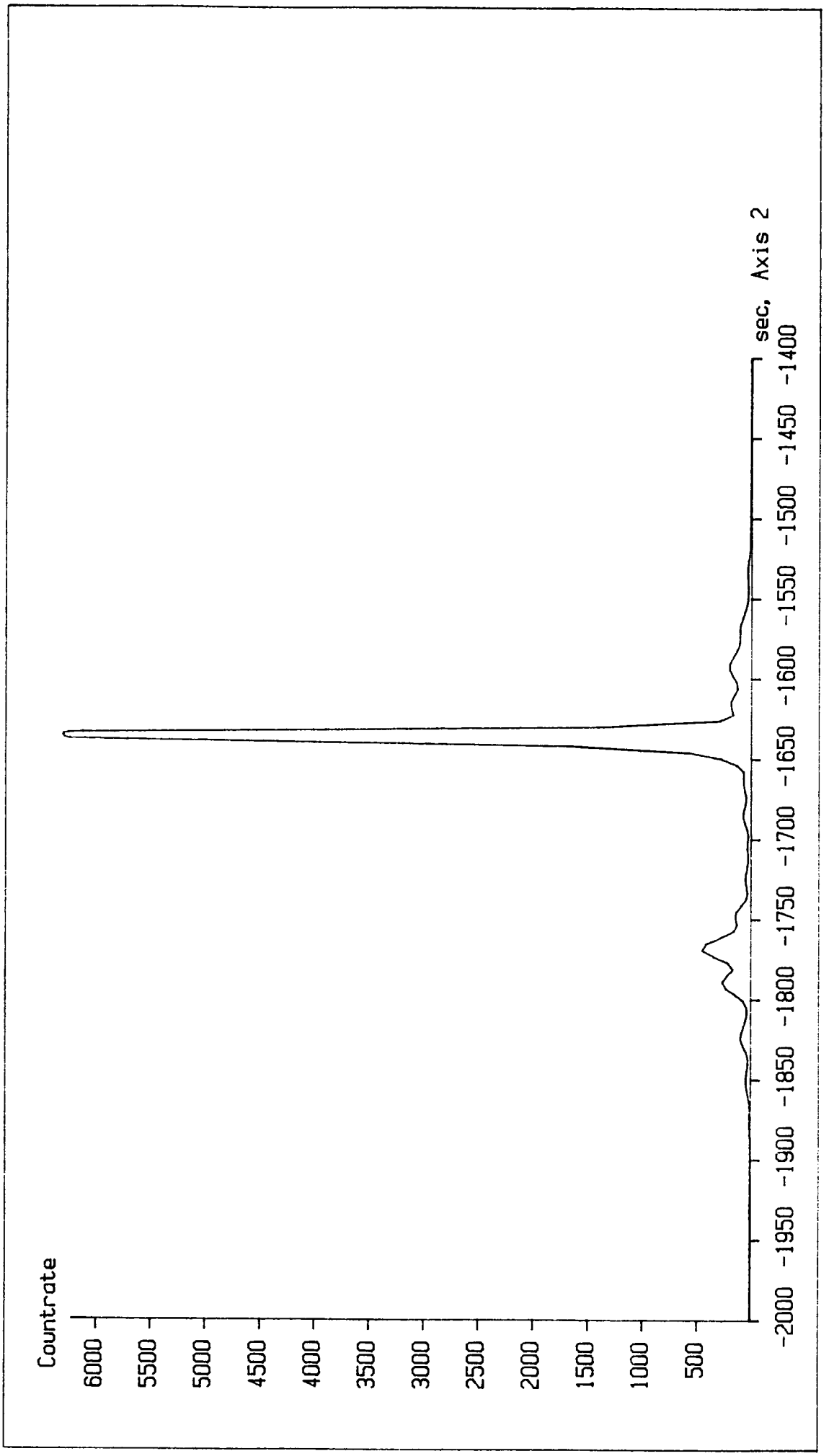

Figure 4.11: 004 rocking curve of INP1.

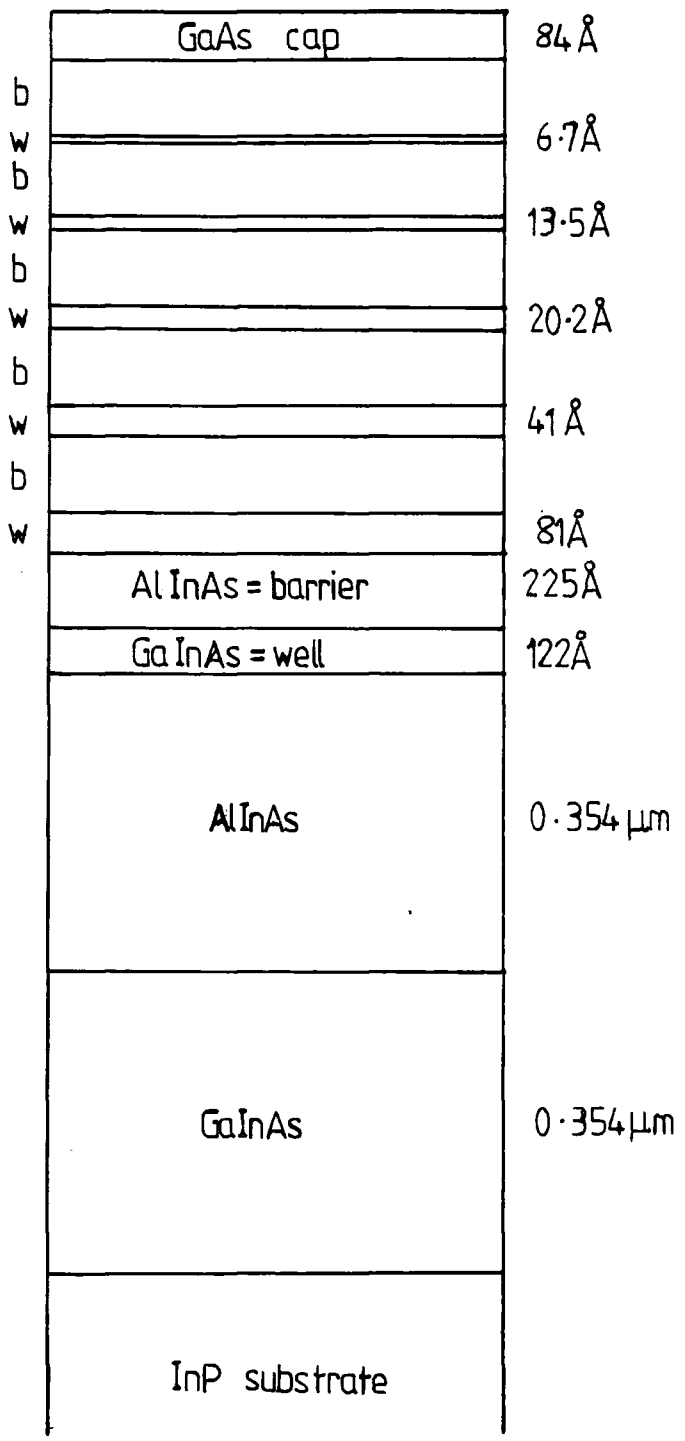

Figure 4.12: Structure of sample INP1.

quantum size effects. The difference between them is that superlattices have barrier widths thin enough to allow coupling between the wells from overlapping wave-functions, and MQW's do not. The basic structure is equivalent however and is described by the superlattice period Λ, which is defined to be the sum of the thicknesses of the well and the barrier,

$$\Lambda = 2n_1a_1 + 2n_2a_2 \ , \qquad 4.15$$

(Segmüller and Blakeslee, 1973; Segmüller, Krishna and Esaki, 1977). n_1 and n_2 are the number of monolayers in each layer, and a_1 and a_2 are the spacings between successive molecular layers. This is illustrated for a $(Ga_{1-x}Al_xAs)n_1$, $(GaAs)n_2$ $/GaAs(001)$ superlattice in figure 4.13 (Kervarec et al., 1984).

The rocking curve of a superlattice is quite complex and a simulated superlattice of $(Ga_{0.38}Al_{0.62}As)n_1 = 40$, $(GaAs)n_1 = 30$ $/GaAs$ with 80 repeat periods is shown in figure 4.14. The curve consists of a substrate peak together with a peak corresponding to the average composition of the superlattice, known as the zeroth order peak. Superimposed symmetrically about this peak is a set of subsidiary maxima, known as satellite peaks, with spacing determined by the periodicity of the superlattice. Their orders are labelled in figure 4.14 and may be analysed to give a great deal of structural information. The following treatment in this section follows that of Fewster (1986, 1987, 1988).

The understanding of the origin of the satellites comes from a consideration of the lattice periodicities contained in the superlattice. Apart from the periodicity due to the average lattice spacing there exist periodicities arising from the lattice spacing $\pm$ the superlattice period. In reciprocal space this will give rise to additional points near each principal point, representing the additional periodicity. Therefore on the rocking curve at least one satellite peak is found on each side of the zeroth order peak, whose spacing from it is determined by the superlattice period. Another approach is to consider the diffraction pattern as the Fourier transform of the structure factor throughout the superlattice. The number of satellite peaks observed will depend on the abruptness of the interface between periods. So, for example, if the periods were graded so that the overall structure factor variation were sinusoidal, only one Fourier component

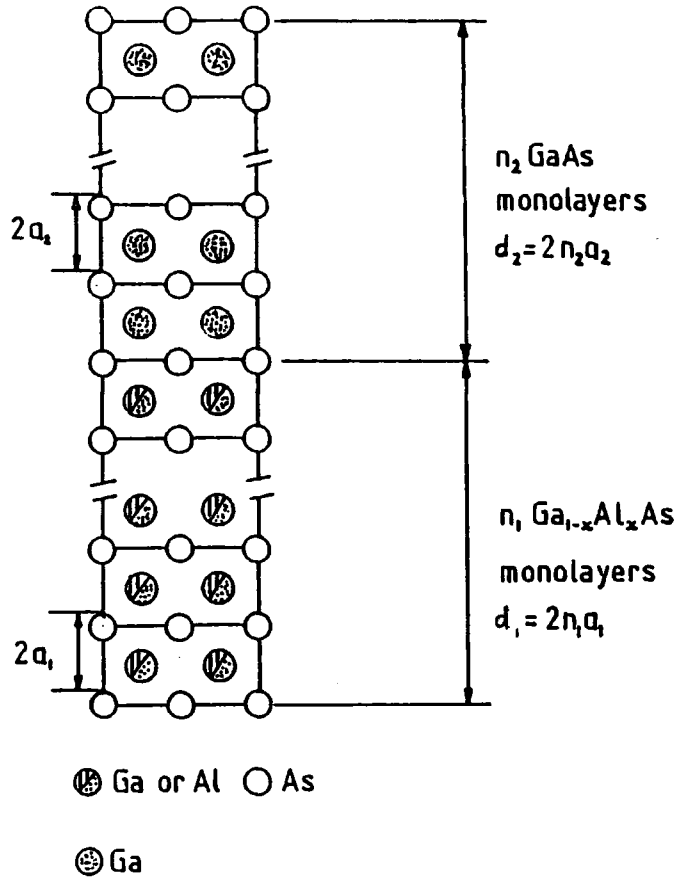

Figure 4.13: The macroscopic and microscopic construction of a *GaAlAs/GaAs* superlattice. The individual layers are an integer number of monolayers which is half a unit cell. After Kervarec et al.(1984).

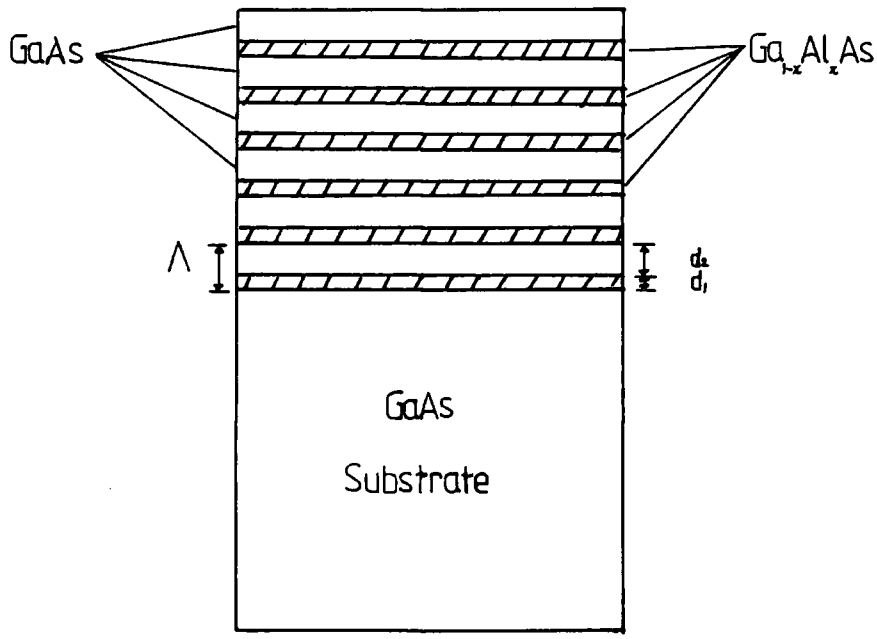

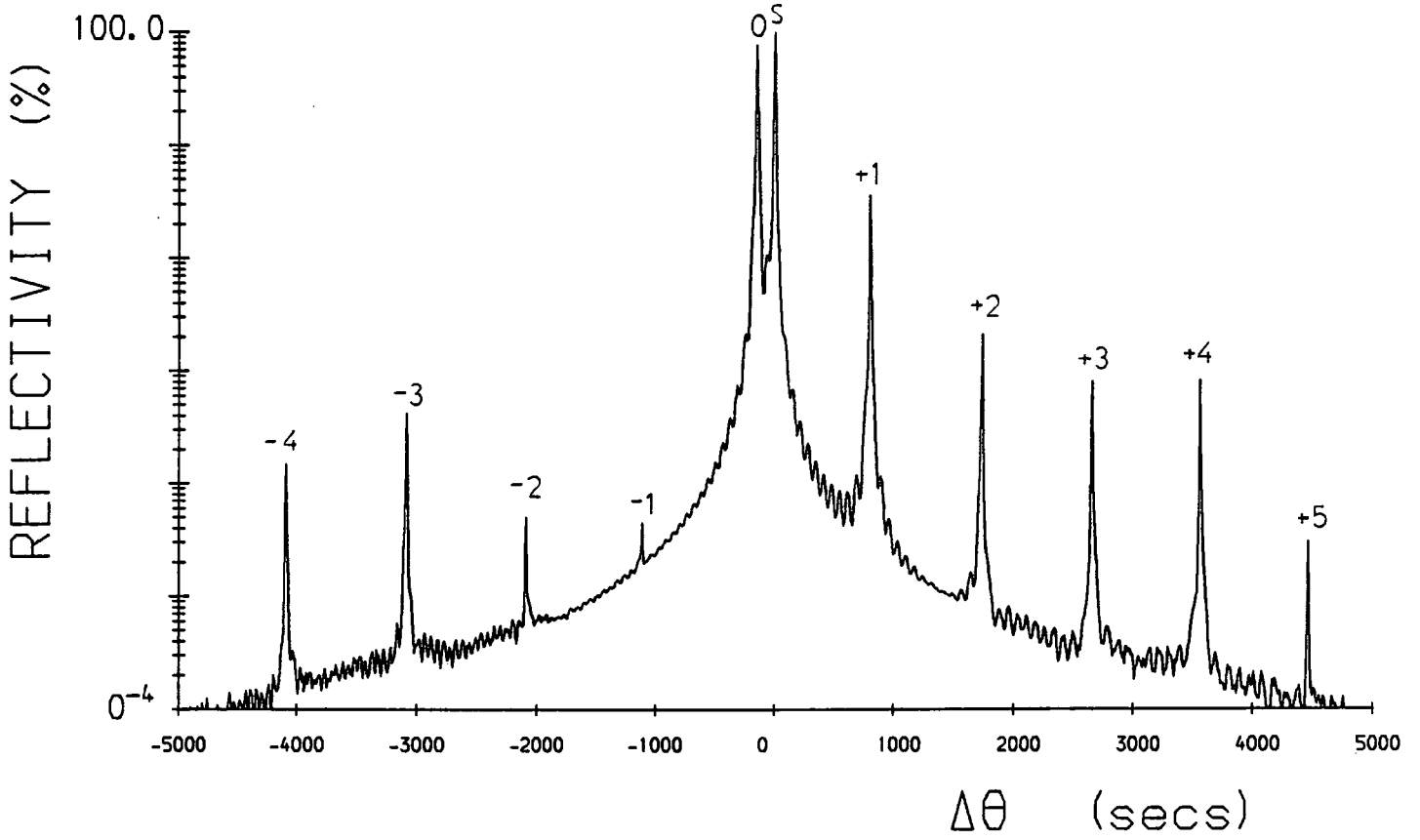

Figure 4.14: Simulated 004 rocking curve of an 80 repeat period $GaAlAs/GaAs$ superlattice.

would exist and thus only one pair of satellites. If the interface is abrupt, this is equivalent to the Fourier transform of a square wave, which consists of an infinite number of odd harmonics and results in a corresponding infinite number of odd satellites. The number of observed satellites therefore gives an indication of the degree of grading in the interfaces.

It is unusual that a superlattice is grown with a perfectly constant period throughout, and variation in period is known as period dispersion. The zeroth order peak remains unchanged because the average composition is the same but the satellite spacings will be slightly different for each of the periods found. This will affect the higher order satellite peaks more than the lower orders and so period dispersion leads to an increase in the width of the satellite peaks with satellite order.

The resolution of higher order satellites from the background requires long data collection periods with a DCD. A powder diffractometer has the advantage of very high intensities which makes it very fast, and it may be used for many of the measurements. Although it cannot usually distinguish the zeroth order peak from the substrate peak, it is accurate enough for measurements of satellite spacing and relative intensity. However, accurate peak profiles are best obtained with double crystal instruments.

The average superlattice composition $\bar{x}$, is determined in the normal way as explained in section 4.3. It is important to note that their zeroth order peak occurs at the average Bragg angle of the superlattice and not of the alloy layers alone. To determine the alloy composition, x, it is necessary to know the well thickness d_1, as well as the period. x is given by

$$x = \frac{\bar{x}\Lambda}{d_1} \,. \qquad 4.16$$

The superlattice period is determined from the separation of the satellites on the rocking curve. For a period of Λ the distance between subsidiary maxima in reciprocal space is $1/\Lambda$, and so by Bragg's law

$$2\Lambda \sin\theta_1 = L_1\lambda \,, \qquad 2\Lambda \sin\theta_2 = L_2\lambda \,, \quad etc.,$$

for the diffraction orders L_1, $L_2, ...L_i, ...$, L_j, and so for symmetric reflections

$$\Lambda = \frac{(L_i - L_j)\lambda}{2(\sin\theta_i - \sin\theta_j)} \ . \qquad 4.17$$

Therefore by measuring the diffraction angles θ for various diffraction orders L, a good estimate of the average period can be obtained by determining Λ for combinations of ΔL.

The satellite intensity is affected by the ratio of the well to barrier thicknesses within a superlattice unit cell. To determine the thicknesses individually, it is necessary to calculate the structure factors of all the observable satellites, summing over atoms in a unit cell, and compare these with the integrated intensities actually measured after correcting for any instrumental effects. The calculation is iterated until the differences between the calculated and measured intensities is minimised as a function of the well:barrier ratio. The differences are expressed as an R factor

$$R = \frac{\Sigma\big||F_o| - |F_c|\big|}{|F_o|} \ , \qquad 4.18$$

where F_o and F_c are the observed and calculated structure factors.

The period dispersion is obtained from the increase of satellite widths as a function of satellite order. The average full width at half maximum (FWHM) of the satellites is first determined after correcting for instrument broadening. This is straightforward since the profiles are Gaussian and the zeroth order width containing the instrumental function, β_0, may simply be subtracted from the satellite width, β_1, to give the required integral width (Fewster, 1988)

$$\beta_s = (\beta_1^2 - \beta_0^2)^{\frac{1}{2}} \ . \qquad 4.19$$

Assuming that the satellite peaks are near the Bragg peak and that over that range $\cos\theta$ does not change appreciably, equation (4.17) can be simplified to

$$\Lambda = \frac{(L_i - L_j)\lambda}{2\cos\theta\Delta\theta} \ . \qquad 4.20$$

To determine the influence of the period variation on the broadening of each satellite equation (4.20) is differentiated to give

$$\Delta\Lambda = \frac{(L_i - L_j)\lambda\delta(\Delta\theta)}{\cos\theta(\Delta\theta)^2} \ , \qquad 4.21$$

where $\delta(\Delta\theta)$ is the difference in angle within the satellite for a period difference of $\Delta\Lambda$. The FWHM of the Gaussian distribution of periods is therefore given by

$$\sigma(\Lambda) = \frac{(L_i - L_j)\lambda\beta_s}{\cos\theta(\Delta\theta)^2} \ , \qquad 4.22$$

where β_s is the statistical average FWHM for all the measured satellites.

Over the region where X-rays are coherently diffracted the diffraction features will be the sum of the intensities from this region. Roughness and grading are indistinguishable to X-rays which average over the coherence width. Fewster's treatment assumes that roughness is confined to less than one monolayer, to account for incommensurability, and that grading accounts for any other variation at the interface. The roughness is introduced by adding coherently the structure factors of two commensurate periods, with well widths straddling the average value. These are then scaled with the previously determined Gaussian dispersion of periods (equation 4.22) and added to give the overall structure factor for that satellite. The structure factor of each satellite is compared with experimental intensities, again using R factors, with the variable being the compositional grading away from the interface, altered by one layer at a time. A linear grading is usually adequate.

Lyons, Scott and Halliwell (1989) have shown that compositional grading in $GaInAs/InP$ superlattices grown by MBE is limited to 2 or 3 monolayers. They have shown that previous methods of modelling superlattices both dynamically (Lyons and Halliwell, 1985, 1986) and kinematically (Vandenberg et al., 1986, 1988) as alternating layers of two materials each having a constant strain and composition have serious limitations. Apart from high computational times the model is not realistic for layers only one or two monolayers thick and has difficulty predicting the way strain varies across the interface (Lyons, 1989).

An alternative approach was used which describes the superlattice period as a tetragonal unit cell with the c parameter equal to the superlattice period. The structure factor for this extended unit cell is then calculated using the standard equations (Segmüller et al., 1977; Kervarec et al., 1984). The interfacial region is modelled by a single variable which describes both the scattering factor and lattice parameter at any point in the period. Although the structure factor approach is essentially kinematic, it is valid for most superlattice structures since satellites are generally very weak. Experimental rocking curves were analysed by assuming a trial structure and calculating the relative intensities of each satellite peak. The first stage was to determine the relative thickness of the individual layers by calculating the satellite intensities assuming a perfect interface and comparing with the experimental curves. Grading was then introduced at the model interfaces to see whether the fit could be further improved.

Although X-rays cannot distinguish between interfacial grading and roughness it is evident that they can give an accurate indication of the quality of interfaces. With the trend towards growth of narrower wells, grading over a few monolayers may significantly change the electrical and optical properties of devices made from superlattices. Simulation programmes modelling experimental rocking curves need to become increasingly sophisticated to allow for compositional grading and roughness over narrow interfaces which is a real problem in the growth of heteroepitaxial layers (Lyons, 1989).

4.6.2 Characterisation of a Periodically Graded Layer

The thickness and average composition of GAS5 were determined in section 4.4. The results suggested that the layer was graded and TEM showed that this grading was periodic. The layer could therefore be expected to behave like a superlattice and display satellite peaks on its rocking curve. However, as explained in the previous section, when the interfaces are graded so much that the compositional profile becomes sinusoidal then only one pair of satellites will result.

A rocking curve was recorded using the 004 reflection over a range of several degrees with a step size of $40''$ and a counting time of 200 seconds per step, using a proportional counter. The grading was known to be greater at the edge

of the wafer and so a point was chosen at $18mm$ from the wafer centre, the short range scan of which is shown in figure 4.3(e), corresponding to a layer thickness of $1.13\mu m$ with 42.8% Aluminium. Figure 4.15 shows the long range rocking curve at 1% and 0.05% of the substrate peak intensity. The first order satellite can be seen on the high angle side of the layer peak. It is a real peak as it is significantly different from the noise. Using equation (4.17) the satellite separation gives the period of the grading to be $\Lambda = 55 \pm 1\mathring{A}$. Unfortunately it was not possible to simulate this to determine the magnitude of the grading as the Durham programme modelled abrupt interfaces only. A qualitative simulation did show, however, that the high angle satellite was stronger than the low angle satellite which explained why only one satellite was seen experimentally.

4.6.3 Experimental Characterisation of a Superlattice

Sample MQW1 was grown by G. Scott of British Telecom using MBE. It consisted nominally of 20 repeat periods of $AlInAs/InGaAs$ of thickness $100/20\mathring{A}$ respectively, grown on InP. A rocking curve was recorded using the symmetric 004 reflection over a range of $6000''$ with a step size of $8''$ and a counting time of 60 seconds. Figure 4.16 shows the experimental and simulated rocking curves. The superlattice is seen to be closely lattice matched to the substrate and because it is thin ($\simeq 0.25\mu m$), the layer peak cannot be distinguished from the substrate peak. The satellite orders of $-2, -1$ and $+1$ can be seen and from their positions the average position of the zeroth order satellite was determined, giving an average superlattice mismatch of $-107 \pm 40ppm$. The superlattice period was also calculated from the average satellite separation and is $\bar{\Lambda} = 161 \pm 3\mathring{A}$. This is significantly larger than the thickness predicted by crystal growth conditions. By measuring the Pendellösung fringe spacing on the wings of the rocking curve the total thickness of the superlattice was calculated to be $0.29 \pm 0.02\mu m$. This gave the number of repeat periods to be 18 ± 2. The simulated rocking curve took the measured period and scaled the individual layer thicknesses by their initial ratio of 5 : 1 and for simplicity made their mismatches equal. Obviously this is not an accurate fit as the simulation also assumes abrupt interfaces, but it gives an idea of the ideal superlattice rocking curve. A background level of 3 counts per second was added for a better fit. Unfortunately, the signal to noise ratio of the experiment is poor and it is difficult therefore to give an indication

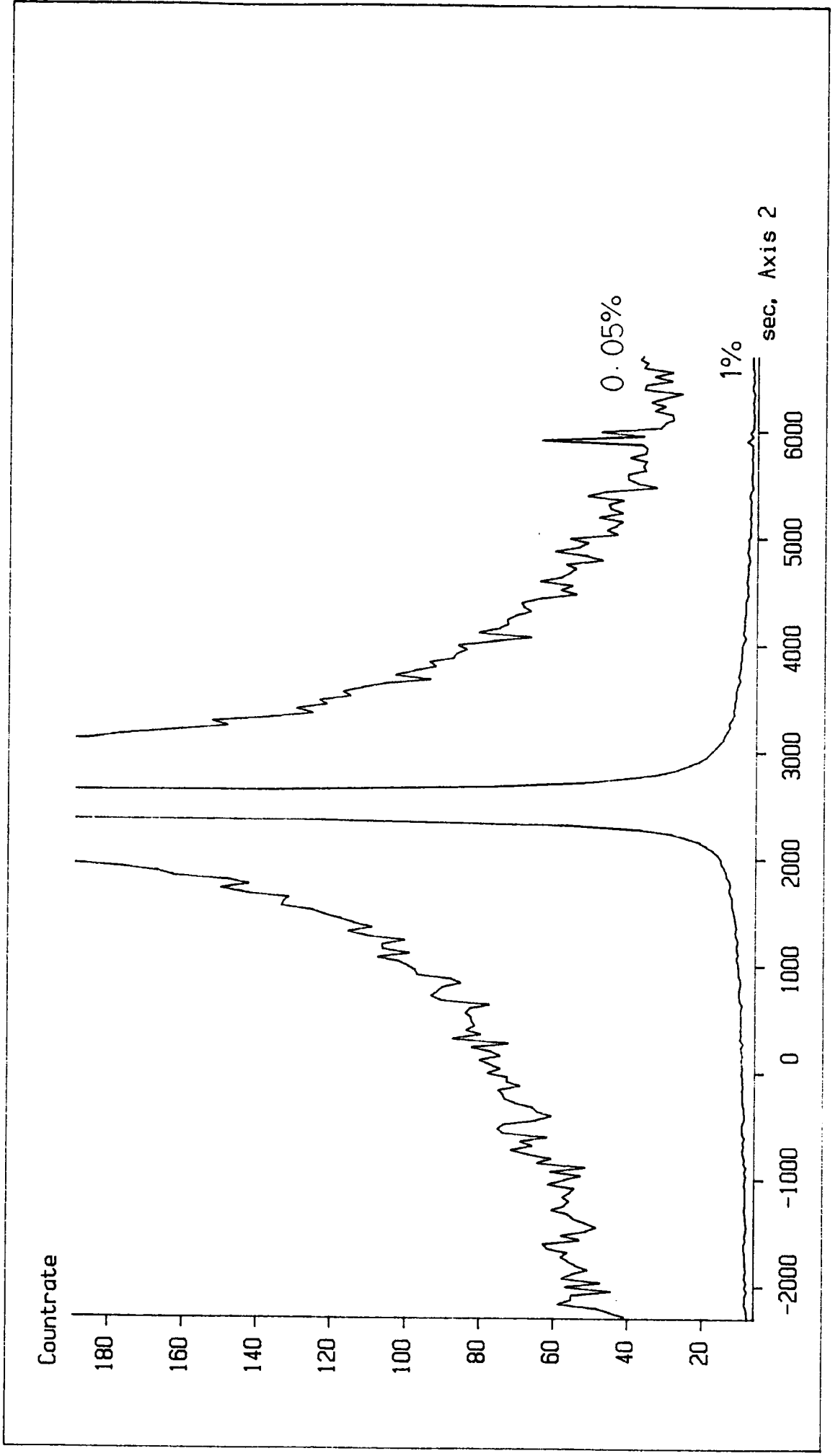

Figure 4.15: 004 long range rocking curve of GAS5 at 1% and 0.05% of the substrate peak intensity.

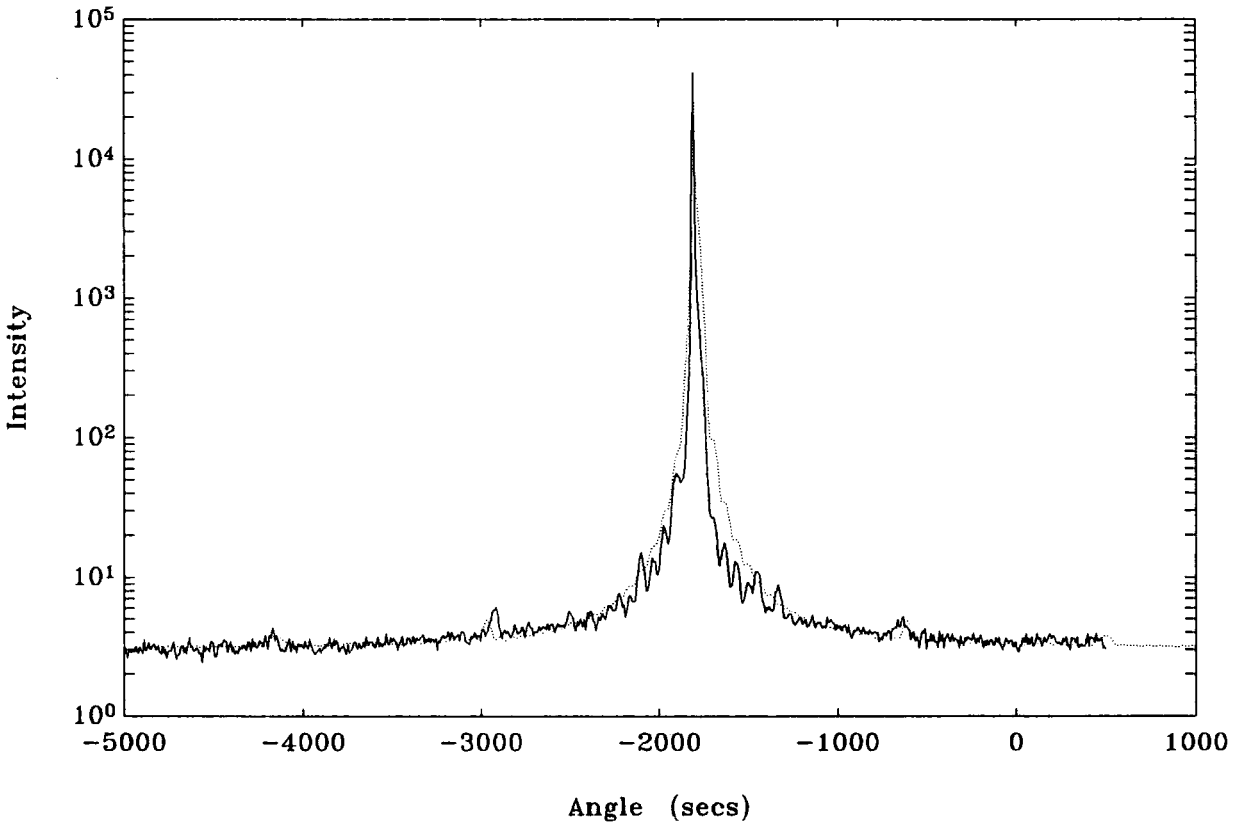

Figure 4.16: 004 experimental (solid) and theoretical (dotted) rocking curves of MQW1.

of interface grading as this requires a detailed comparison of satellite intensities. The use of a proportional counter would be a great improvement.

4.6.4 Superlattice Relaxation

The mechanisms of relaxation occurring in $Si/Si_{1-x}Ge_x$ strained-layer superlattices (SLS) on Si substrates has been described (Fiory et al., 1984; Tuppen et al., 1987). Superlattices can become relaxed in the same way as single heteroepitaxial layers and are more likely to do so if the layer mismatch is large, as it the case in SLS's. The degree of relaxation can be measured more precisely than either Raman spectroscopy or TEM using DCD (Halliwell et al., 1989).

To determine the difference between the substrate and mean lattice tilts, $d\phi$, and Bragg angles, $d\theta$ for incoherent layers, both the high and low angle beam paths of an asymmetric reflection must be used, as explained in section 4.3.1. The Bragg angle θ_m, and the plane tilt ϕ_m, for the mean cell can then be found and used to calculate the a and c parameters of the mean tetragonal unit cell from the known substrate lattice parameter using the following expressions derived from equation (4.6)

$$c = \frac{\lambda l}{2 \sin\theta_m \cos\phi_m} \ , \tag{4.23}$$

$$a = \left\{ \frac{h^2 + k^2}{4 \sin^2\theta_m/\lambda^2 - l^2/c^2} \right\}^{\frac{1}{2}} \ , \tag{4.24}$$

for an hkl reflection. a and c are then substituted into equation (4.25) to calculate the equivalent lattice parameter of a cell with cubic symmetry a_r,

$$a_r = (c - a)\frac{(1-\nu)}{(1+\nu)} + a \ , \tag{4.25}$$

where ν is Poisson's ratio. The mean composition of the superlattice may now be determined.

For asymmetric reflections equation (4.17) is no longer valid for determining the superlattice period. In order to calculate the correct expression which also takes into account lattice tilts, an Ewald construction may be used. This is

essentially a description of Bragg's law in reciprocal space which states that to satisfy Bragg's law for a set of planes hkl the reciprocal lattice point hkl must fall on the surface of a sphere of radius $1/\lambda$. Figure 4.17 shows the Ewald construction for an hkl reflection from the n^{th} order satellite.

The reciprocal lattice vector for the n^{th} order satellite reflection is given by

$$\frac{1}{d} = \sqrt{\frac{h^2+k^2}{a^2} + \frac{n^2}{c^2}} = d^* \ , \tag{4.26}$$

and so

$$\sin\theta = \frac{\lambda}{2}\sqrt{\frac{h^2+k^2}{a^2} + \frac{n^2}{c^2}} = \frac{\lambda}{2}d^* \ . \tag{4.27}$$

Now for a high angle of incidence beam path the satellite spacing is $d(\theta+\phi)/dn$, and for a low angle of incidence the spacing is $d(\theta-\phi)/dn$. Therefore, from equation (4.27)

$$\frac{d\theta}{dd^*} = \frac{1}{\sqrt{\frac{4}{\lambda^2} - d^{*2}}} = \frac{1}{\sqrt{\frac{4}{\lambda^2} - [\frac{h^2+k^2}{a^2} + \frac{n^2}{c^2}]}} \ . \tag{4.28}$$

Now

$$\frac{d\theta}{dn} = \frac{d\theta}{dd^*}.\frac{dd^*}{dn} = \frac{1}{\sqrt{\frac{4}{\lambda^2} - [\frac{h^2+k^2}{a^2} + \frac{n^2}{c^2}]}} \cdot \frac{n/c^2}{\sqrt{\frac{h^2+k^2}{a^2} + \frac{n^2}{c^2}}} \ . \tag{4.29}$$

Using (4.27) we have

$$\cos\theta = \sqrt{1 - \frac{\lambda^2}{4}\Big(\frac{h^2+k^2}{a^2} + \frac{n^2}{c^2}\Big)} \ , \tag{4.30}$$

and combining equations (4.27), (4.29) and (4.30) we find

$$\frac{d\theta}{dn} = \frac{n\lambda^2}{2c^2\sin 2\theta} \ . \tag{4.31}$$

Similarly for $d\phi/dn$, we have

$$\tan\phi = \sqrt{h^2+k^2}.\frac{c}{an} \ , \tag{4.32}$$

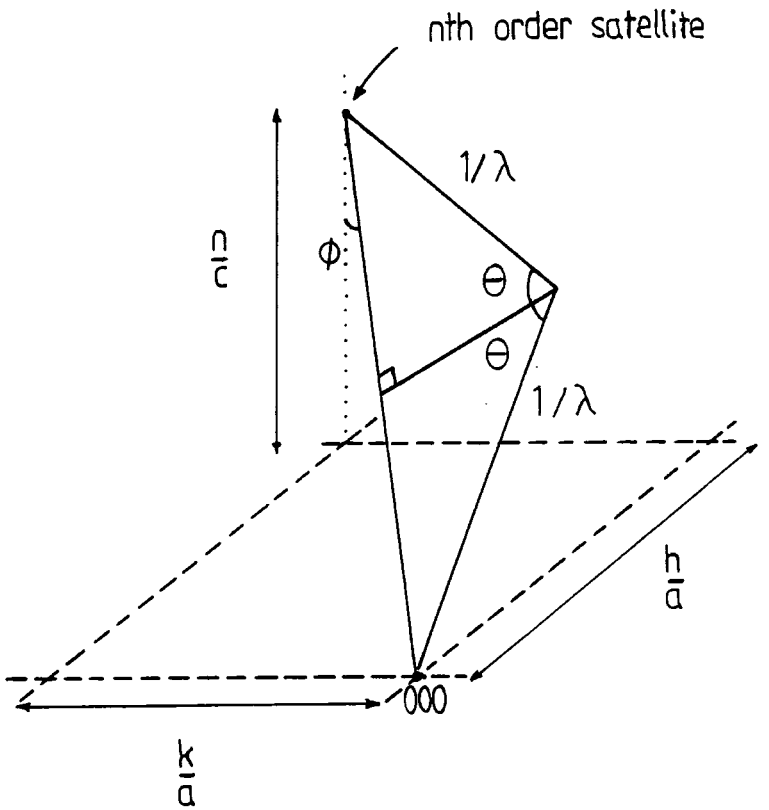

Figure 4.17: Ewald construction for a superlattice reflection.

and so

$$\frac{d\phi}{dn} = \frac{-\sqrt{h^2+k^2}/ca}{\frac{h^2+k^2}{a^2} + \frac{n^2}{c^2}} \,. \tag{4.33}$$

Combining equations (4.31) and (4.33) and using equation (4.27) we have therefore

$$\begin{aligned} \frac{d(\theta+\phi)}{dn} &= \frac{n\lambda^2}{2c^2 \sin 2\theta} - \frac{(h^2+k^2)^{\frac{1}{2}}\lambda^2}{4ca \sin^2\theta} \qquad \textit{High angle,} \\ \frac{d(\theta-\phi)}{dn} &= \frac{n\lambda^2}{2c^2 \sin 2\theta} + \frac{(h^2+k^2)^{\frac{1}{2}}\lambda^2}{4ca \sin^2\theta} \qquad \textit{Low angle.} \end{aligned} \tag{4.34}$$

For satellites close to the substrate peak n/c is approximately the normal component of the substrate reciprocal lattice vector. Hence, if we define S_H and S_L as the angular spacing of the satellites for the high and low angles of incidence respectively, equation (4.34) can now be written as

$$\begin{aligned} S_H\Lambda &= \frac{\lambda \sin\theta_{00l}}{\sin 2\theta_{hkl}} - \frac{(h^2+k^2)^{\frac{1}{2}}\lambda^2}{4a \sin^2\theta_{hkl}} \\ S_L\Lambda &= \frac{\lambda \sin\theta_{00l}}{\sin 2\theta_{hkl}} + \frac{(h^2+k^2)^{\frac{1}{2}}\lambda^2}{4a \sin^2\theta_{hkl}} \,. \end{aligned} \tag{4.35}$$

The percentage relaxation, $R\%$, is given by

$$R\% = \frac{(a-a_0)}{(a_r-a_0)} \times 100 \,, \tag{4.36}$$

where a_0 is the lattice parameter of the substrate (Halliwell et al., 1989). For an unrelaxed superlattice the lattice parameters of the mean unit cell and the substrate match parallel to the surface, with the mean cell tetragonally distorted perpendicular to the surface. This is 0% relaxation. At 100% relaxation the mean unit cell is cubic.

These expressions allowing the mean unit cell parameters to be derived for relaxed superlattices as well as the period of the superlattice using asymmetric reflections can now be applied experimentally. Sample MQW2 was grown by G.

Scott using MBE. It consisted of 50 repeat periods of $GaInAs/InP$ of nominally equal thickness on InP. The experiments were run on a Bede model 150 DCD using a rotary stage and a scintillation detector. In order to determine the extent of relaxation, if any, the asymmetric 115 reflection was used with both high and low angle of incidence beam paths. Also, to determine how the superlattice unit cell was relaxed, rocking curves were taken at sample orientations of 0° and 90° of one of the [110] cleaved edges with respect to the incident beam. In order to take into account the possible epilayer tilt these measurements were repeated at 180° and 270° so that a total of eight rocking curves were recorded. The step size was 0.5″ for the high angle of incidence and 1″ for the low angle of incidence cases, with a counting time of 20 seconds per step. The substrate zeroth order satellite peak separations were then measured as accurately as possible for each curve resulting in eight equations governing $\Delta\theta$, $\Delta\phi$ and $\delta\theta$, the epilayer tilt component. The subscripts in Table 4.4 refer to the sample orientations of 0°, 90°, 180°, and 270° with the incident beam.

High Angle	Low Angle
$\Delta\theta_0 - \Delta\phi_0 - \delta\phi_0 = -128.5''$	$\Delta\theta_0 + \Delta\phi_0 + \delta\phi_0 = -233.0''$
$\Delta\theta_{90} - \Delta\phi_{90} - \delta\phi_{90} = -127.4''$	$\Delta\theta_{90} + \Delta\phi_{90} + \delta\phi_{90} = -241.6''$
$\Delta\theta_{180} - \Delta\phi_{180} + \delta\phi_0 = -116.4''$	$\Delta\theta_{180} + \Delta\phi_{180} - \delta\phi_0 = -245.7''$
$\Delta\theta_{270} - \Delta\phi_{270} + \delta\phi_{90} = -131.1''$	$\Delta\theta_{270} + \Delta\phi_{270} - \delta\phi_{90} = -237.0''$

Table 4.4

Taking the 0° and 180° directions, and the 90° and 270° directions separately, we gain average values of $\Delta\theta$, $\Delta\phi$ and $\delta\phi$, and using equations (4.23), (4.24), (4.25) and (4.36) the a and c parameters and the relaxation can be calculated. Table 4.5 shows the calculated values.

	0° – 180°	90° – 270°
$a(\AA)$	5.86912 ± 0.00005	5.86867 ± 0.00005
$c(\AA)$	5.86277 ± 0.00005	5.86269 ± 0.00005
$R\%$	-14 ± 3	3 ± 3
$\delta\phi(\,''\,)$	6.2 ± 1	-2.1 ± 1

Table 4.5

The relaxation is asymmetric with 14% relaxation occurring in one direction and 3% in the other. In practice asymmetric relaxation is highly likely since there exist four $\{111\}$ slip planes two of which have group III elements uppermost while the other two have group V. The ease of slip along these planes will differ and so strain will tend to be released along the easy direction by the formation of misfit dislocations. However, because the relaxation is asymmetric the unit cell will no longer be tetragonal but orthorhombic, and the calculations of a, c and R will be inaccurate. This explains the apparent small difference between the c values which should of course be equivalent whichever direction of incidence is used.

The maximum component of epilayer tilt is $6.5 \pm 1''$. Had the tilt not been taken into account the relaxation would have been in error by $\pm 10\%$. The substrate tilt was measured to be less than 0.25°, which shows that epilayer tilt can arise even when the substrate is relatively well oriented. This has been confirmed by Auvray, Baudet and Regreny (1989) who have determined a relation between the epilayer tilt and mismatch, and have found that this tilt is even present in growth on non-intentionally misoriented substrates.

The superlattice period may now be calculated from the satellite spacings of long range rocking curves. In order to gain an accurate measurement, four rocking curves were recorded from the 0° and 90° position at high and low incidence beam paths. For the high angle case the scan range was $6000''$ with a $6''$ step size, while for the low angle case the range was $9000''$ with $10''$ step size. A counting time of 75 seconds per step was used in each case. Figure 4.18 (a)-(d) shows the rocking curves. Taking all combinations of satellite separations the

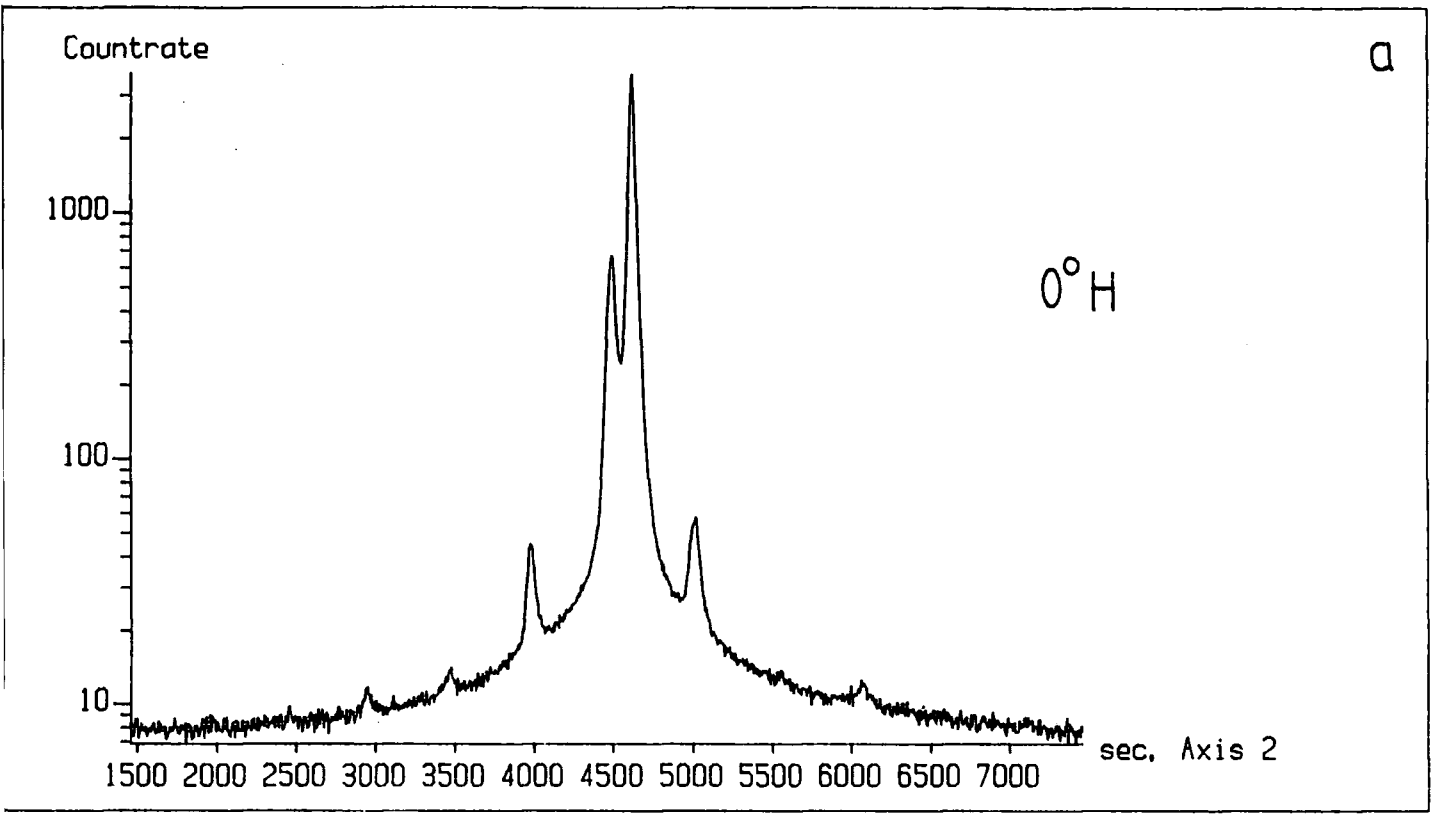

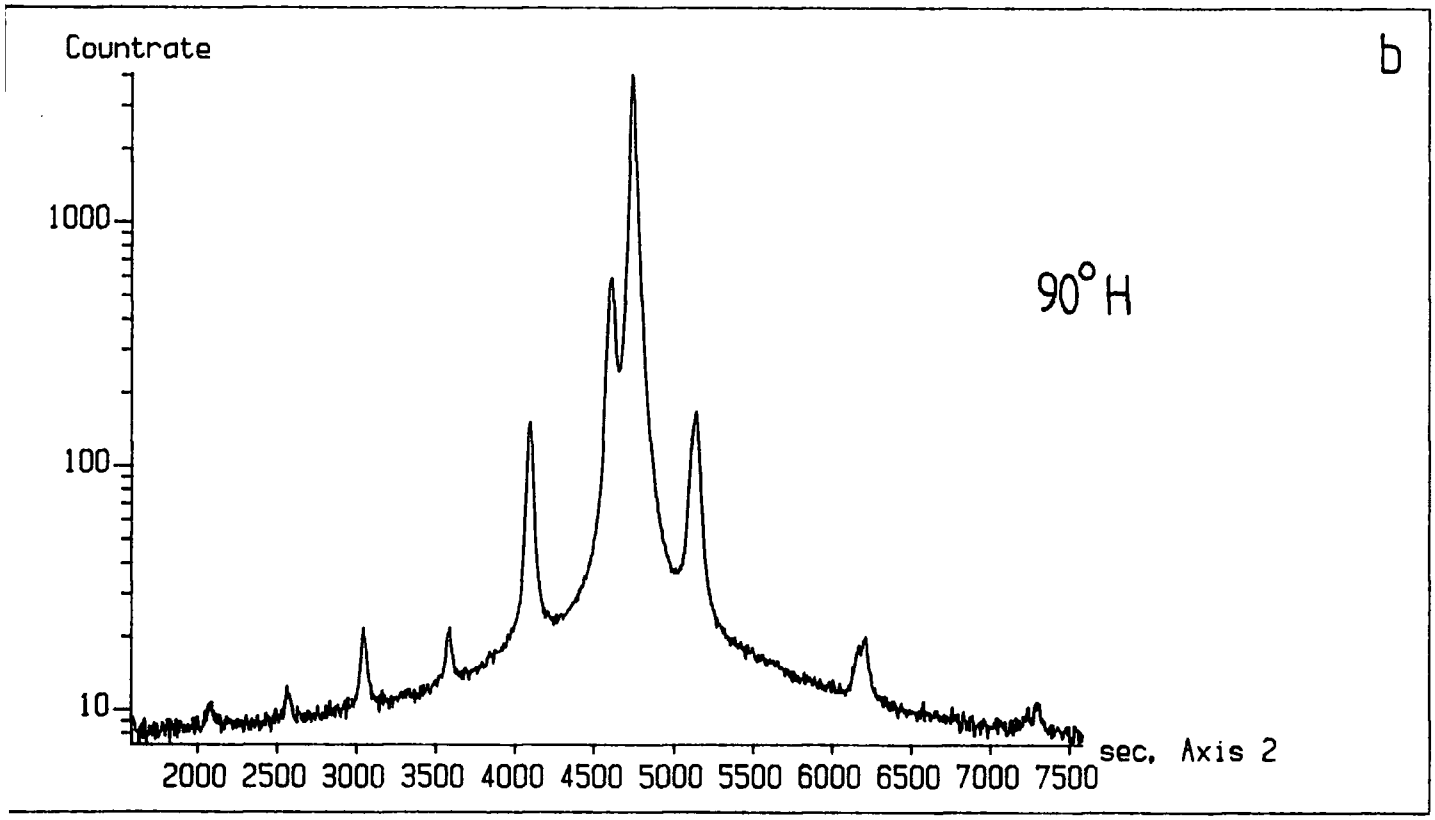

Figure 4.18: 115 experimental rocking curves of MWQ2; (a) 0° rotation, high angle of incidence, (b) 90° rotation, high angle of incidence, (c) 0° rotation, low angle of incidence, (d) 90° rotation, low angle of incidence.

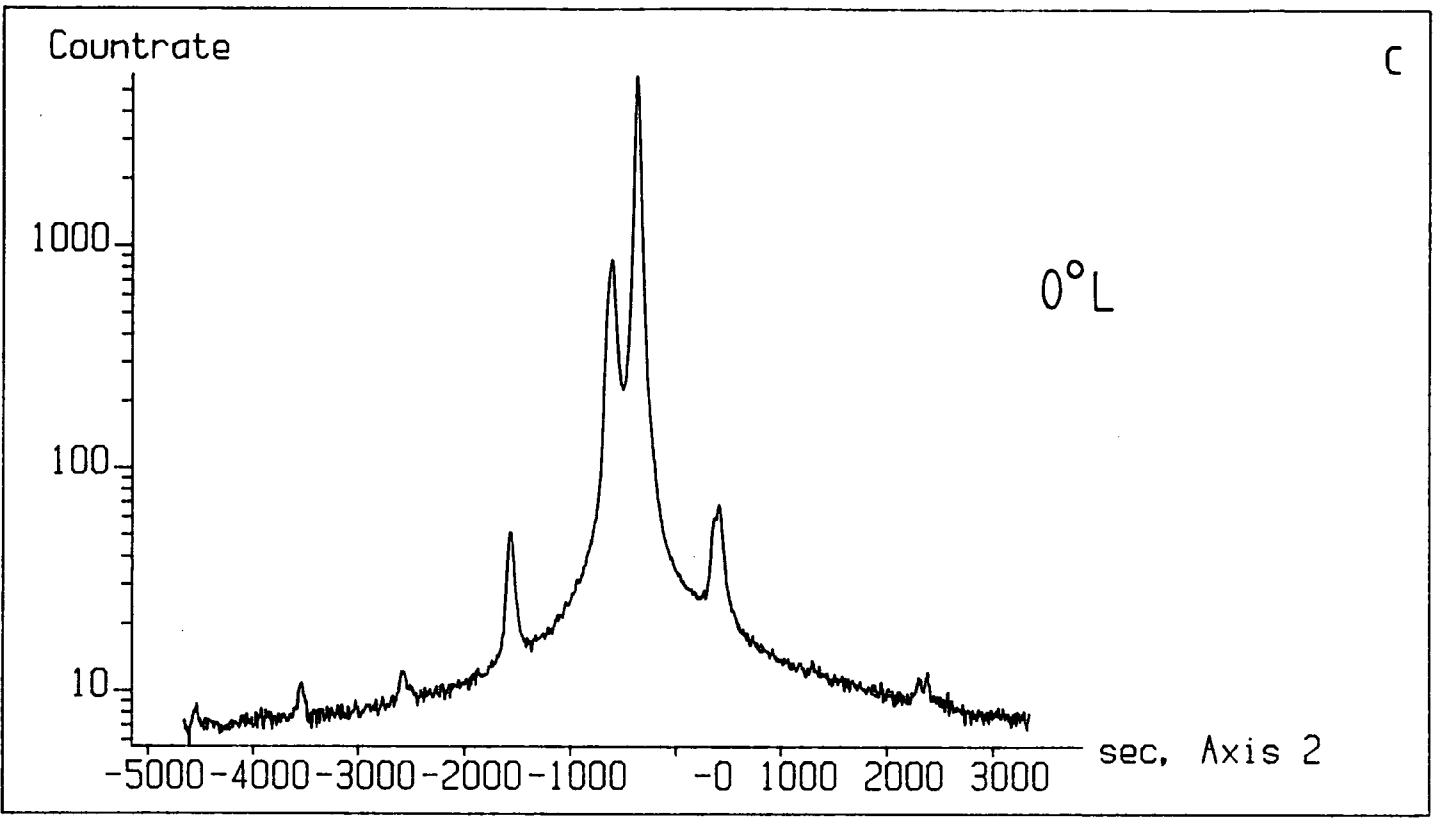
Countrate
c
1000
100
10
0°L
-5000 -4000 -3000 -2000 -1000 -0 1000 2000 3000
sec, Axis 2

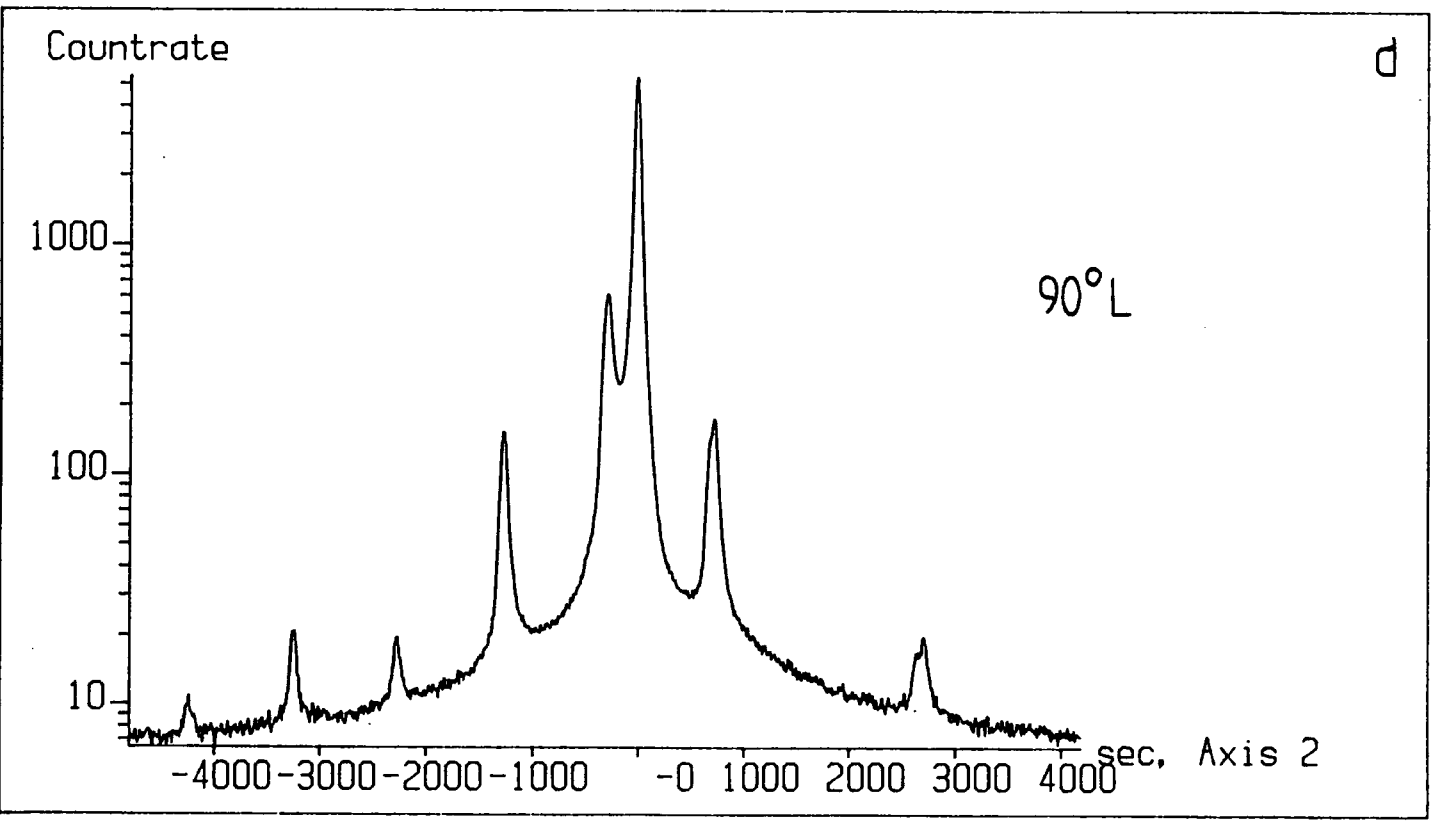
Countrate
d
1000
100
10
90°L
-4000 -3000 -2000 -1000 -0 1000 2000 3000 4000
sec, Axis 2

average separation was $516.6 \pm 1.4''$ for the high incidence case and $990.0 \pm 1.6''$ for the low incidence case, giving an average superlattice period, using equation (4.35) of $276.5 \pm 0.4\mathring{A}$. In order to check this result an 044 glancing incidence rocking curve was recorded over $12000''$ range with $10''$ step size and 55 second counting time, which is shown in figure 4.19. The superlattice period was calculated to be $\Lambda = 283.5 \pm 2.3\mathring{A}$. The overall weighted mean period is therefore $\bar{\Lambda} = 276.7 \pm 0.4\mathring{A}$. It is also interesting that in figure 4.18 (a)-(d) the satellites in the unrelaxed direction are narrower in width and greater in intensity than those in the relaxed direction. In fact the higher order peaks are indistinguishable from the noise. This arises because dislocations within the area irradiated by the X-ray beam lead to small variations in tilt of the diffracting planes across the beam, and so the satellite peaks become broader and less well defined. This supports the previous evidence that the superlattice is asymmetrically relaxed.

4.7 Thin Layer Characterisation using Asymmetric Reflections

From a consideration of structure factors for zinc-blende type crystal structures the strongest allowed symmetric reflection from the 001 plane is the 004. The Bragg angle and hence incidence angle (as the reflecting planes are parallel to the surface) is 31.7° for InP and 33° for $GaAs$. Rocking curve layer peaks are easily resolved using this reflection for relatively thick layers, but when layers become thin, typically less than $0.2\mu m$, the peaks become broad and low in intensity as shown in figure 4.20. For small mismatch the layer peak may be indistinguishable from the tail of the substrate Bragg peak and so the measurement of mismatch then becomes less accurate and longer counting times are required for good statistics. There are some allowed asymmetric reflections which, because of their smaller angles of incidence, increase the layer peak height with respect to the substrate. This arises from an increased path length within the layer. Figure 4.21 shows simulated rocking curves of an $0.15\mu m$ layer of $InGaAs$ with a mismatch of $-1000ppm$ on InP for the 004 reflection and asymmetric 224 and 044 reflections, which have incidence angles of 4.8° and 3° respectively. This is known as glancing incidence, where the incident angle to the surface is $\theta - \phi$. The lower the angle of incidence the more sensitive the reflection is to thin layers. The beam paths may also be reversed to give an incidence angle of $\theta + \phi$ so that the exit beam is at a small angle to the surface. Glancing exit gives the

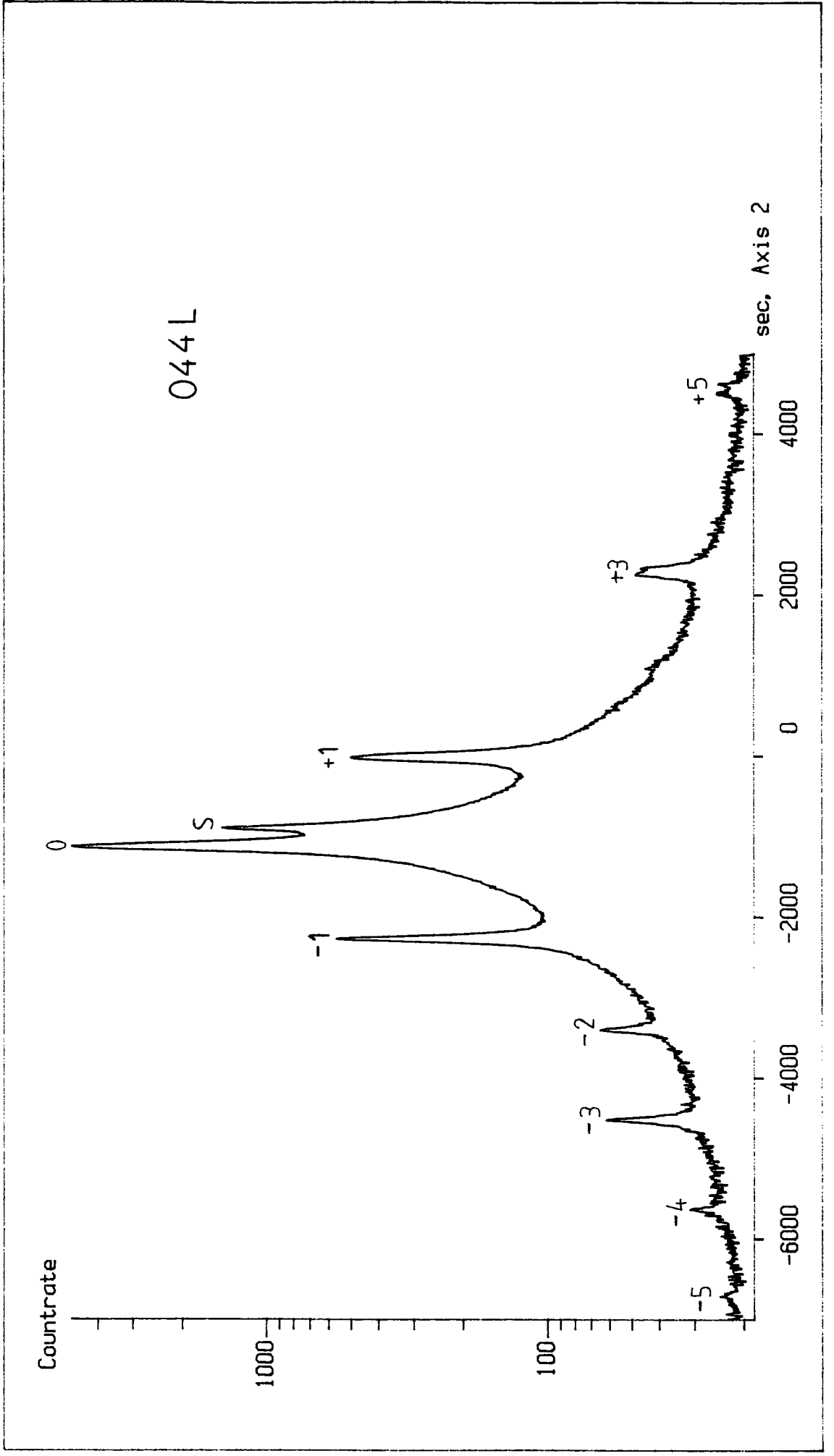

Figure 4.19: 044 low angle of incidence rocking curve of MQW2.

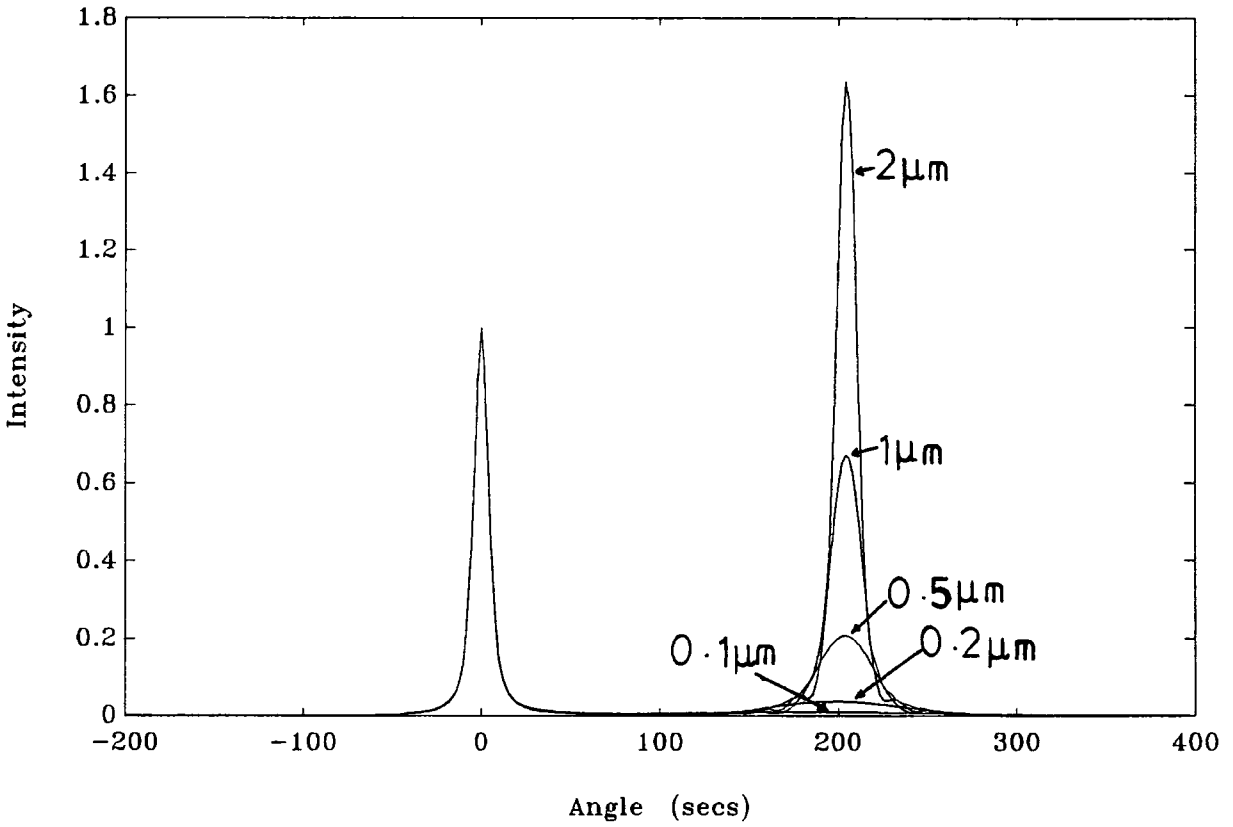

Figure 4.20: Simulated 004 rocking curves showing the variation of layer peak intensity with thickness for an $InGaAs$ layer with a mismatch of $-800ppm$.

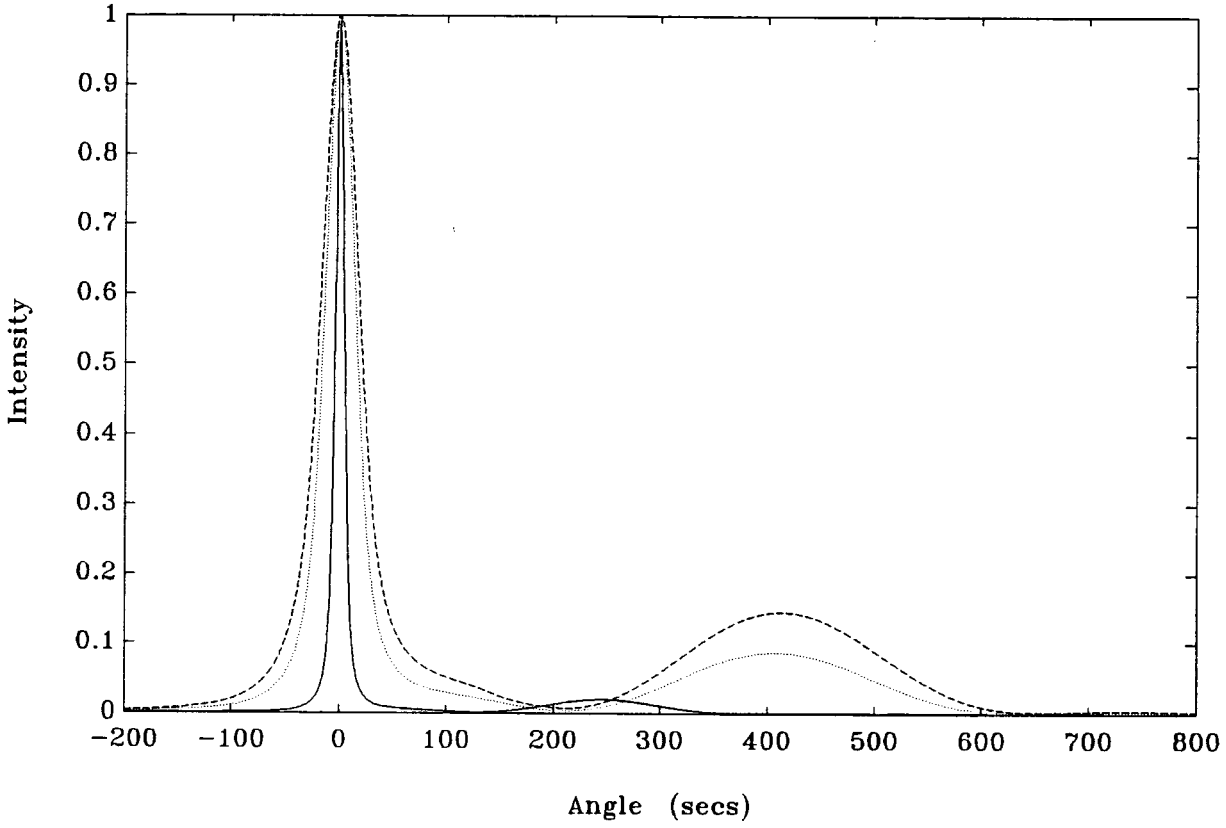

Figure 4.21: Simulated rocking curves of a $0.15\mu m$ $InGaAs$ layer with a mismatch of $-1000ppm$ for the 004 (solid), 224 (dotted) and 044 (dashed) reflections.

same sensitivity to thin layers as glancing incidence since the path length within the layer is the same, but the peak widths are reduced due to the geometry. This is discussed in more detail in Chapter 5.

The asymmetric 044 reflection was applied experimentally to a sample of $AlInAs$ on InP with a nominal thickness of $0.1\mu m$ capped by $50\mathring{A}$ of $GaAs$ (Bates et al., 1988). The sample, code INP2, was grown by G. Scott using MBE. A first crystal 044 reflection from an(011) surface was utilised so that there was no dispersion. The rocking curve was taken on a Bede model 150 diffractometer using a scintillation counter, with a step size of $10''$ and 80 seconds counting time.

Figures 4.22 and 4.23 show the experimental and simulated rocking curves respectively, from three points on the sample separated by $5mm$. The layer thickness variation over the sample is significant with values of $900\mathring{A}$, $500\mathring{A}$ and $250\mathring{A}$ required in the simulation for figures 4.22(a), 4.22(b) and 4.22(c) respectively, with mismatches of $-4785ppm$, $-4630ppm$ and $-4500ppm$. Figure 4.22(c) is plotted on a scale of 2% of the peak intensity so that the layer diffraction features could be seen. The fit between the simulation and experimental curves is not particularly good as the layer is evidently imperfect and some sort of grading probably exists. However an indication of layer thicknesses is yielded. Unfortunately the background noise was too high to allow observation of Pendellösung fringes to give an accurate indication of layer thickness and so the thicknesses given are accurate to no more than $\pm 200\mathring{A}$. Even with the 044 reflection for very thin layers, of less than about $500\mathring{A}$, the diffracted intensity from the layer is low and characterisation becomes inprecise.

4.8 Conclusion

This chapter has illustrated the various techniques used in the characterisation of heteroepitaxial layers as well as some of the problems associated with them. Layers should not be assumed to be perfect and data supplied by crystal growers concerning sample characteristics should be carefully considered. There is an increasing awareness that growth interfaces are not perfectly abrupt and that surface roughness and compositional grading do exist. Epilayer tilt is also a real effect even when substrates are not highly tilted, and must be taken into

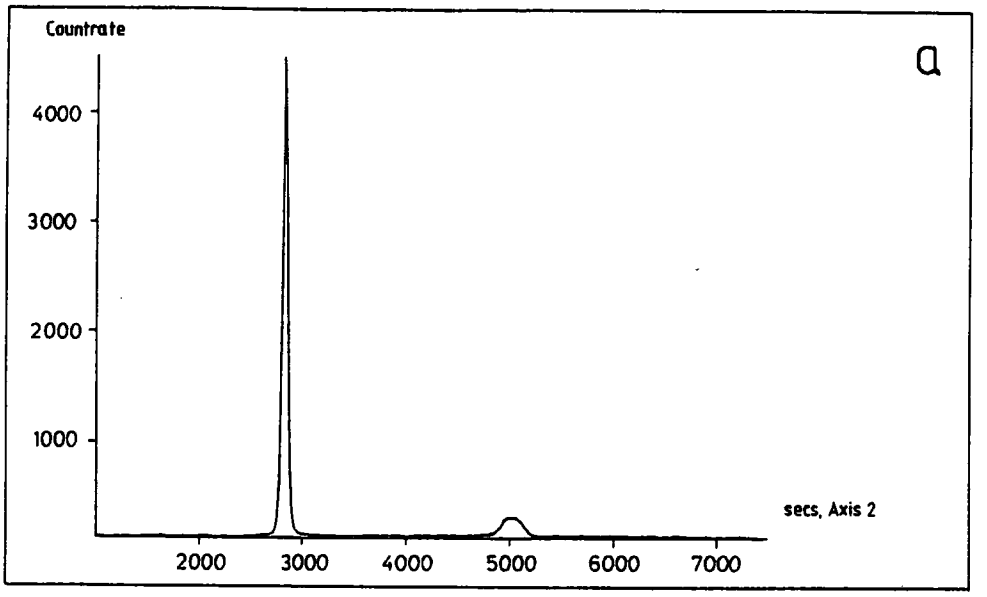

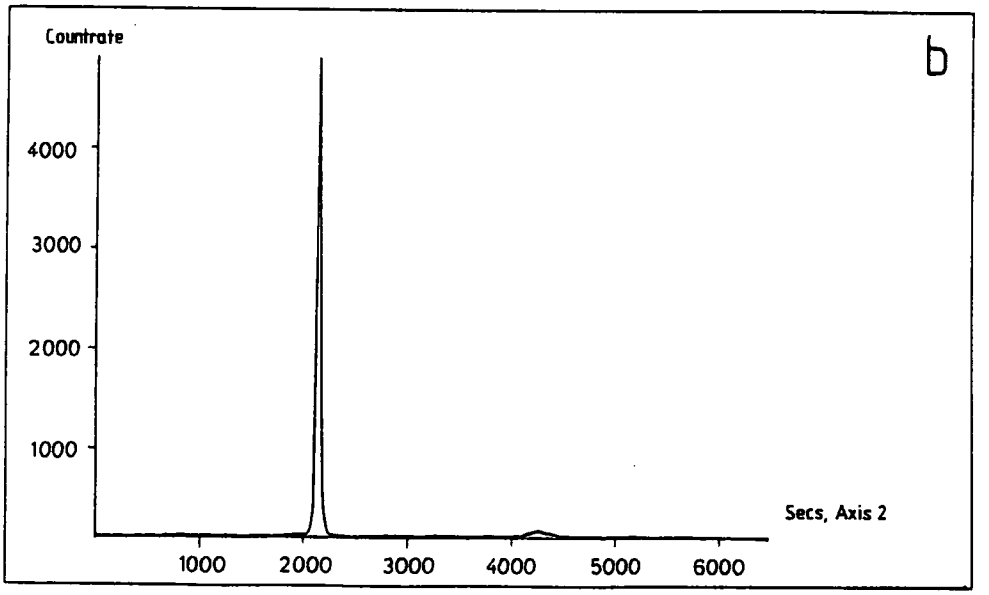

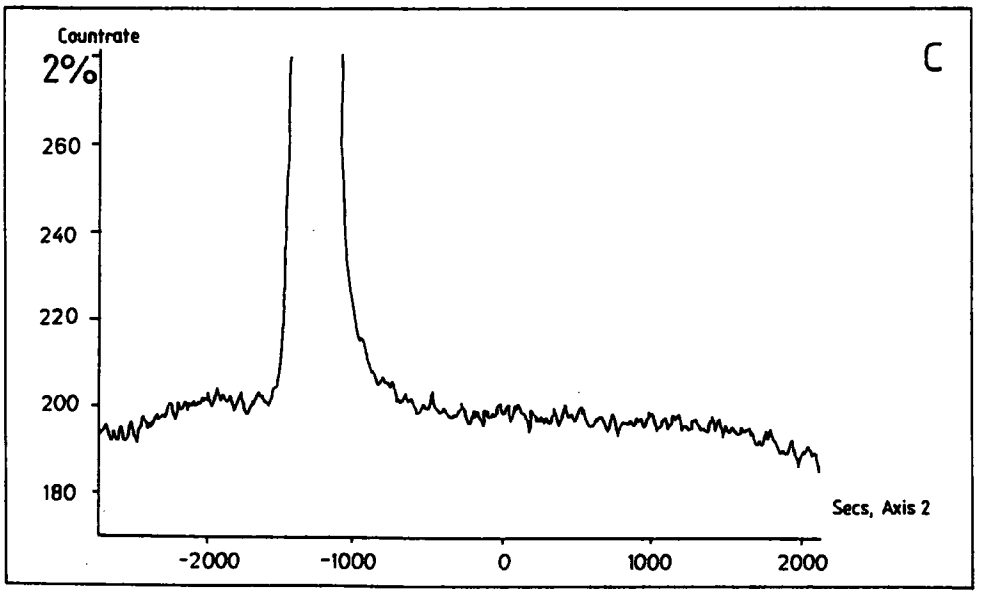

Figure 4.22: 044 experimental rocking curves of INP2

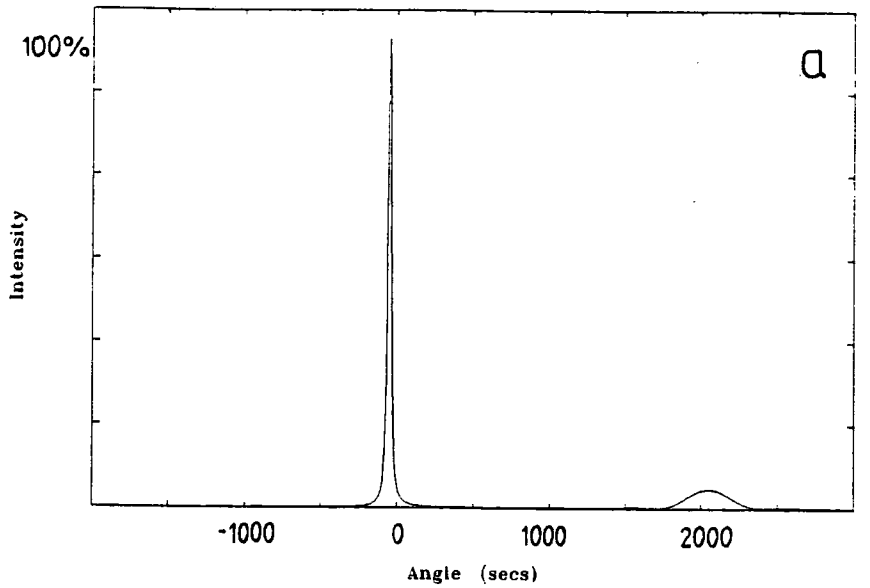

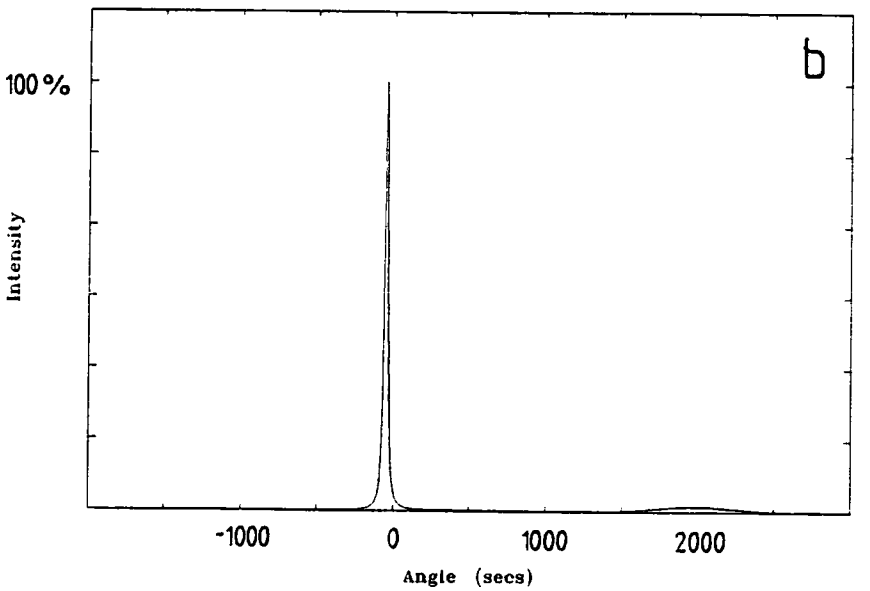

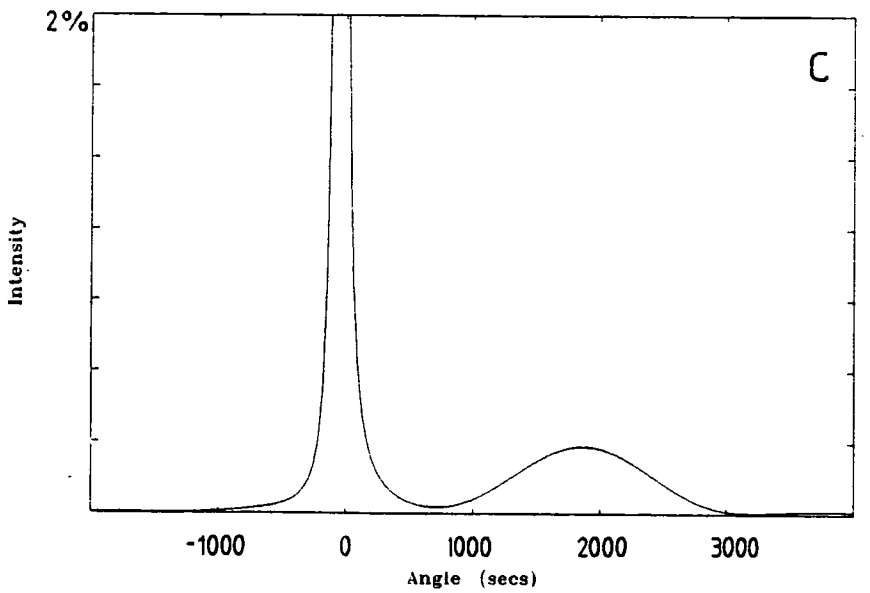

4.23: 044 simulated rocking curves of INP2

account if accurate measurements of lattice parameters are required. The characterisation of superlattices has been discussed and asymmetric relaxation has been found in an $InGaAs/InP$ superlattice. For the measurement of very thin epitaxial layers conventional glancing incidence asymmetric reflections lack sensitivity and it is necessary to consider other geometries which offer enhancement of surface diffraction effects.

Chapter V

Skew Asymmetrical Rocking Curve Analysis

5.1 Introduction

The previous chapter has illustrated the need for asymmetric diffraction geometries in the characterisation of very thin layers. Limitations of the standard glancing angle geometry become apparent however when layers of less than $0.1\mu m$ in thickness are studied. The layer peak on the rocking curve becomes low in intensity, requiring long counting times in order to differentiate the peak from the background. Even when the peak is resolved it is often too broad to give an accurate indication of layer mismatch. In order to obtain strong diffraction features from thin layers the X-ray path length must be increased within the layer.

Tanner and Hill (1986) and Brühl et al. (1988) have used synchrotron radiation to reduce the incident X-ray angle by changing the X-ray wavelength. It is possible with this technique to tune the incident angle by rocking the reference crystal to select the required wavelength. Bubáková et al. (1975) described a technique, using a conventional X-ray source, where the incident angle could be continuously varied which was adopted by Pietsch et al. (1987) to measure lattice parameter differences of heteroepitaxial structures.

This chapter gives a full description of the theoretical aspects of this technique together with its experimental realisation (Miles, Green, Tanner, Halliwell, and Lyons, 1988). Results derived in the discussion have been used in a dynamical simulation program based on the Takagi-Taupin equations to allow theoretical modelling of the technique. Lyons and Halliwell (1985) suggested the acronym SARCA for the method, which stands for Skew Asymmetrical Rocking Curve Analysis.

It is important to differentiate between this technique and the method of structural depth profiling using Glancing Incidence X-ray Scattering known as

GIXS (Brennan, 1986; York and Austin, 1986; Huang, Toney, Brennan and Rek, 1987). In this technique the X-rays are incident to the surface at angles of usually less than 1° and even below the critical angle of total external reflection. For a set incidence angle the detector is scanned along the 2θ circle in a vertical plane to record X-rays diffracted from crystal planes essentially perpendicular to the sample surface. Total external reflection is employed to improve the surface sensitivity of the diffracted beam. The only penetration of X-rays at angles less than the critical angle is due to effervescent waves and it is the diffraction of these waves that makes the experiment possible. A similar technique known as Grazing Incidence Asymmetric Bragg Scattering (GIABS) is also used to study thin films (Toney, Huang, Brennan and Rek, 1988; Toney and Brennan, 1988, 1989). This method differs from GIXS since the detector is scanned to record X-rays diffracted from crystal planes that are inclined to the surface of the specimen, and not X-rays scattered off rows of atoms in the surface plane.

SARCA bears similarities to these techniques in that the angle of incidence may be chosen as desired. However, diffraction from only one set of lattice planes is recorded and it is the incident angle and not the detector angle that is scanned.

5.2 Theoretical Discussion

For a symmetric reflection the angle of incidence, i, is equal to the angle of emergence, e, and the diffracting planes are parallel to the sample surface. The range of possible incident and emergent beams, known as the Bragg cone, is illustrated in figure 5.1(a). The incident angle is equivalent for all positions around the Bragg cone.

For an asymmetric reflection however, the diffracting planes are not parallel to the sample surface and the angle of incidence is not the same as the angle of emergence. Figure 5.1(b) shows the Bragg cone of a typical asymmetric reflection. There is a range of possible incidence angles and corresponding emergence angles that satisfy the Bragg condition as the sample is rotated about the diffraction plane normal. For some reflections where the angle between the diffracting planes and surface, ϕ, is greater than the Bragg angle, θ, there is no allowed reflection in the normal geometry. However as the sample is rotated about the

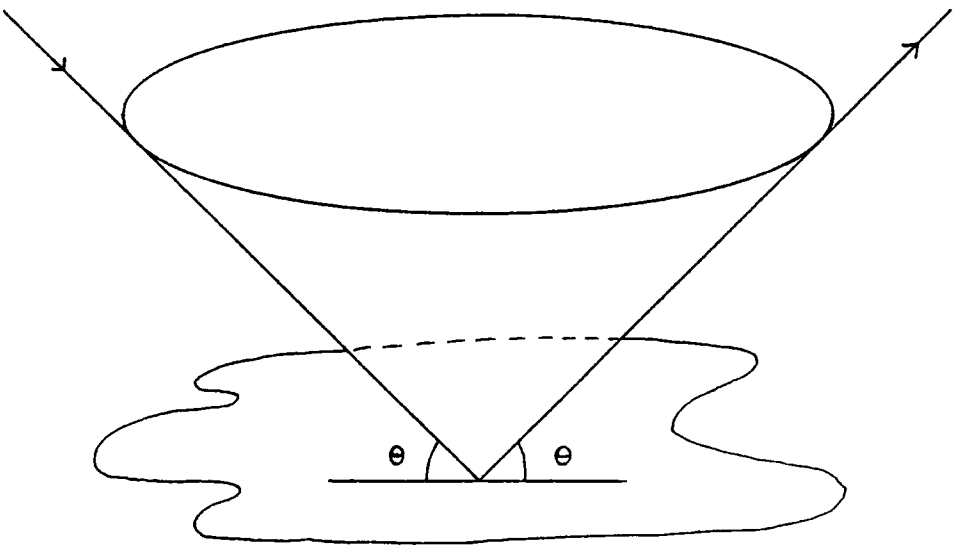

Figure 5.1(a): Symmetric Bragg cone.

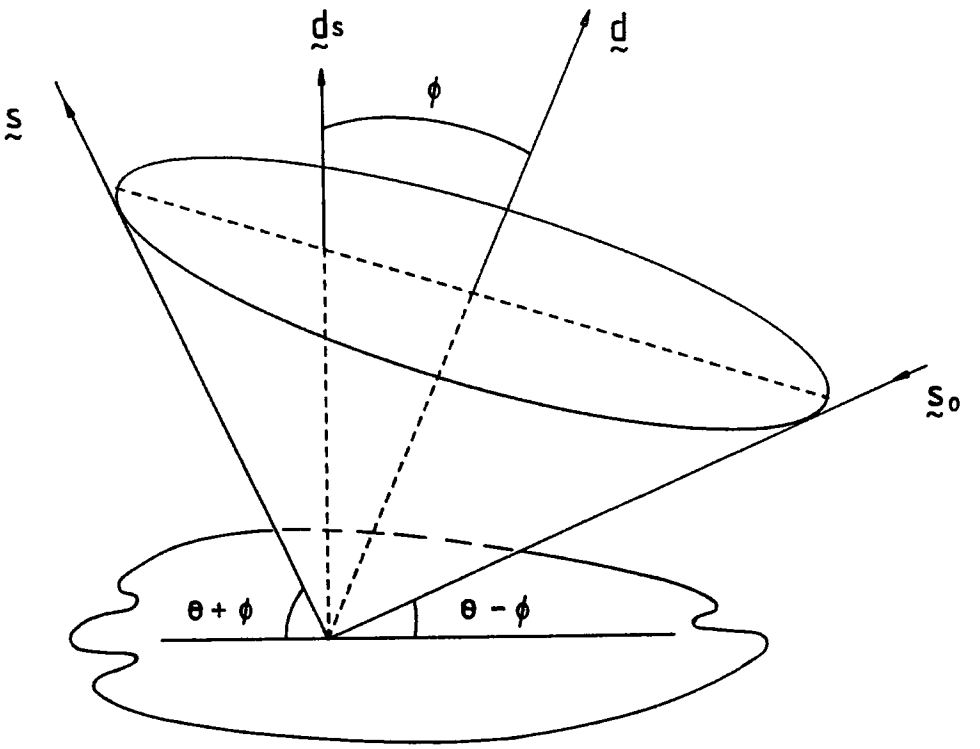

Figure 5.1(b): Asymmetric Bragg cone.

diffraction plane normal there exist a range of beam paths that result in a reflection illustrated in figure 5.2. It is thus possible to reduce the angle of incidence right down to zero degrees by rotating the sample to the required position. This greatly reduces the penetration depth of the incident beam and so enhances the sensitivity to thin surface layers. Similarly, it is possible to adopt the glancing exit geometry which also gives enhanced surface sensitivity but results in narrower diffraction peaks.

Consider the general case of an embedded Bragg cone shown in figure 5.2. Let $\underline{s}_0$ and $\underline{s}$ represent the unit vectors of the incident and emergent X-ray beams at the Bragg angle θ. ϕ is the angle between the reflecting planes and the sample surface. $\underline{d}$ and $\underline{d}_s$ represent the unit vectors of the normals to the reflecting planes and the surface respectively. In order to calculate the relation between incidence angle, i, and the angle of rotation, β, consider the xz projection of the embedded Bragg cone, shown in figure 5.3. As $\underline{s}_0$ is a unit vector then the distances AO and OB are equal to unity. It is then straightforward to show that

$$\sin i = \sin\theta\cos\phi - \cos\theta\sin\phi\cos\beta. \qquad 5.1$$

Similarly the angle of emergence, e, is defined by

$$\sin e = \sin\theta\cos\phi + \cos\theta\sin\phi\cos\beta. \qquad 5.2$$

The rotation angle for which the angle of incidence is zero, β_0, is given by

$$\beta_0 = \cos^{-1}\left(\frac{\tan\theta}{\tan\phi}\right). \qquad 5.3$$

Figure 5.4 illustrates the way the angle of incidence varies with rotation angle for the 044, 333 and 133 reflections for InP, $CuK\alpha$ radiation. Both the 333 and 133 reflections have $\phi > \theta$ and as a consequence it is possible to tune towards zero incidence angle. Only a restricted range of rotations and beam paths are found. The 044 has a full 180° range of possible rotations but a minimum incidence of only 3°. It is interesting to see how the surface sensitivity varies as a function

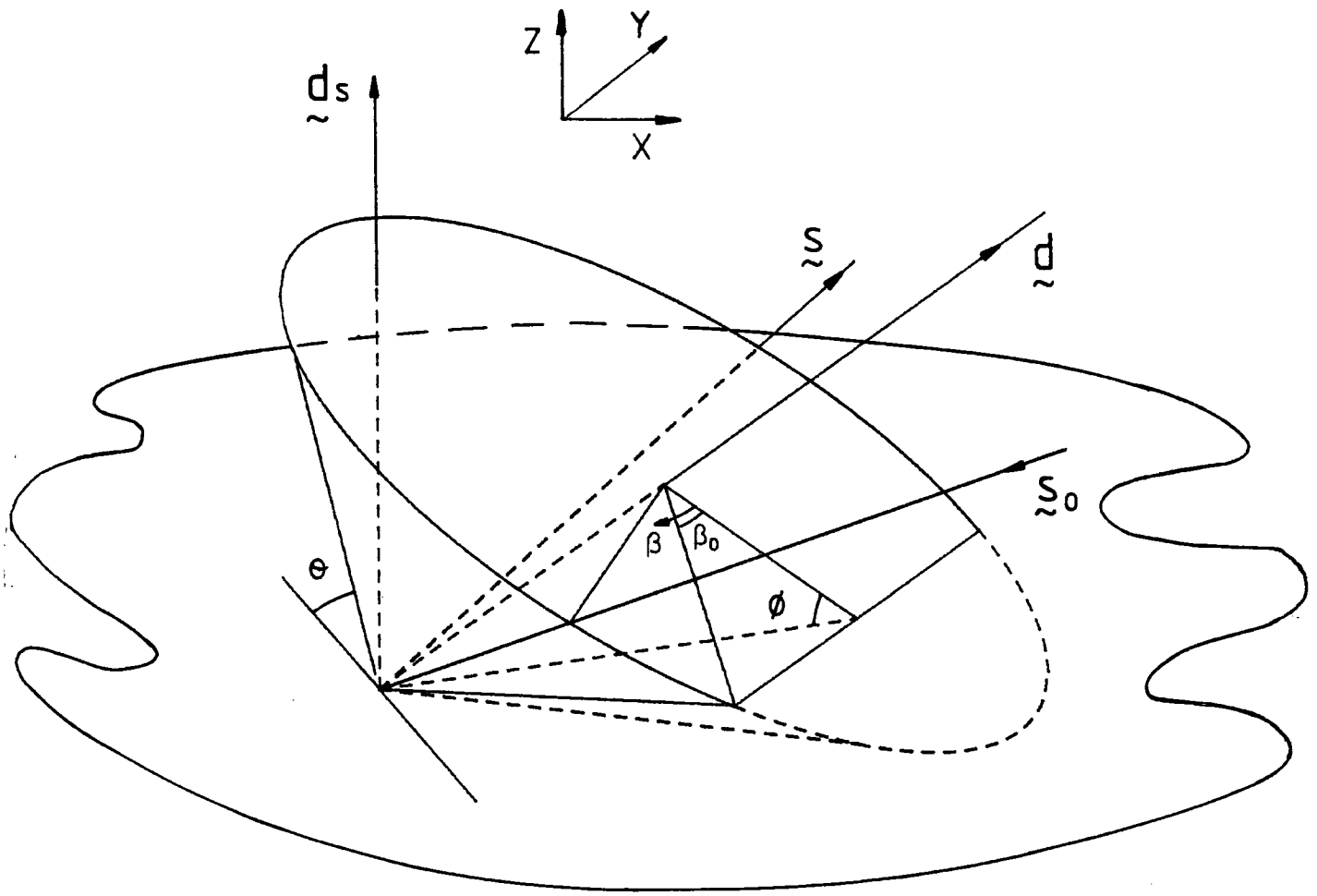

Figure 5.2: Embedded Bragg cone.

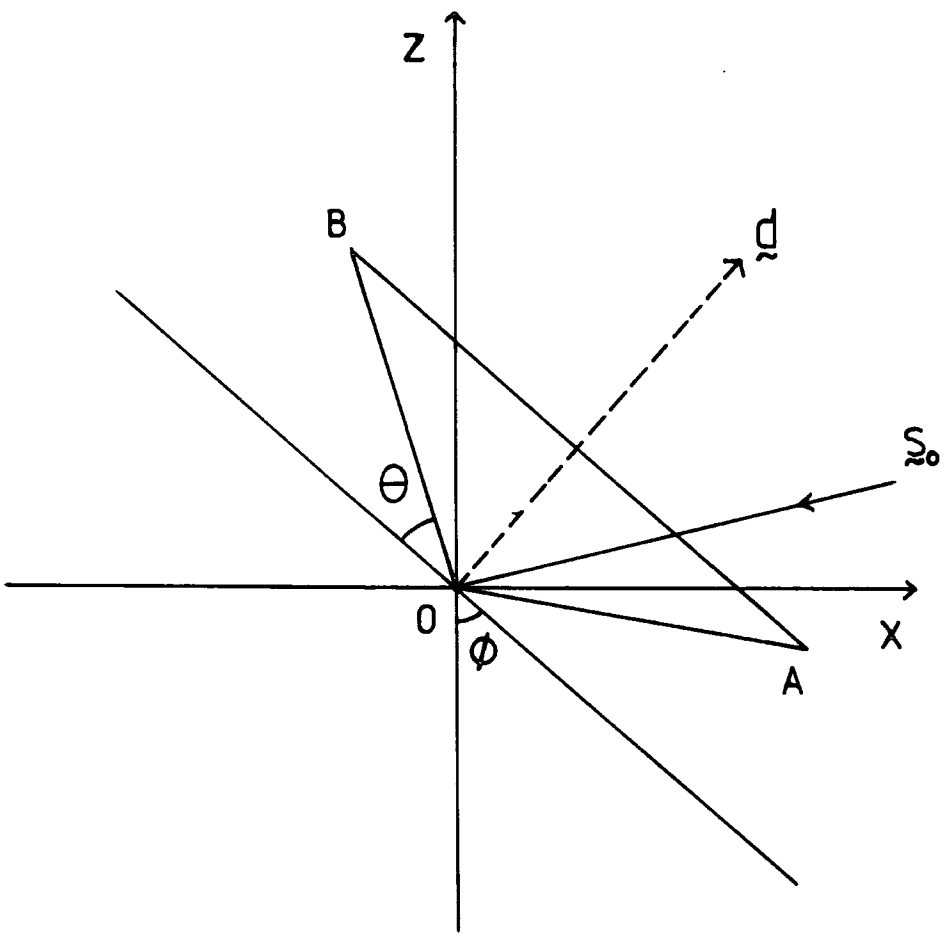

Figure 5.3: xz projection of embedded Bragg cone.

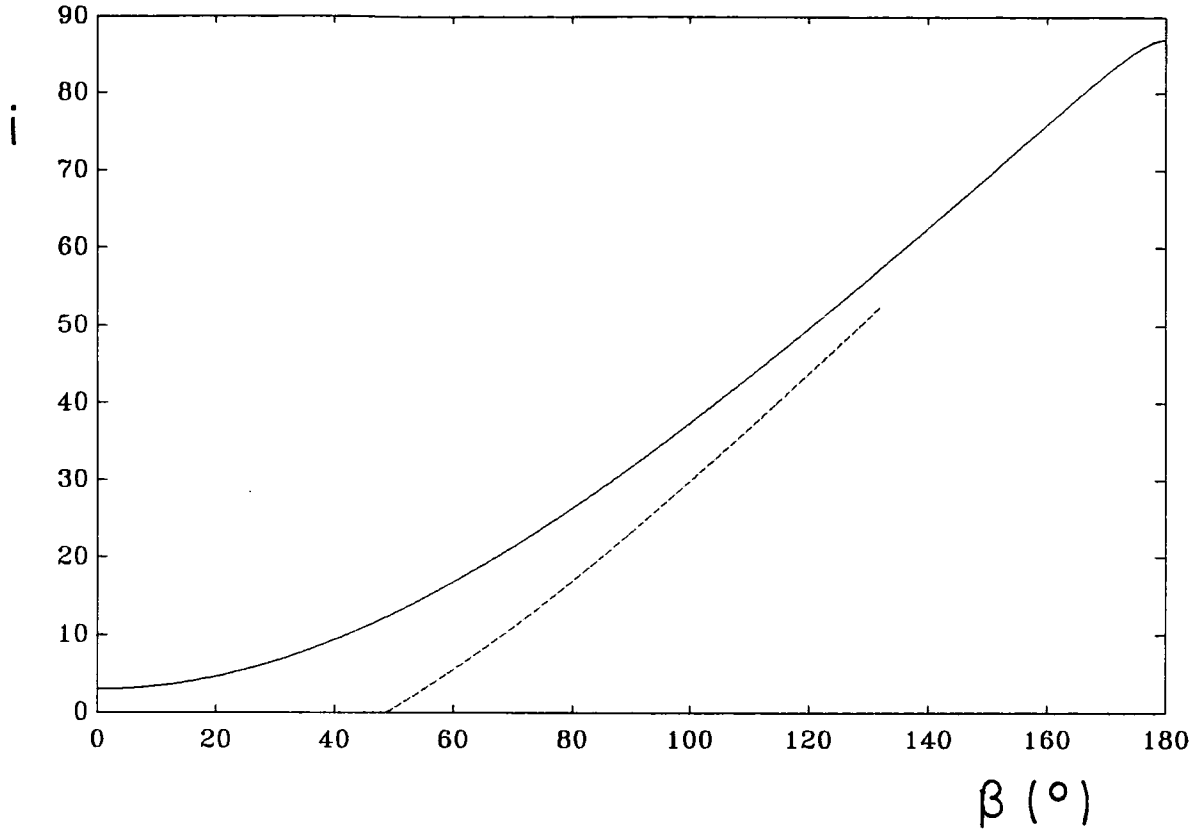

Figure 5.4: Relationship between incidence angle and rotation angle for 044 (solid), 333 (dashed) and 133 (dotted) reflections.

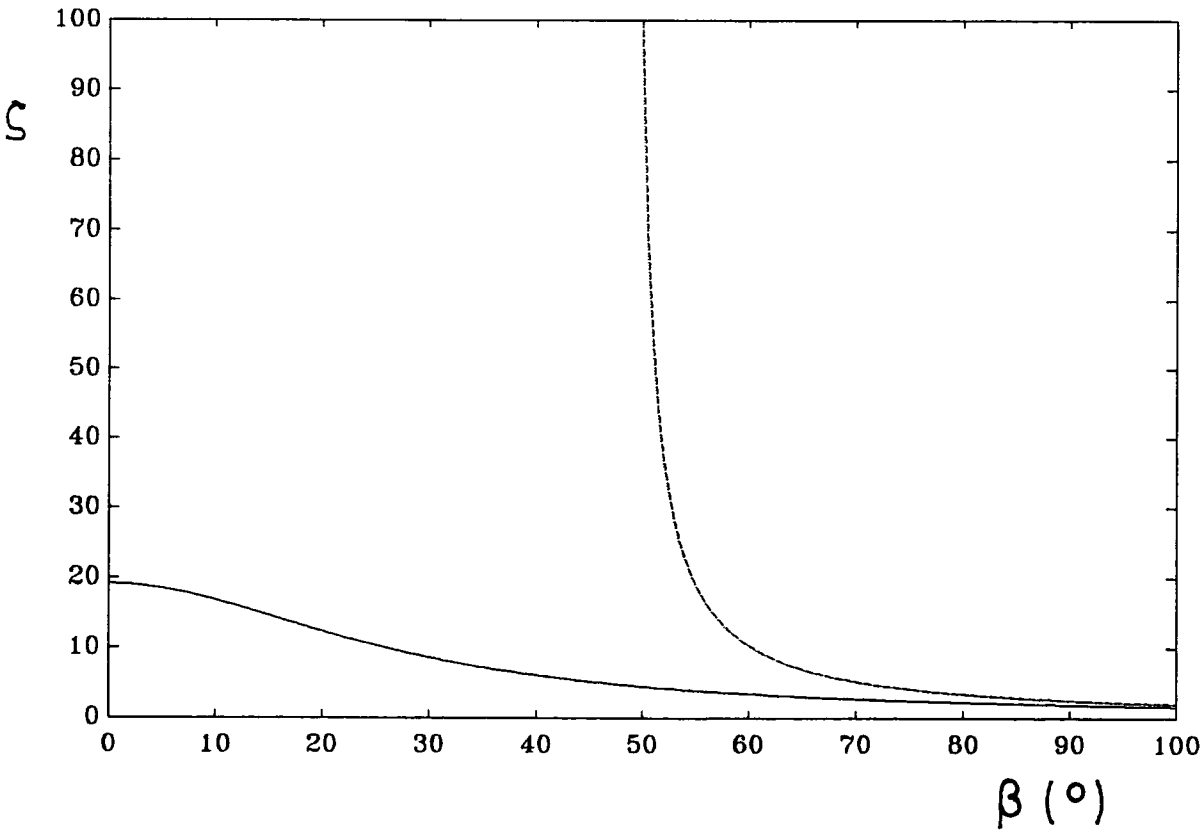

Figure 5.5: Relationship between the path length ratio and rotation angle for 044 (solid), 333 (dashed) and 133 (dotted) reflections.

of rotation. Defining the path length ratio, ζ, to be the ratio of the distance travelled by the incident beam to the depth below the surface, then

$$\zeta = \frac{1}{\sin i} \ . \qquad 5.4$$

The corresponding plot of the ratio as a function of rotation angle for the 044, 333 and 133 reflections is shown in figure 5.5. It is evident that reflections like the 333 and 133 are extremely sensitive to surface features near β_0. As glancing incidence is approached the width of the peaks increases. From dynamical scattering theory (Tanner, 1976), the full width at half maximum (FWHM) is given by

$$\Delta\theta_{1/2} = k\sqrt{\frac{\sin e}{\sin i}} \ , \qquad 5.5$$

where k is a constant for a particular reflection. Figure 5.6 illustrates the relationship between half width and rotation angle for the 333 reflection of InP. In the glancing exit case the half width is expected to become very small. In practice however, it tends to converge to a constant value because of broadening arising from curvature, specimen imperfections and wavelength dispersion.

The relationship between the separation of a mismatched epitaxial layer and the substrate rocking curve peaks, and rotation is not immediately obvious and a geometrical study of two misaligned Bragg cones is necessary. The calculation is simplified by defining a cartesian coordinate system with the z component parallel to the substrate reflecting plane normal as shown in figure 5.7. The locus of the substrate Bragg cone with respect to the origin is defined to be a unit vector

$$\hat{\underline{a}} = a_x\hat{\underline{x}} + a_y\hat{\underline{y}} + a_z\hat{\underline{z}} \ .$$

The components of the locus of the substrate cone are therefore

$$a_x = \cos\theta\cos\beta \quad , \quad a_y = \cos\theta\sin\beta \quad , \quad a_z = \sin\theta \ . \qquad 5.6$$

Now consider a mismatched layer with Bragg angle $\theta - d\theta$ and angle of reflecting plane to sample surface $\phi + d\phi$. The locus of which is given by the unit vector

$$\hat{\underline{b}} = b_x\hat{\underline{x}} + b_y\hat{\underline{y}} + b_z\hat{\underline{z}} \ .$$

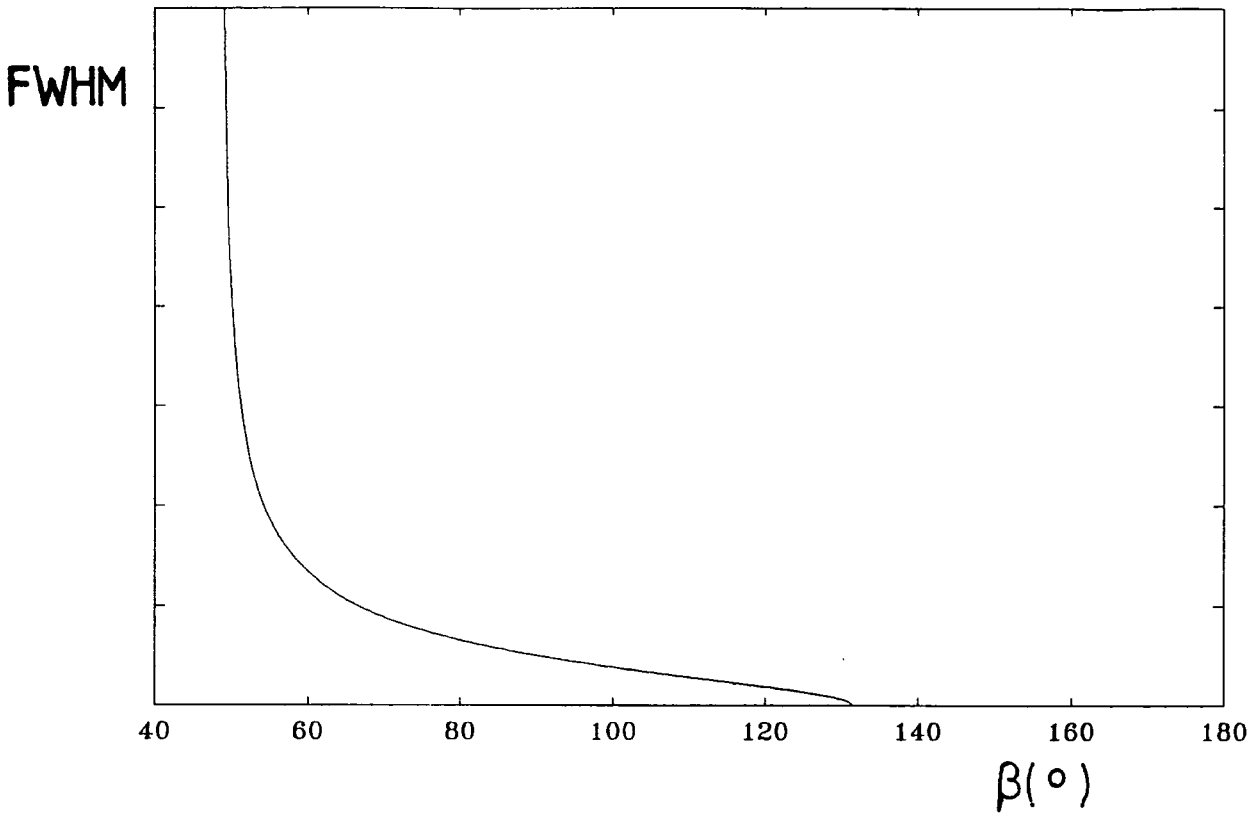

Figure 5.6: Relationship between the FWHM and rotation angle for the 333 reflection.

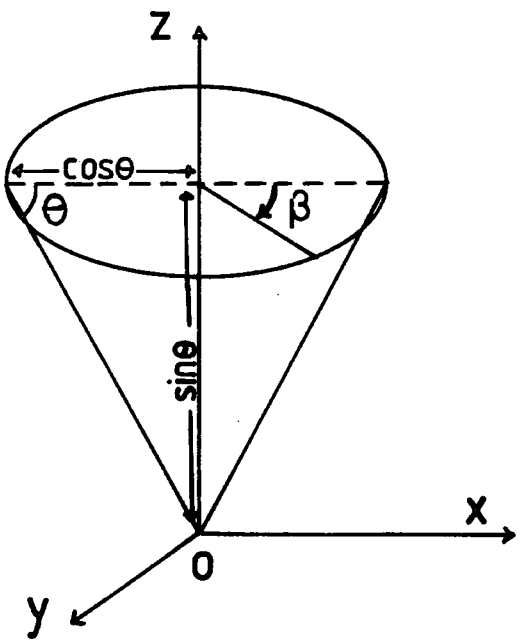

Figure 5.7: Substrate Bragg cone.

The xy projection of the layer cone superimposed over the substrate cone is shown in figure 5.8(a). In this projection the layer cone is seen as an ellipse and the substrate as a circle. The general form of an ellipse not centred on the origin, as shown in figure 5.8(b), is given by

$$\frac{(x-g)^2}{e^2} + \frac{y^2}{f^2} = 1 \ . \tag{5.7}$$

The locus of the layer Bragg cone is determined by finding the intersection of the ellipse with the line OP, given by

$$y = \tan\beta \ x \ . \tag{5.8}$$

Substituting (5.8) into (5.7) results in

$$(f^2 + e^2\tan^2\beta)x^2 - 2f^2gx + f^2(g^2 - e^2) = 0 \ , \tag{5.9}$$

which has the solution

$$x = \frac{f^2g^2 \pm ef\sqrt{f^2 + (e^2 - g^2)\tan^2\beta}}{(f^2 + e^2\tan^2\beta)} \equiv b_x \ , \tag{5.10}$$

where the positive root is taken for $0° \leq \beta \leq 90°$ and negative for $90° < \beta \leq 180°$. Using equation (5.8) it follows that

$$b_y = \tan\beta \ b_x \ . \tag{5.11}$$

The z component of the layer cone locus is determined using the xz projection shown in figure 5.9. It follows that

$$b_z = \frac{\sin(\theta - d\theta)}{\cos d\phi} - b_x \tan d\phi \ . \tag{5.12}$$

b_x is defined using the constants

$$e = \cos(\theta - d\theta)\cos d\phi \quad , \quad f = \cos(\theta - d\theta) \quad , \quad g = \sin(\theta - d\theta)\sin d\phi \ . \tag{5.13}$$

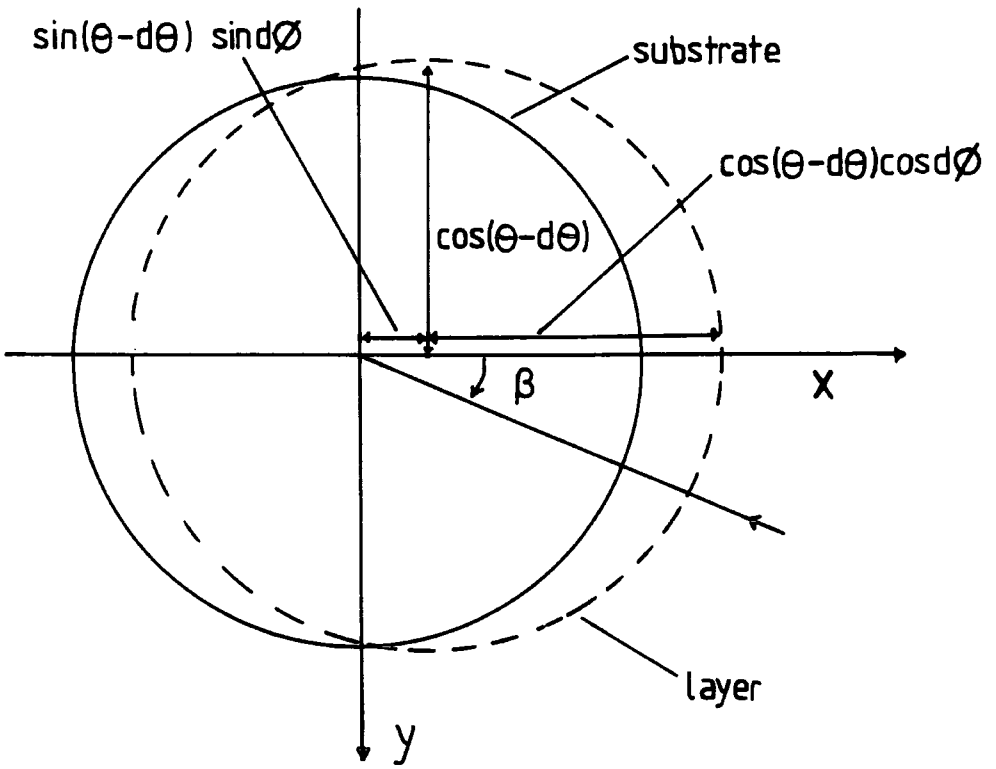

Figure 5.8(a): xy projection of the substrate and layer Bragg cones.

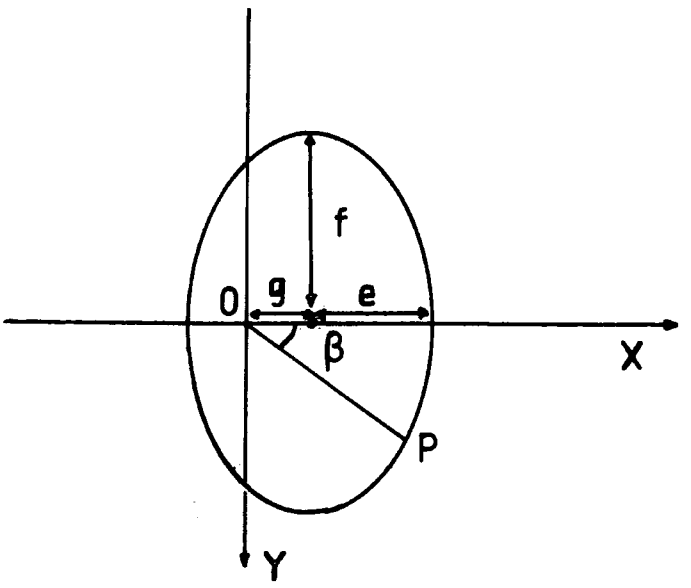

Figure 5.8(b): General form of an ellipse.

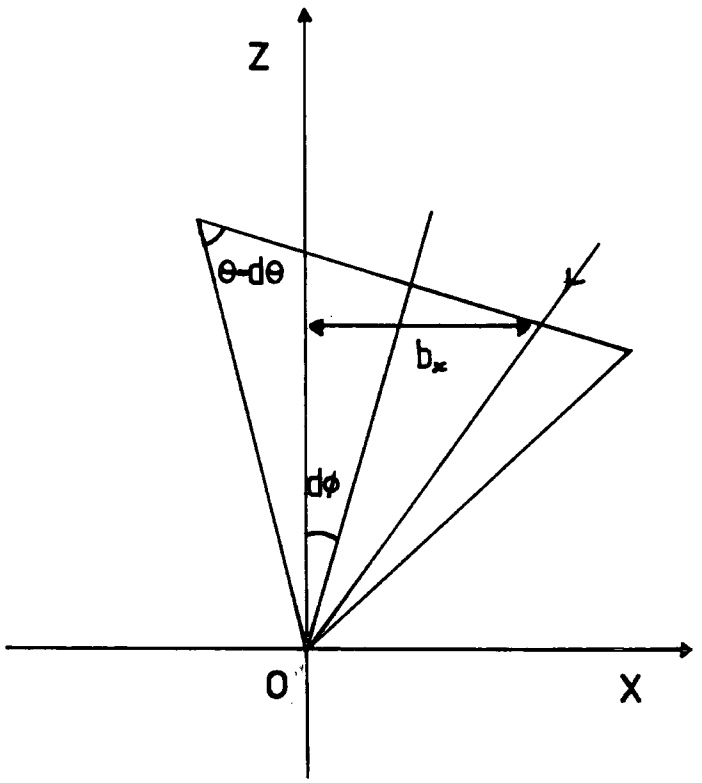

Figure 5.9: xz projection of the layer Bragg cone.

The substrate-layer peak separation, δi, is given by the angular separation of the two vectors $\underline{a}$ and $\underline{b}$ defining the substrate and layer Bragg cones as a function of rotation angle, β. Therefore, it follows that

$$\cos \delta i = \frac{\underline{a}.\underline{b}}{|\underline{a}||\underline{b}|} \ . \qquad 5.14$$

Now, since $\underline{a}$ and $\underline{b}$ are unit vectors

$$\cos \delta i = a_x b_x + a_y b_y + a_z b_z \ .$$

Hence

$$\cos \delta i = \cos\theta \cos\beta \ b_x + \cos\theta \sin\beta \ b_y + \sin\theta \ b_z \ ,$$

and so

$$\delta i = \cos^{-1}\left[(\cos\theta\cos\beta - \sin\theta \tan d\phi + \cos\theta \sin\beta \tan\beta) b_x + \frac{\sin\theta \sin(\theta - d\theta)}{\cos d\phi}\right] , \qquad 5.15$$

where b_x is given by equations (5.10) and (5.13). This equation is used to calculate the mismatch of a layer at any value of β.

5.3 Experimental Details

The experiments were carried out using a prototype of the Bede model 150 double crystal X-ray diffractometer. $CuK\alpha$ radiation was used throughout. The sample was mounted on a wedge of angle equal to that between the reflecting planes and the sample surface, ϕ. This was then mounted on a rotary stage so that the reflecting plane normal was parallel to the axis of rotation. Figure 5.10 shows the experimental arrangement. An important consideration when using asymmetric reflections is the orientation of the sample itself in the plane of its surface. It is incorrect to mount the sample with its cleaved edges at an arbitrary angle as is the case for symmetric reflections. For samples mounted on (001) substrates the cleaved edges are usually $< 110 >$ directions. To calculate the correct orientation consider the vector diagram in figure 5.11 which shows a

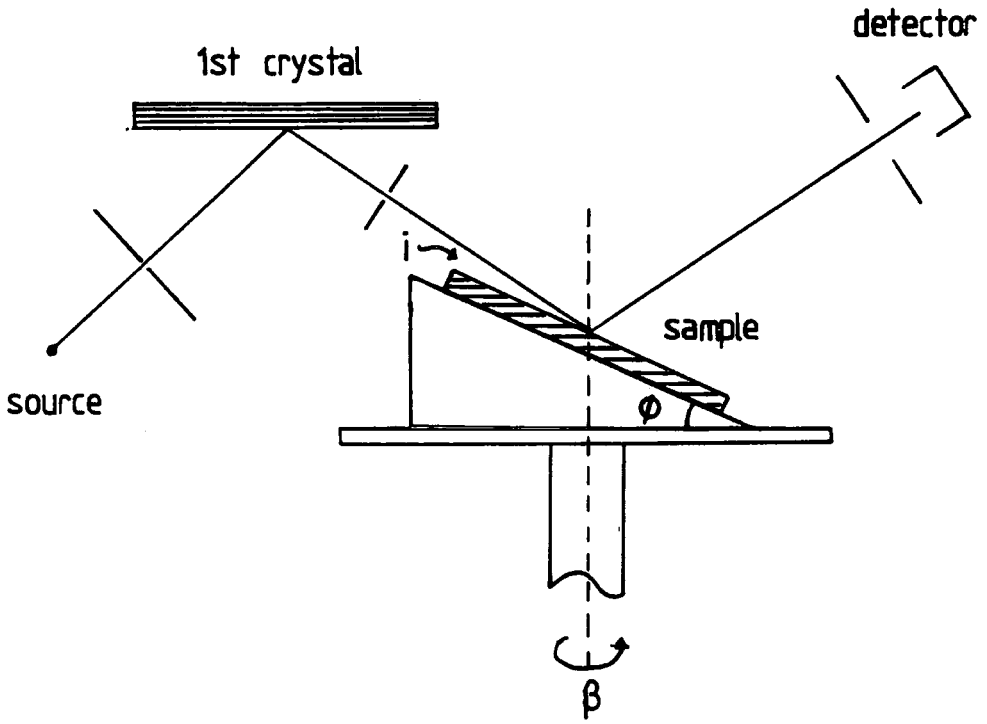

Figure 5.10: SARCA experimental arrangement.

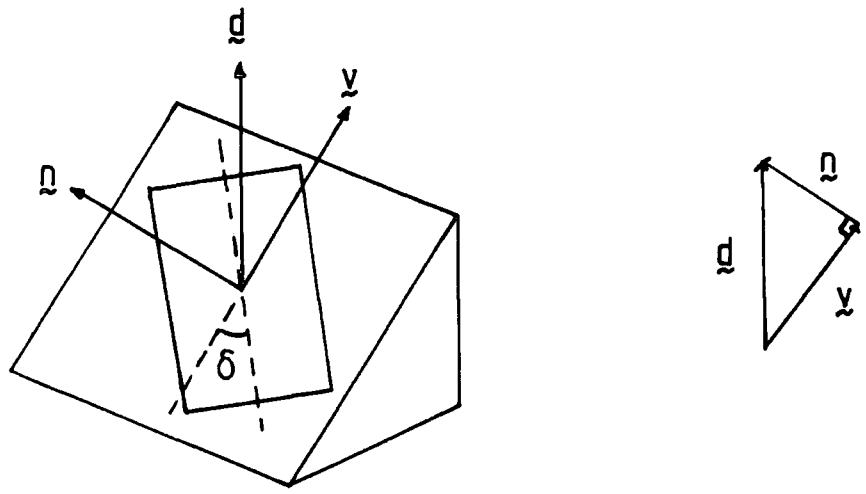

Figure 5.11: Vector diagram of the sample orientation.

Reflection *hkl*	Orientation Angle δ
044	45°
333	0°
133	26.6°
224	0°
115	0°
335	0°

Table 5.1: Angle of orientation with respect to [110] cleaved edges for asymmetric reflections

sample mounted at an angle of δ to the cleaved edges. The sample is mounted such that the diffracting planes are parallel to the base of the wedge, so that rotation occurs about the diffraction plane normal, $\underline{d}$. $\underline{n}$ is a vector parallel to the sample surface normal. δ is then given by the angle between the [110] edge and the vector $\underline{v}$ which lies in the surface plane and also the plane containing $\underline{n}$ and $\underline{d}$. $\underline{v}$ and δ result from the following equations

$$\underline{v}.\underline{n} = 0 \quad , \quad \underline{v} + \underline{n} = \underline{d} \quad , \quad \delta = \cos^{-1}\Big\{\frac{1}{\sqrt{2}|\underline{v}|}\underline{v}.[110]\Big\} \; . \qquad 5.16$$

Table 5.1 shows the values of the angle of orientation for several asymmetric reflections. It is good practice to machine a ledge at the correct angle on the wedge for ease and accuracy of specimen mounting.

It is important when using skew geometry that the incident X-ray beam and the sample surface are accurately aligned over the centre of axis 2. It becomes increasingly important at highly glancing incidence. If this condition is not met then the X-ray beam will either miss the sample entirely or be stopped by the side of the wedge. Obviously, as the angle becomes less glancing the beam will move back on to the sample again, but the most sensitive range of incident angles will be lost. It is also important that the rotation angle is calibrated accurately and the rotational steps are accurate to within 0.1°.

When using first crystal reflections different from that used for the sample it is important to eliminate the $K\alpha_2$ element, to reduce the effects of wavelength dispersion, with a slit between reference and specimen crystals.

5.4 Simulation of SARCA

The simulation program based on the Takagi-Taupin equations of dynamical theory has been described in Chapter 3. In order to model the results of SARCA the equations governing the expected positions of layer peaks need to be adapted for the skew angle case, and the direction cosines have to describe the changing angles of incidence and emergence. Equations (5.1), (5.2) and (5.15) have been used to do this, and Appendix A gives a listing of the adapted program.

In the extreme incidence case the normal assumption in dynamical theory that the asymptotic forms of the dispersion surface and the incidence circle are straight lines is incorrect as they are in fact circles (Brümmer et al., 1976; Rustichelli, 1975). Although the Takagi-Taupin equations do not make this assumption there is some doubt as to their validity at extreme incidence, especially when there is a significant specular reflected beam. Brühl et al. (1988) went down as far as 0.35° incidence angle and interpreted the rocking curves using a semi- kinematic model of Petrashen (1975). Tanner and Hill (1986) used the Takagi-Taupin equations to simulate rocking curves with incidence angle down to 1°. A good match between theory and experiment was found which indicates that the theory is adequate for most practical incident angles.

Pietsch and Borchard (1987) have used SARCA to characterise heteroepitaxial structures of $Ca_{0.43}Sr_{0.57}F_2$ on GaAs. For small incidence angles the effect of refraction becomes more important. They have exploited the fact that both the layer and the substrate peaks are shifted by different amounts from the position calculated from kinematical theory, where absorption and refraction are not taken into account. This permits the characterisation of layers of totally lattice-matched structures. At incident angles of 1° using the 335 reflection they have observed substrate-layer peak splittings of around 35″ from a perfectly lattice-matched layer. The theoretical Bragg shift $\Delta\theta$ from the Bragg angle θ_B has been given by Rustichelli (1975), Brümmer, Höche and Nieber (1976) and Härtwig (1978) to be

$$\Delta\theta = \theta - \theta_B = \frac{-\gamma_0 + \left[\gamma_0^2 + (\gamma_0|\chi_0|/\sin 2\theta_B)(1+\gamma_h/\gamma_0)(1-\gamma_0^2)^{\frac{1}{2}}\right]^{\frac{1}{2}}}{(1-\gamma_0^2)^{\frac{1}{2}}} \leq \theta_C \ , \quad 5.17$$

where γ_0 and γ_h are direction cosines and χ_0 the Fourier component of the polarisability calculated from

$$\chi_0 = \chi_0' + \chi_0'' i = \frac{C r_e \lambda^2}{\pi V}\left[\sum_i (Z_i + f_i') + i\sum_i f_i''\right] . \quad 5.18$$

Here, C is the polarisation factor, r_e the classical electron radius, λ is the wavelength, and f' and f'' are the real and imaginary parts of the dispersion correction. Z_i refers to the ordinary number of atoms involved in the elementary volume

V. When applied to the InP based epitaxial layers of $InGaAs$ and $InGaAsP$ a similar effect is seen for perfectly matched layers, although smaller in magnitude as the polarisabilities are closer than in the $Ca_{0.43}Sr_{0.57}F_2/GaAs$ system. Table 5.2 shows the calculated splittings of perfectly lattice matched layers of $InGaAs$ and $InGaAsP$ (band gap = $1.35\mu m$) on InP for $CuK\alpha$ radiation for several reflections and incident angles. There is little to choose from the 335, 333 and 133 reflections shown in terms of magnitude of peak separation, but the 311 is a lot lower. This is because the γ_h/γ_0 term dominates in equation (5.17) and for the 311 the emergence angle is lower than for the other three reflections. The separation does, however, increase markedly with smaller incidence angles for all reflections. One problem with this technique of characterising lattice matched structures is that as the incident angle decreases the rocking curve peak width increases (equation 5.5), and so splittings of the order of $20''$ become more difficult to observe. Yet Pietsch and Borchard (1987) have demonstrated that it is possible, and without the technique there would be no method of characterising layer thickness of lattice-matched structures using double-crystal X-ray diffraction.

5.5 Results

The sample studied was a single quantum well structure of $GaInAsP$ (band gap $1.35\mu m$) on InP, code INP3, grown by MOCVD at British Telecom research Laboratories by P. Spurdens. Crystal growth information estimated the layer thickness to be between $0.15\mu m$ and $0.16\mu m$, and the mismatch to be around $-800ppm$. SARCA data was collected from the 044, 333 and 133 reflections for a range of rotation angles.

Figure 5.12 shows rocking curves for the 044 reflection over a wide range of rotation angles, from glancing incidence to glancing exit. For the 044 reflection the Bragg cone is not embedded and so only a minimum incidence angle of 3° occurs. The maximum layer to substrate peak ratio occurs at rotations of 0° and 180°, reaching a minimum at 90°. As the geometry moves from glancing incidence to glancing exit the peak separation decreases and the peaks become sharper. However, a constant peak width is achieved before 180° rotation is reached due to broadening from curvature and sample imperfection.

	Incidence Angle i (°)		
335 Reflection	0.75	1.0	1.5
$\Delta\theta$ $InGaAs/InP$	23.5″	18.2″	12.4″
$\Delta\theta$ $InGaAsP/InP$	16.0″	12.4″	8.5″
	Incidence Angle i (°)		
133 Reflection	0.75	1.0	1.5
$\Delta\theta$ $InGaAs/InP$	22.0″	17.0″	11.6″
$\Delta\theta$ $InGaAsP/InP$	15.0″	11.6″	7.9″
	Incidence Angle i (°)		
333 Reflection	0.75	1.0	1.5
$\Delta\theta$ $InGaAs/InP$	20.8″	16.0″	11.0″
$\Delta\theta$ $InGaAsP/InP$	14.2″	10.9″	7.5″
	Incidence Angle i (°)		
311 Reflection	0.75	1.0	1.5
$\Delta\theta$ $InGaAs/InP$	9.1″	6.9″	4.7″
$\Delta\theta$ $InGaAsP/InP$	6.2″	4.7″	3.2″

Table 5.2: Separation of substrate and layer peaks in rocking curves of perfectly matched structures at glancing incidence. (Quaternary band gap = $1.35\mu m$).

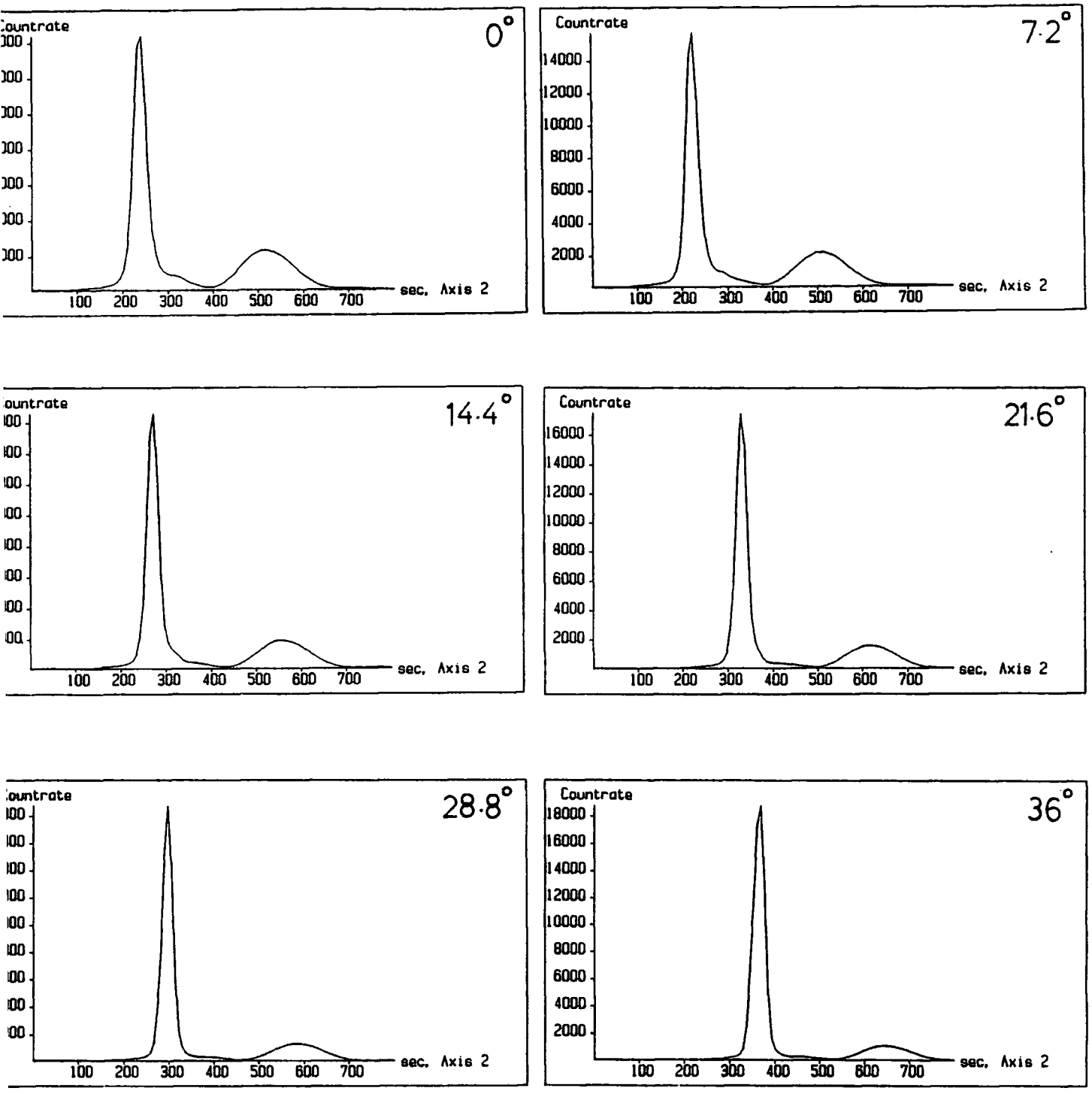

Figure 5.12: SARCA 044 rocking curves of sample $INP3$ over a range of rotation angles.

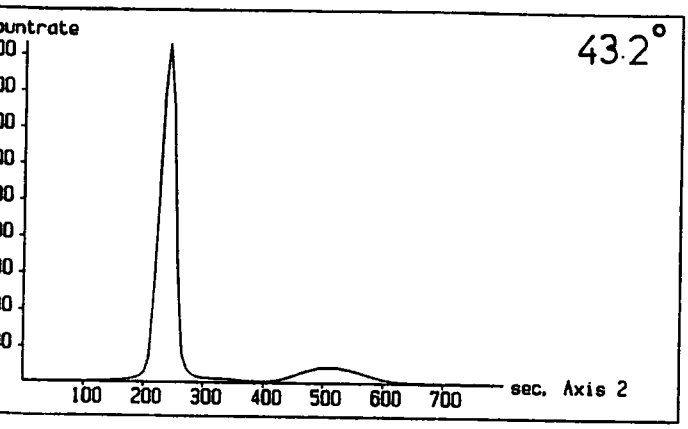
43.2°
100 200 300 400 500 600 700
sec. Axis 2

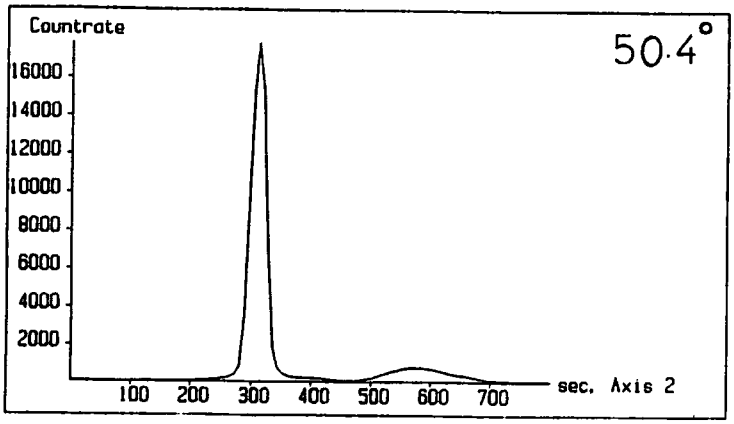
Countrate
16000
14000
12000
10000
8000
6000
4000
2000
50.4°
100 200 300 400 500 600 700
sec. Axis 2

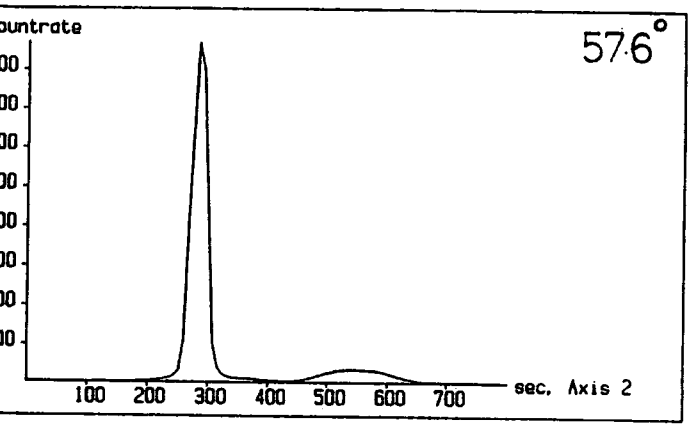
57.6°
100 200 300 400 500 600 700
sec. Axis 2

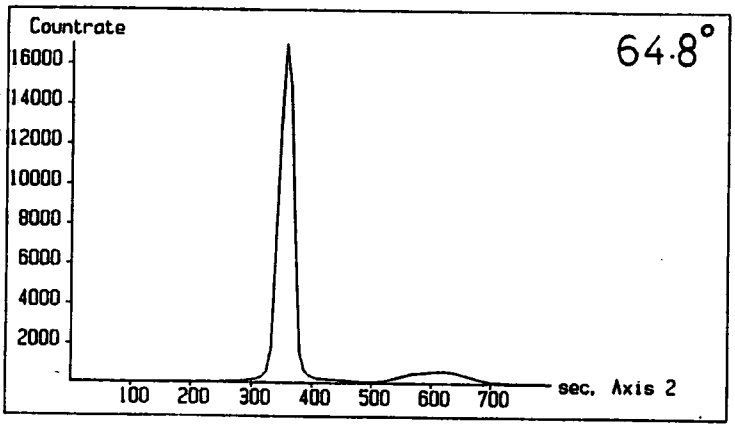
Countrate
16000
14000
12000
10000
8000
6000
4000
2000
64.8°
100 200 300 400 500 600 700
sec. Axis 2

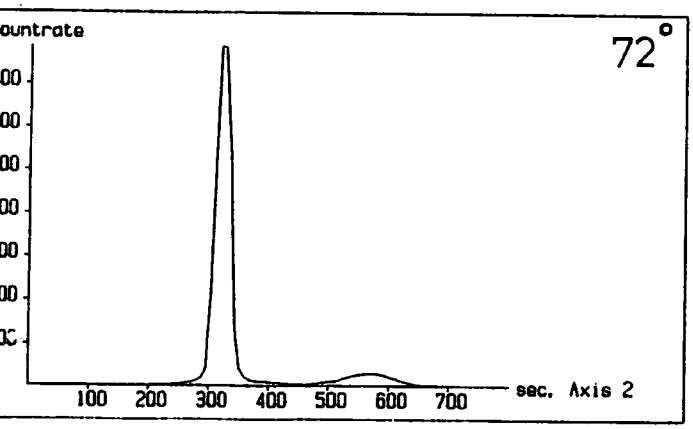
72°
100 200 300 400 500 600 700
sec. Axis 2

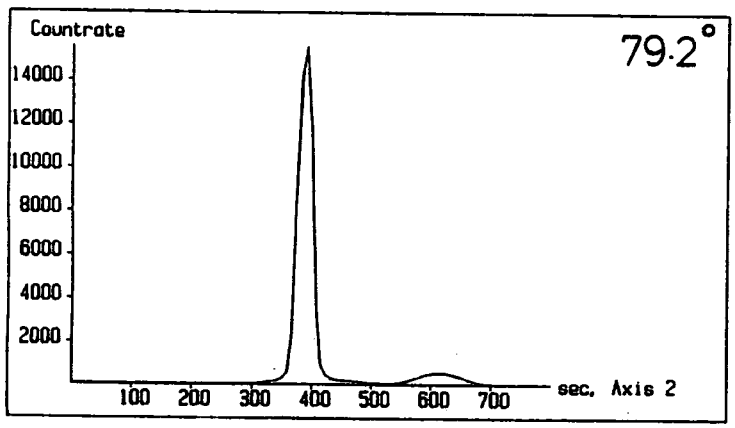
Countrate
14000
12000
10000
8000
6000
4000
2000
79.2°
100 200 300 400 500 600 700
sec. Axis 2

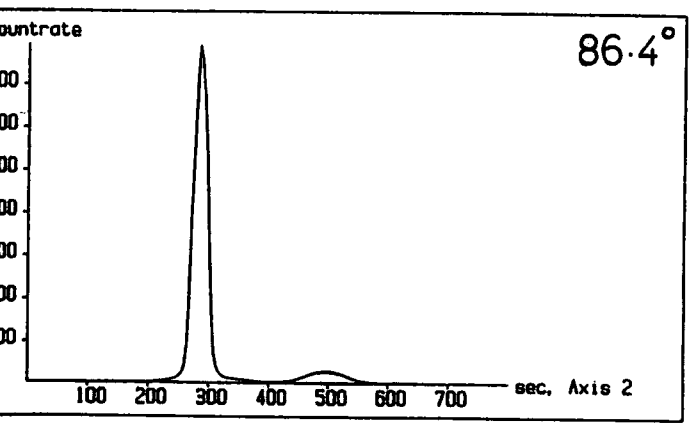
86.4°
100 200 300 400 500 600 700
sec. Axis 2

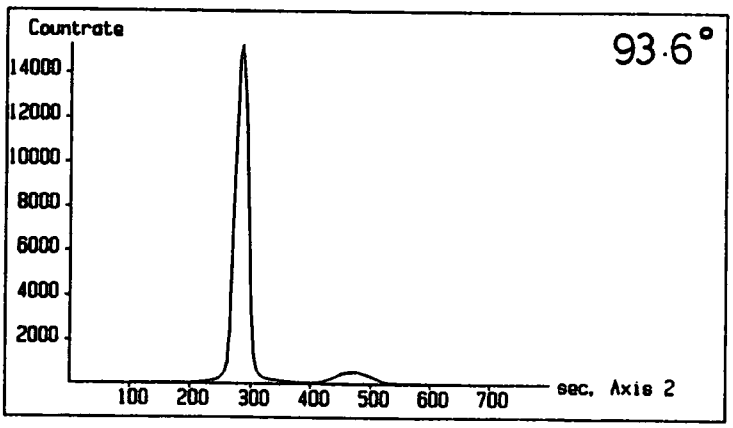
Countrate
14000
12000
10000
8000
6000
4000
2000
93.6°
100 200 300 400 500 600 700
sec. Axis 2

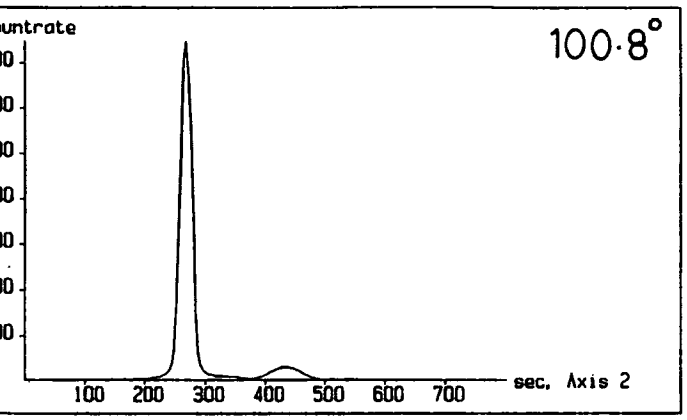
100·8°
sec. Axis 2

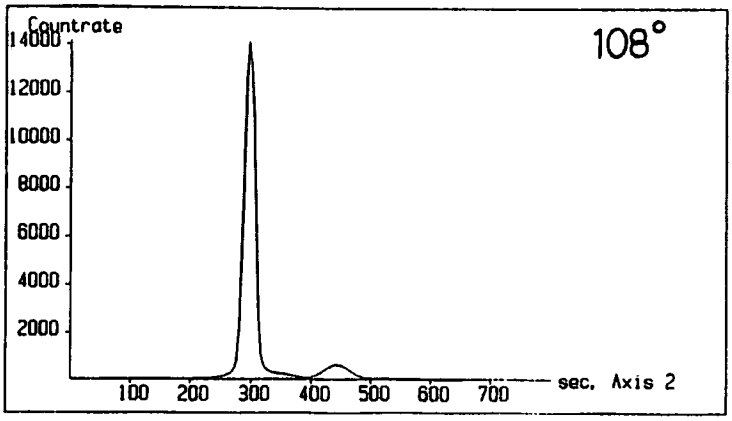
Countrate
14000
12000
10000
8000
6000
4000
2000
108°
100 200 300 400 500 600 700
sec. Axis 2

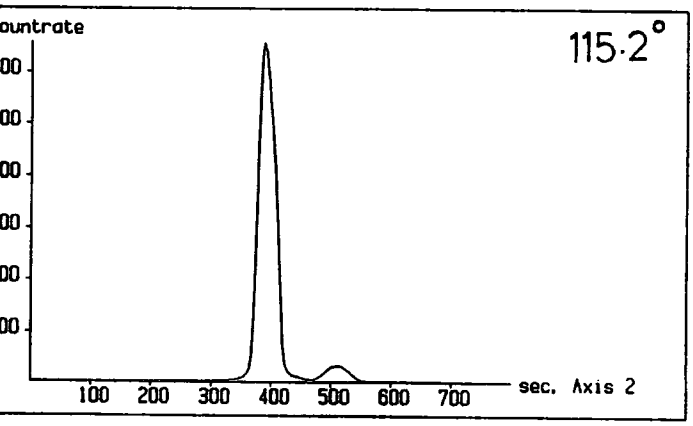
115·2°
sec. Axis 2

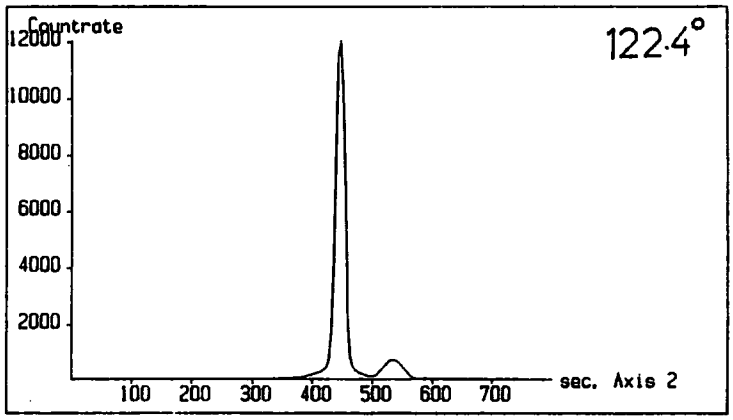
Countrate
12000
10000
8000
6000
4000
2000
122·4°
100 200 300 400 500 600 700
sec. Axis 2

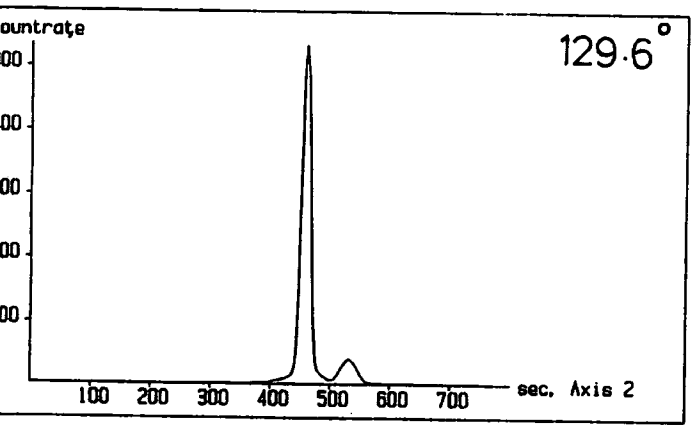
129·6°
sec. Axis 2

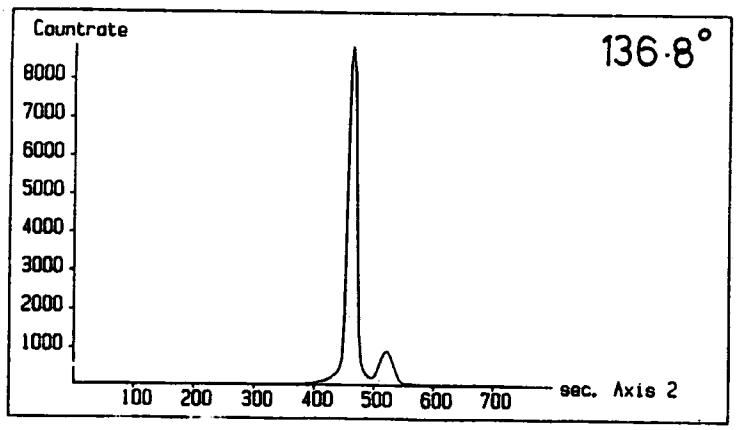
Countrate
8000
7000
6000
5000
4000
3000
2000
1000
136·8°
100 200 300 400 500 600 700
sec. Axis 2

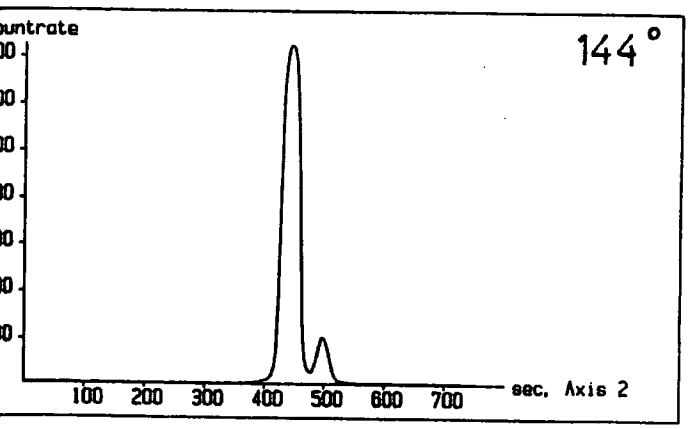
144°
sec. Axis 2

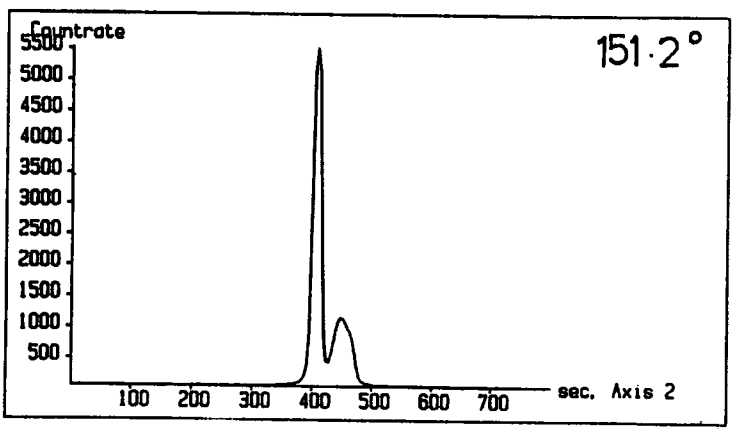
Countrate
5500
5000
4500
4000
3500
3000
2500
2000
1500
1000
500
151·2°
100 200 300 400 500 600 700
sec. Axis 2

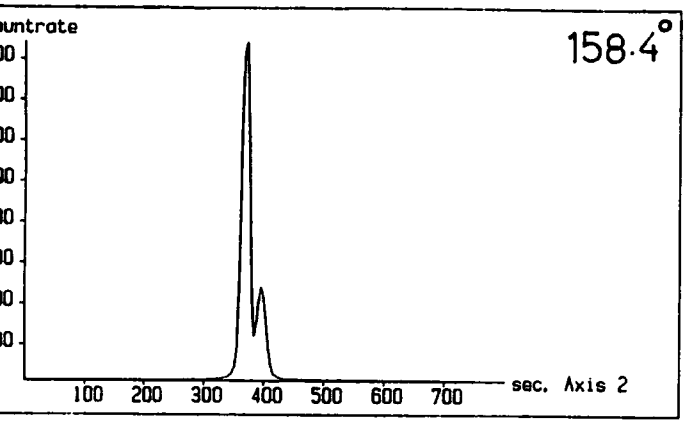
158.4°
100 200 300 400 500 600 700
sec. Axis 2

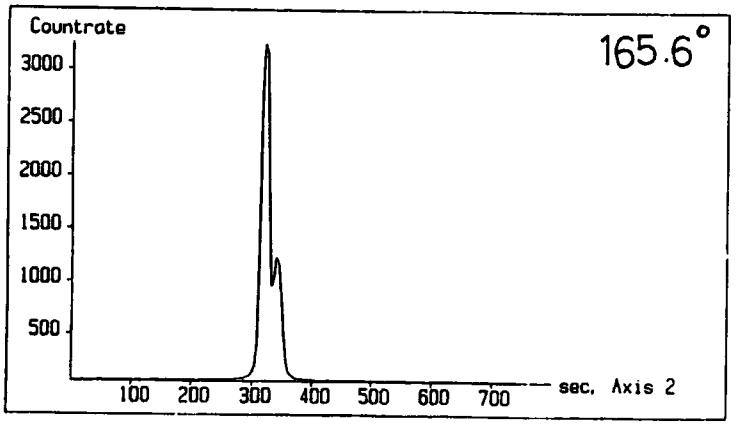
Countrate
3000
2500
2000
1500
1000
500
165.6°
100 200 300 400 500 600 700
sec. Axis 2

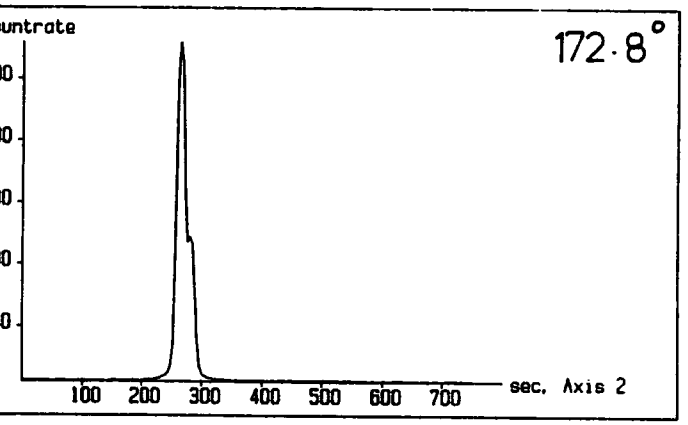
172.8°
100 200 300 400 500 600 700
sec. Axis 2

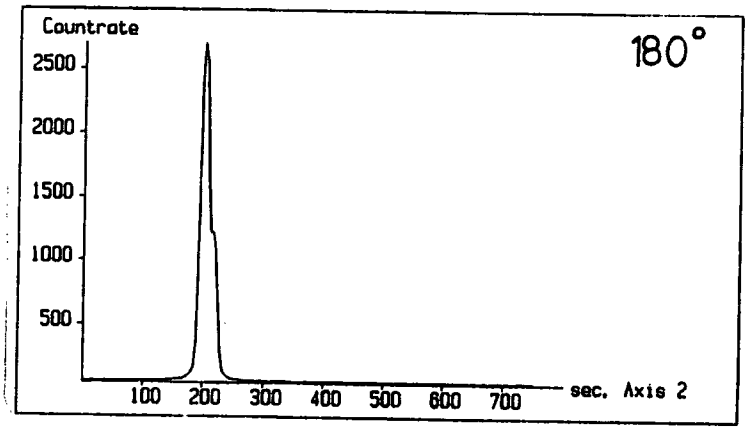
Countrate
2500
2000
1500
1000
500
180°
100 200 300 400 500 600 700
sec. Axis 2

Figure 5.13 shows the corresponding set of rocking curves from the 133 reflection of the same sample. Again, the same features can be observed, with the higher layer to substrate peak ratios at glancing incidence and glancing exit. In this case there is little peak width sharpening as glancing exit is approached. This is because the first crystal used in the experiment was (011) oriented InP, using an 044 reflection, and so wavelength dispersion occurs. Broadening due to dispersion is given by the following equation

$$d\theta = \frac{d\lambda}{\lambda}(\tan\theta_2 - \tan\theta_1) \ . \qquad 5.19$$

There is some $K\alpha_2$ contamination observed on the rocking curve although most of the component was eliminated using a slit. The contamination is small however. Using equation (5.19) the splitting of the $K\alpha_1$ and $K\alpha_2$ peaks on the rocking curve for an 044 first reflection and a 133 second is $-211''$. The rocking curve broadening due to dispersion from the line width of the $K\alpha_1$ component makes the layer peak indistinguishable from the substrate peak at glancing exit. Curvature and sample imperfection also broaden the peaks.

Using the 333 reflection with the same sample an incidence angle of $1.15°$ ($\beta = 51.2°$) was achieved and a full range of rotation angles is shown in figure 5.14. The dotted lines show the simulated rocking curves. The experimental curves closely match the theoretical predictions as the geometry is changed which confirms the validity of the derived geometrical expressions. In order to achieve a close match between the experimental and simulated rocking curves a thin interfacial layer was required. The predicted structure is shown in figure 5.15, with the top layer having a thickness of $0.12\mu m$ and mismatch $-680ppm$. The combined thicknesses of the two layers, and average mismatch agree with the initial crystal growth prediction. The interfacial layer complicated the simulation procedure since the main layer peak position and intensity were highly sensitive to its thickness and mismatch. Changes in thickness of $100\mathring{A}$, or mismatches of $100ppm$ dramatically altered the simulated rocking curve. Figure 5.16 shows a series of simulated rocking curves for different values of thickness and mismatch of the interfacial layer. Figure 5.16(a) is for a mismatch of $-1250ppm$ and varying thickness. As the thickness is increased both the layer peak height and peak separation increase,

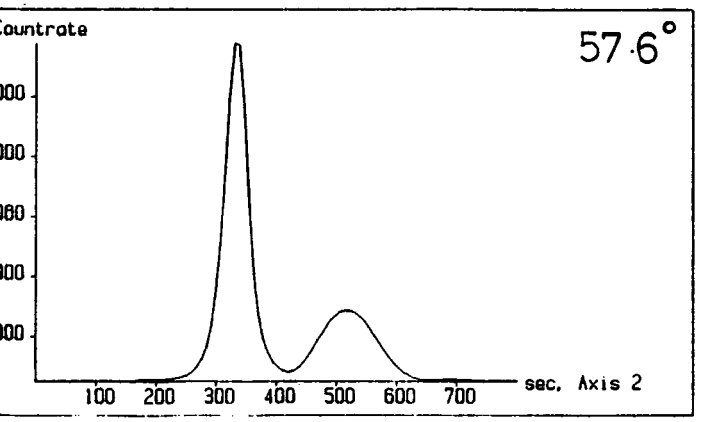

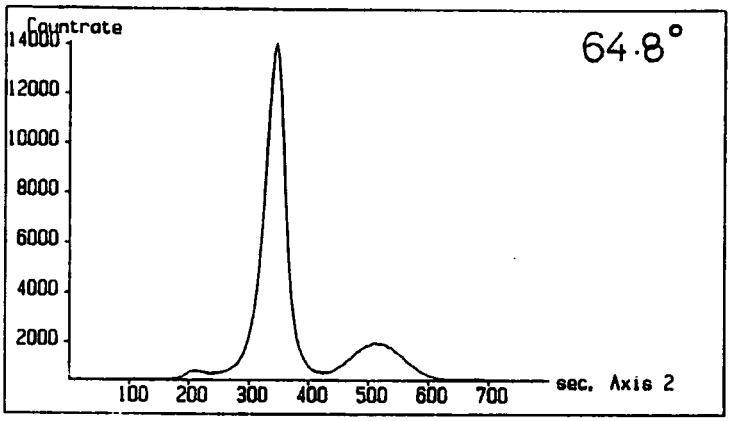

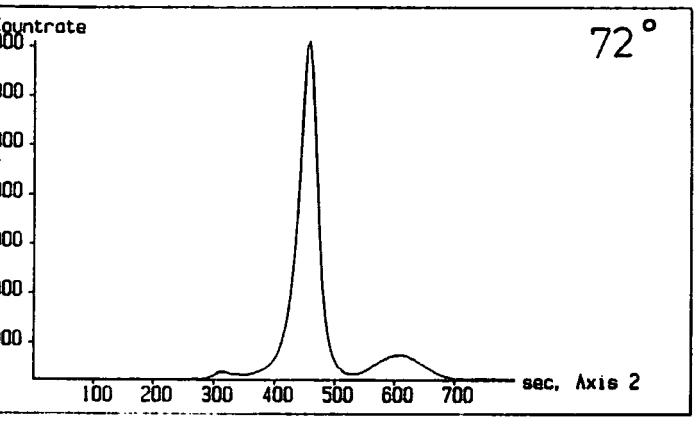

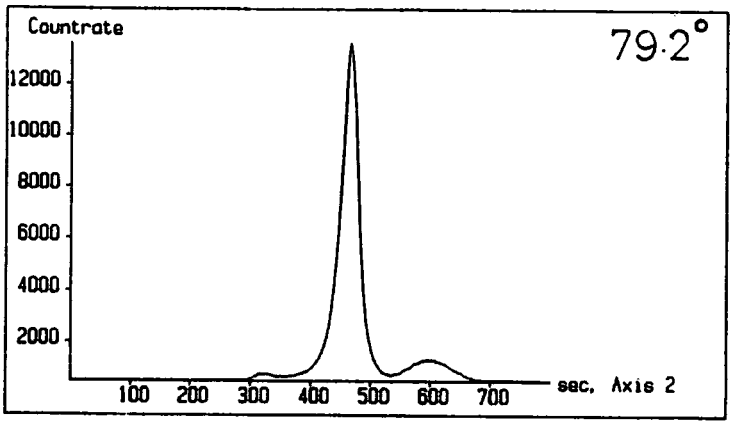

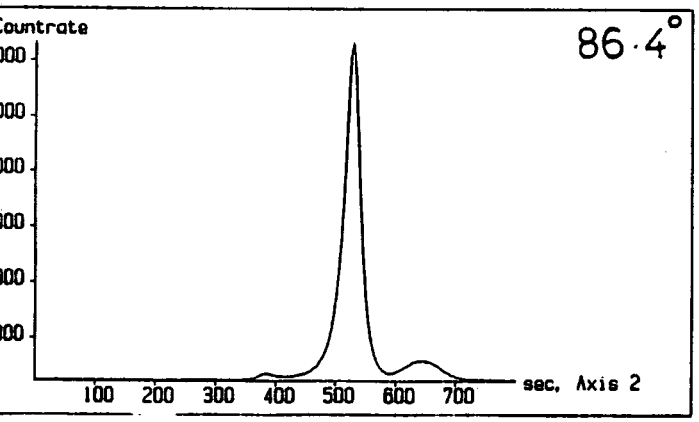

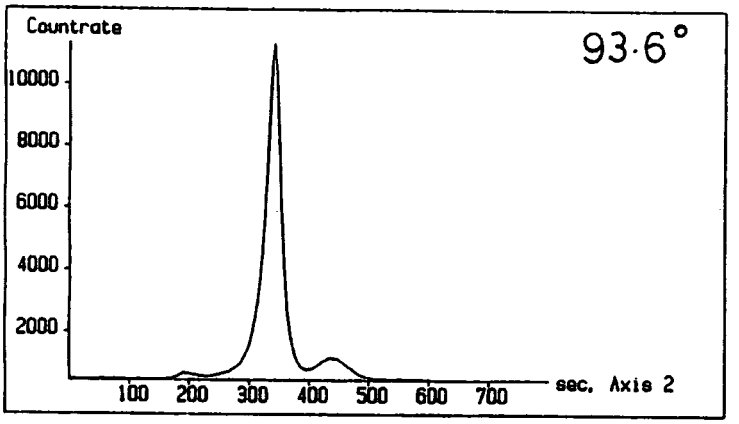

Figure 5.13: SARCA 133 rocking curves of sample $INP3$ over a range of rotation angles.

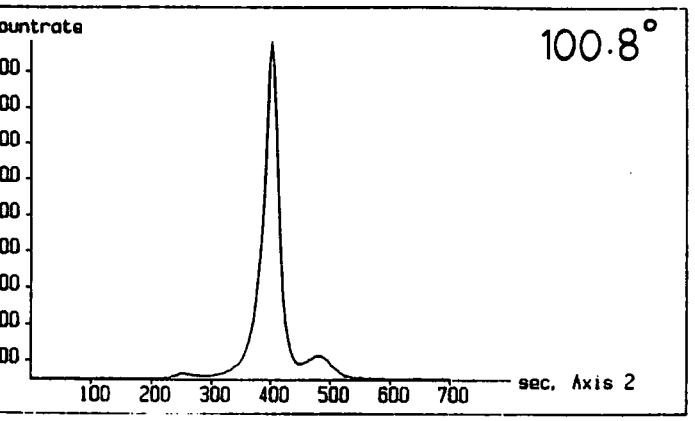
ountrate
00
00
00
00
00
00
00
00
00
100.8°
100 200 300 400 500 600 700
sec. Axis 2

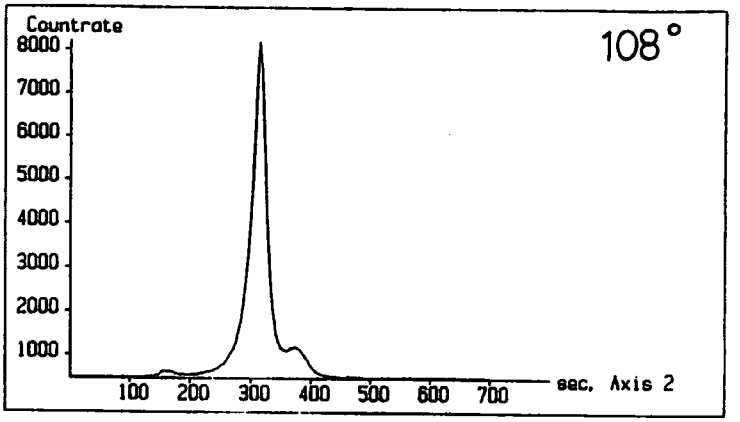
Countrate
8000
7000
6000
5000
4000
3000
2000
1000
108°
100 200 300 400 500 600 700
sec. Axis 2

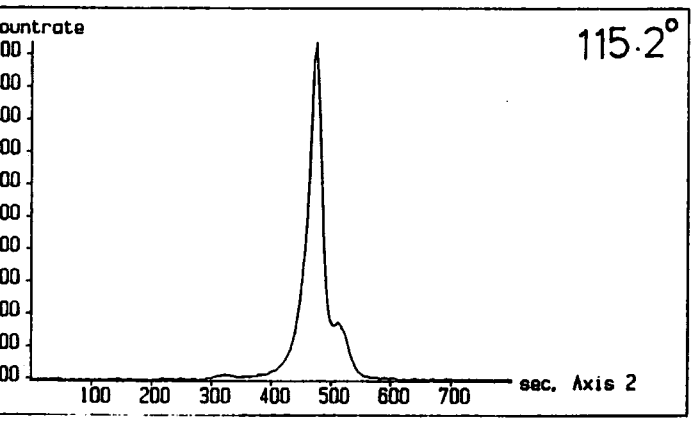
ountrate
00
00
00
00
00
00
00
00
00
00
00
115.2°
100 200 300 400 500 600 700
sec. Axis 2

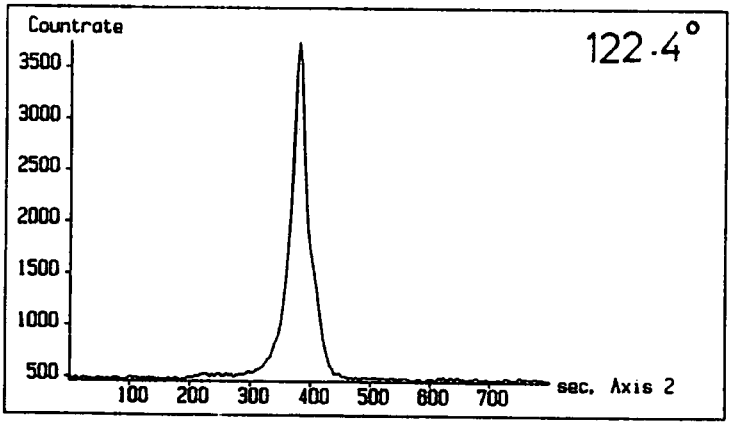
Countrate
3500
3000
2500
2000
1500
1000
500
122.4°
100 200 300 400 500 600 700
sec. Axis 2

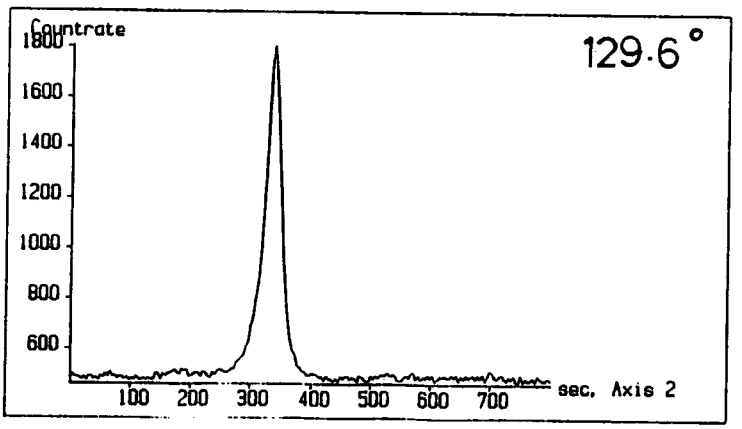
Countrate
1800
1600
1400
1200
1000
800
600
129.6°
100 200 300 400 500 600 700
sec. Axis 2

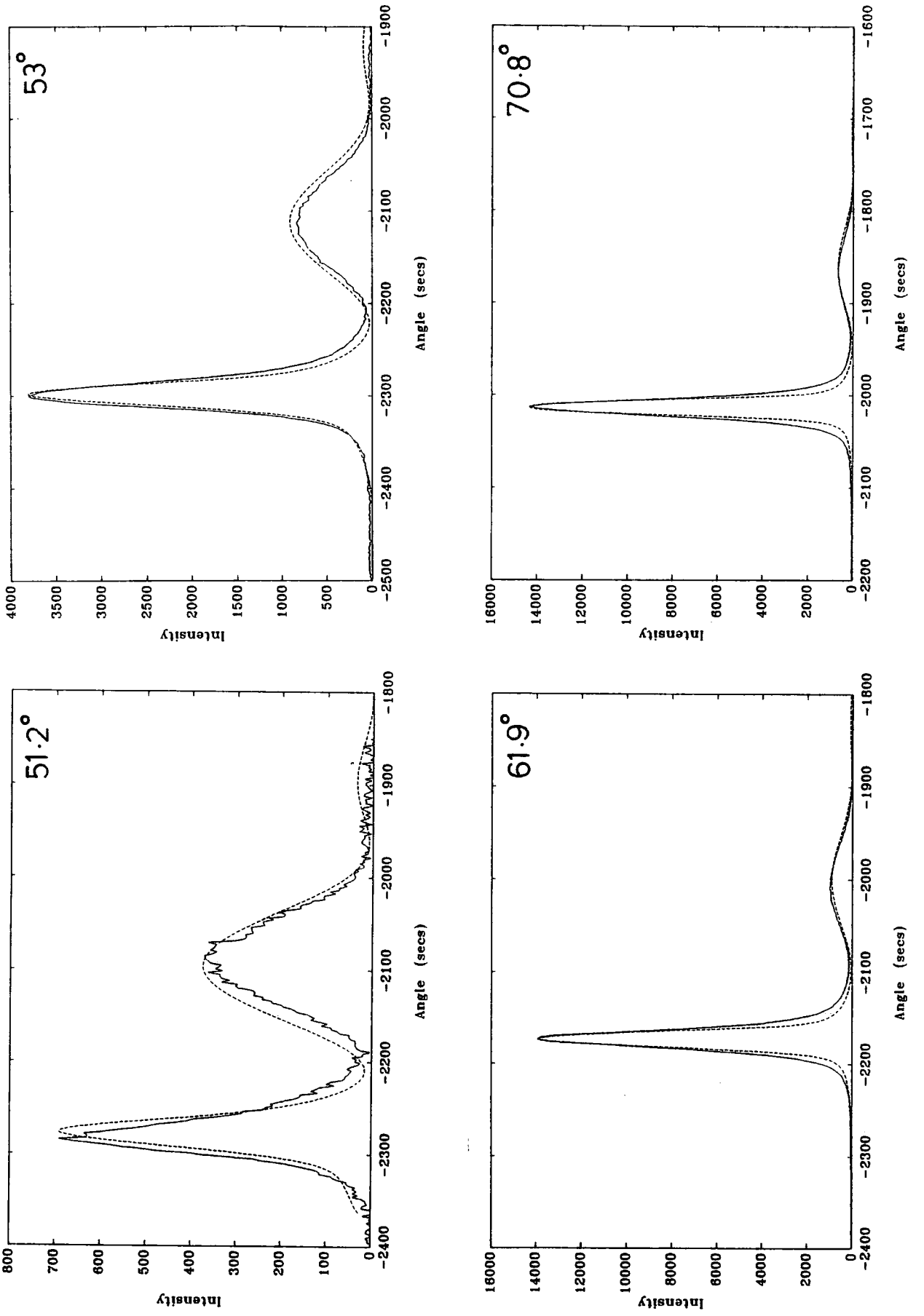

Figure 5.14: Experimental (solid) and theoretical (dashed) SARCA 333 rocking curves of sample $INP3$ over a range of rotation angles.

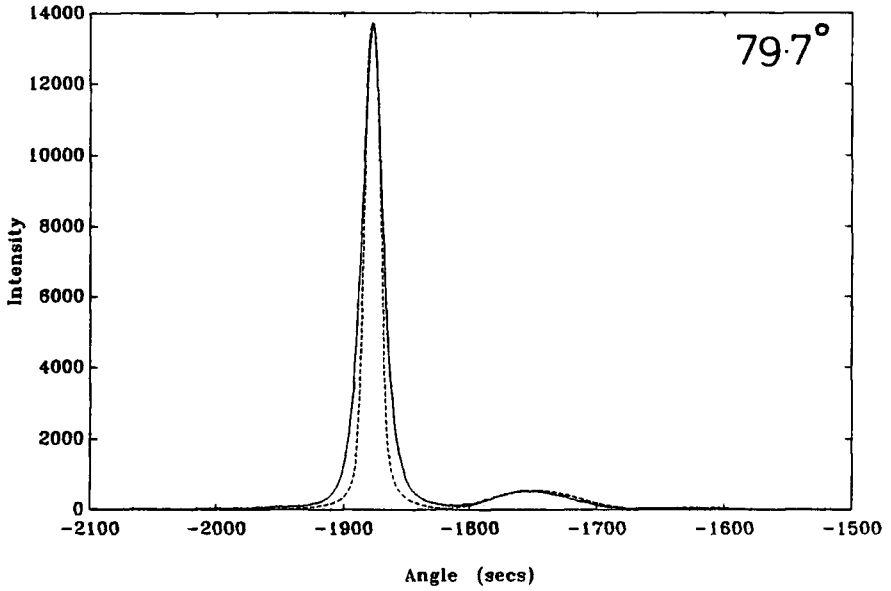
79·7°
Intensity
Angle (secs)
14000
12000
10000
8000
6000
4000
2000
0
-2100
-2000
-1900
-1800
-1700
-1600
-1500

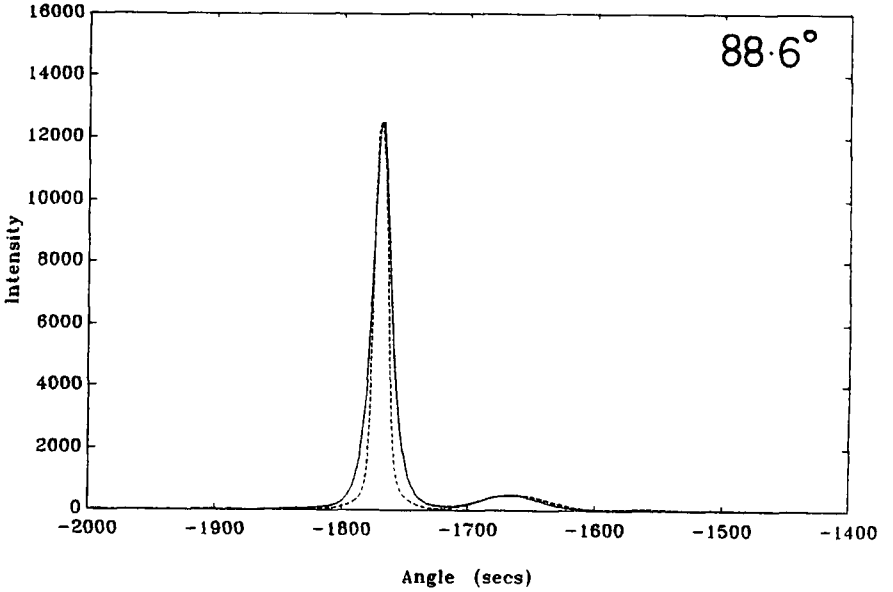
88·6°
Intensity
Angle (secs)
16000
14000
12000
10000
8000
6000
4000
2000
0
-2000
-1900
-1800
-1700
-1600
-1500
-1400

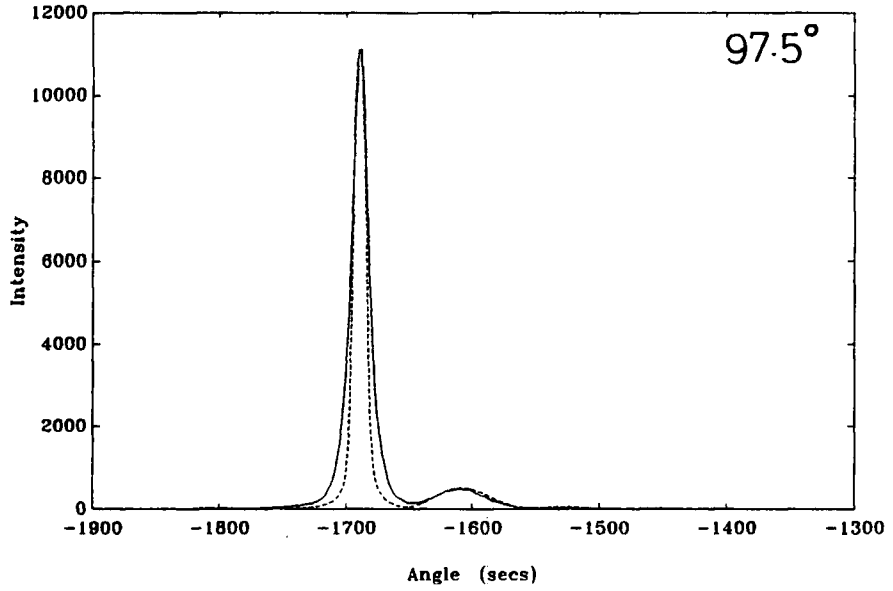
97·5°
Intensity
Angle (secs)
12000
10000
8000
6000
4000
2000
0
-1900
-1800
-1700
-1600
-1500
-1400
-1300

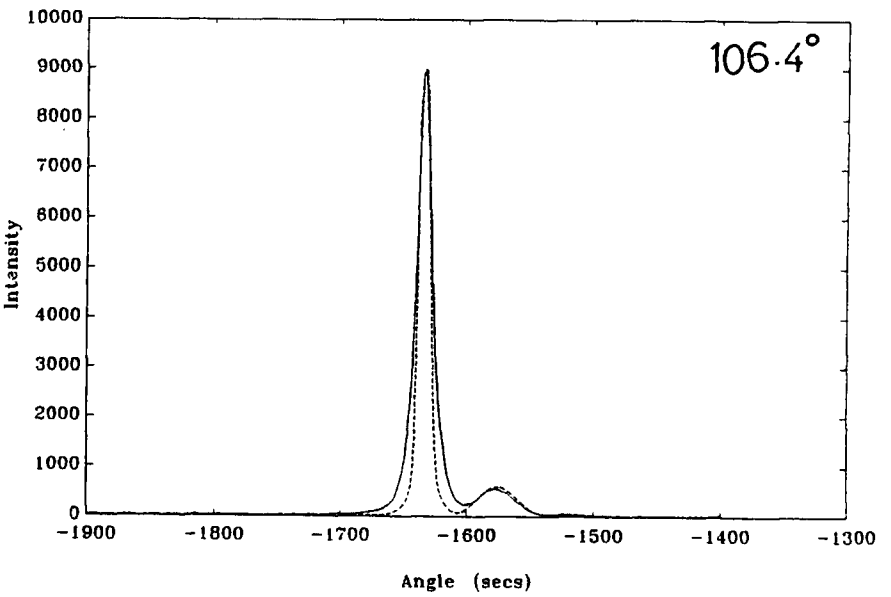
106·4°
Intensity
Angle (secs)
10000
9000
8000
7000
6000
5000
4000
3000
2000
1000
0
-1900
-1800
-1700
-1600
-1500
-1400
-1300

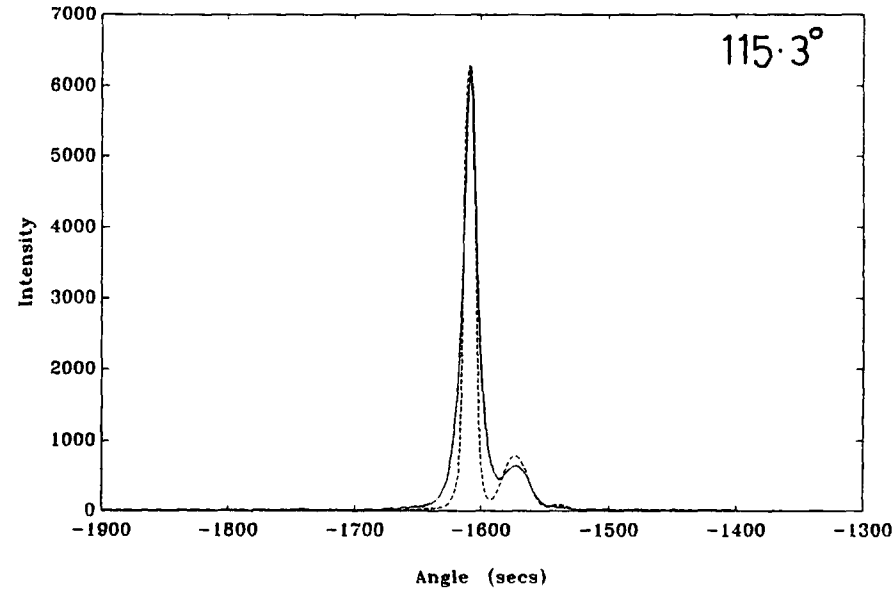
115·3°
Intensity
7000
6000
5000
4000
3000
2000
1000
0
-1900
-1800
-1700
-1600
-1500
-1400
-1300
Angle (secs)

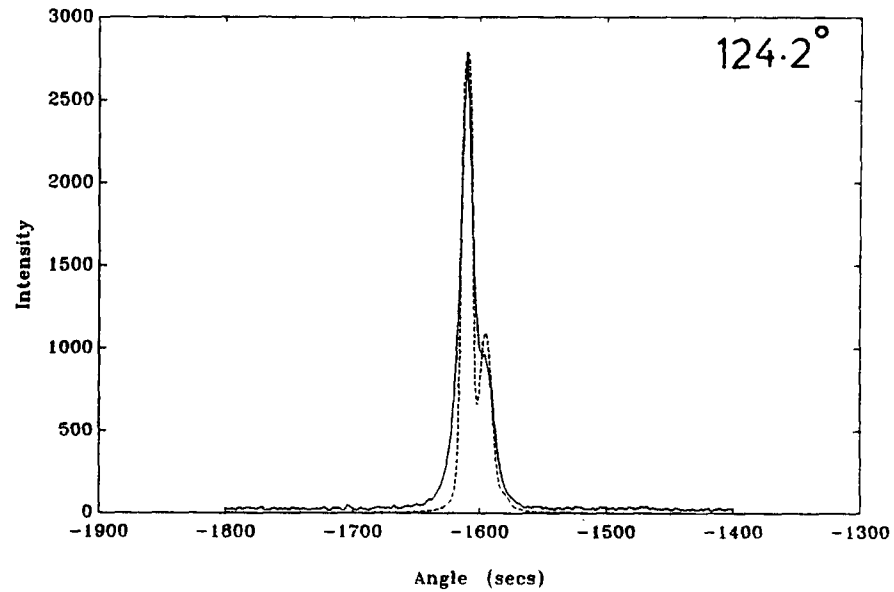
124·2°
Intensity
3000
2500
2000
1500
1000
500
0
-1900
-1800
-1700
-1600
-1500
-1400
-1300
Angle (secs)

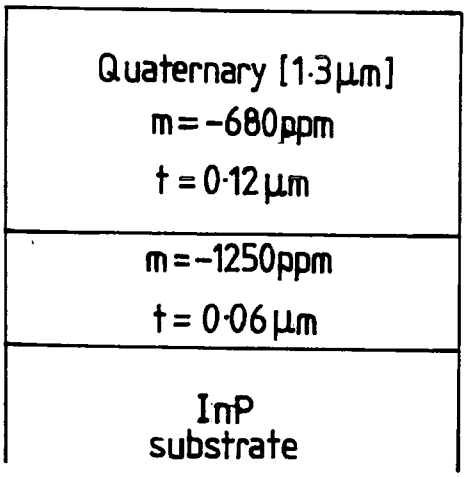

Figure 5.15: Simulated structure of sample $INP3$.

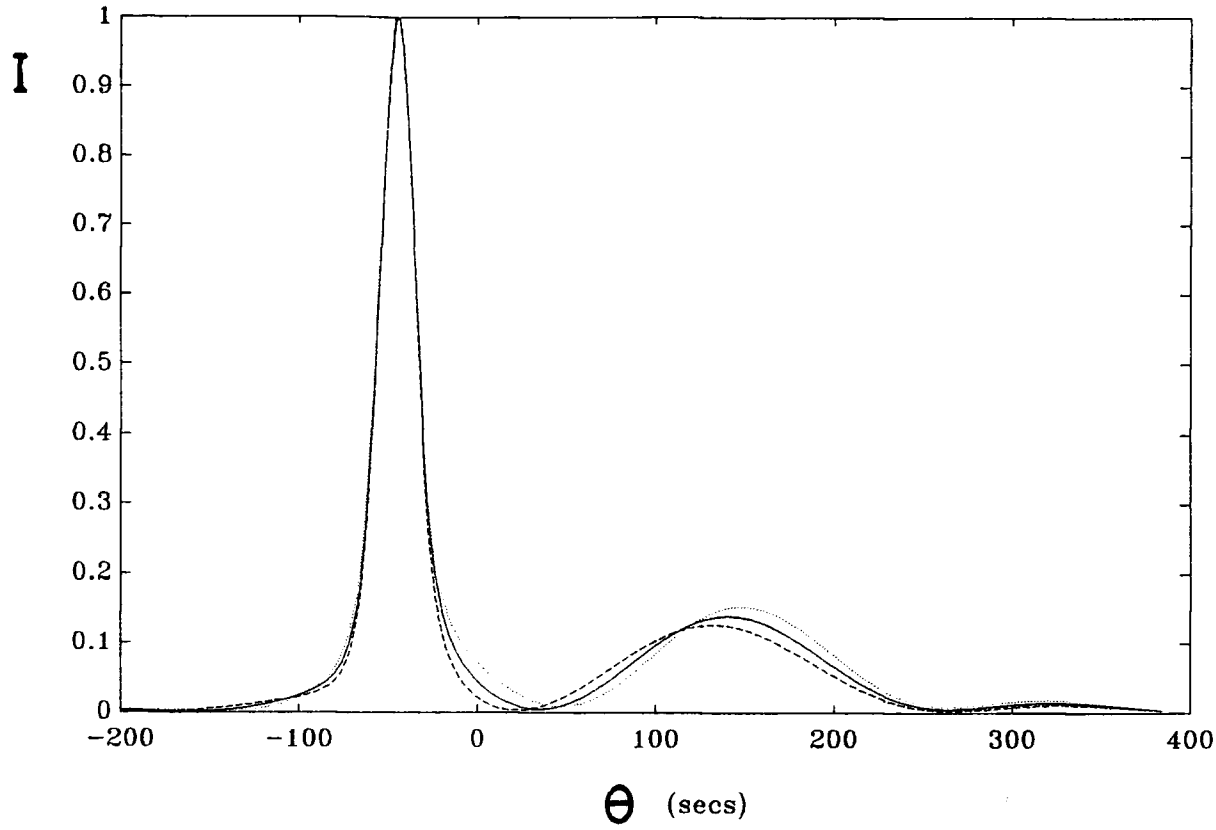

Figure 5.16(a): Simulated SARCA 333 rocking curve at $\beta = 55°$ for the $INP3$ structure but with interfacial layer thickness of $500\mathring{A}$ (dashed), $600\mathring{A}$ (solid) and $700\mathring{A}$ (dotted).

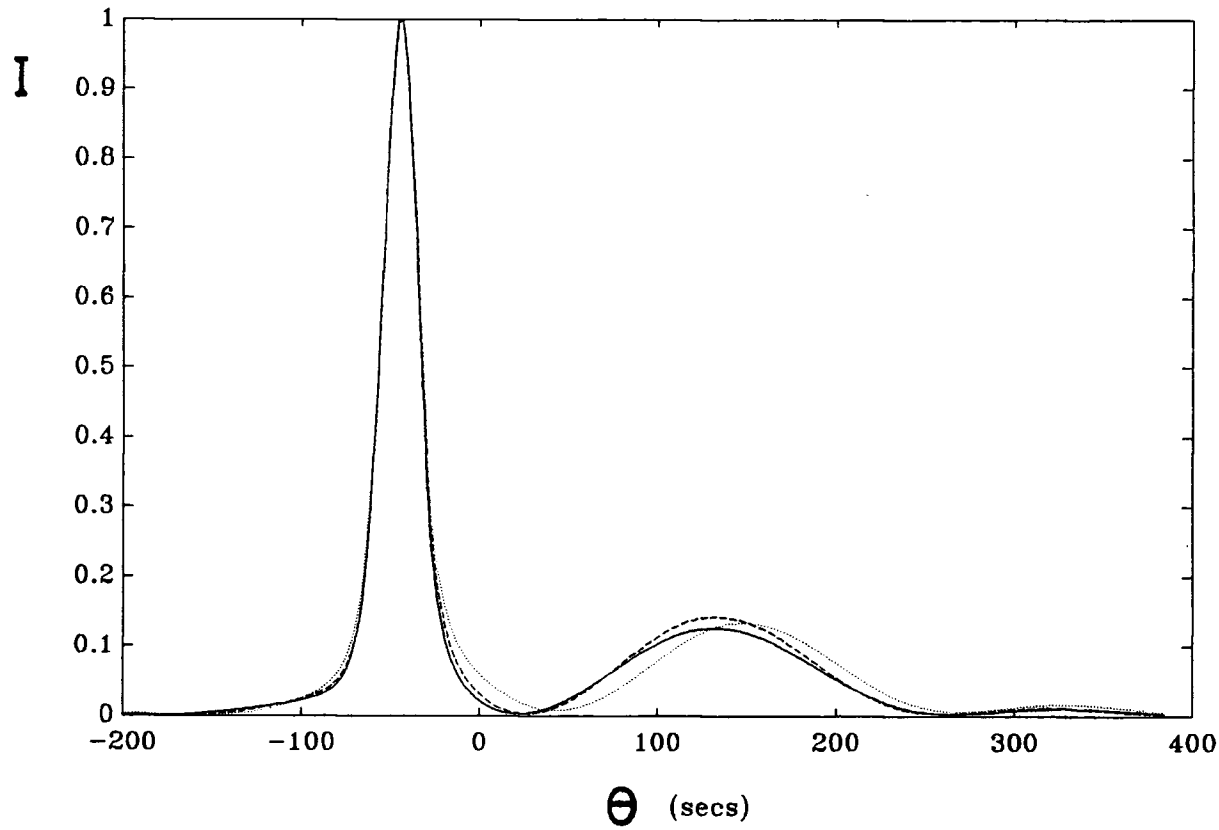

Figure 5.16(b): Simulated SARCA 333 rocking curve at $\beta = 55°$ for the $INP3$ structure but with interfacial layer mismatch of $-1150ppm$ (dashed), $-1250ppm$ (solid) and $-1350ppm$ (dotted).

as well as broadening of the substrate peak tail. Figure 5.16(b) is for a thickness of $0.06\mu m$ and varying mismatch. As the mismatch is increased both the layer peak height and peak separation change, but their relationship with mismatch becomes involved (Cockerton, Miles, Green and Tanner, 1989). In reality, a more complicated structure may exist with the possibility of compositional grading at the interface. In order to fit peak widths as closely as possible the effect of sample curvature has to be considered. At low angles of incidence the broadening due to curvature is greater than at high angles of incidence. The change in angle along the incident X-ray beam due to curvature is given by $D/R\sin i$; where D is the beam diameter, R the radius of curvature and i the angle of incidence. However, it can also be defined as the length sampled in the diffraction plane divided by the radius of curvature. It is interesting to note that for samples of finite size at low angles of incidence the whole length of the sample is irradiated, so that the effect due to curvature tends towards a constant limit. Other broadening effects include wavelength dispersion and poor crystalline quality of the sample and reference crystals.

The first rocking curve in figure 5.14 shows the 1.15° incidence case. The layer to substrate peak intensity ratio has increased to 53%, in comparison with 14% from the standard 044 ($\beta = 0°$) geometry. This is a substantial improvement and shows how much more sensitive to thin layers SARCA can be. In practice a layer of thickness down to a few hundred Ångstroms would be clearly definable on a rocking curve at around 1° incidence, and layers of thickness below $100\mathring{A}$ could be characterised if long counting times to obtain good statistics are used.

The surface sensitivity is governed by the extinction distance, which is given by (Authier, 1969)

$$\mu_e^{-1} = \frac{\lambda}{2\pi}\frac{\sqrt{\gamma_0|\gamma_h|}}{|C||\chi_h|}\,, \qquad 5.20$$

where C is the polarisation factor, γ_0 and γ_0 direction cosines and χ_h the polarisability (equation 5.18). This is effectively the distance penetrated below the sample surface of an X-ray beam. Figure 5.17(a) shows the way the extinction distance changes for the 044 and 133 reflections with rotation angle. For partially

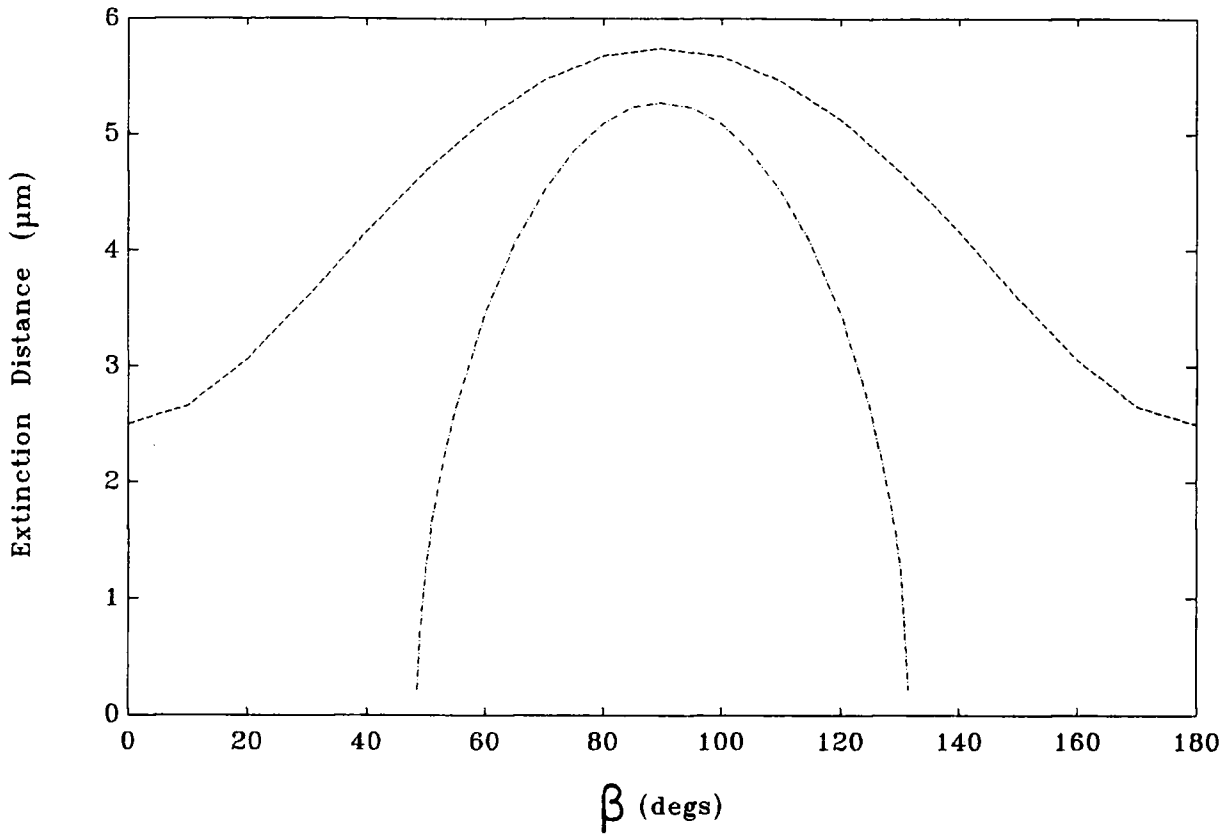

Figure 5.17(a): Relationship between extinction distance and rotation angle for the 044 (dashed) and 133 (dash-dot) reflections.

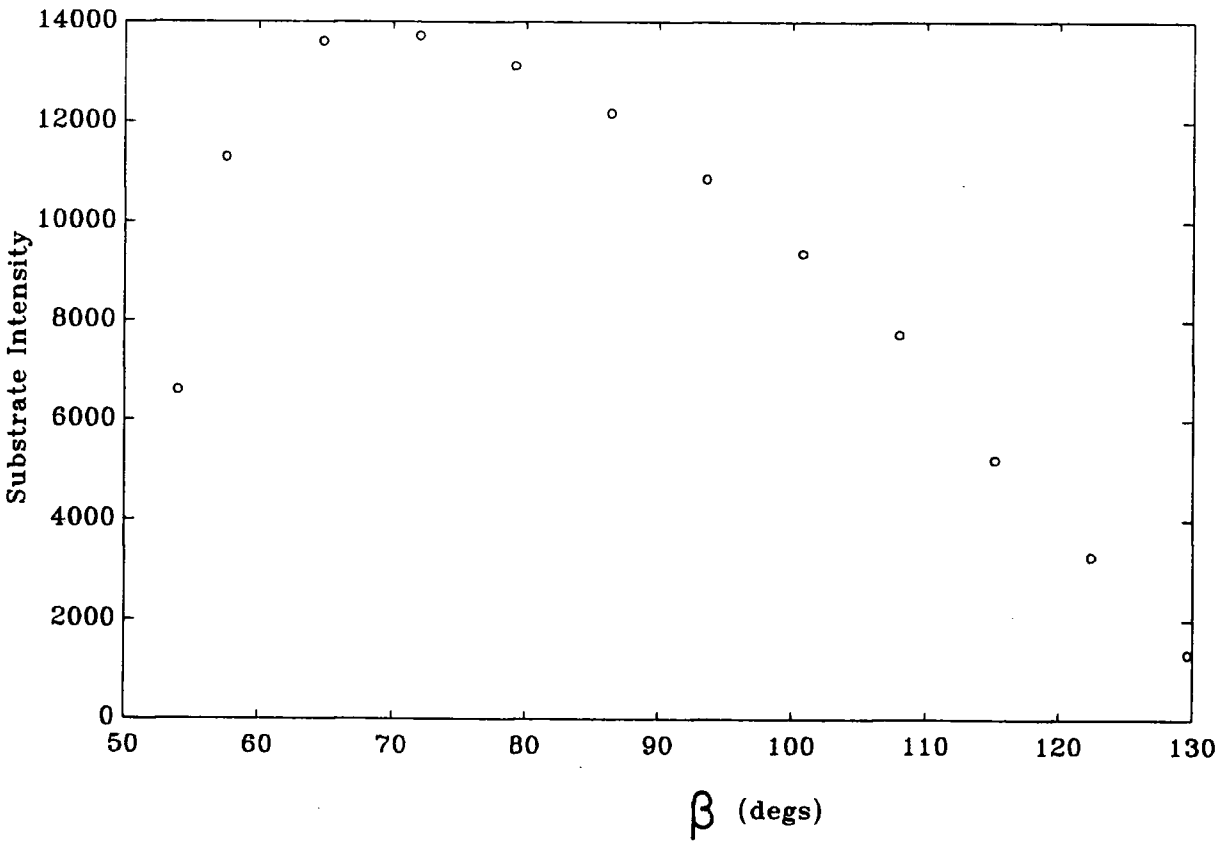

Figure 5.17(b): Substrate peak height found experimentally for the 133 reflection.

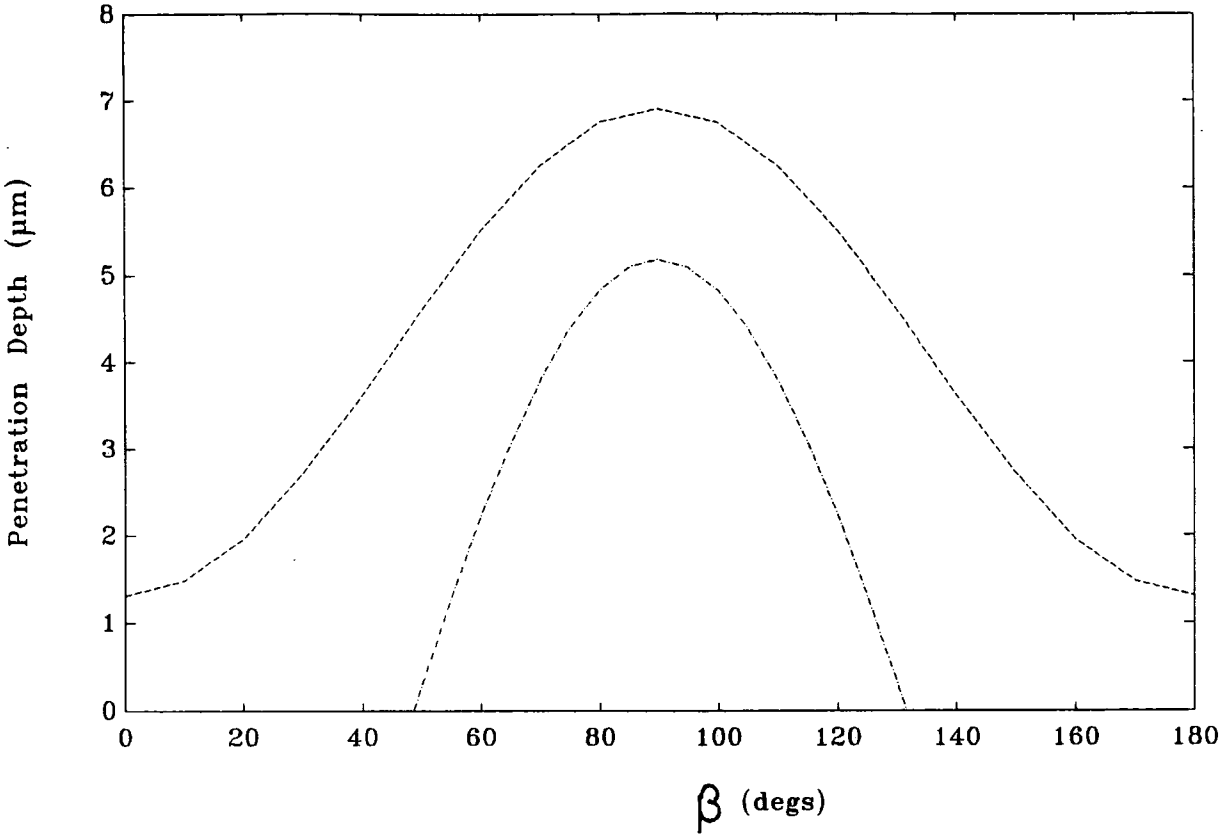

Figure 5.17(c): Relationship between penetration depth and rotation angle for the 044 (dashed) and 133 (dash-dot) reflections.

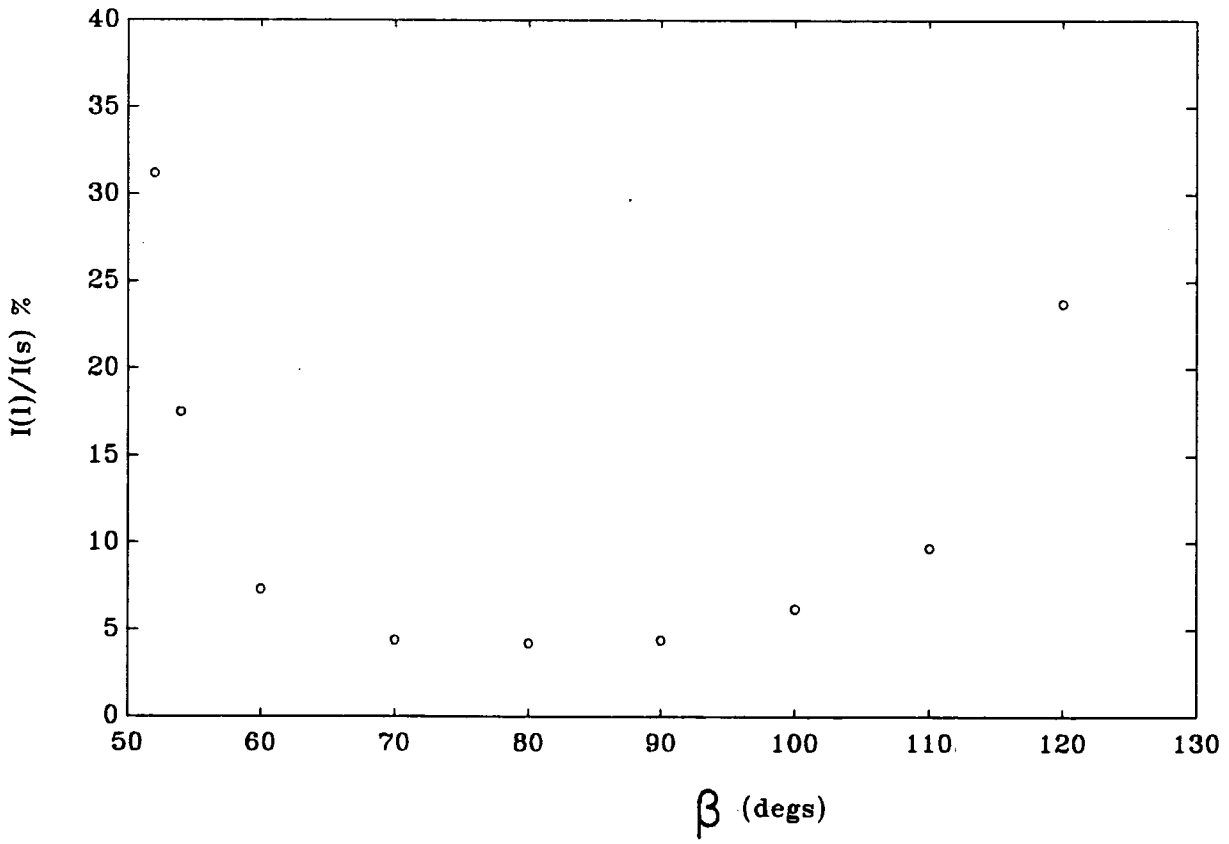

Figure 5.17(d): Layer to substrate peak intensity ratio from simulated data of a 133 reflection.

embedded reflections like the 133 and 333 the incident angle and hence extinction distance can become zero.

It should be noted however, that the total reflected intensity decreases as the incident or emergent beam angle becomes more glancing. If a perfect non-absorbing crystal is considered, (Authier, 1969), both the width of the reflection range and the integrated intensity are proportional to $\sqrt{|\gamma_h|/\gamma_0}$. So that in glancing exit, for instance, the width and integrated intensity decrease but the peak height remains constant. Figure 5.17(b) shows the substrate peak height found experimentally for the 133 reflection. The intensity decreases towards glancing incidence or emergence. This can be explained by increased attenuation due to photoelectric absorption as the beam path within the crystal is increased (Halliwell et al., 1972). Figure 5.17(c) shows the penetration depth, t, for 90% attenuation due to photoelectric absorption, of 133 and 044 reflections from InP with $CuK\alpha$ radiation. For incident and emergent angles approaching zero the depth penetrated by the X-ray beam approaches zero. Figure 5.17(b) also shows that the substrate intensity falls off more rapidly for glancing incidence than it does for glancing exit. This is because finite sized specimens intercept successively smaller fractions of the incident beam as the incident angle drops. Nevertheless, the 1.15° rocking curve in figure 5.14 shows that reasonable statistics may be attained in a few minutes even for very small glancing angles and figure 5.17(d) illustrates the enhanced layer to substrate peak ratio that may be attained for the 133 reflection using glancing angles.

A verification of the validity of the simulated fit was achieved by simulating the 044 SARCA results. In order for a good fit to be achieved the only difference in the predicted structure was that the interfacial layer mismatch needed to be changed to $-900ppm$. There are several possible explanations for this small difference. The first is that the sample may have compositional variation in the surface plane, and since the sample had to be remounted for each SARCA reflection a different part of the sample was in the beam. Another possible difference is the fact that substrate misalignment has been neglected. Most British Telecom substrates are grown to within 0.25° orientation, but even that small value can dramatically affect the results near glancing incidence. As the sample is mounted in a different orientation for each reflection the direction of

tilt may be such to have a lesser or greater effect on each reflection at glancing incidence. The only way around this problem is to investigate the magnitude and direction of this tilt using the method explained in Chapter 4 and include it in the simulation routine to take into account its variation with sample rotation. A more likely explanation is, however, error in mounting the sample. As explained at the beginning of the chapter, the beam and sample surface need to be coincident with the centre of axis 2, the sample needs to be accurately mounted in the plane of its surface, and the wedge needs to be machined at an angle exactly equal to ϕ, for perfect alignment. Small errors in these may have led to slight discrepancies in the characterisation of the sample. Cockerton, Miles, Green and Tanner (1989) have also shown that complications may arise in the simulation of multiple epitaxial layers. The comparisons of the simulation with the 044 experiment for four different rotation angles are shown in figure 5.18.

5.6 Conclusion

It has been demonstrated that when using SARCA in the extreme glancing incidence geometry the sensitivity to thin surface layers is greatly enhanced. SARCA enables layers of thickness down to several hundred Ångstroms to be characterised without much difficulty and thinner ones if longer counting times are employed. An additional application of SARCA is the characterisation of lattice-matched layers, arising from the splitting of layer and substrate peaks due to refraction effects.

The Takagi-Taupin equations together with geometrical adaptations for skew geometries have been used to simulate the experimental results. It is, of course, now well known that a simulation program is a necessary tool in the interpretation of rocking curves to obtain values of thickness and composition of heteroepitaxial structures. Several different reflections have been compared in this chapter for use in SARCA. In practice only one reflection is required for standard characterisation. In order to choose which reflection to use, several factors must be taken into account:

(i) $\phi > \theta$, or else the Bragg cone is not embedded and very low incidence angles cannot be achieved.

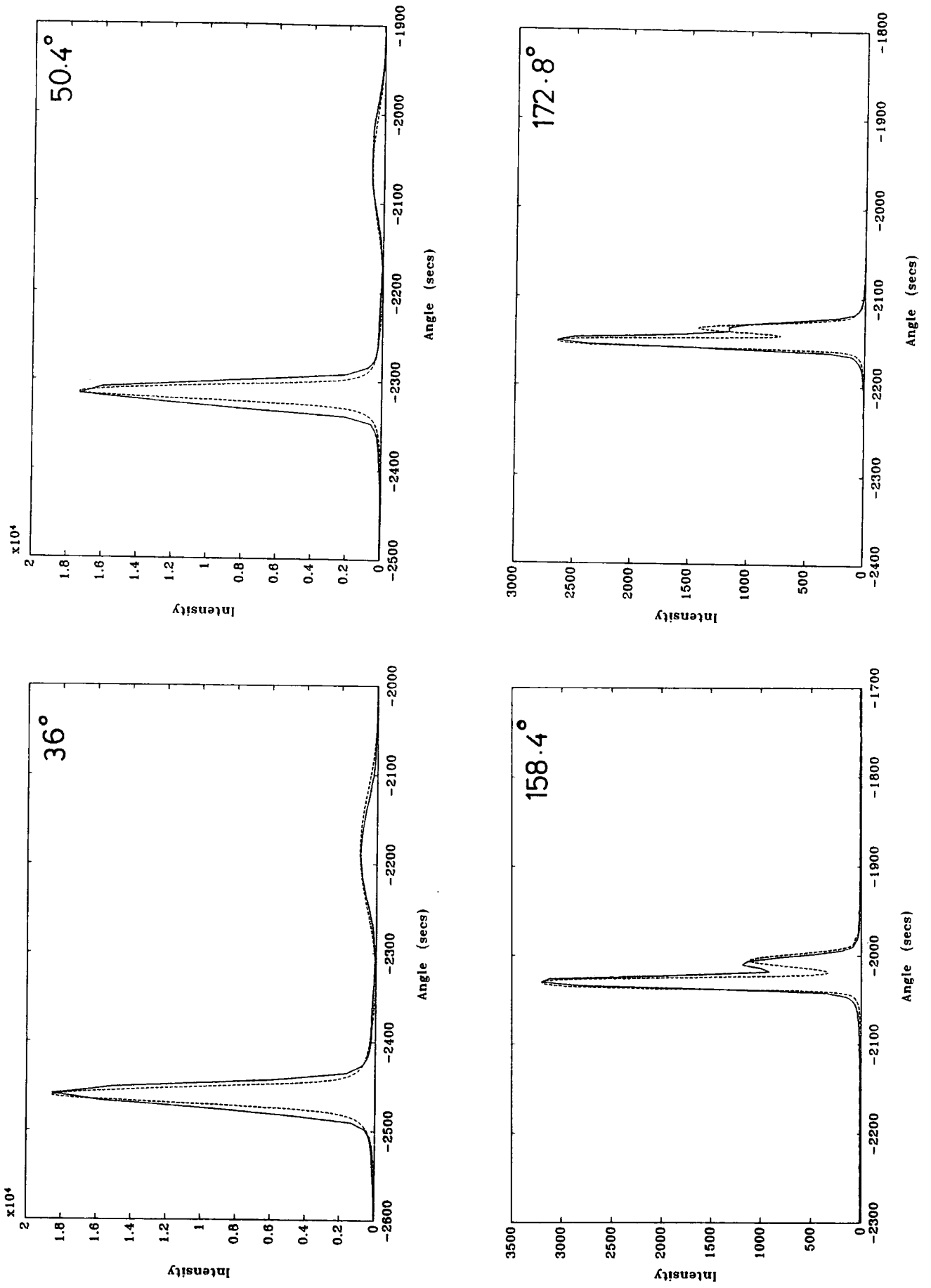

Figure 5.18: Experimental (solid) and theoretical (dashed) SARCA 044 rocking curves from sample $INP3$.

(ii) By increasing the angular range of allowed rotations the sensitivity to incidence angle of rotational steps is enhanced. The 311 for example only had an allowed rotation range of 17.6°.

(iii) It simplifies experimental set up if δ, the orientation angle in the sample surface is 0°.

(iv) The reflection must be intrinsically strong, i.e. the higher the structure factor the better.

Using these criteria, the 333 reflection is a good choice, for layers grown on(001) oriented InP.

For setting up errors to be minimised it is necessary for the procedure to be completely automated. This would involve the provision of a motorised translation stage to allow lateral movement of the sample in and out of the beam so that it may be accurately positioned over the centre of axis 2. In addition, precisely machined sample mounting stages need to be prepared for accurate sample orientation. The most difficult aspect of using SARCA is the initial setting up and if this were automated then the technique would be easily accessible to all users of double crystal diffraction.

Chapter VI

Accurate Determination of Layer Thickness in Double Heterostructures

6.1 Introduction

Chapters 4 and 5 have shown examples of the use of a simulation program to characterise sample structure. By matching an experimental rocking curve with one generated using the Takagi-Taupin equations it is possible to determine layer thickness and composition (Hill, Tanner and Halliwell, 1985). However, the accuracy in this method of characterisation, especially of layer thickness is questionable (Cockerton, Miles, Green and Tanner, 1989). When more than one epitaxial layer exists, or if compositional grading occurs at an interface, (Lyons, 1989), then complex interference of diffracted waves occurs, which can cause peak positions to shift and peak heights to change (Fewster and Curling, 1987). It is necessary to model the experimental rocking curve closely, often studying the long range fine structure to attain an accurate picture of the sample structure (Bensoussan, Malgrange and Sauvage-Simkin, 1987 (a)). There are often too many degrees of freedom, however, and the matching may be expensive in time and computer power. In some cases it is almost impossible to determine layer thickness simply by matching peak heights and positions, especially when structures contain thin buried layers.

In order to gain an accurate indication of layer thickness it is necessary to study the fine structure present in rocking curves known as the Pendellösung fringes (Jeong, Schilesinger and Milnes, 1988; Baümbach, Rhan and Pietsch 1988; Ferrari and Franzosi, 1989). The period of these oscillations, $\Delta\theta$, is related inversely to layer thickness, t_L, by the well known relationship (Batterman, Hilderbrandt, 1968; Bartels and Nijman, 1978)

$$\Delta\theta = \frac{\lambda \sin(\theta + \phi)}{t_L \sin 2\theta} , \qquad 6.1$$

where ϕ is the angle between the sample surface and the Bragg planes. For the symmetric 004 reflection from InP this reduces to

$$t_L = \frac{18.668}{\Delta\theta} \ , \qquad 6.2$$

where t_L is measured in microns and $\Delta\theta$ in seconds of arc.

Use of Pendellösung fringes to determine layer thickness is an established method both for symmetric reflections (Macrander and Strege, 1986; Bensoussan et al., 1987 (b); Bocchi et al., 1987; Ferrari, Franzosi, Gastaldi and Taiariol, 1988; Wie, 1989), and for asymmetric reflections (Prilespki and Sukhodreva, 1985; Paine, 1986). For single layer heterostructures it is adequate to obtain the Pendellösung period by measuring directly from the rocking curve. For multiple layer heterostructures, however, where a superposition of Pendellösung frequencies occurs it becomes more difficult and in some cases the observed fringe spacing appears to deviate from the true Pendellösung period (Tanner and Halliwell, 1988). This chapter describes a method of Fourier Analysis to determine the Pendellösung frequencies and hence layer thicknesses of two layer heterostructures. Macrander, Lau, Strege and Chu (1988) have also independently used the technique to measure the thickness of a thin buried layer of $InGaAsP$ under a thicker InP cap. This chapter determines the optimum conditions for layer thickness characterisation. Several multi-layer structures are studied and close matches between experiment and theory are achieved using the known thicknesses calculated from the Pendellösung fringes.

6.2 Fourier Analysis

When a function consisting of several frequencies is Fourier transformed the resultant function consists of maxima corresponding to each frequency contained in the original function. The greater the amplitude of the oscillation, the greater the amplitude of the peak corresponding to that frequency. Harmonics of the frequencies also exist and peaks corresponding to the sums of individual frequencies occur. So, for a two layer structure, peaks corresponding to the two individual layers and to the sum of the layers are found on the transform of the rocking curve, as well as higher frequency harmonics. It is important that the logarithm

of the rocking curve intensity is transformed and not the absolute intensity. This is because the Pendellösung fringes are usually at low intensities compared to the substrate peak and a Fourier Transform (FT) of the unlogged intensity is dominated by the substrate and layer peaks.

Sensitivity of a FT to layer thickness is dependent on the number and size of steps in a rocking curve. The length of the FT x-axis is proportional to the reciprocal of the step size. Therefore, if thick samples are to be characterised, the rocking curve step size needs to be small in order to pick up the high frequency fringes. The number of points in a FT is equal to the number of points in a rocking curve, so the greater the number, the smaller the FT step size, and so the more accurate the thickness determination. The FT is also symmetrical about the centre of its range which is an important consideration during interpretation, because higher order harmonics from the right hand side of the FT may be visible on the left. Figure 6.1 illustrates the problem with a FT from a simulated rocking curve of a three layer structure given in Table 6.1. The peaks on the FT correspond to individual layer frequencies as well as harmonics from them. The peaks are labelled as such together with an arrow showing their origins. It can be a difficult problem to interpret a FT from a structure with more than two layers.

A_2	$InGaAs$	$-1100ppm$	$0.213\mu m$
B	$InGaAs$	$+560ppm$	$0.24\mu m$
A_1	$InGaAs$	$-1100ppm$	$0.78\mu m$
	InP Substrate		

Table 6.1: Three layer hetreostructure

The mathematical software package PC-MATLAB was used to carry out the FT. When using the fast Fourier transform algorithm contained in the package it is necessary to have the number of steps in a rocking curve equal to a power of two. If this is not the case then the data is padded with zeros until the condition is satisfied, which tends to result in a loss of definition of the peaks from the FT.

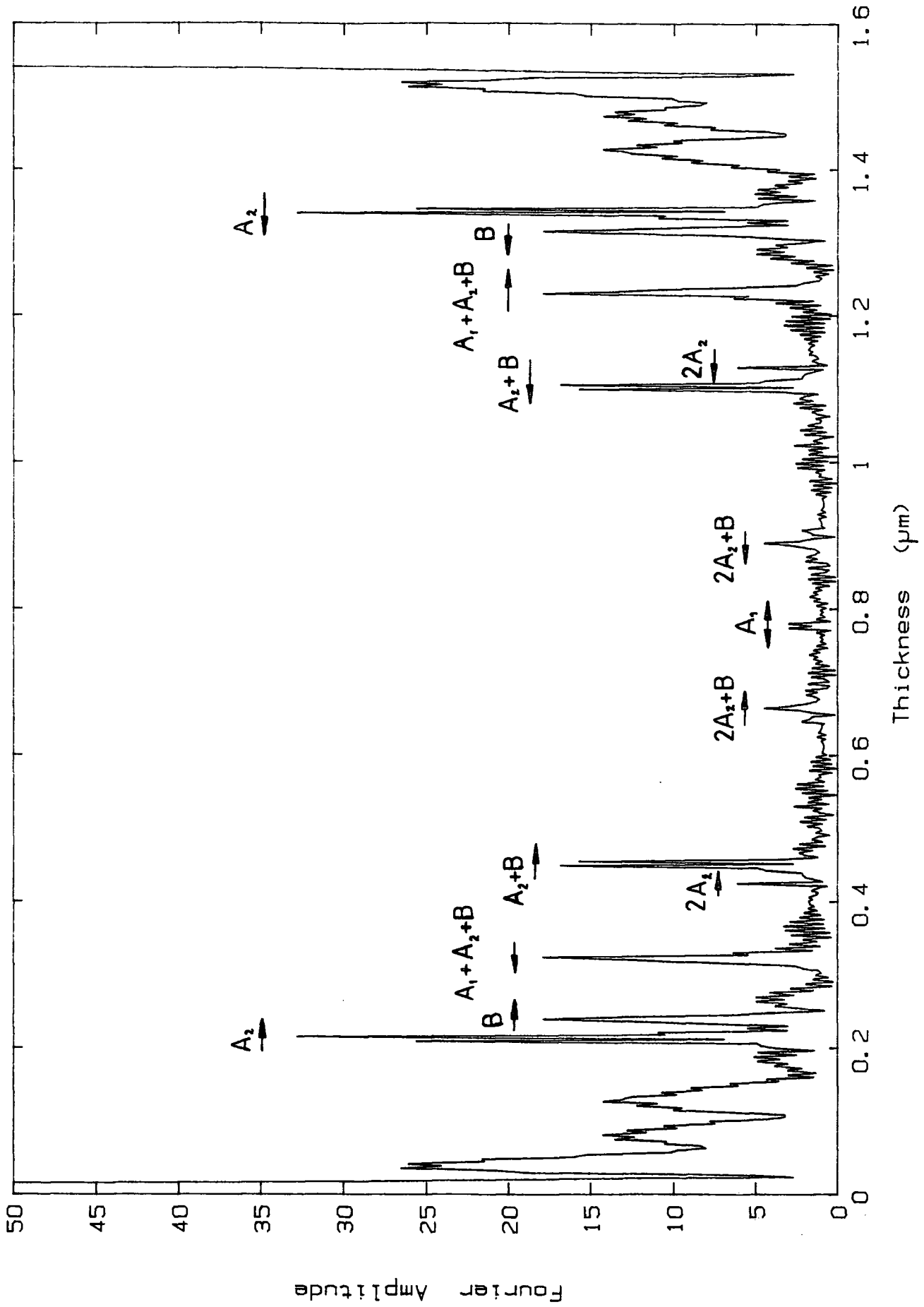

Figure 6.1: Fourier Transform of a rocking curve of the three layer heterostructure given in Table 6.1.

The package is run on a 1512 Amstrad PC with a mathematical co-processor installed.

6.3 Optimum Conditions for Fourier Analysis

A study was based on FT's from simulated rocking curves, generated from the program written at British Telecom, for various scan ranges and step sizes. The sample modelled was a two layer heterostructure composed of an active layer of $InGaAsP$ with $1.35\mu m$ band gap, $-550ppm$ mismatch and $0.18\mu m$ thickness grown on InP, capped by a $0.4\mu m$ thick layer of InP. This sample is fairly typical of those currently being grown by British Telecom for laser devices. Figures 6.2(a) to (n) show rocking curves and corresponding FT's for various ranges and step sizes detailed in Table 6.2.

Figure	Scan Range (″)	Step Size (″)	Number of Steps
2a	512	2	256
2b	512	4	128
2c	512	8	64
2d	512	16	32
2e	1024	2	512
2f	1024	4	256
2g	1024	8	128
2h	1024	16	64
2i	2048	4	512
2j	2048	8	256
2k	2048	16	128
2l	4096	8	512
2m	4096	16	256
2n	8192	16	512

Table 6.2

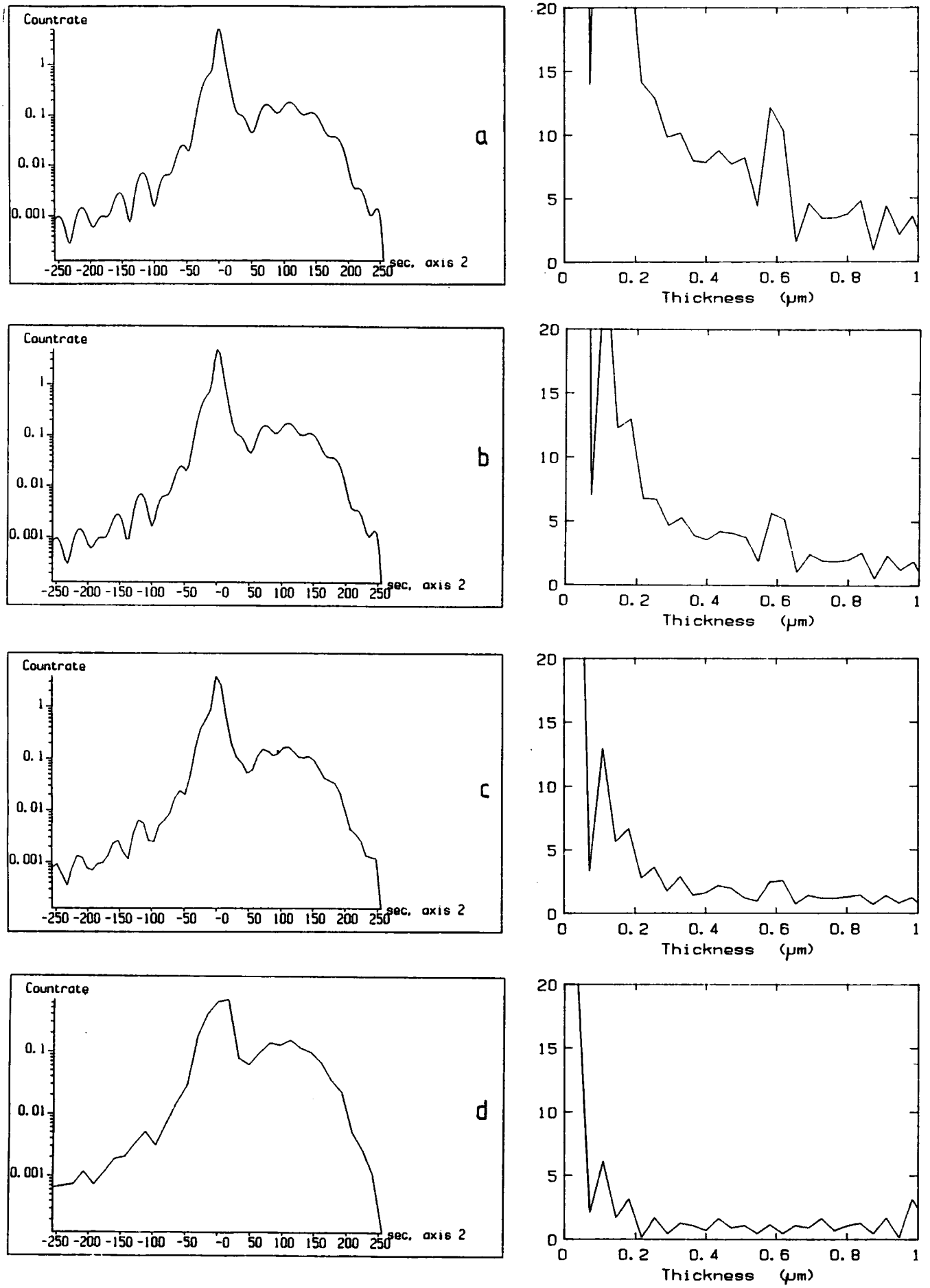

Figure 6.2: 004 rocking curves and corresponding Fourier Transforms for a selection of ranges and step sizes detailed in Table 6.2.

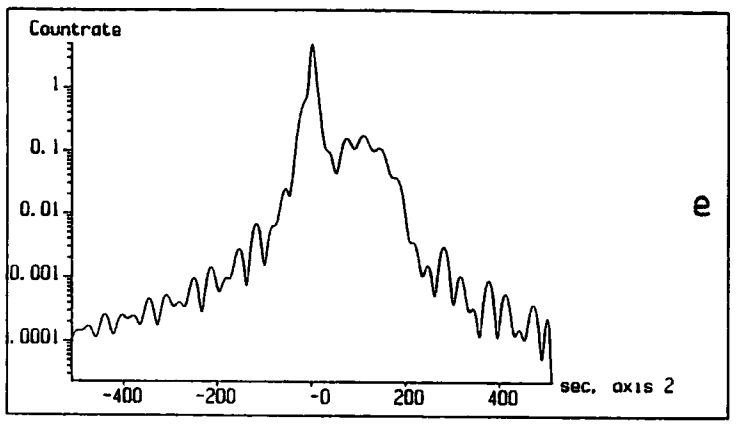
Countrate
1
0.1
0.01
0.001
.0001
-400
-200
-0
200
400
sec, axis 2
e

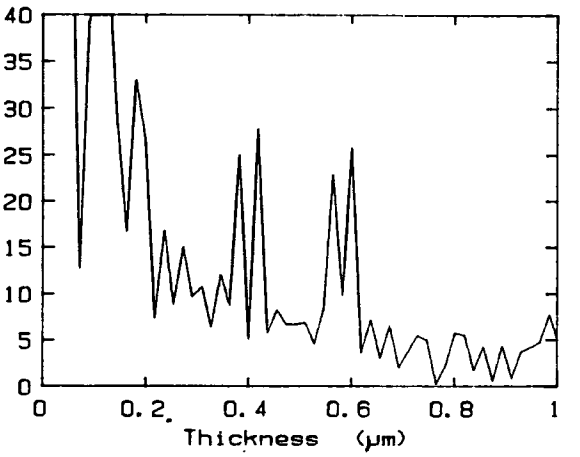
40
35
30
25
20
15
10
5
0
0
0.2
0.4
0.6
0.8
1
Thickness (μm)

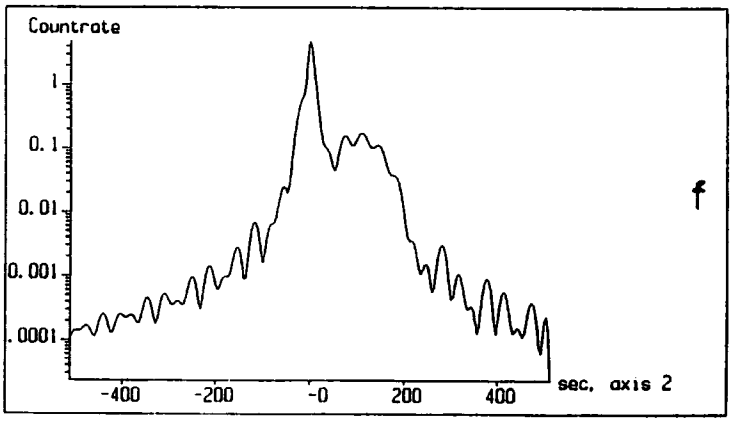
Countrate
1
0.1
0.01
0.001
.0001
-400
-200
-0
200
400
sec, axis 2
f

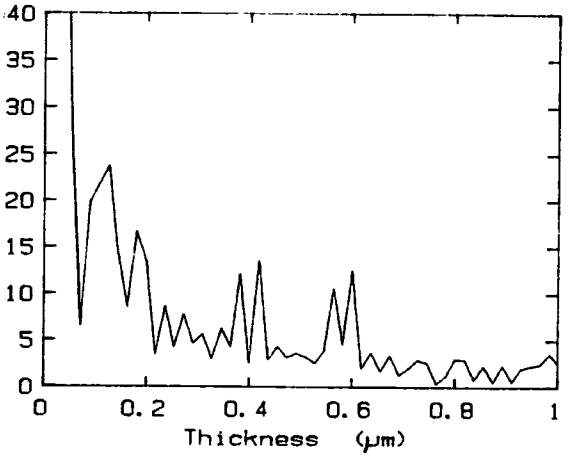
40
35
30
25
20
15
10
5
0
0
0.2
0.4
0.6
0.8
1
Thickness (μm)

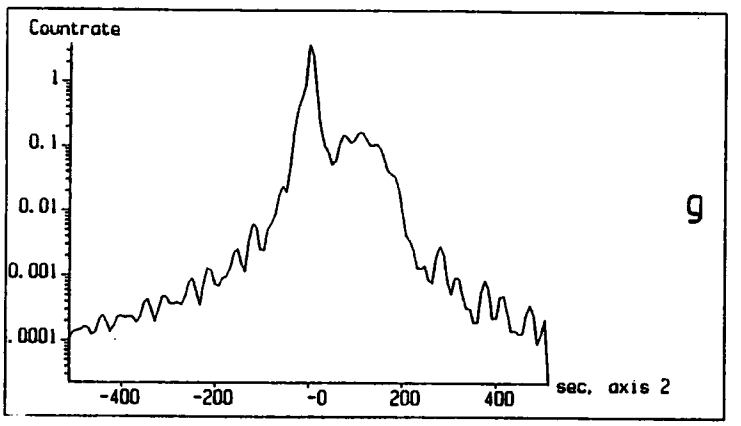
Countrate
1
0.1
0.01
0.001
.0001
-400
-200
-0
200
400
sec, axis 2
g

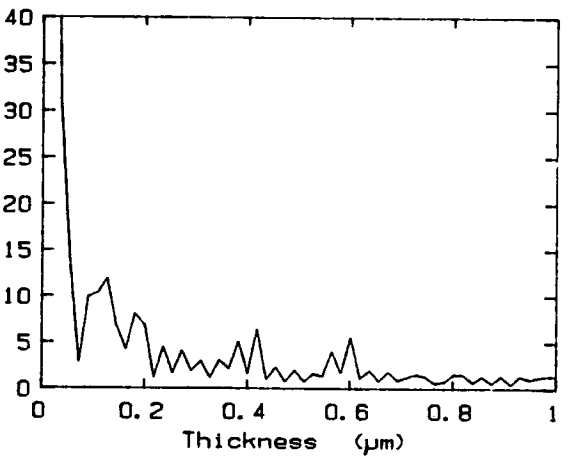
40
35
30
25
20
15
10
5
0
0
0.2
0.4
0.6
0.8
1
Thickness (μm)

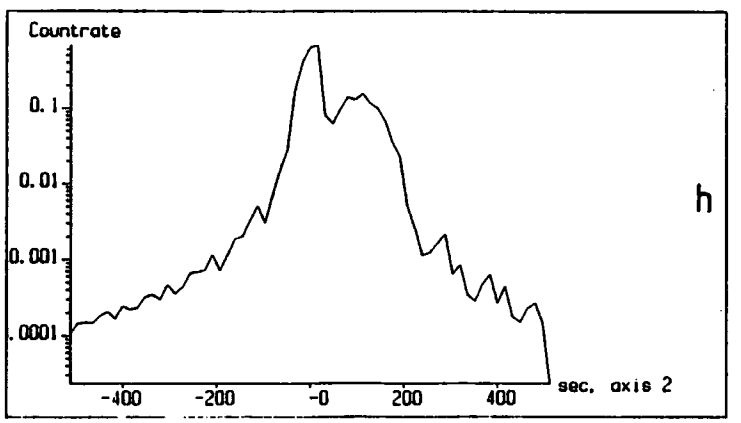
Countrate
0.1
0.01
0.001
.0001
-400
-200
-0
200
400
sec, axis 2
h

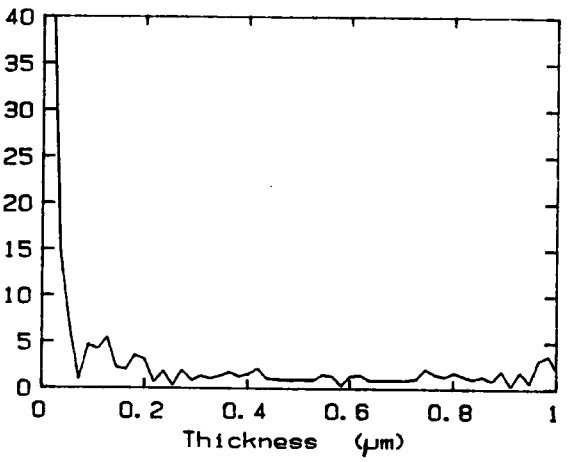
40
35
30
25
20
15
10
5
0
0
0.2
0.4
0.6
0.8
1
Thickness (μm)

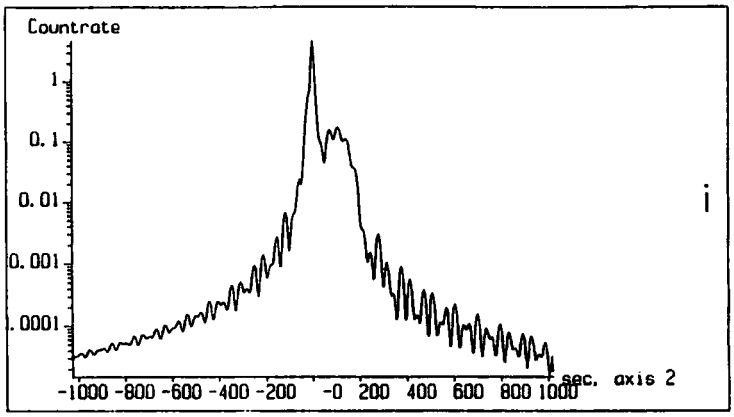
Countrate
1
0.1
0.01
0.001
.0001
-1000 -800 -600 -400 -200 -0 200 400 600 800 1000
sec. axis 2
i

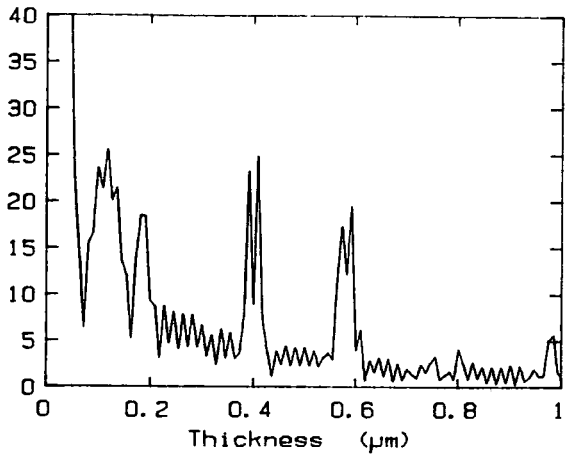
40
35
30
25
20
15
10
5
0
0 0.2 0.4 0.6 0.8 1
Thickness (μm)

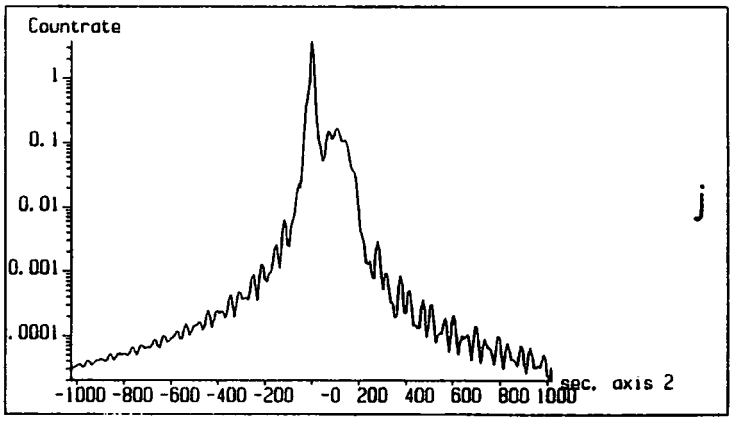
Countrate
1
0.1
0.01
0.001
.0001
-1000 -800 -600 -400 -200 -0 200 400 600 800 1000
sec. axis 2
j

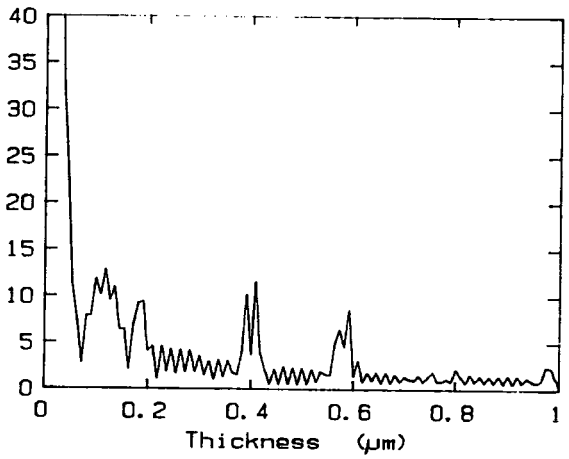
40
35
30
25
20
15
10
5
0
0 0.2 0.4 0.6 0.8 1
Thickness (μm)

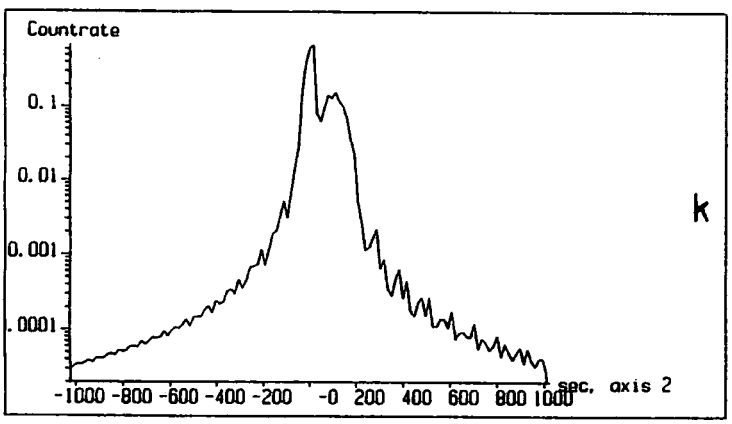
Countrate
0.1
0.01
0.001
.0001
-1000 -800 -600 -400 -200 -0 200 400 600 800 1000
sec. axis 2
k

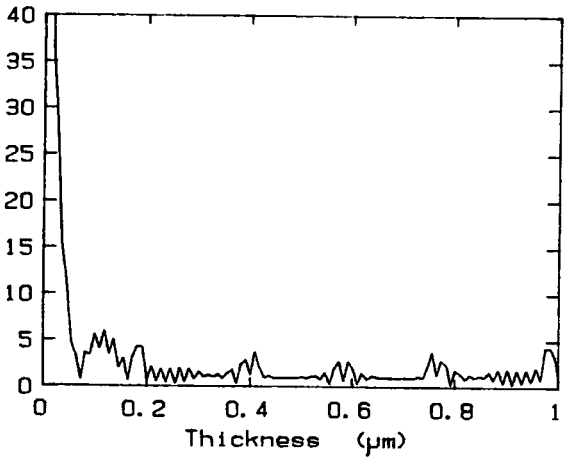
40
35
30
25
20
15
10
5
0
0 0.2 0.4 0.6 0.8 1
Thickness (μm)

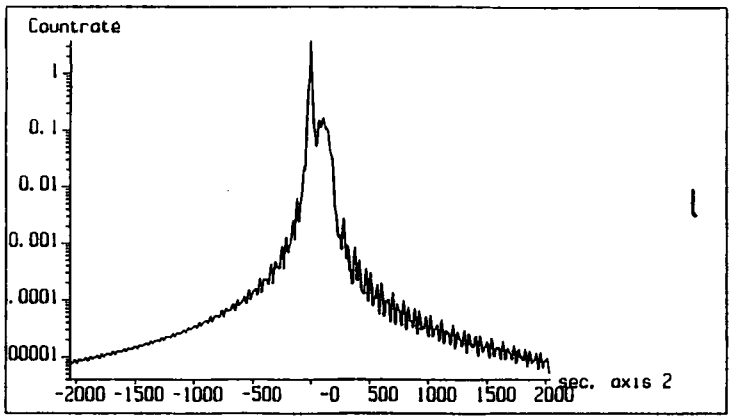
Countrate
1
0.1
0.01
0.001
.0001
00001
-2000 -1500 -1000 -500 -0 500 1000 1500 2000
sec. axis 2
l

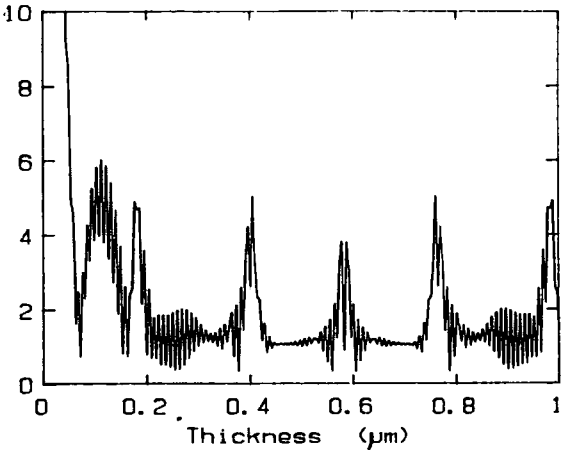
10
8
6
4
2
0
0 0.2 0.4 0.6 0.8 1
Thickness (μm)

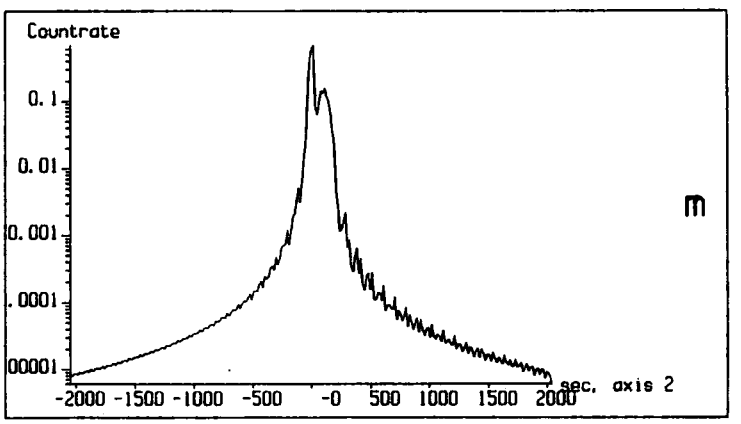
Countrate
0.1
0.01
0.001
.0001
00001
-2000 -1500 -1000 -500 -0 500 1000 1500 2000
sec. axis 2
m

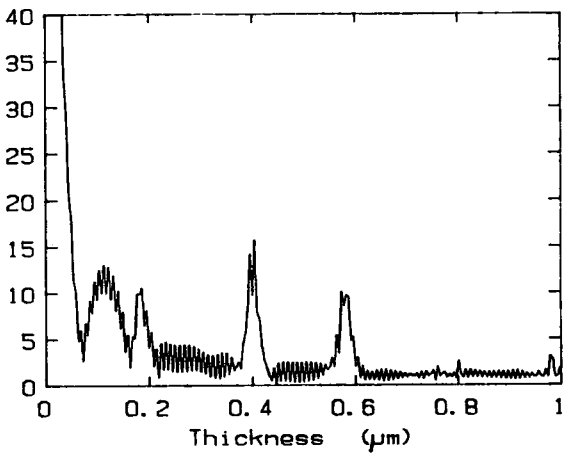
40
35
30
25
20
15
10
5
0
0 0.2 0.4 0.6 0.8 1
Thickness (μm)

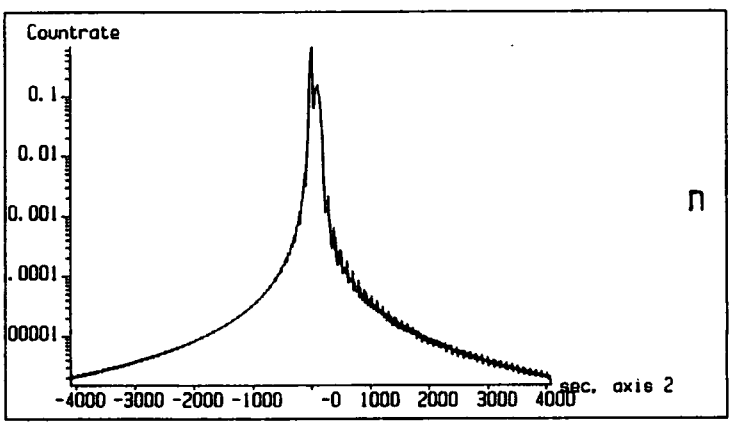
Countrate
0.1
0.01
0.001
.0001
00001
-4000 -3000 -2000 -1000 -0 1000 2000 3000 4000
sec. axis 2
n

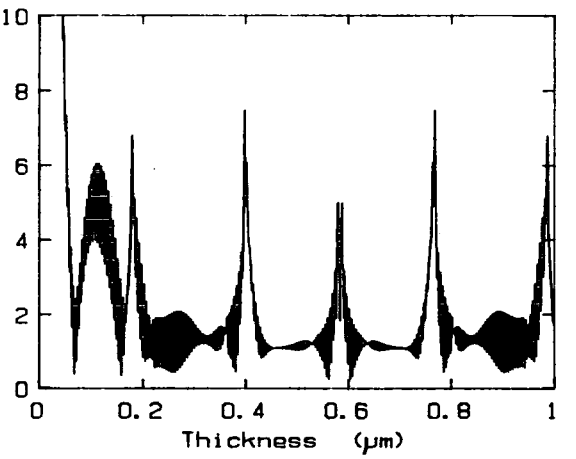
10
8
6
4
2
0
0 0.2 0.4 0.6 0.8 1
Thickness (μm)

Two conclusions can be reached from these curves, both of which follow intuitively:

(i) The longer the range, for a given number of steps, the sharper the peaks from the FT and so the more precise the determination of layer thickness.

(ii) The step size is not an important factor until it becomes larger than about a quarter of the smallest fringe period. Even when it exceeds this, if the range is large enough accurate results are still attained.

These conclusions are not immediately applicable to the experimental case, however, where background noise is an important consideration. In order to model the effect of noise, background levels of 0.001, 0.01 and 0.1% have been included in the simulations and transforms taken. Figures 6.3(a) to (l) show the rocking curves and corresponding FT's for several combinations of range and background, detailed in Table 6.3.

Figure	Scan Range (″)	Step Size (″)	Background (%)
3a	1024	2	0.001
3b	2048	4	0.001
3c	2048	8	0.001
3d	4096	8	0.001
3e	1024	2	0.01
3f	2048	4	0.01
3g	2048	8	0.01
3h	4096	8	0.01
3i	1024	2	0.1
3j	2048	4	0.1
3k	2048	8	0.1
3l	4096	8	0.1

Table 6.3

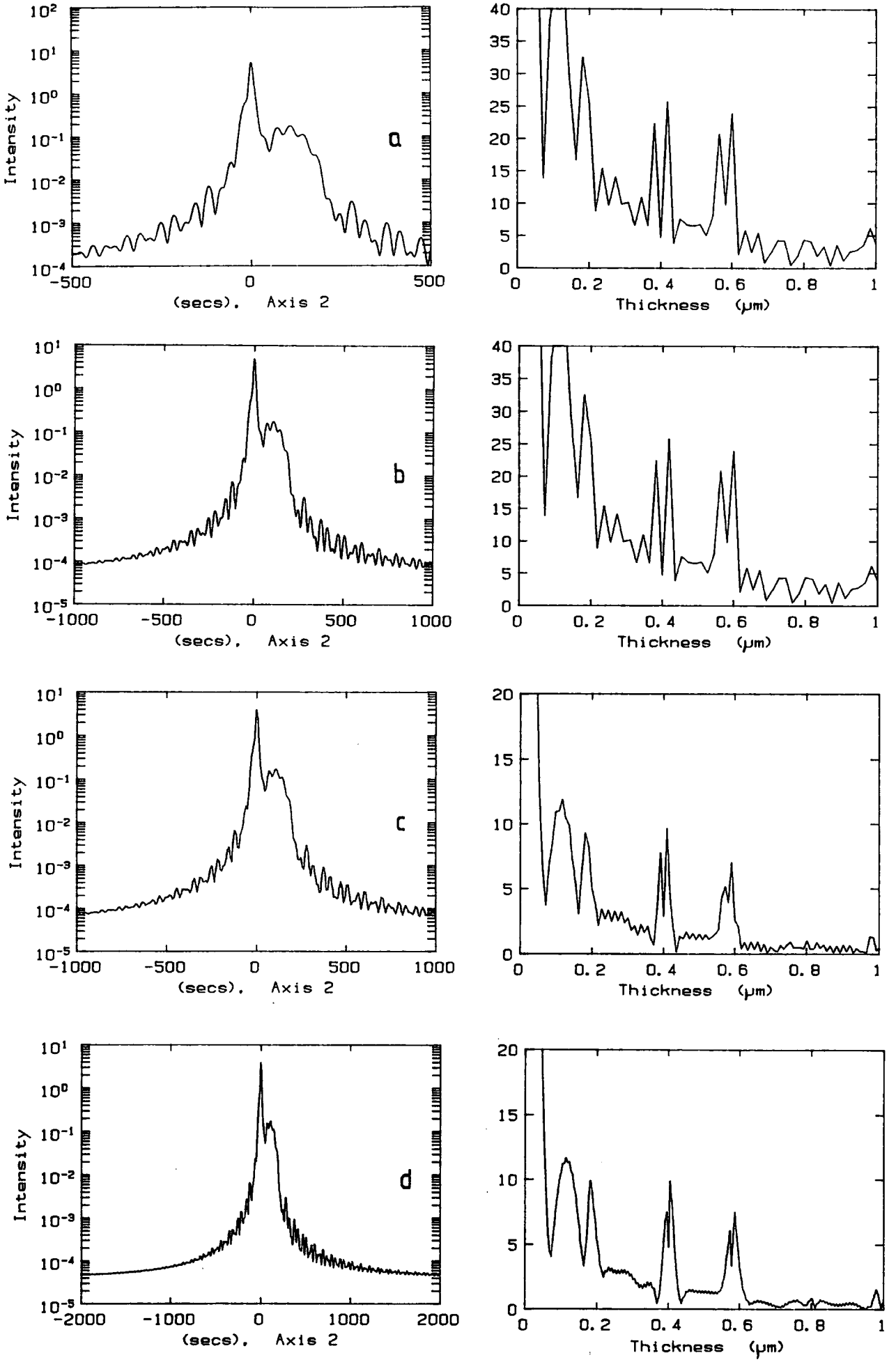

Figure 6.3: 004 rocking curves and corresponding Fourier Transforms for various levels of background detailed in Table 6.3.

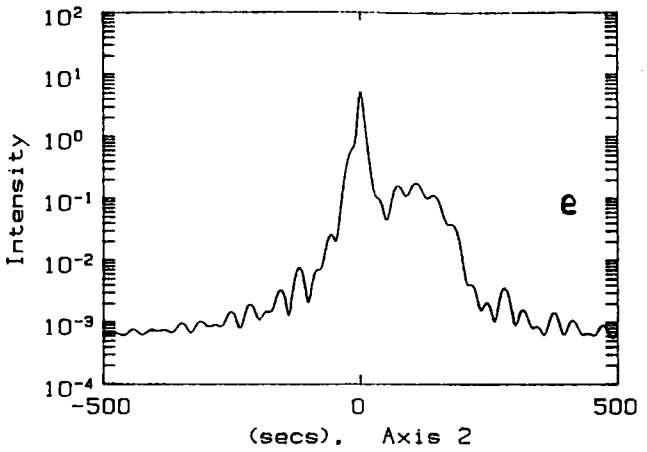
Intensity
e
(secs). Axis 2

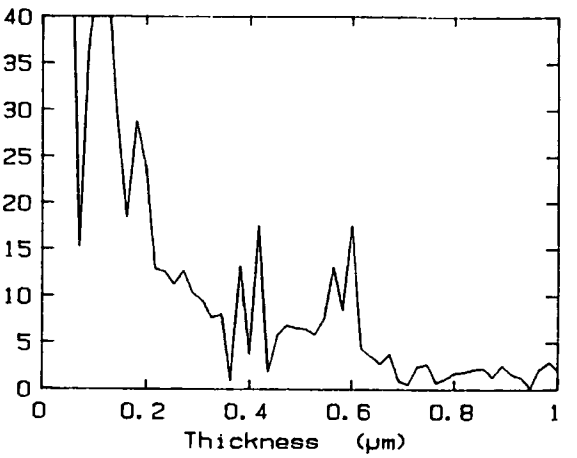
Thickness (μm)

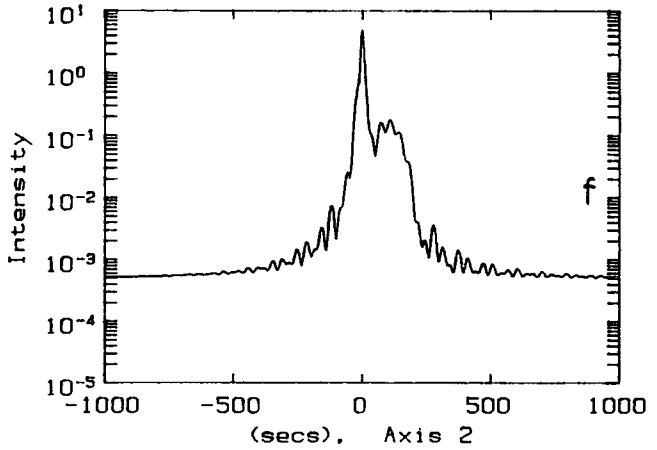
Intensity
f
(secs). Axis 2

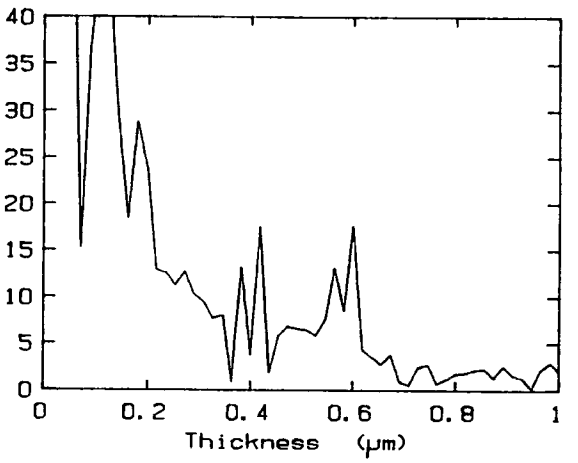
Thickness (μm)

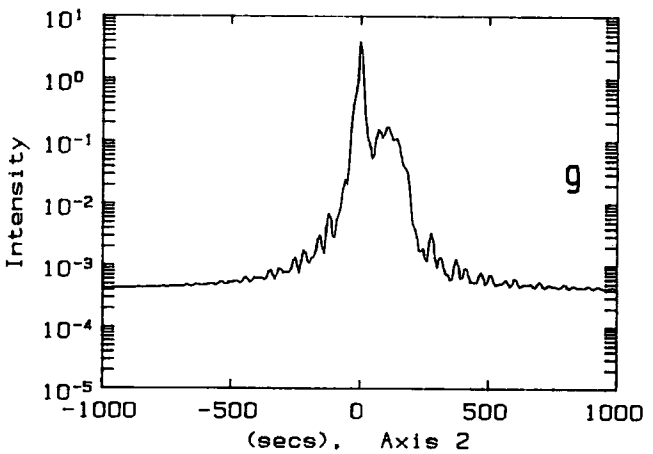
Intensity
g
(secs). Axis 2

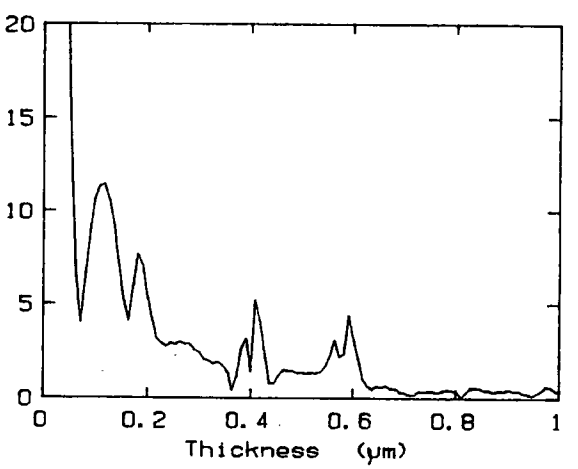
Thickness (μm)

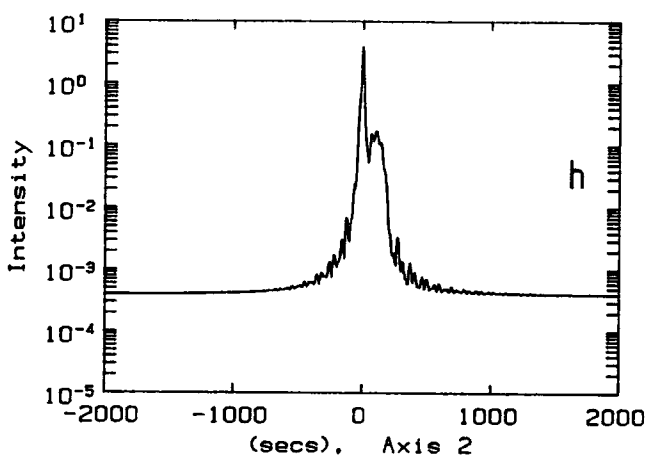
Intensity
h
(secs). Axis 2

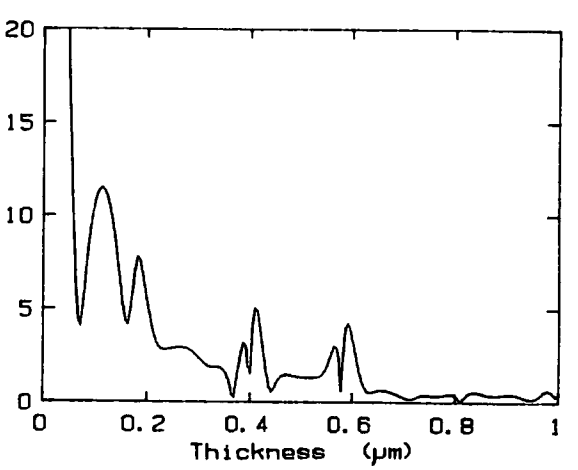
Thickness (μm)

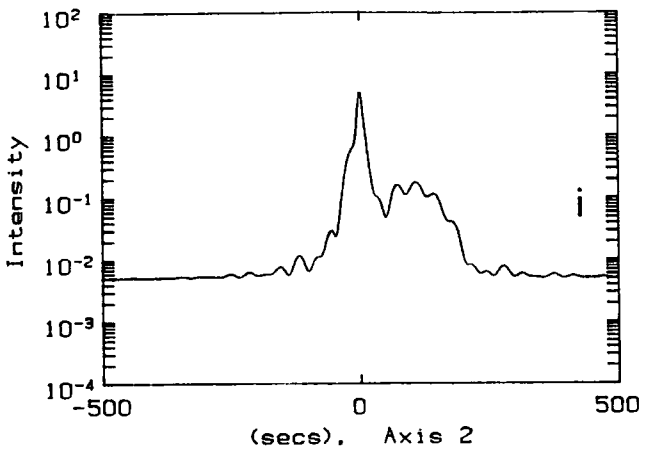
Intensity
i
(secs). Axis 2

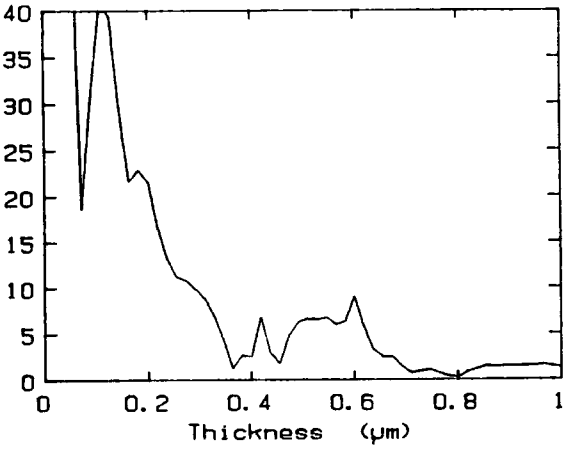
Thickness (μm)

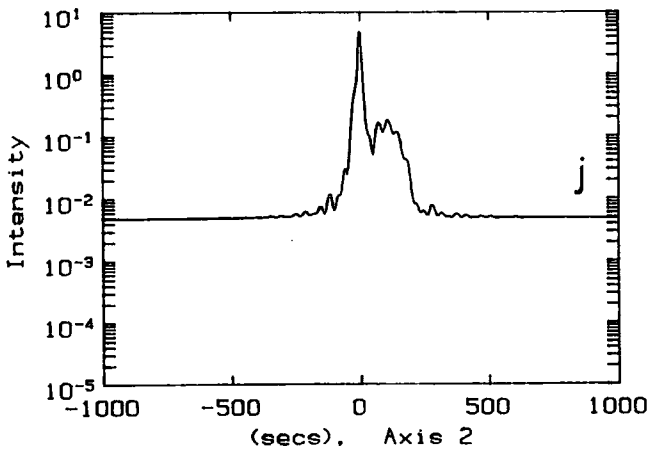
Intensity
j
(secs). Axis 2

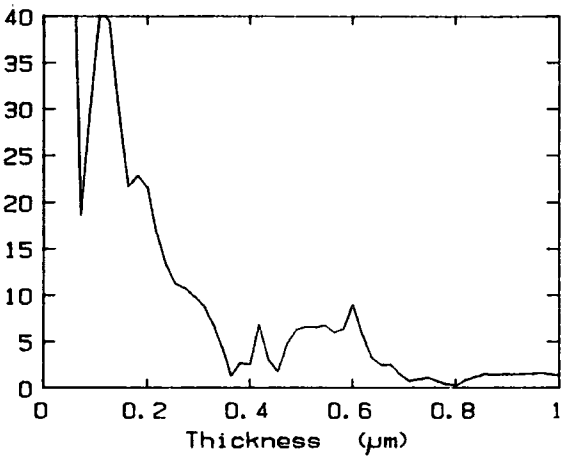
Thickness (μm)

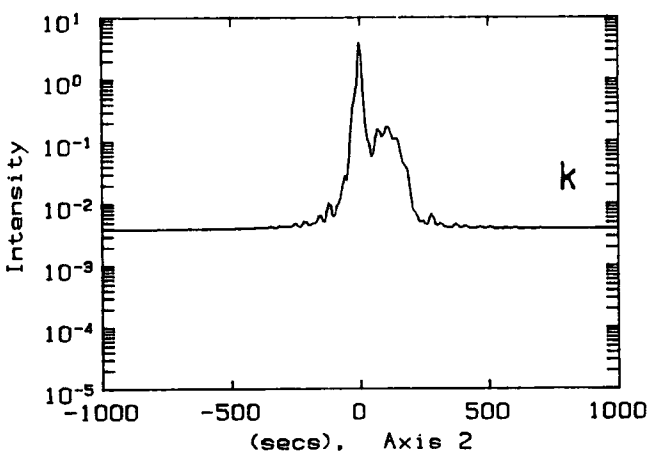
Intensity
k
(secs). Axis 2

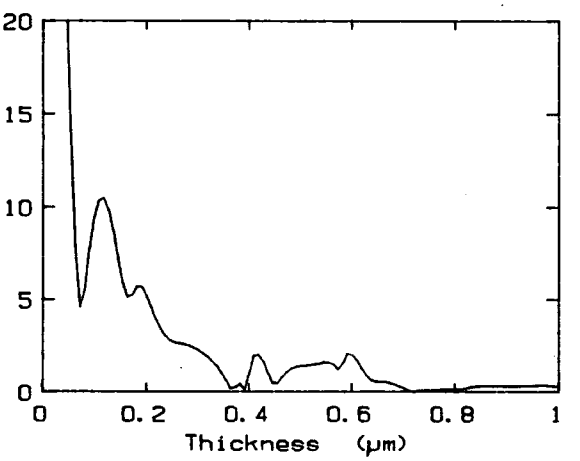
Thickness (μm)

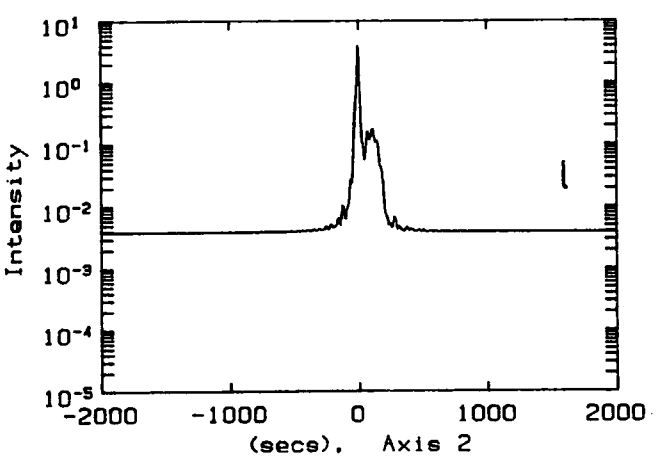
Intensity
l
(secs). Axis 2

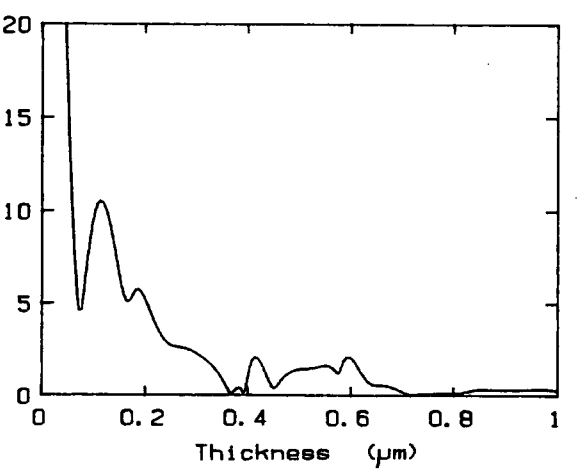
Thickness (μm)

For a background level of 0.001%, (signal to noise ratio, S/N 10^5), the effect on the FT peaks in the ranges studied is negligible, but for 0.1% (S/N 10^3) it is significant and the peak clarity is obscured. With a background level of 0.01% (S/N 10^4) there is no appreciable affect for short ranges, but as longer ranges are approached there is some loss in definition of the FT peaks. It is important to point out that this is a study of simulated rocking curves, with no random statistical variation. So for experimental rocking curves, a good S/N is the primary consideration followed by good counting statistics. It is now possible to make some conclusions in the light of these observations for the experimental case.

(i) The maximum possible range within the limitations of S/N should be used.

(ii) The step size should be as large as possible to maximise counting time, but not larger than about a quarter of the smallest fringe period.

Bearing this in mind, Table 6.4 gives some recommended ranges and step sizes for various S/N ratios for the sample studied.

S/N	Range (″)	Step Size (″)
$\leq 10^3$	S/N not adequate for Fourier analysis	
5×10^3	1000	4
10^4	2000	8
5×10^4	4000	8
$\geq 10^5$	4000+	8+

Table 6.4

Note that for measuring larger thicknesses, it is necessary to have a smaller step size than that shown to be sensitive to higher frequency fringes.

6.4 Measurement of Pendellösung Fringe Spacing

Tanner and Halliwell (1988) reported an apparent deviation from the Pendellösung spacing of the measured fringes arising from a range of simulated rock-

ing curves of two layer structures with varying cap thickness. This is shown in figure 6.4 with the dotted line showing the true Pendellösung frequency. The physical explanation behind this becomes clear from Fourier Analysis. If the FT's of figures 6.2 and 6.3 are studied, the peaks corresponding to the layers in some cases are doublets. Due to complex interference effects, therefore, it appears that two frequencies often arise from each layer. A correct frequency measurement results from taking the average of this doublet. So if measurements of fringe spacing are taken directly from the rocking curve it is possible that an appreciable error could be incurred from measuring only one frequency. It would be impossible to separate this frequency doublet by eye on a rocking curve. Figure 6.5 shows a graph of measured cap thickness using Fourier Analysis against actual cap thickness, from a range of simulated rocking curves with cap thickness varying. The structure used was a layer of $InGaAsP$ of $-500ppm$ mismatch and $0.18\mu m$, capped with InP. The simulations were taken over two ranges: $2044''$ and $4088''$, with an equal number of steps, labelled separately on the graph. Where a frequency doublet occurred on the FT the two thickness are shown. The graph clearly illustrates that the measured cap thickness does not deviate from that expected, unlike the results in figure 6.4. It also shows that the doublet splitting is larger for the smaller scan range. Figure 6.6 shows a similar plot of measured cap + layer thickness against cap thickness. Again the data lies on the Pendellösung line with the larger measurement errors arising from the smaller range. For the $4088''$ range the thickness measurements are accurate to within $50\mathring{A}$.

If the cap thickness is constant and the layer thickness is varied a similar graph results; figure 6.7. A change in the layer mismatch does not affect the frequency of the Pendellösung fringes, although the fringe amplitude does change. Figures 6.8(a) to (d) show rocking curves and corresponding FT's from a structure consisting of a $0.4\mu m$ cap and a $0.18\mu m$ active layer with mismatch varying from $-200ppm$ to $-1500ppm$. The fringe amplitude clearly increases with increasing mismatch and this is reflected in the amplitudes of the FT peaks. The peak due to the layer in particular becomes more clearly defined.

To reinforce the need for Fourier Analysis to measure Pendellösung fringe spacings, figures 6.9(a) to (c) show simulated rocking curves of two layer struc-

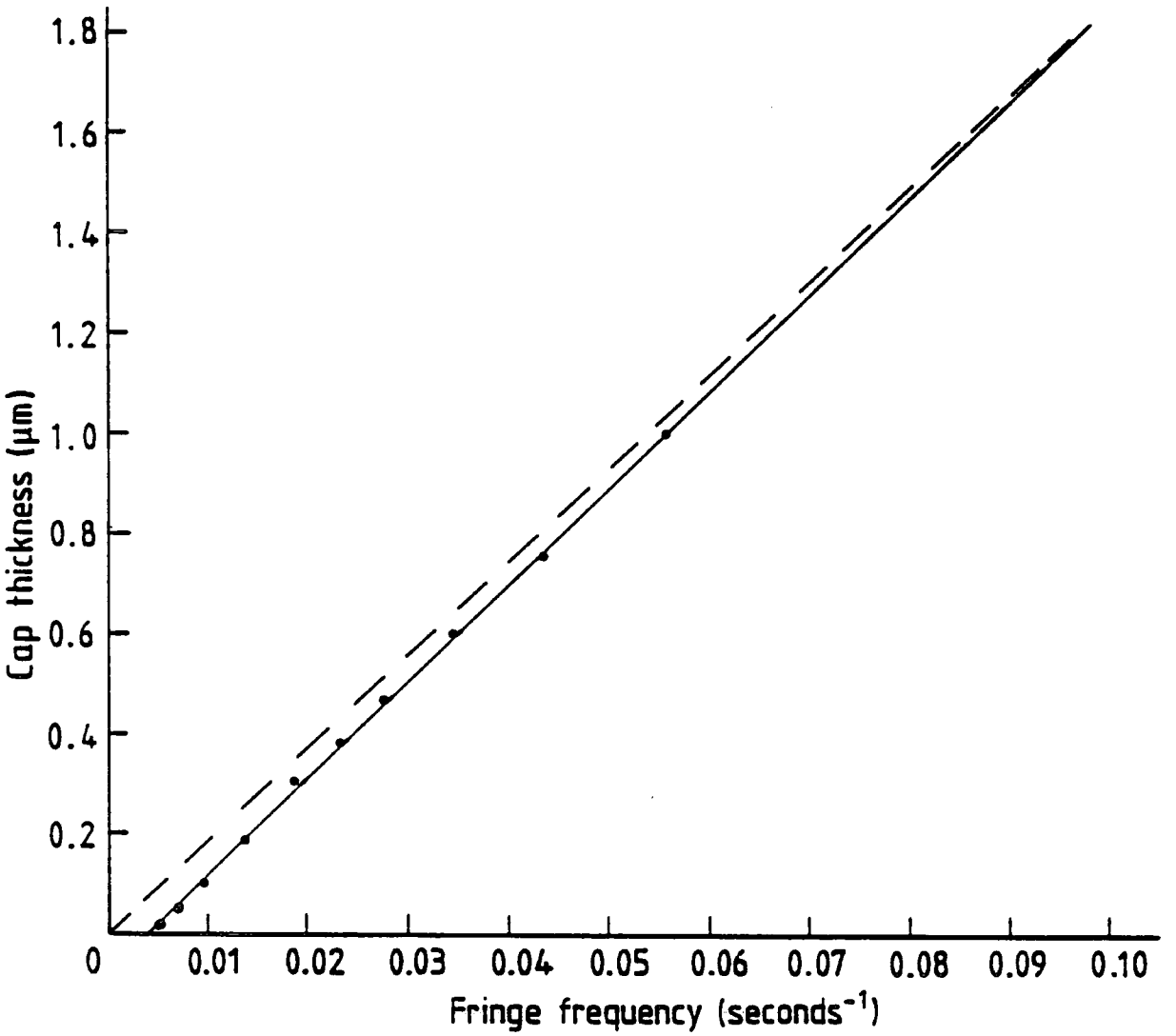

Figure 6.4: Deviation of the cap thickness determined by direct measurement of fringe spacing (points) from the true value (dashed). After Tanner and Halliwell (1988).

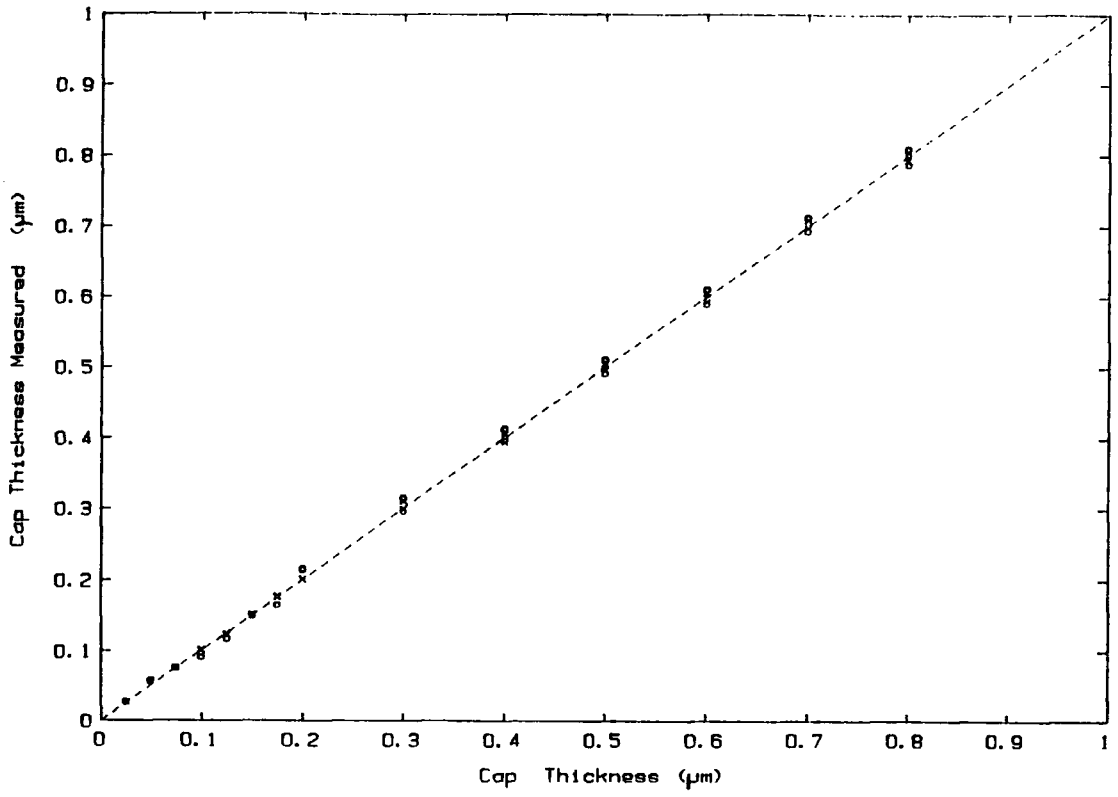

Figure 6.5: Measured cap thickness using Fourier analysis for ranges of 2044″ (circles) and 4088″ (crosses) with 4″ and 8″ step sizes respectively. The dashed line shows the true cap thickness.

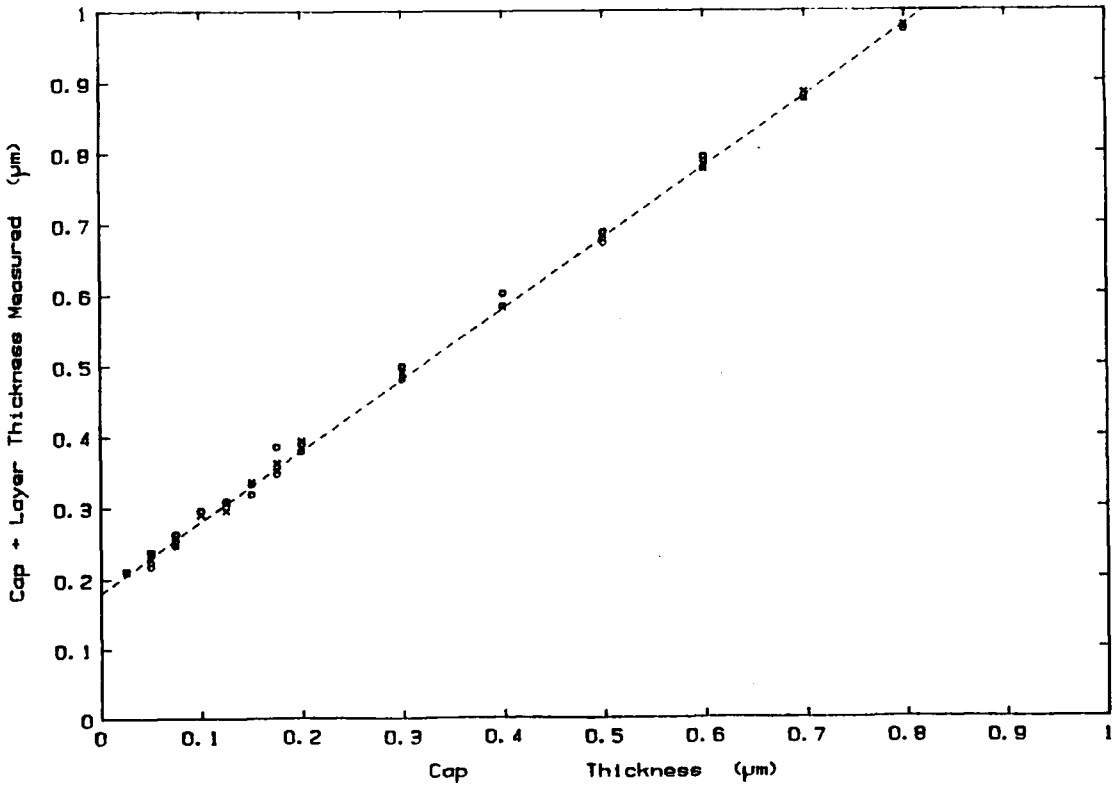

Figure 6.6: Measured cap + layer thickness using Fourier analysis for ranges of 2044″ (circles) and 4088″ (crosses) with 4″ and 8″ step sizes respectively. The dashed line shows the true cap + layer thickness.

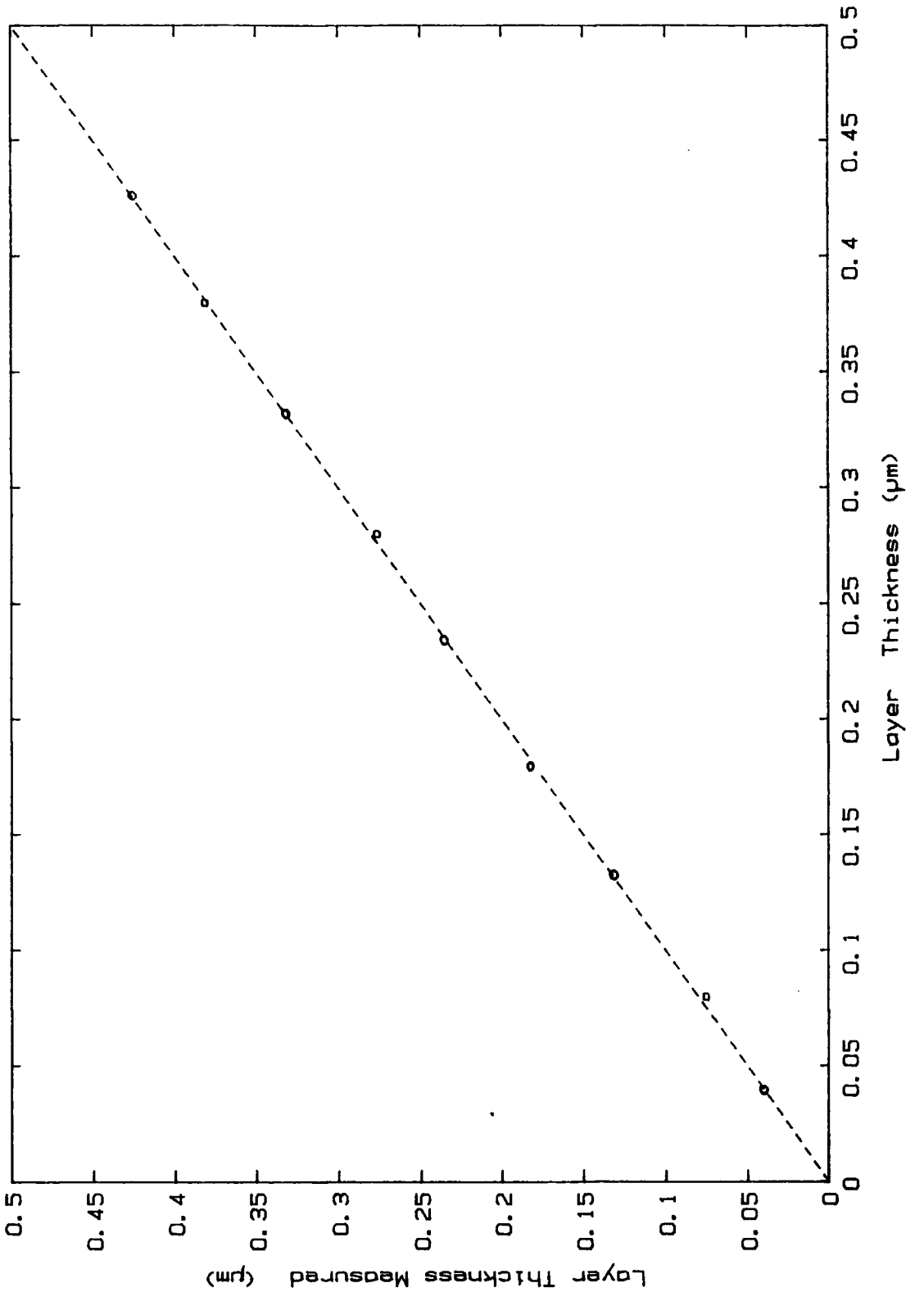

Figure 6.7: Measured layer thickness using Fourier analysis for a constant layer thickness. The dashed line shows the true layer thickness.

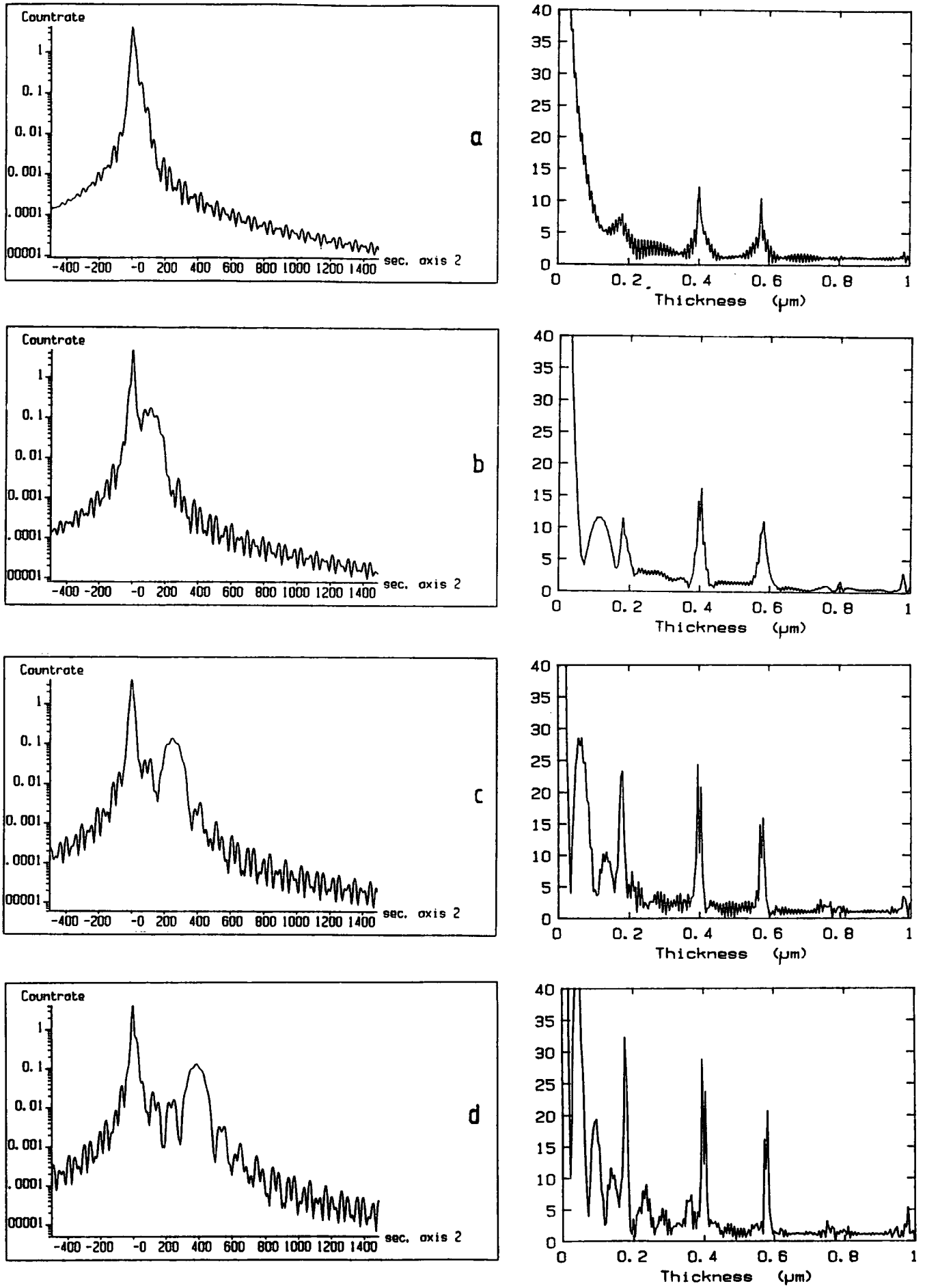

Figure 6.8: 004 rocking curves and Fourier Transforms of a structure comprising of a $0.18\mu m$ active layer with mismatch of (a) $-200ppm$, (b) $-500ppm$, (c) $-1000ppm$ and (d) $-1500ppm$, with a $0.4\mu m$ cap.

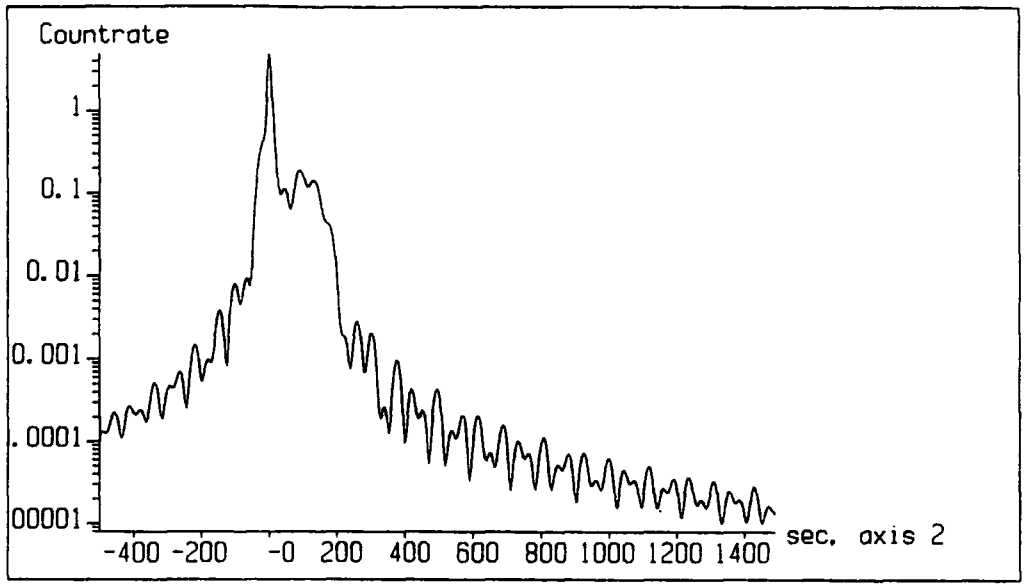

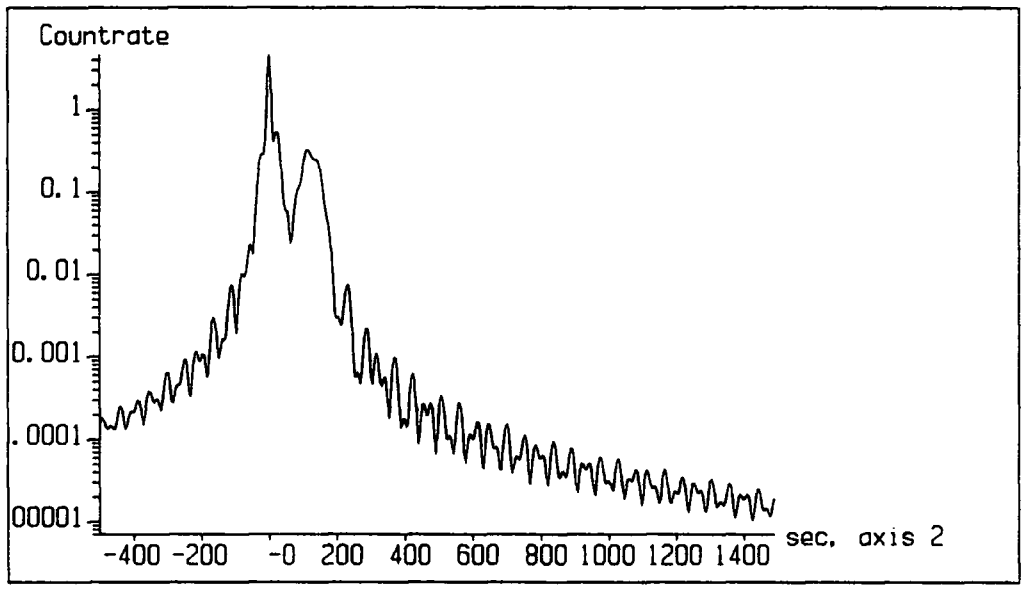

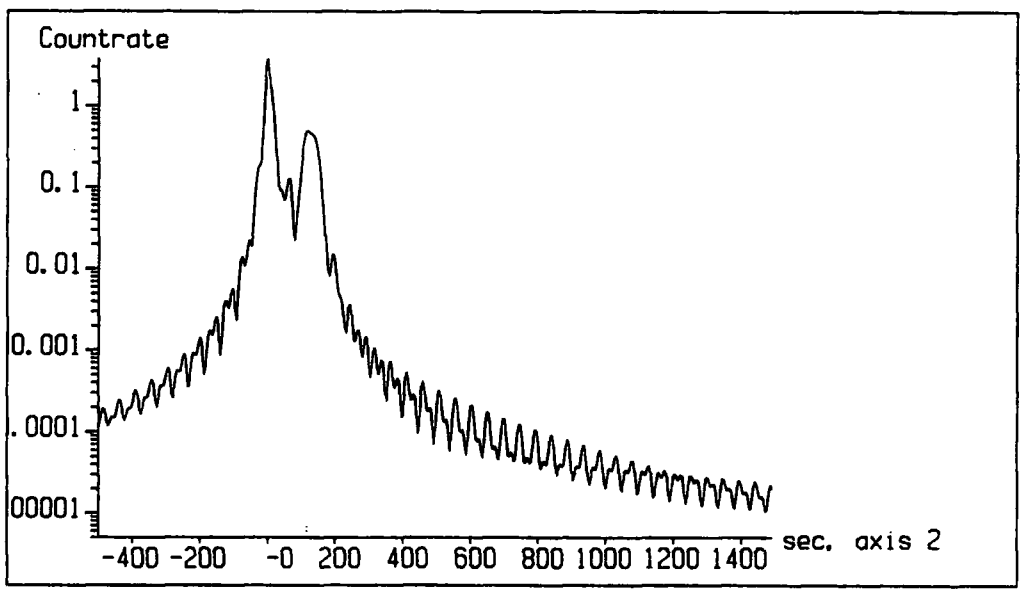

Figure 6.9: 004 rocking curves from a two layer structure with a layer mismatch of $-500ppm$ and thicknesses of (a) cap $0.3\mu m$, layer $0.18\mu m$, (b) cap $0.4\mu m$, layer $0.28\mu m$, (c) cap $0.4\mu m$, layer $0.38\mu m$.

tures where it is extremely difficult to identify individual Pendellösung periods by eye. It would be easy to make substantial errors in the determination of layer thickness without Fourier Analysis.

6.5 Fourier Analysis of Double Heterostructure Rocking Curves

A good signal to noise ratio is vitally important in the study of rocking curve fine structure. Even when the counting time is so high that the statistical variation is negligible, as is the case in simulated rocking curves, if the background count rate is too large then the fine structure cannot be studied. In order to achieve a good S/N it is necessary to shield the detector carefully so that it does not see any part of the direct beam or first crystal diffracted beam. Use of a scatter shield over the first crystal ensures that no X-ray fluorescence reaches the detector. Vertical slits between the first and second crystals ensure that only the wavelength range required reaches the sample, by eliminating the $K\alpha_2$ peak, and horizontal slits can be used to cut down vertical divergence. A slit over the detector may also be used, so long as the detector is moved with the sample in a θ-2θ scan. This again ensures that only the required wavelength range at the correct angle is detected which reduces the dispersive effect of sample curvature. A disadvantage of this, however, is that it cuts down the diffracted intensity, so if curvature is not much of a problem the extra slit is not necessary. A proportional counter with a high quality counting chain is also an important requirement. Electrical noise can be reduced by as much as a factor of ten compared to the conventional scintillation detector.

The Philips 1880 multi-purpose diffractometer at British Telecom with a proportional detector can achieve signal to noise ratios of 10^5 or better. The instrument utilises the Germanium four crystal monochromator discussed in Chapter 2 which eliminates spectral dispersion. This instrument has been used in the (220) monochromator mode to study several examples of two layer heterostructures.

6.5.1 Sample ABA1

This sample was grown by MOCVD at British Telecom by P. Spurdens. It consists of a layer of $GaInAsP$, of $1.35\mu m$ band gap, capped by a layer of InP. Figure 6.10 shows its experimental 004 rocking curve along with two simulated

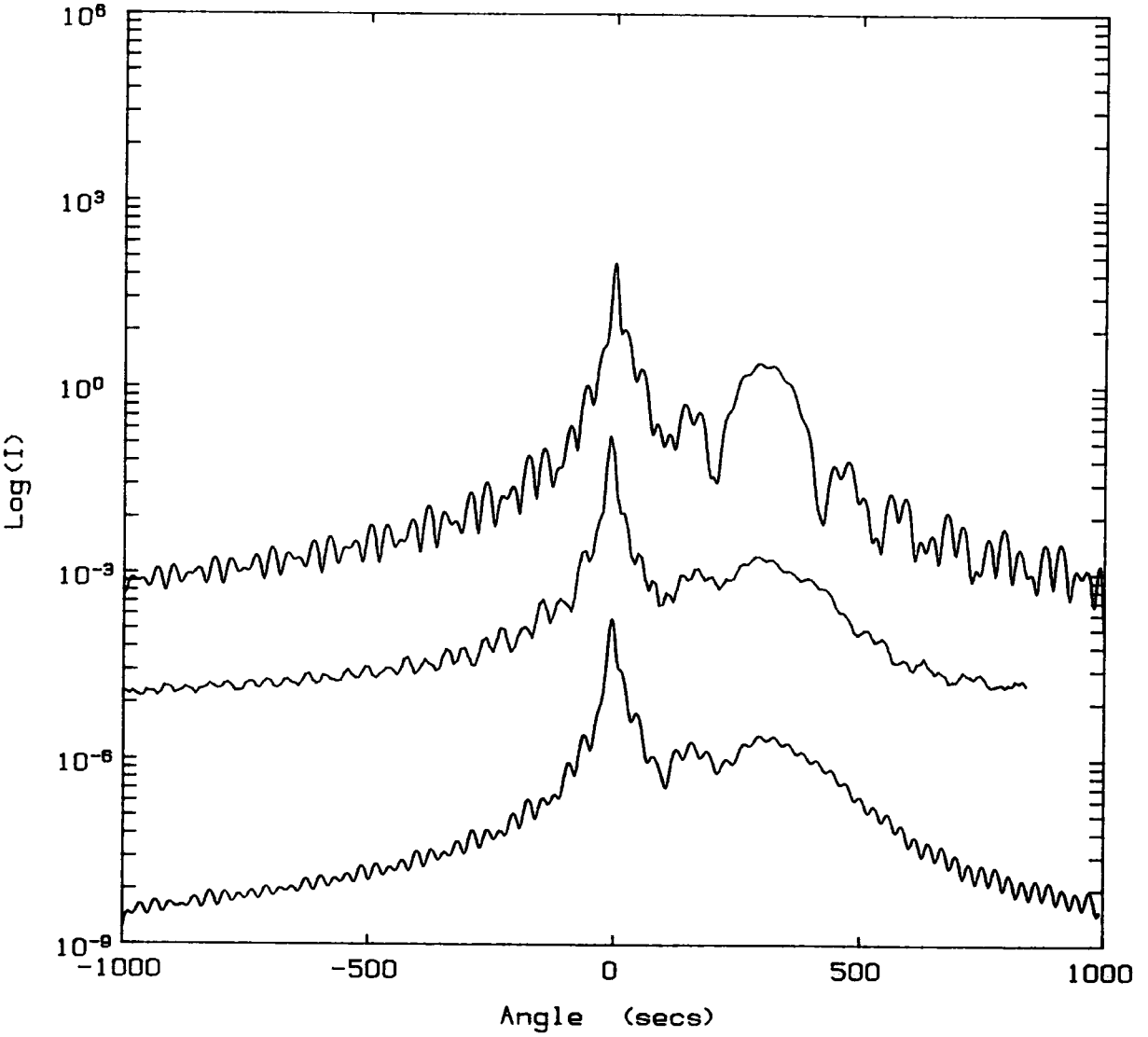

Figure 6.10: Experimental and simulated 004 rocking curves of sample $ABA1$. Upper plot, simulation without grading; middle plot, experiment; lower plot, simulation with grading.

rocking curves. The thicknesses used in the simulations are derived from the experimental FT's shown in figure 6.11, determined from two scan ranges 1843″ and 3686″, each with the same number of steps and a counting time of 20 seconds. The FT's corresponding to the two ranges shown in figure 6.11 exhibit peaks at the same thicknesses. The layer thicknesses are measured to be $0.175\mu m$ for the layer and $0.469\mu m$ for the cap, with an error of $\pm 0.01\mu m$. The top plot in figure 6.10 shows a simulated rocking curve using these values of thickness. However, the layer peak is greater in intensity and narrower than seen in experiment. In order to achieve a close match, therefore, it was necessary to include substantial compositional grading in the active layer, and a small degree of curvature, as shown in the bottom plot of figure 6.11. The two curves now have an almost perfect match of fringe position and amplitude, as well as equivalent layer peak widths, intensities and position relative to the substrate. It is interesting to note that grading does not affect the Pendellösung fringe positions or frequency, but it does reduce the amplitude. The bottom plot of figure 6.11 shows the FT of this simulated structure. Again the positions of the peaks are the same, although sharper due to cleaner statistics.

It is clear that once the layer thicknesses have been determined using Fourier Analysis of the Pendellösung fringes, the process of simulation becomes straightforward, since two degrees of freedom have been removed. Figure 6.12(a) shows the final simulated mismatch and thickness profile of sample ABA1.

6.5.2 Sample ABA2

This sample had the same nominal structure as ABA1 as it was grown at roughly the same time by P. Spurdens under similar growth conditions. An experimental rocking curve was taken over a range of 1843″ with 256 steps and 20 second counting time, under the same conditions as before. Figure 6.13 shows the experimental and simulated rocking curves, the latter derived from the FT shown in figure 6.14. Again the values of thickness determined from the FT made the simulation procedure more straightforward and it was found that grading was required once more to achieve a close match with experiment. It was also necessary to include sample curvature again to provide a match of fringe amplitude. Figure 6.12(b) shows the simulated compositional profile of sample ABA2.

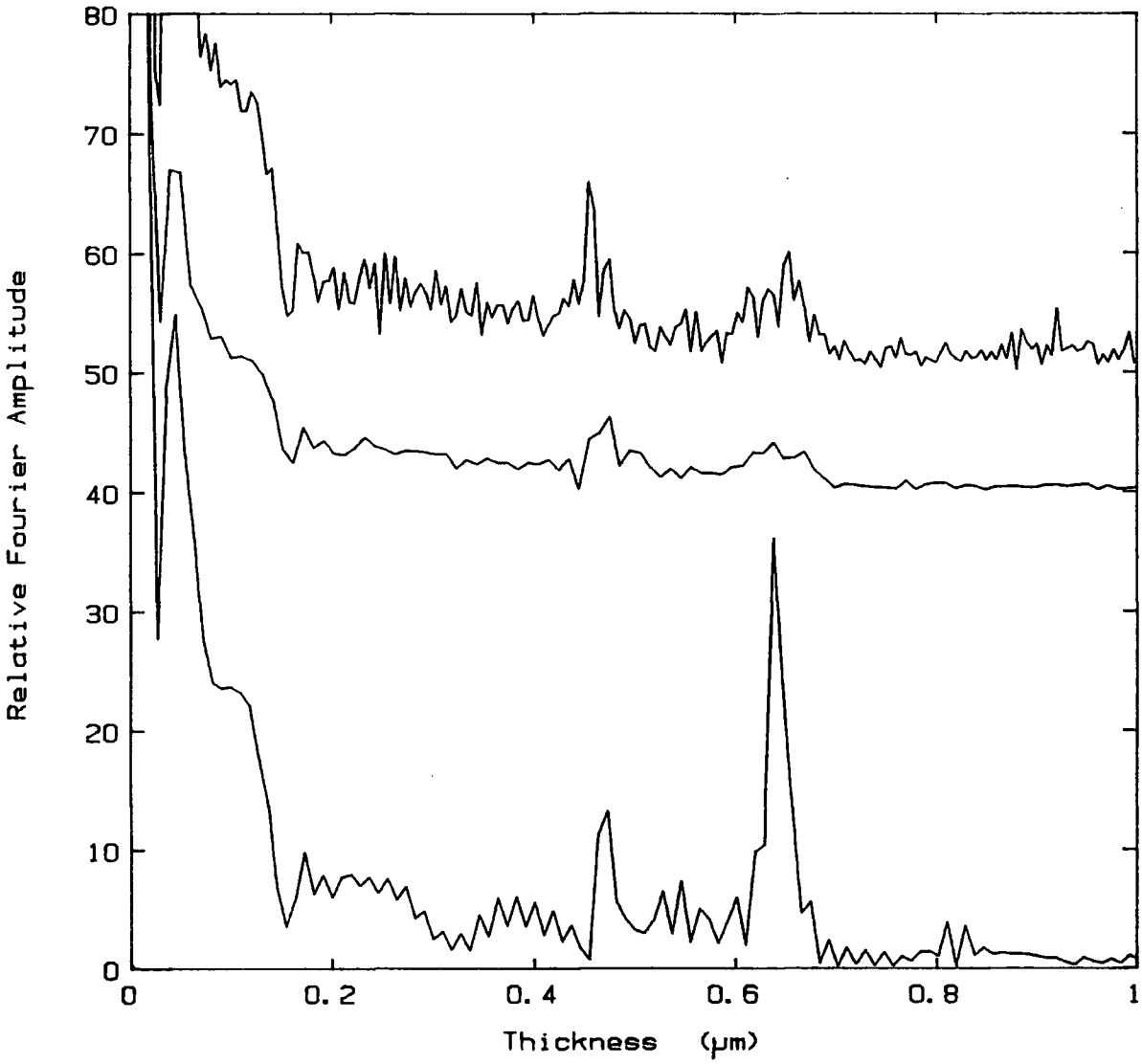

Figure 6.11: Fourier Transforms of experimental and simulated rocking curves of sample $ABA1$. Upper plot, experiment with 3686″ range; middle plot, experiment with 2000″ range; lower plot, simulation.

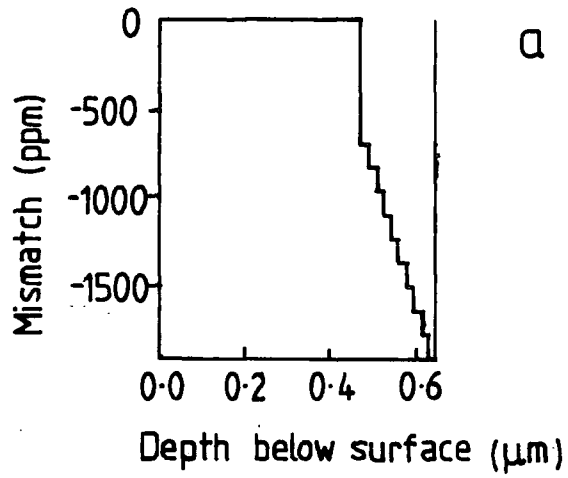

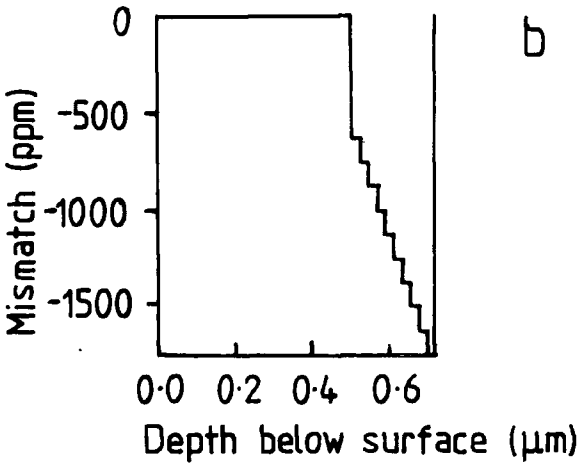

Figure 6.12: Simulated compositional profiles of samples (a) $ABA1$ and (b) $ABA2$.

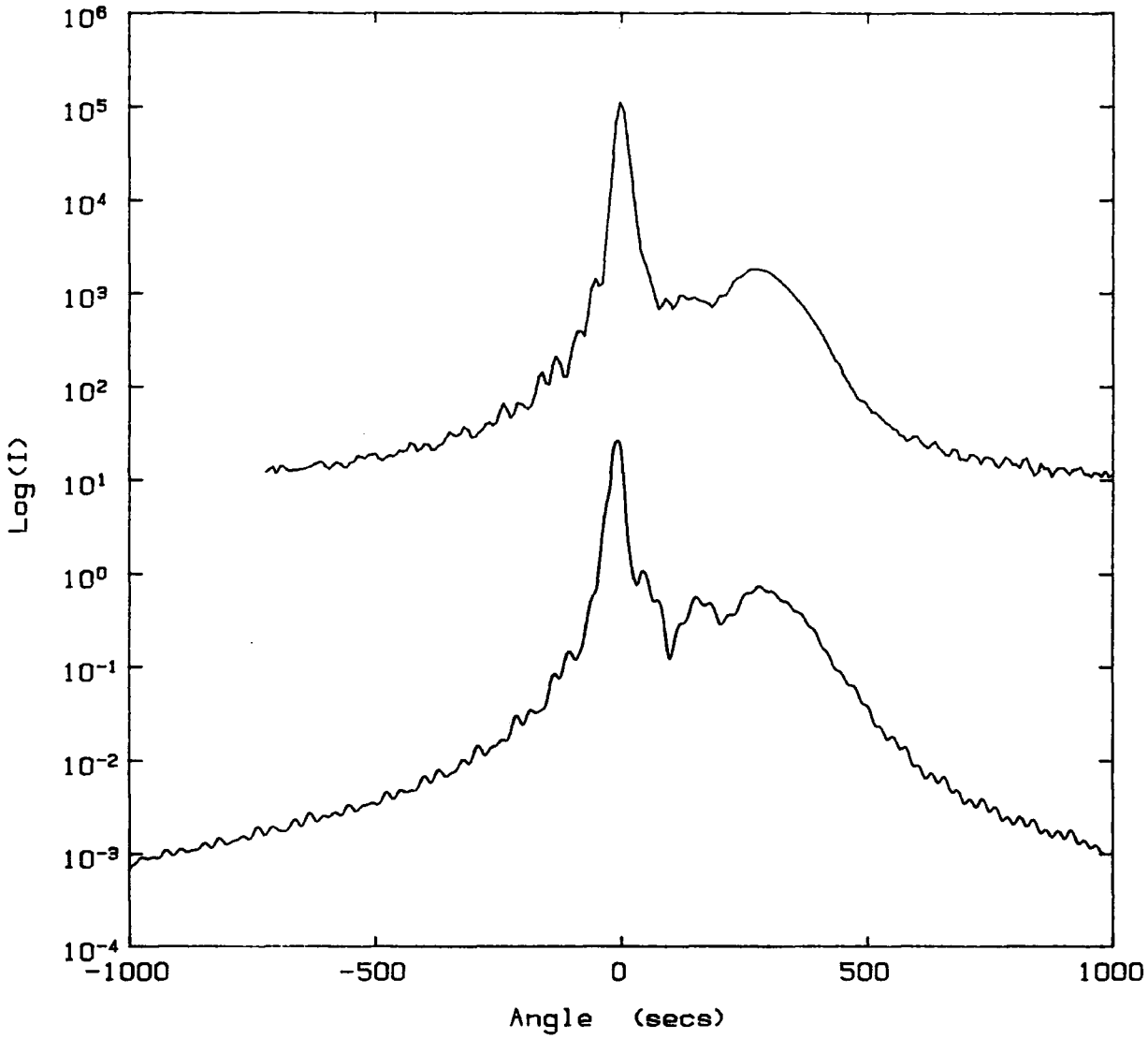

Figure 6.13: Experimental and simulated 004 rocking curves of sample $ABA2$. Upper plot, experiment; lower plot, simulation with grading.

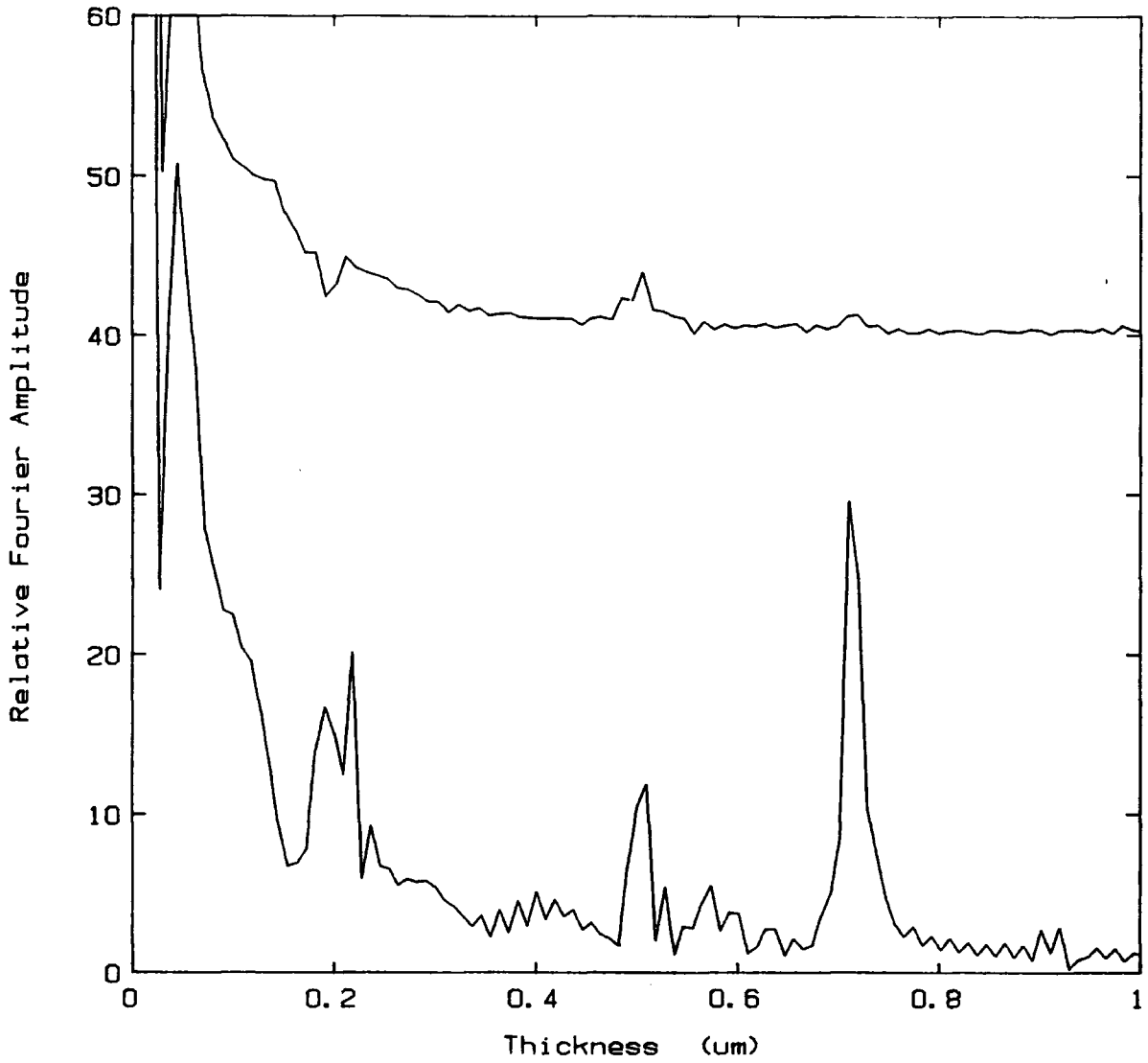

Figure 6.14: Fourier Transforms of experimental and simulated rocking curves of sample $ABA2$. Upper plot, experiment; lower plot, simulation.

6.5.3 Sample ABA3

It is often necessary to know the uniformity of epitaxial growth over an entire wafer of material. In order to obtain an area scan from a wafer, without remounting it each time, an X-Y translation stage is required and software can be used to run the scan loop automatically.

Sample ABA3 was a complete wafer of material grown by S. Cole at British Telecom by MOVPE. Its structure was nominally $0.18\mu m$ of $GaInAsP$, band gap $1.1\mu m$, capped by $0.4\mu m$ of InP. The characterisation of this sample is made more difficult as it is almost perfectly lattice matched. Figure 6.8 showed how the Pendellösung fringe amplitude decreases as the mismatch becomes small. The scan range used was $3686''$ with a step size of $7.2''$ and counting time of 11.4 seconds, for each of the nine points on the area scan.

Figure 6.15 shows the rocking curves obtained from sample ABA3. The mismatch clearly changes across the wafer, but it would be very difficult to directly measure from the rocking curves any change in the Pendellösung period from different points on the sample because the fringe amplitudes are so small. Figure 6.16 shows the corresponding FT's, which all exhibit a broad peak between 0.4 and $0.5\mu m$ due to the cap and a sharper peak at roughly $0.6\mu m$ due to the sum of the cap, and layer frequencies. Unfortunately the data is not good enough to resolve a separate peak due to the layer in most of the cases.

Figure 6.17 gives the measured values of thickness from the FT's for the nine points. The average thicknesses for the cap and layer are $0.44\mu m$ and $0.16\mu m$ respectively, and all of the measurements lie within experimental error of these averages. The layer thicknesses can be said to be constant over the wafer within a measuring accuracy of $\pm 400\mathring{A}$.

6.6 Conclusion

This chapter has illustrated the need for Fourier Analysis as a tool in measuring the Pendellösung fringe spacing. Without it, the errors in thickness determination are large and values may even be incorrect. In some cases it is impossible to measure the fringe spacings directly from the rocking curve, when, for exam-

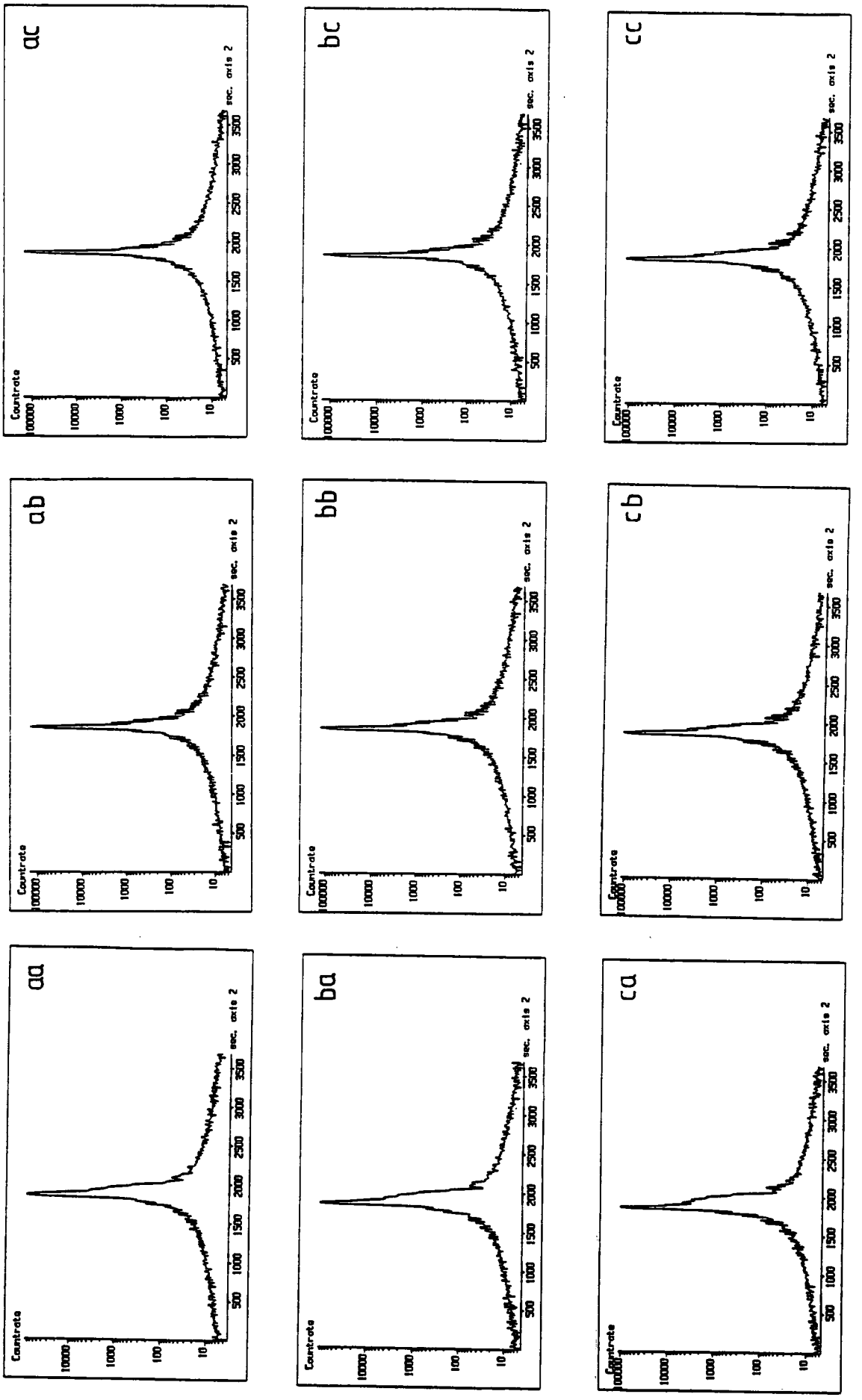

Figure 6.15: 004 reflection area scan of sample $ABA3$

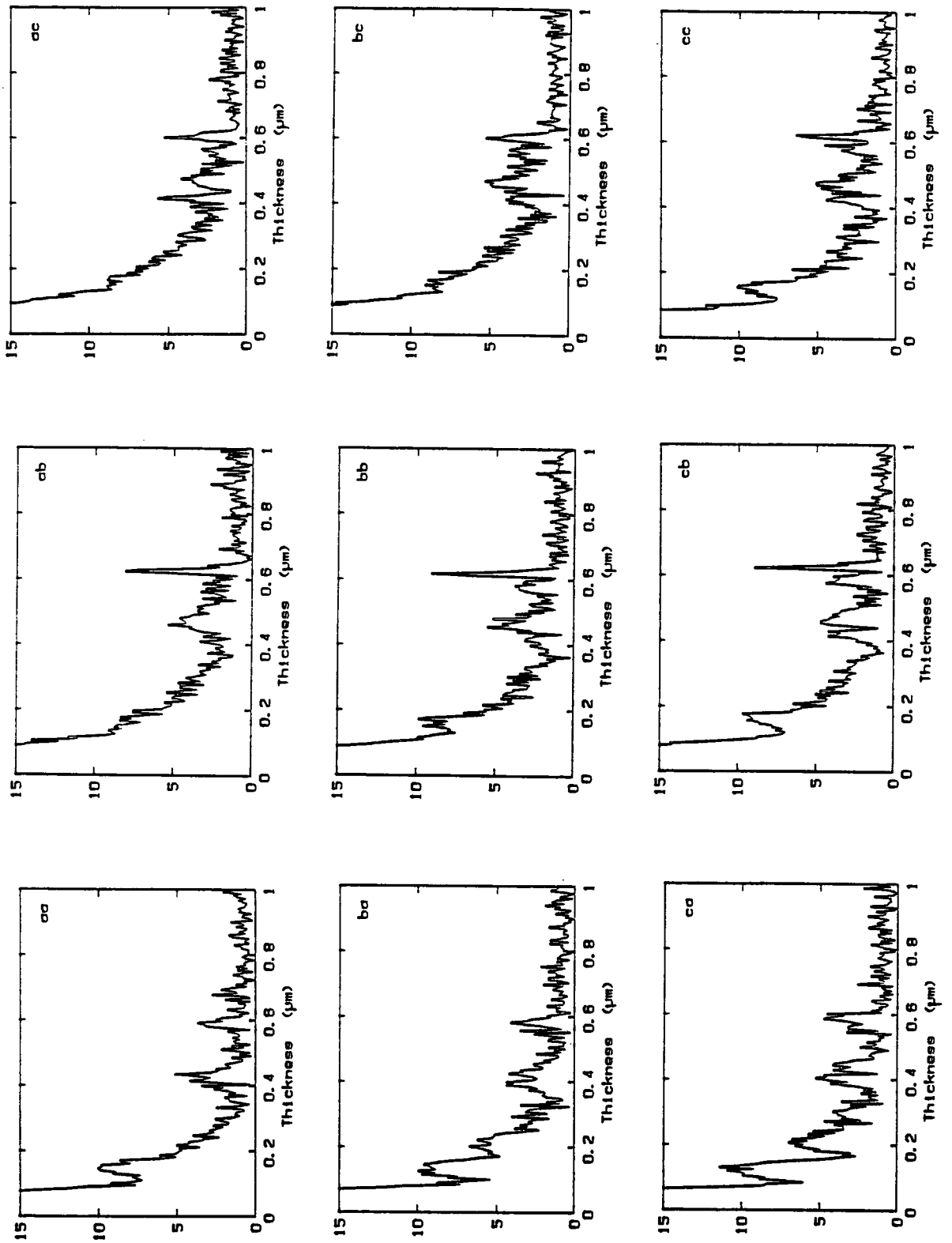

Figure 6.16: Fourier Transforms of the rocking curves of sample $ABA3$ shown in figure 6.15.

Layer	0.15		0.17		0.18	
	aa	±0.02	ab	±0.04	ac	±0.02
Cap	0.44		0.46		0.42	
Layer	0.17		0.16		0.13	
	ba	±0.03	bb	±0.02	ac	±0.03
Cap	0.41		0.46		0.47	
Layer	0.18		0.17		0.16	
	ca	±0.04	cb	±0.02	cc	±0.02
Cap	0.42		0.46		0.46	

Figure 6.17: Measured layer thickness of sample $ABA3$ using Fourier analysis.

ple, the layer thicknesses are such that complex interference patterns result, or when the fringe amplitudes are small as for closely matched structures.

The optimum ranges and step sizes for data collection have been established for a variety of signal to noise ratios. These have been applied to several double layer structures experimentally. Remarkably good fits between simulated and experimental rocking curves have been achieved by utilising the thickness values first determined by Fourier Analysis.

The number of variables to be fitted in a simulation routine needs to be small for a unique, accurate solution to be attained. The complexity of rocking curves from multiple layered epitaxial structures is such, that fitting by simply matching peak heights and positions is inadequate. It is vital that thicknesses are determined accurately from Pendellösung fringes before simulation takes place. This work has shown that by determining layer thicknesses using Fourier Analysis the number of degrees of freedom is reduced making simulation straightforward.

Chapter VII

Triple Crystal Diffraction and X-ray Reflectometry

7.1 Introduction

The theory behind Triple Crystal Diffractometers (TCD's) has been explained in Chapter 2. A major advantage of the TCD over the DCD is the elimination of the effects of sample curvature and small angle diffuse scattering. The third crystal, or analyser, uses angular collimation by Bragg reflection rather than spatial collimation by a slit to define the direction of the scattered X-rays recorded by the detector. The angular resolution of the detector system is effectively the width of the reflection range of the analyser. In addition, by decoupling the sample and analyser crystals a map in reciprocal space can be produced which gives important information on the quality of samples and topography of sample surfaces.

Triple crystal diffraction has not been used to the same extent as double crystal in the characterisation of epitaxial layers probably because, until very recently, no commercial instrument was on the market. It has however, been applied, for example, to the study of phase transitions in prousite (Ag_3AsS_3) (Nelmes et al., 1984; Ryan et al., 1985) as well as structural studies of $BaMn_4F$ (Ryan, 1986; Ryan et al., 1986). Afanas'ev et al. (1984) have used a TCD to study diffraction far from the Bragg peak to gain information on the structural perfection of thin subsurface layers in Ge which had been polished and etched. Multilayers of W/Si, Ni/C and ReW/C have been studied by Hornstrup, Christensen and Schnopper (1986) using TCD, and were all found to show mosaicity. Later work by Christensen, Hornstrup and Schnopper (1987, 1988) on similar materials found evidence of substrate imperfection, interfacial roughness and interdiffusion. Zaumseil et al. (1987) compared TCD and DCD of ion implanted silicon and found that the presence of diffuse scattering in the double crystal rocking curve effectively washed out the fine structure seen in the triple crystal

rocking curve. The signal to noise ratio is of the order of 10^6 for the TCD compared to 10^4 for the DCD. Fewster (1989) has used a four-crystal six-reflection diffractometer to study an $AlGaAs$ laser structure and an $GaAs/AlAs$ MQW. This instrument behaves as a very high resolution TCD. Ryan et al. (1987) have exploited the highly asymmetric geometry to determine layer thickness, composition and internal interface roughness of a buried layer only 230Å thick. This geometry has been used to study a thin layer of $AlInAs$ capped with $GaAs$ using a TCD (Lucas, Hatton, Bates, Ryan, Miles and Tanner, 1988) and the results compared to those obtained with a DCD (Bates, Hatton, Lucas, Ryan, Miles and Tanner, 1988).

X-ray reflectivity is a well established technique used for the characterisation of thin films. As early as 1931, Kiessig showed that measurements of reflectivity of surfaces at angles close to the region of total external reflection gave information on the variation of electron density below the surface. Specular reflectivity depends only on the electron density and hence composition and is independent of crystal structure. Amorphous layers behave in the same way as crystalline layers. A measurement of reflectivity as a function of angle of incidence provides information about the refractive index and hence electron density of the material as a function of depth. As the X-rays penetrate very little into the material, due to the very low incidence angle, reflectivity is a highly sensitive probe of thin surface layers. X-ray reflectivity is well known as a characterisation tool for stratified media such as semiconductor superlattices (Chang, Segmüller and Esaki, 1976; Sugawara et al., 1988) and Langmuir-Blodgett films (Pomerantz, Dacol and Segmüller, 1978; Pomerantz and Segmüller, 1980; Jark et al., 1989). Le Boite et al. (1988) have used it to measure thickness of metallic multilayers with high accuracy, whilst Roberts et al. (1989) have used synchrotron radiation reflectivity to study polyphenylene thin films. Using a triple crystal diffractometer to measure specular reflectivity at grazing incidence, Cowley and Ryan (1987) showed that the thickness and roughness of amorphous films on semiconductor crystals could be determined experimentally. The presence of a thin surface layer causes interference of the X-rays resulting in oscillations in the reflected intensity with angle. This may be explained with Fresnel theory (Compton and Allison, 1935). Parratt (1954) derived a recursion relation for the reflectivity from a multi-layered sample. Parratt's treatment, described in this chapter, is valid for

hard X-ray radiation such as $CuK\alpha$, but for softer X- rays, where the critical angle is larger, multiple reflections as well as absorption need to be taken into account (Heavens, 1965; Jark et al., 1989). Surface and interface roughness have been included in the treatment as a gaussian function (Cowley and Ryan, 1987). Segmüller (1973) used X-ray reflectivity to study thin films of amorphous silicon on sapphire, while Rhan and Pietsch (1988) used it to study nanometer scale heterostructures, determining both layer thickness and roughness accurately. Reflectivity of multilayer structures of W/C and W/Si has been studied by Vidal and Marfaing (1989) and multilayer roughness has been modelled by Rosen et al. (1988). The combination of glancing incidence diffraction and specular reflectivity measurements has been shown to yield structural information on layers as thin as 210$\AA$ (Lucas et al., 1988). Lucas, McMorrow and Bates (1989) have shown that X-ray reflectivity and triple crystal diffraction studies on thin layers of II-VI semiconductors provide complementary information for the characterisation of structures.

A similar technique known as Energy Dispersive Reflectivity has not been used quite as extensively. It is analogous to energy dispersive diffraction, used by Hart, Parrish, and Masciocchi (1987) to study a Pd/Xe thin layer and by Holý, Cummings and Hart (1988) to study mosaic spread in silicon, germanium and calcium fluoride, in that the angle remains constant while the intensity as a function of X-ray energy is recorded. Bilderback and Hubbard (1982) have used energy dispersive reflectivity to study the effect of roughness and etching on X-ray mirrors and the reflectivity of platinum coated mirrors. They used a highly collimated beam of white X-ray radiation at a glancing angle of incidence and recorded the reflected intensity as a function of energy. A similar experiment is described in this chapter together with an explanation of Fresnel theory for both angular reflectivity and energy dispersive reflectivity, which is used to model the results obtained theoretically.

7.2 Triple Crystal Diffraction of a Thin Layer

The experiments were carried out at Edinburgh University using a triple crystal diffractometer based on a Huber 4301 (440) goniometer, and utilising a GEC Avionics $GX21$ rotating anode X-ray generator with a copper target (Lucas

et al., 1988). The monochromator and analyser crystals were $Ge(111)$. The sample, consisting of a thin layer of $AlInAs$ on (100) InP, capped by an ultra-thin layer of $GaAs$, code INP2, was that characterised in Chapter 4 by double crystal diffraction. These measurements found that the thickness of the $AlInAs$ layer varied over the sample (Bates et al., 1988) and thus it was impossible to make a direct comparison between the results of triple and double crystal diffraction. In order to maximise the scattering from the surface layers with respect to the substrate the asymmetric 440 reflection was used, in the glancing incidence mode. The Bragg angle for InP with $CuK\alpha$ is 48° and so the angle of incidence is 3°. The triple crystal diffractometer provides high resolution in two dimensions in the scattering plane and it is therefore possible to map out the intensity distribution of scattered X-rays in an area of reciprocal space. Figure 7.1 illustrates the intensity around the InP (440) reciprocal lattice point for sample INP2. The equal-intensity contours are on a logarithmic scale over four decades of intensity. The small peak at $(4.017, 4, 0)$ has an intensity approximately 10^{-3} that of the substrate (440) Bragg peak and arises from the quantum well layer of $AlInAs$. The width of the Bragg peak in the [010] direction is a measure of the sample mosaicity and homogeneity across the layer. The presence of the secondary Bragg peak is clearer in figure 7.2 which plots the integrated intensity in the [010] direction along the face normal [100] direction over the scan range. The logarithmic scale over five orders of magnitude emphasises the weak scattering observed around the (440) Bragg peak. This profile was simulated using a kinematical model developed at Edinburgh University which is valid in this case because the layer is very thin, although it is not valid near the substrate Bragg peak. The data was fitted with a least squares routine, assuming the heterostructure consisted of a semi-infinite substrate and two thin crystalline layers. The mismatch of the $AlInAs$ layer was found to be $-4450ppm$ and the resulting fit is shown in figure 7.3 with the fitting parameters given in Table 7.1. The results compare well with the findings of DCD from the region on the sample with the thinnest layer. The parameters include roughness and regions of disorder at interfaces which probably correspond to interfacial grading.

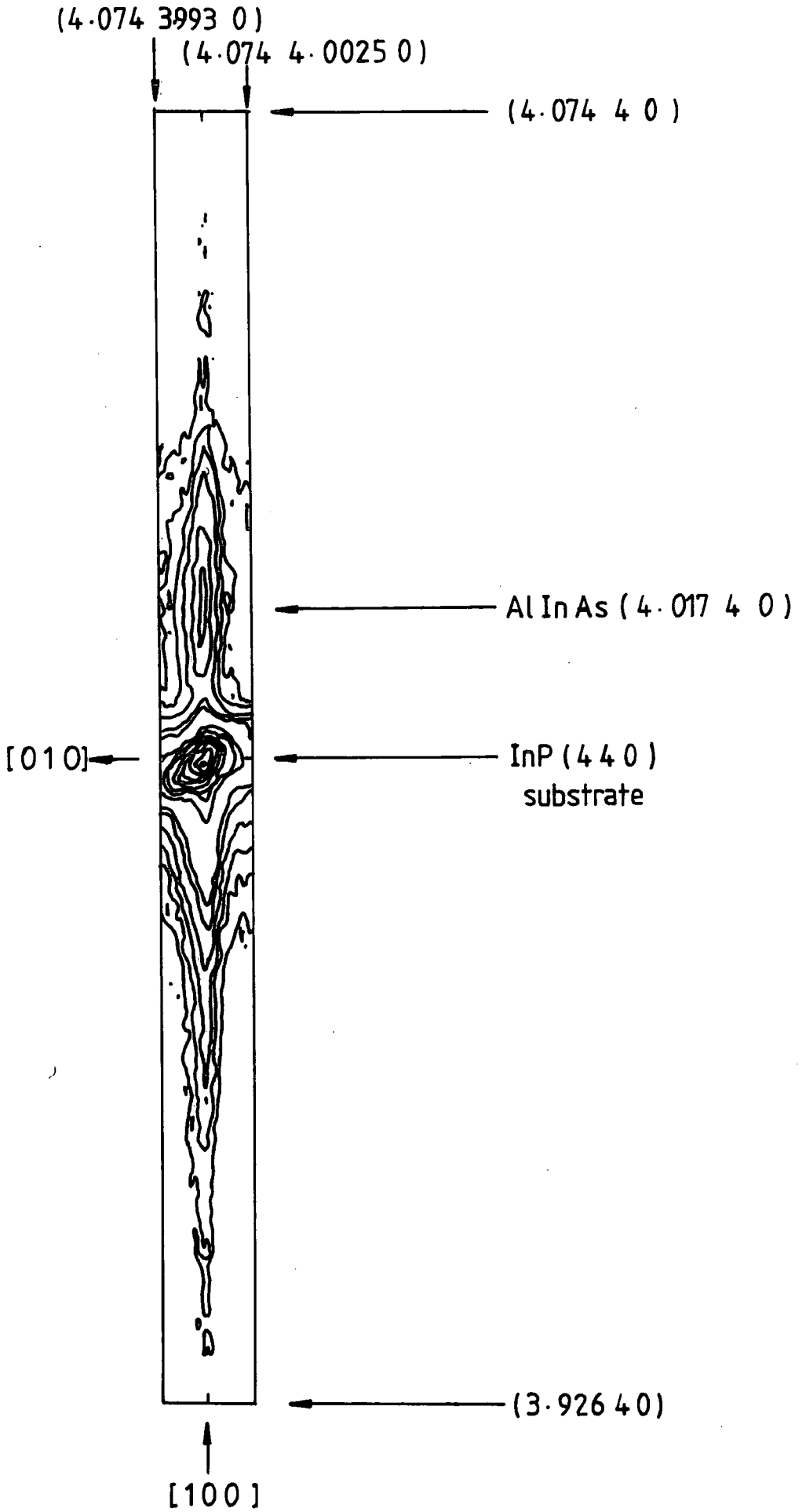

Figure 7.1: Triple crystal diffraction map in reciprocal space of sample INP2.

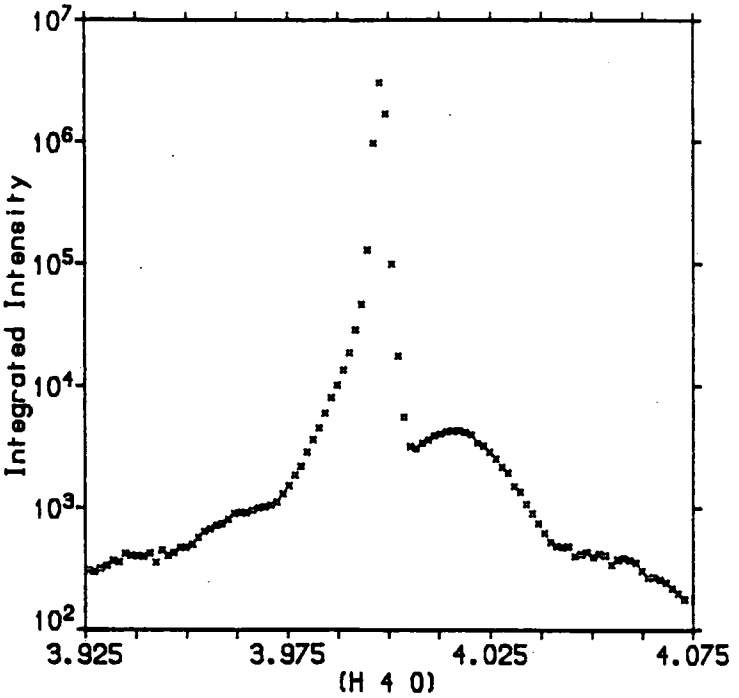

Figure 7.2: The intensity distribution along [100], the face normal direction, through the InP (440) Bragg peak from sample INP2.

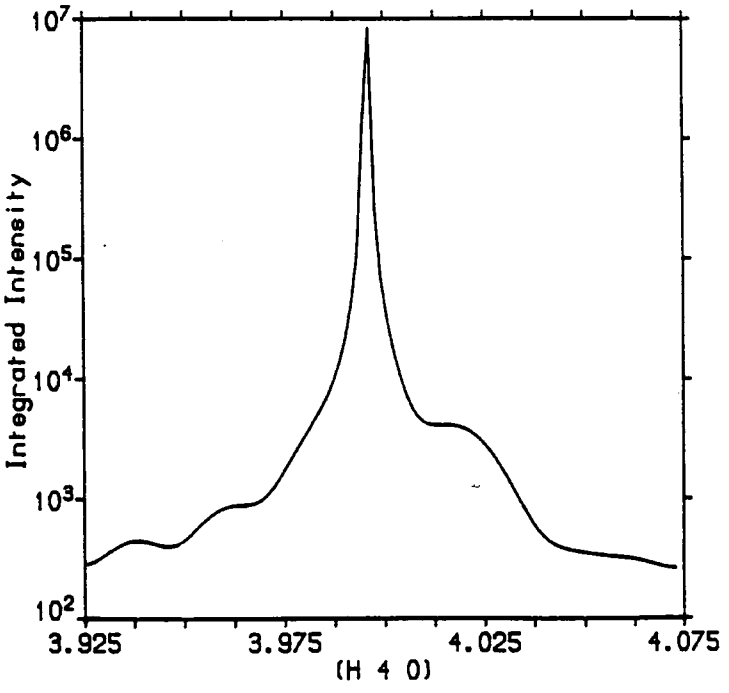

Figure 7.3: A least-squares fit by the Edinburgh group of figure 7.2 with a kinematical scattering model using the parameters shown in Table 7.1.

Layer (2) $GaAs$	$d_2 = 29 \pm 0.4\mathring{A}$	$\sigma_2 \leq 1\mathring{A}$
Disordered Layer (2)	$d = 15 \pm 0.5\mathring{A}$	
Layer (1) $InAlAs$	$d_1 = 204 \pm 0.4\mathring{A}$	$\sigma_1 = 1 \pm 0.7\mathring{A}$
Disordered Layer (1)	$d = 20 \pm 1\mathring{A}$	
InP Substrate		$\sigma_0 = 2.5 \pm 1\mathring{A}$

Table 7.1

It was found that triple crystal diffractometry of sample INP2 was more sensitive to the thin layer diffraction effects than double crystal diffractometry. This is essentially because of the removal of the effects of curvature and reduction of the diffuse scattering background. However, much of the difference can be attributed to the use of a proportional counter with a good quality counting chain. When samples are not appreciably curved double crystal diffraction is almost as sensitive to thin layers as triple, providing care is taken over the experimental set up.

7.3 Theory of X-ray Reflectivity

The refractive index of X-rays in semiconductors is less than one, and so X-rays are totally externally reflected for sufficiently small angles of incidence. Since the X-ray beam then penetrates very little into the material the reflectivity is a probe of the properties of the surface. By rocking the sample crystal through the position of total external reflection, known as the critical angle, and observing the intensity as a function of angle, information on the electron density as a function of depth is yielded. The theory of X-ray reflectivity has been developed by many authors, including Pomerantz (1987) and Névot and Croce (1980), but the treatment of Parratt (1954) is shown here.

7.3.1 Two Homogeneous Media

In order to develop the theory for N layers of varying composition the case of two homogeneous media is first considered. The X-ray beam is incident at an angle ϕ, and a coordinate system in which x-z is the plane of incidence is

used, with z taken as positive into the sample and y parallel to the surface. For any glancing angle, the expressions for the electric vector of the incident beam $E_1(z_1)$, of the reflected beam $E_1^R(z_1)$, and of the refracted beam $E_2(z_2)$ at a perpendicular distance z from the surface, are

$$E_1(z_1) = E_1(0)\exp\Big\{i[\omega t - (k_{1,x}x_1 + k_{1,z}z_1)]\Big\}$$

$$E_1^R(z_1) = E_1^R(0)\exp\Big\{i[\omega t - (k_{1,x}x_1 - k_{1,z}z_1)]\Big\} \qquad 7.1$$

$$E_2(z_2) = E_2(0)\exp\Big\{i[\omega t - (k_{2,x}x_2 + k_{2,z}z_2)]\Big\}$$

where k_1 and k_2 are the propagation vectors (of magnitudes $2\pi/\lambda_1$ and $2\pi/\lambda_2$) outside and inside the sample, respectively. The glancing angle ϕ is always very small for X-rays and we write

$$k_{2,x}^2 + k_{2,z}^2 = k_2^2 = r_2^2 k_1^2 = r_2^2(k_{1,x}^2/\cos^2\phi) \simeq k_{1,x}^2(1 - 2\delta_2 - 2i\beta_2 + \phi^2)\ , \qquad 7.2$$

where $r_2 = 1 - \delta_2 - i\beta_2$ is the refractive index of the sample, $r_1 = 1$ for air or vacuum, and second and higher powers of δ_2 and β_2 are neglected since they are each of the order of 10^{-5} or less. $\beta_2 = \lambda\mu_2/4\pi$ where μ_2 is the linear (incoherent) absorption coefficient of the layer.

The boundary condition for the components of the electric vectors is $k_{2,x} = k_1$, and for small ϕ we can approximate $k_{1,x} \simeq k_1$. It follows that

$$k_{2,z} \simeq k_1(\phi^2 - 2\delta_2 - 2i\beta_2)^{\frac{1}{2}}\ . \qquad 7.3$$

Therefore, we can write

$$f_2 = (\phi^2 - 2\delta_2 - 2i\beta_2)^{\frac{1}{2}}\ , \qquad 7.4$$

and so the expression for the refracted beam becomes

$$E_2(z_2) = E_2(0)\exp[i(\omega t - k_{2,x}x_2)]\exp[-ik_1 f_2 z_2] \ . \qquad 7.5$$

The Fresnel coefficient for reflection, $F_{1,2}$, can be written (Compton and Allison, 1935)

$$F_{1,2} = \frac{E_1^R}{E_1} = \frac{\sin\phi - r_2\sin\phi_2}{\sin\phi + r_2\sin\phi_2} \simeq \frac{\phi - f_2}{\phi + f_2} = \frac{f_1 - f_2}{f_1 + f_2} \ , \qquad 7.6$$

where

$$f_1 = (\phi^2 - 2\delta_1 - 2i\beta_1)^{\frac{1}{2}} = \phi \ . \qquad 7.7$$

7.3.2 N Homogeneous Media

Consider now $N(N \geq 2)$ homogeneous media where the thickness of each lamina $n(\leq N)$ is denoted by d_n. Medium 1 is air and medium N is the substrate. The tangential components of the electric vectors are shown in figure 7.4, and the continuity for the $n-1, n$ boundary may be expressed as

$$a_{n-1}E_{n-1} + a_{n-1}^{-1}E_{n-1}^R = a_n^{-1}E_n + a_n E_n^R \ , \qquad 7.8$$

$$(a_{n-1}E_{n-1} - a_{n-1}^{-1}E_{n-1}^R)f_{n-1}k_1 = (a_n^{-1}E_n - a_n E_n^R)f_n k_1 \ , \qquad 7.9$$

where the amplitude factor a_n for half the perpendicular depth d_n is, from equation (7.5),

$$a_n = \exp\Big(-ik_1 f_n \frac{d_n}{2}\Big) = \exp\Big(-i\frac{\pi}{\lambda} f_n d_n\Big) \ . \qquad 7.10$$

In equations (7.8) and (7.9), the vector amplitudes E_{n-1}, E_{n-1}^R and E_n, E_n^R refer to the values midway through medium $n-1$ and n, respectively. The solutions of equations (7.8) and (7.9) are obtained by dividing their difference by their sum and writing the result as a recursion formula

$$R_{n-1,n} = a_{n-1}^4\Big[\frac{R_{n,n+1} + F_{n-1,n}}{R_{n,n+1}F_{n-1,n} + 1}\Big] \ , \qquad 7.11$$

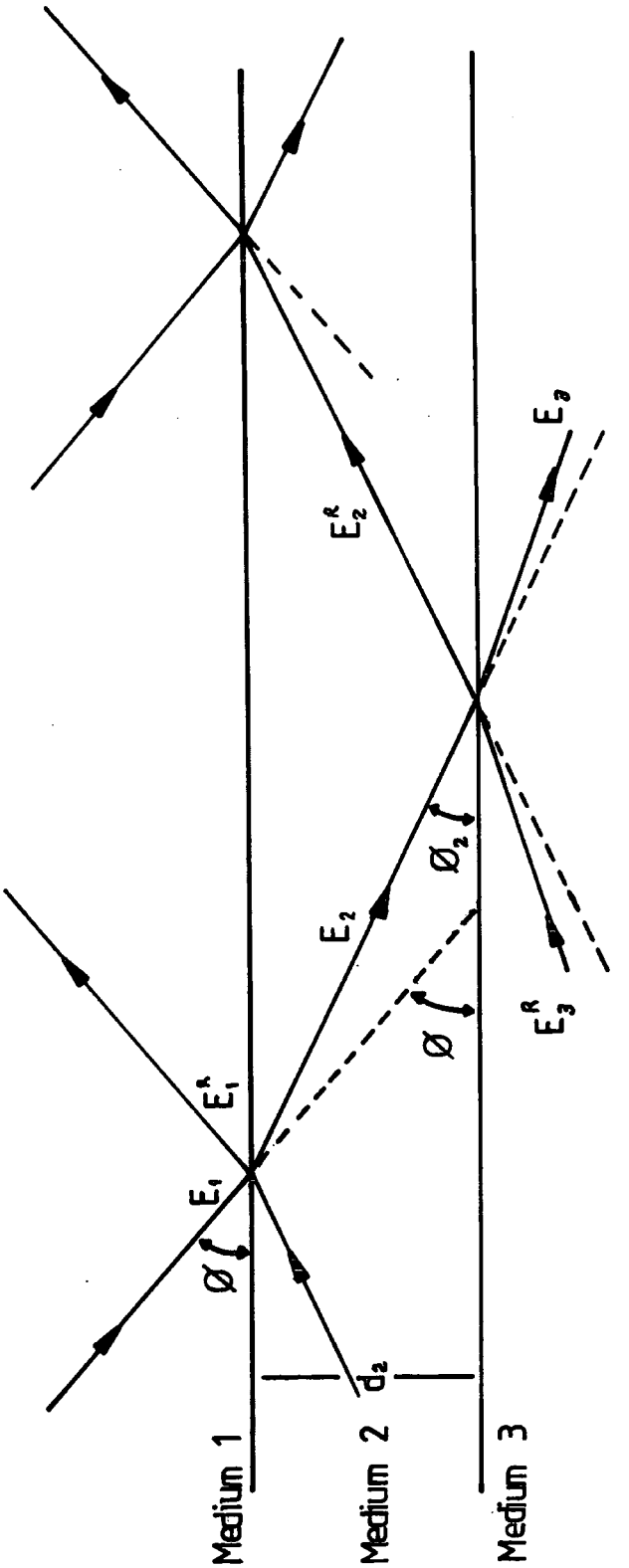

Figure 7.4: Sketch of reflection and refraction for stratified homogeneous media. After Parratt (1954).

where

$$R_{n,n+1} = a_n^2(E_n^R/E_n) \ , \tag{7.12}$$

and

$$F_{n-1,n} = \frac{f_{n-1} - f_n}{f_{n-1} + f_n} \ . \tag{7.13}$$

The solution of equation (7.11) is obtained by starting at the substrate medium, N, and noting that $R_{N,N+1} = 0$ since a_n is zero as the substrate thickness is taken to be infinite. Also as medium 1 is air then a_1 is unity and so $R_{1,2} = E_1^R/E_1$.

The ratio of the reflected to incident intensity is given by the square of the absolute value of $R_{1,2}$ (since it is complex),

$$\frac{I_R}{I_0} = \left|\frac{E_1^R}{E_1}\right|^2 = |R_{1,2}|^2 \ . \tag{7.14}$$

Interface roughness can be accounted for with a gaussian roughness term (Cowley and Ryan, 1987) and equation (7.13) becomes

$$F_{n-1,n} = \frac{f_{n-1} - f_n}{f_{n-1} + f_n}\left\{\exp\left[-\frac{1}{2}(\frac{4\pi\sigma_n \sin\phi}{\lambda})^2\right]\right\} \ , \tag{7.15}$$

where σ_n is the root mean square roughness of the n^{th} layer.

For a given sample layer containing atoms of type $a = A, B, ...$ the refractive index can be written as (James, 1948)

$$n = 1 - \delta^* \ ,$$

where

$$\delta^* = \delta + i\beta = 2.72 \times 10^{14}\frac{1}{A}\rho\lambda^2\sum_a(Z_a + \Delta f_a) \ . \tag{7.16}$$

ρ is the density with units of g/cm^3, A is the atomic weight in g, and λ is the wavelength in $\mathring{A}$. Note that Δf_a is complex since,

$$\Delta f = \Delta f' + i\Delta f'' \ , \tag{7.17}$$

where $\Delta f'$ and $\Delta f''$ are the real and imaginary parts of the dispersion corrections respectively. The compositions of ternary and quaternary alloys are calculated using Végards law as explained in Chapter 1. For normal angular reflectivity with $CuK\alpha$ radiation the X-rays are assumed to be of one wavelength only and the dispersion corrections may be looked up directly from the International Tables for X-ray Crystallography Vol. IV (1974). However, for energy dispersive reflectivity the wavelength of the X-rays varies and so therefore do the dispersion corrections. To a good approximation Hönl's model may be used to calculate Δf for a given λ (James, 1948). The dispersion corrections for a particular element of atomic number Z are given by

$$\Delta f' = g_K \frac{1}{x^2} \log_e |x^2 - 1| \ ,$$

$$\Delta f'' = g_K \frac{\pi}{x^2} \ , \ x > 1 \quad ; \quad = 0 \ , \ x < 1 \ , \tag{7.18}$$

where $x = \lambda_K/\lambda$. λ_K is the wavelength of the K absorption edge of the element while λ is the X-ray wavelength. The oscillator strength, g_K, is given by

$$g_K = \frac{2^8 e^{-4}}{9} \left\{ \frac{2}{(1-\Delta_K)^2} - \frac{1}{3(1-\Delta_K)^3} \right\} \ , \tag{7.19}$$

with

$$\Delta_K = \frac{1}{B}\left(B - \frac{911}{\lambda_K}\right) \ , \tag{7.20}$$

where λ_K is in $\mathring{A}$, and

$$B = (Z - 0.3)^2 + 1.33 \times 10^{-5}(Z - 0.3)^4 \ . \tag{7.21}$$

The value of δ^* may then be calculated for a given composition and wavelength and combined with the angle ϕ to give f_n for a particular layer so that the reflectivity may then be calculated. The algebra becomes extremely tedious for larger values of N and a computer is required to solve the problem quickly. A

Fortran program is included in Appendix B which solves this problem using the equations derived, for both normal reflectivity and energy dispersive reflectivity, for a large range of possible materials.

7.4 Structural Determination using X-ray Reflectivity

The Parratt model has been used in a simulation program to determine the effect of varying different parameters in the reflectivity so that an understanding of experimental curves may be achieved.

7.4.1 Angular Reflectivity

Figure 7.5 shows the angular reflectivity of InP for various wavelengths corresponding to the characteristic $K\alpha$ lines of Ag, Mo, Cu, Fe and Cr. The critical angle varies from approximately 0.1° for Ag with $\lambda = 0.56\mathring{A}$ to 0.4° for Cr with $\lambda = 2.29\mathring{A}$. The reflectivity also falls off more steeply for the harder radiation. The softer radiation of Cr, Fe and Cu is therefore more applicable to the study of semiconductors since experiments are unlikely to achieve more than six decades of intensity and so a larger angular range may be examined.

Figure 7.6 shows the angular reflectivity of InP, $GaAs$ and Si with $CuK\alpha$ radiation. The critical angle for InP and $GaAs$ is approximately 0.3°, while for Si it is 0.2°. This arises because from Snell's law $\cos\phi_c = 1 - \delta$, and as δ is small expanding the cosine gives the critical angle as $\phi_c = \sqrt{2\delta}$. δ is larger for InP and $GaAs$ than for Si.

The effect of surface roughness on the angular reflectivity at $1.54\mathring{A}$ for InP is shown in figure 7.7. The RMS roughness of the surface is applied as a Gaussian function in the model. The reflectivity fall off becomes steeper with increasing surface roughness. Internal interface roughness, however, has a different effect. This is shown in figure 7.8 for a single $400\mathring{A}$ layer of lattice matched $InGaAs$ on InP with interface roughness of $0\mathring{A}$ and $10\mathring{A}$. The reflectivity gradient is unaffected but the interface fringes due to the layer become progressively damped with increasing angle. This is shown for a range of roughnesses in figure 7.9 with the intensity scale of each curve shifted for clarity. The fringe spacing

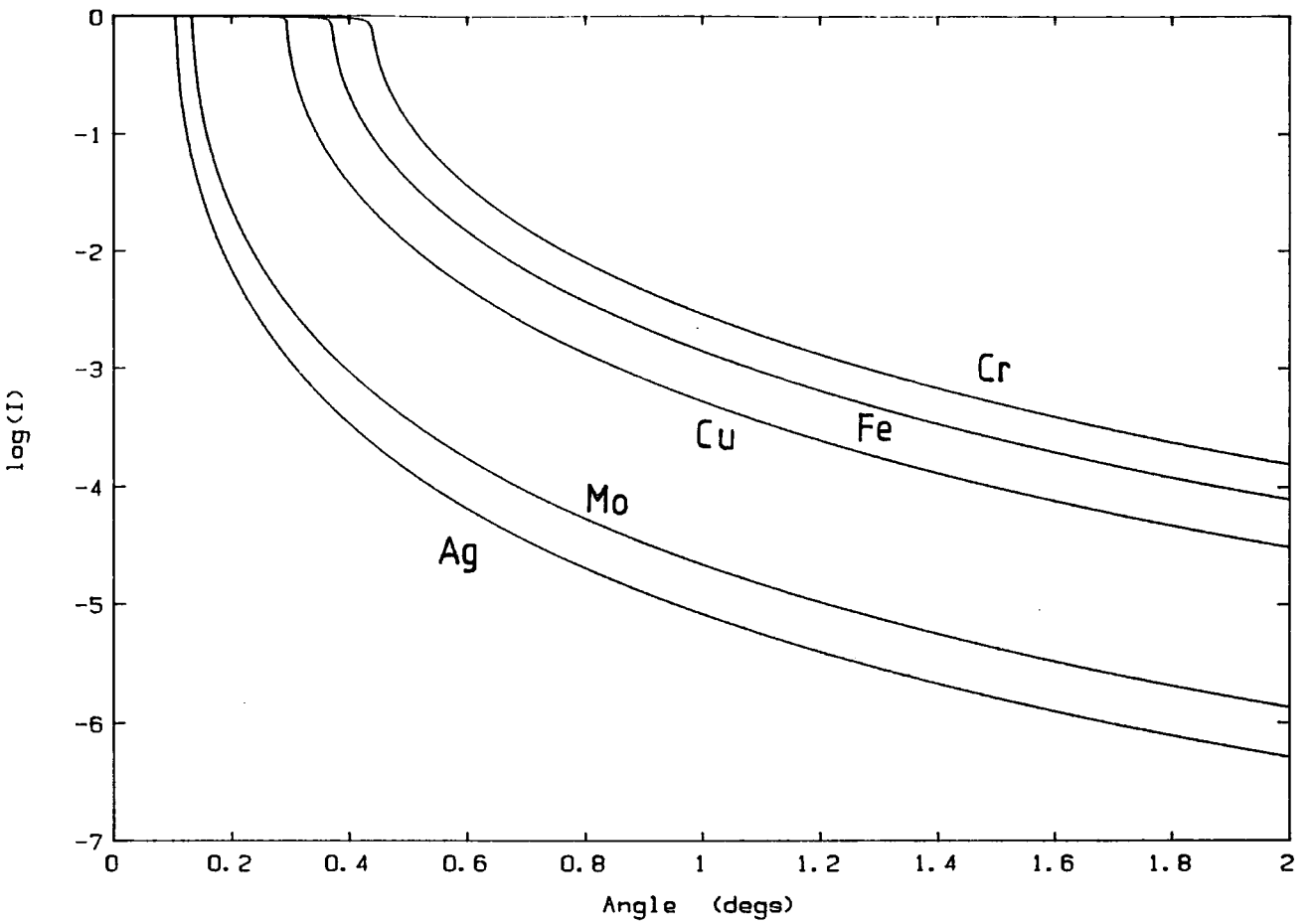

Figure 7.5: Angular reflectivity of InP for various characteristic $K\alpha$ lines.

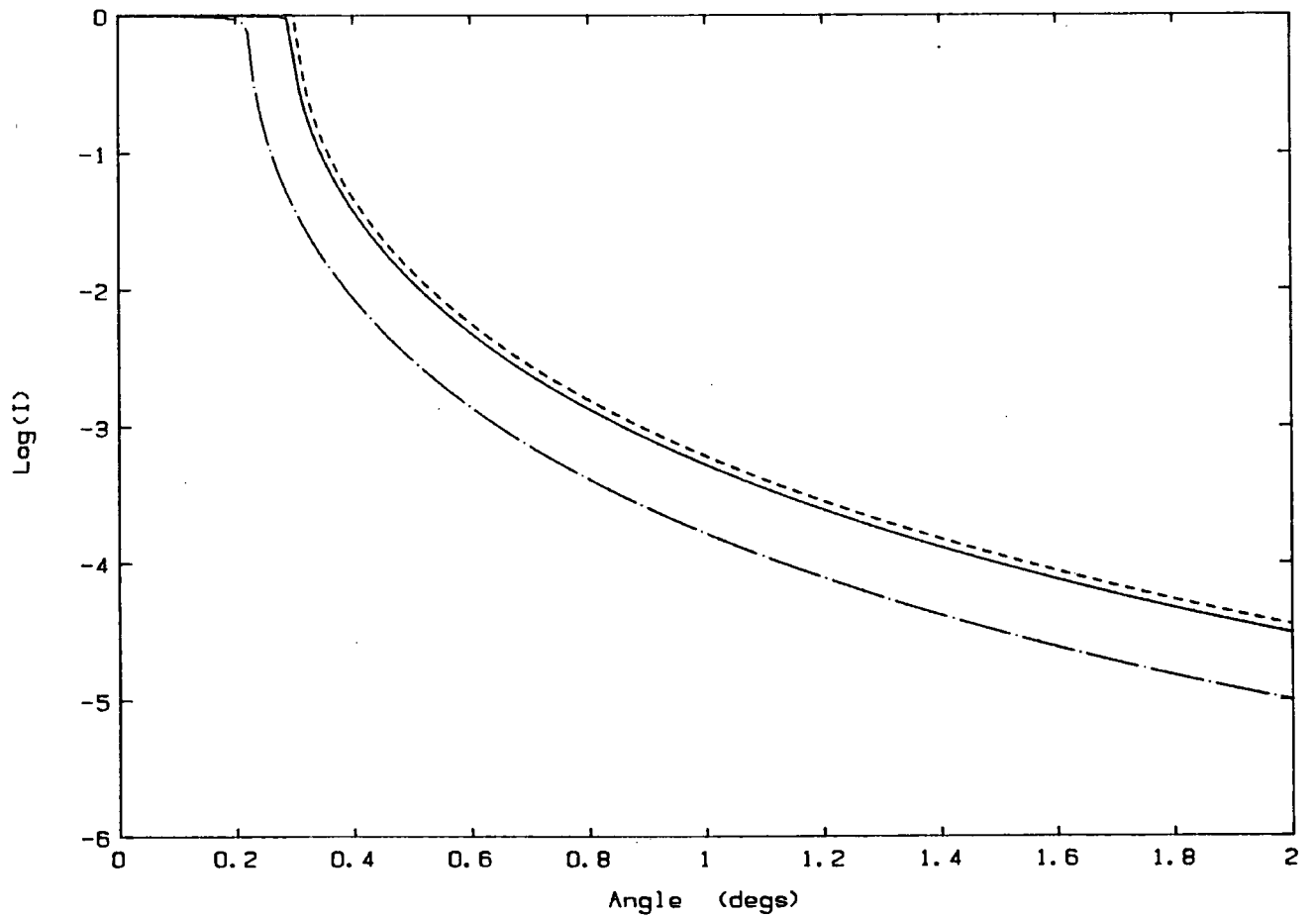

Figure 7.6: Angular reflectivity of InP (solid), $GaAs$ (dashed) and Si (dash-dot) for $CuK\alpha$ radiation.

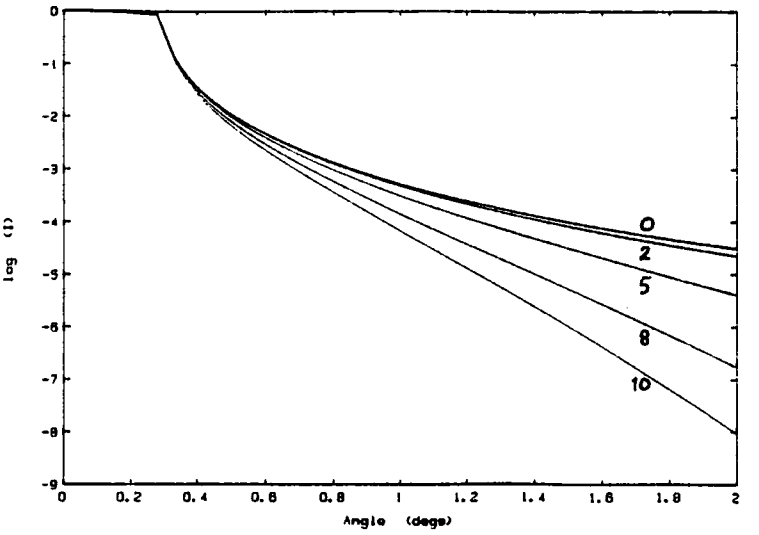

Figure 7.7: The effect of surface roughness on the angular reflectivity of InP for $CuK\alpha$ radiation. The RMS roughness is shown in Ångstroms.

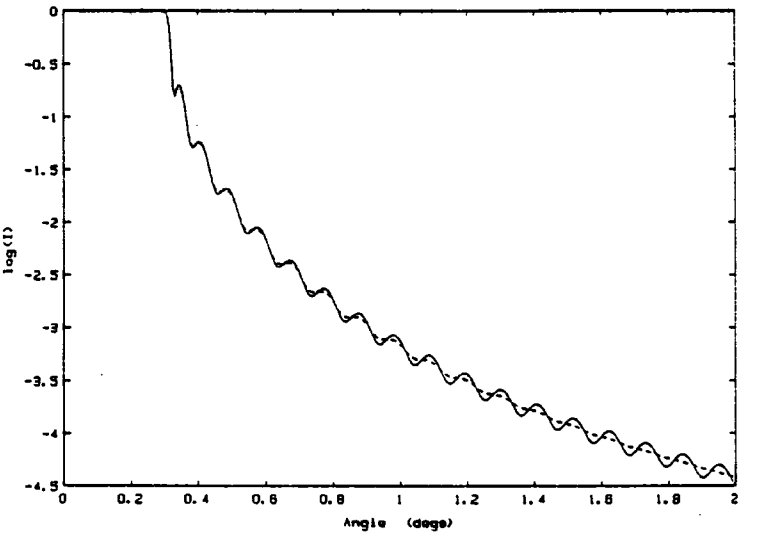

Figure 7.8: Angular reflectivity of a 400$\AA$ layer of lattice matched $InGaAs$ on InP for interface roughnesses of 0$\AA$ (solid) and 10$\AA$ (dashed) with $CuK\alpha$ radiation.

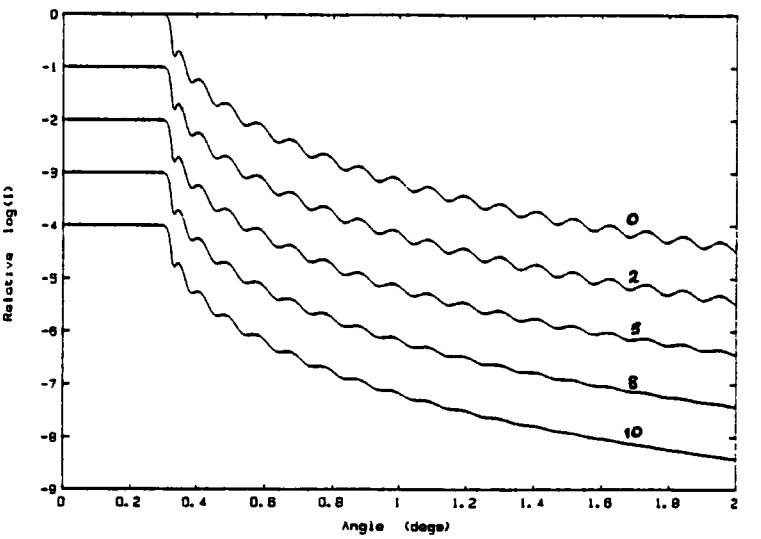

Figure 7.9: Angular reflectivity of a 400$\AA$ layer of lattice matched $InGaAs$ on InP for a range of interface roughnesses (in Ångstroms) with $CuK\alpha$ radiation. The Intensity axes are shifted for clarity.

and reflectivity gradient are unaffected but the damping increases with increasing roughness. It should therefore be possible to separate the effects of surface roughness and internal interface roughness in experimental reflectivity curves.

The frequency of the fringes seen in figure 7.9 is directly related to the thickness of the layer. Figure 7.10 shows the reflectivity at 1.54Å for a lattice matched $InGaAs$ layer on InP for a range of thicknesses. The fringes arise because the electron density of the layer is different to the substrate, even though the lattice parameters are identical. The relationship between fringe period and layer thickness can be deduced by considering the conditions necessary for constructive interference of X-rays. This is effectively Bragg's law with the layer thickness replacing the lattice spacing. Therefore, for angular reflectivity the fringe period, $\Delta\phi$, is given by

$$\Delta\phi = \frac{\lambda}{2t\cos\phi} \simeq \frac{\lambda}{2t} , \qquad 7.22$$

where t is the layer thickness and ϕ is small. Figure 7.11 illustrates the effect of varying layer composition on the fringe amplitude, for a 200Å thick layer of $AlGaAs$ on $GaAs$ at 1.54Å. As the mismatch increases, and hence the Al percentage, the fringe amplitude increases. The effect is not so marked, however, with 200Å of $InGaAs$ on InP as shown in figure 7.12 for roughly the same percentage compositional change. The difference between these two results arises because the electron density difference varies linearly between $AlAs$ and $GaAs$, whereas at the lattice matched condition of $InGaAs$ with InP there is a large electron density difference, but a relatively large change in mismatch can be obtained with a small relative change in electron density. Hence reflectivity is sensitive to layer mismatch only when there is a corresponding difference in electron density.

The case of multi-layer reflectivity is analagous to that of interference of Pendellösung fringes in the symmetric geometry. Fringes arising from each layer will interfere to form a pattern containing the individual and sum of layer frequencies. Figure 7.13 shows the reflectivity of 400Å of lattice matched $InGaAs$ on InP capped by 150Å of InP. The high frequency fringes correspond to the sum of the layer and cap thickness, and are modulated by the individual layer frequencies.

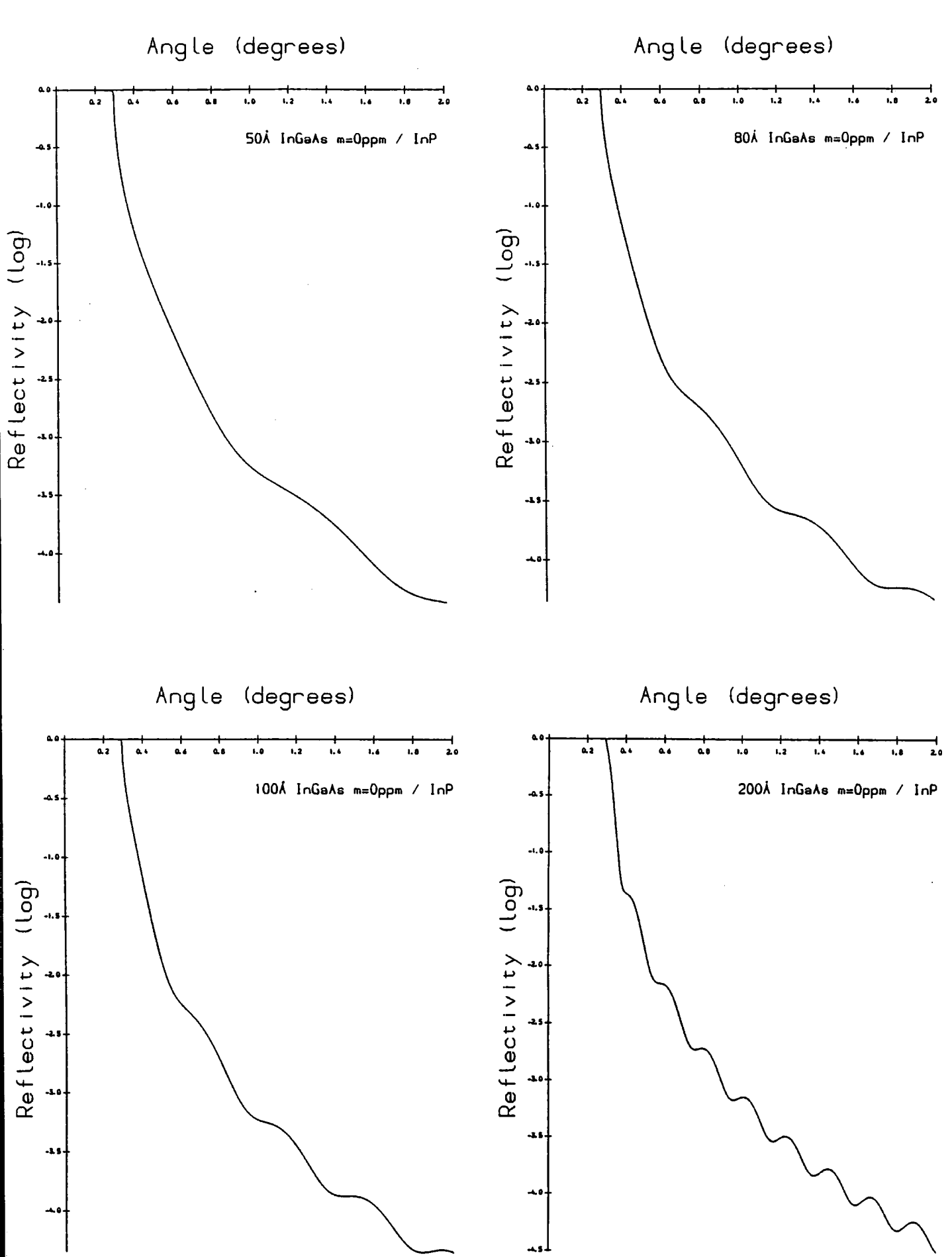

Figure 7.10: Angular reflectivity of a lattice matched $InGaAs$ layer on InP with $CuK\alpha$ radiation for a range of layer thicknesses.

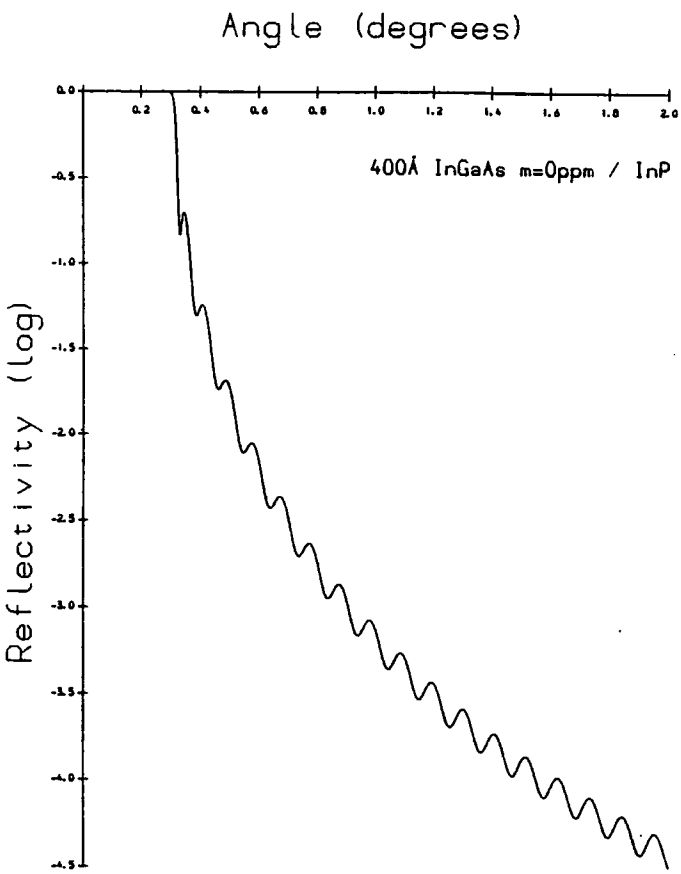
Angle (degrees)
Reflectivity (log)
400Å InGaAs m=0ppm / InP

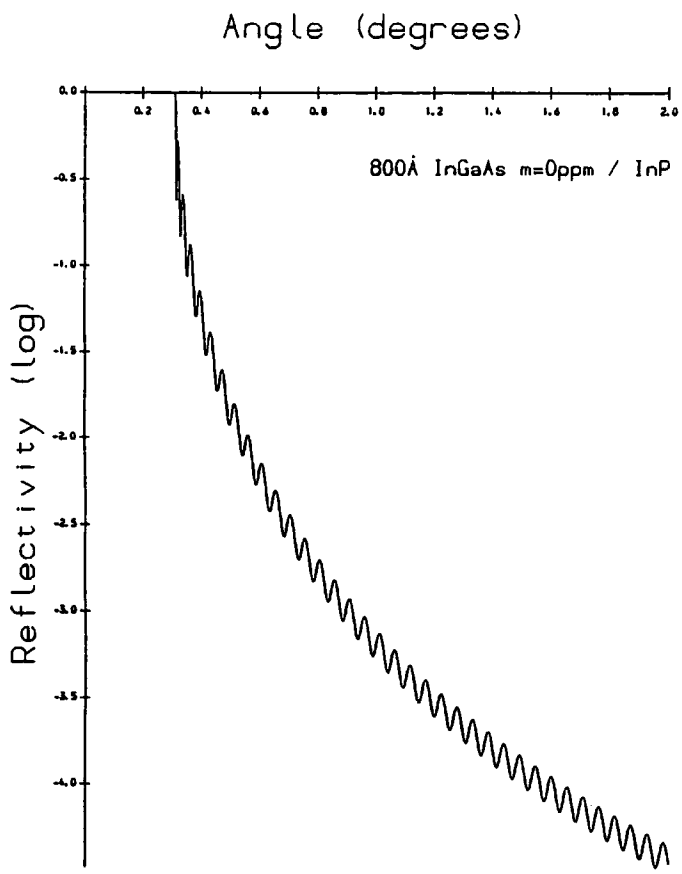
Angle (degrees)
Reflectivity (log)
800Å InGaAs m=0ppm / InP

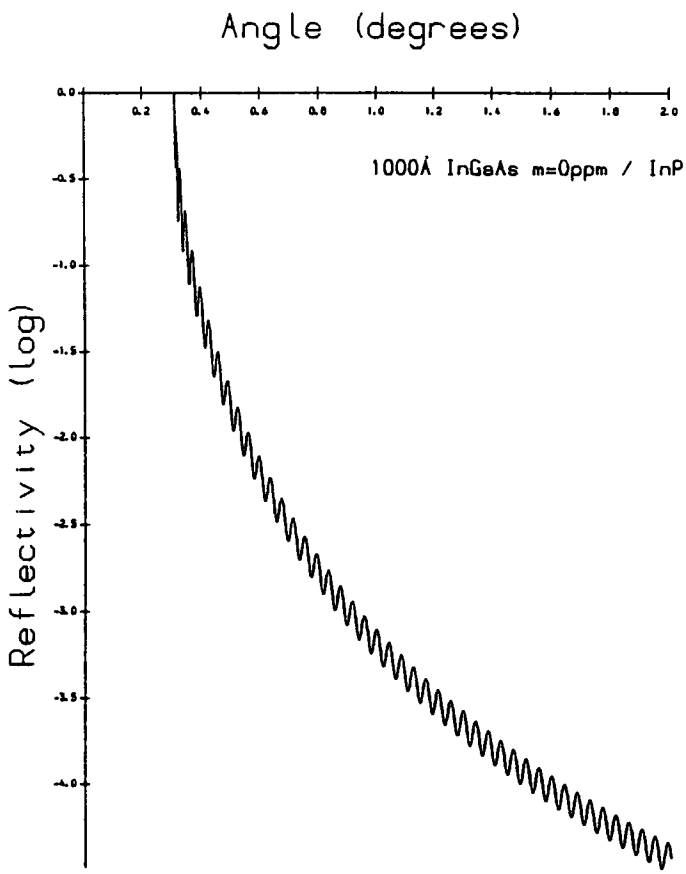
Angle (degrees)
Reflectivity (log)
1000Å InGaAs m=0ppm / InP

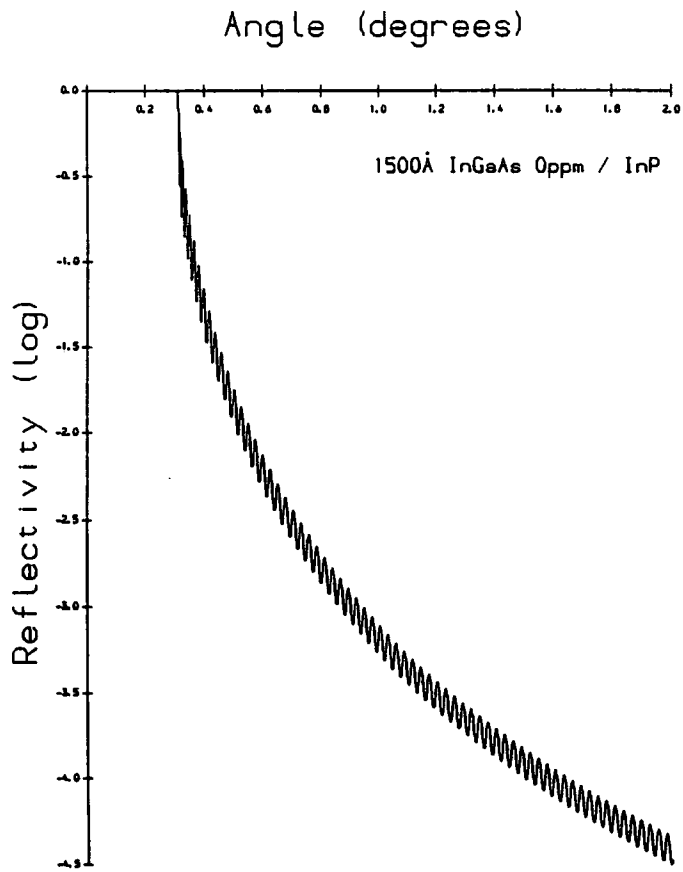
Angle (degrees)
Reflectivity (log)
1500Å InGaAs 0ppm / InP

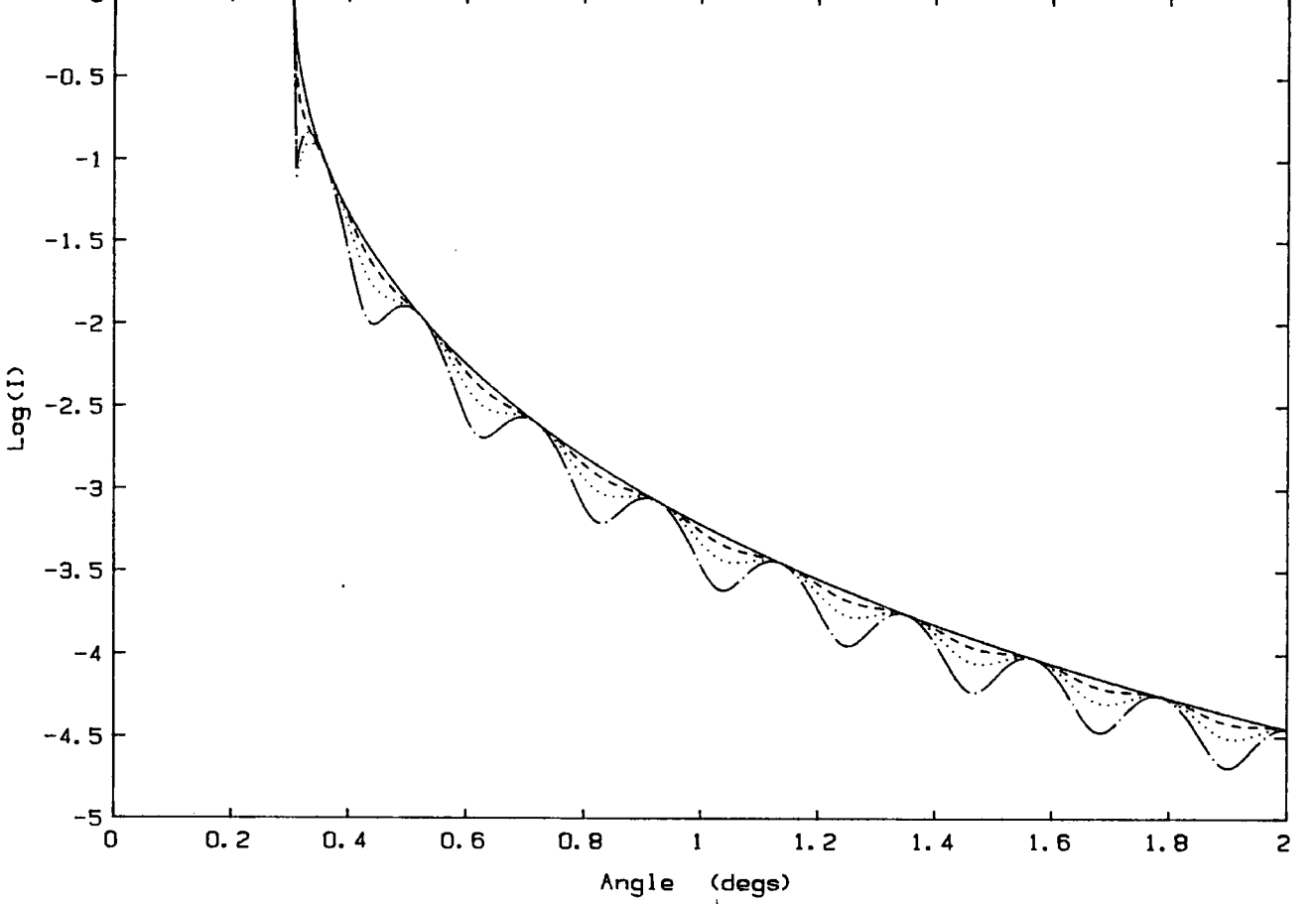

Figure 7.11: Angular reflectivity of a 200$\AA$ layer of $AlGaAs$ on $GaAs$ with a mismatch of 0 (solid), 200 (dashed), 500 (dotted) and 1000ppm (dash-dot) and $CuK\alpha$ radiation.

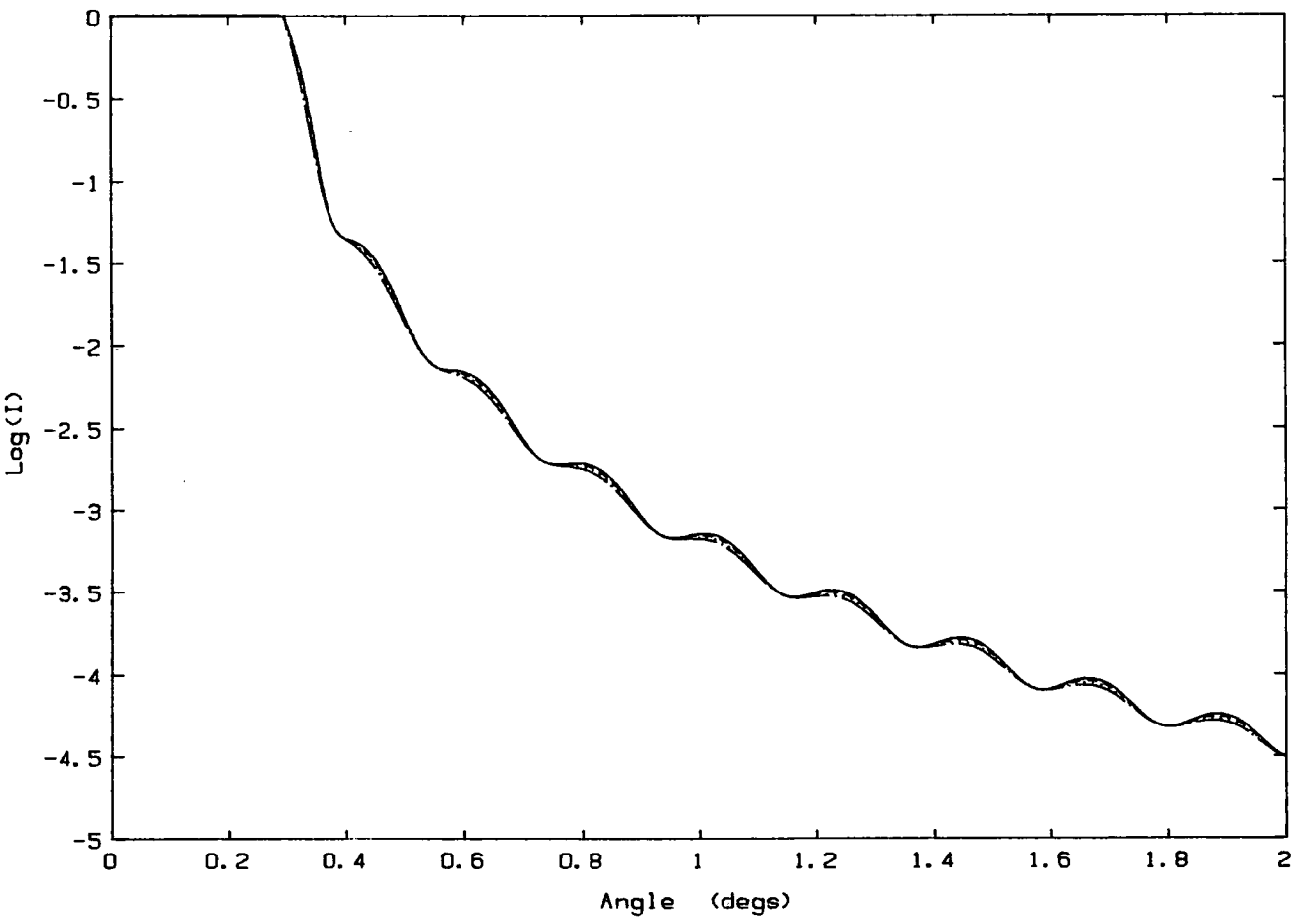

Figure 7.12: Angular reflectivity of a 200$\AA$ layer of $InGaAs$ on InP with a mismatch of 0 (solid), -10000 (dashed), -20000 (dotted) and $-30000ppm$ (dash-dot) and $CuK\alpha$ radiation.

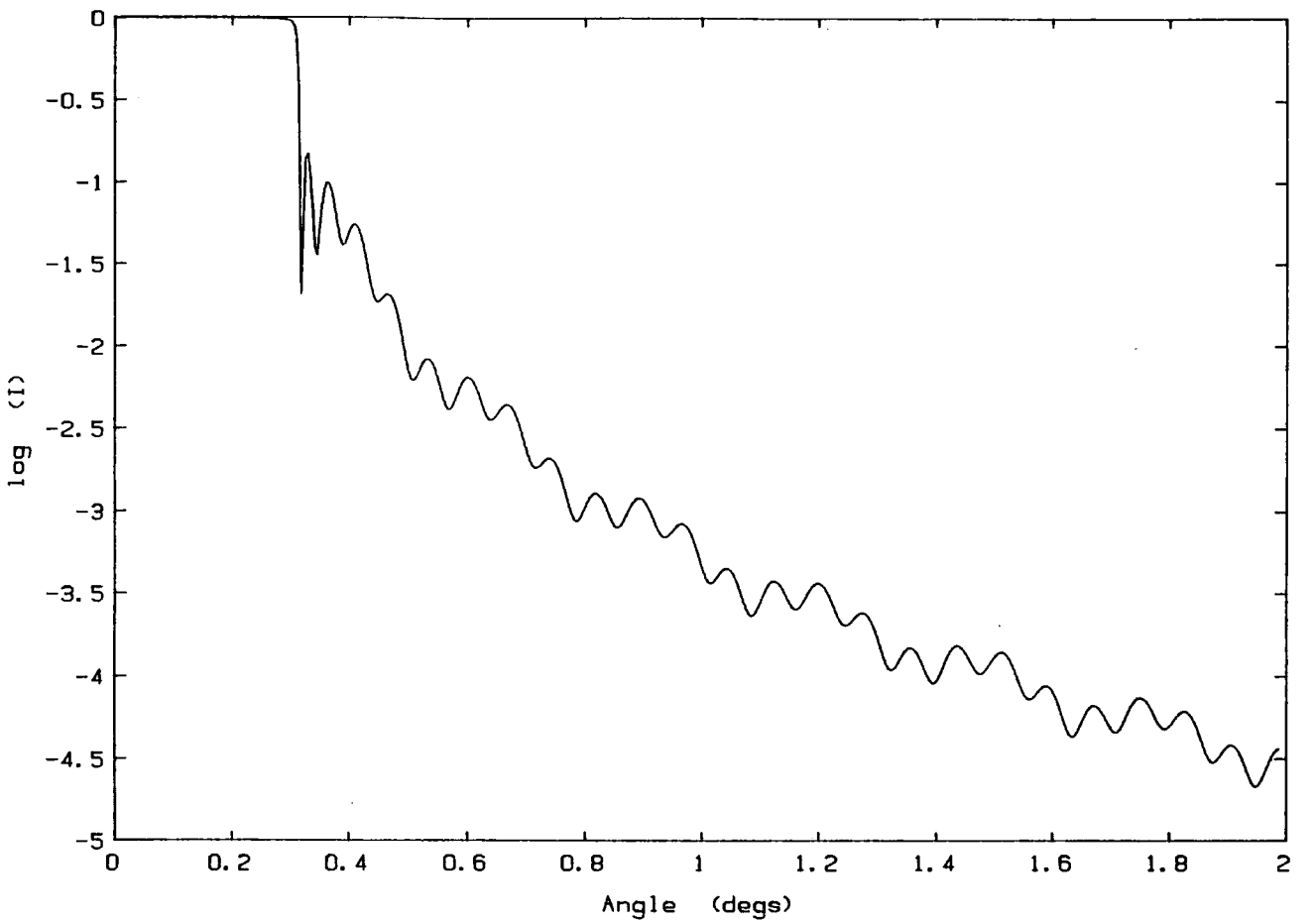

Figure 7.13: Angular reflectivity of a 400$\AA$ layer of lattice matched $InGaAs$ on InP capped by 150$\AA$ of InP with $CuK\alpha$ radiation.

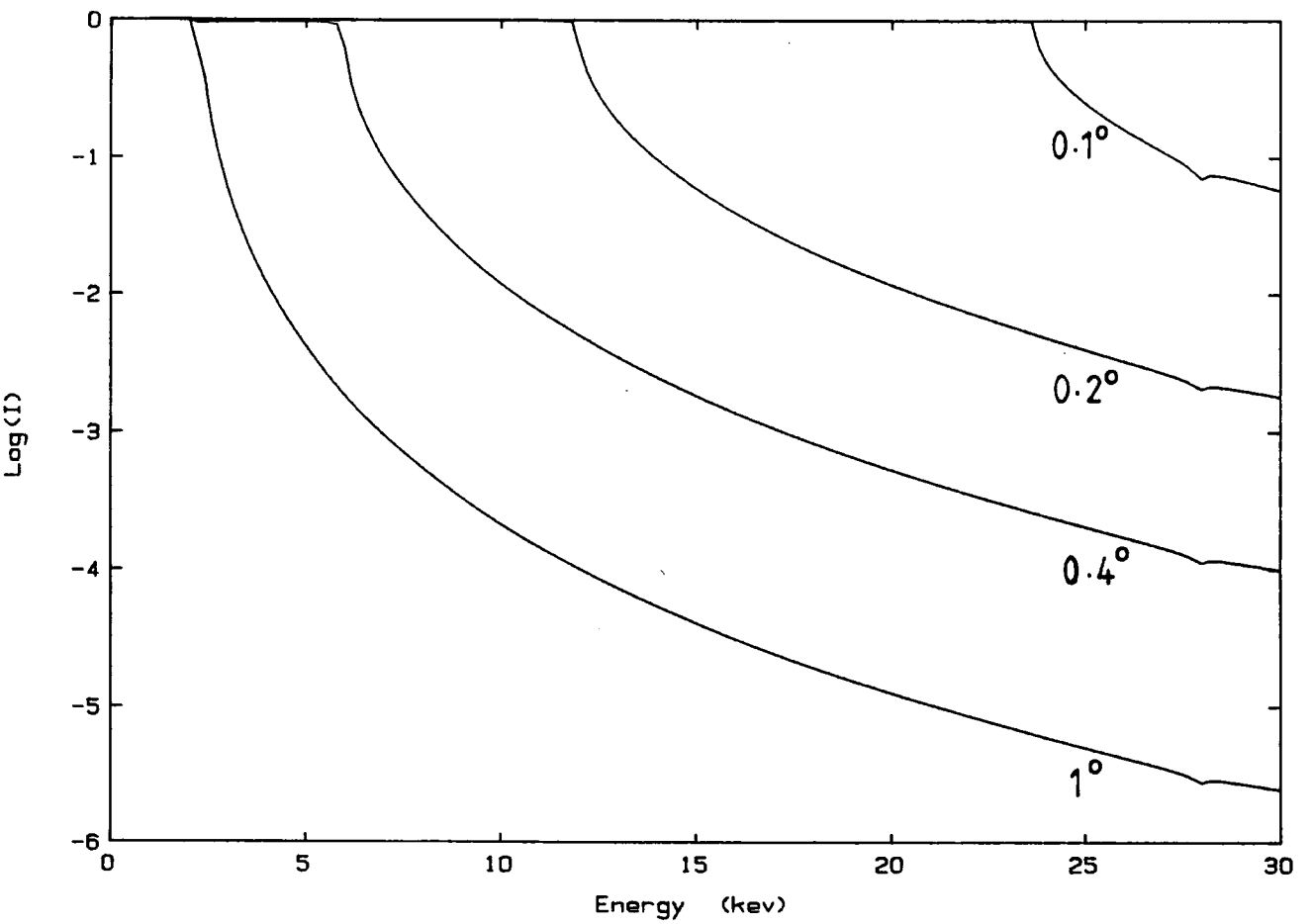

Figure 7.14: Energy dispersive reflectivity of InP for a range of incidence angles.

Fourier analysis may be applied in the same manner explained in Chapter 6 to distinguish between the individual frequencies for multilayer structures.

7.4.2 Energy Dispersive Reflectivity

Energy dispersive reflectivity shows exactly the same behaviour as angular reflectivity, except that energy rather than angle is varied. Figure 7.14 shows the energy reflectivity of InP for various angles of incidence with $CuK\alpha$ radiation. The critical energy increases as the incidence angle becomes smaller but the reflectivity falls off less steeply. It is advantageous therefore, to use a small incidence angle, assuming the X-ray source has enough intensity at higher energies. However, if the incidence angle is too small the experimental set up becomes difficult and the beam spread will be such that intensity may be lost from the beam moving off the sample. In practice, therefore, an angle of incidence between 0.2° and 1° is suitable. The slight dip in the reflectivity at $28keV$ arises from the In K absorption edge at $\lambda = 0.44\mathring{A}$.

Figure 7.15 shows the energy reflectivity for InP, $GaAs$ and Si at 0.5° incidence, with the same trend for the critical energy, given by $E_c = constant\sqrt{\rho}/\phi_c$, as for the critical angle. E_c is therefore proportional to the square root of the reflecting layer density. The kinks on the graph correspond to the K edges of Si at $6.7\mathring{A}$, P at $5.8\mathring{A}$, Ga at $1.2\mathring{A}$, As at $1.0\mathring{A}$ and In at $0.44\mathring{A}$.

The effect of surface roughness on the energy reflectivity at 0.5° incidence for InP is shown in figure 7.16. Again the same trends are found as in angular reflectivity. Figure 7.17 shows the energy reflectivity at 0.5° incidence for a lattice matched $InGaAs$ layer on InP for a range of thicknesses. The relationship between fringe period and layer thickness is given by

$$\Delta E = \frac{hc}{2t\sin\phi} \simeq \frac{hc}{2t\phi} \,. \qquad 7.23$$

Reflectivity is additionally very sensitive to thin buried layers as is shown in figure 7.18, which is the energy reflectivity of a thin, $100\mathring{A}$, quaternary layer with $m = -1000ppm$ on InP capped by $0.1\mu m$ of InP.

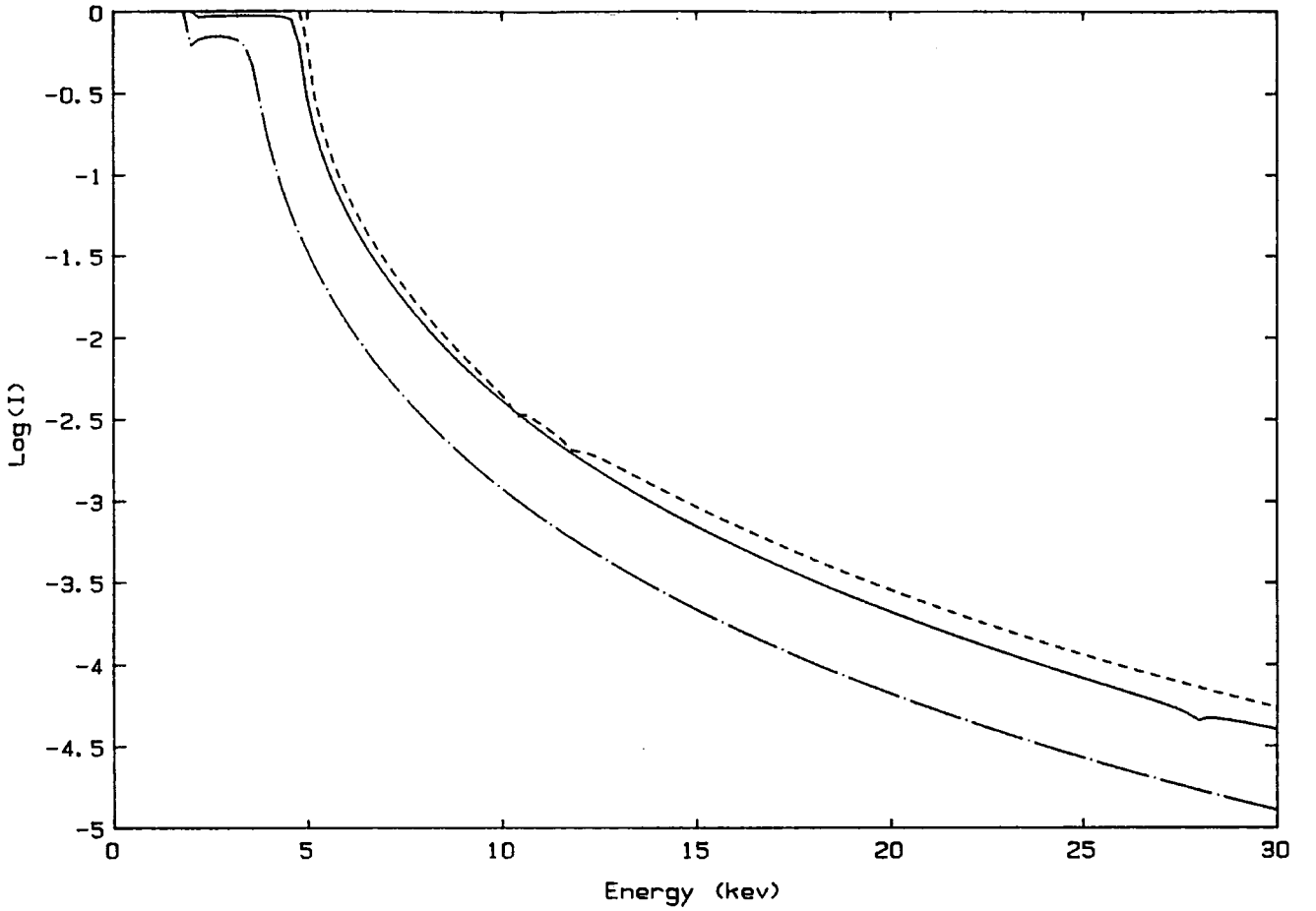

Figure 7.15: Energy dispersive reflectivity of InP (solid), $GaAs$ (dashed) and Si (dash-dot) at 0.5° incidence.

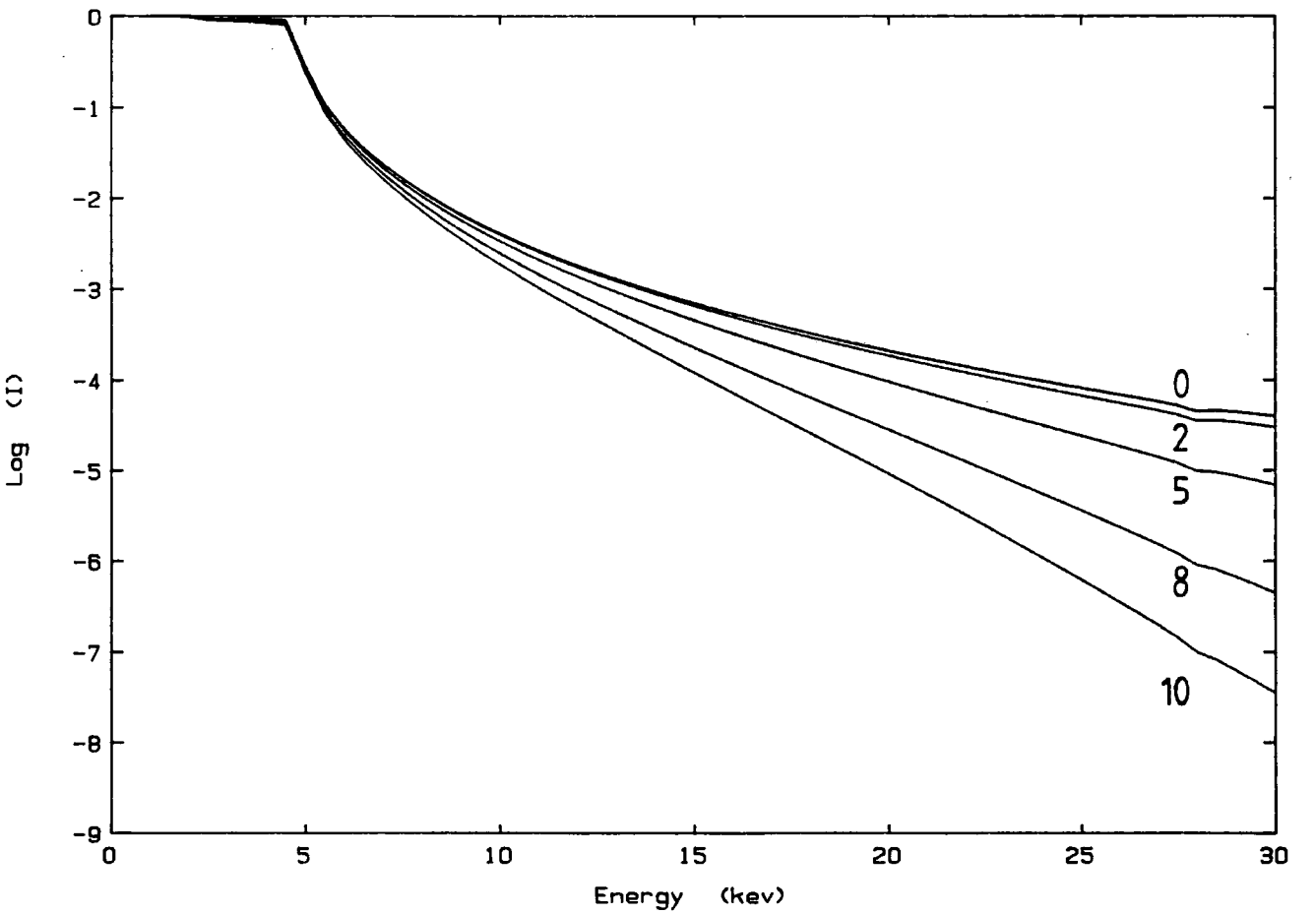

Figure 7.16: Energy dispersive reflectivity of InP for a range of surface rougnesses in Ångstroms at 0.5° incidence.

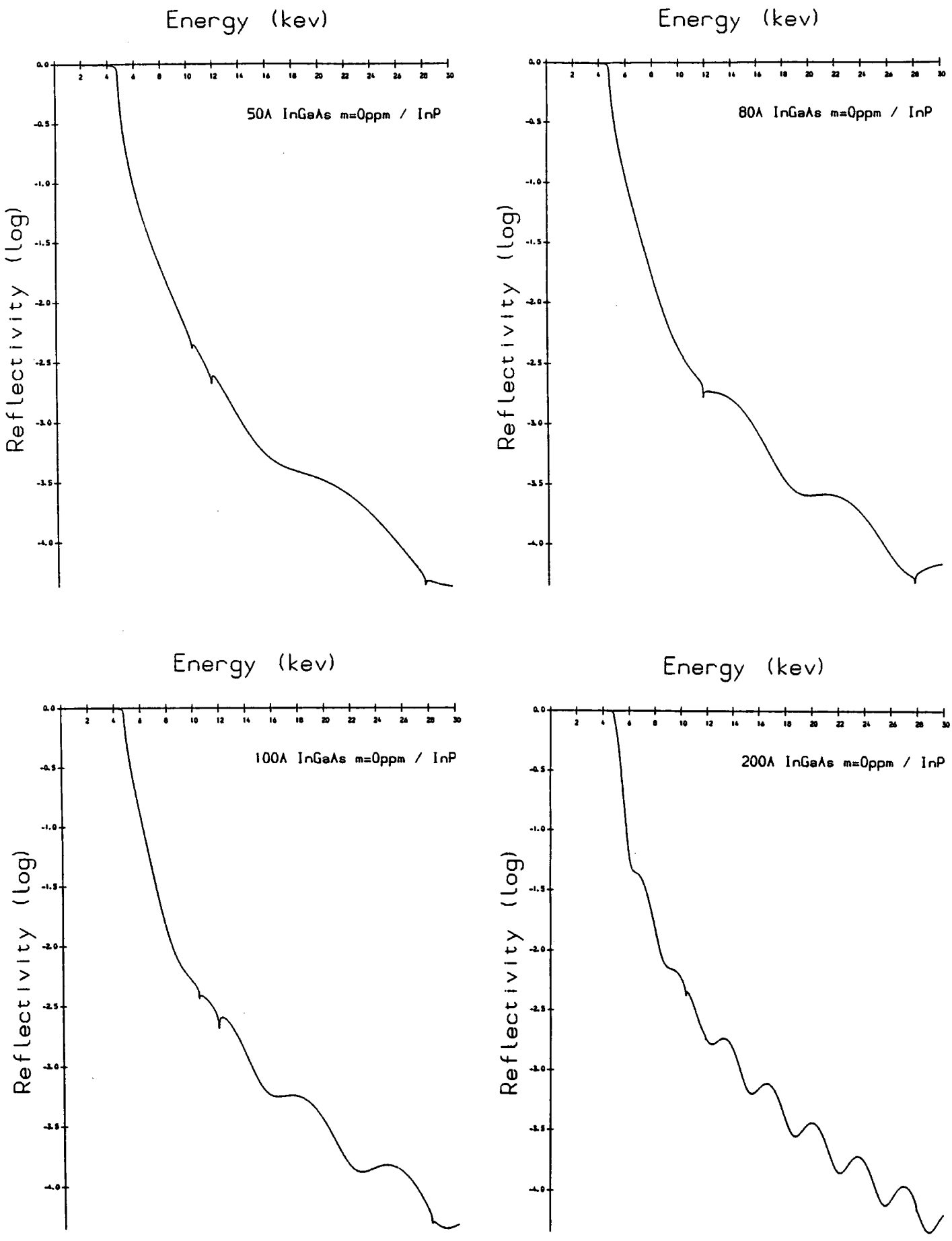

Figure 7.17: Energy dispersive reflectivity of a lattice matched *InGaAs* layer on *InP* with 0.5° incidence for a range of layer thicknesses.

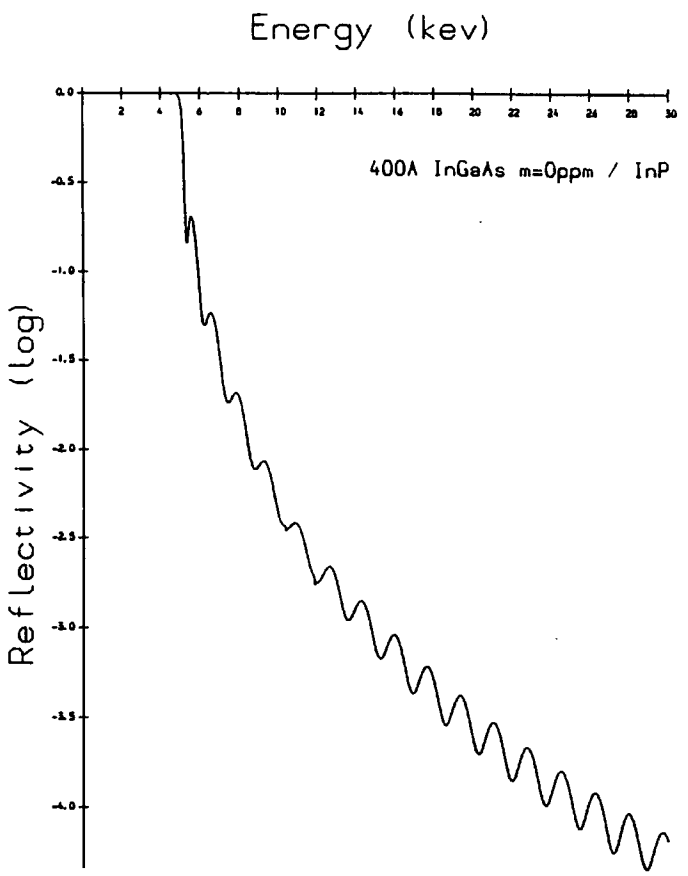
Energy (kev)
400A InGaAs m=0ppm / InP
Reflectivity (log)

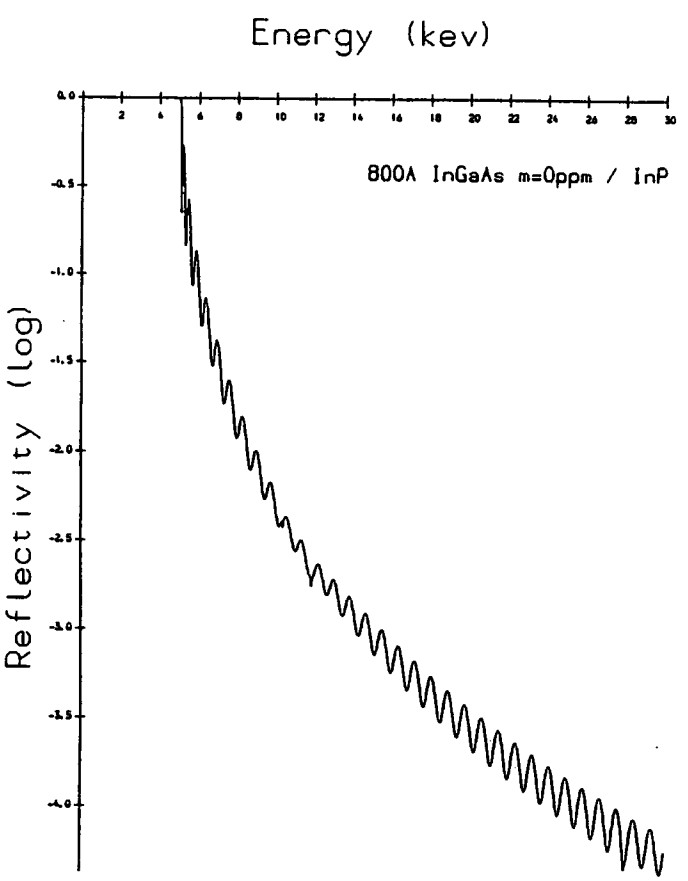
Energy (kev)
800A InGaAs m=0ppm / InP
Reflectivity (log)

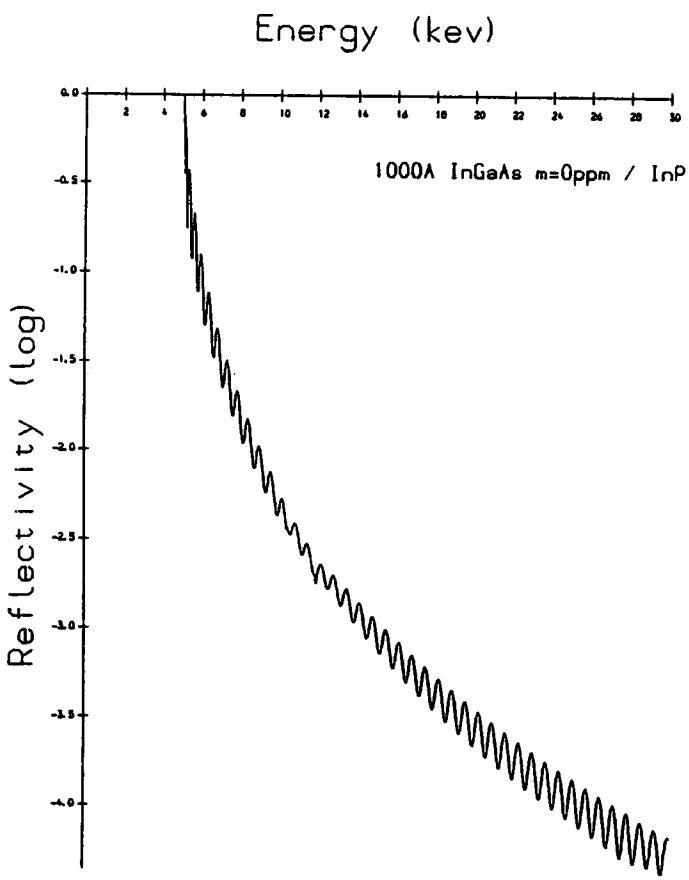
Energy (kev)
1000A InGaAs m=0ppm / InP
Reflectivity (log)

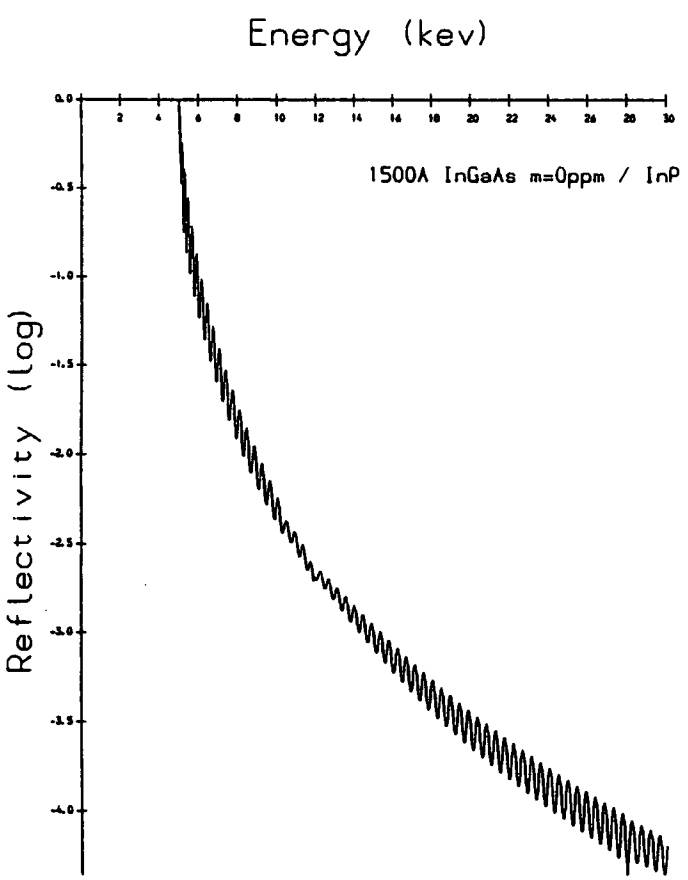
Energy (kev)
1500A InGaAs m=0ppm / InP
Reflectivity (log)

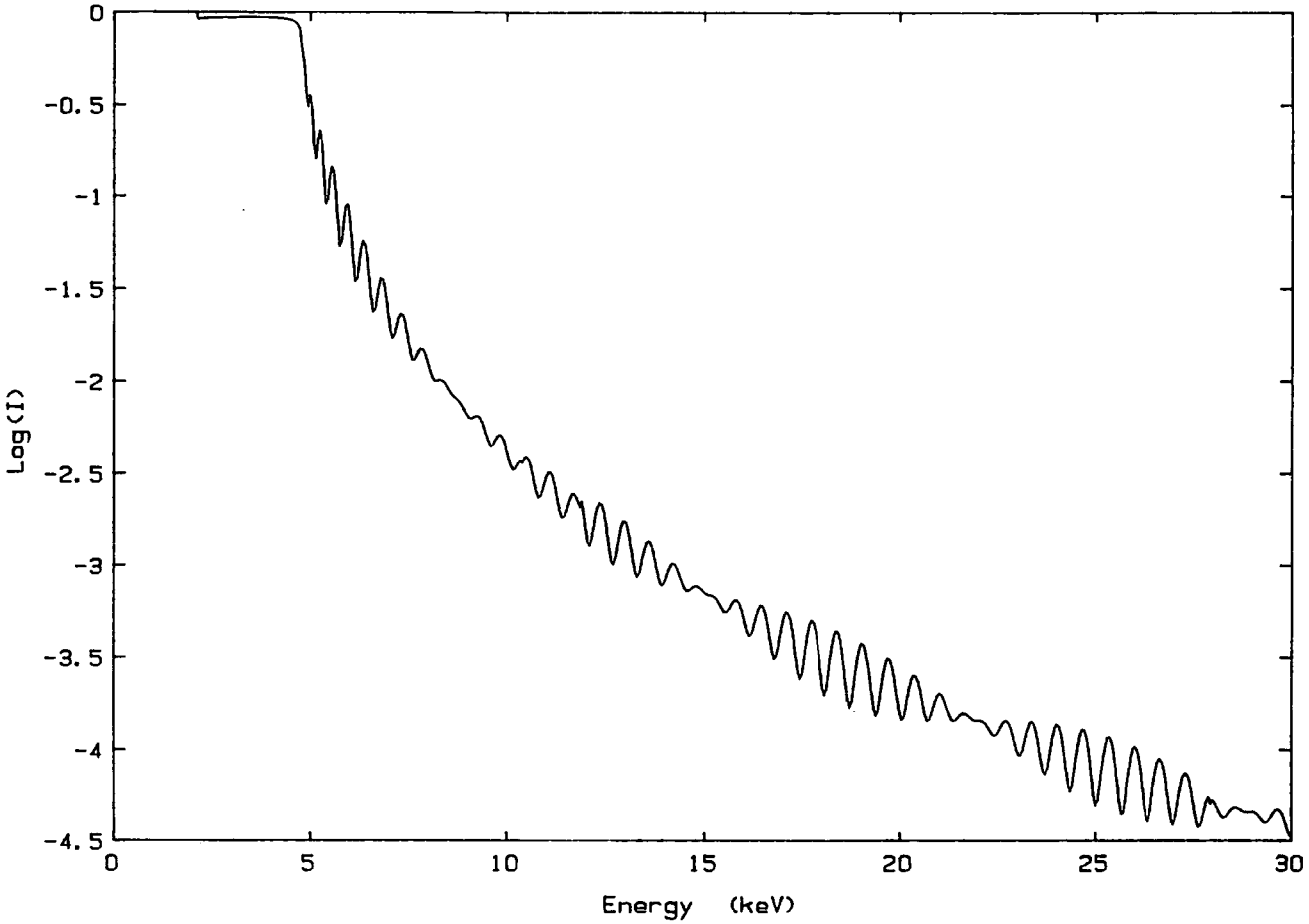

Figure 7.18: Energy dispersive reflectivity of a 100$\mathring{A}$ layer of $InGaAsP$ (1.35μm), mismatch $-1000ppm$ on InP capped with a 0.1μm thick layer of InP at 0.5° incidence.

7.5 X-ray Reflectivity of Thin Epilayers

7.5.1 Double Crystal Reflectivity

Double Crystal Reflectivity (DCR) experiments were performed at Durham University and British Telecom on model 150 and model 300 Bede diffractometers, respectively. Initial work occurred in Durham using an 044 first crystal reflection from (011) InP. A slit was used in between the first and second crystals to reduce background and limit the incident beam size but the detector aperture was not limited. The sample used was INP2. Figure 7.19(a) shows the resulting reflected intensity as a function of incidence angle using a $100''$ step size and 30 second counting time. The peak corresponds to total external reflection; the critical angle for InP being approximately $0.3°$ at $1.54\mathring{A}$ wavelength. The plot shows a poor signal to noise ratio of only 25 : 1 and a large background hump centred at half a degree above the critical angle, which probably arises from direct beam contamination. It was evident that a slit was required over the detector to accurately define the acceptance angle of the reflected beam.

At British Telecom the experiment was repeated using an 004 reflection InP first crystal with a $1mm$ slit over the detector. The sample used here, code INP4, was a single thin layer of $GaInAs$, nominal thickness $400\mathring{A}$ on InP grown by MBE. Great care was taken in the initial alignment of the sample so that at zero incidence angle the sample physically intercepted half of the X-ray beam. This was achieved by a combination of sample translation in and out of the beam, using a Bede X-Y translation stage, and rocking the sample in angle. Figure 7.19(b) shows the resultant reflectivity curve with a $54''$ step size and a count time of 650 seconds. The signal to noise ratio has significantly improved to greater than 10^3 and the background hump has disappeared but there are no sign of any fringes.

The experimental set up is evidently vitally important if interference fringes from the layer are to be observed. As the incidence angles are so small there is a problem with background contamination from the straight through beam since the beam is of finite width and will not be entirely intercepted by the sample at very low angles. Additionally, sample curvature has a substantial degrading effect at very low angles which will tend to wash out any interference fringes. It

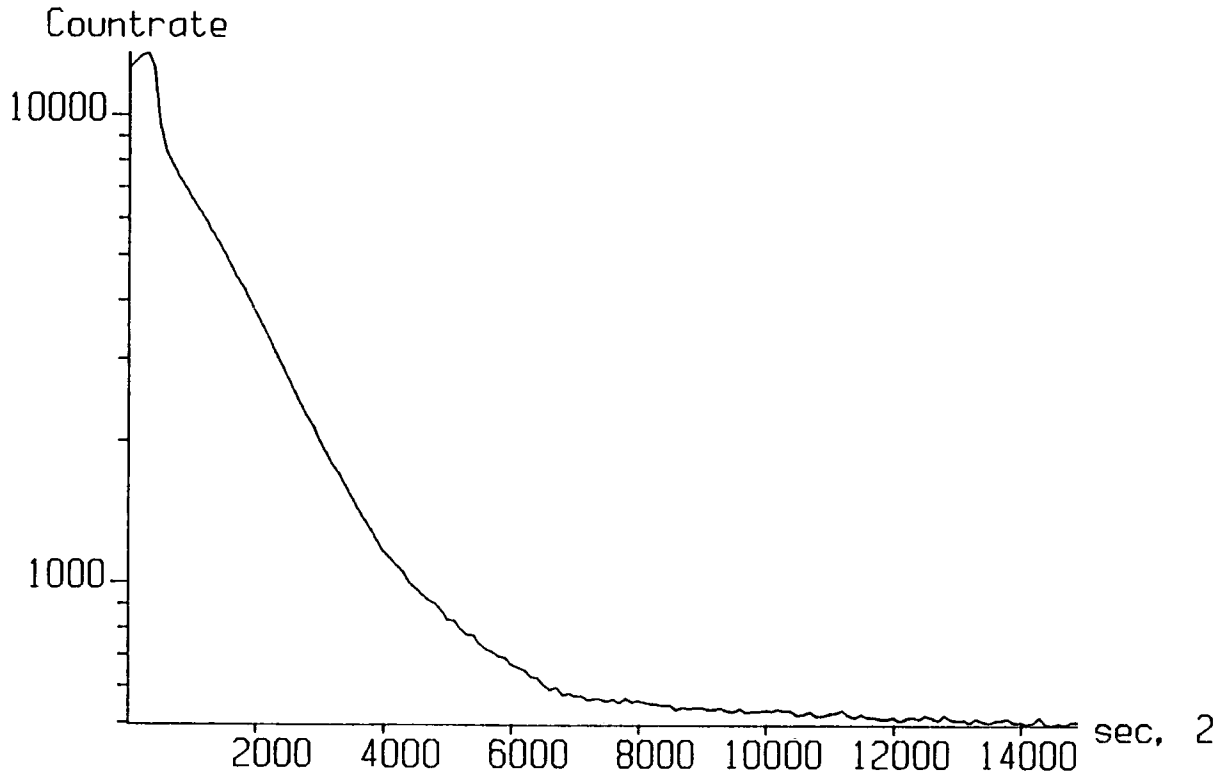

Figure 7.19(a): Double crystal reflectivity of sample INP2 with no detector slit.

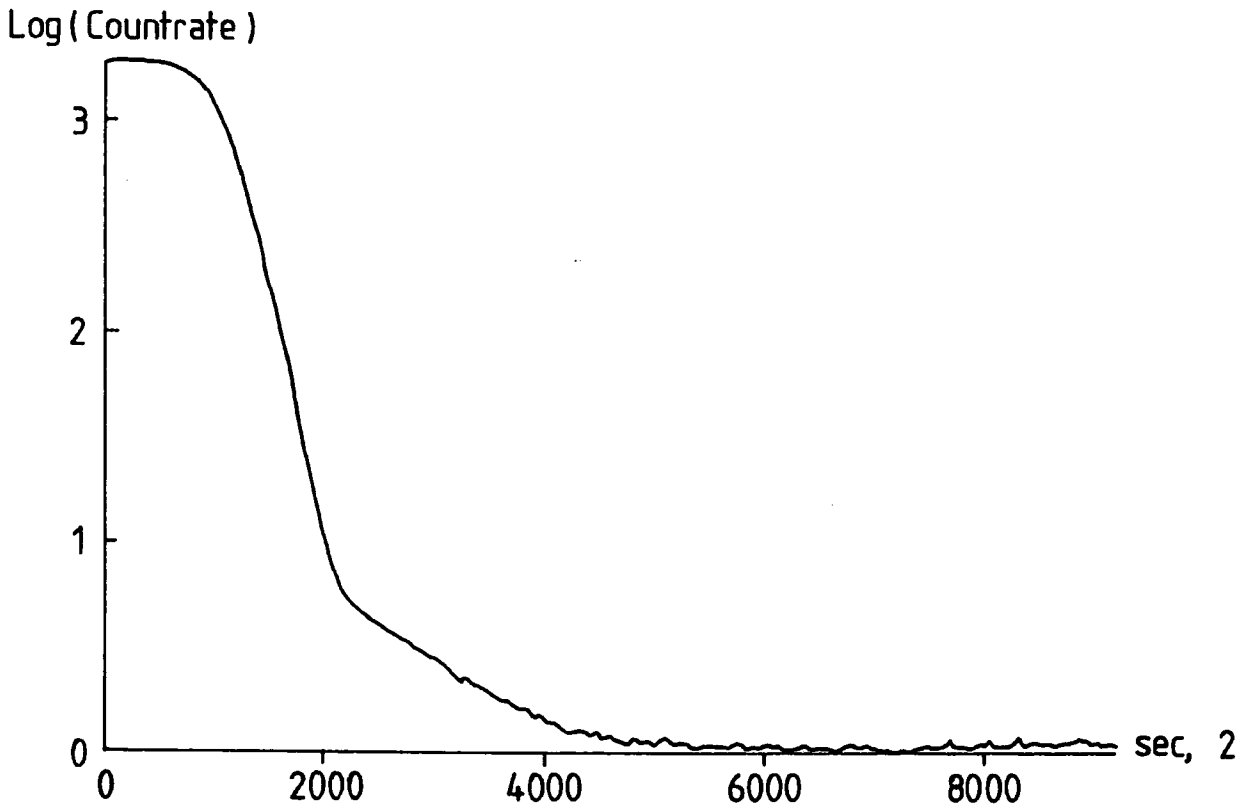

Figure 7.19(b): Double crystal reflectivity of sample INP4 with a $1mm$ detector slit.

was therefore necessary to reduce the slit width to $0.1mm$ and move the sample and detector in a θ-2θ scan. Unfortunately, because the slit was so narrow the reflected beam tended to be lost by simply rotating the detector by twice the sample angle. This was probably due to either some detector or sample misalignment. However, by scanning the detector over a small angular range centred on the 2θ position a peak intensity could be found and measured. The counting time for each detector step of $0.01°$ was up to 300 seconds for the higher sample angle positions. The sample was rotated in steps of $100''$ and a scintillation counter was used to record the reflected intensity. The time for the whole scan of $2300''$ was 48 hours, with the background measured at a relatively high angle over a time of 20 minutes. Figure 7.20 shows the resultant reflectivity data after background subtraction. When an error bar is not indicated the error is contained within the size of the spot. The line drawn through the points is the best fit simulated curve to the data found by minimising the sums of the differences squared, which corresponds to a layer thickness of $362 \pm 10\mathring{A}$. A mismatch of $-500ppm$ based on previous growth data was assumed for the $InGaAs$ layer as the reflectivity was not sensitive to small changes in composition. No surface roughness was necessary to yield a good fit although an interface roughness of $\sigma = 10 \pm 5\mathring{A}$ was used to reduce the fringe amplitude to that of the experimental data. Unfortunately, the error bars are relatively large and the number of points relatively few for a closer fit to be attained. The reflected intensity for total reflection was only 200 counts per second and so very large counting times were required to achieve even these statistics. The fine slit over the detector is necessary however, because of sample curvature. The fact that the beam tended to move off the slit in the simple θ-2θ scan necessitated scanning the detector over a small range containing the 2θ position. If the sample orientation and detector position had been set precisely then this would not have been required and much time could have been saved. Additionally the X-ray tube at British Telecom was nearing the end of its lifetime and had to be run on half power. The use of a good tube together with a proportional counter would have significantly reduced the total data collection time. It is therefore perfectly feasible to use a standard double crystal diffractometer for X-ray reflectivity providing care is taken over the experimental set up.

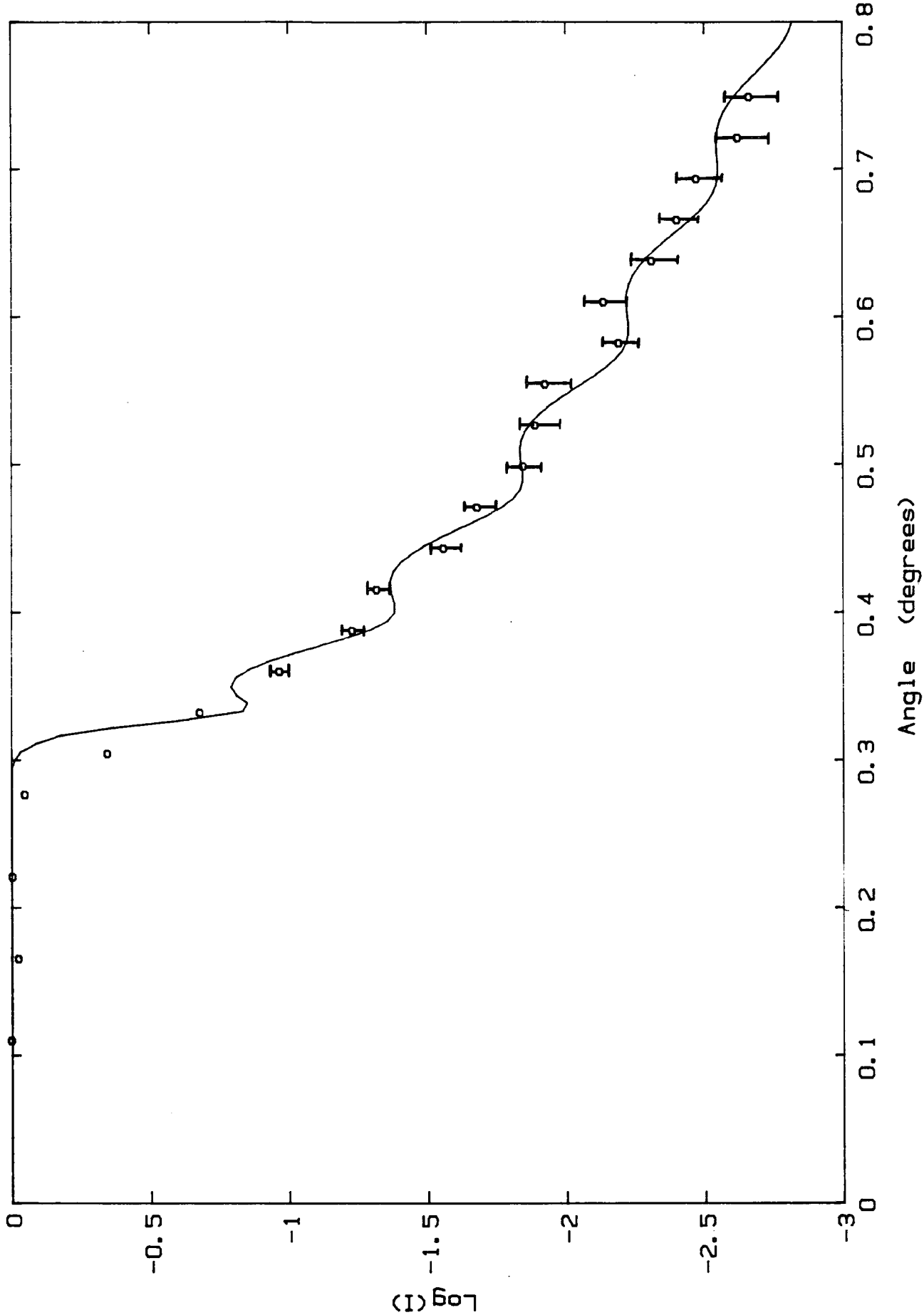

Figure 7.20: Double crystal reflectivity of sample INP4 with a $0.1mm$ detector slit. The circles show the experimental data and the solid line is the best fit simulated curve.

7.5.2 Triple Crystal Reflectivity

The advantage of Triple Crystal Reflectivity (TCR) over DCR is the removal of the effects of sample curvature with the analyser crystal. Rather than using a very fine slit over the detector which reduces the intensity, a third crystal permits angular rather than spatial collimation. The background can also be significantly reduced as the detector is no longer in line with the direct beam from the first crystal.

Experiments were performed at Edinburgh University on sample INP2 (Lucas et al., 1988) using the triple crystal diffractometer described in section 7.2. The reflectivity was recorded over a 2° scan range with a typical data collection time of 24 hours. It was convenient to express the data in terms of a function $T = I\phi^4$, since the general form of the reflectivity is that of a $1/\phi^4$ curve. This arises because, neglecting absorption, $f_n = (\phi^2 - \phi_c^2)^{\frac{1}{2}}$, and for $\phi \gg \phi_c$ we have

$$F_{n-1,n} = \frac{\phi_c^2(n) - \phi_c^2(n-1)}{4\phi^2} \ ,$$

so that the reflected intensity is proportional to $1/\phi^4$. The gradient of the T vs ϕ graph is then only determined by the surface roughness. Figure 7.21 shows this representation of the reflectivity data of INP2 on a logarithmic scale. Fringes arising from the total layer thickness are clearly seen, and the pattern is modulated by a larger period, corresponding to reflection from the thin surface layer. The curve drawn through the points is a least squares fit of Parratt theory by the Edinburgh group. The parameters used to obtain the fit are given in Table 7.2, where σ is the RMS roughness and $\Delta\rho_i/\rho$ the fractional difference in density of the i^{th} layer from the substrate, and this is represented in figure 7.22. Two thin surface layers, in addition to the 210$\AA$ of $AlInAs$ (layer 1) are required to produce the fit. Layer 2 corresponds to the $GaAs$ capping layer of thickness 30$\AA$ and there is an additional surface layer (layer 3) with a very low electron density. Reflectance infrared spectroscopic measurements performed at Edinburgh showed complex absorption features corresponding to OH vibrations near the surface. This indicates a thin layer of surface contaminants. During earlier work investigating contaminant layers on Si/SiO_2 wafers by the Edinburgh group, it

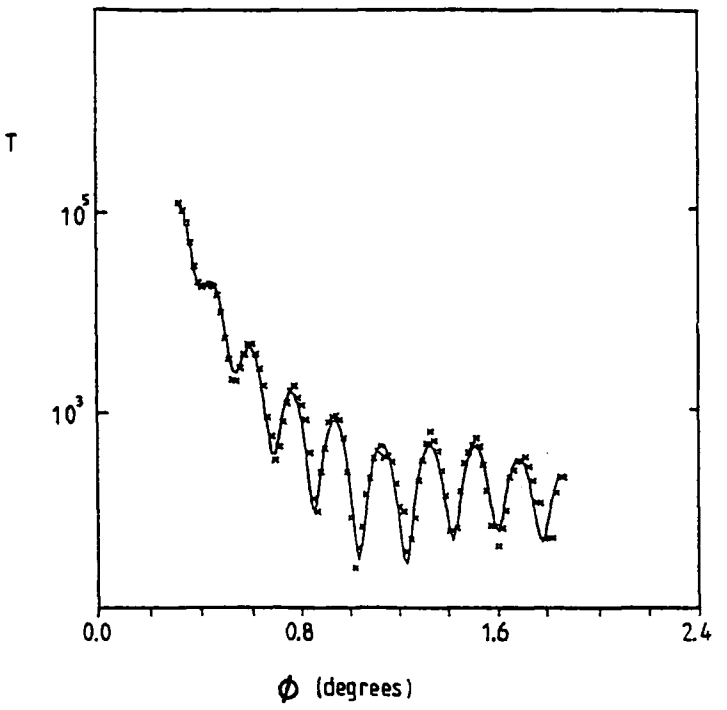

Figure 7.21: Triple crystal reflectivity of sample INP2 shown in the form of a $T = I\phi^4$ vs ϕ curve. The solid line is a least squares fit to the experimental data by the Edinburgh group using Parratt theory.

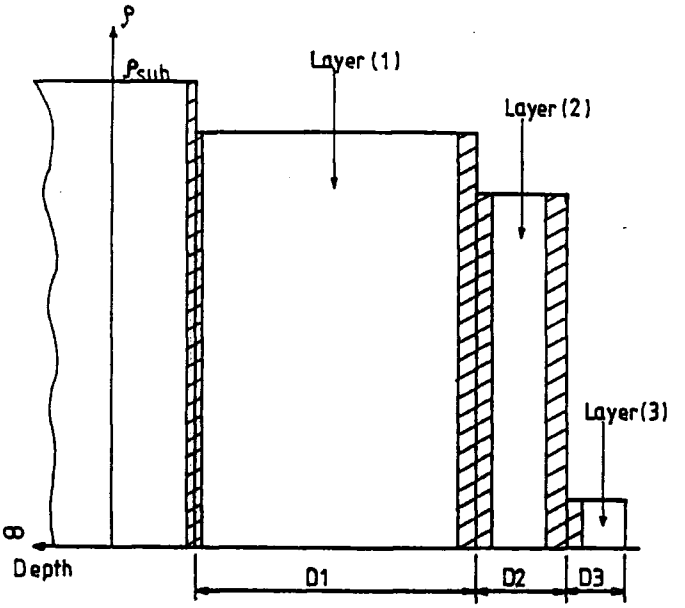

Figure 7.22: The electron density profile used for the calculated fit of figure 7.21.

was discovered that baking of the wafer reduced the contamination to a level at which its effect on the X-ray reflectivity measurements is negligible. The sample was therefore heated in a vacuum oven at $200°C$ for 2 hours before repeating the X-ray reflectivity and infrared measurements. The new reflectivity data is shown in figure 7.23. The parameters used to describe the fit are given in Table 7.3 and the electron density profile is represented in figure 7.24. They are significantly different from those used to describe the original data as the $AlInAs$ layer has decreased in thickness to $197\mathring{A}$, resulting in a proportional increase of layer 2. Considerable roughening of the interface between these layers indicates transfer across the boundary and it is concluded that the heating of the sample reduced oxidation in the $AlInAs$ layer. The roughness in effect represents compositional grading at the interface as the two effects are indistinguishable to X-rays. The roughness of layer 3 was not altered by the heating process and the repeated infrared measurements again indicate the presence of surface contaminants. This manifestation of surface roughness as a low-density surface layer, has also been observed in X-ray reflection studies of metal films (Smirnov, Sotnikov, Anokhin and Taibin, 1979; Smirnov and Anakhin, 1980). A perfect fit to the reflectivity data was impossible to obtain and this may have been due to the inability of the model to account for graded electron density layers. It should be noted that the Edinburgh model neglects the imaginary part of the refractive index which accounts for absorption, and so fitting of parameters to the accuracy quoted is optimistic. In addition, the number of variables to be fitted is too high for a singular solution to be reached and it is therefore necessary to reduce the number of degrees of freedom by use of other techniques. The results obtained from the reflectivity data however, show good agreement with the triple crystal diffraction results of sample INP2. The diffraction measurements are sensitive only to crystalline components of the sample and can be used to measure lattice parameter strain accurately as well as layer thickness. The reflectivity measurements are also sensitive to amorphous layers and so can reveal the presence of oxide or contaminant layers with thicknesses down to $10\mathring{A}$. The two techniques therefore provide complementary information on sample structure.

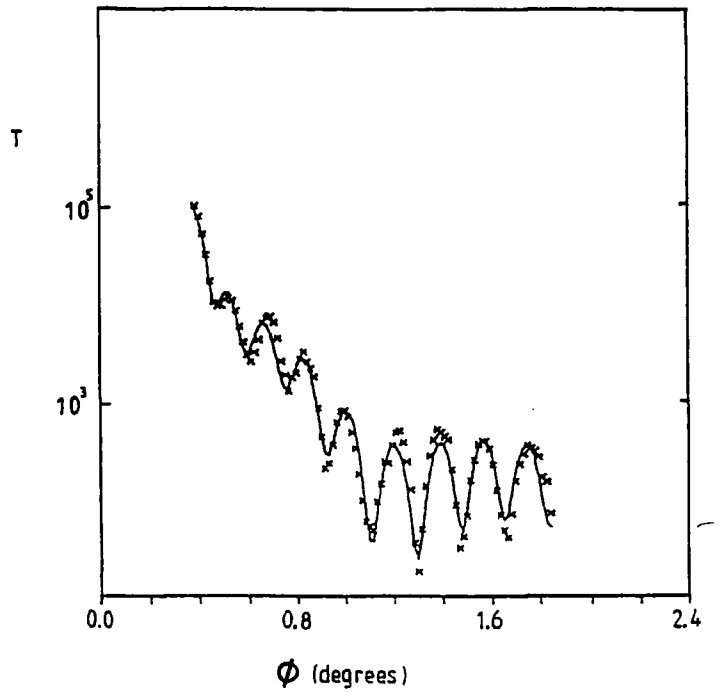

Figure 7.23: Triple crystal reflectivity of sample INP2 after baking. The solid line is a least squares fit to the experimental data by the Edinburgh group using Parratt theory.

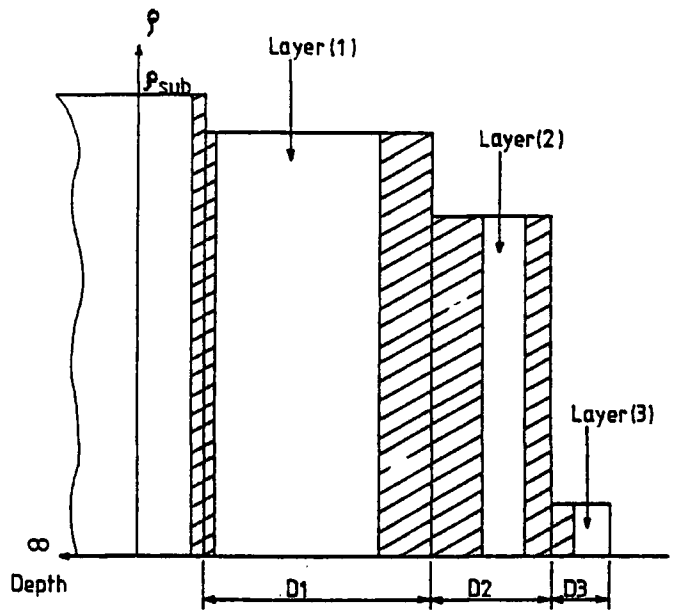

Figure 7.24: The electron density profile used for the calculated fit of figure 7.23 shows how the layer thicknesses have changed after oxidation into the quantum well.

Layer (3)	$d_3 = 22.3 \pm 0.7\mathring{A}$	$\sigma_3 \leq 1\mathring{A}$	$\Delta p_3/p_0 = -0.90 \pm 0.02$
Layer (2)	$d_2 = 30.5 \pm 0.7\mathring{A}$	$\sigma_2 = 8.8 \pm 0.6\mathring{A}$	$\Delta p_2/p_0 = -0.24 \pm 0.02$
Layer (1)	$d_1 = 210.0 \pm 0.8\mathring{A}$	$\sigma_1 = 8.9 \pm 0.7\mathring{A}$	$\Delta p_1/p_0 = -0.11 \pm 0.04$
InP Substrate		$\sigma_0 = 4.2 \pm 0.8\mathring{A}$	

Table 7.2: Sample INP2 before baking

Layer (3)	$d_3 = 23.1 \pm 0.7\mathring{A}$	$\sigma_3 \leq 1\mathring{A}$	$\Delta p_3/p_0 = -0.89 \pm 0.02$
Layer (2)	$d_2 = 45.4 \pm 0.8\mathring{A}$	$\sigma_2 = 9.3 \pm 0.7\mathring{A}$	$\Delta p_2/p_0 = -0.26 \pm 0.02$
Layer (1)	$d_1 = 197.0 \pm 0.9\mathring{A}$	$\sigma_1 = 20.3 \pm 0.8\mathring{A}$	$\Delta p_1/p_0 = -0.08 \pm 0.04$
InP Substrate		$\sigma_0 = 4.0 \pm 0.8\mathring{A}$	

Table 7.3: Sample INP2 after baking

7.6 Energy Dispersive Reflectivity

The reflectivity of X-ray mirrors has been studied in detail from the very soft end of the spectrum up to about $10keV$ ($1.2\mathring{A}$). Many studies of total reflection have generally explored the region just below $10keV$ (Parratt, 1954; Névot and Croce, 1980). The experimental measurements were extended into the $50keV$ regime by Bilderback and Hubbard (1982) and the reflectivity was measured as a function of energy rather than angle. This technique known as energy dispersive reflectivity is sensitive to surface features in the same way as angular reflectivity. It is also analagous to energy dispersive diffraction which has been used by Hart, Parrish and Masiocchi (1987) to study a thin Pd/Xe film and by Holý, Cummings and Hart (1988) to study mosaic spread in Si, Ge and CaF_2.

The experimental arrangement of Bilderback and Hubbard (1982, (a)) uses a solid state $Si(Li)$ detector to measure the intensity of the X-rays reflected from the specimen and the white spectrum from a Tungsten X-ray tube when the mirror was withdrawn from the incident beam. A multi-channel analyser (MCA) converted the detector output pulse distribution into an energy spectrum. A

similar experiment was constructed at Manchester University using the same set up as described by Holý et al. (1988), shown in figure 7.25. A tungsten X-ray tube was powered by a voltage generator able to deliver up to $150kV$ at $3.5mA$. A *Ge* solid-state detector was used together with an MCA with Canberra software. The parallel slits were made from long bars of molybdenum $5mm$ thick separated by spacers. Slit S_1 had a width of $0.1mm$, while S_2 was separated by $18\mu m$ spacers which gave an effective slit width of $4\mu m$, however, since the slits were not perfectly flat. This value was determined from the drop in intensity recorded when the slit width was reduced from its original known value. This gave an incident beam dispersion on the sample of $0.03\,mrad$ which was comparable to that attained by Bilderback and Hubbard. The slits provided total attenuation of the direct beam in the forward direction even at angles of 1° and yet produced no fluorescent background in the 20 to $150keV$ spectral range. A vertical slit of $1.5mm$ was also used in front of the detector to reduce vertical divergence effects. The generator was run at maximum power of $150kV$ and $3.5mA$ and an incidence angle of $\phi = 0.2°$ was used.

Figure 7.26 shows the energy reflectivity of an $InGaAsP$ layer of nominal thickness $0.15\mu m$ grown by MOVPE on InP by P. Spurdens, code INP5. The data was collected over 12 hours. Several features can be noted on the spectrum including the characteristic lines of Tungsten and the Molybdenum absorption edge at $20keV$. There *is* also a set of fringes near the $20keV$ region arising from the layer, shown on an expanded scale in figure 7.27. The fringe spacing was measured to be $1.38 \pm 0.05keV$ which corresponds to a layer thickness, using equation (7.23), of $0.129 \pm 0.005\mu m$. The experiment was run overnight for convenience, but an estimate of layer thickness could have been obtained after only 10 minutes, as shown in figure 7.28.

In order to model the reflectivity using the simulation program it is necessary to divide the reflected intensity by the straight through spectrum so that the characteristic features of the X-ray profile are removed. Unfortunately it was found that the straight through beam saturated the detector even with the current down to its minimum value of $0.3mA$. When the reflectivity spectrum was divided by the straight through spectrum the characteristic lines were reduced but not lost, but since these occurred either before the critical energy or at high

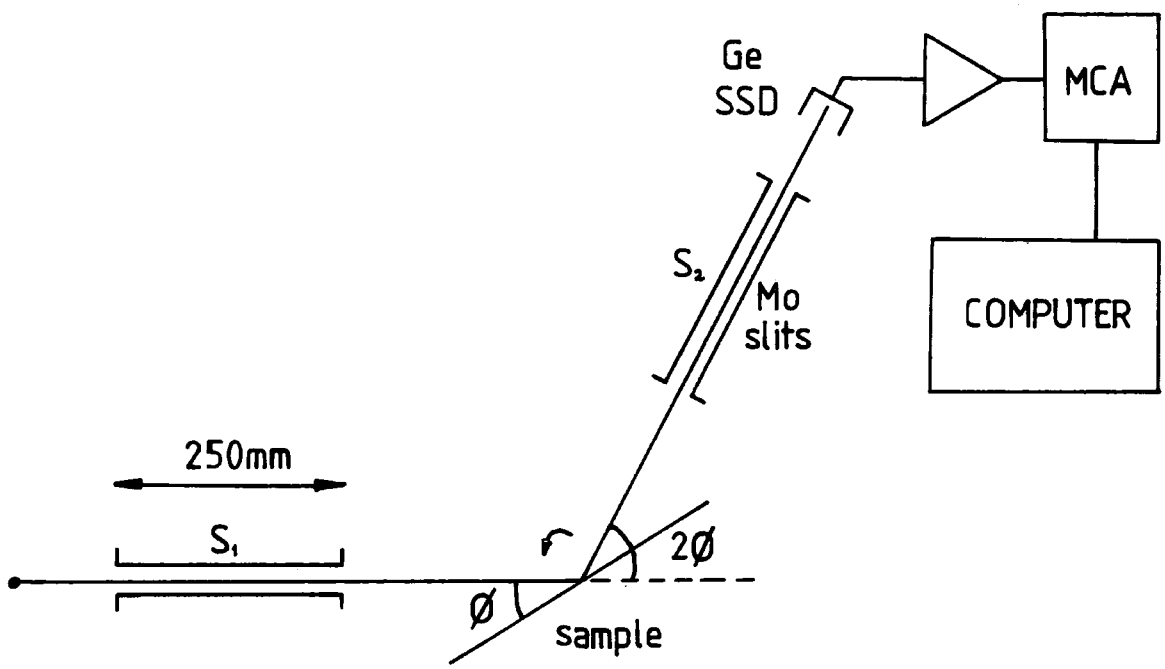

Figure 7.25: Experimental arrangement of the energy dispersive reflectivity apparatus at Manchester University.

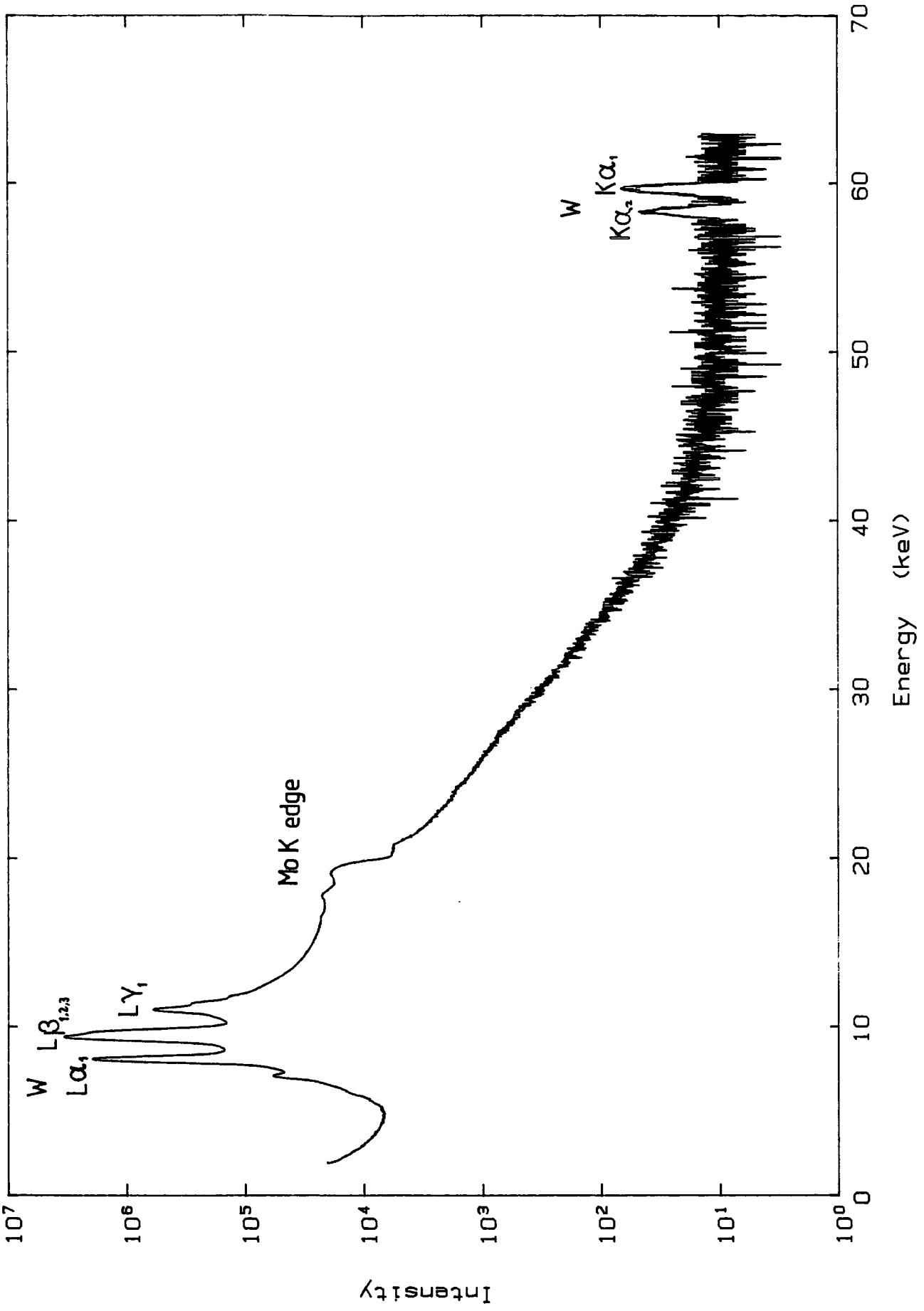

Figure 7.26: Energy dispersive reflectivity of sample INP5.

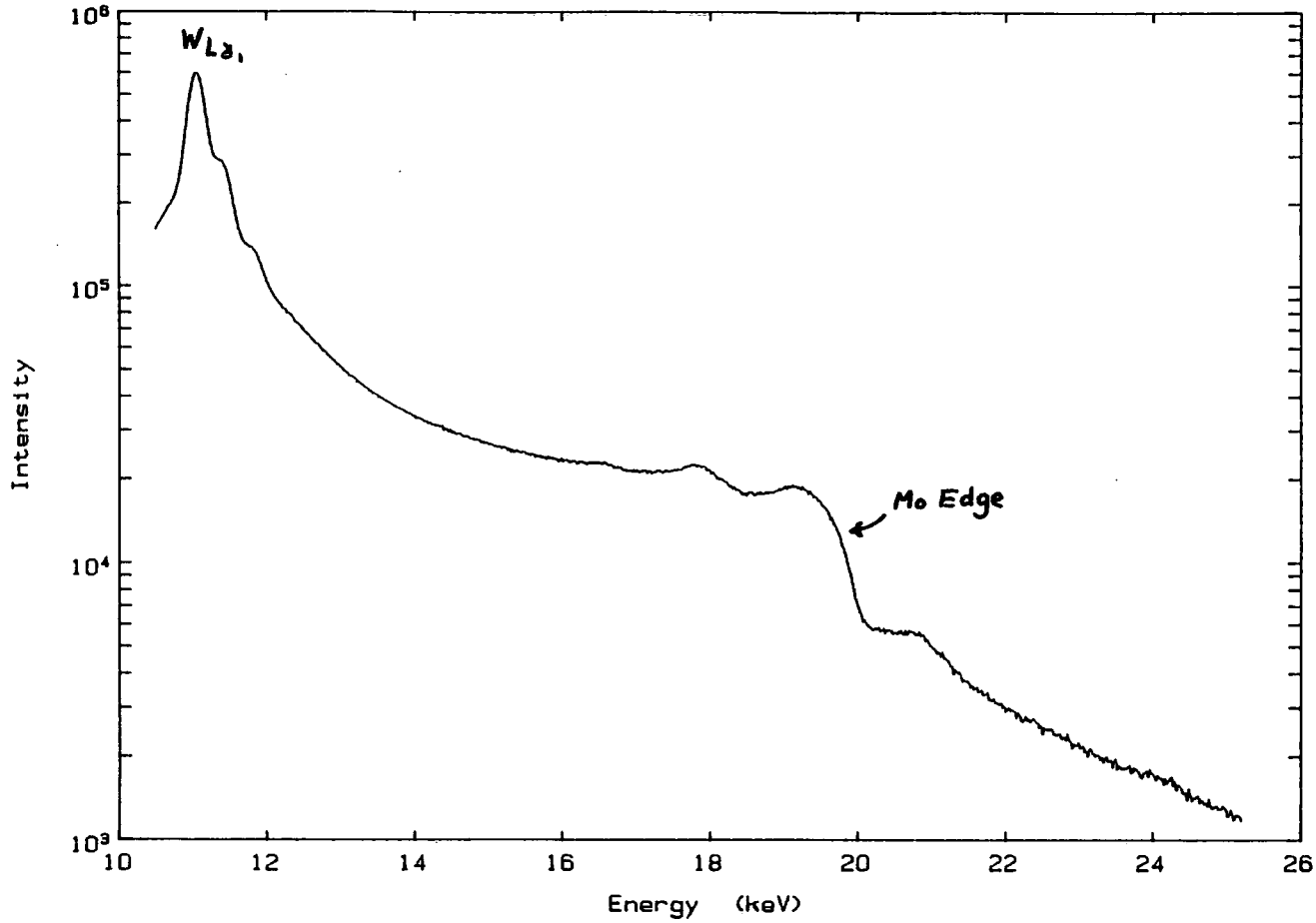

Figure 7.27: Energy dispersive reflectivity of sample INP5 with an expanded scale showing the fringes associated with the interference from the layer, after 12 hours.

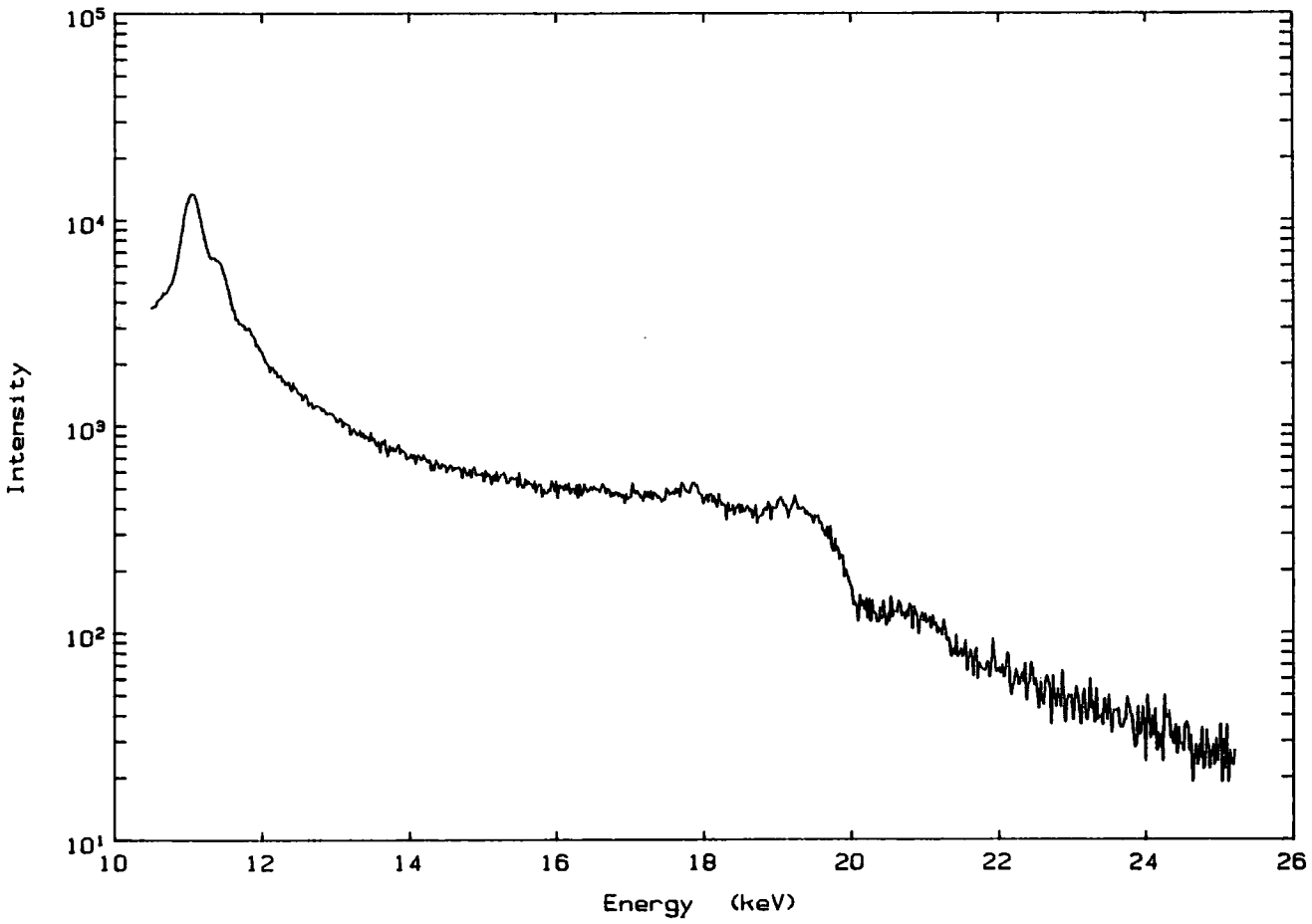

Figure 7.28: Energy dispersive reflectivity of sample INP5 after only 10 minutes data collection time.

energies their presence was not important to the region of interest. It was the Molybdenum absorption edge, however, arising from the slits, which made simulation impossible, although its effect was also reduced. Figure 7.29 shows the straight through spectrum at $150kV$ and $0.6mA$ over a 12 minute data collection time.

Figure 7.30 shows the reflectivity of an annealed ion implanted silicon sample produced by K. Bowen of Warwick University. The sample was implanted to a concentration of 1.8×10^{18} ions/cm^2 with $^{32}O_2^+$ ions, and annealed at a temperature of $T_a = 1300°C$ for 5 hours. The reflectivity data collection time was 10 minutes at $150kV$ and $3.5mA$. A fringe period is clearly visible, even after this short time, giving a thickness for the implanted layer of $0.146 \pm 0.010\mu m$.

The last sample investigated was a Langmuir-Blodgett (LB) film on silicon grown by M. Petty of Durham University. The sample consisted of 50 layers of Cadmium Arachidate ($Cd(Ar)_2$). LB films are prepared by transferring floating organic monolayers onto solid substrates (Roberts, 1985). The technique was first reported over fifty years ago (Blodgett, 1935) however, it is only during the past decade that the extensive potential of these films has been recognised, with applications in electronics, non-linear optics and biological sensors. Various experimental techniques have been used to study LB films including electron spin resonance, infra-red dichroism, surface potential and polarised resonance Raman spectroscopy (Batey, Roberts and Petty, 1983; Kan, Roberts and Petty, 1983; Jones et al., 1987; Swalen, 1987; Howarth, Petty, Davies and Yarwood, 1988). However, for complete assessment of film structure it is advantageous to use transmission electron, X-ray or neutron diffraction. X-ray reflectivity is also a useful tool in the characterisation of LB films (Pomerantz and Segmüller, 1980; Pomerantz, 1987; Jark et al., 1988). This is the first known study of LB films using energy dispersive reflectivity, however.

Figure 7.31 shows the energy reflectivity of the LB film after a data collection time of 150 minutes. There is a strong peak visible at about $39keV$ which corresponds to the (001) Bragg peak of the film. This gives a layer spacing of $45.5 \pm 1.5\AA$, which is twice the length of the molecule. The fringe period observed at lower energies arises from the total thickness of the LB film, giving a thickness

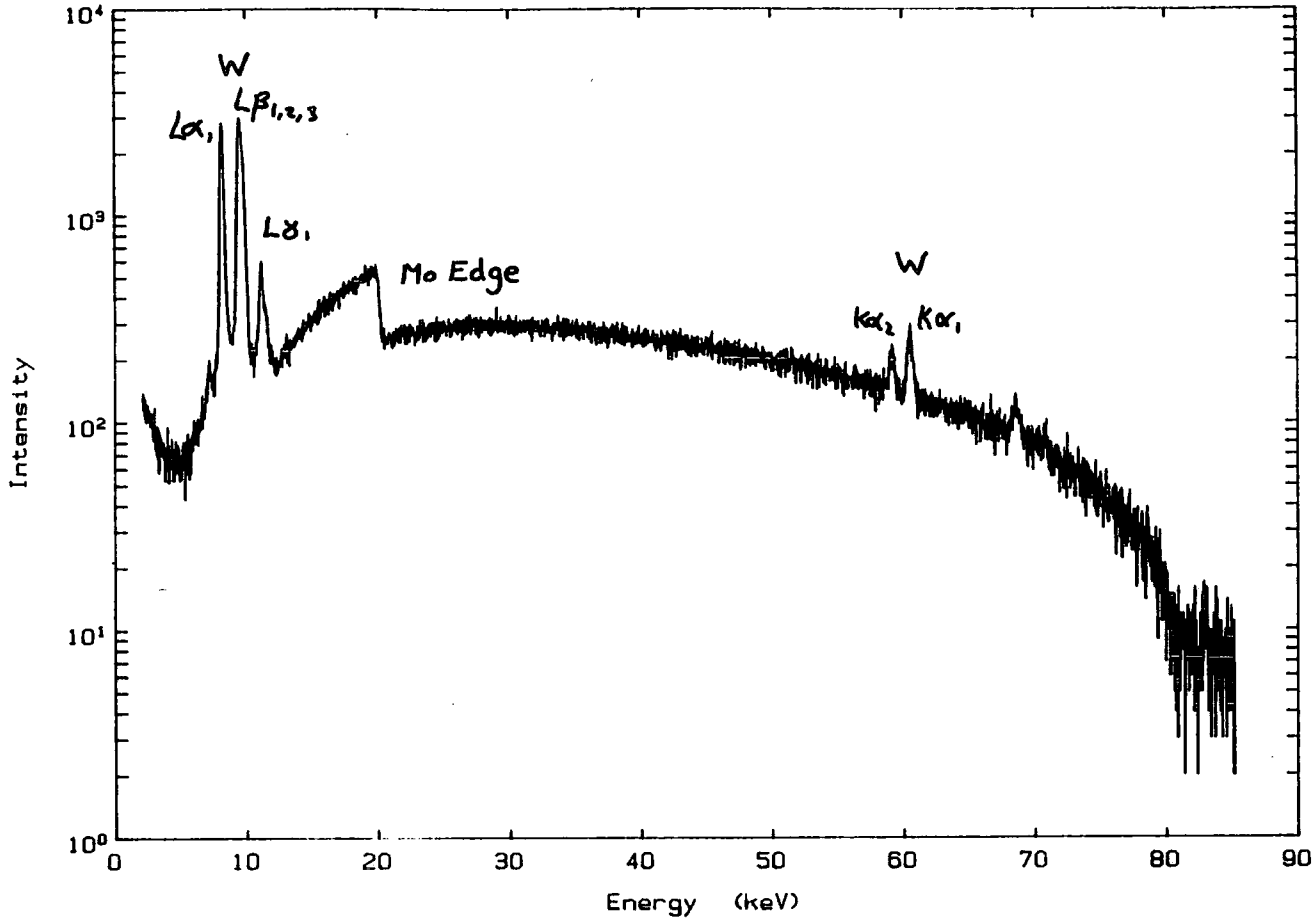

Figure 7.29: Spectrum of the Tungsten X-ray tube at $150kV$ and $0.6mA$

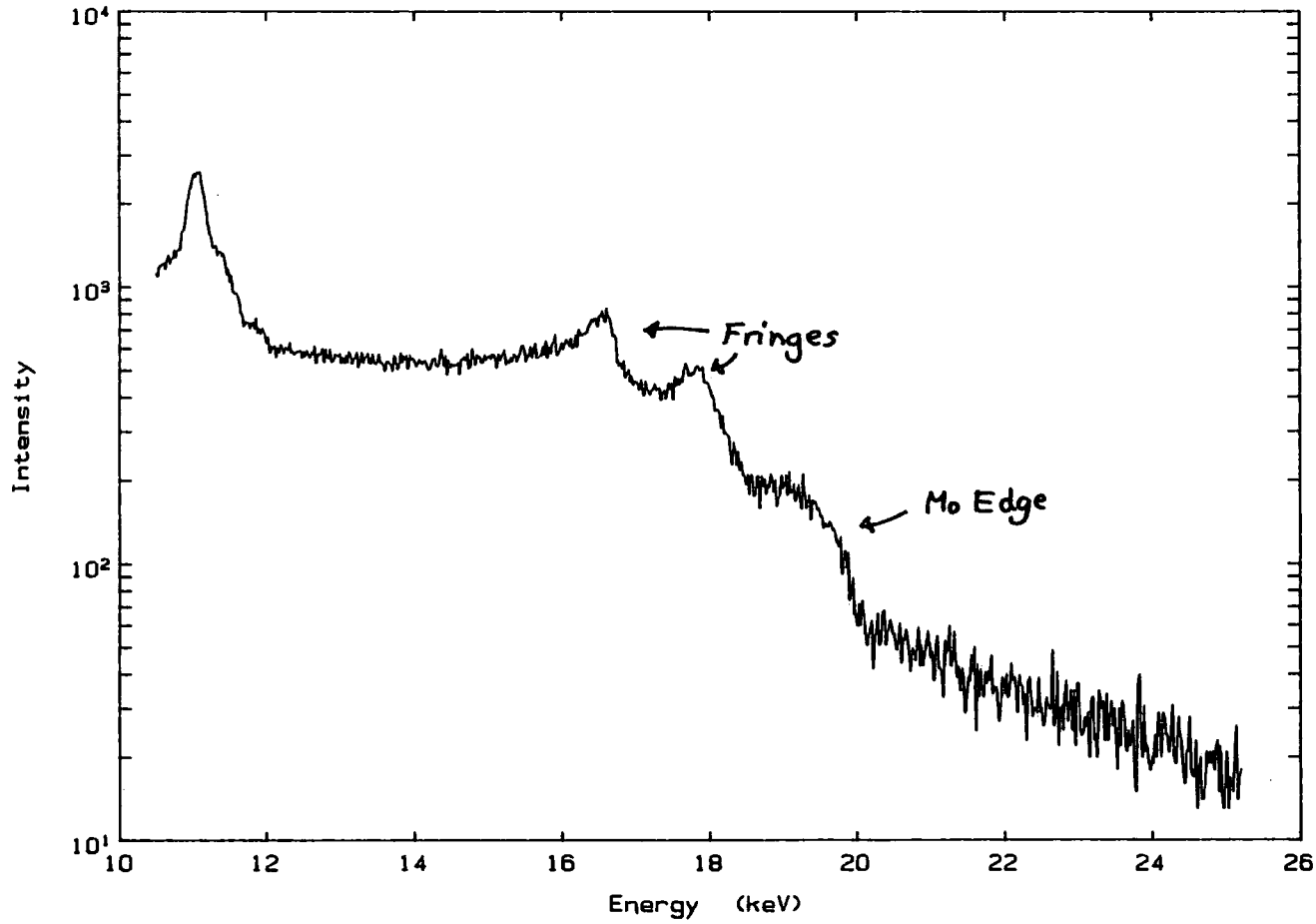

Figure 7.30: Energy dispersive reflectivity of an annealed ion implanted sample after 10 minutes data collection time.

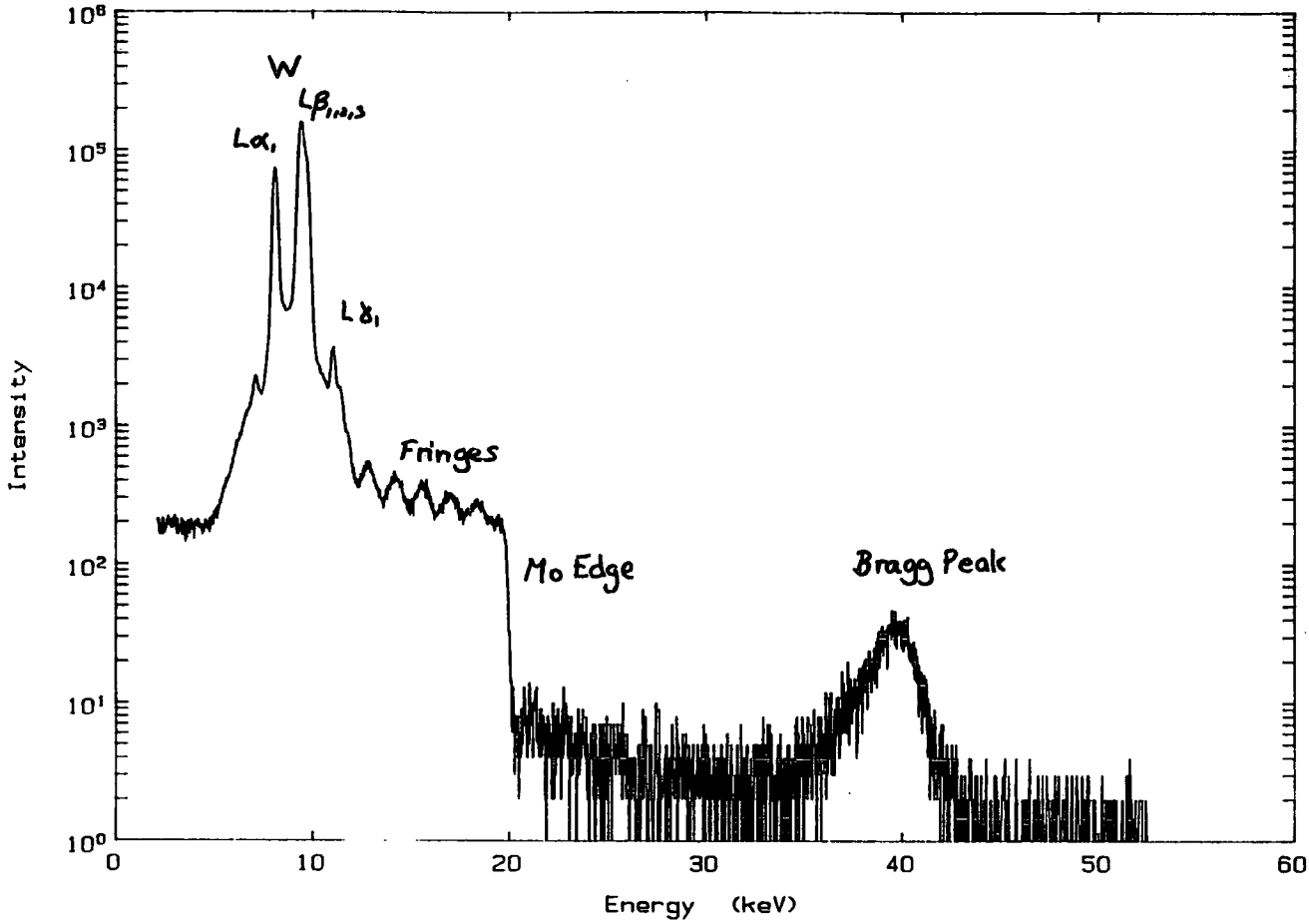

Figure 7.31: Energy dispersive reflectivity of an LB film after 150 minutes data collection time.

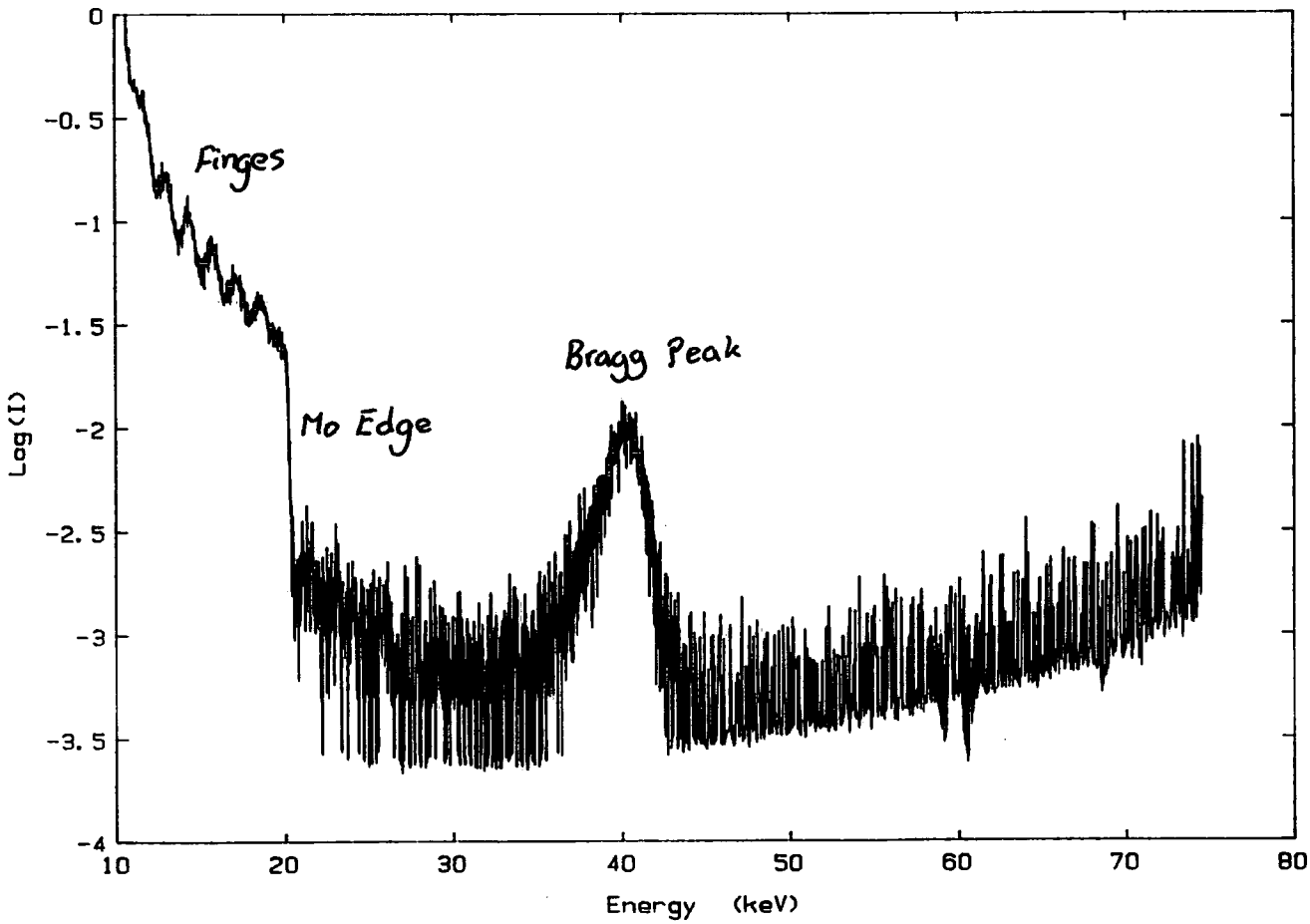

Figure 7.32: Energy dispersive reflectivity of the LB film with the spectrum of figure 7.31 divided by the straight through spectrum of figure 7.29.

of $0.127 \pm 0.005 \mu m$. There is a discrepancy, however, between the bilayer spacing of $45.5 \AA$ and the actual spacing of two cadmium arachidate molecules back to back; $53.9 \AA$. A possible explanation of this is that if the free acid rather than the salt had been deposited then they would be tilted by an angle of about 20°, although this would only reduce the apparent layer thickness to $50.6 \AA$. A more likely conclusion is that the film has been thermally annealed causing it to break up and recrystallise at a different average spacing. This is likely since annealing occurs at as little as $50°C$ and the high energy X-ray beam may have caused an increase in the sample temperature. This would also explain the large peak width and asymmetry of the peak, arising from a range of layer separations within the film. Figure 7.32 shows the result of dividing the reflectivity by the straight through spectrum of figure 7.29. The absorption edge is clearly not removed and the effect of background is detrimental at higher energies, although up to the absorption edge the reflectivity appears to behave as expected.

Angular reflectivity is a well established technique for the characterisation of thin films. Energy dispersive reflectivity is relatively new however, and this work has demonstrated that accurate measurements of thickness may be determined in very short times. Once the experiment had been set up, interchanging of specimens was relatively straightforward and reflectivity plots could be recorded without adjusting any of the angles or alignment. It was not actually necessary to have the full $150kV$ of voltage applied to the X-ray tube since the background at higher energies was significant. In practice $60keV$ would be sufficient as a maximum X-ray energy. For multilayer samples, by varying the incidence angle of the X-rays, higher order Bragg peaks could have been observed and so it would not be necessary to look at higher energies where the background is more significant. Correspondingly, for angular reflectivity, softer radiation than normal could be used for the study of multilayer samples.

7.7 Conclusion

It has been shown that triple crystal diffraction is a sensitive technique for the characterisation of thin layer samples and its advantage over double crystal diffraction is the reduction of curvature effects and diffuse scattering. When used in combination with X-ray reflectivity the techniques provide complementary

information on thickness of both crystalline and amorphous layers, together with interfacial and surface roughness, and composition of layers. X-ray reflectivity, because of its very low incidence angles, can quantify layer thickness down to the monolayer level. Energy dispersive reflectivity, where energy rather than angle is varied, has proved to be an extremely rapid method of thickness determination and is likely to become an important characterisation method for ultra-thin films and multilayers in the future.

Discussion and Suggestions for Further Work

Double crystal diffractometry has been shown to be a highly versatile and sensitive technique for the characterisation of heteroepitaxial layers. With the aid of a rocking curve simulation program much information may be determined about the sample structure. However, due to the large number of varying parameters, especially in multi-layered structures, it is often very difficult to attain a fit to the experimental rocking curve that defines the parameters singularly and accurately. To reduce the number of variables to be modelled the Pendellösung fringe period has been measured to precisely determine layer thickness. Once layer thickness is known the fitting procedure becomes more straightforward.

Two layer structures, comprising of a thin active layer capped by a thicker layer of substrate material, are also difficult to model because the diffracted intensity arising from the buried layer is often weak. Determination of layer thickness from direct measurement of Pendellösung fringe spacing can lead to incorrect values of layer thickness because the fringe pattern is a complicated superposition of frequencies. The use of Fourier Analysis to precisely determine the Pendellösung frequencies and so layer thicknesses, has been investigated and found to significantly speed up the modelling process, allowing very close matches to be achieved.

It has been shown that epilayer tilt must be taken into account when determining layer compositions. In addition, relaxation of epilayers must not be neglected. Asymmetric relaxation was found in an $InGaAs/InP$ superlattice, even with a relatively small lattice mismatch. To gain an accurate picture of the layer unit cell, therefore, including the magnitude and direction of tilt, it is necessary to record rocking curves from several sample orientations.

Asymmetric geometries enhancing surface diffraction effects are necessary for the study of very thin layers. A technique which utilises skew beam paths, known as SARCA, has been used to improve the surface sensitivity. Very low incidence or emergence angles can be achieved with this method and so ultra thin layers may be studied. The Durham rocking curve simulation program has been adapted to include SARCA, so that experimental curves may be fitted for any geometry. The most difficult aspect of using SARCA is the initial sample alignment, and if this were automated then the technique would be easily accessible to all users of double crystal diffraction.

X-ray reflectivity has also been used for the study of thin layers to give an accurate indication of layer thickness. A simulation program has been written to model reflectivity of heteroepitaxial layers based on Parratt theory. Angular reflectivity with a double crystal diffractometer requires accurate specimen alignment, and a special specimen mounting stage would need to be designed to make the technique more straightforward. The triple crystal diffractometer uses an analyser crystal to remove the effects of specimen curvature and can also be used for X-ray reflectivity. The reflectivity method is very useful for determining layer thickness and gives an indication of internal interface and surface roughness.

Energy dispersive reflectivity has been used to determine layer thickness rapidly in epilayers, ion implanted samples and Langmuir-Blodgett films. It has the potential to become a routine assessment technique for sample characterisation, because once the experiment has been set up samples may be interchanged easily and recording of reflectivity curves is rapid. A method needs to be investigated which allows the incident spectrum to be recorded without detector saturation, so that it can be removed from the reflected spectrum to allow modelling of reflectivity curves. Reflectivity is especially useful for the study of MQW's and providing the right combination of radiation and angle of incidence are chosen, several orders of superlattice reflection could be studied.

As the demand on characterisation techniques to provide even more accurate and detailed information on sample structure increases, so the techniques must develop with the demand. For high precision diffractometry it is necessary to use more than the two reflections of a conventional double crystal diffractometer.

Utilisation of a four crystal monochromator as a first crystal removes the problems of both wavelength dispersion and angular dispersion allowing any reflection from the sample without rocking curve broadening and loss of fine structure. In addition, an analyser crystal using one or more reflections, removes the problem of sample curvature so that specimens may be characterised to high precision. If the sample were mounted on a stage which allowed rotation about the sample normal as well as about the axis, translation in three dimensions as well as tilt, then reflectivity, SARCA and conventional X-ray diffraction would all be possible on one high precision instrument, allowing complete sample characterisation.

Appendix A

X-ray Rocking Curve Simulation Program

This program, originally written by M. Hill (Hill, 1985), has been substantially amended to correct previous mistakes and to allow for simulation of SARCA data. The program is divided into two parts; the first, INPUT, dealing with the entry of sample structure and the second, CRUNCH, calculating the rocking curve. A listing of CRUNCH is shown with most of the changes occurring in subroutines SUBREF and LAYREF. INPUT has been expanded to include new combinations of layer materials as well as II-VI compounds but a print out is not included here.

```
C*********************************************************
C*  THIS PROGRAM DOES THE NUMBER CRUNCHING FOR           *
C*               ROCKING CURVES                          *
C*          USING THE DATA FROM FILE INPDAT              *
C*     WHICH IS GENERATED BY THE PASCAL PROGRAM          *
C*                  INPUT.PAS                            *
C*********************************************************
C     Substantially amended by S J Miles, Sept  1988
C
      REAL ALPHA(2000), FSUB(2000), THETA, PHI, PHIF, PI
      REAL CLAYR(200), THICK(200), FLAY(2000), FSIG(2000)
      REAL BETA(2000), FPI(2000)
      REAL ROT, PROT
      INTEGER H, K, L, II, JJ, KK, PASS
      COMPLEX FH1, FH2, FO, ZSUB(2000), FFH1, FFH2, FFO
      COMPLEX LFH1(200), LFH2(200), LFO(200)
      CHARACTER*10 POLAR, SUBST, FIRST, DIFF
      COMMON /AREA1/ ALPHA, ALSTEP, START, FINISH, NOPNTS, WAVE,
     1       POLAR, SUBST, FIRST, DIFF, ROT
      COMMON /AREA2/ FH1, FH2, FO, DSUB, THETA, PHI
      COMMON /AREA3/ FFH1, FFH2, FFO, DFIRST, THETF, PHIF
      COMMON /AREA4/ BETA, BSTEP, BSTART, BFIN
      COMMON /AREA5/ LFH1, LFH2, LFO, CLAYR, THICK, NOLAYS,
     1       H, K, L, II, JJ, KK
C
C  Read data from file INPDAT
C
      CALL READAT
C
C  No of data points in single crystal reflectivity curves
C
      NOPNTS = INT((FINISH - START)/ALSTEP + 1.5)
      PASS = 1
      WRITE (6,10)
   10 FORMAT ('&Enter additional tilt angle (degrees) ?')
      READ (5,*) TILT
      TILT = TILT * 3.14159 / 180.
C  For SARCA , enter angular rotation about Bragg norma
      ROT = 0.
      IF (PHI .EQ. 0) GO TO 20
   11 WRITE (6,12)
   12 FORMAT ('Enter rotation angle in degrees')
      WRITE (6,13)
   13 FORMAT (' 0 for glancing incidence,  180 for glancing exit')
      READ (5,*) ROT
      IF((ROT.GE.0.0).AND.(ROT.LE.180.0)) GOTO 15
      PRINT *,'Incorrect entry , try again'
      GO TO 11
   15 ROT = ROT * 3.14159 / 180.
      PROT = ROT
C
C  Calculate substrate reflectivity curve
C
   20 CALL SUBREF(FH1, FH2, FO, DSUB, THETA, PHI, FSUB, ZSUB,
     1            TILT)
C
C  Calculate layer reflectivity curve
C
      CALL LAYREF(FSUB, ZSUB, FLAY, TILT)
C
```

```
C  Set rotation to zero for first crystal reflectivity calculation
C
      ROT = 0
C
C  If first crystal <> substrate calculate its reflectivity
C
      IF (DIFF(1:1) .EQ. 'Y') CALL SUBREF(FFH1, FFH2, FFO,
     1     DFIRST, THETF, PHIF, FSUB, ZSUB, 0.)
      IF (DIFF(1:1) .EQ. 'Y') GO TO 25
      CALL SUBREF(FH1, FH2, FO, DSUB, THETA, PHI, FSUB, ZSUB,
     1            TILT)
   25 CONTINUE
C
C  Convolute reflectivity of first and second crystals
C
      IF (PASS .EQ. 1) CALL CONVOL(FSUB, FLAY, FSIG)
      IF (PASS .EQ. 2) CALL CONVOL(FSUB, FLAY, FPI)
C
C  If random polarisation redo with pi polarisation
C
      IF ((POLAR(1:1) .NE. 'R') .AND. (PASS .EQ. 1)) GO TO 50
      IF (PASS .EQ. 2) GO TO 30
      POLAR = 'PI'
      PASS = 2
      ROT = PROT
      GO TO 20
C
C  Add sigma and pi polarisations if random
C
   30 DO 40 I = 1, NOPNTS
        FSIG(I) = FSIG(I) + FPI(I)
   40 CONTINUE
C
C  Write data to output file
C
   50 WRITE (1,*) NOPNTS
      WRITE (1,*) BSTEP
      WRITE (1,*) BETA(1)
      DO 60 I = 1, NOPNTS
        WRITE (1,*) FSIG(I)
   60 CONTINUE
      STOP
      END
C
C ********************************************************
C *  SUBREF - CALCULATES INFINITE CRYSTAL REFLECTIVITY   *
C *   OVER A RANGE OF ANGLES RELATIVE TO BRAGG ANGLE     *
C ********************************************************
C
      SUBROUTINE SUBREF(FH1, FH2, FO, DS, THETA, PHI, FSUB,
     1   ZSUB, TILT)
      REAL ALPHA(2000), FSUB(2000), THETA, PHI, DS, PI, CABS
      REAL AI, AE, TEM
      COMPLEX ZSUB(2000), FH1, FH2, FO, CHIH1, CHIH2, CHIO
      COMPLEX CSQRT, SQ, B, CH1, CH2
      CHARACTER*10 POLAR, SUBST, FIRST, DIFF
      COMMON /AREA1/ ALPHA, ALSTEP, START, FINISH, NOPNTS, WAVE,
     1       POLAR, SUBST, FIRST, DIFF, ROT
      WRITE (6,10)
   10 FORMAT (' CALCULATING SUBSTRATE REFLECTIVITY')
```

```
      PI = 3.141592654
      CER = 2.817914E-15
      VUC = DS ** 3
      FFACT = -(WAVE**2*CER) / (VUC*PI)
      CHIH1 = FH1 * FFACT
      CHIH2 = FH2 * FFACT
      CHIO = FO * FFACT
C Calculate angles of incidence and emergence at the Bragg angle
      AI = SIN(THETA)*COS(PHI)-SIN(PHI)*COS(THETA)*COS(ROT)
      AI = ARSIN(AI)-TILT
      AE = SIN(THETA)*COS(PHI)+SIN(PHI)*COS(THETA)*COS(ROT)
      AE = ARSIN(AE)+TILT
      TEM = AI*(180.0/PI)
      WRITE (6,13) TEM
   13 FORMAT ('Angle of incidence S = ', F10.5, '  degrees')
      ALPHA(1) = START
      WRITE (6,20) THETA, PHI
   20 FORMAT (' THETA = ', F10.5, ' PHI = ', F10.5, ' RADIANS')
      DO 40 I = 1, NOPNTS
        THS = ALPHA(I) * PI / (3600.0*180.0)
        GAMMAO = SIN(AI+THS)
        GAMMAH = -SIN(AE-THS)
        CH1 = CHIH1
        CH2 = CHIH2
        IF (POLAR(1:1) .NE. 'P') GO TO 30
        CH1 = CHIH1 * COS(2.0*(THETA + THS))
        CH2 = CHIH2 * COS(2.0*(THETA + THS))
   30   CONTINUE
        B = (CHIO/GAMMAO - CHIO/GAMMAH + 2.0*THS*SIN(2.0*THETA)/
     1       GAMMAH) / 2.0
        SQ = CSQRT(B**2 + CH1*CH2/(GAMMAO*GAMMAH))
        ZSUB(I) = -(B + SQ*SIGN(1.,AIMAG(SQ))) / (CH2/GAMMAO)
        FSUB(I) = (CABS(ZSUB(I))) ** 2*ABS(GAMMAH/GAMMAO)
        ALPHA(I + 1) = ALPHA(I) + ALSTEP
   40 CONTINUE
      RETURN
      END
C
C ***************************************************
C *  LAYREF - CALCULATES LAYER REFLECTIVITIES USING  *
C *  REFLECTIVITIES FROM SUBSTRATE AS STARTING POINT *
C ***************************************************
C
      SUBROUTINE LAYREF(FSUB, ZSUB, FLAY, TILT)
      REAL ALPHA(2000), FSUB(2000), CLAYR(200), THICK(200), PHI
      REAL FLAY(2000), PI
      REAL T, AI, AE
      INTEGER H, K, L, II, JJ, KK
      DOUBLE PRECISION DTHETA, DPHI, DTI
      COMPLEX ZSUB(2000), LFH1(200), LFH2(200), LFO(200)
      COMPLEX FH1, FH2, FO, B, SQ, NUM, DEN, CSQRT, CCOS, CSIN
      COMPLEX CHIH1, CHIH2, CHIO, CH1, CH2, CTN
      CHARACTER*10 POLAR, SUBST, FIRST, DIFF
      COMMON /AREA1/ ALPHA, ALSTEP, START, FINISH, NOPNTS, WAVE,
     1       POLAR, SUBST, FIRST, DIFF, ROT
      COMMON /AREA2/ FH1, FH2, FO, DSUB, THETA, PHI
      COMMON /AREA5/ LFH1, LFH2, LFO, CLAYR, THICK, NOLAYS,
     1       H, K, L, II, JJ, KK
      PI = 3.1415926535897932
      CER = 2.817914E-15
```

```
      WRITE (6,10)
   10 FORMAT (' CALCULATING LAYER REFLECTIVITY')
      AH = FLOAT(H)
      AK = FLOAT(K)
      AL = FLOAT(L)
      AII = FLOAT(II)
      AJJ = FLOAT(JJ)
      AKK = FLOAT(KK)
      DO 50 I = 1, NOLAYS
        VUC = DSUB ** 2 * CLAYR(I)
        FFACT = -(WAVE**2*CER) / (PI*VUC)
        CHIH1 = LFH1(I) * FFACT
        CHIH2 = LFH2(I) * FFACT
        CHIO = LFO(I) * FFACT
        DLAY = SQRT(1/(AH**2/DSUB**2 + AK**2/DSUB**2 +
     1         AL**2/CLAYR(I)**2))
        THETL = ARSIN(WAVE/(2.0*DLAY))
        PHIL = (AH*AII/DSUB**2 + AK*AJJ/DSUB**2 +
     1          AL*AKK/CLAYR(I)**2) ** 2
        PHIL = PHIL / ((AH**2/DSUB**2 + AK**2/DSUB**2 + AL**2/
     1  CLAYR(I)**2)*(AII**2/DSUB**2 + AJJ**2/DSUB**2 + AKK**2/
     1  CLAYR(I)**2))
        PHIL = SQRT(PHIL)
        PHIL = ARCOS(PHIL)
C Calculate apparent layer Bragg angle for a given ROT
        DTHETA = THETA - THETL
        DPHI = PHIL - PHI
        WRITE(6,11)DTHETA*3600.*180./PI,DPHI*3600.
     1             *180/PI
   11   FORMAT(' DTHETA = ',F10.5,'DPHI = ',F10.5)
        CALL THSEP(DTI,DTHETA,DPHI,THETA,ROT)
        THETL = THETA + DTI
        WRITE(6,15) DTI*3600.0*180.0/PI
   15   FORMAT(' Peak seperation',F10.5,' seconds')
        WRITE (6,20) I, THETL, PHIL
   20   FORMAT (' LAYER NO ', I3, '  THETA = ', F10.5, ' PHI = ',
     1          F10.5)
        AI = SIN(THETA)*COS(PHI) - SIN(PHI)*COS(THETA)*COS(ROT)
        AI = ARSIN(AI) - TILT
        AE = SIN(THETA)*COS(PHI) + SIN(PHI)*COS(THETA)*COS(ROT)
        AE = ARSIN(AE) + TILT
        DO 40 J = 1, NOPNTS
          THS = ALPHA(J)*PI/(3600.0*180.0) + THETA - THETL
          GAMMAO = SIN(AI+THS)
          GAMMAH = -SIN(AE-THS)
          D = PI / WAVE
          CH1 = CHIH1
          CH2 = CHIH2
          IF (POLAR(1:1) .NE. 'P') GO TO 30
          CH1 = CHIH1 * COS(2.0*(THETL + THS))
          CH2 = CHIH2 * COS(2.0*(THETL + THS))
   30     CONTINUE
          B = (CHIO/GAMMAO - CHIO/GAMMAH + 2.0*THS*
     1          SIN(2.0*THETL)/GAMMAH) / 2.0
          SQ = CSQRT(B**2 + CH1*CH2/(GAMMAO*GAMMAH))
          CTN = CSIN(SQ*D*(-THICK(I))) / CCOS(SQ*D*(-THICK(I)))
          NUM=ZSUB(J)*SQ+(0.0,1.0)*(ZSUB(J)*B-CH1/GAMMAH) * CTN
          DEN = SQ - (0.0,1.0) * (B + ZSUB(J)*CH2/GAMMAO) * CTN
          ZSUB(J) = NUM / DEN
          FLAY(J) = CABS(ZSUB(J)) ** 2*ABS(GAMMAH/GAMMAO)
```

```
   40   CONTINUE
   50 CONTINUE
      RETURN
      END
C*********************************************************
C subroutine to calculate substrate - layer peak
C separation for SARCA
      SUBROUTINE THSEP(DTI,DTH,DPHI,THBR,BETA)
      DOUBLE PRECISION DTI,DTH,DPHI,THBR,BETA,PI
      DOUBLE PRECISION A,B,C,BX,T
      PI=3.1415926535897932
      A=DCOS(THBR-DTH)*DCOS(DPHI)
      B=DCOS(THBR-DTH)
      C=DSIN(THBR-DTH)*DSIN(DPHI)
      T=DTAN(BETA)
      IF ((BETA.LT.0.5*PI).AND.(BETA.GT.-0.5*PI))GOTO 20
      BX=-1.0*A*B*DSQRT(B*B+(A*A-C*C)*T*T)
      GOTO 30
  20  BX=A*B*DSQRT(B*B+(A*A-C*C)*T*T)
  30  BX=(B*B*C+BX)/(B*B+A*A*T*T)
      DTI=(DCOS(THBR)*DCOS(BETA)-DSIN(THBR)*DTAN(DPHI)+
     1DCOS(THBR)*DSIN(BETA)*T)*BX
      DTI=DTI+DSIN(THBR)*DSIN(THBR-DTH)/DCOS(DPHI)
      DTI=-DACOS(DTI)*(DTH/ABS(DTH))
      RETURN
      END
C*********************************************************
C * CONVOL - CALCULATES CONVOLUTION OF DATA SETS FSUB & FLAY *
C ***********************************************************
C
      SUBROUTINE CONVOL(FSUB, FLAY, FCON)
      REAL FSUB(2000), FLAY(2000), BETA(2000), FCON(2000)
      REAL ALPHA(2000), F(2000)
      CHARACTER*10 POLAR, SUBST, FIRST, DIFF
      COMMON /AREA1/ ALPHA, ALSTEP, START, FINISH, NOPNTS, WAVE,
     1       POLAR, SUBST, FIRST, DIFF, ROT
      COMMON /AREA4/ BETA, BSTEP, BSTART, BFIN
      NPNTS = INT((BFIN - BSTART)/BSTEP + 1.5)
      WRITE (6,10)
   10 FORMAT (' CALCULATING CONVOLUTION')
      BETA(1) = BSTART
      DO 20 I = 1, NPNTS
        CALL MULT(FSUB, FLAY, BETA(I), F, NDP)
        FCON(I) = AINTG(ALPHA,F,NDP)
        BETA(I + 1) = BETA(I) + BSTEP
   20 CONTINUE
      RETURN
      END
C
C ***************************************************************
C * MULTIPLIES TWO DATA SETS, ONE OFFSET FROM THE OTHER BY BETA *
C ***************************************************************
C
      SUBROUTINE MULT(FSUB, FLAY, BETA, F, NDP)
      REAL FSUB(2000), FLAY(2000), F(2000), ALPHA(2000)
      CHARACTER*10 POLAR, SUBST, FIRST, DIFF
      COMMON /AREA1/ ALPHA, ALSTEP, START, FINISH, NOPNTS, WAVE,
     1       POLAR, SUBST, FIRST, DIFF, ROT
      NDP = 0
      N = NOPNTS - 1
```

```
      L = 1
      IF ((ALPHA(1) + BETA) .GT. ALPHA(NOPNTS)) RETURN
      IF ((ALPHA(NOPNTS) + BETA) .LT. ALPHA(1)) RETURN
      DO 50 I = 1, NOPNTS
        IF ((ALPHA(I) + BETA) .GT. ALPHA(NOPNTS)) GO TO 60
        IF ((ALPHA(I) + BETA) .LT. ALPHA(1)) GO TO 40
        DO 20 J = L, N
          H = ALPHA(I) + BETA - ALPHA(J)
          SH = ALPHA(J + 1) - ALPHA(J)
          IF (H .GT. SH) GO TO 10
          G = FLAY(J) * (1 - H/SH) + FLAY(J + 1) * H / SH
          GO TO 30
   10     CONTINUE
   20   CONTINUE
   30   NDP = NDP + 1
        F(NDP) = FSUB(I) * G
        L = J
   40   CONTINUE
   50 CONTINUE
   60 CONTINUE
      RETURN
      END
C
C *********************************************************
C * AINTG - CALCULATES AREA UNDER MULTIPLIED DATA SET F *
C *********************************************************
C
      FUNCTION AINTG(ALPHA, F, NDP)
      REAL ALPHA(2000), F(2000)
      N = NDP - 1
      AINTG = 0.0
      DO 10 I = 1, N
        H = ALPHA(I + 1) - ALPHA(I)
        AINTG = AINTG + (F(I) + F(I + 1)) * H / 2.0
   10 CONTINUE
      RETURN
      END
C
C ****************************************
C *  READAT - READS DATA FROM FILE INPDAT  *
C ****************************************
C
      SUBROUTINE READAT
      REAL ALPHA(2000), BETA(2000), FSUB(2000), PHI, PHIF
      REAL THICK(200), CLAYR(200)
      INTEGER H, K, L, II, JJ, KK
      COMPLEX ZSUB(2000), FH1, FH2, F0, FFH1, FFH2, FF0
      COMPLEX LFH1(200), LFH2(200), LF0(200)
      CHARACTER*10 POLAR, SUBST, FIRST, DIFF, DATE, TIME
      COMMON /AREA1/ ALPHA, ALSTEP, START, FINISH, NOPNTS, WAVE,
     1       POLAR, SUBST, FIRST, DIFF, ROT
      COMMON /AREA2/ FH1, FH2, F0, DSUB, THETA, PHI
      COMMON /AREA3/ FFH1, FFH2, FF0, DFIRST, THETF, PHIF
      COMMON /AREA4/ BETA, BSTEP, BSTART, BFIN
      COMMON /AREA5/ LFH1, LFH2, LF0, CLAYR, THICK, NOLAYS,
     1       H, K, L, II, JJ, KK
C
C  Read data from file INPDAT
C
      CALL FTNCMD('ASSIGN 3=INPDAT;')
```

```
      READ (3,10) DATE
      READ (3,10) TIME
      READ (3,10) SUBST
      READ (3,10) FIRST
      READ (3,10) DIFF
      READ (3,*) WAVE
      READ (3,10) POLAR
      READ (3,*) START, FINISH
      READ (3,*) ALSTEP
      READ (3,*) BSTART, BFIN
      READ (3,*) BSTEP
   10 FORMAT (' ', A10)
      WRITE (6,20) TIME, DATE
   20 FORMAT (' DATA GENERATED AT ', A10, ' ON ', A10)
      WRITE (6,30) FIRST, SUBST
   30 FORMAT (' First crystal is ', A10, '  Second crystal is ',
     1       A10)
      WRITE (6,40) WAVE
   40 FORMAT (' Wavelength = ', E12.5)
      WRITE (6,50) POLAR
   50 FORMAT (' Polarization state is ', A10)
      WRITE (1,*) DATE
      WRITE (1,*) TIME
      WRITE (1,*) SUBST
      WRITE (1,*) FIRST
      WRITE (1,*) WAVE
      WRITE (1,*) POLAR
C
C  Read substrate variables
C
      READ (3,*) THETA
      READ (3,*) PHI
      READ (3,*) FH1
      READ (3,*) FH2
      READ (3,*) FO
      READ (3,*) DSUB
      THETA = ARSIN(THETA)
      PHI = ARCOS(PHI)
      WRITE (1,*) THETA, PHI, DSUB
C
C  Read layer variables
C
      READ (3,*) NOLAYS
      READ (3,*) H, K, L
      READ (3,*) II, JJ, KK
      DO 60 I = 1, NOLAYS
        READ (3,*) CLAYR(I)
        READ (3,*) THICK(I)
        READ (3,*) LFH1(I)
        READ (3,*) LFH2(I)
        READ (3,*) LFO(I)
   60 CONTINUE
      WRITE (1,*) NOLAYS
      WRITE (1,*) H, K, L
      WRITE (1,*) II, JJ, KK
      DO 70 I = 1, NOLAYS
        WRITE (1,*) CLAYR(I), THICK(I)
   70 CONTINUE
C
C  Read first crystal variables if necessary
```

```
C
      IF (DIFF(1:1) .EQ. 'N') GO TO 90
      WRITE (6,80)
   80 FORMAT (' Reading first crystal parameters')
      READ (3,*) THETF
      READ (3,*) PHIF
      READ (3,*) FFH1
      READ (3,*) FFH2
      READ (3,*) FFO
      READ (3,*) DFIRST
      THETF = ARSIN(THETF)
      PHIF = ARCOS(PHIF)
   90 CONTINUE
      RETURN
      END
```

Appendix B

X-ray Reflectivity Simulation Program

The program was written in FORTRAN on the Durham Amdahl 5860 mainframe computer, using the GHOST80 graphics package. For a given sample structure it calculates the specular reflectivity using the equations given in Chapter 7, for either angular or energy dispersive reflectivity. The program is divided into five basic subprograms which utilise the subroutines and functions detailed below.

Subprogram SAMPLE

Reads the sample details: number of layers, composition, thickness and roughness of each layer, and substrate composition. For ternary and quaternary alloys the mismatch is read together with the band gap in quaternaries.

Subprogram PRNTS

Writes the sample data to the screen.

Subprogram XSCALE

Asks for the experimental details for either fixed angle or fixed wavelength in terms of angular or energy step size, together with the start and end values for the reflectivity data.

Subprogram CONTRO

This is the controlling subprogram which calculates the reflectivity for a given wavelength or angle using the subroutines CRYS, FN and RATIO, and the function ROG.

Subprogram GRAPH

Produces the graphical output using the GHOST80 suite of programs.

Subroutine CRYS

Determines the dispersion corrections for a particular compound and wavelength using subroutine HONL and then calculates δ^*.

Subroutine HONL

Calculates the dispersion corrections for a particular element and wavelength.

Subroutine FN

Calculates f_n for a particular material, wavelength and angle.

Subroutine RATIO

Calculates the recursion relation ratio for the sample at a particular wavelength and angle.

Function DEG

Converts radians to degrees.

Function RAD

Converts degrees to radians.

Function WAV

Converts energy in keV to wavelength in Ångstroms.

Function ROG

Calculates Gaussian roughness factor.

The operation of the program is illustrated in the following series of flow diagrams, which is followed by a full listing of the program.

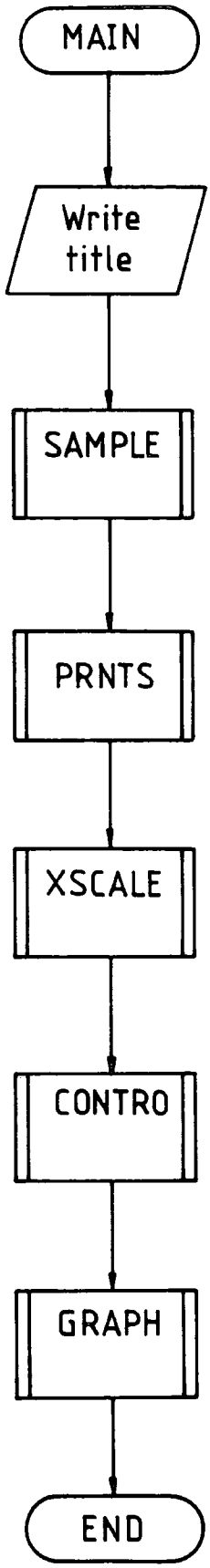
MAIN
Write title
SAMPLE
PRNTS
XSCALE
CONTRO
GRAPH
END

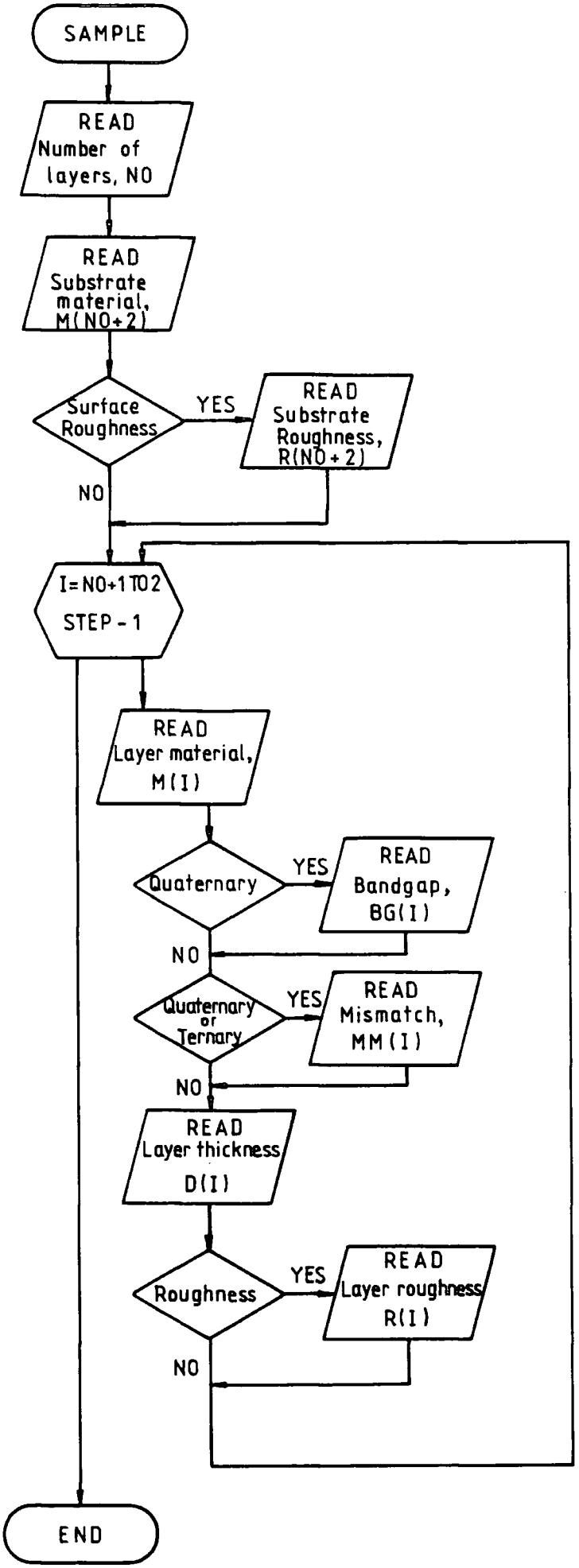
SAMPLE
READ Number of layers, NO
READ Substrate material, M(NO+2)
Surface Roughness
YES
READ Substrate Roughness, R(NO+2)
NO
I=NO+1 TO 2 STEP-1
READ Layer material, M(I)
Quaternary
YES
READ Bandgap, BG(I)
NO
Quaternary or Ternary
YES
READ Mismatch, MM(I)
NO
READ Layer thickness D(I)
Roughness
YES
READ Layer roughness R(I)
NO
END

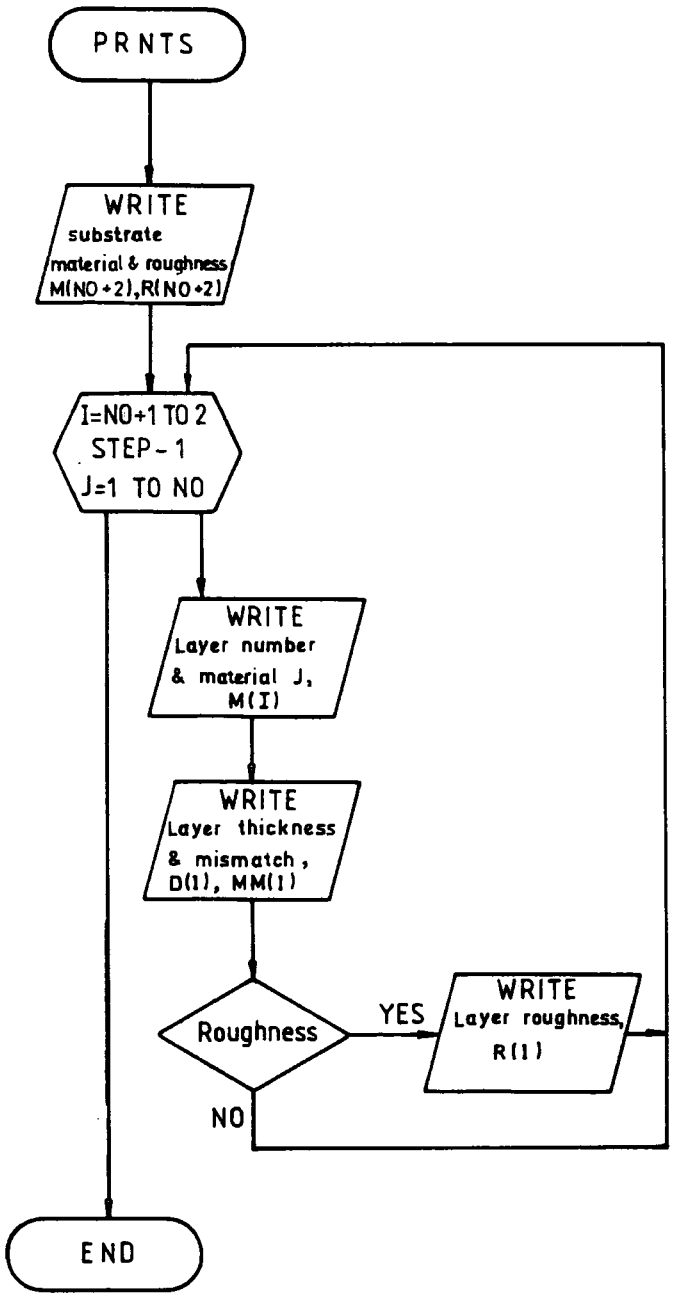
PRNTS
WRITE
substrate
material & roughness
M(NO+2),R(NO+2)
I=NO+1 TO 2
STEP-1
J=1 TO NO
WRITE
Layer number
& material J,
M(I)
WRITE
Layer thickness
& mismatch,
D(1), MM(1)
Roughness
YES
WRITE
Layer roughness,
R(1)
NO
END

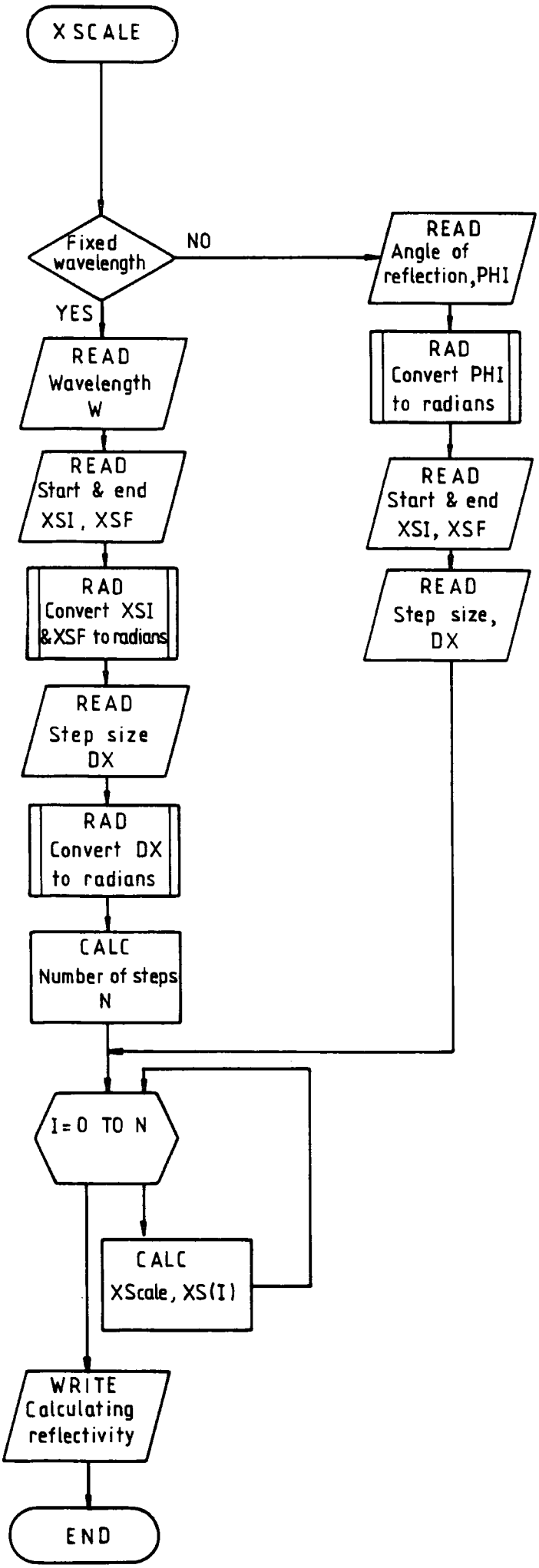
XSCALE
Fixed wavelength
NO
YES
READ Angle of reflection, PHI
READ Wavelength W
RAD Convert PHI to radians
READ Start & end XSI, XSF
READ Start & end XSI, XSF
RAD Convert XSI &XSF to radians
READ Step size, DX
READ Step size DX
RAD Convert DX to radians
CALC Number of steps N
I=0 TO N
CALC XScale, XS(I)
WRITE Calculating reflectivity
END

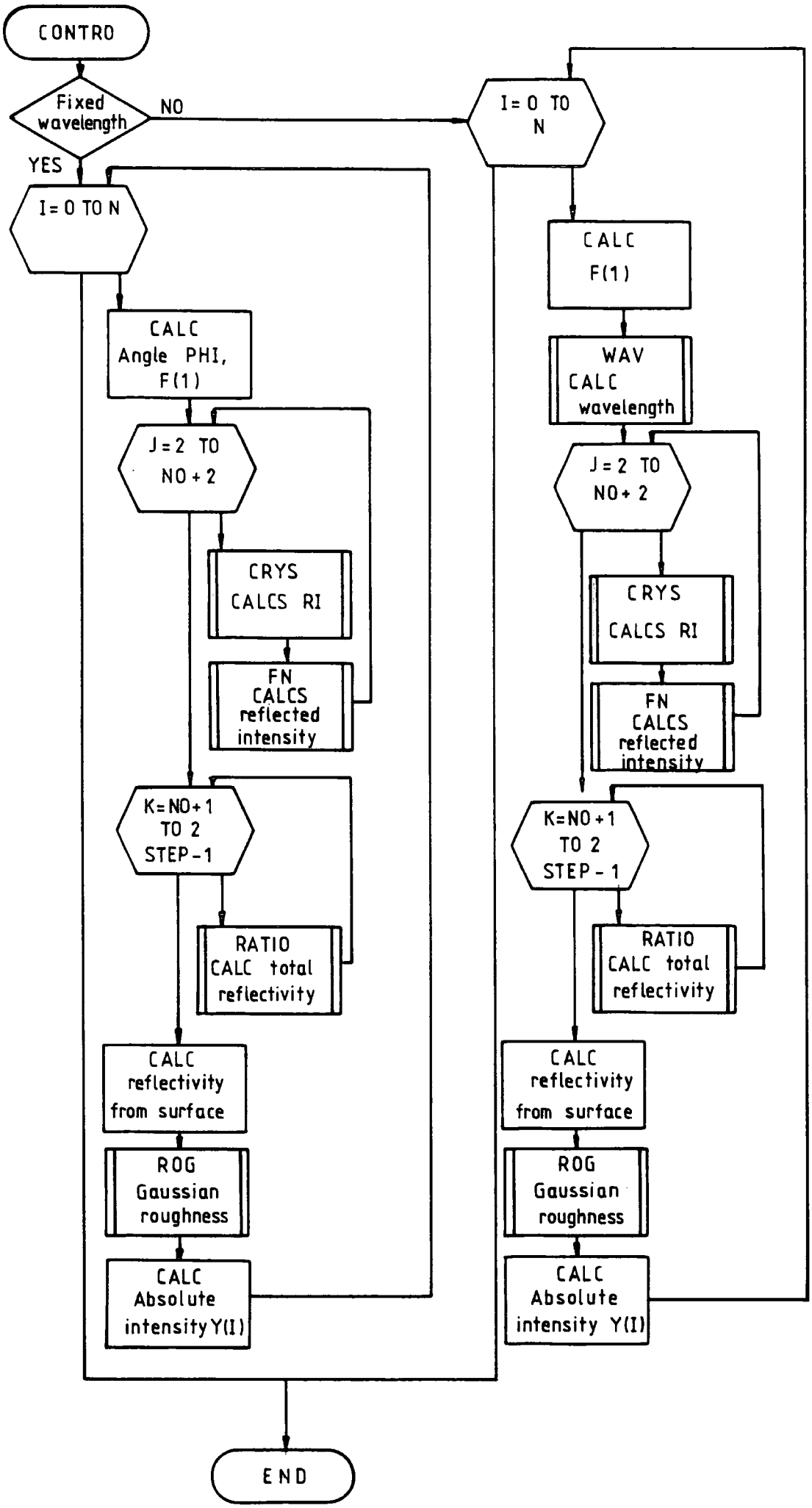
CONTRO
Fixed wavelength
NO
YES
I = 0 TO N
CALC Angle PHI, F(1)
J = 2 TO NO + 2
CRYS CALCS RI
FN CALCS reflected intensity
K = NO + 1 TO 2 STEP - 1
RATIO CALC total reflectivity
CALC reflectivity from surface
ROG Gaussian roughness
CALC Absolute intensity Y(I)
I = 0 TO N
CALC F(1)
WAV CALC wavelength
J = 2 TO NO + 2
CRYS CALCS RI
FN CALCS reflected intensity
K = NO + 1 TO 2 STEP - 1
RATIO CALC total reflectivity
CALC reflectivity from surface
ROG Gaussian roughness
CALC Absolute intensity Y(I)
END

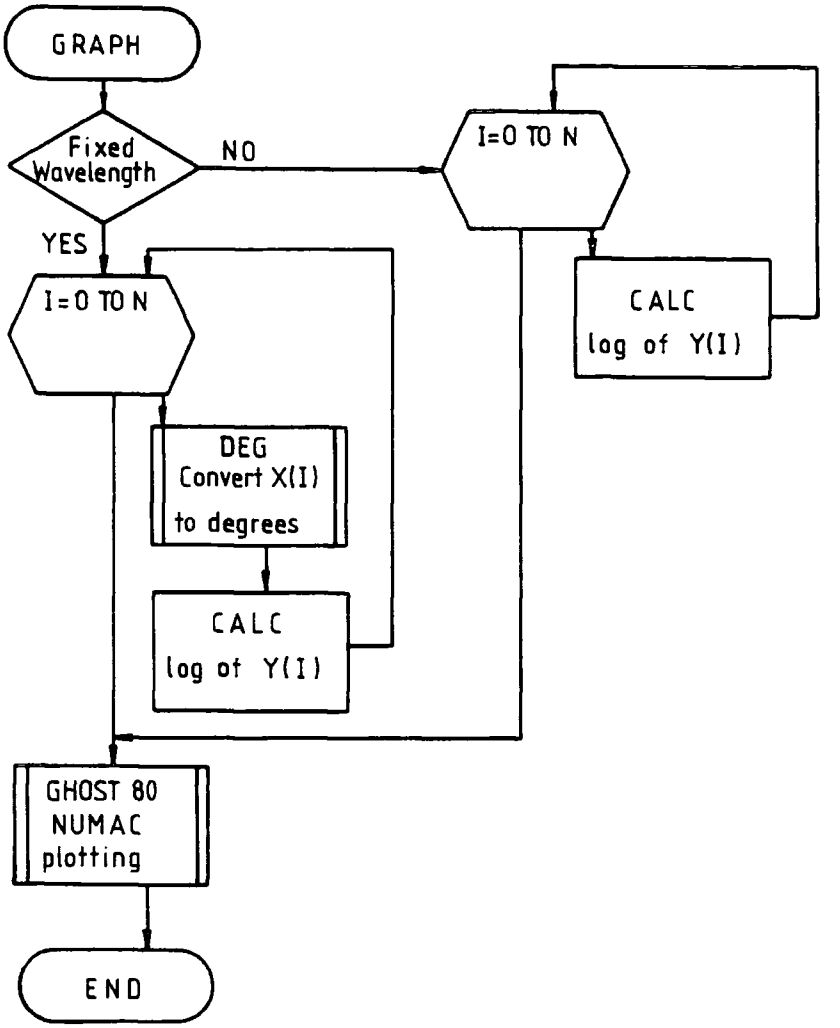
GRAPH
Fixed Wavelength
NO
YES
I=0 TO N
CALC log of Y(I)
I=0 TO N
DEG Convert X(I) to degrees
CALC log of Y(I)
GHOST 80 NUMAC plotting
END

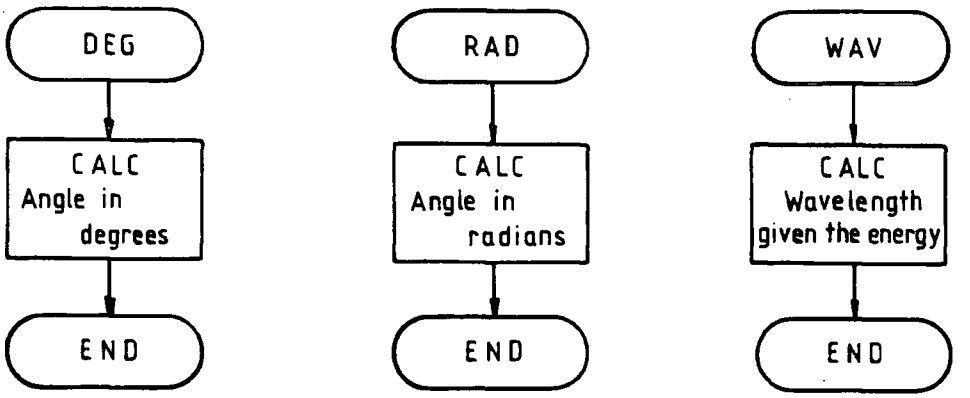
DEG
CALC Angle in degrees
END
RAD
CALC Angle in radians
END
WAV
CALC Wavelength given the energy
END

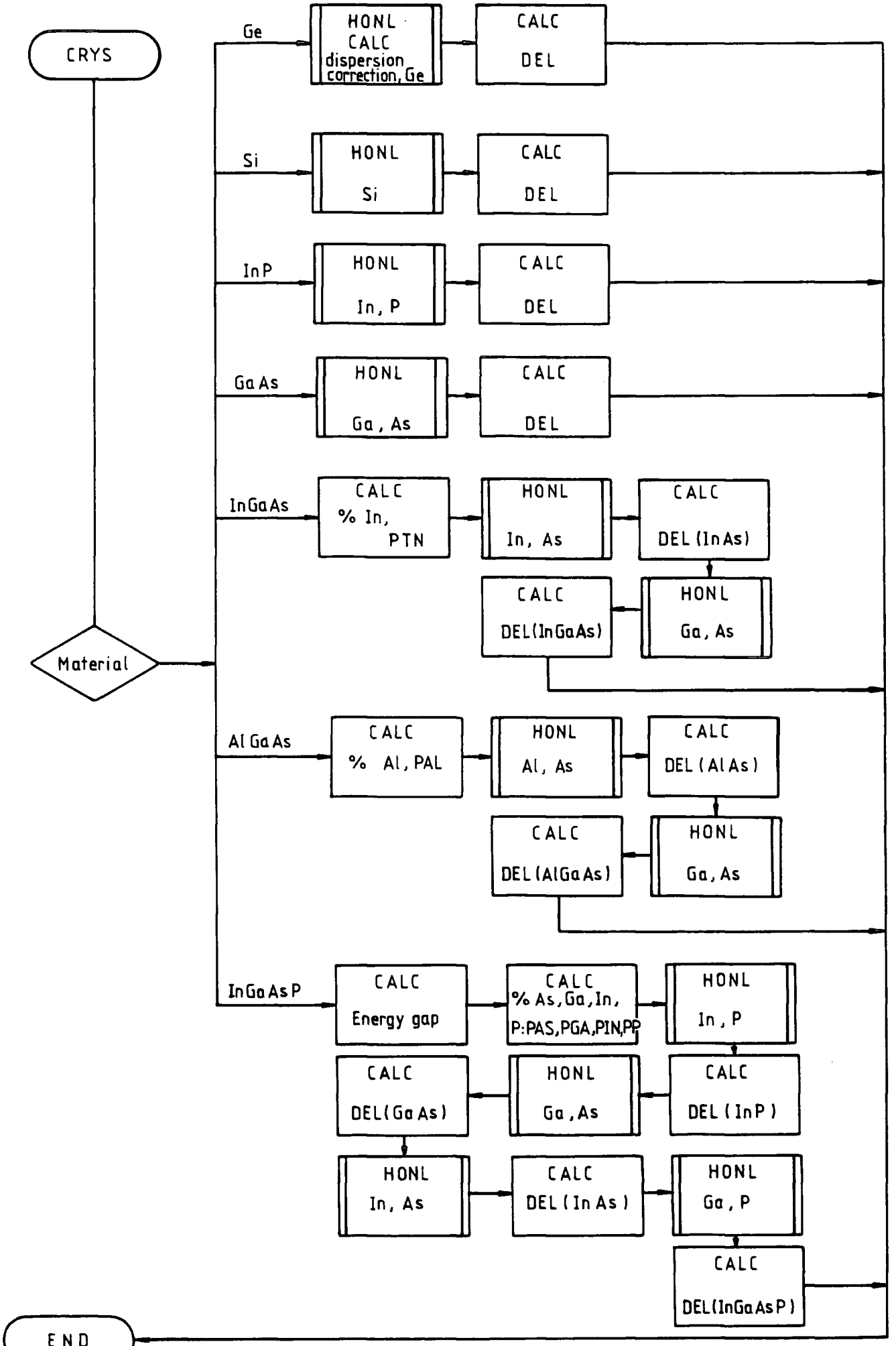
CRYS
Material
Ge
HONL
CALC
dispersion
correction, Ge
CALC
DEL
Si
HONL
Si
CALC
DEL
InP
HONL
In, P
CALC
DEL
GaAs
HONL
Ga, As
CALC
DEL
InGaAs
CALC
% In,
PTN
HONL
In, As
CALC
DEL (InAs)
CALC
DEL(InGaAs)
HONL
Ga, As
AlGaAs
CALC
% Al, PAL
HONL
Al, As
CALC
DEL (AlAs)
CALC
DEL (AlGaAs)
HONL
Ga, As
InGaAsP
CALC
Energy gap
CALC
% As, Ga, In,
P:PAS, PGA, PIN, PP
HONL
In, P
CALC
DEL(GaAs)
HONL
Ga, As
CALC
DEL (InP)
HONL
In, As
CALC
DEL (InAs)
HONL
Ga, P
CALC
DEL(InGaAsP)
END

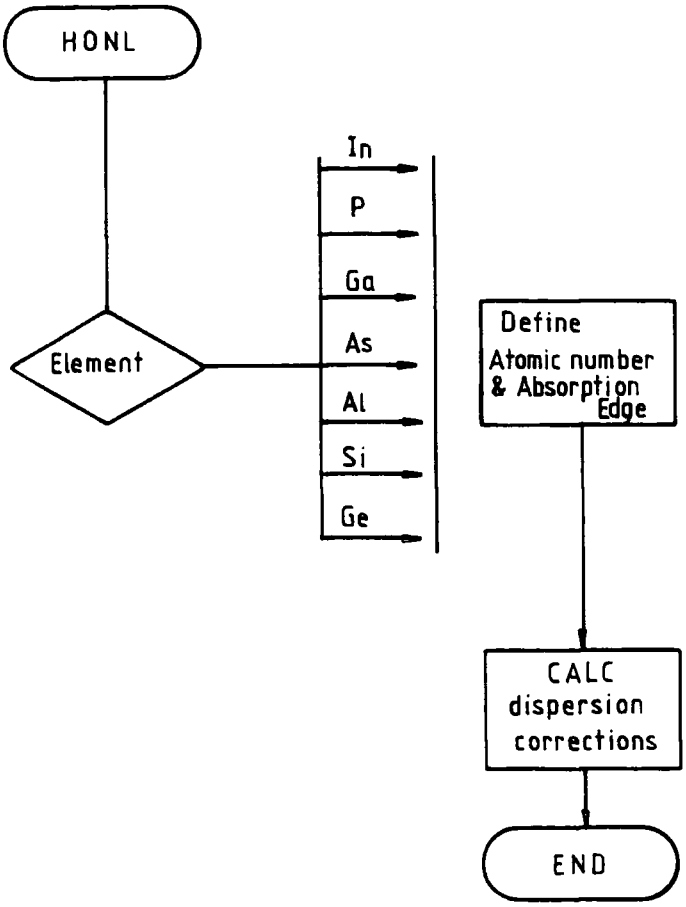
HONL
Element
In
P
Ga
As
Al
Si
Ge
Define
Atomic number
& Absorption
Edge
CALC
dispersion
corrections
END

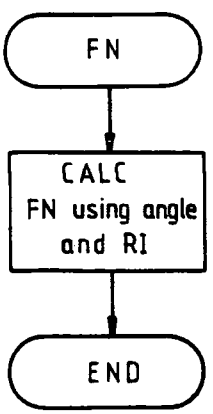
FN
CALC
FN using angle
and RI
END

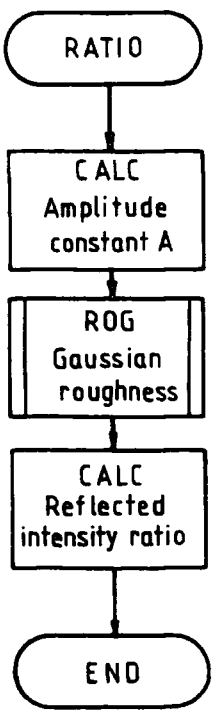
RATIO
CALC
Amplitude
constant A
ROG
Gaussian
roughness
CALC
Reflected
intensity ratio
END

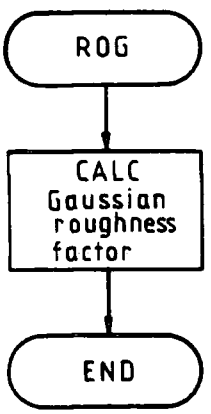
ROG
CALC
Gaussian
roughness
factor
END

```
C*********************************************************
C
C      Program   REFLECT   by   S.J.Miles
C
C            10/1/1989
C
C*********************************************************
C
      INTEGER NO,I,J,BG(2:101),N
      REAL D(2:101),R(2:102),MM(2:101),XS(0:10000),W,PHI
      REAL Y(0:10000)
      COMPLEX DF,DELT(2:102)
      CHARACTER M(2:102)*7,Q,E*2
C
C*********************************************************
C  Display title
      PRINT *,'    ************************************'
      PRINT *,'    *  Reflectivity Simulation Program  *'
      PRINT *,'    *  written by S.J.Miles  10/1/89    *'
      PRINT *,'    ************************************'
      PRINT *,' '
      PRINT *,'! This program can generate reflectivity'
      PRINT *,'! data from layered structures in the'
      PRINT *,'! case where the wavelength is fixed and'
      PRINT *,'! the incident angle is varied or the'
      PRINT *,'! case where the angle is fixed and the'
      PRINT *,'! wavelength varied.'
      PRINT *,'!'
C  Enter sample details
      CALL SAMPLE(NO,M,MM,D,R,BG)
C  Print sample details
      CALL PRNTS(NO,M,MM,D,R)
      CALL XSCALE(Q,PHI,W,XS,N)
      CALL CONTRO(M,D,MM,R,BG,XS,NO,Q,N,Y,W,PHI)
      CALL GRAPH(Q,N,XS,Y)
      STOP
      END
C
C*********************************************************
C* SAMPLE - reads sample data interactively             *
C*********************************************************
C
      SUBROUTINE SAMPLE(NO,M,MM,D,R,BG)
      INTEGER NO,N,L,BG(2:102)
      REAL D(2:101),R(2:102),MM(2:101)
      CHARACTER M(2:102)*7,V
C
      PRINT *,' Entry of Sample Characteristics'
   10 PRINT *,'enter number of layers :'
      READ *,NO
      IF((NO.GE.1).AND.(NO.LE.100))GO TO 20
      PRINT *,'Incorrect entry, no more than 100 layers'
      GO TO 10
C substrate
   20 PRINT *,' Substrate :'
      WRITE(*,30)
   30 FORMAT('Please choose material from ',/,'InP',/,
     1       'GaAs',/,'Si')
      READ '(A7)',M(NO+2)
      IF((M(NO+2).EQ.'InP').OR.(M(NO+2).EQ.'Si'))GO TO 40
```

```
      IF(M(NO+2).EQ.'GaAs')GO TO 40
      PRINT *,' Incorrect entry try again'
      GO TO 20
   40 PRINT *,'Do you want to include surface roughness?'
      READ '(A1)',V
      R(NO+2)=0.0
      IF((V.NE.'Y').AND.(V.NE.'y'))GO TO 60
   50 PRINT *,'Enter the mean roughness of the substrate'
      PRINT *,'interface in Angstroms'
      READ *,R(NO+2)
      IF((R(NO+2).GE.0.0).AND.(R(NO+2).LT.1000.0))GO
     1 TO 60
      PRINT *,'Incorrect entry try again'
      GO TO 50
C  layers
   60 L=0
      DO 130 N=NO+1,2,-1
        MM(N)=0.0
        R(N)=0.0
        BG(N)=0
        L=L+1
   70   PRINT *,'Enter the material type of layer ',L
        PRINT *,'You may choose from :'
        WRITE(*,80)
   80   FORMAT('InP',/,'GaAs',/,'Si',/,'InGaAs',/,
     1        'AlGaAs',/,'InGaAsP',/,'Ge',/,'AlInAs')
        READ '(A7)',M(N)
        IF((M(N).EQ.'InP').OR.(M(N).EQ.'GaAs'))GO TO 100
        IF((M(N).EQ.'Si').OR.(M(N).EQ.'Ge'))GO TO 100
        IF((M(N).EQ.'InGaAs').OR.(M(N).EQ.'AlGaAs'))GO
     1   TO 90
        IF(M(N).EQ.'AlInAs')GO TO 90
        IF(M(N).EQ.'InGaAsP')GO TO 85
        PRINT *,'Incorrect entry try again'
        GO TO 70
C for quaternaries enter band gap
   85   PRINT *,'Enter the band gap of the Quaternary'
        PRINT *,'1 = Q1.05, 2 = Q1.35, 3 = Q1.55'
        READ *,BG(N)
        IF((BG(N).EQ.1).OR.(BG(N).EQ.2))GO TO 90
        IF(BG(N).EQ.3)GO TO 90
        PRINT *,'Incorrect entry, try again'
        GO TO 85
C for ternaries and quaternaries enter mismatch
   90   PRINT *,'Enter the mismatch of layer ',L
        PRINT *,' in ppm'
        READ *,MM(N)
  100   PRINT *,'Enter thicknes of layer ',L,
     1          ' in Angstroms'
        READ *,D(N)
        IF(D(N).GT.0.0)GO TO 110
        PRINT *,'Incorrect entry try again'
        GO TO 100
  110   IF((V.NE.'Y').AND.(V.NE.'y'))GO TO 130
  120   PRINT *,'Enter the mean roughness of layer ',L,
     1          ' in Angstroms'
        READ *,R(N)
        IF((R(N).GE.0.0).AND.(R(N).LT.1000.0))GO TO 130
        PRINT *,'Incorrect entry try again'
        GO TO 120
```

```
  130 CONTINUE
      RETURN
      END
C*********************************************************
C* PRNTS  -  prints out sample data                      *
C*********************************************************
      SUBROUTINE PRNTS(NO,M,MM,D,R)
      REAL D(2:101),R(2:102),MM(2:101)
      CHARACTER M(2:102)*7
      INTEGER I,NO,J
      PRINT *,'Sample details :'
      PRINT *,'Substrate : ',M(NO+2)
      IF(R(NO+2).NE.0.0)THEN
        PRINT *,'Roughness =',R(NO+2),'A'
      ENDIF
      J=0
      DO 100 I=NO+1,2,-1
        J=J+1
        PRINT *,'Layer ',J,' Material ',M(I)
        PRINT *,'Thickness =',D(I),'A',
     1          '  Mismatch =',MM(I),'ppm'
        IF(R(I).NE.0.0)THEN
          PRINT *,'Roughness =',R(I),'A'
        ENDIF
  100 CONTINUE
      RETURN
      END
C*********************************************************
C  CRYS  -  calculates refractive index correction,     *
C           delta, for a given material and wavelength  *
C*********************************************************
      SUBROUTINE CRYS(MA,W,MIS,EG,DEL)
C this subroutine uses subroutine Honl to calculate
C individual element disprsion corrections
      INTEGER EG
      REAL MIS,W,B,AR,PIN,PAL,PGA,PP,PAS,Y
      COMPLEX DEL,DE,DF
      CHARACTER MA*7,E*2
C calculate constant factor
      B=2.72E-6*W*W
C determine dispersion corrections for each material then
C calculate refractive index
C Si
      IF(MA.EQ.'Si')THEN
        E='Si'
        CALL HONL(W,E,DF)
        DEL=B*(14.0+DF)*2.3283/28.086
      ENDIF
C Ge
      IF(MA.EQ.'Ge')THEN
        E='Ge'
        CALL HONL(W,E,DF)
        DEL=B*(32.0+DF)*5.3234/72.59
      ENDIF
C InP
      IF(MA.EQ.'InP')THEN
        E='In'
        CALL HONL(W,E,DF)
        DEL=DF
        E='P'
```

```
        CALL HONL(W,E,DF)
        DEL=B*(64.0+DEL+DF)*4.787/145.794
      ENDIF
C GaAs
      IF(MA.EQ.'GaAs')THEN
        E='Ga'
        CALL HONL(W,E,DF)
        DEL=DF
        E='As'
        CALL HONL(W,E,DF)
        DEL=B*(64.0+DEL+DF)*5.316/144.642
      ENDIF
C InGaAs
      IF(MA.EQ.'InGaAs')THEN
        AR=5.86875*(MIS*1.0E-6+1.0)
        PIN=(AR-5.65315)/0.40523
        E='In'
        CALL HONL(W,E,DF)
        DEL=DF
        E='As'
        CALL HONL(W,E,DF)
        DEL=B*PIN*(82.0+DEL+DF)*5.66/189.742
        E='Ga'
        CALL HONL(W,E,DF)
        DE=DF
        E='As'
        CALL HONL(W,E,DF)
        DEL=DEL+B*(1.0-PIN)*(64.0+DE+DF)*5.316/144.642
      ENDIF
C AlGaAs
      IF(MA.EQ.'AlGaAs')THEN
        AR=5.65315*(MIS*1.0E-6+1.0)
        PAL=(AR-5.65315)/0.00905
        E='Al'
        CALL HONL(W,E,DF)
        DEL=DF
        E='As'
        CALL HONL(W,E,DF)
        DEL=B*PAL*(46.0+DEL+DF)*3.81/101.904
        E='Ga'
        CALL HONL(W,E,DF)
        DE=DF
        E='As'
        CALL HONL(W,E,DF)
        DEL=DEL+B*(1.0-PAL)*(64.0+DE+DF)*5.316/144.642
      ENDIF
C AlInAs
      IF(MA.EQ.'AlInAs')THEN
        AR=5.86875*(MIS*1.0E-6+1.0)
        PIN=(AR-5.6622)/0.39618
        E='In'
        CALL HONL(W,E,DF)
        DEL=DF
        E='As'
        CALL HONL(W,E,DF)
        DEL=B*PIN*(82.0+DEL+DF)*5.66/189.742
        E='Al'
        CALL HONL(W,E,DF)
        DE=DF
        E='As'
```

```
        CALL HONL(W,E,DF)
        DEL=DEL+B*(1.0-PIN)*(46.0+DE+DF)*3.81/101.904
      ENDIF
C InGaAsP
      IF(MA.EQ.'InGaAsP')THEN
        IF(EG.EQ.1)Y=1.05
        IF(EG.EQ.2)Y=1.35
        IF(EG.EQ.3)Y=1.55
        Y=1.2408/Y
        PAS=(0.72-SQRT(0.5184-0.48*(1.35-Y)))/0.24
        PGA=5.86875*MIS*1.0E-6 - PAS*0.18963
        PGA=PGA/(PAS*5.65315+(1.0-PAS)*5.4505-PAS*6.05838
     1  -(1.0-PAS)*5.86875)
        PIN=1.0-PGA
        PP=1.0-PAS
        E='In'
        CALL HONL(W,E,DF)
        DE=DF
        E='P'
        CALL HONL(W,E,DF)
        DEL=B*PP*PIN*(64.0+DE+DF)*4.787/145.794
        E='Ga'
        CALL HONL(W,E,DF)
        DE=DF
        E='As'
        CALL HONL(W,E,DF)
        DEL=DEL+B*PGA*PAS*(64.0+DE+DF)*5.316/144.642
        E='In'
        CALL HONL(W,E,DF)
        DE=DF
        E='As'
        CALL HONL(W,E,DF)
        DEL=DEL+B*PAS*PIN*(82.0+DE+DF)*5.66/189.742
        E='Ga'
        CALL HONL(W,E,DF)
        DE=DF
        E='P'
        CALL HONL(W,E,DF)
        DEL=DEL+B*PGA*PP*(46.0+DE+DF)*4.13/100.694
      ENDIF
      RETURN
      END
C*********************************************************
C  HONL  -  calculates dispersion corrections for a     *
C           given element and wavelength using Holn's   *
C           method                                      *
C*********************************************************
      SUBROUTINE HONL(W,E,DF)
      REAL W,WK,Z,X,DK,GK,PI
      COMPLEX DF
      CHARACTER E*2
      PI=3.141592654
C for the element type define the atomic number and the
C absorbtion edge for use in the calculation
      IF(E.EQ.'In')THEN
        Z=49
        WK=0.444
      ENDIF
      IF(E.EQ.'P')THEN
        Z=15
```

```
        WK=5.7886
      ENDIF
      IF(E.EQ.'Ga')THEN
        Z=31
        WK=1.196
      ENDIF
      IF(E.EQ.'As')THEN
        Z=33
        WK=1.045
      ENDIF
      IF(E.EQ.'Al')THEN
        Z=13
        WK=7.9511
      ENDIF
      IF(E.EQ.'Si')THEN
        Z=14
        WK=6.7446
      ENDIF
      IF(E.EQ.'Ge')THEN
        Z=32
        WK=1.117
      ENDIF
C calculate the ratio of the wavelength to the edge
      X=WK/W
      A=(Z-0.3)**2+1.33E-5*(Z-0.3)**4
C oscillator strength
      DK=(A-911/WK)/A
      GK=0.520978*(2/((1.0-DK)**2)-1/(3*(1-DK)**3))
C real dispersion correction
      DF=GK*(LOG(ABS(1.0-X*X)))/(X*X)
C imaginary correction
      IF(X.GE.1.0)THEN
      DF=DF+(0.0,1.0)*PI*GK/(X*X)
      ENDIF
      RETURN
      END
C*********************************************************
C*  XSCALE  -  determines experimental details           *
C*********************************************************
      SUBROUTINE XSCALE(Q,PHI,W,XS,N)
      REAL PHI,W,XS(0:10000),XSI,XSF
      CHARACTER Q
      INTEGER N
C determine experimental details
      PRINT *,'Do you wish to keep the wavelength fixed?'
      READ '(A1)',Q
      IF((Q.EQ.'Y').OR.(Q.EQ.'y'))THEN
C fixed wavelength - variable angle
   10   PRINT *,'Enter the wavelength in Angstroms'
        READ *,W
        IF(W.GT.0.0)GO TO 20
        PRINT *,'Incorrect entry try again'
        GO TO 10
   20   PRINT *,'Enter range of reflection (degrees)'
        PRINT *,'(start,finish)='
        READ *,XSI,XSF
        IF(XSF.LE.XSI)GO TO 30
        IF((XSI.GE.0.0).AND.(XSF.GE.0.0))GO TO 40
   30   PRINT *,'Incorrect entry try again'
        GO TO 20
```

```
   40   XSI=RAD(XSI)
        XSF=RAD(XSF)
   50   PRINT *,'Enter step size (seconds)'
        READ *,DX
        DX=RAD(DX)/3600.0
        IF((DX.GT.0.0).AND.(DX.LE.(XSF-XSI)))GO TO 60
        PRINT *,'Incorrect entry try again'
        GO TO 50
   60   N=(XSF-XSI)/DX
        IF(N.GT.10000)THEN
          PRINT *,'Too many steps try again'
          GO TO 50
        ENDIF
      ELSE
C fixed angle , variable wavelength
   80   PRINT *,'Enter the angle of reflection (degrees)'
        READ *,PHI
        IF((PHI.GT.0.0).AND.(PHI.LT.90.0))GO TO 90
        PRINT *,'Incorrect entry try again'
        GO TO 80
   90   PHI=RAD(PHI)
  100   PRINT *,'Enter the range in Energy (kev)'
        PRINT *,'(Start,Finish)='
        READ *,XSI,XSF
        IF(XSF.LE.XSI)GO TO 110
        IF((XSI.GE.0.0).AND.(XSF.GE.0.0))GO TO 120
  110   PRINT *,'Incorrect entry try again'
        GO TO 100
  120   PRINT *,'Enter step size (kev)'
        READ *,DX
        IF((DX.GT.0.0).AND.(DX.LE.(XSF-XSI)))GO TO 130
        PRINT *,'Incorrect entry try again'
        GO TO 120
  130   N=(XSF-XSI)/DX
        IF(N.LE.10000)GO TO 140
        PRINT *,'Too many steps try again'
        GO TO 120
  140 ENDIF
C produce xscale
      DO 150 I=0,N
        XS(I)=XSI+DX*FLOAT(I)
  150 CONTINUE
      PRINT *,'Calculating Reflectivity......Please Wait'
      RETURN
      END
C*********************************************************
C*  RAD  -  function to convert degrees to radians      *
C*********************************************************
      FUNCTION RAD(ANGLE)
      REAL PI,ANGLE
      PI=3.141592654
      RAD=ANGLE*PI/180.0
      RETURN
      END
C*********************************************************
C*  FN  -  calculates reflected intensity for a given   *
C*         wavelength and material                      *
C*********************************************************
      SUBROUTINE FN(ANGLE,DELTA,F)
      COMPLEX DELTA,F
```

```
      REAL ANGLE
      F=CSQRT(ANGLE*ANGLE-2.0*DELTA)
      RETURN
      END
C*********************************************************
C*  RATIO  -  calculation of reflected intensity        *
C*********************************************************
      SUBROUTINE RATIO(FN,FN1,T,RN,RN1,SIG,ANGLE,WL)
C subroutine to evaluate E-vector ratio , R(n-1)
      COMPLEX FN,FN1,RN,RN1,FF,A
      REAL WL
      PI=3.141592654
C evaluate amplitude factor , a , to 4th power
      A=(0.0,-1.0)*FN1*T*PI/WL
      A=(CEXP(A))**4
C evaluate capital F values
      FF=((FN1-FN)/(FN1+FN))*(ROG(SIG,ANGLE,WL))
C evaluate R(n-1)
      RN1=A*(RN+FF)/(RN*FF+1.0)
      RETURN
      END
C*********************************************************
C*  ROG  -  function to calculate the Gaussian roughness*
C*          factor for a given wavelength and angle     *
C*********************************************************
      FUNCTION ROG(SIG,ANGLE,WL)
      REAL PI,ANGLE,WL,ROG
      PI=3.141592654
      ROG=PI*SIG*(SIN(ANGLE/WL))
      ROG=EXP(-8.0*ROG*ROG)
      RETURN
      END
C*********************************************************
C*  CONTRO  -  subroutine to execute reflectivity      *
C*              routines for given experimental and     *
C*              sample details                          *
C*********************************************************
      SUBROUTINE CONTRO(M,D,MM,R,BG,XS,NO,Q,N,Y,W,PHI)
      REAL D(2:101),MM(2:101),R(2:102),XS(0:10000)
      REAL Y(0:10000),W,PHI
      COMPLEX RR(102),F(102),DEL,FF
      INTEGER NO,N,BG(2:102),I,J,K,KK
      CHARACTER M(2:102)*7,Q
C set initial constants
      RR(NO+2)=(0.0,0.0)
      IF((Q.EQ.'Y').OR.(Q.EQ.'y'))THEN
C fixed wavelength , variable angle
        DO 200 I=0,N
          PHI=XS(I)
          F(1)=PHI
C calculate f values
          DO 100 J=2,NO+2
            CALL CRYS(M(J),W,MM(J),BG(J),DEL)
            CALL FN(PHI,DEL,F(J))
  100     CONTINUE
C calculate ratios
          DO 150 K=NO+1,2,-1
            KK=K+1
            CALL RATIO(F(KK),F(K),D(K),RR(KK),RR(K),R(KK)
     1                 ,PHI,W)
```

```
  150     CONTINUE
C calculate intensity from top layer
          FF=(F(1)-F(2))/(F(1)+F(2))*
     1       (ROG(R(2),PHI,W))
          RR(1)=(RR(2)+FF)/(RR(2)*FF+1.0)
          Y(I)=(CABS(RR(1)))*(CABS(RR(1)))
  200   CONTINUE
      ELSE
C fixed angle , variable wavelength
        DO 400 I=0,N
          F(1)=PHI
          W=WAV(XS(I))
C calculate f values
          DO 300 J=2,NO+2
            CALL CRYS(M(J),W,MM(J),BG(J),DEL)
            CALL FN(PHI,DEL,F(J))
  300     CONTINUE
C calculate ratios
          DO 350 K=NO+1,2,-1
            KK=K+1
            CALL RATIO(F(KK),F(K),D(K),RR(KK),RR(K),R(KK)
     1                 ,PHI,W)
  350     CONTINUE
C calculate intensity from top layer
          FF=(F(1)-F(2))/(F(1)+F(2))*
     1       (ROG(R(2),PHI,W))
          RR(1)=(RR(2)+FF)/(RR(2)*FF+1.0)
          Y(I)=(CABS(RR(1)))*(CABS(RR(1)))
  400   CONTINUE
      ENDIF
      RETURN
      END
C*********************************************************
C*  WAV  - function to calculate wavelength in Angstroms*
C*         for a given energy                            *
C*********************************************************
      FUNCTION WAV(KEV)
      REAL WAV,KEV
      WAV=1.0E10*6.626E-34*3.0E8/(KEV*1.602E-16)
      RETURN
      END
C*********************************************************
C*  DEG  -  function to convert radians to degrees      *
C*********************************************************
      FUNCTION DEG(RADN)
      REAL DEG,RADN,PI
      PI=3.141592654
      DEG=RADN*180.0/PI
      RETURN
      END
C*********************************************************
C*  GRAPH  -  plots out results using Ghost80           *
C*********************************************************
      SUBROUTINE GRAPH(Q,N,X,Y)
C subroutine to plot data using GHOST80 programs
      REAL XMIN,XMAX,YMIN,YMAX,X(0:10000),Y(0:10000)
      REAL TX,TY,XLX,XLY,YLX,YLY
      CHARACTER TEXT*30,Q
      INTEGER N,I
C
```

```
      PRINT *,'Generating graph - use *view -p* to see'
      PRINT *,'and *rlaser -p* for a hard copy'
      IF((Q.EQ.'Y').OR.(Q.EQ.'y'))THEN
C fixed wavelength
C convert radians to degrees for scale
        YMAX=-100.0
        YMIN=1.0
        DO 100 I=0,N
          X(I)=DEG(X(I))
C convert data to log
          Y(I)=LOG10(Y(I))
C set maxima and minima
          IF(YMIN.GT.Y(I))YMIN=Y(I)
  100   CONTINUE
      ELSE
C fixed angle
        YMAX=-100.0
        YMIN=1.0
        DO 200 I=0,N
C convert data to log
          Y(I)=LOG10(Y(I))
C set maxima and minima
          IF(YMIN.GT.Y(I))YMIN=Y(I)
  200   CONTINUE
      ENDIF
        XMIN=0.0
        XMAX=X(N)
        YMAX=0.0
C write data to file
      DO 205 I=0,N
        WRITE(1,*)X(I),Y(I)
  205 CONTINUE
C switch on output device and define ranges
      CALL PAPER(1)
      CALL PSPACE(0.1,0.7,0.1,0.9)
      CALL MAP(XMIN,XMAX,YMIN,YMAX)
C read title
      PRINT*,'Enter title details'
      READ '(A30)',TEXT
      CALL AXES
      CALL CURVEO(X,Y,0,N)
C set position of title
      TX=0.5*XMAX
      TY=0.1*YMIN
      XLX=0.5*XMAX
      XLY=-0.08*YMIN
      YLX=-0.1*XMAX
      YLY=0.5*YMIN
      CALL CTRMAG(15)
      CALL PLOTCS(TX,TY,TEXT)
      CALL CTRMAG(25)
      IF((Q.EQ.'Y').OR.(Q.EQ.'y'))THEN
        CALL PCSCEN(XLX,XLY,'Angle (degrees)')
      ELSE
        CALL PCSCEN(XLX,XLY,'Energy (kev)')
      ENDIF
      CALL CTRORI(90.0)
      CALL PCSCEN(YLX,YLY,'Reflectivity (log)')
C terminate the graph
      CALL FRAME
```

```
CALL GREND
CLOSE(5)
RETURN
END
```

References

Afanas'ev, A. M., Aleksandrov, P. A., Imamov, R. M., Lomov, A. A. and Zavylov A. A. (1984) Acta Cryst. **A40** 352.

Agrawal, G. P. and Dutta, N. K. (1986) *Long Wavelangth Semiconductor Lasers*, Van Nostrand, New York.

Ahlgren, W. L., James, J. B., Ruth, R. P., Patten, E. A. and Staudenmann, J. -L. (1987) Mat. Res. Soc. Symp. Proc. **90** 405.

Alavi, K., Petroff, P., Wagner, W. R. and Cho, A. Y. (1983) J. Vac. Sci. Technol. **B1**(2) 146.

Allison, S. K. and Williams, J. H. (1930) Phys. Rev. **35** 1476.

Allison, S. K. (1932) Phys. Rev. **41** 1.

Ambridge, T. and Wakefield, B. (1985) Br. Telecom. Technol. J. **3**(1) 47.

Andrews, S. R. and Cowley, R. A. (1986) J. Phys. C: Solid State Phys. **18** 6427.

Asher, S. (1988) Adv. X-Ray Anal. **31** 53.

Authier, A. (1970) In *Advances in Structure Research by Diffraction Methods* (ed: Brill and Mason) **3** 1.

Auvray, P., Baudet, M. and Regreny, A. (1987) J. Appl. Phys. **62**(2) 456.

Auvray, P., Baudet, M. and Regreny, A. (1989) J. Cryst. Growth. **95** 288.

Aydinli, A., Camera, A., Drigo, A. V., Genova, F., Moro, L., Ferrari, C. and Franzosi, P. (1987) Les Editions de Physique **16** 193.

Bachmann, K. J. and Gaslowsky, H. (1987) Mat. Res. Soc. Symp. Proc. **90** 69.

Baribeau, J. -M. (1988) Appl. Phys. Lett. **52**(2) 105.

Baribeau, J. -M., Houghton, D. C. and Kerchang, S. (1989) Proc. Symp. on *Heteroepitaxial Approaches in Semiconductors: Lattice Mismatch and its Consequences* **89-5** 287.

Barnett, S. J., Brown, G. T., Courtney, S. J., Bass, S. J. and Taylor, L. L. (1988) J. Appl. Phys. **64**(3) 1185.

Barnett, S. J., Brown, G. T.,Houghton, D. C. and Baribeau, J. -M. (1989) Appl. Phys. Lett. **54**(18) 1781.

Bartels, W. J. and Nijman, W. (1978) J. Cryst. Growth **44** 518.

Bartels, W. J. (1983) J. Vac. Sci. Technol. **B1**(2) 338.

Bartels, W. J., Hornstra, J. and Lobeek, D. J. W. (1986) Acta Cryst. **A42** 539.

Bassingnana, I. C., Springthorpe, A. J. and Tan, C. C. (1987) Inst. Phys. Conf. Ser. **91** 267.

Bassingnana, I. C. and Tan, C. C. (1989) J. Appl. Cryst. **22** 269.

Bates, S., Hatton, P. D., Lucas, C. A. Ryan, T. W., Miles, S. J. and Tanner B. K. (1988) Adv. X-Ray Anal. **31** 155.

Batey, J., Roberts, G. G. and Petty, M. C. (1983) Thin Solid Films **99** 283.

Batterman, B. W. and Cole, H. (1964) Rev. Mod. Phys. **3** 681.

Batterman, B. W. and Hilderbrandt, G. (1968) Acta Cryst. **A24** 150.

Baumbach, T., Rhan, H. and Pietsch, U. (1988) Phys. Stat. Sol. (a) **109** K7.

Beaumont, J. H. and Hart, M. (1974) J. Phys. E: Sci. Inst. **7** 823.

Bede Scientific Instruments (1987) J. Appl. Phys. **20** 272.

Bell, T. E. (1983) IEEE Spectrum (Dec) 38.

Bensoussan, S., Malgrange, C. and Sauvage-Simkin, M. (1987) J. Appl. Cryst. **20** 222.

Bensoussan, S., Malgrange, C., Sauvage-Simkin, M., N'Guesson, K. and Gibart, P. (1987) J. Appl. Cryst. **20** 230.

Bhat, B., Taskar, N. R., Ayers, J. E. Patel, K. and Ghandi, S. K. (1987) Mat. Res. Soc. Symp. Proc. **90** 471.

Bhat, B., Patel, K., Taskar, N. R., Ayers, J. E. and Ghandi, S. K. (1988) J. Cryst. Growth **88** 23.

Bhat, H. L. (1985) Prog. Cryst. Growth Charact. **2** 57.

Bilderback, D. H. and Hubbard, J. (1982) Nucl. Instr. Meth. **195** 85 and 91.

Blodgett, K. B. (1935) J. Am. Chem. Soc. **57** 1007.

Bocchi, C., Ferrari, C., Franzosi, P., Fornuto, G., Pellegrino, S. and Taiariol, F. (1987) J. Electron. Mat. **16**(4) 245.

Le Boite, M. G., Traverse, A., Névot, L., Pardo, B. and Corno, J. (1988) J. Mat. Res. **3**(6) 1089.

Bonse, U. and Kappler, E. (1958) Z. Naturforschung **13a** 792.

Bowen, D. K., Hill, M. J. and Tanner, B. K. (1987) Mat. Res. Soc. Symp. Proc. **82** 447.

Brantley, W. A. (1973) J. Appl. Phys. **44** 534.

Brennan, S. (1986)Proc SPIE Int. Soc. Opt. Eng. **690** 124.

Brühl, H. -G., Pietsch, U. and Lengeler, B. (1988) J. Appl. Cryst. **21** 240.

Brümmer, O., Höche, H. R. and Nieber, J. (1976) Phys. Stat. Sol. (a) **37** 529.

Bubáková, R., Drahokoupil, J. and Fingerland, A. (1961) Czech. J. Phys. **B11** 205.

Bubáková, R., Hrivnáková, M. and Šourek, Z. (1975) Czech. J. Phys. **B25** 1321.

Capano, M. A., Kavanagh, K. L., Bensoussan, S. and Hobbs, L. W. (1988) Rigaku J. **5**(1) 3.

Carey, K. W. (1985) Appl. Phys. Lett. **46** 89.

Chang, K. H., Bhattacharya, P. K. and Gibala, R.(1989) J. Appl. Phys. **65**(9) 3391.

Chang, L. L., Segmüller, A. and Esaki, L. (1976) Appl. Phys. Lett. **28**(1) 39.

Chang, L. L. (1983) J. Vac. Sci. Technol. **B1**(2) 120.

Chang, L. L. (1986) Mat. Res. Soc. Symp. Proc. **56** 267.

Chatterjee, A. K., Faktor, M. M., Lyons, M. H. and Moss, R. H. (1982) J. Cryst. Growth. **56** 591.

Cho, A. Y. and Arthur, J. R. (1975) Prog. Solid State Chem. **10**(3) 1975.

Christensen, F. E., Hornstrup, A. and Schnopper, H. W. (1988) J. Appl. Cryst. **21** 252.

Chu, R., Wie, C. R., Kim, H. M. and Lau, K. M. (1988) Proc SPIE Int. Soc. Opt. Eng. **877** 41.

Chu, X. and Tanner, B. K. (1986) Appl. Phys. Lett. **49**(26) 1773.

Chu, X. and Tanner, B. K. (1987) Semicond. Sci. Technol. **2** 765.

Cockerton, S., Green, G. S. and Tanner, B. K. (1989) Mat. Res. Soc. Symp. Proc. **138** 65.

Cockerton, S., Miles, S. J., Green, G. S. and Tanner, B. K. (1989) J. Cryst. Growth (in press).

Compton, A. H. (1931) Rev. Sci. Instrum. **2**(7) 365.

Compton, A. H. and Allison, S. K. (1936) *X-Rays in Theory and Experiment*, MacMillon.

Cook, L. W., Tashima, M. M., Tabatabaie, N., Low, T. S. and Stillman, G. E. (1982) J. Cryst. Growth. **56** 475.

Cowley, R. A. and Ryan, T. W. (1987) J. Phys. D: Appl. Phys. **20** 61.

Darwin, C. (1914) Phil. Mag. **27** 315 and 675.

Davey, S. T., Wakefield, B. and Ambridge, T. (1987) Br. Telecom. Technol. J. **5**(4) 19.

Davey, S. T., Scott, E. G., Wakefield, B. and Davies, G. J. (1987) Semicond. Sci. Technol. **2** 683.

Davey, S. T., Halliwell, M. A. G., Rogers, D. C., Taylor, M. R. and Scott, E. G. (1989) J. Cryst. Growth. **96** 258.

Davies, G. J. and Andrews, D. A. (1985) Br. Telecom. Technol. J. **3**(2) 59.

Diebold, A. C., Steinhauser, S. W. and Mariella, R. P. (1989) J. Vac. Sci. Technol. **B7**(2) 365.

DuMond, J. W. M. (1937) Phys. Rev. **52** 872.

DuMond, J. W. M. and Marlow, D. (1937) Rev. Sci. Instrum. **8** 112.

Dupuis, R. D., Bean, J. C., Brown, J. M., Macrander, A. T., Miller, R. C. and Hopkins, L. C. (1987) J. Electron. Mat. **16**(1) 69.

Dyer, L. R. (1983) Electrochem. Soc. Ext. Abstr. **83-2** 553.

Eaglesham, D. J., Kvam, E. P., Maher, D. M., Humphreys, C. J., Green, G. S., Tanner, B. K. and Bean, J. C. (1988) Appl. Phys. Lett. **53**(21) 2083.

Esaki, L. and Tsu, R. (1970) IBM J. Res. Dev. **14** 61.

Estrop, E., Izrael, A. and Sauvage, M. (1976) Acta Cryst. **A32** 627.

Ewald, P. P. (1916) Ann. Physik. **49** 117.

Ewald, P. P. (1917) Ann. Physik. **54** 519.

Fatner, E. J. (1987) Adv. X-Ray Anal. **29** 367.

Ferrari, C., Franzosi, P., Gastaldi, L. and Taiariol, F. (1988) J. Appl. Phys. **63**(8) 2628.

Ferrari, C. and Franzosi, P. (1989) J. Appl. Phys. **65**(4) 1544.

Fewster, P. F. (1985) J. Appl. Cryst. **18** 334.

Fewster, P. F. (1986) Phillips J. Phys. **41** 268.

Fewster, P. F. (1987) *Thin Film Techniques for Low Dimmensional Structures* NATO ASI Series B: Physics, **163** ed: Farrow, Parkin, Dobson, Neave and Arrot, 417.

Fewster, P. F. and Curling, C. J. (1987) J. Appl. Phys. **62** 4154.

Fewster, P. F. (1988) J. Appl. Cryst. **21** 524.

Fewster, P. F. (1989) J. Appl. Cryst. **22** 64.

Fewster, P. F. (1989) Proc. Symp. on *Heteroepitaxial Approaches in Semiconductors: Lattice Mismatch and its Consequences* **89-5** 278.

Fiory, A. T., Bean, J. C., Feldman, L. C. and Robinson, I. K. (1984) J. Appl. Phys. **56**(4) 1227.

Fleming, R. M., McWhan, D. B., Gossard, A. C.,Wiegmann, W. and Logan, R. A. (1980) J. Appl. Phys. **51**(1) 357.

Fukui, T. (1984) Japn. J. Appl. Phys. **23**(4) L208.

Glisson, T. H., Hauser, J. R., Littlejohn, M. A. and Williams, C. K. (1978) J. Electron. Mat. **7**(1) 1.

Goetz, K. -H., Bimberg, D., Jürgensen, H., Selders, J., Solomonov, A. V., Glinskii, G. F. and Razeghi, M. (1983) J. Appl. Phys. **54**(8) 4543.

Griesche, J., Enderlein, R. and Schikora, D. (1988) Phys. Stat. Sol. (a) **109** 11.

Grundy, P. J. and Jones, G. H. (1976) *Electron Microscopy in the Study of Materials*, Arnold, London.

Halliwell, M. A. G., Childs, J. B. and O'Hara, S. (1972) Proc. Symp. GaAs Rel. Comp. 98.

Halliwell, M. A. G. (1981) Inst. Phys. Conf. Ser. **60**(5) 271.

Halliwell, M. A. G., Juler, J. and Norman, A. G. (1983) Inst. Phys. Conf. Ser. **67**(7) 365.

Halliwell, M. A. G., Lyons, M. H. and Hill, M. J. (1984) J. Cryst. Growth. **68** 523.

Halliwell, M. A. G., Taylor M. R. and Ambridge, T. (1985) Br. Telecom. Technol. J. **3**(3) 30.

Halliwell, M. A. G., Lyons, M. H., Davey, S. T., Hockly, M., Tuppen, C. G. and Gibbings, C. J. (1989) Semicond. Sci. Technol. **4** 10.

Hart, M. (1971) Rept. Prog. Phys. **34** 435.

Hart, M. (1975) J. Appl. Cryst. **8** 436.

Hart, M. (1980) In *Characterisation of Crystal Growth Defects by X-Ray Methods* ed: Tanner and Bowen, London, Plenum Press, 216 and 483.

Hart, M. (1981) J. Cryst. Growth. **55** 409.

Hart, M., Parrish, W. and Masciocchi, N. (1987) Appl. Phys. Lett. **50**(14) 897.

Härtwig, J. (1978) Kristall Techn. **13**(9) 1117.

Hattanda, T. and Takeda, A. (1973) Japn. J. Appl. Phys. **12**(7) 1104.

Heavans, O. S. (1965) *Optical Properties of Thin Solid Films*, Dover, New York.

Hill, M. J. (1985) Ph.D. Thesis, University of Durham.

Hill, M. J., Tanner, B. K. and Halliwell, M. A. G. (1985) Mat. Res. Soc. Symp. Proc. **37** 53.

Hill, M. J., Tanner, B. K., Halliwell, M. A. G. and Lyons, M. H. (1985) J. Appl. Cryst. **18** 446.

Holah, G. D., Meeks, E. L. and Eisele, F. L. (1983) J. Vac. Sci. Technol. **B1**(2) 182.

Holý, V., Cummings, S. and Hart, M. (1988) J. Appl. Cryst. **21** 516.

Hornstra, J. and Bartels, W. J. (1978) J. Cryst. Growth. **44** 513.

Hornstrup, A., Christensen, F. E. and Schnopper, H. W. (1987) Proc SPIE Int. Soc. Opt. Eng. **733** 333.

Howarth, V. A., Petty, M. C., Davies, G. H. and Yarwood, J. (1988) Thin Solid Films **160** 483.

Huang, T. C., Toney, M. F., Brennan, S. and Rek, Z. (1987) Thin Solid Films **154** 439.

International Tables of X-Ray Crystallography (1974) Vol III and IV, Kynoch Press, Birmingham.

Isherwood, B. J., Brown, B. R. and Halliwell, M. A. G. (1981) J. Cryst. Growth **54** 449.

Isherwood, B. J., Brown, B. R. and Halliwell, M. A. G. (1982) J. Cryst. Growth **60** 33.

James, R. W. (1948) *The Optical Principles of the Diffraction of X-Rays*, Bell, London.

Jark, W., Comelli, G., Russel, T. P. and Stöhr, J. (1989) Thin Solid Films **170** 309.

Jeong, J., Schilesinger, T. E. and Milnes, A. G. (1988) J. Cryst. Growth **87** 265.

Jones, C. A., Petty, M. C., Roberts, G. G., Davies, G., Yarwood, J., Ratcliffe, N. M. and Barton, J. W. (1987) Thin Solid Films **155** 187.

Kamigaki, K., Sakashita, H., Kato, H., Nakayama, M., Sang, N. and Terauchi, H. (1987) J. Appl. Phys. **62**(3) 1124.

Kan, K. K., Roberts, G. G. and Petty, M. C. (1983) Thin Solid Films **99** 291.

Kao, K. C. and Hockham, G. A. (1961) Proc. IEEE **13** 1151.

Kato, H., Nakayama, M., Chika, S., Iguchi, N., Kubota, K. and Sano, N. (1986) Surf. Sci. **174** 579.

Kawamura, Y. and Okamoto, H. (1979) J. Appl. Phys. **50**(6) 4457.

Kervarec, J., Baudet, M., Caulet, J., Auvray, P., Emery, J. Y. and Regreny, A. (1984) J. Appl. Cryst. **17** 196.

Kiessig, H. Von (1931) Ann. Physik. **10** 715 and 769.

Kleiman, J., Park, R. M. and Mar, H. A. (1988) J. Appl. Phys. **64**(3) 1201.

Lambert, B., Caulet, J., Regreny, A., Baudet, M., Deveaud, B. and Chomette, A. (1987) Semicond. Sci. Technol. **2** 491.

Larson, B. C. and Barhorst, J. F. (1980) J. Appl. Phys. **51**(6) 3181.

Laue, M. Von (1952) Acta Cryst. **5** 619.

Li, R. and Xu, S. (1988) J. Appl. Cryst. **21** 902.

Lucas, C. A., Hatton, P. D., Bates, S., Ryan, T. W., Miles, S. J. and Tanner, B. K. (1988) J. Appl. Phys. **63**(6) 1936.

Lucas, C. A., McMorrow, D. F. and Bates, S. (1989) Proc. Symp. on *Heteroepitaxial Approaches in Semiconductors: Lattice Mismatch and its Consequences* **89-5** 271.

Lucas, C. A., Garstein, E. and Cowley, R. A. (1989) Acta Cryst. **A45** 416.

Lyons, M. H. and Halliwell, M. A. G. (1985) Inst. Phys. Conf. Ser. **76**(10) 445.

Lyons, M. H. and Halliwell, M. A. G. (1986) Les Editions de Physique 323.

Lyons, M. H., Halliwell, M. A. G., Tuppen, C. G. and Gibbings, C. J. (1987) Inst. Phys. Conf. Ser. **87**(9) 609.

Lyons, M. H. (1989) J. Cryst. Growth. **96** 339.

Lyons, M. H., Scott, E. G. and Halliwell, M. A. G. (1989) Inst. Phys. Conf. Ser.

Macrander, A. T. and Strege, K. (1986) J. Appl. Phys. **59**(2) 442.

Macrander, A. T. and Strege, K. (1986) Mat. Res. Soc. Symp. Proc. **56** 115.

Macrander, A. T. and Swaminathan, W. (1987) J. Electrochem. Soc. **134** 1247.

Macrander, A. T., Lau, S., Strege, K. and Chu, S. N. G. (1988) Appl. Phys. Lett. **52**(23) 1985.

Mellor, P. J. T. (1987) Br. Telecom. Technol. J. **5** 5.

Mikkelsen, J. C. and Boyce, J. B. (1982) Phys. Rev. Lett. **49**(19) 1412.

Miles, S. J., Green, G. S., Tanner, B. K., Halliwell, M. A. G. and Lyons, M. H. (1989) Mat. Res. Soc. Symp. Proc. **138** 539.

Miltat J. (1987) Phil. Mag. **55** 543.

Miltat J. (1988) Phil. Mag. **57** 79 and 685.

Miya, T., Terunuma, Y., Hosaku, T. and Miyashita, T. (1979) Electron. Lett. **15** 106.

Moss, R. H. and Spurdens, P. C. (1984) Electron. Lett. **26** 978.

Nagai, H. (1974) J. Appl. Phys. **45**(9) 3789.

Nahory, R. E., Pollock, M. A., Johnston, W. D. and Barns, R. L. (1978) Appl. Phys. Lett. **33**(7) 659.

Nakajima, K., Komiya, S., Akita, K., Yamaoka, T. and Ryuzun, O. (1980) J. Electrochem. Soc. **127** 1568.

Nakayama, K., Hashizume, H., Miyoshi, A., Kikuta, S. and Kohra, K. (1973) Z. Naturforsch. **A28** 632.

Nelmes, R. J., Howard, C. J., Ryan, T. W., David, W. I. F., Schultz, A. J. and Leung, P. C. W. (1984) J. Phys. C: Solid State Phys. **17** L861.

Nelson, A. W., Moss, R. H., Spurdens, P. C., Cole, S. and Wong, S. (1986) Br. Telecom. Technol. J. **4** 85.

Névot, L. and Croce, P. (1975) J. Appl. Cryst. **8** 304.

Névot, L. and Croce, P. (1980) Rev. Phys. Appl. **15** 761.

Oe, K., Shinoda, Y. and Sugiyama, K. (1978) Appl. Phys. Lett. **33**(11) 962.

Okamoto, K., Edahiro, T., Kawana, A. and Miya, T. (1979) Electron. Lett. **15**(22) 729.

Okamoto, K., Itoh, N., Ogawa, H., Kawabata, T. and Koike, S. (1988) Japn. J. Appl. Phys. **27**(5) L756.

Olsen, G. H. and Smith, R. T. (1975) Phys. Stat. Sol. (a) **31** 739.

Orders, P. J. and Usher, B. F. (1987) Appl. Phys. Lett. **50**(15) 980.

Orton, J. M., Fewster, P. F., Gowers, J. P., Dawson, P., Moore, K. J., Dobson, P. J., Curling, C. J., Foxon, C. T., Woodbridge, K., Duggan, G. and Ralph, H. I. (1987) Semicond. Sci. Technol. **2** 597.

Orton, J. M. (1989) Phys. World **2**(7) 39.

Paine, B. M. (1986) Mat. Res. Soc. Symp. Proc. **56** 121.

Paine, B. M., Vreeland, T. and Cheung, J. T. (1986) Mat. Res. Soc. Symp. Proc. **56** 313.

Paine, B. M. (1986) Mat. Res. Soc. Symp. Proc. **69** 39.

Paine, B. M., Hurvitz, N. N. and Speriosu, V. S. (1987) J. Appl. Phys. **61**(4) 1335.

Panish, M. B. (1987) Mat. Res. Soc. Symp. Proc. **90** 3.

Parratt, L. G. (1954) Phys. Rev. **95**(2) 359.

Petrashen', P. V. (1975) Sov. Phys. Solid State **16** 1417.

Petrashen', P. V. (1975) Sov. Phys. Solid State **17** 1882.

Pietsch, U. and Borchard, W. (1987) J. Appl. Cryst. **20** 8.

Pinsker, Z. G. (1978) *Dynamical Scattering of X-Rays in Crystals*, Springer-Verlag, Berlin.

Pomerantz, M., Dacol, F. H. and Segmüller, A. (1978) Phys. Rev. Lett. **40**(4) 246.

Pomerantz, M. and Segmüller, A. (1980) Thin Solid Films **68** 33.

Pomerantz, M. (1987) Thin Solid Films **152** 165.

Prilepskii, M. V. and Sukhodreva, J. M. (1985) Phys. Chem. Mech. Surf. **3**(1) 188.

Qadri, S. B., Jonker, B. T., Prinz, G. A. and Krebs, J. J. (1988) J. Vac. Sci. Technol. **A6**(3) 1526.

Renninger, M. Von (1955) Acta Cryst. **8** 597.

Rhan, H. and Pietsch, U. (1988) Phys. Stat. Sol. (a) **107** K93.

Riglet, P., Sauvage, M., Petroff, J. F. and Epelboin, Y. (1980) Phil. Mag. **A42**(3) 339.

Roberts, G. G. (1985) Adv. Phys. **34**(4) 475.

Roberts, K. J., Sherwood, J. N., Shripathi, T., Oldman, R. J., Holmes, P. A. and Nevin, A. (1989) J. Phys. D: Appl. Phys. *(in press)*.

Rosen, D. L., Brown, D., Gilfrich, J. and Burkhalter, P. (1988) J. Appl. Cryst. **21** 136.

Rustichelli, F. (1975) Phil. Mag. **31** 1.

Ryan, T. W., Gibaud, A. and Nelmes, R. J. (1985) J. Phys. C: Solid State Phys. **18** 5279.

Ryan, T. W. (1986) Ph.D. Thesis, University of Edinburgh.

Ryan, T. W. (1986) J. Phys. C: Solid State Phys. **19** 1097.

Ryan, T. W., Cowley, R. A. and Andrews, S. R. (1986) J. Phys. C: Solid State Phys. **19** L113.

Ryan, T. W., Hatton, P. D., Bates, S., Watt, M., Sotomayor-Torres, C., Claxton, P. A. and Roberts, J. S. (1987) Semicond. Sci. Technol. **2** 241.

Schaus, C. F., Shealy, J. R., Eastman, L. F., Cooman, B. C. and Carter, C. B. (1986) J. Appl. Phys. **59**(2) 678.

Schnopper, H. W. (1965) J. Appl. Phys. **36**(4) 1415.

Schumacher, U. (1987) Nucl. Instr. Meth. **A259** 538.

Schwarzschild, M. M. (1928) Phys. Rev. **32** 162.

Scott, E. G., Davey, S. T., Halliwell, M. A. G. and Davies, G. J. (1988) J. Vac. Sci. Technol. **B6**(2) 603.

Segmüller, A. and Blakeslee, A. E. (1973) J. Appl. Cryst. **6** 19.

Segmüller, A. (1973) Thin Solid Films **18** 287.

Segmüller, A., Krishna, P. and Esaki, L. (1977) J. Appl. Cryst. **10** 1.

Segmüller, A. (1986) Adv. X-Ray Anal. **29** 353.

Shaffner, T. J. (1986) Scan. Elect. Microsc. **1** 11.

Skolnick, M. S., Tapster, P. R., Bass, S. J., Pitt, A. D., Apsley, N. and Aldred, S. P. (1986) Semicond. Sci. Technol. **1** 29.

Slusky, S. E. G. and Macrander, A. T. (1987) J. Appl. Cryst. **20** 522.

Slusky, S. E. G. and Macrander, A. T. (1988) Appl. Phys. Lett. **53**(21) 2042.

Smirnov, L. A., Sotnikova, T. U., Anokhin, B. S. and Taibin, B. Z. (1979) Opt. Spectrosc. **46**(3) 329.

Smirnov, L. A. and Anokhin, B. S. (1980) Opt. Spectrosc. **48**(3) 315.

Smith, K. K. (1981) Thin Solid Films **84** 171.

Speriosu, V. S. (1981) J. Appl. Phys. **52**(10) 6094.

Speriosu, V. S. and Wilts, C. H. (1983) J. Appl. Phys. **54**(6) 3325.

Speriosu, V. S. and Vreeland, T. (1984) J. Appl. Phys. **56**(6) 1591.

Stallhofer, P. and Huber, D. (1983) Solid. State Technol., August, 233.

Stringfellow, G. B. (1985) Semiconductors and Semimetals **22** 209.

Sugawara, M., Kondo, M., Yamazaki, S. and Nakajima, K. (1988) J. Cryst. Growth **93** 318.

Sugimura, A., Daikoku, K., Imoto, N. and Miya, T. (1980) IEEE J. Quantum Elect. **QE-16**(2) 215.

Swalen J. D. (1987) Thin Solid Films **152** 151.

Takagi, S. (1962) Acta Cryst. **15** 1311.

Takagi, S. (1969) J. Phys. Soc. Japn. **26**(5) 1239.

Tanaka, A., Masa, Y., Seto, S. and Kawasaki, T. (1987) Mat. Res. Soc. Symp. Proc. **90** 111.

Tanner, B. K. (1976) *X-Ray Diffraction Topography*, Pergamon, Oxford.

Tanner, B. K. and Hill, M. J. (1986) Adv. X-Ray Anal. **29** 337.

Tanner, B. K. and Hill, M. J. (1986) J. Phys. D: Appl. Phys. **19** L229.

Tanner, B. K., Chu, X. and Bowen, D. K. (1986) Mat. Res. Soc. Symp. Proc. **69** 191.

Tanner, B. K. and Halliwell, M. A. G. (1988) Semicond. Sci. Technol. **3** 967.

Tanner, B. K., Miles, S. J., Peterson, G. G. and Sacks, R. N. (1988) Mat. Lett. **7**(5,6) 239.

Taupin, D. (1964) Bull. Soc. Franç. Minér. Crist. **87** 469.

Toney, M. F., Huang, T. C., Brennan, S. and Rek, Z. (1988) J. Mater. Res. **3**(2) 351.

Toney, M. F. and Brennan, S. (1988) IBM Surf. Sci. Phys. Res. Rep. RJ 6441

Toney, M. F. and Brennan, S. (1989) J. Appl. Phys. **65**(12) 4763.

Tuppen, C. G., Gibbings, C. J., Davey, S. T., Lyons, M. H., Hockly, M. and Halliwell, M. A. G. (1987) J. Electrochem. Soc. Proc. **88** 36.

Vandenberg, J. M., Hamm, R. A., Macrander, A. T., Panish, M. B. and Temkin, H. (1986) Appl. Phys. Lett. **48**(17) 1153.

Vandenberg, J. M., Hamm, R. A., Panish, M. B. and Temkin, H. (1987) J. Appl. Phys. **64**(2) 1278.

Vandenberg, J. M., Panish, M. B., Temkin, H. and Hamm, R. A. (1988) Appl. Phys. Lett. **53**(20) 1920.

Van der Merwe, J. H. and Jesser, W. A. (1989) Proc. Symp. on *Heteroepitaxial Approaches in Semiconductors: Lattice Mismatch and its Consequences* **89-5** 3.

Vidal, B. A. and Marfaing, J. C. (1989) J. Appl. Phys. **65**(9) 3453.

Villaflor, A. B., Inoue, Y. and Kimata, M. (1988) Japn. J. Appl. Phys. **27**(9) 1580.

Wang, X. R., Chi, X. Y., Zheng, H., Miao, Z. L., Wang, J., Zhang, Z. S. and Jin, Y. S. (1988) J. Vac. Sci. Technol. **B6**(1) 34.

Warren, B. E. (1969) *X-Ray Diffraction*, Addison Wesley.

Wie, C. R., Vreeland, T. and Tombrello, T. A. (1985) Mat. Res. Soc. Symp. Proc. **35** 305.

Wie, C. R. (1989) J. Appl. Phys. **65**(3) 1036.

Wie, C. R. (1989) J. Appl. Phys. **65**(6) 2267.

Wood, D. R. and Ambridge, T. (1986) Br. Telecom. Technol. J. 4(2) 69.

Xu, S. and Li, R. (1988) J. Appl. Cryst. **21** 213 and 218.

York, B. R. and Austin, A. B. (1986) Proc SPIE Int. Soc. Opt. Eng. **690** 135.

Yoshimura, J. (1984) J. Appl. Cryst. **17** 426.

Zachariasen, W. H. (1945) *Theory of X-Ray Diffraction in Crystals*, Wiley, New York.

Zaumseil, P., Winter, U., Cembali, F., Servidor, M. and Sourek, Z. (1987) Phys. Stat. Sol. (a) **100** 95.